© Copyright 2023

Jonathan Augustine Kephart

Dancing at the Interface: Surface-Mediated Active Site Dynamics within Molecular Nanoclusters

Jonathan Augustine Kephart

A dissertation

submitted in partial fulfillment of the

requirements for the degree of

Doctor of Philosophy

University of Washington

2023

Reading Committee:

Alexandra Velian, Chair

Brandi M. Cossairt

Dianne J. Xiao

Program Authorized to Offer Degree:

Chemistry

University of Washington

Abstract

Dancing at the Interface: Surface-Mediated Active Site Dynamics within Molecular Nanoclusters

Jonathan Augustine Kephart

Chair of the Supervisory Committee:
Alexandra Velian
Department of Chemistry

The key to accessing next-generation heterogeneous catalysts, which lie at the heart of many industrial manufacturing and energy conversion processes, is the identification and detailed surveillance of the catalytic active site. However, owing in part to the myriad interfacial dynamics that dictate active site identity, reactivity and selectivity, these catalytic systems are notoriously challenging to study. As Muetterties proposed years ago via the cluster-surface analogy, polynuclear molecular clusters provide an environment to study and harness these surface processes with atomic precision. Through this work, we introduce a new family of M/Co/Se nanoclusters that not only enables detailed investigations of active site identity and

mechanism, but also reveals the presence of multi-site allosteric effects that orchestrate surface dynamics.

Herein, homoleptic $Co_6Se_8L^{R,H}_6$ clusters decorated with bifunctional aminophosphine ligands ($L^{R,H}$ = $Ph_2PN(H)R$; R = 4-tolyl, isopropyl) serve as redox-active, inorganic platforms that are pre-templated to host three substrate-accessible "active sites" at their surface. After deprotonation of the pendent amino groups, this cluster-ligand is trimetallated with a wide array of first-row transition metal ions to afford a family of propeller-shaped M/Co/Se nanoclusters, $M_3Co_6Se_8L^{Tol}_6$ (**M$_3$**; L^{Tol} = $Ph_2PN^{(-)}Tol$; M = Cr^{2+}, Mn^{2+}, Fe^{2+}, Co^{2+}). Owing to their unique physicochemical properties, these nanoclusters provide an atomically defined, molecular environment to study the metal-support interactions that govern heterogeneous catalytic interfaces.

In Chapter 1, we find the surface Fe centers of the triiron nanocluster, **Fe$_3$**, engage in dynamic coordinative and electronic interactions with the Co_6Se_8 support, "dancing" with one another on this well-defined inorganic surface. These interactions are facilitated by hemilabile Fe···Se bonding, the strength of which exhibits a clear redox-state dependence. The electronic structure of **Fe$_3$** was investigated in detail using a suite of synthetic and electrochemical methods, extensive single crystal X-ray diffraction analysis, electronic absorption and infrared spectroscopy, and ^{57}Fe Mössbauer spectroscopy. We find that the Fe edge sites communicate electronically with the Co_6Se_8 core and that these interactions are responsive to ligand binding. In turn, the Co_6Se_8 core is demonstrated as a redox non-innocent ligand platform. Ultimately, **Fe$_3$** serves as an excellent catalyst for the conversion of tosyl azide (TsN_3) and *tert*-butyl isocyanide (CN^tBu) to the asymmetric carbodiimide, $TsN{=}C{=}N^tBu$, via a multi-electron redox transformation.

In Chapter 2, detailed synthetic investigations reveal how supporting aminophosphine ligands impact product distribution in the synthesis of the related cluster-ligand, $Co_6Se_8L^{iPr,H}_6$, granting access to a series of smaller Co/Se cluster intermediates. Introduction of more sterically demanding isopropyl substituents at the edge sites enables isolation of pseudo-D_3 symmetric trimetallated clusters, $M_3Co_6Se_8L^{iPr}_6$ (**M$_3$**^{iPr}; L^{iPr} = $Ph_2PN^{(-)}iPr$; M = Fe^{2+}, Zn^{2+}), wherein no ancillary ligands are bound at the edge metals.

In Chapter 3, the binding of surface ligands is found to have a collective impact on the surface sites of **Fe$_3$**, as multi-active site domino interactions promote allosteric ligand substitution at discrete Fe centers on the cluster surface. In an unprecedented molecular example of the inter-adsorbate effect, we resolve these inter-adsorbate dynamics at the cluster surface crystallographically. By combining a battery of crystallographic, spectroscopic, and computational techniques, we demonstrate how delocalized Fe/Se/Co bonding interactions promote ligand exchange at Fe sites positioned on the same α/β cluster face. In Chapter 4, these allosteric effects are harnessed to encode structural anisotropy within a family of redox-active two-dimensional nanosheets built via self-assembly of **Co$_3$**.

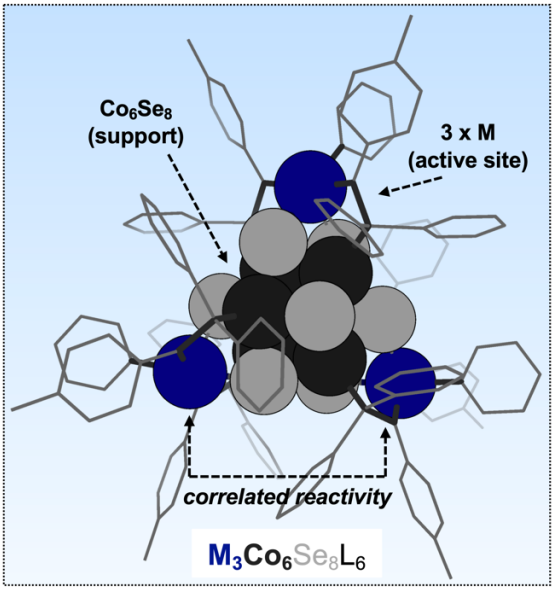
In Chapter 5, we return to the catalytic synthesis of asymmetric carbodiimide to conduct a thorough investigation of active site identity and reaction mechanism. Following our initial discovery of this reactivity using **Fe$_3$**, a trichromium derivative, **Cr$_3$**$(py)_3$, is developed to conduct a detailed analysis of catalytic azide activation and nitrene transfer through a series of stoichiometric and catalytic reactivity studies. Through the isolation of key mono-, bis- and tris(imido) intermediates, we pin-point the identity of the catalytic active site within **Cr$_3$**$(py)_3$ and discover the presence of multi-active site interactions that regulate nitrene transfer kinetics. In Chapter 6, a comparative crystallographic study of **Cr$_3$** clusters unearths counter-intuitive

bonding trends in the structural site-differentiation of the Cr edge sites. Building upon this crystallographic analysis, we apply a combination of computational, electrochemical, spectroscopic, and synthetic techniques to explore the mechanism of active site speciation within the trichromium nanocluster. Through this study, we establish a molecular orbital basis for electronic active site differentiation at within these M/Co/Se nanocluster.

IT TAKES THREE TO TANGO: AN OVERVIEW

This text represents the culmination of several years of hard work and determination in lab. Initially, this work was focused on the synthesis and characterization of a new class of "nanopropeller" clusters, which entailed detailed analysis using a range of techniques including cyclic voltammetry, ^{57}Fe Mössbauer spectroscopy, solid-state magnetometry, and many others. After recognizing more nuanced traits inherent to the M/Co/Se platform, many of which stem from their intrinsic preference to form low-symmetry (α,α,β) isomers, we came to appreciate the unique choreography of their molecular "dance". Pushing and pulling on one another through an inorganic Co_6Se_8 support, the three appended surface metals are intertwined as they react with organic substrates. By studying these correlated dynamics, we gain insights into complex solid-state processes such as surface restructuring, inter-adsorbate effects, and active site speciation — for these M/Co/Se nanoclusters, it truly takes three to tango.

In Chapter 1, we introduce the M/Co/Se cluster platform, outlining the coordinative and electronic interactions between appended surface metals (Fe) and the Co_6Se_8 support. Chapter 2 outlines our initial efforts in lab, as detailed synthetic investigations grant access to a family of Co/Se cluster intermediates *en route* to the Co_6Se_8 cluster-ligand. Here, we also explore the influence of the supporting amido ligand in a derivatized set of trimetallated clusters. In Chapter 3, thoughtful inspection of what was initially perceived as a lackluster result, namely the disordered crystal structure of [$\mathbf{Fe_3}$(CN^{t}Bu)$_2$(THF)][PF_6], gives rise to a rich study of how ligand binding at the cluster surface collectively impacts all Fe active sites. In Chapter 4, we demonstrate how we can harness allosteric (α,α,β) site-differentiation to encode structural anisotropy within a family of two-dimensional hierarchical nanosheets. In Chapter 5, we embark on a thorough investigation of active site identity and mechanism by isolating key reactive intermediates formed in the catalytic conversion of tosyl azide and *tert*-butyl isocyanide into the asymmetry carbodiimide, TsN=C=N^{t}Bu. In Chapter 6, we outline a molecular orbital basis for electronic active site differentiation on the surface of M/Co/Se nanoclusters.



There is a road, no simple highway,
between the dawn and the dark of night.
And if you go, no one may follow.
That path is for your steps alone.

Ripple in still water
when there is no pebble tossed
nor wind to blow.

You who choose to lead must follow,
but if you fall you fall alone.
If you should stand then who's to guide you?
If I knew the way, I would take you home.

—Ripple—
Written by Robert Hunter, Performed by the Grateful Dead

TABLE OF CONTENTS

List of Figures ix

List of Schemes xxxviii

List of Tables xxxix

CHAPTER 1. Atomically Defined Fe/Co/Se Nanoropellers: Functional Models for the Electronic Metal-Support Interaction Effect and High Catalytic Activity for Carbodiimide Formation 1

1.1 Harnessing Electronic Metal-Support Interactions 1

1.2 Atomically Defined Fe/Co/Se Nanopropeller 2

1.2.1 Abstract 2

1.2.2 Synthesis and Characterization of a Fe/Co/Se Nanopropeller Cluster 3

1.2.3 Probing the Electronic Structure of Fe/Co/Se Nanopropellers 6

1.2.4 Edge-support Redox Cooperativity Facilitates Group Transfer Catalysis 11

1.2.5 Influence of Ligand Binding on Fe/Co/Se Electronic Structure 13

1.2.6 Correlating the Solid-state Structure of **Fe$_3$** with its Unexpected ^{1}H NMR Profile .. 16

1.3 Experimental Details 16

1.3.1 General Considerations 16

1.3.2 Synthesis and Isolation of $Co_6Se_8L^{Tol,H}_6$ 18

1.3.3 Synthesis and Isolation of $[Co_6Se_8L^{Tol,H}_6][OTf]$ 19

1.3.4 Synthesis and Isolation of $Li_6(py)_6Co_6Se_8L^{Tol}_6$, **Li$_6$**(py)$_6$ 20

1.3.5 Synthesis and Characterization of $Fe_3Co_6Se_8L^{Tol}_6$, **Fe$_3$** 20

1.3.6 Synthesis and Characterization of $Fe_3(CN^tBu)_3Co_6Se_8L^{Tol}_6$, **Fe$_3$**(CN^{t}Bu)$_3$ 21

1.3.7 Synthesis and Characterization of $[Fe_3(CN^tBu)_2Co_6Se_8L^{Tol}_6][PF_6]$, $[\mathbf{Fe_3}(CN^tBu)_2][PF_6]$ 22

1.3.8 Synthesis and Characterization of $[Fe_3(phen)_3Co_6Se_8L^{Tol}_6][PF_6]$, $[\mathbf{Fe_3}(phen)_3][PF_6]$ 23

1.3.9 Synthesis of $[Na(18\text{-crown-}6)(MeCN)_2][Fe_3Co_6Se_8L^{Tol}_6]$, $[Na(18\text{-C-}6)][\mathbf{Fe_3}]$ 24

1.3.10 Synthesis and Characterization of $[^nBu_4N][Fe_3Co_6Se_8L^{Tol}_6]$, $[^nBu_4N][\mathbf{Fe_3}]$ 25

1.3.11 Catalytic Synthesis of Carbodiimide $TsNCN^tBu$ 26

1.3.12 UV-vis-nIR Absorption Spectra 28

1.3.13 Determination of CN^tBu Binding Constants 30

1.3.14 ^1H NMR Response to Solvation 35

1.3.15 Evans Method Determination of Solution-phase Magnetic Moment 36

1.3.16 Electrochemical Analysis 37

1.3.17 ^{57}Fe Mössbauer Spectroscopy 44

1.3.18 X-ray Structure Determination 46

1.4 References 56

CHAPTER 2. Inorganic Clusters as Metalloligands: Ligand Effects on the Synthesis and Properties of Ternary Nanopropeller Clusters 62

2.1 Abstract 62

2.2 Introduction 63

2.3 Ligand effects in the Synthesis of M/Co/Se Clusters 64

2.3.1 Aminophosphine ^{i}Pr2PN(H)^{i}Pr halts cluster formation to Co dimer $\mathbf{Co_2}$ 66

2.3.2 Aminophosphine $L^{iPr,H}$ alters optimal reagent stoichiometry 67

2.3.3 Square-capped [4,2] cluster $Co_4Se_2(CO)_6(L^{iPr,H})_4$ and its conversion to $Co_6Se_8L^{iPr,H}_6$ 68

2.3.4 Isolation of a trapped [Co3Se] intermediate cluster $Co_3Se(\mu_2\text{-}PPh_2)(CO)_4(L^{iPr,H})_3$. 70

2.3.5 Homoleptic cluster $Co_6Se_8L^{iPr,H}_6$ and its chemical mono-oxidation..... 74

2.3.6 Ternary nanopropeller clusters $M_3Co_6Se_8L^{iPr}_6$ (M = Fe, Zn) 77

2.4 Electronic Influence of Surface Ligands..... 80

2.5 Experimental Details..... 84

2.5.1 General Considerations..... 84

2.5.2 Synthesis and Isolation of $Co_6Se_8(Ph_2P(H)N^iPr)_6$, $Co_6Se_8L^{iPr,H}_6$ 86

2.5.3 Synthesis and Isolation of $[Co_6Se_8L^{iPr,H}_6][PF_6]$; $[Co_6Se_8L^{iPr,H}_6]^+$ 87

2.5.4 Synthesis and Isolation of $Co_4Se_2(CO)_6L^{iPr,H}_6$, **$Co_4Se_2$** 87

2.5.5 Thermal Conversion of **Co_4Se_2** to $Co_6Se_8L^{iPr,H}_6$..... 88

2.5.6 Synthesis of $Co_3Se(\mu_2\text{-}PPh_2)(CO)_4L^{iPr,H}_3$, **$Co_3Se$** 88

2.5.7 Synthesis and Isolation of $[Co(CO)_3(^iPr_2PN(H)^iPr)]_2$, **$Co_2$** 90

2.5.8 Synthesis and Isolation of $Fe_3Co_6Se_8L^{iPr}_6$, **Fe_3^{iPr}** 91

2.5.9 Synthesis and Isolation of $Zn_3Co_6Se_8L^{iPr}_6$, **Zn_3^{iPr}** 93

2.5.10 Electronic Absorption Spectra 95

2.5.11 Electrochemical Analysis..... 96

2.5.12 Effect of Reagent Stoichiometry in the Synthesis of $Co_6Se_8L^{iPr,H}_6$ 96

2.5.13 X-ray Structure Determination 100

2.5.14 X-ray Tables..... 108

2.6 References..... 111

CHAPTER 3. Caught in the act of substitution: inter-adsorbate effects on an atomically precise Fe/Co/Se nanocluster with multiple active sites 117

3.1 Abstract 117

3.2 Capturing Inter-adsorbate Dynamics 117

3.3 Inter-Adsorbate Dynamics within Fe/Co/Se Clusters 119

3.3.1 Ligand Binding Induces Stereoisomerism in **Fe$_3$** Clusters 119

3.3.2 Structural Trends in the Site-differentiation of [**Fe$_3$**]$^+$ 120

3.3.3 Solution-phase Ligand Exchange with [**Fe$_3$**(CN^{t}Bu)$_2$]$^+$ 122

3.3.4 Single-crystal Resolution of the Inter-adsorbate Effect 123

3.4 ^{57}Fe Mössbauer Spectroscopy Analysis 125

3.5 Multi-site Solvolysis Mechanism 126

3.5.1 Computational Modelling of Multi-site Ligand Substitution. 128

3.5.2 Electronic Origins of the Inter-adsorbate Effect 130

3.6 Chemical Disorder in Solid-State Structure of **Fe$_3$**(py)$_3$ 134

3.7 Molecular Formalism for the Inter-adsorbate Dynamics 135

3.8 Experimental Details 135

3.8.1 General Considerations 135

3.8.2 Synthesis and Isolation of [Fe$_3$(MeCN)Co$_6$Se$_8$L$^{Tol}_6$][OTf], **Fe$_3$**(MeCN)(OTf) 136

3.8.3 Synthesis and Isolation of [Fe$_3$(THF)$_2$Co$_6$Se$_8$L$^{Tol}_6$][PF$_6$], [**Fe$_3$**(THF)$_2$][PF$_6$] 137

3.8.4 Adapted Synthesis of [Fe$_3$(CN^{t}Bu)$_2$Co$_6$Se$_8$L$^{Tol}_6$][PF$_6$], [**Fe$_3$**(CN^{t}Bu)$_2$][PF$_6$] 138

3.8.5 Solution-phase Fourier Transform Infrared Spectroscopy 139

3.8.6 Magnetic Characterization of [**Fe$_3$**(CN^{t}Bu)$_2$][PF$_6$] 141

3.8.7 X-ray Structure Determination 143

3.8.8 DFT Calculations 155

3.9 References 161

CHAPTER 4. Hierarchical Nanosheets Built from Superatomic Clusters: Properties, Exfoliation and Single-Crystal-to-Single-Crystal Intercalation 167

4.1 Abstract 167

4.2 Introduction 168

4.3 Synthesis and Characterization of Co/Se/Co Nanoblock 170

4.4 Self-Assembly of Anisotropic Nanosheets 174

4.5 Solid-state Magnetic Analysis 177

4.6 Redox-Active Hybrid Nanosheets 179

4.6.1 Electrochemical Characterization of Co/Se/Co Nanosheets 179

4.6.2 Single-crystal-to-single-crystal Redox Intercalation 181

4.7 Mechanical Exfoliation of **Co$_3$**(bpy$_\sigma$) into Ultrathin Nanosheets 183

4.8 Conclusions 184

4.9 Experimental Details 184

4.9.1 General Considerations 184

4.9.2 Synthesis and Isolation of $Co_3(py)_3Co_6Se_8L^{Tol}_6$, **Co$_3$**(py)$_3$ 186

4.9.3 Synthesis and Isolation of $Co_3(bpy)_{1.5}Co_6Se_8L^{Tol}_6$, **Co$_3$**(bpy) 187

4.9.4 Synthesis and Isolation of $Co_3(bpy_\pi)_{1.5}Co_6Se_8L^{Tol}_6$, **Co$_3$**(bpy$_\pi$) 187

4.9.5 Synthesis and Isolation of $Co_3(bpy_\sigma)_{1.5}Co_6Se_8L^{Tol}_6$, **Co$_3$**(bpy$_\sigma$) 188

4.9.6 Synthesis and Isolation of $[Co_3(bpy_\sigma)_{1.5}Co_6Se_8L^{Tol}_6][TCNE]_2$, [**Co$_3$**(bpy$_\sigma$)][TCNE]$_2$ 188

4.9.7 Magnetic Measurements 189
4.9.8 Electrochemical Measurements 193
4.9.9 X-ray Structure Determination 197
4.10 References 204
CHAPTER 5. Multi-active Site Dynamics on a Molecular Cr/Co/Se Cluster Catalyst 211
5.1 Abstract 211
5.2 Introduction 212
5.3 Synthesis of a Catalytically Active Cr/Co/Se Nanopropeller 214
5.4 Isolation of a Catalytically Competent Tris(Imido) Nanocluster 216
5.5 Isolation of Nitrene Transfer Intermediates 219
5.5.1 Isolation of the Catalyst Resting State, $\mathbf{Cr_3}(NTs)_3(CN^tBu)_3$ 223
5.5.2 Isolation of a Site-differentiated Cr(NTs)/Cr(CN^tBu) Intermediate 225
5.5.3 Conclusions 227
5.5.4 CN^tBu Binding Constant Determination 228
5.6 Experimental Details 234
5.6.1 General Information 234
5.6.2 Synthesis and Isolation of $Cr_3(py)_3Co_6Se_8L^{Tol}_6$, $\mathbf{Cr_3}(py)_3$ 235
5.6.3 Synthesis and Isolation of $Cr_3(NTs)_3Co_6Se_8L^{Tol}_6$, $\mathbf{Cr_3}(NTs)_3$ 236
5.6.4 Synthesis and Isolation of $Cr_3(NTs)_3(CN^tBu)_3Co_6Se_8L^{Tol}_6$, $\mathbf{Cr_3}(NTs)_3(CN^tBu)_3$ .. 240
5.6.5 Synthesis and Isolation of $Cr_3(NTs)(CN^tBu)_2Co_6Se_8L^{Tol}_6$, $\mathbf{Cr_3}(NTs)(CN^tBu)_2$ 241
5.6.6 Synthesis and Isolation of $Cr_3(CN^tBu)_3Co_6Se_8L^{Tol}_6$, $\mathbf{Cr_3}(CN^tBu)_3$ 243
5.6.7 Electronic Absorption Spectra 245
5.6.8 Nitrene Transfer Catalysis 246

5.6.9 In situ Reaction Monitoring with 10 mol% Catalyst Loading 247
5.6.10 Stoichiometric Azide Activation and Nitrene Transfer Experiments 254
5.6.11 X-ray Structure Determination 256
5.7 References 264
CHAPTER 6. Allosteric Active Site Speciation in Molecular Cr/Co/Se Clusters 270
6.1 Abstract 270
6.2 Introduction 271
6.3 Site-differentiated Azide Activation and Nitrene Transfer 273
6.4 Crystallization of a Diastereomeric Bis(imido) Nanocluster 279
6.5 Structural Trends in Site-differentiated Cr/Co/Se Clusters 281
6.5.1 Activation of Benzyl Azide Affords Benzaldimine-Bound Nanocluster 282
6.6 Computational Analysis Provides Molecular Orbital Basis for Active Site Differentiation 284
6.6.1 Density of States Analysis 284
6.6.2 Inspection of Frontier Molecular Orbitals 289
6.6.3 Molecular Orbital Basis for Active Site Differentiation 290
6.7 Edge-support Bonding Induces Ordered Structural Distortions within the Co/Se Support 293
6.8 Physicochemical Properties of Cr/Co/Se Nanoclusters 295
6.9 Magnetic Characterization 298
6.10 Chemical Redox Reactivity of **Cr$_3$**(NTs)$_3$ 299
6.11 Conclusions 302
6.12 Experimental Details 303

6.12.1 General Information 303

6.12.2 Synthesis and Isolation of $Cr_3(NTs)(py)_2Co_6Se_8L^{Tol}_6$, $\mathbf{Cr_3}(NTs)(py)_2$ 304

6.12.3 Synthesis and Isolation of $Cr_3(NTs)_2(py)Co_6Se_8L^{Tol}_6$, $\mathbf{Cr_3}(NTs)_2(py)$ 306

6.12.4 Synthesis of $Cr_3(NTs)_2(CN^tBu)Co_6Se_8L^{Tol}_6$, $\mathbf{Cr_3}(NTs)_2(CN^tBu)$ 307

6.12.5 Synthesis and Isolation of $[Cr_3(NTs)_3Co_6Se_8L^{Tol}_6][PF_6]$, $[\mathbf{Cr_3}(NTs)_3][PF_6]$ 309

6.12.6 Synthesis of [K(18-crown-6)]$[Cr_3(NTs)_3Co_6Se_8L^{Tol}_6]$, [K(18-C-6][$\mathbf{Cr_3}(NTs)_3$] 310

6.12.7 Stoichiometric Azide Activation and Nitrene Transfer Experiments 311

6.12.8 Electrochemical Analysis 315

6.12.9 Magnetic Measurements 320

6.12.10 DFT Calculations 325

6.12.11 X-ray Structure Determination 332

6.13 References 340

Appendix A 347

LIST OF FIGURES

Figure 1.1. The $[Co_6Se_8L^{Tol}{}_6]^{6-}$ cluster-ligand acts as a non-innocent inorganic support to host three low-coordinate Fe active sites. 3

Figure 1.2. Single-crystal X-ray structure of [Na(18-C-6)][**Fe$_3$**] illustrating the deconstruction of the pseudo-D_3 symmetric $Fe_3Co_6Se_8$ inorganic core. Thermal ellipsoids shown at a 50% probability level. Selected interatomic distances (Å): Fe4-Se9 2.47(4), Fe4-Se10 2.46(1), Fe5-Se11 2.46(2), Fe5-Se12 2.46(3), Fe6-Se13 2.44(4), Fe6-Se14 2.47(3); Fe4…Co7 2.820(9), Fe4…Co8 2.80(2); Co7…Co8 2.78(3), Co7…Co12 2.94(5), Co7…Co11 3.00(3); Co7…Se9 2.39(3), Co7…Se10 2.40(3), Co7…Se14 2.44(3); Se15…Se16 5.34(7), Se9…Se12 5.79(5), Se10…Se3 5.87(9), Se11…Se14 5.92(8). 5

Figure 1.3. Single crystal X-ray diffraction structures of nanopropellers highlighting the coordinative versatility in the κ^4, κ^3 and κ^2 binding modes at the Fe sites, and the corresponding $\tau4$ values (zoom-in left). Select interatomic distances (Å): (A) [Na(18-crown-6)$(MeCN)_2$][**Fe$_3$**], Fe2-Se3 2.48(2), Fe2-Se4 2.46(4); (B) **Fe$_3$**$(CN^tBu)_3$, Fe2-Se3 2.487(3), Fe2-Se4 3.102(5) and (C) [**Fe$_3$**$(phen)_3$][PF_6], Fe3...Se5 2.99(1), Fe3...Se6 2.990(6). H atoms, solvents, counterions, and any disorder are omitted for clarity. Thermal ellipsoids are plotted at 50%. 7

Figure 1.4. ATR-FTIR spectra of **Fe$_3$**, **Fe$_3$**$(CN^tBu)_3$, [**Fe$_3$**$(CN^tBu)_2$][PF_6], and CN^tBu, highlighting the isocyanide CN stretching region. 8

Figure 1.5. Investigations in the electronic structure of the nanopropellers. (A) Zero-field ^{57}Fe Mössbauer spectra (90K) of [**Fe$_3$**$(CN^tBu)_2$][PF_6], **Fe$_3$**, and [^{n}Bu$_4$N][**Fe$_3$**]. (B) UV-vis-nIR absorption spectra (THF) of $[Co_6Se_8L^{Tol,H}{}_6]$[OTf], **Fe$_3$**, [**Fe$_3$**$(CN^tBu)_2$][PF_6] and [**Fe$_3$**$(phen)_3$][PF_6]. (C) Cyclic voltammograms of **Fe$_3$**, [**Fe$_3$**$(CN^tBu)_2$][PF_6], and $Co_6Se_8L^{Tol,H}{}_6$ recorded in DCM (dashed lines) or THF (solid lines) solutions with [^{n}Bu$_4$N][PF_6] (0.1 M) at 200 mV/s. 10

Figure 1.6. Monitoring the conversion of TsN_3 and CN^tBu to $TsNCN^tBu$ at 25 °C. *Control reactions prepared in situ. The data for **Fe$_3$** was obtained in pyridine-d_5, while all other data was obtained in benzene-d_6. Percent conversion was determined based on ^{1}H NMR

integrations of the reagents and products versus an internal mesitylene standard. Both **Fe$_3$** and $Co_6Se_8L^{Tol,H}_6$ were used with 2.5 mol% loading, while the other control experiments were performed with 5.0 mol% loading. 12

Figure 1.7. a) Cyclic voltammograms of **Fe$_3$**, **Fe$_3$**(MeCN)(OTf), [**Fe$_3$**(CN^{t}Bu)$_2$][PF_6], and [**Fe$_3$**(phen)$_3$][PF_6] (0.1 M [^{n}Bu$_4$N][PF_6] in DCM or THF). b) UV-vis-*n*IR spectra recorded in DCM (λ_{max}, ε) for **Fe$_3$** (435 nm, 60400 M^{-1} cm^{-1}), **Fe$_3$**(MeCN)(OTf) (431 nm, 38500 M^{-1} cm^{-1}), [**Fe$_3$**(CN^{t}Bu)$_2$][PF_6] (430 nm, 38400 M^{-1} cm^{-1}), and [**Fe$_3$**(phen)$_3$][PF_6] (380 nm, 42800 M^{-1} cm^{-1}; 448 nm, 36500 M^{-1} cm^{-1}; 509 nm, 27400 M^{-1} cm^{-1}). 13

Figure 1.8. a) ^{1}H NMR (MeCN-d_3, 25 °C, 300 MHz) spectrum of [^{n}Bu$_4$N][**Fe$_3$**], with proton resonances associated with either the [**Fe$_3$**]$^-$ cluster or [^{n}Bu$_4$N]$^+$ counterion denoted red or gray, respectively. b) The solid-state structure of [**Fe$_3$**]$^-$ illustrates how phosphinoamide phenyl substituents adopt either an axial (red) or equatorial (blue) orientation after being locked into D_3 symmetry upon trimetallation. Hydrogen atoms and the [Na(18-C-6)(MeCN)$_2$]$^+$ counterion are omitted for clarity and all other atoms have been shown in gray. The black arrow represents the C_3 rotational z-axis of the compound. 15

Figure 1.9. ^{1}H NMR (C_6D_6, 25 °C, 300 MHz) spectrum of **Fe$_3$**. 21

Figure 1.10. ^{1}H NMR (CD_2Cl_2, 25 °C, 300 MHz) spectrum of [**Fe$_3$**(phen)$_3$][PF_6]. 24

Figure 1.11. ^{1}H NMR (pyridine-d_5, 25 °C, 300 MHz) spectra of the paramagnetic region (A) and emphasizing the diamagnetic region (B) of the catalytic reaction mixture before and 3 h after addition of TsN_3. A catalyst loading of 10 mol% **Fe$_3$** was employed to enhance the visibility of the paramagnetic species. The reaction was run in the presence of TsN_3 (0.11 M) and CN^{t}Bu (0.19 M). 27

Figure 1.12. UV-vis-*n*IR absorption spectra of $Co_6Se_8L^{Tol,H}_6$ and [$Co_6Se_8L^{Tol,H}_6$][OTf](blue lines); **Fe$_3$**, [Na(18-C-6)][**Fe$_3$**], and [**Fe$_3$**(CN^{t}Bu)$_2$][PF_6] (pink lines); and [**Fe$_3$**(phen)$_3$][PF_6] (burgundy line) acquired in THF with extinction coefficient (ε) plotted *vs* wavenumber (A) or wavelength (B). 28

Figure 1.13. UV-vis-*n*IR absorption spectra of (A) $Co_6Se_8L^{Tol,H}_6$ and **Fe$_3$**; (B) **Fe$_3$**, [**Fe$_3$**(CN^{t}Bu)$_2$][PF_6], and [Na(18-C-6)][**Fe$_3$**$Co_6Se_8L_6$]; and (C) [$Co_6Se_8L^{Tol,H}_6$][OTf], [**Fe$_3$**(CN^{t}Bu)$_2$][PF_6], and [**Fe$_3$**(phen)$_3$][PF_6]. 29

Figure 1.14. Normalized electronic absorption spectra of **Fe$_3$**, **Fe$_3$**(MeCN)(OTf), [**Fe$_3$**(CN^{t}Bu)$_2$][PF$_6$], and [**Fe$_3$**(phen)$_3$][PF$_6$] recorded in DCM at 25 °C. Here, the triiron cluster **Fe$_3$** is denoted as **1**. 30

Figure 1.15. ^{1}H NMR (C_6D_6, 25 °C, 300 MHz) spectra of $Fe_3Co_6Se_8L_6$ (**Fe$_3$**) with varying equivalents of CN^{t}Bu, increasing from the bottom to the top spectrum as indicated. The binding constants were calculated based on the change in the farthest downfield chemical shift at each inflection point (1.5 and 5 equiv) and the starting and ending chemical shift values (0 and 288 equiv). 32

Figure 1.16. ^{1}H NMR (CD_2Cl_2, 25 °C, 300 MHz) spectra of [Fe_3(CN^{t}Bu)$_2Co_6Se_8L_6$][PF$_6$] ([**Fe$_3$**(CN^{t}Bu)$_2$][PF$_6$]) with varying equivalents of CN^{t}Bu, increasing from the bottom to the top spectrum as indicated. The binding constant was calculated based on the change in chemical shift of the far downfield signal (~57 ppm, 0 equiv CN^{t}Bu). Note that after adding 288 equiv of CN^{t}Bu and allowing the sample to sit for ~24 h at 25 °C, the analyte appears to have been reduced to yield fully coordinated **Fe$_3$**. 33

Figure 1.17. ^{1}H NMR (C_6D_6, 25 °C, 300 MHz) spectra of [^{n}Bu$_4$N][**Fe$_3$**] with varying equivalents of CN^{t}Bu that are increasing from the bottom to the top spectrum as indicated. A binding constant was not calculated as it appears that CN^{t}Bu does not coordinate to the mono-reduced species, suggesting that the Fe-Se interaction is more robust for the mono-anionic species. Note that as the excess of CN^{t}Bu increases the mono-reduced undergoes oxidation to produce neutral CN^{t}Bu-bound **Fe$_3$**. 34

Figure 1.18. ^{1}H NMR (CD_2Cl_2, 25 °C, 500 MHz) spectra of crude **Fe$_3$**, **Fe$_3$**(MeCN)(OTf), [**Fe$_3$**CN^{t}Bu)$_2$][PF$_6$], and [**Fe$_3$**(phen)$_3$][PF$_6$], highlighting variation of the tolyl-C*H*$_3$ and ancillary ligand-based resonances. Here, **1** is used as an abbreviation for **Fe$_3$.** 35

Figure 1.19. ^{1}H NMR (CD_3CN, 25 °C, 500 MHz) spectra of crude **Fe$_3$**(MeCN)(OTf), [**Fe$_3$**(CN^{t}Bu)$_2$][PF$_6$], [**Fe$_3$**(phen)$_3$[PF$_6$], and [**Fe$_3$**(bipy)$_3$][PF$_6$] highlighting variation of the tolyl-C*H*$_3$ and ligand-based resonances. Note that the similarities between the spectra obtained for **Fe$_3$**(MeCN)(OTf) and [**Fe$_3$**(CN^{t}Bu)$_2$][PF$_6$] are consistent with displacement of the surface ligands MeCN and by the coordinating CD_3CN solvent. Here, **1** is used as an abbreviation for **Fe$_3$.** 36

Figure 1.20. The solution-phase magnetic moments of **Fe$_3$** and [**Fe$_3$**(CN^{t}Bu)$_2$][PF$_6$] as determined using the Evans Method in dichloromethane-d_2 between 188 and 297 K. 37

Figure 1.21. Cyclic voltammograms of $Co_6Se_8L^{Tol,H}_6$ recorded between 50 and 500 mV s^{-1} in 0.1 M [^{n}Bu$_4$N][PF$_6$] DCM and referenced to ferrocene (left) and a plot of current density (j_p) versus the square root of scan rate ($v^{1/2}$) with linear fits used to model the data with the Randles–Sevcik equation (right). 38

Figure 1.22. Cyclic voltammograms of **Fe$_3$** recorded between 50 and 500 mV s^{-1} in 0.1 M [^{n}Bu$_4$N][PF$_6$] DCM and referenced to ferrocene (left) and a plot of current density (j_p) versus the square root of scan rate ($v^{1/2}$) with linear fits used to model the data with the Randles–Sevcik equation (right). 38

Figure 1.23. Cyclic voltammograms of [**Fe$_3$**(CN^{t}Bu)$_2$][PF$_6$] recorded between 50 and 500 mV s^{-1} in 0.1 M [^{n}Bu$_4$N][PF$_6$] DCM and referenced to ferrocene (left) and a plot of current density (j_p) versus the square root of scan rate ($v^{1/2}$) with linear fits used to model the data with the Randles–Sevcik equation (right). 39

Figure 1.24. Cyclic voltammograms of [**Fe$_3$**(phen)$_3$][PF$_6$] recorded at scan rates (left) between 50 and 500 mV s^{-1}, (right) of 200 mV/s with a wider potential window, in 0.1 M [^{n}Bu$_4$N][PF$_6$] DCM and referenced to ferrocene. 39

Figure 1.25. Plot of current density (j_p) versus the square root of scan rate ($v^{1/2}$) derived from cyclic voltammograms of [**Fe$_3$**(phen)$_3$][PF$_6$] in in 0.1 M [^{n}Bu$_4$N][PF$_6$] DCM. Linear fits used to model the data with the Randles–Sevcik equation. 40

Figure 1.26. Cyclic voltammograms of **Fe$_3$**(MeCN)(OTf) recorded between 50 and 500 mV s^{-1} in 0.1 M [^{n}Bu$_4$N][PF$_6$] DCM and referenced to ferrocene (left) and plot of current density (j_p) versus the square root of scan rate ($v^{1/2}$) with linear fits used to model the data with the Randles-Sevcik equation (right). 40

Figure 1.27. Cyclic voltammograms of $Co_6Se_8L^{Tol,H}_6$ (1.1 mM) recorded before (black) and after (blue/green) addition of CN^{t}Bu (8 equiv, 8.8 mM) in 0.1 M [^{n}Bu$_4$N][PF$_6$] DCM. Importantly, the 2+/3+ redox couple does not shift to lower potentials in the presence of excess CN^{t}Bu. Note that irreversible events are introduced if the 3+/4+ transition is accessed in the presence of CN^{t}Bu, but that the first three oxidation events appear to be reversible. 42

Figure 1.28. Zero-field ^{57}Fe Mössbauer spectrum (90 K) of **Fe$_3$**(CN^{t}Bu)$_3$. [δ, |ΔE$_Q$| (mm/s)]: component 1 (cyan fit): 0.84, 1.43, 89%; component 2 (magenta): 0.42, 1.16, 11%.44

Figure 1.29. Zero-field ^{57}Fe Mössbauer spectrum (90 K) of [**Fe$_3$**(phen)$_3$][PF$_6$]. [δ, |ΔE$_Q$| (mm/s)]: component 1 (dark blue fit): 0.94, 1.55, 100%. 45

Figure 1.30. Given the similarity between the Mössbauer spectra obtained for **Fe$_3$** and [(^{n}Bu)$_4$N][**Fe$_3$**], ^{1}H NMR (CD$_3$CN, 25 °C, 300 MHz**)** spectra of [(^{n}Bu)$_4$N][**Fe$_3$**] were recorded before (bottom) and after (top) Mössbauer analysis. 45

Figure 1.31. Solid-state structure of $Co_6Se_8L^{Tol,H}_6$ with thermal ellipsoids plotted at a 50% probability level. Hydrogen atoms have been omitted for clarity..... 47

Figure 1.32. Solid-state structure of [$Co_6Se_8L^{Tol,H}_6$][OTf] with thermal ellipsoids plotted at a 50% probability level. Hydrogen atoms have been omitted for clarity. 48

Figure 1.33. Molecular structure of **Fe$_3$**(CN^{t}Bu)$_3$ with thermal ellipsoids shown at a 50% probability level. All hydrogen atoms, disorder and co-crystallized solvent molecules are omitted for clarity. Selected interatomic distances (Å): Fe1-C115 2.126(5), Fe2-C120 2.127(5), Fe3-C125 2.140(4); Fe1-Se2 2.526(4), Fe2-Se3 2.488(4), Fe3-Se6 2.509(2); Se1…Se4 5.644(9), Se2…Se5 5.701(5), Se3…Se6 5.757(8), Se7…Se8 5.499(2).. 49

Figure 1.34. Molecular structure of [**Fe$_3$**(CN^{t}Bu)$_2$][PF$_6$] with thermal ellipsoids shown at a 50% probability level. All hydrogen atoms, disorder, the [PF$_6$]$^-$ counterion and co-crystallized solvent molecules are omitted for clarity. Selected interatomic distances (Å): Fe1-C115 2.04(2), Fe2-C120 2.08(2); Fe1-Se1 2.488(7), Fe2-Se2 2.546(7), Fe3-Se4 2.397(6), Fe3-Se5 2.433(5); Fe3-Co5 2.661(8), Fe3-Co6 2.853(7); Co5-Co6 2.800(7); Se7-Se8 5.486(3), Se1-Se4 5.734(8), Se2-Se5 5.83(1), Se3-Se6 5.58(2). 50

Figure 1.35. Molecular structure of [**Fe$_3$**(phen)$_3$][PF$_6$] with thermal ellipsoids plotted at a 50% probability level. Hydrogen atoms, disorder, co-crystallized solvent molecules, and the [PF$_6$]$^-$ counterion are omitted for clarity. One of two [**Fe$_3$**(phen)$_3$]$^+$ molecules in the asymmetric unit is displayed. Selected interatomic distances (Å): Fe1-Se1 2.780(6), Fe1…Se2 3.097(6), Fe2-Se4 2.815(9), Fe2…Se3 3.640(6), Fe3…Se5 2.99(1), Fe3…Se6 2.990(6); Fe1-N13 2.04(2), Fe1-N14 2.27(2), Fe2-N15 2.18(2), Fe2-N16 2.16(2), Fe3-N17 2.18(2), Fe3-N18 2.19(2); Se7…Se8 5.549(6), Se1…Se4 5.707(5), Se2…Se5 5.659(5), Se3…Se6 5.698(9). 51

Figure 1.36. Molecular structure of [Na(18-C-6)][**Fe$_3$**] with thermal ellipsoids shown at a 50% probability level. All hydrogen atoms, disorder and co-crystallized solvent molecules are omitted for clarity. One of two [**Fe$_3$**]$^-$ molecules in the asymmetric unit is displayed. Selected interatomic distances (Å): Fe4-Se9 2.47(4), Fe4-Se10 2.46(1), Fe5-Se11 2.46(2), Fe5-Se12 2.46(3), Fe6-Se13 2.44(4), Fe6-Se14 2.47(3); Fe4…Co7 2.820(9), Fe4…Co8 2.80(2); Co7…Co8 2.78(3), Co7…Co12 2.94(5), Co7…Co11 3.00(3), Co8…Co10 3.01(3), Co8…Co9 2.94(3); Se15…Se16 5.34(7), Se9…Se12 5.79(5), Se10…Se3 5.87(9), Se11…Se14 5.92(8). 52

Figure 2.1. Capping phosphine ligands affect the speciation of intermediates formed en route to $Co_6Se_8L^{iPr,H}_6$, which can support three κ^4-bound surface metals. 63

Figure 2.2. Heterometallic clusters featuring (a) active sites rigidly embedded within the polymetallic framework, (b) dangler sites tethered at the cluster surface. 64

Figure 2.3. Solid-state structure of **Co$_2$** with thermal ellipsoids shown at a 50% probability level. All hydrogen atoms and three-fold rotational disorder have been omitted for clarity. Selected interatomic distances (Å): Co1-Co1 2.6731(6); Co1-P1 2.19(1); P1-N1 1.47(2). 67

Figure 2.4. UV-visible absorption (in toluene; left) and ATR-FTIR (carbonyl region; right) spectra of **Co$_4$Se**. 69

Figure 2.5. Single crystal X-ray diffraction structure of **Co$_4$Se$_2$** depicted (a) in full and (b) trimmed to only the inorganic core and the immediate coordination sphere. Selected interatomic distances(Å): Co1–Co1 2.54(1), Co1–Co2 2.746(1), Co2–Co2 2.51(1); Co1–Se1 2.386(5), Co2–Se1 2.405(2). Thermal ellipsoids are plotted at 50% probability level. All hydrogen atoms are omitted, and the aminophosphine carbon atoms are plotted as wireframes for clarity. 70

Figure 2.6. Thermal conversion of **Co$_4$Se$_2$** to $Co_6Se_8L^{iPr,H}_6$ in the presence of excess $L^{iPr,H}$ and Se. UV-vis absorption analysis of the reaction mixture before and after the thermal conversion, revealing a clear transition to the absorption profile characteristic of [Co_6Se_8] clusters. 71

Figure 2.7. ^{1}H NMR (C_6D_6, 25 °C, 300 MHz) spectra of the starting material and crude products in the thermal conversion of **Co$_4$Se$_2$** to $Co_6Se_8L^{iPr,H}_6$. 71

Figure 2.8. ^{31}P NMR (C_6D_6, 25 °C, 300 MHz) spectrum of **Co_3Se**. 72
Figure 2.9. UV-visible absorption (in toluene; left) and ATR-FTIR (carbonyl region; right) spectra of **Co_3Se**..... 72
Figure 2.10. Single crystal X-ray diffraction structure of **Co_3Se** in full (a), and trimmed to only the inorganic core (b). Selected interatomic distances(Å): Co1–Co2 2.57(2), Co1–Co3 2.62(1), Co2–Co3 2.47(1); Co1–Se1 2.29(1), Co2–Se1 2.30(2), Co3–Se1 2.314(9); Co2–P4 2.179(9), Co3–P4 2.19(1). Thermal ellipsoids are plotted at 50% probability level. All hydrogen atoms and co-crystallizing solvent molecules are omitted. The aminophosphine carbon atoms are plotted as wireframes for clarity. 73
Figure 2.11. Single crystal X-ray diffraction structure of (a) neutral cluster $Co_6Se_8L^{iPr,H}_6$ and (b) its packing in the lattice governed by π-π stacking of phenyl rings..... 75
Figure 2.12. Single crystal X-ray structure of the mono-oxidized cluster, $[Co_6Se_8L^{iPr,H}_6][PF_6]$. 76
Figure 2.13. Single crystal X-ray structures of the nanopropeller clusters, Λ-**Fe_3^{iPr}** (a) and Δ-**Zn_3^{iPr}** (b), with insets highlighting the κ^4-bound edge sites. (a) Selected interatomic distances (Å): (a) Fe1–Se1 2.5360(2), Fe1–Se6 2.496(2), Fe1–N1 1.962(2), Fe1–N4 1.952(4), Fe1–Co1 2.885(1), Fe1–Co6 2.831(2), Co1–Co6 2.780(5), Co1–Se1 2.373(2), Co6–Se6 2.401(2), Co6–P4 2.171(2), P4–N4 1.6512(6); (b) Zn1–Se1 2.711(2), Zn1–Se6 2.660(5), Zn1–N1 1.882(7), Zn1–N4 1.888(8), Zn1–Co1 3.181(4), Zn1–Co6 3.181(3), Co1–Co6 2.910(4), Co1–Se1 2.369(2), Co6–Se6 2.385(1), N1–P1 1.648(8), Co1–P1 2.163(3). For **Zn_3^{iPr}**, plotted is only the major component (88% occupancy), omitting for clarity the co-crystallizing $Co_6Se_8L^{iPr,H}_6$ (12% occupancy; see Figure 2.36). Thermal ellipsoids plotted at 50% probability. Hydrogen atoms, co-crystallizing solvent, and disorder are omitted. All carbon atoms are displayed as wireframes for clarity. 78
Figure 2.14. (a) UV-vis-*n*IR spectra including the λ_{max} (nm) and corresponding extinction coefficient ϵ (M^{-1} cm^{-1}) for **Fe_3^{iPr}** (428; 34100), **Fe_3** (444, 39800) and **Zn_3^{iPr}** (397; 37100), acquired in toluene. (b) Cyclic voltammograms of **Fe_3^{iPr}** and **Zn_3^{iPr}** recording in DCM or THF (0.1 M [^{n}Bu$_4$N][PF_6]) at 50 mV/s. (c) Comparison between the electrochemical profiles of **Fe_3^{iPr}** and **Fe_3**, acquired in DCM (0.1 M [^{n}Bu$_4$N][PF_6]) at 50 mV/s. 81

Figure 2.15. Space filling models for a single κ^4–Fe edge site in (a) **Fe$_3$**$^{i\mathrm{Pr}}$ and (b) [**Fe$_3$**]$^-$, including a zoom-in on the side view, highlighting the isolated edge site, and the full cluster viewed from the top of the outlined edge site. 82

Figure 2.16. Comparison of CN infrared stretches of free CN^{t}Bu (black), **Fe$_3$**(CN^{t}Bu)$_3$ (blue) and **Fe$_3$**$^{i\mathrm{Pr}}$(CN^{t}Bu)$_x$ (red). 83

Figure 2.17. ^{1}H NMR (C_6D_6, 25 °C, 500 MHz) spectrum of $Co_3Se(\mu_2\text{-}PPh_2)(CO)_4L^H{}_3$.. 90

Figure 2.18. ^{13}C NMR (C_6D_6, 25 °C, 125 MHz) spectrum of $Co_3Se(\mu_2\text{-}PPh_2)(CO)_4L^H{}_3$. 90

Figure 2.19. UV-vis absorption (in toluene; left) and ATR-FTIR (solids; carbonyl region; right) spectra of $[Co(CO)_3(^i\mathrm{Pr}_2\mathrm{PN(H)}^i\mathrm{Pr})]_2$. 91

Figure 2.20. ^{1}H NMR (CD_2Cl_2, 25 °C, 500 MHz) spectrum of **Fe$_3$**$^{i\mathrm{Pr}}$. Here, **Fe$_3$**$^{i\mathrm{Pr}}$ is abbreviated as **1**$^{i\mathrm{Pr}}$-Fe$_3$. 92

Figure 2.21. ^{1}H NMR (C_6D_6, 25 °C, 300 MHz) spectra **Fe$_3$**$^{i\mathrm{Pr}}$ (0.012 M, 1 equiv) without ligand (bottom), and in the presence of either *tert*-butyl isocyanide (0.18 M, 15 equiv) or pyridine (0.18 M, 15 equiv). Here, **Fe$_3$**$^{i\mathrm{Pr}}$ is abbreviated as **1**$^{i\mathrm{Pr}}$-Fe$_3$..... 93

Figure 2.22. ^{1}H NMR (CD_2Cl_2, 25 °C, 500 MHz) spectrum of **Zn$_3$**$^{i\mathrm{Pr}}$. Here, **Zn$_3$**$^{i\mathrm{Pr}}$ is abbreviated as **1**$^{i\mathrm{Pr}}$-Zn$_3$. 94

Figure 2.23. ^{13}C NMR (CD_2Cl_2, 25 °C, 125 MHz) spectrum of **Zn$_3$**$^{i\mathrm{Pr}}$. 95

Figure 2.24. UV-vis-*n*IR spectra of **Fe$_3$**$^{i\mathrm{Pr}}$, **Zn$_3$**$^{i\mathrm{Pr}}$, and $Co_6Se_8L^{i\mathrm{Pr,H}}{}_6$, recorded in toluene. Here, **Fe$_3$**$^{i\mathrm{Pr}}$, **Zn$_3$**$^{i\mathrm{Pr}}$, and $Co_6Se_8L^{i\mathrm{Pr,H}}{}_6$ are abbreviated as **1**$^{i\mathrm{Pr}}$-Fe$_3$, **1**$^{i\mathrm{Pr}}$-Zn$_3$, and **1**$^{i\mathrm{Pr}}$-H$_6$, respectively. 95

Figure 2.25. ^{1}H NMR (C_6D_6, 25 °C, 300 MHz) spectrum of the crude mixture obtained in the reaction of $Co_2(CO)_8$ (3 equiv) with Se=L$^{i\mathrm{Pr,H}}$ (12 equiv). Here, $Co_6Se_8L^{i\mathrm{Pr,H}}{}_6$ and L$^{i\mathrm{Pr,H}}$ are abbreviated as **1**$^{i\mathrm{Pr}}$-H$_6$ and L^H, respectively. 97

Figure 2.26. ^{1}H NMR ($CDCl_3$, 25 °C, 300 MHz) spectrum of the crude mixture obtained in the reaction of $Co_2(CO)_8$ (3 equiv) with Se (8 equiv) and L$^{i\mathrm{Pr,H}}$ (6 equiv). Here, $Co_6Se_8L^{i\mathrm{Pr,H}}{}_6$ and L$^{i\mathrm{Pr,H}}$ are abbreviated as **1**$^{i\mathrm{Pr}}$-H$_6$ and L^H, respectively..... 98

Figure 2.27. ^{1}H NMR (C_6D_6, 25 °C, 300 MHz) spectrum of the crude mixture obtained in the reaction of $Co_2(CO)_8$ (3 equiv) with Se (8 equiv) and L$^{i\mathrm{Pr,H}}$ (12 equiv). Here, $Co_6Se_8L^{i\mathrm{Pr,H}}{}_6$ and L$^{i\mathrm{Pr,H}}$ are abbreviated as **1**$^{i\mathrm{Pr}}$-H$_6$ and L^H, respectively..... 99

Figure 2.28. ^{1}H NMR (C_6D_6, 25 °C, 300 MHz) spectrum of the crude reaction mixture obtained in the reaction of $Co_2(CO)_8$ (3 equiv) with Se (10 equiv) and $L^{iPr,H}$ (15 equiv). Here, $Co_6Se_8L^{iPr,H}_6$ and $L^{iPr,H}$ are abbreviated as $\mathbf{1}^{iPr}$-H_6 and L^{H}, respectively. 100

Figure 2.29. Solid-state structure of $Co_6Se_8L^{iPr,H}_6$. Thermal ellipsoids displayed at a 50% probability level. All hydrogen atoms are omitted for clarity. Selected interatomic distances (Å): Co1-Se1 2.3334(5), Co1-Se2 2.3448(5); Co1…Co1 2.9390(5); Se1…Se1 5.5081(9), Se2…Se2 5.6655(7); Co1…P1 2.1354(9). 101

Figure 2.30. Molecular structure of $[Co_6Se_8L^{iPr,H}_6][PF_6]$ with thermal ellipsoids shown at a 50% probability level. All hydrogen atoms and disorder in the $[PF_6]^-$ counterion are omitted for clarity. Selected interatomic distances (Å): Co1-Se1 2.349(2), Co1-Se3 2.343(8), Co1-Se2 2.343(4), Co1-Se4 2.336(2); Se1…Se1 5.633(3), Se2…Se2 5.53(2), Se3…Se3 5.657(5), Se4…Se4 5.710(3); Co3-P3 2.163(4). 102

Figure 2.31. Molecular structure of $\mathbf{Co_4Se_2}$ with thermal ellipsoids shown at a 50% probability level. All hydrogen atoms are omitted for clarity. Selected interatomic distances (Å): Co1-Co1 2.54(1), Co1-Co2 2.746(1), Co2-Co2 2.51(1); Co1-Se1 2.387(5), Co2-Se1 2.361(5). 103

Figure 2.32. Molecular structure of $\mathbf{Co_3Se}$ with thermal ellipsoids shown at a 50% probability level. All hydrogen atoms and a co-crystallizing solvent molecule are omitted for clarity. Selected interatomic distances (Å): Co1-Co2 2.57(2), Co1-Co3 2.62(1), Co2-Co3 2.47(1); Co1-Se1 2.29(1), Co2-Se1 2.30(2), Co3-Se1 2.314(9); Co2-P4 2.179(9), Co3-P4 2.19(1); Co1-P1 2.20(1), Co2-P2 2.173(4), Co3-P3 2.17(1). 104

Figure 2.33. Solid-state structure of $\mathbf{Co_2}$ with thermal ellipsoids shown at a 50% probability level. All hydrogen atoms and three-fold rotational disorder have been omitted for clarity. Selected interatomic distances (Å): Co1-Co1 2.6731(6); Co1-P1 2.19(1); P1-N1 1.47(2). 105

Figure 2.34. Molecular structure of $\mathbf{Fe_3}^{iPr}$ with thermal ellipsoids shown at a 50% probability level. All hydrogen atoms and co-crystallizing solvent molecules are omitted for clarity. Selected interatomic distances (Å): Fe1-Se1 2.5360(2), Fe1-Se6 2.492(2), Fe2-Se2 2.5193(5), Fe2-Se3 2.5304(9), Fe3-Se4 2.534(2), Fe3-Se5 2.519(2); Fe1…Co1 2.885(1),

Fe1…Co6 2.831(2); Co1…Co6 2.780(5), Co1…Co2 2.959(1), Co1…Co3 2.989(2); Se7…Se8 5.412(8), Se1…Se4 5.800(6), Se2…Se5 5.756(3), Se3…Se6 5.7607(7).106

Figure 2.35. Molecular structure of **Zn$_3$**$^{i\text{Pr}}$ with thermal ellipsoids shown at a 50% probability level. All co-crystallizing solvent molecules and disorder have been omitted for clarity. Selected interatomic distances (Å): Zn1-Se1 2.711(2), Zn1-Se6 2.660(5), Zn2-Se2 2.733(2), Zn2-Se3 2.658(2), Zn3-Se4 2.648(2), Zn3-Se5 2.780(4); Co1…Co6 2.910(4), Co1…Co2 3.036(2), Co1…Co3 2.949(2); Se7…Se8 5.613(3), Se1…Se4 5.642(9), Se2…Se5 5.685(2), Se3…Se6 5.671(3). 107

Figure 2.36. (top) The major component of the asymmetric unit consisting of a racemic pair of **Zn$_3$**$^{i\text{Pr}}$ clusters with Zn(II) ions occupying each of the metal binding edge sites. (bottom) The minor component of the asymmetric unit, consisting of two molecules of $Co_6Se_8L^{i\text{Pr,H}}{}_6$. All hydrogen atoms omitted for clarity. Thermal ellipsoids plotted at a 50% probability level. 107

Figure 3.1. Atomically precise M/Co/Se nanoclusters with multiple active sites enable probing inter-adsorbate interactions at neighboring active sites. Red arrows illustrate the correlated reactivity of neighboring active sites. 118

Figure 3.2. Changes in the coordination environment of a single Fe edge site in response to ligand binding at the edge metals of **Fe$_3$**, and b) the stereochemical implications of ligands binding at multiple Fe edge sites. 120

Figure 3.3. Single-crystal X-ray diffraction structures for a family of *cis*-(α,β) nanoclusters including a) [**Fe$_3$**(CN^{t}Bu)$_2$][PF$_6$], b) [**Fe$_3$**(THF)$_2$][PF$_6$], and c) **Fe$_3$**(MeCN)(OTf). Phosphinoamide ligands, chemical disorder and solvent molecules are omitted for clarity. 122

Figure 3.4. Solution-phase FTIR absorption (25 °C, 7.8 mM, 2 mm pathlength) spectra of [**Fe$_3$**(CN^{t}Bu)$_2$][PF$_6$] recorded in neat DCM or THF. Solvent contributions were accounted for via solvent subtraction. 123

Figure 3.5. a) Solid-state structures of the co-crystallized intermediates (α,α,β)-[**Fe$_3$**(CN^{t}Bu)$_2$(THF)][PF$_6$] and *trans*-(α,β)-[**Fe$_3$**(CN^{t}Bu)(THF)][PF$_6$]. Thermal ellipsoids plotted at 50% probability. Insets included to highlight the dynamic exchange of isocyanide at the b) major and c) minor components of the crystal. All hydrogen atoms,

phosphinoamide carbon atoms, and the $[PF_6]^-$ counterion have been omitted for clarity. Selected interatomic distances (Å): Fe1a-Se2 2.498(7), Fe1a-Se1 3.258(3), Fe1b-Se2 2.471(8), Fe1b-Se1 2.404(5), Fe2-Se3 2.541(7), Fe3-Se6 2.450(2), Fe3-Se5 2.699(3); Fe1a-C115 2.13(1); Fe1b-C129 2.41(3), Fe2-C120 2.11(3). 124

Figure 3.6. Zero-field ^{57}Fe Mössbauer spectra (90 K) collected on bulk solid samples of disordered [**Fe$_3$**(CN^{t}Bu)$_2$(THF)][PF$_6$], [**Fe$_3$**(CN^{t}Bu)$_2$][PF$_6$], and [**Fe$_3$**(THF)$_2$][PF$_6$], with quadrupole doublets tentatively assigned to distinct Fe environments. 126

Figure 3.7. Calculated energetics and optimized geometries for the proposed ligand substitution reaction coordinate. Calculations were run at the uB3LYP+/cc-PVTZ level of theory. 128

Figure 3.8. Variable-temperature *dc* magnetic susceptibility (χ_MT, filled circles) data recorded for [**Fe$_3$**(CN^{t}Bu)$_2$][PF$_6$] upon warming from 5 to 300K under applied fields of 0.1, 0.5, and 1.0 T. 129

Figure 3.9. Partial density of states plots and b) molecular orbital diagrams of the crystallographically resolved [**Fe$_3$**]$^+$ ligand exchange series, *cis*-(α,β)-[**Fe$_3$**(CNMe)$_2$]$^+$, (α,α,β)-[**Fe$_3$**(CNMe)$_2$(THF)]$^+$ and *trans*-(α,β)-[**Fe$_3$**(CNMe)(THF)]$^+$. Here, *a* and *b* are used to abbreviate the up and down spin-manifolds. Calculations were run at the uB3LYP+/cc-PVTZ level of theory. 131

Figure 3.10. Isosurface plots are provided for select frontier orbitals of *cis*-(α,β)-[**Fe$_3$**(CNMe)$_2$]$^+$, (α,α,β)-[**Fe$_3$**(CNMe)$_2$(THF)]$^+$ and *trans*-(α,β)-[**Fe$_3$**(CNMe)(THF)]$^+$ (bottom, 0.04 au). Here, *a* and *b* are used to abbreviate the up and down spin-manifolds. Calculations were run at the uB3LYP+/cc-PVTZ level of theory. 132

Figure 3.11. a) Solid-state structure of neutral **Fe$_3$**(py)$_x$ (x = 2, 3) containing major and minor components of (α,α,β)-**Fe$_3$**(py)$_3$ and *cis*-(α,β)-**Fe$_3$**(py)$_2$, respectively. All phosphinoamide carbon atoms and hydrogen atoms are omitted for clarity. Thermal ellipsoids are plotted with 50% probability. Select interatomic distances (Å): Fe2-Se3 2.555(5), Fe1-Se2 2.507(5), Fe3-Se5 2.487(4), Fe3b-Se5 2.544(6), Fe3b-Se6 2.353(7). 134

Figure 3.12. FTIR absorption spectra for [**Fe$_3$**(CN^{t}Bu)$_2$][PF$_6$] collected in neat THF (left) and DCM (right). 140

Figure 3.13. FTIR absorption spectra recorded for [**Fe$_3$**(THF)$_2$][PF$_6$] upon titration with varying equivalents of CN^{t}Bu in neat THF both after (left) and before solvent subtraction (right). 140
Figure 3.14. FTIR absorption spectra recorded for [**Fe$_3$**(THF)$_2$][PF$_6$] upon titration with varying equivalents of CN^{t}Bu in neat DCM after (left) and before solvent subtraction (right).141
Figure 3.15. Representative gaussian fits used to assess the concentrations of bound and free CN^{t}Bu (dark gray curves) in both THF (left) and DCM (right). Light grey curves are attributed to overtone bands and were necessary to achieve a good fit to the line shape for the major CN^{t}Bu stretches. 141
Figure 3.16. (left) Variable-temperature, variable-field reduced magnetization data for [**Fe$_3$**(CN^{t}Bu)$_2$][PF$_6$], collected upon warming from 2.5 to 10 K at each applied field. This plot confirms the presence of a high-spin ground state, but the sample resists magnetic saturation under applied magnetic fields up to 7.0 T. (right) Magnetization of [**Fe$_3$**(CN^{t}Bu)$_2$][PF$_6$] recorded on sweeping the applied field from 0 and 7 T at 50 K. This plot confirms the absence of ferromagnetic impurities..... 142
Figure 3.17. Single-crystal X-ray structure of [**Fe$_3$**(THF)$_2$][PF$_6$] (thermal ellipsoids plotted at 50% probability). Disordered amidophosphine substituents are plotted over two positions. All hydrogen atoms have been omitted for clarity..... 144
Figure 3.18. Single-crystal X-ray structure of **Fe$_3$**(MeCN)(OTf) with thermal ellipsoids plotted at 50% probability. All hydrogen atoms, the disordered triflate fragment and two co-crystallizing diethyl ether molecules have been omitted for clarity. 145
Figure 3.19. Solid-state structure of co-crystallized [**Fe$_3$**(CN^{t}Bu)$_2$(THF)]$^+$ and *trans*-(α,β)-[**Fe$_3$**(CN^{t}Bu)(THF)]$^+$ plotting both disordered components, which are present in a 76:24 ratio, respectively. Atoms associated only with the secondary component, *trans*-(α,β)-[**Fe$_3$**(CN^{t}Bu)(THF)]$^+$ are depicted as hollow spheres. All hydrogen atoms and the rotationally disordered [PF$_6$]$^-$ counterion have been omitted for clarity. 146
Figure 3.20. Single-crystal X-ray structure of (α,α,β)-[**Fe$_3$**(CN^{t}Bu)$_2$(THF)][PF$_6$] with thermal ellipsoids plotted at 50% probability. All hydrogen atoms and the rotationally disordered [PF$_6$]$^-$ counterion have been omitted for clarity. 147

Figure 3.21. Single-crystal X-ray structure of *trans*-(α,β)-[**Fe$_3$**(CN^{t}Bu)(THF)]$^+$ including a dissociated CN^{t}Bu molecule proximal to Fe1B. Thermal ellipsoids are plotted at 50% probability. All hydrogen atoms and the rotationally disordered [PF_6]$^-$ counterion have been omitted for clarity. 147

Figure 3.22. (2nd Measurement) Solid-state structure of co-crystallized [**Fe$_3$**(CN^{t}Bu)2(THF)]$^+$ and *trans*-(α,β)-[**Fe$_3$**(CN^{t}Bu)(THF)]$^+$ plotting both disordered components, which are present in a 85:15 ratio, respectively. Atoms associated only with the secondary component, *trans*-(α,β)-[**Fe$_3$**(CN^{t}Bu)(THF)]$^+$ are depicted as hollow spheres. All hydrogen atoms and the rotationally disordered [PF_6]$^-$ counterion have been omitted for clarity. 148

Figure 3.23. (2nd Measurement) Single-crystal X-ray structure of the two components of the disordered crystal structure: (α,α,β)-[**Fe$_3$**(CN^{t}Bu)$_2$(THF)][PF_6] (85%) and *trans*-(α,β)-[**Fe$_3$**(CN^{t}Bu)(THF)]$^+$ (15%). Thermal ellipsoids plotted at 50% probability. All hydrogen atoms and the rotationally disordered [PF_6]$^-$ counterion have been omitted for clarity. 149

Figure 3.24. Single-crystal X-ray structure of **Fe$_3$**(py)$_x$ (x = 2, 3) (thermal ellipsoids plotted at 50% probability) with all disorder included. Three amidophosphine ligands and one Fe center are plotted over two positions. All hydrogen atoms have been omitted for clarity. 150

Figure 3.25. Single-crystal X-ray structure of **Fe$_3$**(py)$_2$ (46% abundance) (thermal ellipsoids plotted at 50% probability), which co-crystallizes with **Fe$_3$**(py)$_3$ (54% abundance). All hydrogen atoms and disorder have been omitted for clarity. 150

Figure 4.1. Pre-formed inorganic Co/Se/Co clusters serve as templated building blocks to guide the self-assembly of two-dimensional nanosheets. 168

Figure 4.2. UV-vis-*n*IR absorption spectra of $Co_3(py)_3Co_6Se_8L_6$ (**Co$_3$**(py)$_3$) and $Co_6Se_8L^{Tol,H}{}_6$ recorded in THF. 171

Figure 4.3. Single-crystal X-ray structure of the Λ enantiomer of **Co$_3$**(py)$_3$, with selected interatomic distances (Å): Co7–Se2 2.534(1), Co7…Se1 3.200(2), Co8–Se3 2.524(1), Co9–Se6 2.573(2). Thermal ellipsoids plotted at 50%. Disordered ligands, solvent and hydrogen atoms hidden for clarity. Inset: top (a) and side (b) view of **Co$_3$**(py)$_3$ illustrating (α,α,β)

orientation with respect to the plane of the Co edge sites, with two Se bound above this triangle (α) and one below(β). 171
Figure 4.4. ^{1}H NMR (benzene-d_6, 25 °C, 300 MHz) spectrum of **Co$_3$**(py)$_3$..... 173
Figure 4.5. ^{1}H NMR (pyridine-d_5, 25 °C, 300 MHz) spectrum of **Co$_3$**(py)$_3$. 173
Figure 4.6. (a) Single crystal X-ray structure for single layers of **Co$_3$**(bpy), **Co$_3$**(bpy$_\sigma$) and **Co$_3$**(bpy$_\pi$) (top and side views), illustrating the variations in tile sizes and layer corrugation. (b) In-plane anisotropy and quasi-chiral phase separation in **Co$_3$**(bpy$_\sigma$). Linkers and nanopropeller blades are colored blue when linked to β-Se, and teal when associated with α-Se sites. 176
Figure 4.7. Post-assembly, **Co$_3$**(py)$_3$ preserves its individual magnetic properties within the nanosheets. (a) Plotted are the variable-temperature *dc* magnetic susceptibility (χ_MT, filled circles), the reciprocal molar susceptibility ($1/\chi_M$, hollow circles) data for nanoblock **Co$_3$**(py)$_3$ (blue) and nanosheet **Co$_3$(**bpy$_\pi$) (teal), collected between 2 to 300 K, at 0.1 T, and the linear fit (25 to 150 K) used to obtain the Weiss constant. (b) Variable-temperature, variable-field reduced magnetization data for **Co$_3$**(py)$_3$, collected upon warming from 1.8 to 10 K at each applied field. 178
Figure 4.8. Solution and solid-state cyclic voltammograms of **Co$_3$**(py)$_3$ and **Co$_3$**(bpy$_\sigma$), respectively, recorded in DCM (solid lines), THF (dotted lines) or MeCN (dashed lines) solutions of [^{n}Bu$_4$N][PF$_6$] (0.1 M), at a scan rate of 200 mV/s. The data for **Co$_3$**(bpy$_\sigma$) was recorded by dropcasting a slurry of crystalline **Co$_3$**(bpy$_\sigma$) in toluene on a glassy carbon disk electrode. 180
Figure 4.9. a) Single-crystal-to-single-crystal synthesis of [**Co$_3$**(bpy$_\sigma$)][TCNE]$_2$ via redox intercalation. b) ATR-FTIR analysis of [**Co$_3$**(bpy$_\sigma$)][TCNE]$_2$ and TCNE, highlighting the CN stretching region. c) Single crystal X-ray structure of [**Co$_3$**(bpy$_\sigma$)][TCNE]$_2$ (top and side views). 182
Figure 4.10. The laminar structure of **Co$_3$**(bpy$_\sigma$) revealed by imaging pre- and post-mechanical exfoliation of a single crystal. (a) Optical microscopy image of a bulk single crystal. (b) Scanning electron microscopy image focused on laminar edge of the bulk crystal. (c) Optical microscopy of a mechanically exfoliated flake. (d) Atomic force microscopy

characterization of the exfoliated flake, including height profiles and a zoom-in inset of a thin flake. 183
Figure 4.11. ATR-FTIR spectra of [**Co$_3$**(bpy$_\sigma$)][TCNE]$_2$ (blue) and neutral TCNE (black), displaying the full spectral window acquired (zoom in included in Figure 4.9). In this figure, [**Co$_3$**(bpy$_\sigma$)][TCNE]$_2$ is denoted as **[2-bpy$_\sigma$]**[TCNE]$_2$. 189
Figure 4.12. A comparison of the variable-temperature dc magnetic susceptibility of **Co$_3$**(py)$_3$, **Co$_3$**(bpy), **Co$_3$**(bpy$_\pi$), and **Co$_3$**(bpy$_\sigma$) recorded at 0.1 T. We attribute the slight deviation in the data recorded for **Co$_3$**(bpy$_\sigma$) to a small amount of an unidentified impurity. In these figures, **Co$_3$**(py)$_3$, **Co$_3$**(bpy), **Co$_3$**(bpy$_\pi$), and **Co$_3$**(bpy$_\sigma$) are denoted as **1**, **2-bpy**, **2-bpy$_\pi$**, and **2-bpy$_\sigma$**, respectively. 190
Figure 4.13. (left) Variable-temperature dc magnetic susceptibility of **Co$_3$**(py)$_3$ recorded at 0.1 and 0.5 T, upon warming from 2 to 300 K. (right) Magnetization of **Co$_3$**(py)$_3$ recorded between 0 and 7 T at 100 K. These plots indicate that the sample is free of ferromagnetic impurities. 191
Figure 4.14. Inverse molar susceptibility of **Co$_3$**(py)$_3$ recorded upon warming from 2 to 300 K at 0.1 T. A linear fit to the data between 25 and 150 K, which was used to calculate Curie (C) and Weiss (θ) constants. 191
Figure 4.15. (left) Variable-temperature dc magnetic susceptibility of **Co$_3$**(bpy) recorded at 0.1 and 0.5 T upon warming from 5 to 300 K. The polynomial fit (R^2 = 0.9999) to the data recorded at 0.1 T was used to generate a truncated data set for the susceptibility of **Co$_3$**(bpy) shown above. (right) Magnetization of **Co$_3$**(bpy) recorded at 100 K between 0 and 7 T. These plots indicate the absence of ferromagnetic impurities. 192
Figure 4.16. (left) Variable-temperature dc magnetic susceptibility of **Co$_3$**(bpy$_\pi$) recorded at 0.1 and 1 T upon warming from 2 to 300 K. (right) Magnetization of **Co$_3$**(bpy$_\pi$) recorded between 0 and 7 T at 100 K. These plots confirm the absence of ferromagnetic impurities. 192
Figure 4.17. (left) Variable-temperature dc magnetic susceptibility of **Co$_3$**(bpy$_\sigma$) recorded at 0.1 and 0.5 T, upon warming from 5 to 300 K. The polynomial fit to the data (R^2 = 0.9999) recorded at 0.1 T was used to generate the truncated data set for the susceptibility of

Co$_3$(bpy$_\sigma$) shown above. (right) Magnetization of **Co$_3$**(bpy$_\sigma$) recorded between 0 and 7 T at 100 K. Both plots indicate the absence of ferromagnetic impurities. 193

Figure 4.18. (a) A comparison of the solution-phase cyclic voltammograms recorded for **Co$_3$**(py)$_3$ to the solid-state cyclic voltammograms recorded for **Co$_3$**(bpy), **Co$_3$**(bpy$_\pi$), and **Co$_3$**(bpy$_\sigma$) in THF, DCM, or MeCN solutions with 0.1 M $TBAPF_6$ electrolyte. The solid-state voltammograms for **Co$_3$**(bpy), **Co$_3$**(bpy$_\pi$), and **Co$_3$**(bpy$_\sigma$) were obtained by first dropcasting crystalline material on a glassy carbon working electrode. (b) A cyclic voltammogram of **1** in 0.1 M $TBAPF_6$ THF, revealing a third, irreversible reduction event (n_{red}/n_{ox} = –3/–2) at –2.45 V. All voltammograms were recorded with a scan rate of 200 mV/s. In these figures, **Co$_3$**(py)$_3$, **Co$_3$**(bpy), **Co$_3$**(bpy$_\pi$), and **Co$_3$**(bpy$_\sigma$) are denoted as **1**, **2-bpy**, **2-bpy$_\pi$**, and **2-bpy$_\sigma$**, respectively. 194

Figure 4.19. (left) A plot of current density (j_p) versus the square root of scan rate ($v^{1/2}$) for **Co$_3$**(py)$_3$ in 0.1 M [^{n}Bu$_4$N][PF_6] THF. Linear fits were used to extract diffusion coefficients using the Randles-Sevcik equation. (right) Cyclic voltammograms of **Co$_3$**(py)$_3$ recorded in 0.1 M [^{n}Bu$_4$N][PF_6] THF. 195

Figure 4.20. (left) A plot of current density (j_p) versus the square root of scan rate ($v^{1/2}$) for **Co$_3$**(py)$_3$ in 0.1 M [^{n}Bu$_4$N][PF_6] DCM. Linear fits were used to extract diffusion coefficients using the Randles-Sevcik equation. (right) Cyclic voltammograms of **Co$_3$**(py)$_3$ recorded in 0.1 M [^{n}Bu$_4$N][PF_6] DCM..... 195

Figure 4.21. Solid-state structure of **Co$_3$**(py)$_3$ with thermal ellipsoids plotted at a 50% probability level. All hydrogen atoms are omitted for clarity. Selected interatomic distances (Å): Co(7)-Se(2) 2.534(1), Co(7)-Se(1) 3.200(2), Co(8)-Se(3) 2.524(1), Co(8)-Se(4) 3.243(2), Co(9)-Se(6) 2.573(2), Co(9)-Se(5) 3.147(1), Co(1)-Se(8) 2.334(1), Co(1)-Se(2) 2.347(2), Co(9)-N(9) 2.101(2), Co(7)-N(1) 1.941(2), Se(1)-Se(4) 5.587(2), Se(2)-Se(5) 5.657(3), Se(7)-Se(8) 5.5524(8), Se(3)-Se(6) 5.830(3), Co(1)-Co(2) 2.868(1), Co(3)-Co(4) 2.8383(6), Co(5)-Co(6) 2.831(1), Co(1)-Co(6) 2.8934(6), Co(2)-Co(3) 2.922(1), Co(4)-Co(5) 2.954(1), N(1)-P(1) 1.673(3). 198

Figure 4.22. The asymmetric unit of **Co$_3$**(bpy) with thermal ellipsoids plotted at a 50% probability level. All hydrogen atoms are omitted and phosphinoamide carbon atoms are plotted as wireframes for clarity. 199

Figure 4.23. The asymmetric unit of **Co$_3$**(bpy$_\pi$) with thermal ellipsoids plotted at a 50% probability level. All hydrogen atoms are omitted and phosphinoamide carbon atoms are plotted as wireframes for clarity. 199
Figure 4.24. The asymmetric unit of **Co$_3$**(bpy$_\sigma$) with thermal ellipsoids plotted at a 50% probability level. All hydrogen atoms are omitted and phosphinoamide carbon atoms are plotted as wireframes for clarity. 200
Figure 4.25. The asymmetric unit of **Co$_3$**(bpy$_\sigma$) with thermal ellipsoids plotted at a 50% probability level. All hydrogen atoms are omitted and phosphinoamide carbon atoms are plotted as wireframes for clarity. 201
Figure 5.1. The Cr/Co/Se nanocluster grants enhanced stability to key intermediates formed upon azide activation and nitrene transfer, enabling their isolation and single-crystal X-ray characterization. 211
Figure 5.2. Structural resemblance between a) MoS_2, b) edge-doped MoS_2, and c) M/Co/Se nanoclusters. Image a) reproduced from Besenbacher *et al*. *ACS Nano* **2010**, *4*, 4677–4682. Copyright 2010 American Chemical Society. Image b) reproduced with permission from Besenbacher *et al*. *J. Catal.* **2007**, *249*, 220–233. Copyright 2007 Elsevier. 213
Figure 5.3. Single crystal X-ray diffraction structure of **Cr$_3$**(py)$_3$, including an inset to highlight the Cr(py) edge coordination environment. Select interatomic distances (Å): Cr1-Se2 2.581(2), Cr1-Se1 2.726(7), Cr1-N1 2.022(9), Cr1-N7 2.101(8). Thermal ellipsoids plotted at 50% probability. All hydrogen atoms and co-crystallizing solvent molecules omitted for clarity. 215
Figure 5.4. ^{1}H NMR (benzene-d_6, 25 °C, 300 MHz) spectrum of **Cr$_3$**(py)$_3$. Gray dots indicate toluene/*n*-pentane resonances. 215
Figure 5.5. Catalytic carbodiimide formation using nanoclusters **Cr$_3$**(py)$_3$ and **Fe$_3$**, including kinetic monitoring by ^{1}H NMR spectroscopy. 216
Figure 5.6. Single crystal X-ray diffraction structure of **Cr$_3$**(NTs)$_3$, including an inset to highlight the Cr(NTs) edge coordination environment. Select interatomic distances (Å): Cr2-Se3 2.475(7), Cr2-N8 1.83(1), Cr2-N4 1.90(2), Cr2-O3 2.12(1). Thermal ellipsoids plotted at 50% probability. All hydrogen atoms and co-crystallizing solvent molecules omitted for clarity. 218

Figure 5.7. ^{1}H NMR (benzene-d_6, 25 °C, 300 MHz) spectrum of **Cr$_3$**(NTs)$_3$. The C_1 symmetry is reflected in solution, where we observe a highly desymmetrized NMR profile with a range of different ^{1}H resonances. Gray dots indicate toluene/*n*-pentane resonances. 218

Figure 5.8. Step-wise nitrene transfer mechanism wherein the reactivity of Cr(NTs) edges is differentiated under stoichiometric conditions. 219

Figure 5.9. ^{1}H NMR (benzene-d_6, 25 °C, 500 MHz) spectra of the *in situ* reaction mixture of **Cr$_3$**(NTs)$_3$ with CN^{t}Bu (6 equiv) recorded after 15 min and 4 h at 25 °C, and after an additional 48 h at 60 °C. The C(CH_3)$_3$ resonances of Cr(CN^{t}Bu) (reagent) and TsNCN^{t}Bu (product) are integrated against the internal standard mesitylene to track the reactions progress (see Section 5.6.10 for more details). 220

Figure 5.10. *In situ* ^{1}H NMR (benzene-d_6, 25 °C, 300 MHz) spectra collected for the catalytic reaction mixture formed using either **Cr$_3$**(py)$_3$, **Cr$_3$**(NTs)(CN^{t}Bu)$_2$, or **Cr$_3$**(NTs)$_3$ (10 mol%) as a pre-catalyst 20 min after the addition of TsN_3, plotted in comparison to the spectrum obtained 15 min after stoichiometric treatment of **Cr$_3$**(NTs)$_3$ with CN^{t}Bu (6 equiv) (top). 221

Figure 5.11. *In situ* ^{1}H NMR (benzene-d_6, 25 °C, 500 MHz) reaction monitoring of **Cr$_3$**(NTs)$_3$ treated with CN^{t}Bu (3 equiv) recorded after 48 h at 25 °C. The C(CH_3)$_3$ resonances of CN^{t}Bu (reagent) and TsNCN^{t}Bu (product) are integrated to reveal the ~1:1 distribution of Cr(CN^{t}Bu) and TsNCN^{t}Bu. This spectrum is plotted in comparison to *in situ* ^{1}H NMR (toluene-d_8, 25 °C, 500 MHz) spectra monitoring the reactivity of crystalline **Cr$_3$**(NTs)$_3$(CN^{t}Bu)$_3$ upon dissolution after 5 min at 25 °C (bottom) and 24 h at 60 °C (middle). *For the latter spectra, overlap between toluene-d_8 and TsNCN^{t}Bu CH_3 resonances makes Cr(CN^{t}Bu) and TsNCN^{t}Bu integration challenging..... 222

Figure 5.12. Single crystal X-ray diffraction structure of **Cr$_3$**(NTs)$_3$(CN^{t}Bu)$_3$, including an inset to highlight the Cr(NTs)(CN^{t}Bu) edge coordination environment. Select interatomic distances (Å): Cr1-Se2 2.574(4), Cr1-N7 1.75(1), Cr1-N2 1.916(9), Cr1-C136 2.07(1). Thermal ellipsoids plotted at 50% probability. All hydrogen atoms and co-crystallizing solvent molecules omitted for clarity. 223

Figure 5.13. ATR-FTIR spectra of crystalline **Cr$_3$**(CN^{t}Bu)$_3$, **Cr$_3$**(NTs)(CN^{t}Bu)$_2$, **Cr$_3$**(NTs)$_3$(CN^{t}Bu)$_3$, and neat CN^{t}Bu, highlighting the isocyanide CN stretching frequencies. 224

Figure 5.14. Single crystal X-ray diffraction structure of **Cr$_3$**(NTs)(CN^{t}Bu)$_2$, including an inset to highlight the Cr(CN^{t}Bu) edge coordination environment. Select interatomic distances (Å): Cr2-Se3 2.611(3), Cr2-Se4 2.663(4), Cr2-N4 2.04(1), Cr-C122 2.09(2). Thermal ellipsoids plotted at 50% probability. All hydrogen atoms and co-crystallizing solvent molecules omitted for clarity. 225

Figure 5.15. Proposed catalytic cycle for carbodiimide formation at an isolated Cr edge site, informed by the isolation of key reactive intermediates. 227

Figure 5.16. Partition of CN^{t}Bu as it engages in reversible coordinative at a Cr(NTs) edge, or undergoes migratory (1,2)-insert with the imido group to afford carbodiimide product. 228

Figure 5.17. In situ ^{1}H NMR (benzene-d_6, 25 °C, 500 MHz) spectra recorded 15 min after treatment of **Cr$_3$**(NTs)$_3$ with varying amounts of CN^{t}Bu (1, 2, 3, 4, 5, 6 equiv) at 25 °C. Mesitylene CH_3 resonance (internal standard) at ~1.8 ppm omitted for clarity. 231

Figure 5.18. *In situ* ^{1}H NMR (benzene-d_6, 25 °C, 500 MHz) spectrum recorded 15 min after treatment of **Cr$_3$**(NTs)$_3$ with CN^{t}Bu (6 equiv) at 25 °C. Depicted integrations are representative of those used to calculate the isocyanide binding constant. 232

Figure 5.19. ^{1}H NMR (benzene-d_6, 25 °C, 500 MHz) spectra recorded in situ upon treatment of **Cr$_3$**(NTs)(CN^{t}Bu)$_2$ with CN^{t}Bu (3 equiv) at 25 °C (top), and of isolated **Cr$_3$**(NTs)(CN^{t}Bu)$_2$ (bottom)..... 233

Figure 5.20. ATR-FTIR spectrum of **Cr$_3$**(NTs)$_3$ (solids). Here, the trichromium cluster **Cr$_3$** is denoted as **1**..... 237

Figure 5.21. ATR-FTIR spectra of **Cr$_3$**(NTs)$_3$ (red) and **Cr$_3$**(py)$_3$ (black), highlighting the fingerprint region. Here, the trichromium cluster **Cr$_3$** is denoted as **1**. 238

Figure 5.22. Variable-temperature ^{1}H NMR (benzene-d_6, 700 MHz) spectra collected for **Cr$_3$**(NTs)$_3$. Spectra were recorded as the sample temperature was increased from 283 to 343 K, and then a final spectrum was collected upon cooling back to 298 K. These data indicate

that **Cr$_3$**(NTs)$_3$ remains locked in a low-symmetry (α,α,β) conformation in solution. Here, the trichromium cluster **Cr$_3$** is denoted as **1**. 238
Figure 5.23. Variable-temperature ^{1}H NMR (benzene-d_6, 700 MHz) spectra collected for **Cr$_3$**(NTs)$_3$. Here, we highlight the diagnostic N-tosyl ^{1}H resonances between 0 and –8 ppm. Spectra were recorded as the sample temperature was increased from 283 to 343 K, and then a final spectrum was collected upon cooling back to 298 K. These data indicate that **Cr$_3$**(NTs)$_3$ remains locked in a low-symmetry (α,α,β) conformation in solution. Here, the trichromium cluster **Cr$_3$** is denoted as **1**. 239
Figure 5.24. ATR-FTIR spectra of **Cr$_3$**(NTs)$_3$(CN^{t}Bu)$_3$ (solids, green) and neat CN^{t}Bu (dropcast, black). Here, the trichromium cluster **Cr$_3$** is denoted as **1**..... 241
Figure 5.25. ^{1}H NMR (benzene-d_6, 25 °C, 300 MHz) spectrum of **Cr$_3$**(NTs)(CN^{t}Bu)$_2$. Gray dots indicate toluene/*n*-pentane resonances..... 242
Figure 5.26. ATR-FTIR spectra of **Cr$_3$**(NTs)(CN^{t}Bu)$_2$ (dropcast, red) and neat CN^{t}Bu (dropcast, black). Here, the trichromium cluster **Cr$_3$** is denoted as **1**..... 243
Figure 5.27. ^{1}H NMR (benzene-d_6, 25 °C, 300 MHz) spectrum of **Cr$_3$**(CN^{t}Bu)$_3$. Gray dots indicate toluene/*n*-pentane resonances..... 244
Figure 5.28. ATR-FTIR spectra of **Cr$_3$**(CN^{t}Bu)$_3$ (solids, blue) and neat CN^{t}Bu (dropcast, black). Here, the trichromium cluster **Cr$_3$** is denoted as **1**..... 245
Figure 5.29. UV-vis-*n*IR Absorption Spectra of **Cr$_3$**(NTs)$_3$ and **Cr$_3$**(py)$_3$ recorded in toluene. Here, the trichromium cluster **Cr$_3$** is denoted as **1**..... 245
Figure 5.30. Monitoring the catalytic conversion of TsN_3 and CN^{t}Bu to TsNCN^{t}Bu at 25 °C. CN^{t}Bu (165 equiv), TsN_3 (100 equiv), and **Cr$_3$**(py)$_3$ (2.8 mM, 2.5 equiv) in benzene-d_6. Data was collected in triplicate, and percent conversion was calculated based on ^{1}H NMR integrations of the reagents and products versus an internal mesitylene standard. Control experiments were run with 7.5 mol% loading of $CrCl_2$ with 15 mol% $Ph_2PN(H)Tol$ or $Se{=}Ph_2PN(H)Tol$ (2 equiv per $CrCl_2$). The control samples exhibit no reaction with TsN_3 or formation of the carbodiimide product. Here, the trichromium cluster **Cr$_3$** is denoted as **1**. 247
Figure 5.31. ^{1}H NMR (benzene-d_6, 25 °C, 300 MHz) spectra of the catalytic reaction mixture prior to the addition of TsN_3 (bottom), 10 min (middle) and 6 h (top) after the addition of

TsN_3. A catalyst loading of 10 mol% **Cr$_3$**(py)$_3$ (0.0085 M, 10 equiv) was employed to increase the visibility of the paramagnetic species, and the reaction was performed in the presence of TsN_3 (100 equiv, 0.085 M) and CN^{t}Bu (165 equiv, 0.140 M). Here, the trichromium cluster **Cr$_3$** is denoted as **1**. 248

Figure 5.32. ^{1}H NMR (benzene-d_6, 25 °C, 500 MHz) spectra of the catalytic reaction upon mixing **Cr$_3$**(py)$_3$, TsN_3 and CN^{t}Bu. A catalyst loading of 10 mol% **Cr$_3$**(py)$_3$ (0.0085 M, 10 equiv) was employed to increase the visibility of the paramagnetic species, and the reaction was performed in the presence of TsN_3 (100 equiv, 0.085 M) and CN^{t}Bu (165 equiv, 0.140 M). Here, the trichromium cluster **Cr$_3$** is denoted as **1**..... 249

Figure 5.33. ^{1}H NMR (benzene-d_6, 25 °C, 500 MHz) spectra of the catalytic reaction upon mixing **Cr$_3$**(py)$_3$, TsN_3 and CN^{t}Bu, highlighting the diamagnetic region to show the clean conversion of tosyl azide to carbodiimide. A catalyst loading of 10 mol% **Cr$_3$**(py)$_3$ (0.0085 M, 10 equiv) was employed to increase the visibility of the paramagnetic species, and the reaction was performed in the presence of TsN_3 (100 equiv, 0.085 M) and CN^{t}Bu (165 equiv, 0.140 M). Here, the trichromium cluster **Cr$_3$** is denoted as **1**..... 250

Figure 5.34. ^{1}H NMR (benzene-d_6, 25 °C, 500 MHz) spectra of the catalytic reaction upon mixing **Cr$_3$**(NTs)(CN^{t}Bu)$_2$, TsN_3 and CN^{t}Bu. A catalyst loading of 10 mol% **Cr$_3$**(NTs)(CN^{t}Bu)$_2$ (0.0085 M, 10 equiv) was employed to increase the visibility of the paramagnetic species, and the reaction was performed in the presence of TsN_3 (100 equiv, 0.085 M) and CN^{t}Bu (165 equiv, 0.140 M). Here, the trichromium cluster **Cr$_3$** is denoted as **1**..... 251

Figure 5.35. ^{1}H NMR (benzene-d_6, 25 °C, 500 MHz) spectra of the catalytic reaction upon mixing **Cr$_3$**(NTs)(CN^{t}Bu)$_2$, TsN_3 and CN^{t}Bu, highlighting the diamagnetic region to show the clean conversion of tosyl azide to carbodiimide. A catalyst loading of 10 mol% **Cr$_3$**(NTs)(CN^{t}Bu)$_2$ (0.0085 M, 10 equiv) was employed to increase the visibility of the paramagnetic species, and the reaction was performed in the presence of TsN_3 (100 equiv, 0.085 M) and CN^{t}Bu (165 equiv, 0.140 M). Here, the trichromium cluster **Cr$_3$** is denoted as **1**..... 252

Figure 5.36. ^{1}H NMR (benzene-d_6, 25 °C, 500 MHz) spectra of the catalytic reaction upon mixing **Cr$_3$**(NTs)$_3$, TsN_3 and CN^{t}Bu. A catalyst loading of 10 mol% **Cr$_3$**(NTs)$_3$ (0.0085 M,

10 equiv) was employed to increase the visibility of the paramagnetic species, and the reaction was performed in the presence of TsN_3 (100 equiv, 0.085 M) and CN^{t}Bu (165 equiv, 0.140 M). Here, the trichromium cluster **Cr$_3$** is denoted as **1**. 253

Figure 5.37. ^{1}H NMR (benzene-d_6, 25 °C, 500 MHz) spectra of the catalytic reaction upon mixing **Cr$_3$**$(NTs)_3$, TsN_3 and CN^{t}Bu, highlighting the diamagnetic region to show the clean conversion of tosyl azide to carbodiimide. A catalyst loading of 10 mol% **Cr$_3$**$(NTs)_3$ (0.0085 M, 10 equiv) was employed to increase the visibility of the paramagnetic species, and the reaction was performed in the presence of TsN_3 (100 equiv, 0.085 M) and CN^{t}Bu (165 equiv, 0.140 M). Here, the trichromium cluster **Cr$_3$** is denoted as **1**..... 254

Figure 5.38. ^{1}H NMR (benzene-d_6, 25 °C, 500 MHz) spectra tracking the reaction of **Cr$_3$**$(py)_3$ with TsN_3 (3 equiv). The *in situ* reaction mixture after 15 min is plotted in comparison to that of isolated **Cr$_3$**$(NTs)_3$ in benzene-d_6. Here, the trichromium cluster **Cr$_3$** is denoted as **1**. 255

Figure 5.39. Solid-state structure of **Cr$_3$**$(py)_3$ with thermal ellipsoids plotted at a 50% probability level. All hydrogen atoms are omitted for clarity. Selected interatomic distances (Å): Cr1-Se2 2.581(1), Cr1-Se1 2.726(1), Cr2-Se3 2.647(2), Cr2-Se4 2.703(2), Cr3-Se6 2.637(1), Cr3-Se5 2.719(2), Cr1-N7 2.102(7), Cr2-N8 2.150(8), Cr3-N9 2.116(7), Cr1-N1 2.022(7), Cr2-N3 2.059(8), Cr3-N6 2.047(7), Cr3…Co5 3.25(1). 257

Figure 5.40. Solid-state structure of **Cr$_3$**$(NTs)_3 \cdot 2\ CH_2Cl_2$ with thermal ellipsoids plotted at a 50% probability level. All hydrogen atoms and co-crystallizing DCM molecules are omitted for clarity. Selected interatomic distances (Å) and angles (°): Cr1-Se1 2.513(5), Cr2-Se3 2.471(5), Cr3-Se6 2.463(5), Cr1-N7 1.81(2), Cr2-N8 1.82(2), Cr3-N9 1.84(2), Cr1-O1 2.12(2), Cr2-O2 2.10(2), Cr3-O3 2.05(2), Cr1-N1 1.88(2), Cr2-N3 1.91(2), Cr3-N5 1.87(2), Cr1…Co1 3.750(5), Cr1-N7-S1 95.2(1), Cr2-N8-S2 96.2(13), Cr3-N9-S3 95.8(13).258

Figure 5.41. Solid-state structure of **Cr$_3$**$(NTs)_3(CN^tBu)_3$ with thermal ellipsoids plotted at a 50% probability level. All hydrogen atoms and disorder are omitted for clarity. Selected interatomic distances (Å): Cr1-Se2 2.574(3), Cr2-Se4 2.605(3), Cr3-Se6 2.656(6), Cr1-N7 1.746(8), Cr2-N8 1.747(8), Cr3-N9 1.745(8), Cr1-C136 2.07(1), Cr2-C141 2.07(1), Cr3-C146 2.07(1), Cr1-N7-S1 143.7(6), Cr2-N8-S2 142.7(5), Cr3-N9-S3 144.5(6).... 259

Figure 5.42. Solid-state structure of **Cr$_3$**(NTs)$_3$(CN^{t}Bu)$_3$ plotting both disordered components (each with ~50% abundance). The two components are compositionally identical but exhibit slight structural differences. 260

Figure 5.43. Solid-state structure of **Cr$_3$**(NTs)(CN^{t}Bu)$_2$ with thermal ellipsoids plotted at a 50% probability level. All hydrogen atoms and disorder are omitted for clarity. Selected interatomic distances (Å): Cr1A-Se2 2.444(2), Cr2-Se3 2.611(2), Cr2-Se4 2.663(2), Cr3-Se6 2.648(2), Cr3-Se5 2.655(2), Cr1A-N7 1.86(1), Cr1A-N1A 2.02(2), Cr3-N5 2.059(9), Cr2-C122 2.09(1), Cr3-C127 2.07(1). 261

Figure 6.1. Cr/Co/Se nanoclusters enable a molecular investigation of the electronic forces that guide active site speciation. 270

Figure 6.2. ^{1}H NMR (C_6D_6, 25 °C, 500 MHz) spectra tracking the reaction of **Cr$_3$**(NTs)$_3$ with CN^{t}Bu (4 equiv). Spectra recorded at different timepoints in the reaction were plotted in comparison to the starting material, **Cr$_3$**(NTs)$_3$, and the purified product, **Cr$_3$**(NTs)(CN^{t}Bu)$_2$. 275

Figure 6.3. ^{1}H NMR (C_6D_6, 25 °C, 300 MHz) spectra of **Cr$_3$**(CN^{t}Bu)$_3$, **Cr$_3$**(NTs)(CN^{t}Bu)$_2$, **Cr$_3$**(NTs)$_2$(CN^{t}Bu), **Cr$_3$**(NTs)$_3$, **Cr$_3$**(NTs)$_2$(py), **Cr$_3$**(NTs)(py)$_2$, and **Cr$_3$**(py)$_3$ (listed from top to bottom), with boxes included to highlight diagnostic spectral features. 276

Figure 6.4. ^{1}H NMR (C_6D_6, 25 °C, 300 MHz) spectra of **Cr$_3$**(NTs)(CN^{t}Bu)$_2$, **Cr$_3$**(NTs)$_2$(CN^{t}Bu), **Cr$_3$**(NTs)$_3$, **Cr$_3$**(NTs)$_2$(py), and **Cr$_3$**(NTs)(py)$_2$, highlighting the N-tosyl ^{1}H region.277

Figure 6.5. ^{1}H NMR (C_6D_6, 25 °C, 500 MHz) spectra tracking the reaction of **Cr$_3$**(py)$_3$ with TsN_3 (2 equiv). The *in situ* reaction mixture after 15 min is plotted in comparison to that of purified **Cr$_3$**(NTs)$_2$(py) in C_6D_6. 278

Figure 6.6. a) Single crystal X-ray structure of *trans*-(α,β,α)-**Cr$_3$**(NTs)$_2$(py) with insets highlighting Cr(py) and Cr(NTs) edge sites. b) Comparison of Cr···Se (α, black; β, gray) and Cr-NTs (blue) bond metrics across the crystallographically characterized Cr(NTs)/Cr(py)/Cr(CN^{t}Bu) series. Thermal ellipsoids plotted at 50% probability. Hydrogen atoms and co-crystallizing solvent omitted for clarity. 280

Figure 6.7. Single crystal X-ray structure of **Cr$_3$**(NHCHPh)$_3$ with an inset highlighting the Cr(NHCHPh) edge site. Select interatomic distances (Å): Cr1-N7 2.073(6), Cr1-Se1 2.633(1), Cr1-Se2 2.697(1), Cr1-N1 2.046(5), C115-N7 1.274(8). 283

Figure 6.8. Mulliken spin density (*a*-*b*) isosurface plots (0.004 a.u.) of **Cr$_3$**(py)$_3$′ and **Cr$_3$**(NTs)$_3$′. Positive spin density values (green) are tabulated for the Cr edge metals and Co_6Se_8 core. 285

Figure 6.9. Partial density of states plots illustrating Co 3d , Se 4p and Cr 3d orbital contributions for **Cr$_3$**(py)$_3$′, **Cr$_3$**(NTs)(py)$_2$′, **Cr$_3$**(NTs)$_2$(py)′, and **Cr$_3$**(NTs)$_3$′. Calculations run at the uB3LYP+/cc-PVTZ level of theory. 285

Figure 6.10. Frontier molecular orbital diagrams of **Cr$_3$**(py)$_3$′, **Cr$_3$**(NTs)(py)$_2$′, **Cr$_3$**(NTs)$_2$(py)′, and **Cr$_3$**(NTs)$_3$′, normalized to the highest-lying core-centered electronic states. Orbital topology is denoted in text that is color-coded to pair with representative molecular orbital plots provided below. Separate spin manifolds are denoted as *a* and *b*. All calculations run at the uB3LYP+/cc-PVTZ level of theory. 286

Figure 6.11. Isosurface plots (0.04 a.u.) for select frontier orbitals of **Cr$_3$**(py)$_3$′ and **Cr$_3$**(NTs)$_2$(py)′. All calculations run at the uB3LYP+/cc-PVTZ level of theory. .. 287

Figure 6.12. Isosurface plots (0.04 a.u.) for select frontier orbitals of **Cr$_3$**(NTs)(py)$_2$′ and **Cr$_3$**(NTs)$_3$′. All calculations run at the uB3LYP+/cc-PVTZ level of theory..... 288

Figure 6.13. Dative Cr–Se *σ*-bonds form as a symmetry adapted linear combination of in-line Cr, Se, and Co atoms. Note that in the case of the weak axial Cr(py)–Se bond, the first antibonding state is singly occupied. 291

Figure 6.14. Qualitative depictions of the primary molecular orbitals responsible for Cr/Se/Co bonding. Red traces indicate topology of Cr–Se bonding interactions between Cr $3d_{z2}/3d_{x2-y2}$ and Se $4p_z$. Blue orbitals indicate topology of Cr–Se antibonding interactions between Cr $3d_{z2}/3d_{x2-y2}$ and Se $4p_z$, which are singly occupied along the weakened axial Cr–Se interactions present at Cr(py) edges. Red, purple, and blue dots denote Se atoms where these orbitals intersect via the provided interference patterns. 292

Figure 6.15. Single crystal X-ray comparison of **Cr$_3$**(py)$_3$, **Cr$_3$**(NTs)(py)$_2$, **Cr$_3$**(NTs)$_2$(py), and **Cr$_3$**(NTs)$_3$. Interatomic distances (Å), depicted in red or blue to pair with the orbital traces in Figure 6.14, are reflective of the presence of Cr–Se···Co–Se bonding interactions. All hydrogen atoms, chemical disorder, co-crystallizing solvents, and phosphinoamide carbon and phosphorous atoms are omitted to clarify the structure of the inorganic core. 294

Figure 6.16. Comparison of the single crystal X-ray structures of **Cr$_3$**(NTs)$_3$(CN^{t}Bu)$_3$ and **Cr$_3$**(NTs)$_3$, with outlines to highlight the topology of *Cr–Se···Co–Se* bonding interactions. Orbital crossing points are denoted by red dots. 295

Figure 6.17. Cyclic voltammograms of $Co_6Se_8L^{Tol,H}_6$, **Cr$_3$**(py)$_3$, and **Cr$_3$**(NTs)$_3$ recorded at 50 mV/s with 0.1 M [^{n}Bu$_4$N][PF$_6$] as the supporting electrolyte. The dashed trace represents a differential pulse voltammogram collected in DFB. Open circuit potentials are denoted with black arrows. 296

Figure 6.18. Variable-temperature dc magnetic susceptibility of **Cr$_3$**(py)$_3$ and **Cr$_3$**(NTs)$_3$, [**Cr$_3$**(NTs)$_3$][PF$_6$] and [K(2,2,2-crypt)]$_3$[**Cr$_3$**(NTs)$_3$] collected upon warming from 2.5 to 300 K with an applied field of 0.5 T. 298

Figure 6.19. ^{1}H NMR (C$_6$D$_6$, 25 °C, 300 MHz) spectrum of [**Cr$_3$**(NTs)$_3$][PF$_6$]. Gray dot indicate solvent (toluene, *o*-DFB) resonances. 300

Figure 6.20. Single-crystal X-ray structures of a) [**Cr$_3$**(NTs)$_3$][PF$_6$] and b) [K(18-C-6)][**Cr$_3$**(NTs)$_3$]. Insets provided to highlight Cr(NTs) and [K(18-C-6)][Cr(NTs)] edge sites, with thermal ellipsoids plotted at 30% probability. All hydrogen atoms, positional disorder and solvent molecules omitted for clarity. 301

Figure 6.21. ^{1}H NMR (C$_6$D$_6$, 25 °C, 300 MHz) spectrum of **Cr$_3$**(NTs)(py)$_2$. Gray dot indicates *n*-pentane resonance. 305

Figure 6.22. ^{1}H NMR (C$_6$D$_6$, 25 °C, 300 MHz) spectrum of **Cr$_3$**(NTs)$_2$(py). Gray dots indicate toluene/*n*-pentane resonances. 307

Figure 6.23. ^{1}H NMR (C$_6$D$_6$, 25 °C, 300 MHz) spectrum of **Cr$_3$**(NTs)$_2$(CN^{t}Bu). Gray dot indicates *n*-pentane or toluene resonances. Here, the trichromium cluster **Cr$_3$** is denoted as **1**. 308

Figure 6.24. ^{1}H NMR (C$_6$D$_6$, 25 °C, 300 MHz) spectrum recorded for crystalline [K(18-C-6)][**Cr$_3$**(NTs)$_3$], revealing that the compound undergoes disproportionation in solution. Here, the trichromium cluster **Cr$_3$** is denoted as **1**. 311

Figure 6.25. ^{1}H NMR (C$_6$D$_6$, 25 °C, 500 MHz) spectra tracking the reaction of **Cr$_3$**(py)$_3$ with TsN$_3$ (2 equiv). The *in situ* reaction mixture after 15 min is plotted in comparison to that of purified **Cr$_3$**(NTs)$_2$(py) in C$_6$D$_6$. Here, the trichromium cluster **Cr$_3$** is denoted as **1**. 312

Figure 6.26. ^{1}H NMR (THF-d_8 {top}, benzene-d_6 {bottom}, 25 °C, 500 MHz) spectra tracking the reaction of **Cr$_3$**(py)$_3$ with TsN_3 (1 equiv). The *in situ* reaction mixture in THF-d_8 is plotted in comparison to that of the starting material in benzene-d_6. Here, the trichromium cluster **Cr$_3$** is denoted as **1**. 313

Figure 6.27. ^{1}H NMR (C_6D_6, 25 °C, 500 MHz) spectra tracking the reaction of **Cr$_3$**(NTs)$_3$ with CN^{t}Bu (2 equiv). Spectra recorded at different timepoints in the reaction were plotted in comparison to the starting material **Cr$_3$**(NTs)$_3$ and the purified product **Cr$_3$**(NTs)$_2$(CN^{t}Bu). Here, the trichromium cluster **Cr$_3$** is denoted as **1**..... 314

Figure 6.28. Cyclic voltammograms of **Cr$_3$**(py)$_3$ recorded between 25 and 500 mV s^{-1} in 0.1 M [^{n}Bu$_4$N][PF_6] DCM and referenced to ferrocene (top) and a plot of current density (j_p) versus the square root of scan rate ($v^{1/2}$) with linear fits used to model the data with the Randles–Sevcik equation (bottom). 316

Figure 6.29. Cyclic voltammograms of **Cr$_3$**(py)$_3$ recorded between 25 and 500 mV s^{-1} in 0.1 M [^{n}Bu$_4$N][PF_6] THF and referenced to ferrocene (top) and a plot of current density (j_p) versus the square root of scan rate ($v^{1/2}$) with linear fits used to model the data with the Randles–Sevcik equation (bottom). 317

Figure 6.30. Cyclic voltammograms of **Cr$_3$**(NTs)$_3$ recorded between 25 and 500 mV s^{-1} in 0.1 M [^{n}Bu$_4$N][PF_6] DFB and referenced to ferrocene (top) and a plot of current density (j_p) versus the square root of scan rate ($v^{1/2}$) with linear fits used to model the data with the Randles–Sevcik equation (bottom). 318

Figure 6.31. Cyclic voltammograms of **Cr$_3$**(py)$_3$, **Cr$_3$**(NTs)$_3$, **Cr$_3$**(NTs)$_2$(py) and **Cr$_3$**(NTs)(py)$_2$, recorded at 50 mV s^{-1} in 0.1 M [^{n}Bu$_4$N][PF_6] DFB, THF or DCM and referenced to ferrocene. Open circuit potentials denoted with black arrows. In the case of **Cr$_3$**(NTs)(py)$_2$, multiple potential windows were sample to verify the reversibility of the electrochemical events. 319

Figure 6.32. Differential pulse voltammogram of the three reduction processes of **Cr$_3$**(NTs)$_3$ in 0.1 M [^{n}Bu$_4$N][PF_6] in DFB solution. Step size = 2 mV, Pulse amplitude = 25 mV, Sample period = 2 s, Pulse time = 0.5 s. 320

Figure 6.33. (left) Variable-temperature *dc* magnetic susceptibility ($\chi_M T$, filled circles) data recorded for **Cr$_3$**(py)$_3$ upon warming from 5 to 300K under applied fields of 0.1, 0.5, and

1.0 T. (right) Reciprocal molar susceptibility ($1/\chi_M$) data recorded for **Cr$_3$**(py)$_3$ upon warming from 5 to 300K with an applied field of 0.5 T. A linear fit to the data between 25 and 150 K was used to calculate Curie (C) and Weiss (θ) constants. 321

Figure 6.34. (left) Variable-temperature, variable-field reduced magnetization data for **Cr$_3$**(py)$_3$, collected upon warming from 2.5 to 10 K at each applied field. This plot confirms the presence of a high-spin ground state, but the sample resists magnetic saturation under applied magnetic fields up to 7.0 T. (right) Magnetization of **Cr$_3$**(py)$_3$ recorded on sweeping the applied field from 0 and 14 T at 50 K. 322

Figure 6.35. (left) Variable-temperature *dc* magnetic susceptibility (χ_MT, filled circles) data recorded for **Cr$_3$**(NTs)$_3$ upon warming from 5 to 300K under applied fields of 0.1, 0.5, and 1.0 T. (right) Reciprocal molar susceptibility ($1/\chi_M$) data recorded for **Cr$_3$**(NTs)$_3$ upon warming from 5 to 300K with an applied field of 0.5 T. 322

Figure 6.36. (left) Variable-temperature, variable-field reduced magnetization data for **Cr$_3$**(NTs)$_3$, collected upon warming from 2.5 to 10 K at each applied field. This plot confirms the presence of a high-spin ground state, but the sample resists magnetic saturation under applied magnetic fields up to 7.0 T. (right) Magnetization of **Cr$_3$**(NTs)$_3$ recorded on sweeping the applied field from 0 and 14 T at 50 K. 323

Figure 6.37. (left) Variable-temperature *dc* magnetic susceptibility (χ_MT, filled circles) data recorded for [**Cr$_3$**(NTs)$_3$][PF$_6$] upon warming from 5 to 300K under applied fields of 0.1, 0.5, and 1.0 T. (right) Reciprocal molar susceptibility ($1/\chi_M$) data recorded for [**Cr$_3$**(NTs)$_3$][PF$_6$] upon warming from 5 to 300K with an applied field of 0.5 T... 323

Figure 6.38. (left) Variable-temperature, variable-field reduced magnetization data for [**Cr$_3$**(NTs)$_3$][PF$_6$], collected upon warming from 2.5 to 10 K at each applied field. This plot confirms the presence of a high-spin ground state, but the sample resists magnetic saturation under applied magnetic fields up to 7.0 T. Magnetization of [**Cr$_3$**(NTs)$_3$][PF$_6$] recorded on sweeping the applied field from 0 and 14 T at 50 K. 324

Figure 6.39. (left) Variable-temperature *dc* magnetic susceptibility (χ_MT, filled circles) data recorded for [K(222-crypt)]$_3$[**Cr$_3$**(NTs)$_3$] upon warming from 5 to 300K under applied fields of 0.1, 0.5, and 1.0 T. (right) Reciprocal molar susceptibility ($1/\chi_M$) data recorded for

[K(222-crypt)]$_3$[**Cr$_3$**(NTs)$_3$] upon warming from 5 to 300K with an applied field of 0.5 T. 324

Figure 6.40. (left) Variable-temperature, variable-field reduced magnetization data for [K(222-crypt)]$_3$[**Cr$_3$**(NTs)$_3$], collected upon warming from 2.5 to 10 K at each applied field. This plot confirms the presence of a high-spin ground state, but the sample resists magnetic saturation under applied magnetic fields up to 7.0 T. (right) Magnetization of [K(222-crypt)]$_3$[**Cr$_3$**(NTs)$_3$] recorded on sweeping the applied field from 0 and 14 T at 50 K.325

Figure 6.41. Isosurface plots (0.04 a.u.) for select molecular orbitals of **Cr$_3$**(py)$_3$′ and **Cr$_3$**(NTs)$_3$′. The orbitals are illustrative of the following interactions: 1) **Cr$_3$**(py)$_3$′ *a*-(HOMO-23) depicts the *Cr–Se···Co–Se* bonding orbital that projects along the axial Cr–Se bond, and represents a bonding counterpart to the HOMO; 2) **Cr$_3$**(py)$_3$′ *a*-(HOMO-24) depicts an analogous equatorial *Cr–Se···Co–Se* bonding orbital; 3) **Cr$_3$**(NTs)$_3$′ *a*-(HOMO-8) exhibits *Cr–Se···Co–Se* character, confirming presence of the same bonding motif at Cr(NTs) edge sites; 4) **Cr$_3$**(NTs)$_3$′ *a*-(HOMO-9) exhibits *Cr–Se–Co–Se* all-bonding character. Outlines included to aid inspection, which is admittedly very challenging, even for the author. All calculations run at the B3LYP+/cc-PVTZ level of theory. 326

Figure 6.42. Solid-state structure of *trans*-(α,β,α)-**Cr$_3$**(NTs)$_2$(py) with thermal ellipsoids plotted at 50% probability. All hydrogen atoms, co-crystallizing solvent molecules and instances of chemical disorder are omitted for clarity. Selected interatomic distances (Å) and angles (°): Cr1-N7 2.073(8), Cr2-N8 1.829(8), Cr3-N9 1.832(8), Cr2-O1 2.097(6), Cr3-O3 2.062(6), Cr1-Se2 2.6392(16), Cr1-Se1 2.7243(17), Cr2-Se3 2.4755(15), Cr3-Se6 2.4801(17), Cr1-N1 2.053(7), Cr2-N3 1.904(7), Cr3-N5 1.926(7), Cr2-N8-S1 95.5(4), Cr3-N9-S2 94.5(4). 333

Figure 6.43. Solid-state structure of **Cr$_3$**(NHCHPh)$_3$ with thermal ellipsoids plotted at 50% probability. All hydrogen atoms, co-crystallizing solvent molecules and instances of chemical disorder are omitted for clarity. Selected interatomic distances (Å) and angles (°): Cr1-N7 2.073(6), Cr2-N8 2.095(17), Cr3-N9 2.053(6); Cr1-Se1 2.633(1), Cr1-Se2 2.697(1), Cr2-Se4 2.653(1), Cr2-Se3 2.711(1), Cr3-Se6 2.613(1), Cr3-Se5 2.714(1), Cr1-N1 2.046(5), Cr1-N2 2.053(6), Cr2-N3 2.051(5), Cr2-N4 2.062(5), C122-N8 1.252(17), C115-N7 1.274(8), C129-N9 1.237(13). 334

Figure 6.44. Solid-state structure of [**Cr$_3$**(NTs)$_3$][PF$_6$] with thermal ellipsoids plotted at 50% probability. All hydrogen atoms, co-crystallizing solvent molecules and instances of chemical disorder are omitted for clarity. Selected interatomic distances (Å) and angles (°): Cr4-N16 1.81(3), Cr5-N17 1.92(3), Cr6-N18 1.80(2), Cr5-O9 2.04(2), Cr4-Se10 2.547(6), Cr5-Se12 2.469(7), Cr6-Se9 2.499(6), Se10-Co8 2.546(5), Co8-Se14 2.280(6), Cr4-N10 1.91(3), Cr5-N12 1.98(3), Cr6-N8 1.88(3). 335

Figure 6.45. Solid-state structure of [K(18-C-6)][**Cr$_3$**(NTs)$_3$] with thermal ellipsoids plotted at 50% probability. All hydrogen atoms, co-crystallizing solvent molecules and instances of chemical disorder are omitted for clarity. Selected interatomic distances (Å) and angles (°): Cr1-Se2 2.563(5), Cr2-Se3 2.371(5), Cr3-Se6 2.359(5), Cr1-N7 1.732(19), Cr2-N8 1.78(2), Cr3-N9 1.75(2), Cr1-N1 1.873(17), Cr1-N2 1.797(16), Cr2-N3 1.821(16), Cr3-N5 1.786(17), Cr2-O3 1.977(18), Cr3-O5 1.988(17), Co3-Se2 2.263(4), Co3-Se4 2.230(4), Co1-Se6 2.299(4), Co1-Se2 2.221(4). 336

LIST OF SCHEMES

Scheme 1.1. Synthesis of nanopropeller $Fe_3Co_6Se_8L^{Tol}_6$ (**Fe$_3$**). 4

Scheme 1.2. Chemical redox transformations of $Co_6Se_8L^{Tol,H}_6$ and **Fe$_3$** clusters. 6

Scheme 2.1. Attempted cluster synthesis with the aminophosphine $^{i}Pr_2PN(H)^{i}Pr$ leads to formation of dimer **Co$_2$**, with no other detectable products. 67

Scheme 2.2. Effects of the stoichiometry of reagents on the nuclearity and ratio of the cobalt selenide clusters produced in the reaction of $Co_2(CO)_8$, Se, $L^{iPr,H}$ or $Se{=}L^{iPr,H}$ in refluxing toluene. 68

Scheme 2.3. Chemical oxidation of the homoleptic [Co_6Se_8] cluster, $Co_6Se_8L^{iPr,H}_6$. 76

Scheme 2.4. Synthesis of trimetallated nanopropellers **Fe$_3$**$^{i\text{Pr}}$ and **Zn$_3$**$^{i\text{Pr}}$. 77

Scheme 3.1. Chemical oxidation of **Fe$_3$** to yield a family of bis-ligated adducts. 121

Scheme 3.2. Proposed multi-site mechanism for the interconversion of [**Fe$_3$**$(CN^{t}Bu)_2]^+$ and [**Fe$_3$**$(THF)_2]^+$ via allosteric ligand substitution. 127

Scheme 4.1. Synthesis of tritopic nanocluster building block, **Co$_3$**$(py)_3$; $L^{Tol,H} = Ph_2PN(H)Tol$; py = pyridine. 170

Scheme 4.2. Self-assembly of van der Waals nanosheets, **Co$_3$**(bpy), **Co$_3$**(bpy_σ), and **Co$_3$**(bpy_π), from tritopic nanoblock **Co$_3$**$(py)_3$ and pyridyl-based ditopic linkers. 175

Scheme 5.1. Synthesis of the Cr/Co/Se nanocluster, **Cr$_3$**$(py)_3$. 214

Scheme 5.2. Stoichiometric syntheses and isolated yields of catalytically competent azide activation and nitrene transfer intermediates. 217

Scheme 6.1. Stoichiometric azide activation and nitrene transfer to yield a series of site-differentiated Cr(NTs)/Cr(py)/Cr($CN^{t}Bu$) nanoclusters. 274

Scheme 6.2. Chemical redox transformations of the tris(imido) nanocluster **Cr$_3$**$(NTs)_3$.299

LIST OF TABLES

Table 1.1. A compilation of the *tert*-butyl isocyanide binding constants for the neutral, oxidized and reduced tri-iron clusters **Fe$_3$**, [**Fe$_3$**(CN^{t}Bu)$_2$][PF$_6$], and [^{n}Bu$_4$N][**Fe$_3$**]..... 31

Table 1.2. Half-wave potentials ($E_{1/2}$) and peak-to-peak separation potentials (ΔE_p) of **Fe$_3$**, **Fe$_3$**(MeCN)(OTf), [**Fe$_3$**(CN^{t}Bu)$_2$][PF$_6$], and [**Fe$_3$**(phen)$_3$][PF$_6$] recorded in 0.1 M [^{n}Bu$_4$N][PF$_6$] DCM (or THF) solutions at a scan rate of 200 mV/s. 41

Table 1.3. Diffusion coefficients (D_0) obtained by applying the Randles–Sevcik equation assuming n_e=1 for various oxidation states determined from cyclic voltammograms of **Fe$_3$**, **Fe$_3$**(MeCN)(OTf), [**Fe$_3$**(CN^{t}Bu)$_2$][PF$_6$], and [**Fe$_3$**(phen)$_3$][PF$_6$] recorded in 0.1 M [^{n}Bu$_4$N][PF$_6$] DCM. 41

Table 1.4. Half-wave potentials ($E_{1/2}$), peak-to-peak separation potentials (ΔE_p), and open circuit potentials (OCP) of Co$_6$Se$_8$L$^{Tol,H}_6$ and **Fe$_3$** recorded in 0.1 M [^{n}Bu$_4$N][PF$_6$] DCM or (THF) with a scan rate of 200 mV/s..... 42

Table 1.5. Diffusion coefficients (D_0) obtained by applying the Randles–Sevcik equation assuming n_e=1 for various oxidation states determined from cyclic voltammograms of Co$_6$Se$_8$L$^{Tol,H}_6$, **Fe$_3$**, and [**Fe$_3$**(CN^{t}Bu)$_2$][PF$_6$] recorded in 0.1 M [^{n}Bu$_4$N][PF$_6$] DCM.43

Table 1.6. Zero-field ^{57}Fe Mössbauer parameters for [**Fe$_3$**(CN^{t}Bu)$_2$][PF$_6$], [**Fe$_3$**(phen)$_3$][PF$_6$], **Fe$_3$**(CN^{t}Bu)$_3$, **Fe$_3$**, and [^{n}Bu$_4$N][**Fe$_3$**Co$_6$Se$_8$L$_6$] collected at 90 K. 44

Table 1.7. Minimum and maximum values for select interatomic distances as determined by single crystal X-ray diffractometry. 53

Table 1.8. Crystallographic information for Co$_6$Se$_8$L$^{Tol,H}_6$, [Co$_6$Se$_8$L$^{Tol,H}_6$][OTf], and **Fe$_3$**(CN^{t}Bu)$_3$. 54

Table 1.9. Crystallographic information for [**Fe$_3$**(phen)$_3$][PF$_6$], [Na(18-C-6)(MeCN)$_2$][**Fe$_3$**], and [**Fe$_3$**(CN^{t}Bu)$_2$][PF$_6$]. 55

Table 2.1. Half-wave potentials ($E_{1/2}$) and open circuit potentials (OCP) of **Zn$_3$**$^{i\text{Pr}}$ and **Fe$_3$**$^{i\text{Pr}}$ recorded in 0.1 M [^{n}Bu$_4$N][PF$_6$] THF or (DCM) at 50 mV/s. 96

Table 2.2. Crystallographic information for Co$_6$Se$_8$L$^{iPr,H}_6$, [Co$_6$Se$_8$L$^{iPr,H}_6$][PF$_6$]. 108

Table 2.3. Crystallographic information for **Co$_4$Se$_2$**, **Co$_3$Se**, and **Co$_2$**. 109

Table 2.4. Crystallographic information for **Fe$_3$**$^{i\text{Pr}}$, **Zn$_3$**$^{i\text{Pr}}$. 110

Table 3.1. Select interatomic distances for **Fe$_3$**(MeCN)(OTf), [**Fe$_3$**(CN^{t}Bu)$_2$][PF$_6$], and [**Fe$_3$**(phen)$_3$][PF$_6$]. Bonding parameters involving Fe centers as well as τ4 values are listed for Fe1, Fe2, and Fe3 from top to bottom. 151

Table 3.2. Select interatomic distances for [**Fe$_3$**(THF)$_2$][PF$_6$] and both measurements of [**Fe$_3$**(CN^{t}Bu)$_2$(THF)]/*trans*-(α,β)-[**Fe$_3$**(CN^{t}Bu)(THF)][PF$_6$]. Parameters involving Fe centers as well as τ4 values are listed for Fe1, Fe2, and Fe3 from top to bottom. 152

Table 3.3. Crystallographic data for duplicate measurements of disordered [**Fe$_3$**(CN^{t}Bu)$_2$(THF)]/*trans*-(α,β)-[**Fe$_3$**(CN^{t}Bu)(THF)][PF$_6$]. Separate measurements denoted at (1) or (2). 153

Table 3.4. Crystallographic data for [**Fe$_3$**(THF)$_2$][PF$_6$], **Fe$_3$**(MeCN)(OTf), and **Fe$_3$**(py)$_x$ (x = 2, 3). 154

Table 3.5. Comparison of bond metrics of the DFT optimized structures of [**Fe$_3$**(CNMe)$_2$]$^+$ and [**Fe$_3$**(CNMe)$_2$(THF)]$^+$ and those of the related single-crystal X-ray diffraction structures of [**Fe$_3$**(CN^{t}Bu)$_2$][PF$_6$] and [**Fe$_3$**(CN^{t}Bu)$_2$(THF)][PF$_6$]. 156

Table 3.6. Comparison of bond metrics of the DFT optimized structures of *trans*-(α,β)-[**Fe$_3$**(CNMe)(THF)]$^+$ and *cis*-(α,β)-[**Fe$_3$**(THF)$_2$] and those of the related single-crystal X-ray diffraction structures of *trans*-(α,β)-[**Fe$_3$**(CN^{t}Bu)(THF)][PF$_6$] and *cis*-(α,β)-[**Fe$_3$**(THF)$_2$][PF$_6$]. 157

Table 3.7. Total energies calculated for *cis*-(α,β)-[**Fe$_3$**(CNMe)$_2$]$^+$, [**Fe$_3$**(CNMe)$_2$(THF)]$^+$, [**Fe$_3$**(CNMe)(THF)]$^+$, [**Fe$_3$**(CNMe)(THF)$_2$]$^+$, [**Fe$_3$**(THF)$_2$]$^+$, *trans*-(α,β)-[**Fe$_3$**(CNMe)$_2$]$^+$, and (α,α)-[**Fe$_3$**(CNMe)$_2$]$^+$ at the B3LYP+/cc-pVTZ level of theory. 158

Table 3.8. Hirshfeld spin-density values calculated for [**Fe$_3$**(CNMe)$_2$]$^+$, [**Fe$_3$**(CNMe)$_2$(THF)]$^+$, [**Fe$_3$**(CNMe)(THF)]$^+$, [**Fe$_3$**(CNMe)(THF)$_2$]$^+$, and [**Fe$_3$**(THF)$_2$]$^+$ at the B3LYP+/cc-pVTZ level of theory. 159

Table 3.9. Hirshfeld charges calculated for [**Fe$_3$**(CNMe)$_2$]$^+$, [**Fe$_3$**(CNMe)$_2$(THF)]$^+$, [**Fe$_3$**(CNMe)(THF)]$^+$, [**Fe$_3$**(CNMe)(THF)$_2$]$^+$, and [**Fe$_3$**(THF)$_2$]$^+$ at the B3LYP+/cc-pVTZ level of theory. 160

Table 4.1. Half-wave potentials ($E_{1/2}$), peak-to-peak separation potentials (ΔE_p), and open circuit potentials (OCP) of **Co$_3$**(py)$_3$ recorded in 0.1 M [^{n}Bu$_4$N][PF$_6$] DCM or (THF) at 200 mV/s. 196

Table 4.2. Diffusion coefficients (D_0) obtained by applying the Randles–Sevcik equation assuming n_e=1 for various oxidation states determined from cyclic voltammograms of **Co$_3$**(py)$_3$ recorded in 0.1 M [^{n}Bu$_4$N][PF$_6$] DCM or (THF). 196
Table 4.3. Half-wave potentials ($E_{1/2}$), peak-to-peak separation potentials (ΔE_p), and open circuit potentials (OCP) of **Co$_3$**(bpy), **Co$_3$**(bpy$_\pi$), and **Co$_3$**(bpy$_\sigma$) recorded in 0.1 M [^{n}Bu$_4$N][PF$_6$] DCM or (MeCN) at 200 mV/s. 196
Table 4.4. Crystallographic information for **Co$_3$**(py)$_3$ and **Co$_3$**(bpy). 202
Table 4.5. Crystallographic information for **Co$_3$**(bpy$_\pi$), **Co$_3$**(bpy$_\sigma$), and [**Co$_3$**(bpy$_\sigma$)][TCNE]$_2$. 203
Table 5.1. Binding constants collected for **Cr$_3$**(NTs)$_3$ and **Cr$_3$**(NTs)(CN^{t}Bu)$_2$ in the presence of varying equivalents of added isocyanide in benzene-d_6. 230
Table 5.2. Crystallographic information for **Cr$_3$**(py)$_3$ and **Cr$_3$**(NTs)$_3$ 262
Table 5.3. Crystallographic information for **Cr$_3$**(NTs)$_3$(CN^{t}Bu)$_3$ and **Cr$_3$**(NTs)(CN^{t}Bu)$_2$. 263
Table 6.1. Half-wave potentials ($E_{1/2}$) and open circuit potentials (OCP) of **Cr$_3$**(py)$_3$ and **Cr$_3$**(NTs)$_3$ recorded in 0.1 M [^{n}Bu$_4$N][PF$_6$] THF, DCM, or DFB solutions at 50 mV/s. 315
Table 6.2. Diffusion coefficients (D_0) obtained by applying the Randles–Sevcik equation assuming n_e=1 for various oxidation states determined from cyclic voltammograms of **Cr$_3$**(py)$_3$ recorded in either THF or (DCM) and **Cr$_3$**(NTs)$_3$ recorded in DFB, with 0.1 M [^{n}Bu$_4$N][PF$_6$] supporting electrolyte. 315
Table 6.3. Comparison of bond metrics of the DFT optimized structures of **Cr$_3$**(py)$_3$′ and **Cr$_3$**(NTs)$_3$′ to those extracted from the single-crystal X-ray diffraction structures of **Cr$_3$**(py)$_3$ and **Cr$_3$**(NTs)$_3$. Parameters listed from top to bottom correspond to α1, α2, and β edge sites, respectively. 327
Table 6.4. Comparison of bond metrics of the DFT optimized structures of **Cr$_3$**(NTs)(py)$_2$′ and **Cr$_3$**(NTs)$_2$(py)′ to those extracted from the single-crystal X-ray diffraction structures of **Cr$_3$**(NTs)(CN^{t}Bu)$_2$ and **Cr$_3$**(NTs)$_2$(py). Parameters listed from top to bottom correspond to α1, α2, and β edge sites, respectively. 328

Table 6.5. Total energies calculated for **Cr$_3$**(py)$_3$′, **Cr$_3$**(NTs)(py)$_2$′, *trans*-(α,β,α)-**Cr$_3$**(NTs)$_2$(py)′, *cis*-(α,β,α)-**Cr$_3$**(NTs)$_2$(py)′, *trans*-(α,α,β)-**Cr$_3$**(NTs)$_2$(py)′, **Cr$_3$**(NTs)$_3$′, and **Cr$_3$**(NTs)$_3$(CN^{t}Bu)$_3$′ calculated at the B3LYP+/cc-pVTZ level of theory. 329

Table 6.6. Composition analysis for the highest lying core-centered orbitals of **Cr$_3$**(py)$_3$′, **Cr$_3$**(NTs)(py)$_2$′, **Cr$_3$**(NTs)$_2$(py)′, and **Cr$_3$**(NTs)$_3$′ at the B3LYP+/cc-pVTZ level of theory. Orbital composition analysis conducted using Multiwfn (see Ref. 62)..... 330

Table 6.7. Hirshfeld spin-density (α−β) values calculated for **Cr$_3$**(py)$_3$′, **Cr$_3$**(NTs)(py)$_2$′, *trans*-(α,α,β)-**Cr$_3$**(NTs)$_2$(py)′, and **Cr$_3$**(NTs)$_3$′ at the B3LYP+/cc-pVTZ level of theory.331

Table 6.8. Hirshfeld charges calculated for **Cr$_3$**(py)$_3$′, **Cr$_3$**(NTs)(py)$_2$′, *trans*-(α,α,β)-**Cr$_3$**(NTs)$_2$(py)′, and **Cr$_3$**(NTs)$_3$′ at the B3LYP+/cc-pVTZ level of theory. 331

Table 6.9. Crystallographic information for **Cr$_3$**(NTs)(CN^{t}Bu)$_2$, **Cr$_3$**(NHCHPh)$_3$, and **Cr$_3$**(NTs)$_2$(py). 337

Table 6.10. Crystallographic information for [**Cr$_3$**(NTs)$_3$][PF$_6$] and [K(18-C-6)][**Cr$_3$**(NTs)$_3$]. 338

Table 6.11. Select interatomic distances for **Cr$_3$**(py)$_3$, **Cr$_3$**(NTs)$_2$(py), **Cr$_3$**(NTs)$_3$ · 2 CH_2Cl_2, **Cr$_3$**(NTs)$_3$(CN^{t}Bu)$_3$, and **Cr$_3$**(NTs)(CN^{t}Bu)$_2$. 339

ACKNOWLEDGEMENTS

This work did not take place within a vacuum – in fact, by and large it took place at room temperature under an atmosphere of dinitrogen within CHB 328. My educational experience has been shaped and defined by my interactions with countless mentors, friends, and family members. There are many people that I need to thank here.

First, I'd like to thank my advisor, Alexandra, whose fiery passion for science and determination to explore the unknown are the entire reason that I came to the University of Washington. I met Alexandra as a visiting student at her first recruitment weekend, where, after only briefly discussing her proposed research at her poster, I immediately knew I would pursue research in her lab. Not only has Alexandra has always pushed me to be the best scientist that I can be, but she has pushed me to truly believe in myself and ultimately draw strength from within. She shares an infectious excitement for her science and has always been willing to discuss new ideas or discoveries on the fly. Graduate school has its many peaks and valleys, and I am very grateful to have had an advisor who was always willing to discuss challenges and problems with an open heart. There are many lessons that I've learned from Alexandra over the years. My favorite, perhaps, draws from her adage "*If Lady Fortuna is in the lab, you don't want to leave until she does.*". Over these past few years, there were indeed many times that Lady Fortuna and I enjoyed late nights in lab, exploring the depths of our science together. Thank you, Alexandra, for all your support, advice, encouragement, and friendship over these past few years. It has been an honor to work with you.

Next, I'd like to thank the committee members and faculty who have enriched my experience here at UW, including Brandi Cossairt, Daniel Gamelin, Dianne Xiao, Julie Kovacs and Michael Heinekey. On that same visiting weekend described above, I met with Brandi Cossairt, whose InP cluster chemistry was the original draw for me to apply to the UW chemistry program. Stepping into Brandi's office, I was amazed to find she had photos of Sasha DiGiulian decorating her wall, which I appreciated as an avid rock climber. Brandi, I'm very grateful for the

opportunities to walk and talk, not only about science, but about life in general. Your support will always be greatly appreciated. I'm also grateful to Daniel Gamelin for the opportunities to discuss science, either in his office, after CHEM508, at the ORCAS conference, or over a beer at Big Time Brewing. It might sound crazy, but if I could, I would audit CHEM508 again each year. I thank Dianne Xiao for sharing kind words of support after several Inorganic Division Meeting presentations and for providing sage advice as I applied for postdoctoral research opportunities. I thank Julie Kovacs for her genuine excitement in discussing my graduate research, which often transpired not only during formal exams, but spontaneously in the hallway or the offices of CHB. Finally, I thank Michael Heinekey, whose course on organometallic chemistry I enjoyed immensely.

Many thanks are due to Velian group members, past and present. I'll start here with the present. Benjamin Mitchell is one of the most hard working, determined, and genuine people I've ever met. Ben, we had such a great dynamic working together in lab, with countless funny moments and discoveries made side-by-side. I could not have asked for a better glovebox partner than you. Thank you for the many brewery trips, the fly fishing, the ping-pong matches, and for confirming that you know how to bust-a-move on the dance floor at my wedding. Daniel Zhou, thank you for all the hard work you have put into **Fe$_3$** solvolysis project – as a glovebox partner, you give Ben a run for his money! Sebastian Krajewski, thank you for all your thoughtful feedback on writing projects and presentations over the years, and for sharing your cat-dad enthusiasm with me. I've enjoyed working with you both these past few years, and I'm excited to see which direction graduate school takes you. It has also been my privilege to work with Robert Love, who is a genuinely kind and thoughtful person. I thank the "2D" subgroup members, especially Kendahl Walz-Mitra, who frequently gave invaluable advice on writing styles, figure aesthetics, and professional correspondence, and Daniel Tofan, who shared his encyclopedic knowledge of coordination chemistry. I also thank Ella Spurlock, Michael Riehs, and Andrei Draguicevic for the good times in lab and in the office and wish them the very best in graduate school. I've found a real family here in the Velian group, and I'm grateful for each of you. I could not have made it through graduate school without you guys!

I have so many great memories from the early days in lab, and I must thank the members that were present those first years as we set up the lab space and established research projects. It

is entirely possible that Yuka Sakazaki is the most genuinely kind person I've ever had the great fortune to meet. Yuka, you are I truly were a dynamic duo setting up the lab together. You and Charles have been great friends and I wish you the very best. Christine Chang and Andrei Chirila shared such a positive energy in the lab space and always managed to keep things lively, even on those surprisingly late Friday nights. Christine's drawing skills and handwriting are impeccable. Andrei also shared his deep knowledge of coordination chemistry; I'm grateful to have learned from him as we worked to metallate our nanoclusters and explore their reactivity.

Next, I'll thank the undergraduate students that I've had the pleasure of working with. Andrew Boggiano joined us in that very first summer and demonstrated true grit by working late with all the graduate students and contributing to our early projects. Xiaory (Steven) Yu was another stellar undergraduate student who worked tirelessly to make *hundreds of grams* of pure starting materials that have catalyzed many research efforts in the lab. If asked how he was doing, Steven's typical reply was "Standard.". Finally, Catherine Romero was an excellent REU student joined the team over the summer of 2019 and played a key role in the **Co_3** self-assembly project. I am very proud of all these students and their accomplishments, and I'm thankful for their hard work in lab. Although he wasn't an undergraduate researcher, I also thank local high-school student Kailai Wang, for his after-school trips to the office where we discussed many fundamental topics in inorganic chemistry.

Outside of the Velian group, there are many students and postdocs throughout UW Chemistry and Physics that deserve thanks. I am eternally grateful to Louise Guard for her friendship, mentorship, and guidance throughout the first two years of my Ph.D. Louise, I grant you sole credit for introducing me to the Seattle craft beer scene. Dylan Rogers, who has become one of my absolute best friends. Your determination throughout graduate school has not gone unnoticed. Dmitry Ovchinnikov was a postdoc in the Xu group (UW Physics) whom I had the great fortune of meeting late one night in the MRSEC shared space as I worked to exfoliate my 2D van der Waals crystals. Dmitry periodically asked for well-activated 3Å molecular sieves prepared by "a good chemist", which I happily supplied in exchange for his advice on 2D materials. Dmitry has since become a dear friend and mentor and I am very grateful for that chance encounter so long ago. Jose Araujo has been an excellent mentor and friend – whenever I was performing a new measurement in lab, I knew he would have great advice. Several Cossairt group members

including Cecilia Johnson, Danielle Henckel, David Ung, Ian Murphy, and Michael Enright shared a sense of community, belonging, and friendship in those early years that I am grateful for. I'm also thankful to all of my collaborators, Kevin Anderton (Betley group, Harvard University), Paul Malinowski (Chu group, UW Physics), Chun-Chih Tseng (Yankowitz group, UW Physics), Jason Sandwisch (Khalil group, UW Chemistry), Nathalia Caijao (Neidig group, University of Rochester); Ryan Beck (Li group, UW Chemistry), and Avijit Hazra (Lalic group, UW Chemistry), who not only supported my research but taught me so much along the way. I was so lucky to interface with all of you during graduate school.

I want to thank the UW Chemistry instrumentation and office staff, who ensure all students have the resources and support they need. In particular, I thank Werner Kaminsky, with whom I've enjoyed many conversations over the years while conducting single crystal X-ray diffractometry. I also thank Rajan Paranji and Adrienne Rochelle, who work tirelessly to keep the NMR facility up and running. I want to thank Lochlan Hickok, who has always been extremely reliable and supportive throughout graduate school. Fun fact about Loch: in case you were wondering, he *is* related to Wild Bill Hickok of the Old West. Finally, I would like to thank Diana Knight and Christine Gormley for their support of myself and other graduate students here at UW Chemistry. The UW is very lucky to have all of you!

I thank the NSF for their financial support of our research (NSF CAREER Award #1944843). The UW Department of Chemistry provided generous support in the form of teaching assistantships, the Alvin L. Kwiram Graduate Research Fellowship, a Graduate Student Merit Fellowship, and the Alma Mater Travel award. The Clean Energy Institute provided generous support in the form of a CEI Graduate Research Fellowship and two travel grants. The American Chemical Society provided financial support to present my research at the Spring 2022 ACS National Meeting via a Division of Inorganic Chemistry travel award.

I was very fortunate throughout graduate school to enjoy good times and adventures with friends. Shayne Magstadt was my first climbing partner, and in the summer of 2019, was the best man at my wedding. Shayne, you really are like a brother to me. Thank you for standing by me all these years. I often reflect on our many days in the mountains together – let's get out and climb sometime soon. Bryce Tappan is my oldest running partner, which as it turns out also equates to a particularly strong bond. Although neither of us planned it, we've both ended up completing

Ph.D.'s in inorganic chemistry. Bryce, you've been an incredible support to me and a true friend for all these years – I'm looking forward to seeing you in Cambridge. I also thank Lucy Corro, Bonita Julius, Andrew Marotz, Mike Flynn, Adam Langland, Adam Stary, and Nick Bien, who have always kept me out of trouble. I thank Aaron Strom for being a great friend and for unnecessarily mailing me two boxes of organic synthesis textbooks. I'm grateful for new friendships I've made here in Seattle: Ethan Zilz, who is a real marvel at the climbing gym, and Corey who has taught me so much about myself these past few years. I was very fortunate to stay in the household of Karin Sidhu when I first arrived in Seattle, and I am grateful for her support and friendship throughout graduate school. Finally, I thank Tim Nichols, who was the officiant at my wedding, and helped me through some particularly difficult times during my undergraduate.

I express my sincere thanks to the mentors who led me down the path toward my Ph.D. First, I need thank Elliott Hulley, who I was lucky enough to conduct research with as an undergraduate at the University of Wyoming. Elliott, you've been an incredible support throughout my career and I am extremely grateful for everything you do. You're a great mentor and friend – thank you for everything. I also thank Bob Corcoran, who pushed me to be my very best during my undergraduate, and who has been an incredible advisor over the years. I will always cherish our many discussions of organic synthesis in your office. I also thank the other faculty at the University of Wyoming, including John Hoberg, Bruce Parkinson, Brian Leonard, and Ed Clennan, who made my undergraduate experience everything that it was. Finally, I thank Prof. Janis Louie, whose lab I worked in as an NSF-REU student where I was first introduced to inorganic chemistry research. I've learned so much from all of you, and I appreciate your support. I also need to thank the high school teachers that taught me the fundamentals and encouraged me to apply myself. In particular, I thank Mr. Steve Keppen and Mr. Chad Caldwell, who taught me AP-calculus and chemistry, respectively, at Brookings High School. Mr. Keppen was an incredible lecturer and pushed me to truly apply myself in my studies, which is a skill I've relied on every day since. Mr. Caldwell truly immersed me in "the central science". He made learning both challenging and fun, and it meant the world to know that he truly believed in me. I often reflect on the advice you gave me after graduation to "stoke the fire".

Having saved the best for last, I need to thank my family who have supported me throughout all of this. First, my mother who taught me to be kind and to enjoy all people. Mom,

you've always been my biggest supporter; I can always hear you rooting from the sidelines at a climbing competition or cross-country meet. "Go Jonny!". You've always reflected on the way Grampy would expound on the light patterns diffracting off facetted glassware. These types of conversations showed me that there is so much beauty to uncover and understand in this world. Second, my father who is a scientist himself and taught me to always ask questions. Dad, you showed me what it means to truly work hard and to put others ahead of oneself. Whether it be mowing the lawn, schoolwork, or planting a garden, you taught me to apply myself and to trust in the process. I am especially grateful for all the days we have spent fly-fishing, hiking, and hunting together. Summiting Longs Peak with you and mom will always be one of my proudest accomplishments. Many thanks to my older sisters, Jojo and Natalie, who have always been there for me. Jojo, sharing time with you in Seattle was a true gift throughout graduate school. Sally and I had so much fun with you and Tom at concerts, fancy restaurants, and in the Washington wilderness. Natalie, I still give you credit for teaching me how to multiply when we were in elementary school. I'm so grateful for all the love and support from you, Sam and Jonny. We all ought to thank my little sister Abbey, who became a nurse at the beginning of the COVID-19 pandemic and is the epidemy of strength. Abbey, I'm so proud of you and thankful for all your love and support over the years. My family got a little (or a lot?) bigger in the summer of 2019 after Sally and I were married. My sincere thanks go out to my mother- and father-in-law, Judy and Critter, for their unending support and many great times throughout graduate school. I also thank my brothers-in-law, Slim, Sam, and Ned, for all the good times. Like it or not, you three have become some of my very best friends. I'm thankful to Uncle Andrew for our many days spent in the mountains together, and to my cousin Alexander for being a true friend all these years. I'm proud of you, Alex! I'm thankful to Patty Dever, who taught me how to saddle a horse and has always treated me like one of her own. "Did ya' love it?!" Yes, I did love it, Patty. I thank Cheeks Kephart, who has been the true mastermind behind my graduate studies and is covered in soft white fur. Finally, I thank my grandmother, Josephine Lucy Rosauer, who endured true hardships with grace and showed us all that life is full of beauty and joy. Grammy passed away in September 2020, and she is dearly missed. Thank you for bringing me to the mountains all those years ago.

Last, but certainly not least, I thank my wife, Sally, who is my partner in crime and by far the best thing to have ever happened to me. Sally, I love you more than you could ever know. I

have had so much fun exploring all of Washington with you, and I can't wait for our adventures on the East Coast. I'm so proud of you for your hard work, endurance, and determination throughout graduate school, and I'm forever grateful for the countless ways that you've supported me.

DEDICATION

For Sally, who brightens each and every day.

CHAPTER 1.

ATOMICALLY DEFINED FE/CO/SE NANOROPELLERS: FUNCTIONAL MODELS FOR THE ELECTRONIC METAL-SUPPORT INTERACTION EFFECT AND HIGH CATALYTIC ACTIVITY FOR CARBODIIMIDE FORMATION

1.1 HARNESSING ELECTRONIC METAL-SUPPORT INTERACTIONS

Nanostructured transition metal chalcogenides are potent catalysts for challenging multielectron energy conversion reactions, including the oxidation of water, the reduction of oxygen, and even the reduction of carbon dioxide.[1–4] The availability of a high number of surface d states ready to engage in strong interactions with intermediates generated during the reaction is arguably the most important factor responsible for their success.[5–7] The exact crystal type and even the composition are relatively less consequential, as reflected in the wide variety of types of materials with similar reactivity profiles.[7] For example, Chevrel cluster phases — of mixed-metal [$Mo_{6-x}M_xSe_8$] or ternary $M_x[Mo_6Se_8]$ composition — are highly active electrocatalysts in the multielectron oxygen reduction reaction.[1,8,9] Binary, ternary, or doped cobalt chalcogenides of diverse stoichiometries and structures (e.g., Co/FeS, pyrite and marcasite $CoSe_2$, Fe- or Ni-doped $CoSe_2$, Co_3S_4, Co_7Se_8, Co_9S_8) are active electrocatalysts for oxygen reduction or evolution, albeit some via an active layer of surface oxide.[1,2,8]

Importantly, the exposed active sites have coordination environments and redox properties distinct from those of the bulk. The electronic interaction between the two impacts the interfacial chemical and electron transfer processes, which in turn govern catalytic performance and selectivity. This is perhaps best illustrated when the active site and the support are compositionally different, such as in Co or Ni edge-doped layered MoS_2[4,10] or, more broadly, the rapidly growing

---

Adapted in part with permission from:
1. Kephart, J. A.; Mitchell, B. S.; Chirila, A.; Anderton, K. J.; Rogers, D.; Kaminsky, W.; Velian, A. *J. Am. Chem. Soc.* **2019**, *141* (50), 19605-19610. Copywrite 2019 American Chemical Society.

class of single-atom catalysts on redox-active supports.[11] Indeed, this "electronic metal–support interaction" effect has recently been shown to dramatically enhance catalytic performance.[12,13] However, the synthesis of well-defined active interfaces at the nanoscale that harness this cooperativity to facilitate challenging multielectron transformations, or that allow the study of the chemical and redox interactions among the substrate, active site, and support remains a considerable challenge. By contrast, in homogeneous systems the role noninnocent ligands play in enhancing and altering the reactivity of single metal sites is comparatively well understood.[14–20] More recent investigations have focused on increasingly complex multimetallic molecular systems,[21,22] such as site-differentiated iron/vanadium polyoxometalates[23,24] and tetrairon suboxide clusters $[Fe_4(\mu_4\text{-}O)]$[25–27] in which the "active" iron site is rigidly embedded within a cluster. While such platforms shed light on the interplay between substrate binding or activation and redox fluctuations within the polymetallic system, they have yet to demonstrate catalytic competency.

1.2 Atomically Defined Fe/Co/Se Nanopropeller

1.2.1 *Abstract*

Atomically defined interfaces that maximize the density of active sites and harness the electronic metal–support interaction are desirable to facilitate challenging multielectron transformations, but their synthesis remains a considerable challenge. We report the rational synthesis of the atomically defined metal chalcogenide nanopropeller $Fe_3Co_6Se_8L^{Tol}_6$ (**Fe$_3$**;L^{Tol} = $Ph_2PN^{(-)}Tol$, Ph = phenyl, Tol = 4-tolyl) featuring three Fe edge sites, and its ensuing catalytic activity for carbodiimide formation. The complex interaction between the Fe edges and Co_6Se_8 support, including the interplay between oxidation state, substrate coordination, and metal–support interaction, is probed in detail using chemical and electrochemical methods, extensive single crystal X-ray diffraction, and electronic absorption and Mössbauer spectroscopy.

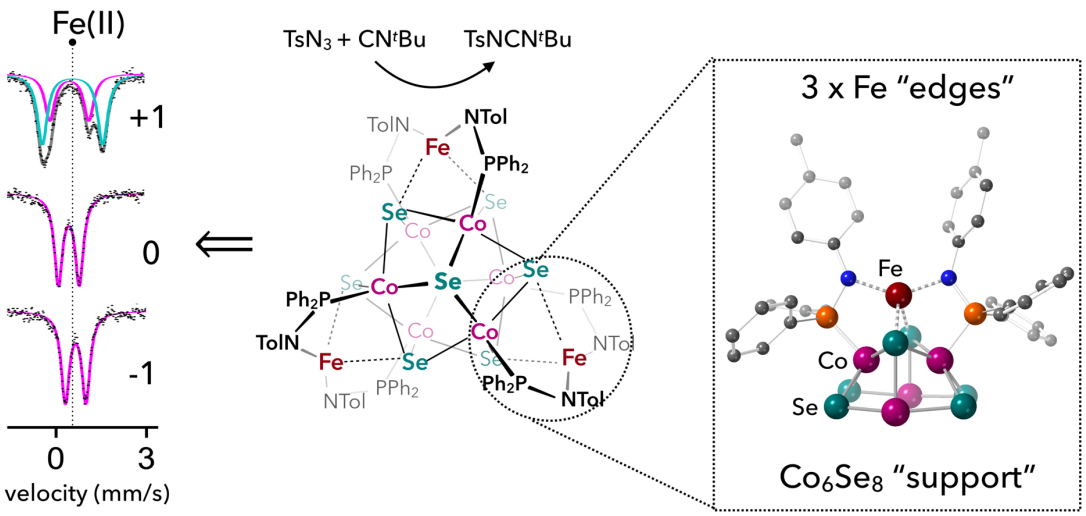


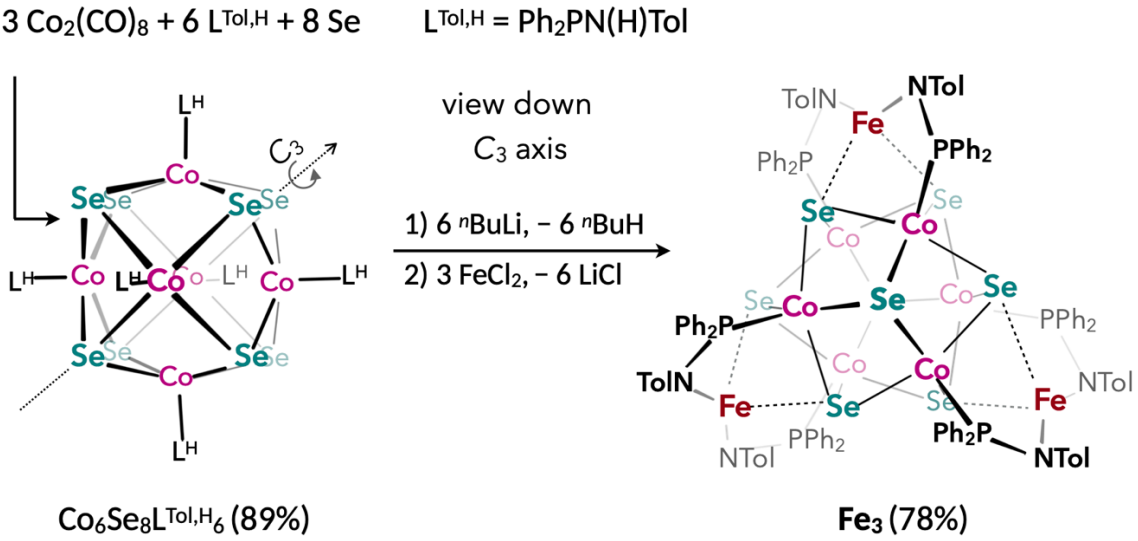
Figure 1.1. The $[Co_6Se_8L^{Tol}_6]^{6-}$ cluster-ligand acts as a non-innocent inorganic support to host three low-coordinate Fe active sites.

We seek to create atomically defined transition metal chalcogenide nanostructures that not only embed the redox and coordination complexity of the bulk material support but also maximize the number of low-coordinate "edge" sites deemed catalytically active in both molecular and heterogeneous systems.[5] Herein, we introduce a family of $Fe_3Co_6Se_8L^{Tol}_6$ nanopropeller-shaped clusters (**Fe$_3$**) prepared via surface functionalization of the Chevrel-type cluster $Co_6Se_8L^{Tol,H}_6$ ($L^{Tol,H}$ = $Ph_2PN(H)Tol$, Ph = phenyl, Tol = 4-tolyl).[28] The three edge Fe sites are in direct contact with the redox-active Co_6Se_8 "support" by reversible coordination to the exposed selenium atoms and remain anchored to the cluster surface via amide chelation. We report on the electronic and structural changes incurred by the edge sites and support upon substrate coordination and oxidation state changes. Further, we demonstrate the ensuing high activity of the edge sites in catalyzing a multielectron transformation, namely, the formation of carbodiimide from an organic azide.

1.2.2 *Synthesis and Characterization of a Fe/Co/Se Nanopropeller Cluster*

The homoleptic cluster $Co_6Se_8L^{Tol,H}_6$ was prepared in a large-scale one-pot reaction using an adapted literature protocol for the synthesis of [6,8] cobalt selenide clusters (Scheme 1.1).[29] Hexadeprotonation of $Co_6Se_8L^{Tol,H}_6$ proceeded to completion to yield $Li_6(py)_6Co_6Se_8L_6$ (**Li$_6$**$(py)_6$) with no complications from decomposition. This hexalithiated cluster is in a molecular sense an unusual multidentate ligand with three binding sites, each of which can chelate a metal in κ^2, κ^3, or κ^4 fashion via two amides and zero, one, or two selenium atoms, respectively. In our initial

Scheme 1.1. Synthesis of nanopropeller $Fe_3Co_6Se_8L^{Tol}_6$ (**Fe$_3$**).



study, we chose Fe(II) as the edge site metal, as this metal can report on oxidation state changes via Mössbauer spectroscopy. After 14 h of stirring at 50 °C, the red-orange slurry of **Li$_6$**(py)$_6$ (1 equiv) and anhydrous ferrous chloride, $FeCl_2$ (3.1 equiv), in toluene/THF adopts a deeper maroon color. After removal of volatiles, a single paramagnetic species was detected by ^{1}H NMR spectroscopy (Figure 1.9). Following a brief solvent workup, this species was isolated and identified as the triiron nanopropeller **Fe$_3$** (Scheme 1.1). Indeed, the UV−vis−*n*IR absorption profile of **Fe$_3$** reveals a marked increase in overall absorptivity and a red-shift in λ_{max} and broadening of the three diagnostic absorption bands observed for $Co_6Se_8L^{Tol,H}_6$ (see Figure 1.13). These changes likely result from ligand-to-metal charge transfer (LMCT) adsorption between the Fe metals and the Se lone pairs, though a complete interpretation is challenging. These changes in the absorption profile are indicative of electronic interactions between the Fe surface metals and the Co_6Se_8 support.

Isolated as racemic mixtures, the triiron nanoclusters exhibit a distinctive three-blade propeller geometry with (Δ/Λ)-helical chirality. This geometry is best illustrated in the single crystal X-ray diffraction structure of the monoreduced cluster [Na(18-crown-6)(MeCN)$_2$][$Fe_3Co_6Se_8L^{Tol}_6$] ([Na(18-C-6)][**Fe$_3$**]), where no solvent molecules are bound to the Fe sites (see below and Figure 1.3a). With an inorganic $Fe_3Co_6Se_8$ core of nearly perfect D_3 symmetry, the cluster ligand chelates in a κ^4 fashion to each iron atom via two amides and two μ_4-Se atoms oriented at the corners of a distorted tetrahedron (τ_4 = 0.81).[30] The $Fe_3Co_6Se_8$ core can be deconstructed into three Se-bicapped $FeCo_2$ triangles that are interconnected along their

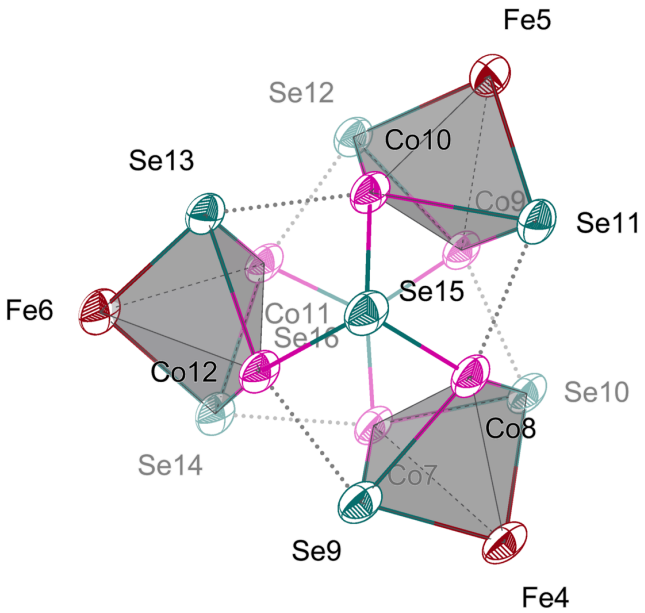
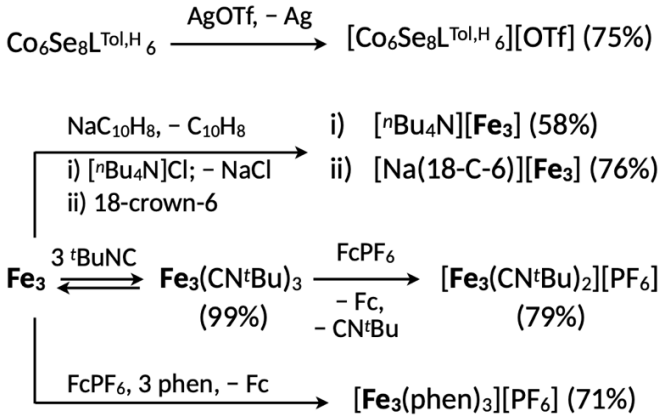


Figure 1.2. Single-crystal X-ray structure of [Na(18-C-6)][**Fe$_3$**] illustrating the deconstruction of the pseudo-D_3 symmetric $Fe_3Co_6Se_8$ inorganic core. Thermal ellipsoids shown at a 50% probability level. Selected interatomic distances (Å): Fe4-Se9 2.47(4), Fe4-Se10 2.46(1), Fe5-Se11 2.46(2), Fe5-Se12 2.46(3), Fe6-Se13 2.44(4), Fe6-Se14 2.47(3); Fe4…Co7 2.820(9), Fe4…Co8 2.80(2); Co7…Co8 2.78(3), Co7…Co12 2.94(5), Co7…Co11 3.00(3); Co7…Se9 2.39(3), Co7…Se10 2.40(3), Co7…Se14 2.44(3); Se15…Se16 5.34(7), Se9…Se12 5.79(5), Se10…Se3 5.87(9), Se11…Se14 5.92(8).

Co···Co edge by two apical μ_3-Se atoms — which also define the C_3 axis of the propeller (Figure 1.2). Each $FeCo_2$ triangle has comparable intermetallic distances Co···Co and Co···Fe distances (avg. 2.78 and 2.80 Å, respectively), which are markedly contracted relative to the Co···Co distances observed within $Co_6Se_8L^{Tol,H}_6$ (avg. 2.94 ± 0.02 Å). These $FeCo_2Se_2$ fragments are somewhat separated from one another as inter-triangle Co···Co distances are elongated to at least 2.94(5) Å. These changes are illustrative of the distortional impact that installation of Fe(II) admetals has on the Co_6Se_8 support.

We hypothesized that unlike lighter congeners, selenium could provide access to masked low-coordinate surface metal sites by forming comparatively more labile bonds, effectively masking the active site on the cluster surface during dormant states. Indeed, in the presence of a suitable monodentate ligand (CN^tBu), the **Fe$_3$** clusters form adducts that feature the κ^3 chelation mode of the cluster, where a single M–Se bond is retained. In the solid state, the adducts deviate from the D_3 symmetry of the parent propeller. For example, the triiron cluster can be crystallized as a tris-adduct with tert-butyl isocyanide, $Fe_3(CN^tBu)_3Co_6Se_8L^{Tol}_6$ (**Fe$_3$**$(CN^tBu)_3$; Figure 1.3b).

Scheme 1.2. Chemical redox transformations of $Co_6Se_8L^{Tol,H}{}_6$ and **Fe$_3$** clusters.



Upon coordination, the incoming ligand substitutes a Se atom from the cluster surface, inverting the coordination tetrahedron of the Fe (τ_4 = 0.80).

1.2.3 *Probing the Electronic Structure of Fe/Co/Se Nanopropellers*

To investigate the effect of the surface metal ions on the electronic levels of the Co6Se8 support, we probed the redox properties of the **Fe$_3$** cluster using both chemical and electrochemical methods. Chemically, monoreduction was conveniently accomplished using sodium naphthalenide. The monoreduced nanopropeller [**Fe$_3$**]$^-$ was isolated as the [Na(18-crown-6)(MeCN)$_2$]$^+$ ([Na(18-C-6)]$^+$) salt (Figure 1.3a), or, following cation exchange, as a tetra-*n*-butyl ammonium ([^{n}Bu$_4$N]$^+$) salt (Scheme 1.2).

Mono-oxidation was achieved using ferrocenium hexafluorophosphate ($FcPF_6$) in the presence of coordinating ligands, and in contrast to the neutral or monoreduced species, the resulting salt was isolated only with surface-bound ligands (Scheme 1.2). For example, mono-oxidation of **Fe$_3$**(CN^{t}Bu)$_3$ yielded a bis(isocyanide) adduct, [Fe$_3$(CN^{t}Bu)$_2$Co$_6$Se$_8$L$_6$][PF$_6$] ([**Fe$_3$**(CN^{t}Bu)$_2$]$^+$). The selective dissociation of CN^{t}Bu from one Fe edge site reveals a chemical preference of mono-oxidized triiron clusters to form site-differentiated [**Fe$_3$**(L)$_2$]$^+$ adducts. This intriguing observation is probed in greater detail below in Section Chapter 3. High-spin terminal Fe(II) isocyanide complexes are exceedingly rare;[31] adding to this class, **Fe$_3$**(CN^{t}Bu)$_3$ exhibits the longest reported terminal Fe−CN^{t}Bu bonds (avg. 2.13 Å), which are slightly longer than those in the mono-oxidized complex (avg. 2.06 Å). In conjunction with their CN stretching frequencies (ν_{CN} = 2168, 2117 cm^{-1} and 2192, 2174 cm^{-1}, respectively), which are

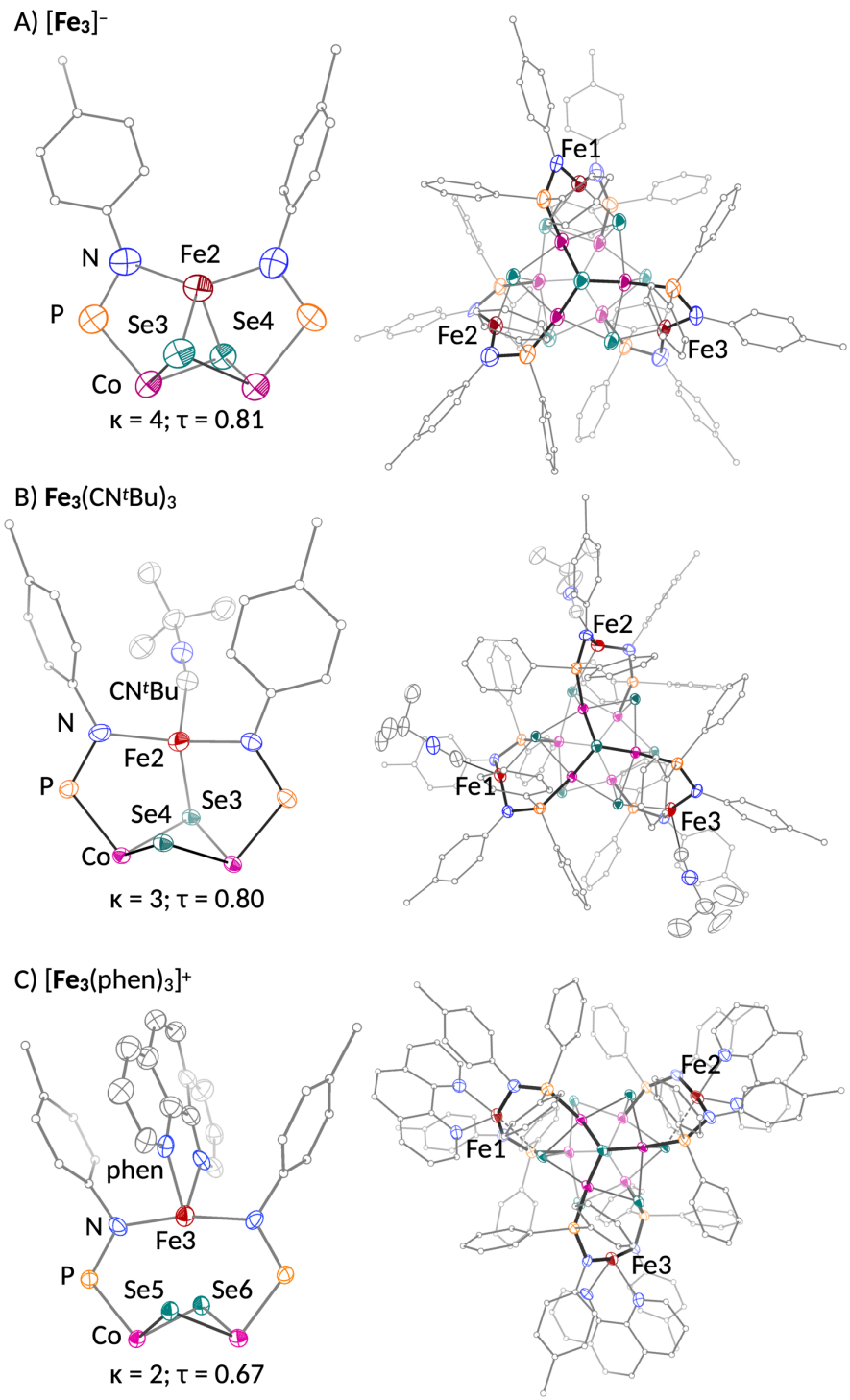


Figure 1.3. Single crystal X-ray diffraction structures of nanopropellers highlighting the coordinative versatility in the κ^4, κ^3 and κ^2 binding modes at the Fe sites, and the corresponding $\tau 4$ values (zoom-in left). Select interatomic distances (Å): (A) [Na(18-crown-6)(MeCN)$_2$][**Fe$_3$**], Fe2-Se3 2.48(2), Fe2-Se4 2.46(4); (B) **Fe$_3$**(CN^{t}Bu)$_3$, Fe2-Se3 2.487(3), Fe2-Se4 3.102(5) and (C) [**Fe$_3$**(phen)$_3$][PF$_6$], Fe3...Se5 2.99(1), Fe3...Se6 2.990(6). H atoms, solvents, counterions, and any disorder are omitted for clarity. Thermal ellipsoids are plotted at 50%.

blue-shifted from that of free isocyanide (2133 cm^{-1}), these parameters indicate highly electron-deficient iron centers that do not back-bond to activate the π-acidic substrate.[32,33] Interestingly, qualitative binding constants derived from NMR spectroscopy indicate that the affinity for CN^{t}Bu increases when an electron is removed from the neutral nanopropeller and decreases to zero upon monoreduction (see Section 1.3.13). This unique behavior stands in stark contrast to that of typical Fe–(π-acid) complexes,[27] where the binding affinity decreases with increasing oxidation state. However, this is in alignment with our interpretation that it is the Co_6Se_8 support, as opposed to the Fe edge metals, that hosts the first electron and hole: when reduced, the exposed Se atoms are more electron-rich and outcompete the external ligand; when oxidized, the Se sites are depleted of electrons, and the Fe binds to ligands such as isocyanide. The hemilability of the Se atoms distinguishes the $[Co_6Se_8L^{Tol}_6]^{(6-)}$ ligand framework from other polymetallic clusters, providing unprecedented structural and coordinative versatility.[23,34]

While monodentate ligands displace only one of the Fe–Se bonds, the iron sites completely detach from the Se surface in the presence of the bidentate ligand 1,10-phenanthroline (phen). Indeed, in its presence (3 equiv), the mono-oxidized salt was isolated as the tris(phen) adduct $[Fe_3(phen)_3Co_6Se_8L^{Tol}_6][PF_6]$ ($[\mathbf{Fe_3}(phen)_3][PF_6]$). Solid-state structural analysis reveals an unusual see-saw coordination geometry at the iron sites, each κ^2-coordinated by the cluster (τ_4 = 0.67; Figure 1.3C) little-to-no Fe–Se bonding interactions (Fe–Se bond lengths ranging between

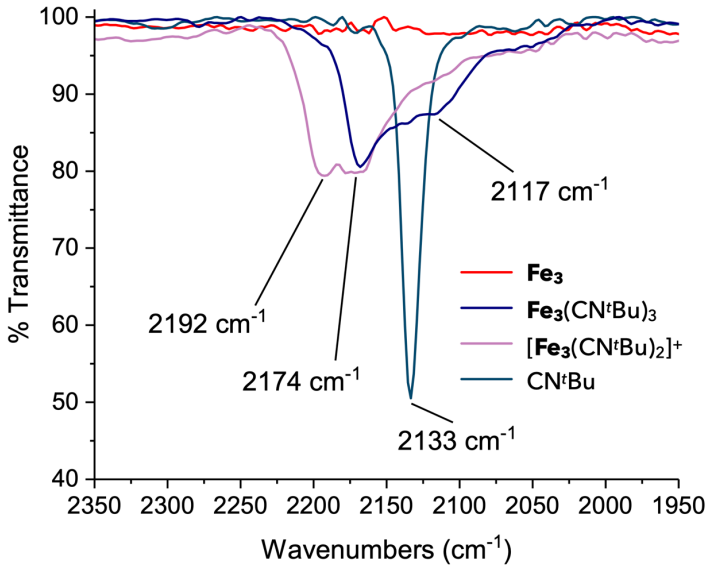


Figure 1.4. ATR-FTIR spectra of $\mathbf{Fe_3}$, $\mathbf{Fe_3}(CN^tBu)_3$, $[\mathbf{Fe_3}(CN^tBu)_2][PF_6]$, and CN^{t}Bu, highlighting the isocyanide CN stretching region.

2.780(6) and 3.641(6) Å). Intriguingly, two of the Fe(phen) edges (Fe1 and Fe2) distort slightly toward the Co_6Se_8 surface to form weak contacts (2.780 (6) and 2.816(9) Å) with Se atoms oriented on opposing ends of the Co_6Se_8 core, suggesting that even after coordination of a strong bidentate ligand, the Co_6Se_8 attempts to interact with the edge metals. This major disruption of the bonding interactions between the Fe and the support elicits a clear response in the electronic absorption profile. The UV−vis−*n*IR absorption profile of [**Fe$_3$**(phen)$_3$][PF_6] reveals how ligand binding, and concomitant disruption of Fe–Se bonding, can also perturb the electronic interaction between edge and support. [**Fe$_3$**(phen)$_3$][PF_6] has a significantly less intense absorption tail than the [**Fe$_3$**(CN^{t}Bu)$_2$][PF_6] salt, where the Fe is still engaged in bonding with the inorganic core. Further, we note a decrease in overall absorptivity and a blue-shift in λ_{max} to afford an absorption profile that is more reminiscent of the mono-oxidized non-metallated parent cluster, [$Co_6Se_8L^{Tol,H}{}_6$][OTf] (Figure 1.5B). For a more comprehensive comparison of UV-vis results, see Section 1.3.12.

Zero-field ^{57}Fe Mössbauer spectroscopy, together with Evans method magnetic susceptibility measurements, reveal that the surface sites are three high-spin Fe(II) ions that stay this way across the +1, 0, and −1 redox series (Figure 1.5A; also see the SI).[19,35,36] This observation reaffirms that the inorganic support undergoes redox changes while the surface sites remain oxidatively unchanged. We attribute the unusually low quadrupole splitting values associated with the κ^4 coordination mode, as measured for **Fe$_3$** and [**Fe$_3$**]$^-$, to the distorted tetrahedral geometry of this unprecedented $FeSe_2N_2$ coordination environment.[37,38] Indeed, a substantial increase in the quadrupole splitting and isomer shift to values more typical for high-spin Fe(II) occurs when the Fe disengages with one of the exposed Se atoms, as in the neutral isocyanide adduct **Fe$_3$**(CN^{t}Bu)$_3$ or the mono-cation [**Fe$_3$**(phen)$_3$]$^+$ ($|\Delta E_Q|$, ∂ (in mm/s): 1.43, 0.84 and 1.55, 0.94, respectively; see Section 1.3.17). In the bis(isocyanide) cation [**Fe$_3$**(CN^{t}Bu)$_2$]$^+$, we observe two distinct signals in a 2:1 area ratio, corresponding to the isocyanide-bound and isocyanide-free sites, respectively. We attribute the substantial change in quadrupole splitting for the isocyanide-free site to a structural distortion. Indeed, solid-state analysis of [**Fe$_3$**(CN^{t}Bu)$_2$][PF_6] revealed an equatorial elongation of the Co_6Se_8 core along the C_2 axis that pierces the isocyanide-free site as well as shortened Fe–Se distances (see Figure 1.34).

The nanopropellers retain the rich electrochemical profile of the parent cluster.[39] The triiron cluster features five one-electron redox events, which Randles−Sevcik analysis indicates are reversible (see Section 1.3.16).[40] Interestingly, trimetallation significantly narrows the

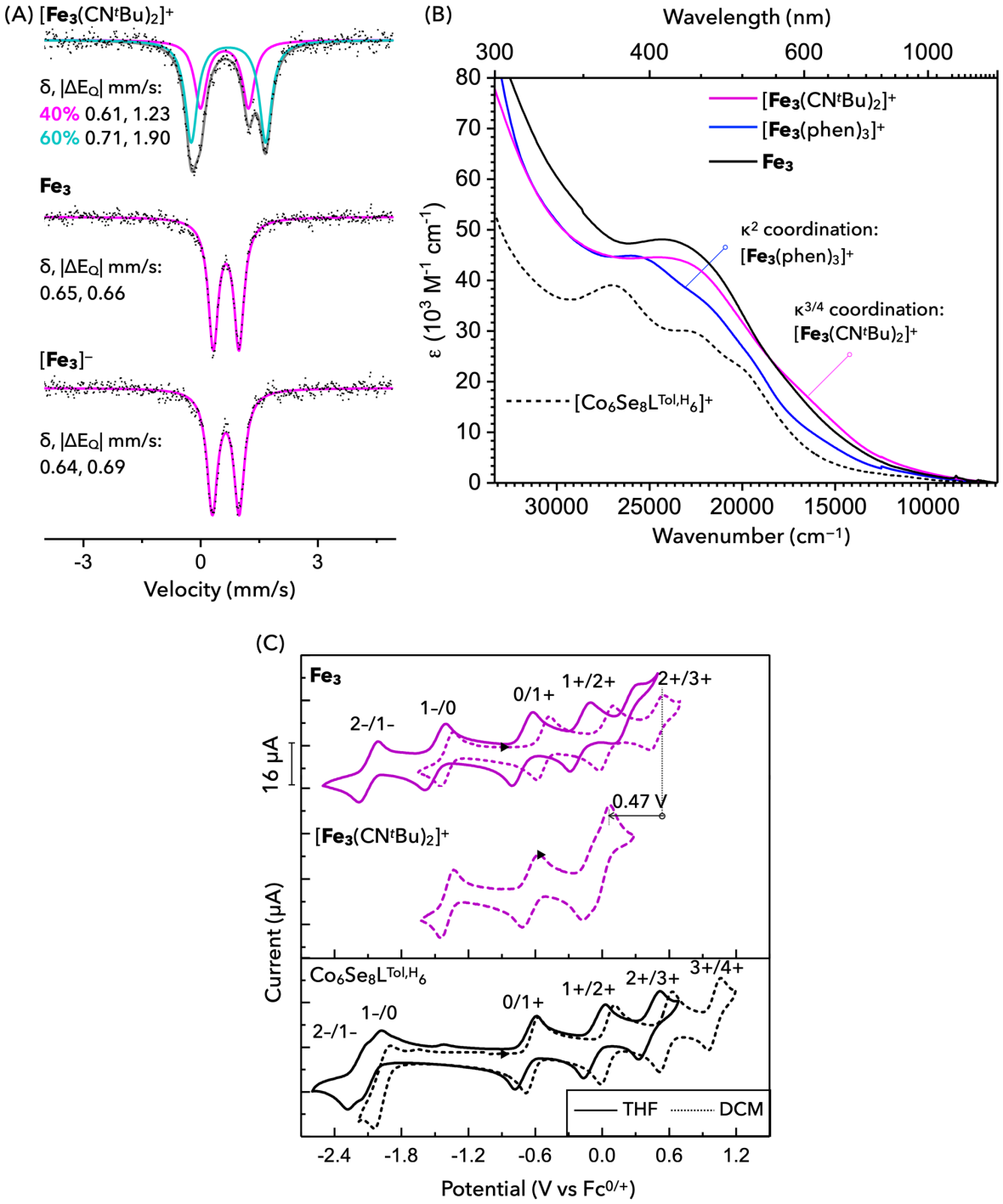


Figure 1.5. Investigations in the electronic structure of the nanopropellers. (A) Zero-field ^{57}Fe Mössbauer spectra (90K) of [**Fe$_3$**(CN^{t}Bu)$_2$][PF$_6$], **Fe$_3$**, and [^{n}Bu$_4$N][**Fe$_3$**]. (B) UV-vis-nIR absorption spectra (THF) of [Co$_6$Se$_8$L$^{Tol,H}_6$][OTf], **Fe$_3$**, [**Fe$_3$**(CN^{t}Bu)$_2$][PF$_6$] and [**Fe$_3$**(phen)$_3$][PF$_6$]. (C) Cyclic voltammograms of **Fe$_3$**, [**Fe$_3$**(CN^{t}Bu)$_2$][PF$_6$], and Co$_6$Se$_8$L$^{Tol,H}_6$ recorded in DCM (dashed lines) or THF (solid lines) solutions with [^{n}Bu$_4$N][PF$_6$] (0.1 M) at 200 mV/s.

HOMO−LUMO gap, estimated as the separation between the 1–/0 and 0/1+ redox couples, from 1.44 to 0.79 V vs $Fc^{0/+}$ in DCM (Figure 1.5c). By coordinating to the exposed Se sites, the electrophilic Fe sites withdraw electron density from the Co_6Se_8 core, effectively lowering the energy of the LUMO.

The electrochemical response to changes in the coordination environment of the surface iron sites, corroborated with the ^{57}Fe Mössbauer measurements, reinforces that the HOMO−LUMO and (HOMO−1)/(LUMO+1) levels are located on the Co_6Se_8 support, which is formally mixed valence $(Co^{III})_4(Co^{II})_2$ when neutral. Comparing the electrochemical profiles of **Fe$_3$** and [**Fe$_3$**$(CN^tBu)_2$][PF_6] in DCM, we find that the third oxidation responds dramatically to changes in the coordination environment at Fe, shifting cathodically by 0.5 V vs $Fc^{0/+}$ (also see Figure 1.21). This allows us to tentatively assign this event to the Fe(II/III) redox couple, and illustrates how substrate coordination tunes the redox potentials of the edge sites (Figure 1.5C), akin to other polymetallic systems.[21,22]

1.2.4 *Edge-support Redox Cooperativity Facilitates Group Transfer Catalysis*

Eager to test the cooperativity between the "edge" and "support" sites in multielectron transformations, in a proof-of-principle experiment we tested the reactivity of the triiron clusters with tosyl azide (TsN_3). Preliminary data suggest that **Fe$_3$** is a remarkably good catalyst for the formation of the asymmetric carbodiimide, $TsNCN^tBu$, from TsN_3 and CN^tBu (Figure 1.6).

The reaction occurred quantitatively in 3 h at room temperature with catalyst loadings as low as 2.5% (turnover frequency ≈ 26 h^{-1}). It is noteworthy that no decomposition of the triiron cluster was observed (see also Figure 1.11). While the amides anchor the Fe sites to the cluster surface, the Fe−Se hemilability likely engenders the catalytic competence. The background reactivity was negligible under a series of control conditions, including in the presence of the unmetallated cluster $Co_6Se_8L^{Tol,H}_6$. This high catalytic activity is intriguing because the formation of carbodiimides from azides and isocyanides is known as a stoichiometric or low-yielding catalytic transformation.[41–48] Moreover, electron-deficient N-sulfonyl organoazides, such as TsN_3, usually form stable imido complexes that do not transfer the nitrene "NR" moiety catalytically to isocyanides to form carbodiimides.[49] In contrast, the few isolated catalysts of late transition metals involve metals in

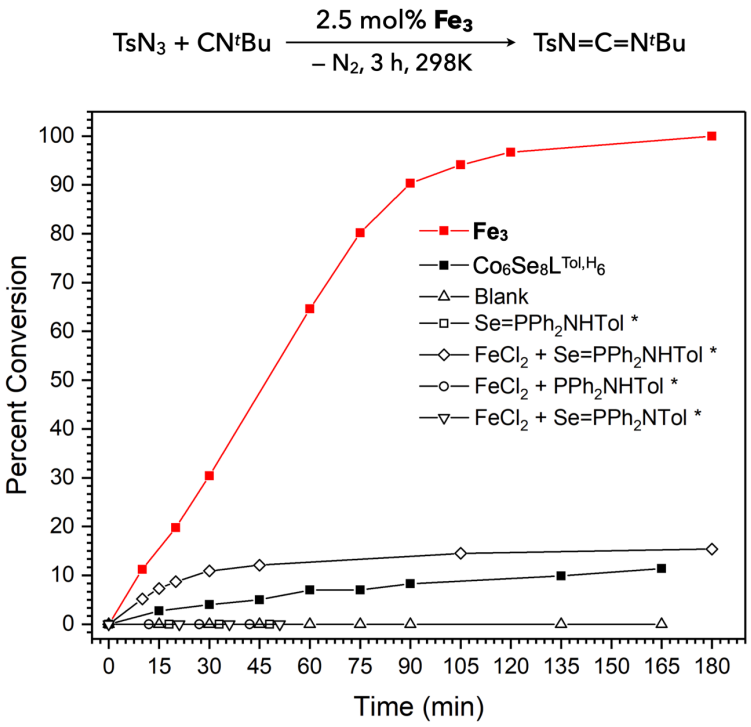


Figure 1.6. Monitoring the conversion of TsN_3 and CN^tBu to $TsNCN^tBu$ at 25 °C. *Control reactions prepared in situ. The data for **Fe$_3$** was obtained in pyridine-d_5, while all other data was obtained in benzene-d_6. Percent conversion was determined based on ^{1}H NMR integrations of the reagents and products versus an internal mesitylene standard. Both **Fe$_3$** and $Co_6Se_8L^{Tol,H}{}_6$ were used with 2.5 mol% loading, while the other control experiments were performed with 5.0 mol% loading.

low oxidation states, such as Fe(0), Fe(I), or Ni(I), and require relatively long reaction times at temperatures higher than 60 °C while producing moderate yields of the product.[49–52]

The dichotomy between the chemically inaccessible inorganic core, which is able to provide the first two holes and electrons, and the high-spin surface sites, which are ready to engage in substrate coordination and activation is an intriguing and unique feature of the **Fe$_3$** nanopropellers. In a chemical transformation, the substrate-accessible surface metals are poised to retain their (formal) oxidation state over a range of 2 V, while the redox-rich Co_6Se_8 core may funnel electrons and holes to the reaction site akin to an electrode. Together with the atomic definition and hemilability of the exposed chalcogens, this new class of soluble nanostructures bridges the gap between traditional clusters and heterogeneous systems, presenting intriguing opportunities for designer, atomically defined nanocatalysts that harness the electronic interaction with the support to facilitate challenging multielectron transformations.

1.2.5 *Influence of Ligand Binding on Fe/Co/Se Electronic Structure*

Above, a comparison of the electrochemical behavior of **Fe$_3$** and [**Fe$_3$**(CN^{t}Bu)$_2$][PF$_6$] enabled assigning the third oxidation couple (2+/3+) to an Fe edge based on its sizeable cathodic shift upon isocyanide coordination (Figure 1.5). Here, we extend this analysis to include two additional clusters, **Fe$_3$**(MeCN)(OTf) (introduced in section 3.3.2) and [**Fe$_3$**(phen)$_3$][PF$_6$], bound to weak (acetonitrile, triflate) and strong-field ligands (phenanthroline), respectively. Randles-Sevcik analysis reveals most electrochemical transformations reported here are diffusion-limited, as expected based on the nanocluster size, and chemically reversible.[53,54]

The surface ligands bound to **Fe$_3^+$** in the solid state are displaced differently upon dissolution. For example, tetrahydrofuran (THF) displaces weaker ligands (MeCN, OTf$^-$, CN^{t}Bu) giving rise to the same solvent adduct [**Fe$_3$**(THF)$_x$]$^+$, but does not displace the stronger, bidentate ligand phenanthroline. This is evident when inspecting the cyclic voltammograms of **Fe$_3$**(MeCN)(OTf) and [**Fe$_3$**(CN^{t}Bu)$_2$][PF$_6$] which are identical to that of **Fe$_3$** in THF, but distinct

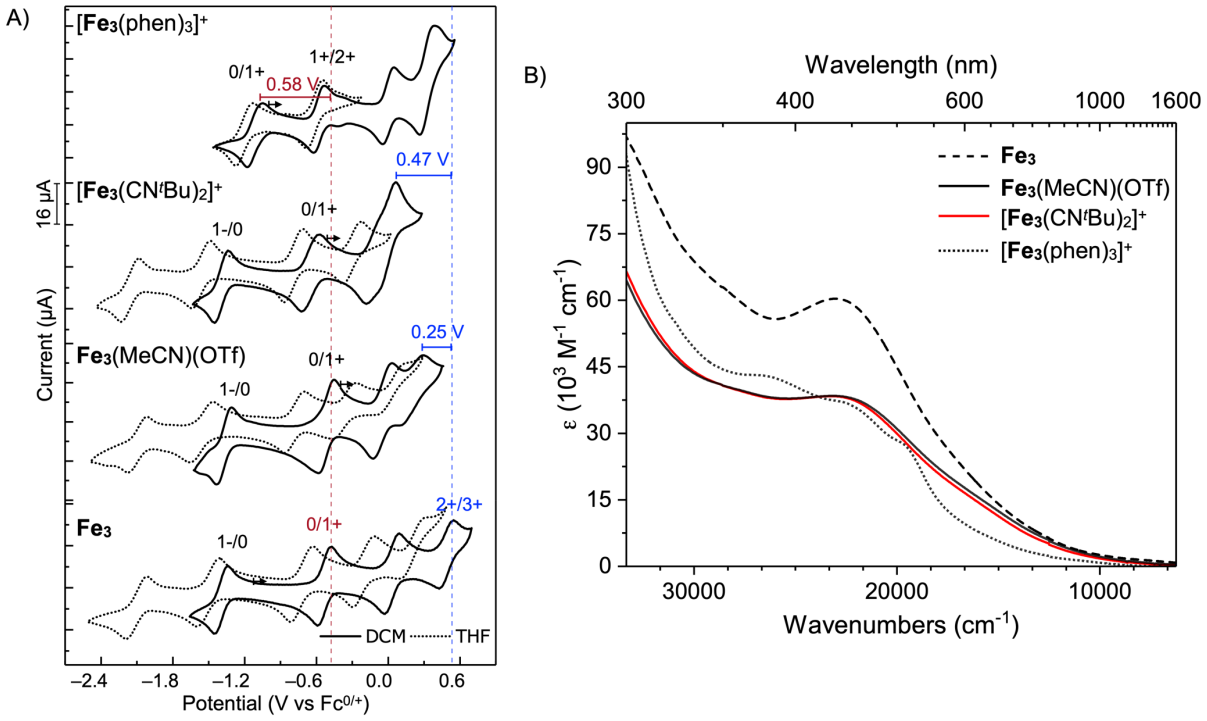


Figure 1.7. a) Cyclic voltammograms of **Fe$_3$**, **Fe$_3$**(MeCN)(OTf), [**Fe$_3$**(CN^{t}Bu)$_2$][PF$_6$], and [**Fe$_3$**(phen)$_3$][PF$_6$] (0.1 M [^{n}Bu$_4$N][PF$_6$] in DCM or THF). b) UV-vis-*n*IR spectra recorded in DCM (λ_{max}, ε) for **Fe$_3$** (435 nm, 60400 M^{-1} cm^{-1}), **Fe$_3$**(MeCN)(OTf) (431 nm, 38500 M^{-1} cm^{-1}), [**Fe$_3$**(CN^{t}Bu)$_2$][PF$_6$] (430 nm, 38400 M^{-1} cm^{-1}), and [**Fe$_3$**(phen)$_3$][PF$_6$] (380 nm, 42800 M^{-1} cm^{-1}; 448 nm, 36500 M^{-1} cm^{-1}; 509 nm, 27400 M^{-1} cm^{-1}).

from that of [**Fe$_3$**(phen)$_3$][PF$_6$] (Figure 1.7a). A similar solvation behavior was observed by NMR, upon dissolution in acetonitrile-*d*$_3$, wherein both **Fe$_3$**(MeCN)(OTf) and [**Fe$_3$**(CN^{t}Bu)$_2$][PF$_6$] exhibit nearly-identical ^{1}H resonances, consistent with formation of [**Fe$_3$**(MeCN)$_x$]$^+$ adducts in solution (see Figure 1.19). In contrast, the electrochemical profile of [**Fe$_3$**(phen)$_3$][PF$_6$] does not change significantly when switching from a strongly coordinating solvent to a weak one. Noteworthy, the phenanthroline ligands have a dramatic effect on [**Fe$_3$**(phen)$_3$][PF$_6$], making it significantly more electron rich. The relative position of the 0/1+ redox couple indicates that neutral **Fe$_3$**(phen)$_3$ is 0.58 V more reducing than **Fe$_3$**. Since Mössbauer analysis revealed the 0/1+ oxidation is not Fe-centered, the phenanthroline ligands appear to pump electron density into the nanocluster cobalt core as they coordinate to the edge sites.[53]

To resolve the effects of weaker ligands on the electronic structure of **Fe$_3$**, electrochemical measurements were also conducted in a poorly coordinating solvent. In dichloromethane, the redox couples of **Fe$_3$**(MeCN)(OTf) and [**Fe$_3$**(CN^{t}Bu)$_2$][PF$_6$] are almost identical to those of **Fe$_3$**, with one notable exception. The 2+/3+ oxidation progressively shifts cathodically in the **Fe$_3$**, **Fe$_3$**(MeCN)(OTf) and [**Fe$_3$**(CN^{t}Bu)$_2$][PF$_6$] series (Figure 1.7a). This trend is in line with the relative donating strength of the surface ligands present in these clusters, DCM < MeCN and/or [OTf]$^-$ < CN^{t}Bu, and reinforces the conclusion that the 2+/3+ oxidation is localized on an Fe edge site. This is a unique feature of the surface/support structure of the nanoclusters **Fe$_3$** facilitated by the hemilabile Fe/Se interactions; often surface ligands affect all redox couples in polymetallic clusters.[21,54,55]

The UV-vis-*n*IR electronic absorption spectra of **Fe$_3$**, [**Fe$_3$**(CN^{t}Bu)$_2$][PF$_6$] and [**Fe$_3$**(phen)$_3$][PF$_6$] were previously measured and compared in THF, revealing the striking effect of breaking the Fe–Se bonds upon phenanthroline coordination. To investigate the effect weaker ligands have on the electronic structure, the absorption spectra of **Fe$_3$**, [**Fe$_3$**(CN^{t}Bu)$_2$][PF$_6$], [**Fe$_3$**(phen)$_3$][PF$_6$] and **Fe$_3$**(MeCN)(OTf) were measured and compared in dichloromethane. This weakly coordinating solvent does not displace acetonitrile, CN^{t}Bu or phenanthroline, as revealed from the electrochemical analysis discussed above.

Inspecting the electronic absorption spectra plotted in Figure 1.7b, the drastic effect of detaching the Fe sites from the selenium surface sites is immediately apparent. Like **Fe$_3$**, **Fe$_3$**(MeCN)(OTf) and [**Fe$_3$**(CN^{t}Bu)$_2$][PF$_6$] have one main absorption feature and an increased absorbance tail in the visible/near IR region. In contrast, [**Fe$_3$**(phen)$_3$][PF$_6$], features three broad

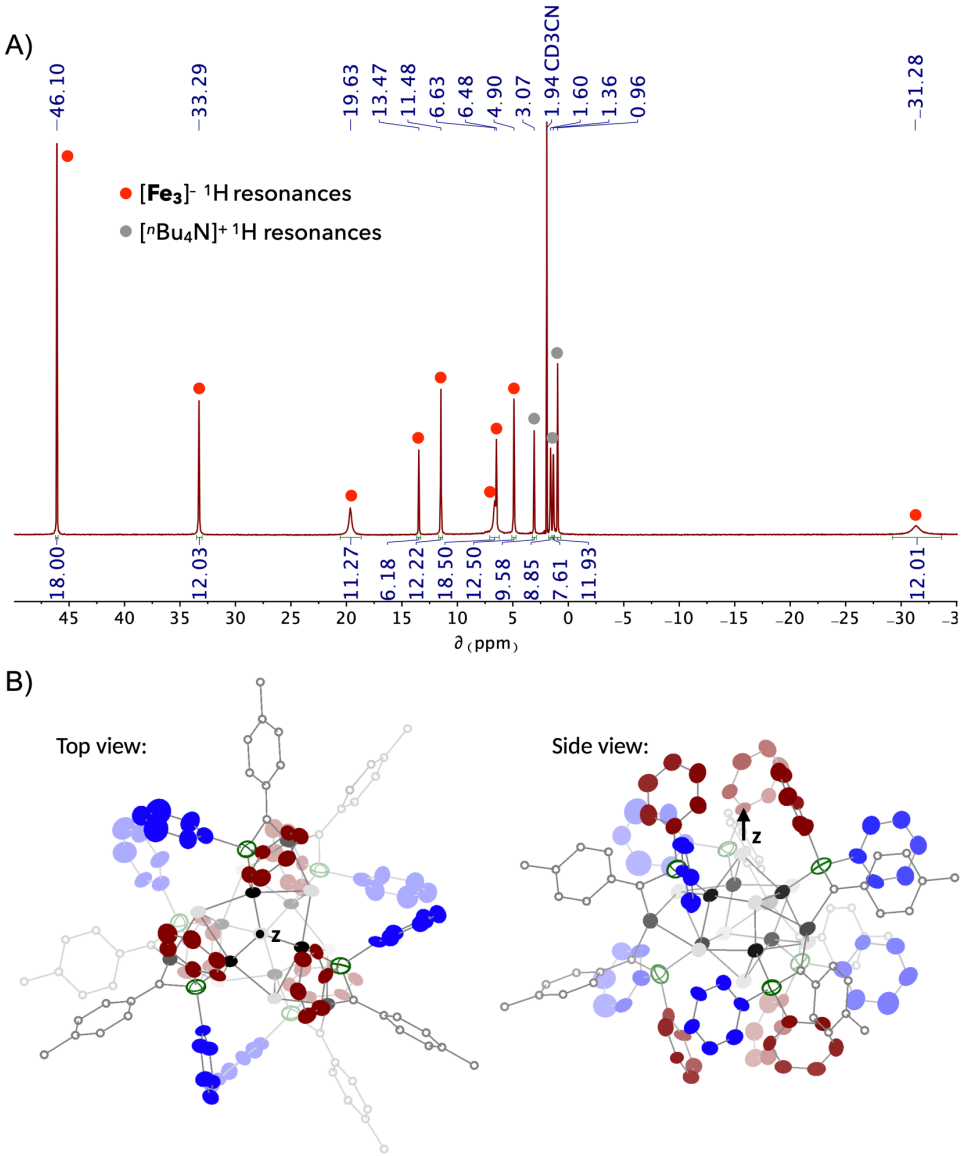


Figure 1.8. a) ^{1}H NMR (MeCN-d_3, 25 °C, 300 MHz) spectrum of [^{n}Bu$_4$N][**Fe$_3$**], with proton resonances associated with either the [**Fe$_3$**]$^{-}$ cluster or [^{n}Bu$_4$N]$^{+}$ counterion denoted red or gray, respectively. b) The solid-state structure of [**Fe$_3$**]$^{-}$ illustrates how phosphinoamide phenyl substituents adopt either an axial (red) or equatorial (blue) orientation after being locked into D_3 symmetry upon trimetallation. Hydrogen atoms and the [Na(18-C-6)(MeCN)$_2$]$^{+}$ counterion are omitted for clarity and all other atoms have been shown in gray. The black arrow represents the C_3 rotational z-axis of the compound.

absorption bands (λ_{max} = 509, 448, 380 nm) closely reminiscent of the parent $Co_6Se_8L^{Tol,H}_6$ cluster (λ_{max} = 504, 444, 367 nm), and a significantly decreased visible/near IR absorption tail.[53] These key differences in the absorption profiles of the three mono-oxidized clusters are attributed to the presence (in **Fe$_3$**, **Fe$_3$**(MeCN)(OTf) and [**Fe$_3$**(CN^{t}Bu)$_2$][PF$_6$]) or absence (in [**Fe$_3$**(phen)$_3$][PF$_6$]) of

Fe–Se bonds, and are a direct consequence of the nature of the surface ligand. Only a negligeable (1 nm) redshift is associated with replacing acetonitrile/triflate with isocyanide, as observed when comparing the visible-near IR absorption of **Fe$_3$**(MeCN)(OTf) with that of [**Fe$_3$**(CN^{t}Bu)$_2$][PF$_6$].

1.2.6 *Correlating the Solid-state Structure of **Fe$_3$** with its Unexpected ^{1}H NMR Profile*

For instances wherein the ligands on the cluster are symmetry related, as is the case for the O_h symmetric cluster-ligand $Co_6Se_8L^{Tol,H}{}_6$, we observe a single set of seven ^{1}H NMR resonances for the six $Ph_2PN(H)Tol$ ligands bound to the Co_6Se_8 core. The observation that **Fe$_3$** clusters exhibit a set of nine paramagnetically shifted ^{1}H resonances, ranging between 45 and –35 ppm was initially perplexing in that a singular $Ph_2PN^{(-)}Tol$ ligand environment should exhibit a total of six ^{1}H NMR resonances. The observed nine resonances is therefore intermittent between one and two unique phosphinoamide environments. Furthermore, I anticipated all six $Ph_2PN^{(-)}Tol$ ligands to be symmetrically equivalent due to the cluster's C_3 rotational symmetry. Careful inspection of the pseudo-D_3 symmetrical structure of [**Fe$_3$**]$^-$ reveals that this discrepancy is a reflection of a desymmetrization of the phenyl substituents on each phosphine. Upon trimetallation, the phenyl substituents are locked into place such that they adopt either an equatorial or axial orientation with respect to the C_3 axis of the Fe/Co/Se core (Figure 1.8). Accordingly, in the corresponding ^{1}H NMR profile we observe a total of nine ^{1}H resonances, three for each phenyl group and three for the tolyl substituent.

1.3 Experimental Details

1.3.1 *General Considerations*

All syntheses were conducted under a dinitrogen atmosphere using standard Schlenk or glovebox techniques (LC Technology Solutions glovebox equipped with a freezer set to −35 °C). All glassware was dried at 160 °C for a minimum of 12 h and cooled in an evacuated antechamber prior to use in the glovebox. Solvents were purchased from Fischer Scientific and degassed, dried and purified using solvent purification columns housed in a stainless-steel cabinet and dispensed by a stainless-steel Schlenk line manufactured by JC Meyer Solvent Systems. Tetrahydrofuran (THF), diethyl ether, acetonitrile, and methylene chloride (DCM) are passed through two packed columns of neutral alumina. In the cases of *n*-pentane and toluene, one of the columns is alumina

and the other is Q5 reactant, a copper(II) oxide oxygen scavenger. All solvents were passed through an in-line, 2 μm filter, then stored over activated 3Å molecular sieves in the glovebox for a minimum of 72 h. 3Å molecular sieves were purchased from Sigma Aldrich and activated under vacuum at 300 °C for 48 h.

Deuterated solvents ($CDCl_3$, C_6D_6, CD_2Cl_2, CD_3CN) were purchased from Cambridge Isotope Laboratories, Inc. degassed and dried over activated 3Å molecular sieves in the glovebox for a minimum of 72 h. $FeCl_2$ (98+%) was purchased from Strem Chemicals, Inc. and dried under vacuum at 120 °C for 24 h prior to use. $Co_2(CO)_8$ (stabilized with 2-5% hexanes) was purchased from Strem Chemicals, Inc. stored in the glovebox freezer and used as received without further purification. Chlorodiphenylphosphine (97%) and *p*-toluidine (99+%) were purchased from Alfa Aesar and used without further purification. The aminophosphine $Ph_2PN(H)Tol$ (Ph = phenyl, Tol = 4-tolyl; $L^{Tol,H}$) was prepared according to the literature.[57] Selenium (99.5%, powder, 200 mesh) and *n*-butyl lithium (2.5 M in hexanes) were purchased from Sigma Aldrich and used without further purification. *Tert*-butyl isocyanide (CN^tBu, 98%) was purchased from Sigma Aldrich and stored over activated 3Å molecular sieves in the glovebox for 72 h prior to use. Ferrocenium hexafluorophosphate was purchased from Sigma Aldrich and recrystallized from dry acetone and diethyl ether prior to its use. Silver triflate was purchased from Strem Chemicals, Inc. and used as is. Naphthalene (99%) and 1,10-phenanthroline (99%, anhydrous) were purchased from Sigma Aldrich and used without further purification. Sodium metal (99.9%, cubes in mineral oil) was purchased from Sigma Aldrich and washed thoroughly with *n*-pentane under a nitrogen atmosphere prior to its use. Tetra(*n*-butyl)ammonium hexafluorophosphate ($[^nBu_4N][PF_6]$, 98%) was purchased from Sigma Aldrich and recrystallized from ethanol upon cooling from 78 to –35 °C three times followed by removal of volatiles under reduced pressure at 110 °C for 24 h prior to its use. Tetra(*n*-butyl)ammonium chloride ($[^nBu_4N][Cl]$, ≥97.0%) was purchased from Sigma Aldrich and recrystallized three times from acetone and diethyl ether followed by drying under reduced pressure at 80 °C prior to its use.

Samples were prepared for elemental analysis by crushing single crystalline material into a powder and then drying under reduced pressure for 12 h. C, H, N combustion analysis was conducted by Atlantic Microlabs Inc. For the lithium and iron containing samples, there was difficulty achieving complete combustion. Co, Se, P, Fe elemental analysis was conducted using a Perkin-Elmer Nexion 2000B inductively-coupled plasma mass spectrometer (ICP-MS). Prior to

ICP-MS analysis, samples were digested in neat nitric acid (Fisher Scientific, ICP-MS grade) at 50 °C.

UV-vis-*n*IR absorption spectra were acquired using a Varian Cary 5000 UV-Vis-nIR spectrometer, in nIR quartz cuvettes (Spectrocell Inc., 10 mm path length, 220–3500 nm spectral window). Attenuated total reflectance infrared (ATR-IR) spectra were recorded on a Bruker Alpha IR instrument equipped with a Platinum ATR accessory stored within a nitrogen glovebox. NMR spectra were acquired at 25 °C on Bruker 300, 500 or 700 MHz spectrometers. ^{1}H and ^{13}C NMR spectra were referenced to residual deuterated solvent peaks. ^{31}P NMR spectra were externally referenced to phosphoric acid and ^{19}F NMR spectra were referenced externally to CCl_3F. Zero-field ^{57}Fe Mössbauer spectra were measured with a constant acceleration spectrometer (SEE Co., Minneapolis, MN) at 90 K. Solid samples (ca. 40 mg) were restrained with Parabar 10312 (Hampton Research Co., Aliso Viejo, CA). Isomer shifts are reported relative to α-Fe metal at 298 K. The data were analyzed and simulated with Igor Pro 7 software (WaveMetrics, Inc., Portland, OR) using Lorentzian fitting functions. Cyclic voltammetry was conducted using a μAutolabIII/FRA2 potentiostat by Metrohm. A three-electrode cell setup was used with a glassy carbon disk working electrode, a platinum wire counter electrode, and a silver-wire pseudo-reference electrode. All potentials were referenced to the $Fc^{0/+}$ redox couple by adding a small amount of ferrocene after each measurement. All electrochemical measurements were conducted under a dinitrogen atmosphere, at 25 °C.

1.3.2 *Synthesis and Isolation of $Co_6Se_8L^{Tol,H}{}_6$*

A 100 mL Schlenk flask equipped with a magnetic stir bar and a rubber septum was charged with $Co_2(CO)_8$ (5.884 g, 17.2 mmol, 3 equiv), selenium powder (3.643 g, 45.9 mmol, 8 equiv), and $L^{Tol,H}$ (10.021 g, 34.4 mmol, 6 equiv) inside a nitrogen glove box. Outside the box, the reaction flask was connected to a nitrogen-flushed Schlenk line and left open to allow venting through an oil bubbler. Toluene (24 mL) was injected to the flask using a syringe, causing rapid evolution of gas. *Caution: roughly 3.3 L of carbon monoxide gas is produced.* The deep red mixture was stirred at room temperature for 1.5 h and then heated at reflux in a 115 °C oil bath for 18 h. Reaction progress was monitored by analyzing aliquots *via* IR spectroscopy. After 18 h, carbonylated intermediates (most likely Co_6Se_8 $L^{Tol,H}{}_6(CO)$) were still present in the reaction mixture. A second portion of $L^{Tol,H}$ (1.671 g, 5.73 mmol, 1 equiv) was added in toluene (4 mL) and the mixture was

heated at 115 °C for an additional 6 h. Volatiles were removed under reduced pressure, and the oily residue was triturated with *n*-pentane (3 x 10 mL). The crude powder was then washed with successive portions of diethyl ether (3 x 30 mL) and MeCN (3 x 20 mL), before a final extraction of the crude product in DCM (100 mL). The DCM extracts were dried under reduced pressure to yield $Co_6Se_8L^{Tol,H}_6$ as an analytically pure, dark-red powder (13.186 g, 4.82 mmol, 89%).

^{1}H NMR (CD_2Cl_2, 500 MHz) δ: 7.51 (t, 24H, J = 8.9 Hz, PPh_2 *m*-Ar*H*), 7.28 (d, 12H, J = 6.9 Hz, PPh_2 *o*-Ar*H*), 7.21 (t, 24H, J = 6.8 Hz, PPh_2 *p*-Ar*H*), 6.67 (d, 12H, J = 7.8 Hz, tolyl *m*-Ar*H*), 5.99 (d, 12H, J = 7.8 Hz, tolyl *o*-Ar*H*), 5.07 (d, 6H, J = 13.6 Hz, N*H*), 2.10 (s, 18 H, tolyl-CH_3) ppm. ^{13}C NMR (CD_2Cl_2, 125 MHz) δ: 180.5 (d, $^2J_{PC}$ = 11.3 Hz, *i*-tolyl), 140.38 (d, $^1J_{PC}$ = 50.9 Hz, *i*-PPh_2), 131.98 (d, J_{PC} = 10.2 Hz, PPh_2 *o*-*C*H), 129.06 (*p*-tolyl), 129.02 (*m*-tolyl), 128.96 (*p*-PPh_2), 127.71 (d, J_{PC} = 10.1 Hz, *o*-tolyl), 118.50 (d, J_{PC} = 4.6 Hz, *m*-PPh_2), 20.51 (4-tolyl-*C*H_3) ppm. ^{31}P NMR (C_6D_6, 283 MHz) δ: +90.4 ($\nu_{1/2}$ = 464 Hz) ppm. Elemental analysis found (calc.) for $Co_6Se_8L^{Tol,H}_6$: C 50.10 (50.10), H 3.97 (3.98), N 3.07 (3.07).

1.3.3 *Synthesis and Isolation of [$Co_6Se_8L^{Tol,H}_6$][OTf]*

A 20 mL scintillation vial equipped with a magnetic stir bar, was charged with $Co_6Se_8L^{Tol,H}_6$ (0.400 g, 0.146 mmol, 1.0 equiv) and DCM (10 mL). AgOTf (0.0376 g, 0.146 mmol, 1.0 equiv) was added slowly as a solid to the stirring solution. The resulting mixture was allowed to stir at room temperature for 2 h and then passed through a plug of Celite on a fritted-glass funnel. The volatiles were removed from the filtrate under reduced pressure to yield [$Co_6Se_8L^{Tol,H}_6$][OTf] as an analytically pure, dark red, crystalline solid (0.3146 g, 0.109 mmol, 75%).

^{1}H NMR (CD_3CN, 500 MHz) δ: 7.66 (t, 12H, J = 7.4 Hz , PPh_2 *p*-Ar*H*), 7.40 (d, 24H, J = 7.3 Hz, PPh_2 *o*-Ar*H*), 6.87 (t, 24H, J = 7.4 Hz, PPh_2 *m*-Ar*H*), 6.60 (d, 12H, J = 7.9 Hz, tolyl *o*-Ar*H*), 6.21 (d, 12H, J = 8.1 Hz, tolyl *m*-Ar*H*), 3.62 (s, 6H, , N*H*), 1.87 (s, 18 H, tolyl-CH_3) ppm. ^{13}C NMR (CD_3CN, 125 MHz) δ: 132.6, 131.5, 130.4, 129.9, 129.6, 129.4, 119.4, 118.3, 20.8 ppm. ^{31}P NMR (C_6D_6, 283 MHz) δ: –423.0 ($\nu_{1/2}$ = 1083 Hz) ppm. ^{19}F NMR (C_6D_6, 471 MHz): δ –77.1 ppm. Elemental analysis found (calc.) for [$Co_6Se_8L^{Tol,H}_6$][OTf]: C 47.82 (47.92), H 3.63 (3.78), N 2.96 (2.92).

1.3.4 *Synthesis and Isolation of $Li_6(py)_6Co_6Se_8L^{Tol}_6$, **$Li_6(py)_6$***

A 500 mL Schlenk flask equipped with a Teflon valve and a large magnetic stir bar was charged with $Co_6Se_8L^{Tol,H}_6$ (4.184 g, 1.53 mmol, 1 equiv) and toluene (300 mL). The flask was brought outside the glovebox and connected to a dinitrogen manifold, and then vigorously stirred at 110 °C for 2 h to ensure complete dissolution of starting material. After returning the flask to the glovebox, pyridine (3 mL) was added to the solution, and the resulting mixture was partially frozen within a glovebox cold-well. Upon thawing, *n*-butyl lithium (2.5 M in hexanes, 4.41 mL, 11.02 mmol, 7.2 equiv) was added dropwise over the course of 5 minutes with vigorous stirring. The reaction was slowly warmed to room temperature, allowing for periodic venting of any pressure buildup in the first 4 h. This mixture was stirred for a total of 14 h, during this time a fine black precipitate developed. The solids were collected on a fine-porosity fritted-glass filter and washed with toluene (20 mL) and diethyl ether (50 mL) until the filtrate ran colorless. Residual volatiles were removed *in vacuo* to yield $Li_6(py)_6Co_6Se_8L^{Tol}_6$ (**Li_6**$(py)_6$) as an analytically pure, red-brown powder (4.799 g, 1.48 mmol, 97% yield). The compound is sparingly soluble in toluene, highly soluble in THF and pyridine, and decomposes in DCM.

^{1}H NMR (C_6D_6, 300 MHz): δ 8.23 (d, 12H, J = 4.1 Hz, *o*-py), 8.00 (t, 12H, *J* = 8.1 Hz, PPh_2 *o*-Ar*H*), 7.64 (t, 12H, *J* = 8.1 Hz, PPh_2 *p*-Ar*H*), 6.91-7.00 (m, 24H, PPh_2 *m*-Ar*H*), 6.83 (t, 6H, J = 7.08 Hz, *p*-py), 6.59 (t, 12H, J = 6.45 Hz, *m*-py), 6.50 (d, 12H, J = 8.0 Hz, tolyl *o*-Ar*H*), 6.40 (d, 12H, *J* = 7.9 Hz, tolyl *m*-Ar*H*), 1.94 (s, 18 H, tolyl-CH_3) ppm. ^{31}P NMR (C_6D_6, 283 MHz) δ: +82.65 ($\nu_{1/2}$ = 482 Hz) ppm. ^{7}Li NMR (C_6D_6, 272 MHz) δ: +1.83 ($\nu_{1/2}$ = 21.2 Hz) ppm. Elemental analysis found (calc.) for **Li_6**$(py)_6$: Co 10.94 (10.90), Se 19.49 (19.48), P 6.20 (5.73).

1.3.5 *Synthesis and Characterization of $Fe_3Co_6Se_8L^{Tol}_6$, **Fe_3***

A 100 mL Schlenk flask equipped with a Teflon valve and a large magnetic stir bar was loaded with **Li_6**$(py)_6$ (2.000 g, 0.617 mmol, 1 equiv), toluene (72 mL) and THF (6 mL), and the resulting mixture was frozen within the glovebox cold-well. Solid $FeCl_2$ (242 mg, 1.91 mmol, 3.1 equiv) was added portion-wise to the thawing, stirring mixture. The flask was degassed, sealed, and stirred at 60 °C for 14 h, during which time it homogenized to yield a deep-red solution. Volatiles were removed under reduced pressure, and the resulting crude solids were triturated with diethyl

ether (3 x 5 mL), and the product was extracted in DCM (50 mL) through a plug of Celite on a fritted-glass funnel. Volatiles were removed from the filtrate in vacuo to yield a black solid, which was the slurried in acetonitrile (50 mL) for 1 h then collected on a fine-porosity fritted-glass funnel and rinsed with acetonitrile (30 mL), diethyl ether (40 mL) and n-pentane (20 mL) to yield **Fe$_3$** as an analytically pure, fine, red-brown powder (1.4006 g, 0.484 mmol, 78% yield).

^{1}H NMR (C_6D_6, 300 MHz) δ: 44.48 (s, 18H, $\nu_{1/2}$ = 20 Hz, tolyl CH_3); 31.69 (s, 12H, $\nu_{1/2}$ = 22 Hz); 16.22 (s, 12H, $\nu_{1/2}$ = 143 Hz), 12.11 (s, 12H, $\nu_{1/2}$ = 22 Hz); 11.29 (s, 12H, $\nu_{1/2}$ = 122 Hz); 10.96 (s, 6H, $\nu_{1/2}$ = 18 Hz); 7.38 (s, 12H, $\nu_{1/2}$ = 24 Hz); 2.82 (s, 6H, $\nu_{1/2}$ = 17 Hz); −35.66 (s, 12H, $\nu_{1/2}$ = 344 Hz) ppm. ^{31}P NMR (C_6D_6, 700 MHz): no signals observed between ±2000 ppm. Elemental analysis found (calc.) for **Fe$_3$**: Co 12.70 (12.21), Se 21.35 (21.82), P 6.42 (6.84), Fe 6.25 (5.79).

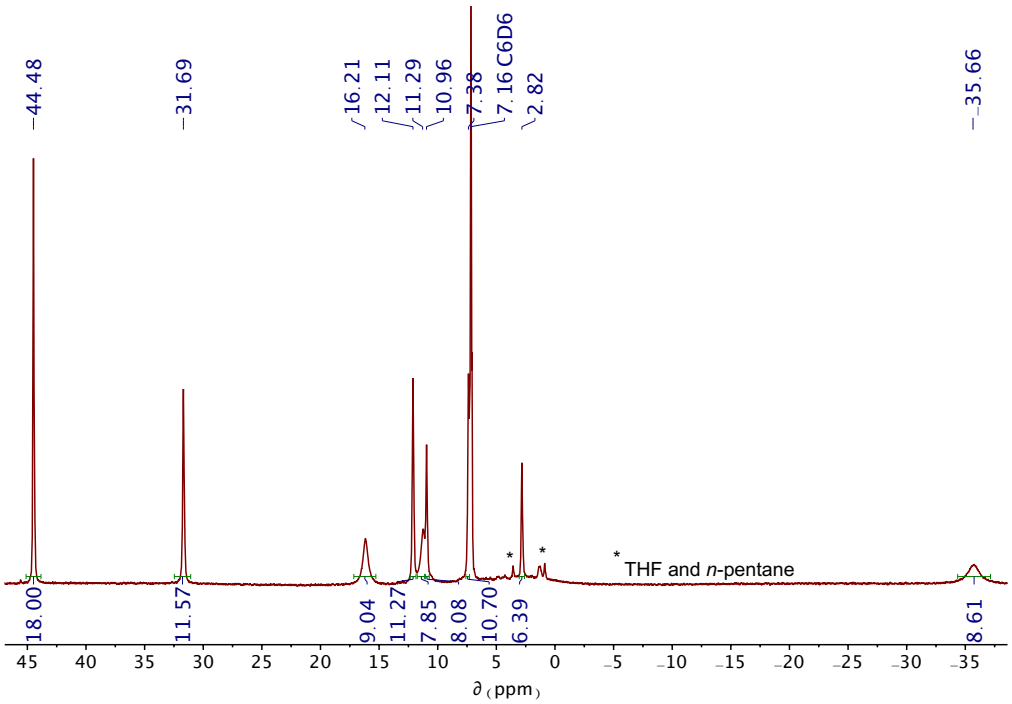


Figure 1.9. ^{1}H NMR (C_6D_6, 25 °C, 300 MHz) spectrum of **Fe$_3$**.

1.3.6 *Synthesis and Characterization of $Fe_3(CN^tBu)_3Co_6Se_8L^{Tol}{}_6$, **$Fe_3(CN^tBu)_3$***

In a nitrogen glovebox, a 20 mL scintillation vial equipped with a small magnetic stir bar was loaded with **Fe$_3$** (0.500 g, 0.173 mmol, 1 equiv) and DCM (12 mL). The sample was cooled to –35 °C in the glovebox freezer before CN^{t}Bu (0.0474 g, 0.570 mmol, 3.3 equiv) was added dropwise

using a microsyringe to the rapidly stirring solution. The mixture was slowly brought to room temperature and stirred for 2h before volatiles were removed under reduced pressure. The resulting solids were triturated with *n*-pentane (3 x 3 mL) and the mixture was dried under reduced pressure to remove excess CN^{t}Bu, yielding **Fe$_3$**(CN^{t}Bu)$_3$ as an analytically pure, dark red powder (0.536 g, 0.170 mmol, 99%). This product has much greater solubility in benzene and toluene than **Fe$_3$**.

^{1}H NMR (C_6D_6, 300 MHz) δ: 41.22 (s, 18 H, $\nu_{1/2}$ =76 Hz, tolyl-C*H*$_3$); 29.27 (s, 12H, $\nu_{1/2}$ =71 Hz); 18.68 (s, 12H, $\nu_{1/2}$ =231 Hz), 12.84 (s, 12H, $\nu_{1/2}$ =42 Hz); 11.09 (s, 6H, $\nu_{1/2}$ =24 Hz); 8.34 (s, 12H, $\nu_{1/2}$ =42 Hz); 3.12 (s, 6H, $\nu_{1/2}$ =29 Hz); 0.62 (s, 27H, $\nu_{1/2}$ =12 Hz, CNC(C*H*$_3$)$_3$); –33.18 (s, 12H, $\nu_{1/2}$ =492 Hz) ppm. ^{31}P NMR (C_6D_6, 700 MHz): no signals observed between ± 2000 ppm. ATR-FTIR (film): ν_{CN} = 2168–2117 cm^{-1}. Elemental analysis found (calc.) for **Fe$_3$**(CN^{t}Bu)$_3$: Co 11.19 (11.25), Se 19.20 (20.09), P 5.90 (5.91), Fe 5.92 (5.33).

1.3.7 *Synthesis and Characterization of [Fe$_3$(CN^{t}Bu)$_2$Co$_6$Se$_8$L$^{Tol}_6$][PF$_6$], [**Fe$_3$**(CN^{t}Bu)$_2$][PF$_6$]*

A 100 mL round bottom flask equipped with a small magnetic stir bar was loaded with **Fe$_3$**(CN^{t}Bu)$_3$ (0.400 g, 0.127 mmol, 1 equiv), ferrocenium hexafluorophosphate ([Fc][PF$_6$], 0.0421 g, 0.127 mmol, 1 equiv), and DCM (32 mL). The mixture was stirred at 25 °C for 2 h, concentrated under reduced pressure to half of its original volume, and then passed through a plug of Celite. ^{1}H NMR analysis this filtrate revealed the presence of three CN^{t}Bu ligands per [**Fe$_3$**]$^+$ cluster, by integration. The filter cake was rinsed with DCM (2 mL) and the filtrate was layered with *n*-pentane (40 mL) before being stored at –35 °C for 24 h. Long black needles grew within the flask, which were collected on a fine-porosity fritted-glass funnel. ^{1}H NMR integrations indicated loss of one isocyanide after crystallization. This material was recrystallized from DCM and *n*-pentane once more, to yield [**Fe$_3$**(CN^{t}Bu)$_2$][PF$_6$] as a crop of spectroscopically pure, black, crystalline needles (321 mg, 0.100 mmol, 79%).

^{1}H NMR (CD_3CN, 300 MHz) δ: 50.03 (s, 18 H, $\nu_{1/2}$ = 97 Hz, 4-tolyl-C*H*$_3$); 33.25 (s, 12H, $\nu_{1/2}$ = 59 Hz); 21.98 (s, 12H, $\nu_{1/2}$ = 211 Hz), 17.08 (s, 12H, $\nu_{1/2}$ = 157 Hz); 14.73 (s, 12H, 24 Hz); 11.25 (s, 6H, $\nu_{1/2}$ = 22 Hz); 10.70 (s, 12H, $\nu_{1/2}$ = 29 Hz); 3.28 (s, 6H, $\nu_{1/2}$ = 21 Hz); 0.89 (s, 18H, $\nu_{1/2}$ = 13 Hz, CNC(C*H*$_3$)$_3$) –36.48 (s, 12H, $\nu_{1/2}$ = 512 Hz) ppm. ^{19}F NMR (CD_3CN, 471 MHz) δ: –72.96 (d,

$^{1}J_{PF}$ = 718 Hz) ppm. ATR-FTIR (film): ν_{CN} = 2192–2174 cm^{-1}. Elemental analysis found (calc.) for [**Fe$_3$**(CN^{t}Bu)$_2$][PF$_6$]: Co 11.04 (11.03), Se 18.56 (19.70), P 7.08 (6.76), Fe 6.14 (5.23). Complete mineralization was not achieved for this sample.

1.3.8 *Synthesis and Characterization of [Fe$_3$(phen)$_3$Co$_6$Se$_8$L$^{Tol}_6$][PF$_6$], [**Fe$_3$**(phen)$_3$][PF$_6$]*

A 20 mL scintillation vial equipped with a small magnetic stir bar was loaded with **Fe$_3$** (0.312 g, 0.108 mmol, 1 equiv) and DCM (16 mL). This mixture was stirred until homogeneous, then quickly transferred to a vial loaded with solid ferrocenium hexafluorophosphate (35.7 mg, 0.108 mmol, 1 equiv). The mixture was stirred at 25 °C for 1 h, before 1,10-phenanthroline (phen, 64.2 mg, 0.356 mmol, 3.3 equiv) in DCM (1.5 mL) was added. During this addition, the solution quickly turned a yellow-brown color. The solution was then concentrated under reduced pressure to half its original volume and passed through a plug of Celite on a fritted-glass filter. The resulting filtrate was layered with *n*-pentane (10 mL) and stored at –35 °C for 24 h to yield a crop of dark-red prismatic crystals. These were collected on a fine-porosity fritted-glass filter and washed with *n*-pentane to yield spectroscopically pure [**Fe$_3$**(phen)$_3$][PF$_6$] (274.9 mg, 0.077 mmol, 71%). This compound is soluble and stable in DCM but decomposes in acetonitrile to yield a mixture of paramagnetic products and an unidentified 1,10-phenanthroline complex.

^{1}H NMR (CD_2Cl_2, 300 MHz) δ: 50.84 (s, 6H, $\nu_{1/2}$ = 39 Hz, phen-*H*$_a$); 24.29 (s, 18H, $\nu_{1/2}$ = 17 Hz, 4-tolyl-C*H*$_3$); 21.15 (s, 6H, $\nu_{1/2}$ = 18 Hz, phen-*H*$_b$), 20.55 (s, 12H, $\nu_{1/2}$ = 47 Hz); 10.00 (s, 18H, $\nu_{1/2}$ = 24 Hz); 9.14 (s, 12H, $\nu_{1/2}$ = 124 Hz); 8.40 (s, 12H, $\nu_{1/2}$ = 35 Hz); 6.43 (s, 6H, $\nu_{1/2}$ = 19 Hz); 2.75 (s, 6H, $\nu_{1/2}$ = 23 Hz, phen-*H*$_c$); –9.50 (s, 6H, $\nu_{1/2}$ = 28 Hz, phen-*H*$_d$), –15.27 (s, 12H, $\nu_{1/2}$ = 809 Hz) ppm. ^{19}F NMR (CD_2Cl_2, 471 MHz) δ: –73.44 (d, $^{1}J_{PF}$ = 713 Hz) ppm. Elemental analysis found (calc.) for [**Fe$_3$**(phen)$_3$][PF$_6$]: Co 10.03 (9.88), Se 16.84 (17.64), P 6.33 (6.05), Fe 5.54 (4.68). Complete mineralization was not achieved for this sample.

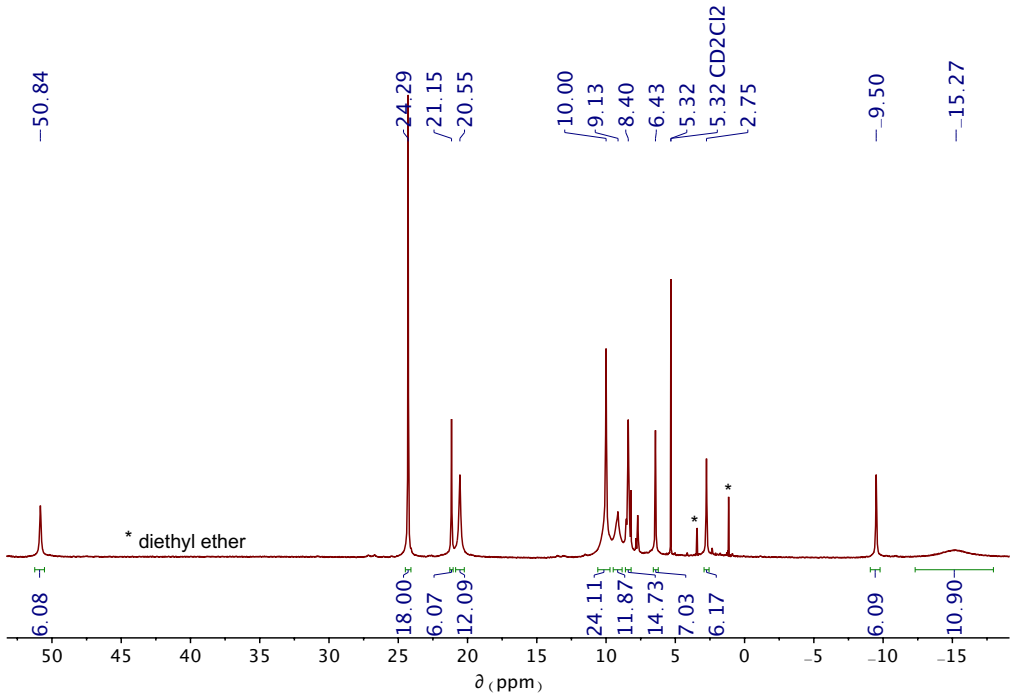


Figure 1.10. ^{1}H NMR (CD_2Cl_2, 25 °C, 300 MHz) spectrum of [**Fe$_3$**(phen)$_3$][PF_6].

1.3.9 *Synthesis of [Na(18-crown-6)(MeCN)$_2$][Fe$_3$Co$_6$Se$_8$L$^{Tol}_6$], [Na(18-C-6)][**Fe$_3$**]*

A 100 mL round bottom flask equipped with a small magnetic stir bar was loaded with **Fe$_3$** (0.811 g, 0.280 mmol, 1 equiv) and THF (50 mL). The flask was sealed with a rubber septum, and the mixture was stirred at room temperature until homogeneous. The deep-red solution was frozen within the glovebox cold-well. Upon thawing, a freshly prepared 0.1 M solution of sodium naphthalenide in THF (2.80 mL, 0.280 mmol, 1 equiv) was added dropwise under rapid stirring, followed by rapid addition of 18-*crown*-6 (74 mg, 0.280 mmol, 1 equiv) in THF (~1.5 mL). The sample was warmed to room temperature and stirred for 2 h, at which point it was concentrated under reduced pressure, then passed through a plug of Celite on fritted-glass filter. The filtrate was layered with diethyl ether (~40 mL) and the solution was stored at –35 °C for 24 h to yield a crop of brick-red powder [Na(18-*crown*-6)][**Fe$_3$**] (678.6 mg, 0.213 mmol, 76%). As a solid, this compound slowly decomposes at room temperature with the formation of neutral **Fe$_3$** and an unidentified diamagnetic species, which precluded elemental analysis. However, the solid appears to be indefinitely stable when stored at –35 °C.

^{1}H NMR (CD_3CN, 300 MHz) δ: 46.01 (s, 18H, 85 Hz, 4-tolyl-C*H*$_3$); 33.24 (s, 12H, $\nu_{1/2}$ = 96 Hz); 19.67 (s, 12H, $\nu_{1/2}$ = 184 Hz); 13.45 (s, 6H, $\nu_{1/2}$ = 83 Hz); 11.47 (s, 12H, $\nu_{1/2}$ = 93 Hz); 6.54 (s, 18H, $\nu_{1/2}$ = 193 Hz); 4.89 (s, 12H, $\nu_{1/2}$ = 102 Hz); 3.53 (s, 24H, $\nu_{1/2}$ = 140 Hz, 18-*crown*-6 *H*); –31.29 (s, 12H, $\nu_{1/2}$ = 392 Hz).

1.3.10 *Synthesis and Characterization of [^{n}Bu$_4$N][Fe$_3$Co$_6$Se$_8$L$^{Tol}_6$], [^{n}Bu$_4$N][**Fe$_3$**]*

A 20 mL scintillation vial equipped with a small magnetic stir bar was loaded with **Fe$_3$** (0.300 g, 0.104 mmol, 1 equiv) and THF (10 mL), and the mixture was stirred at room temperature until homogeneous. The deep-red solution was frozen within the glovebox cold-well. Upon thawing, a freshly prepared 0.1 M solution of sodium naphthalenide in THF (1.04 mL, 0.104 mmol, 1 equiv) was added dropwise with rapid stirring, immediately followed by the addition of solid [(^{n}Bu)$_4$N][Cl] (31.7 mg, 0.114 mmol, 1.1 equiv). The sample was warmed to room temperature and stirred for 1 h, and then concentrated under reduced pressure to half of its original volume. After passing the concentrated solution through a plug of Celite on a fritted-glass funnel, the filtrate was layered with diethyl ether (12 mL) and the solution was stored at –35 °C for 24 h to yield a crop of brick-red crystals. These crystals were dissolved in acetonitrile (10 mL) and the solution was passed through a plug of Celite before volatiles were removed under reduced pressure to yield [(^{n}Bu)$_4$N][**Fe$_3$**] as an analytically pure deep-red, microcrystalline solid (0.188 g, 0.060 mmol, 58%). In contrast with the [Na(18-crown-6)]$^+$ variant, the [^{n}Bu$_4$N]$^+$ salt appears to be indefinitely stable as a solid at room temperature.

^{1}H NMR (CD_3CN, 300 MHz) δ: 46.09 (s, 18H, $\nu_{1/2}$ = 9 Hz, 4-tolyl-C*H*$_3$); 33.28 (s, 12H, $\nu_{1/2}$ = 17 Hz); 19.62 (s, 12H, $\nu_{1/2}$ = 81 Hz); 13.47 (s, 6H, $\nu_{1/2}$ = 17 Hz); 11.47 (s, 12H, $\nu_{1/2}$ = 16 Hz); 6.62 (s, 6H, $\nu_{1/2}$ = 64 Hz); 6.47 (s, 12H, $\nu_{1/2}$ = 18 Hz); 4.89 (s, 12H, $\nu_{1/2}$ = 17 Hz); 3.07 (t, 8H, 6.92 Hz, N-C*H*$_2$CH$_2$CH$_2$CH$_3$); 1.59 (m, 8H, 6.56 Hz, N-CH$_2$CH$_2$C*H*$_2$CH$_3$); 1.35 (dt, 8H, J_1 = 6.56 Hz, J_2 = 6.92, N-CH$_2$C*H*$_2$CH$_2$CH$_3$); 0.96 (t, 12H, 8.38 Hz, N-CH$_2$CH$_2$CH$_2$C*H*$_3$); –31.57 (s, 12H, $\nu_{1/2}$ = 260 Hz). Elemental analysis found (calc. for [^{n}Bu$_4$N][**Fe$_3$**]): Co 11.51 (11.27), Se 19.66 (20.13), P 6.03 (5.92), Fe 5.80 (5.34).

1.3.11 *Catalytic Synthesis of Carbodiimide TsNCN^{t}Bu*

The catalyst **Fe$_3$** (0.005 mmol, 0.02 equiv) is dissolved in 1 mL benzene-d_6, to which CN^{t}Bu (0.300 mmol, 1.20 equiv) is added neat. The reaction mixture is frozen in the glovebox coldwell. Upon thawing, TsN_3 (0.10 M in benzene-d_6, 0.250 mmol, 1.00 equiv) is added dropwise. The reaction mixture is left to warm to 25 °C and stirred for 3 h. The resulting mixture is monitored by NMR spectroscopy using a mesitylene/benzene-d_6 capillary (2% by volume) as an internal standard, as well as by GC-MS spectroscopy. The carbodiimide product is purified by passing the reaction mixture through a 5 cm silica plug and eluting it with dichloromethane. After removal of volatiles under reduced pressure, the carbodiimide TsNCN^{t}Bu is isolated as a spectroscopically pure, white powder (98% isolated yield).[58]

^{1}H NMR (300 MHz, $CDCl_3$) δ: 7.82 (d, J = 8.5 Hz, 2H, Ar), 7.33 (d, J = 8.5 Hz, 2H, Ar), 2.44 (s, 3H, Me), 1.38 (s, 9H, ^{t}Bu). GC-MS (temp program: initial temp = 60 °C, 15.00 °C/min, final temp = 300 °C, hold time = 3.5 min) retention time = 12.78 min; m/z (intensity): 252 (11), 197 (48), 142 (88), 155 (60), 91 (100), 57 (86). ATR-FTIR (film): 2155 ($\nu_{N=C=N}$), 1340 and 1160 (ν_{SO2}) cm^{-1}.

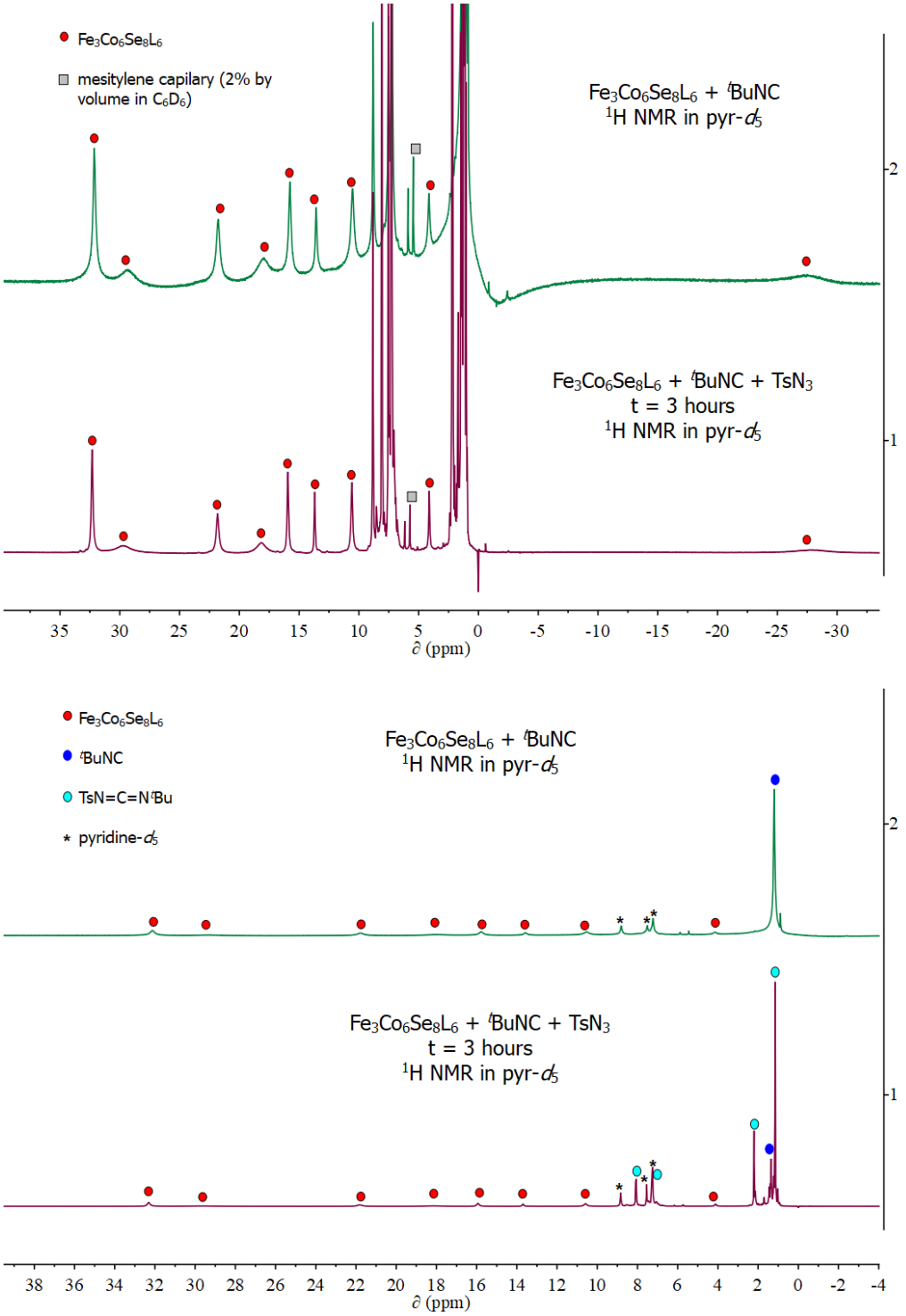


Figure 1.11. ^{1}H NMR (pyridine-d_5, 25 °C, 300 MHz) spectra of the paramagnetic region (A) and emphasizing the diamagnetic region (B) of the catalytic reaction mixture before and 3 h after addition of TsN_3. A catalyst loading of 10 mol% **Fe$_3$** was employed to enhance the visibility of the paramagnetic species. The reaction was run in the presence of TsN_3 (0.11 M) and CN^{t}Bu (0.19 M).

1.3.12 *UV-vis-nIR Absorption Spectra*

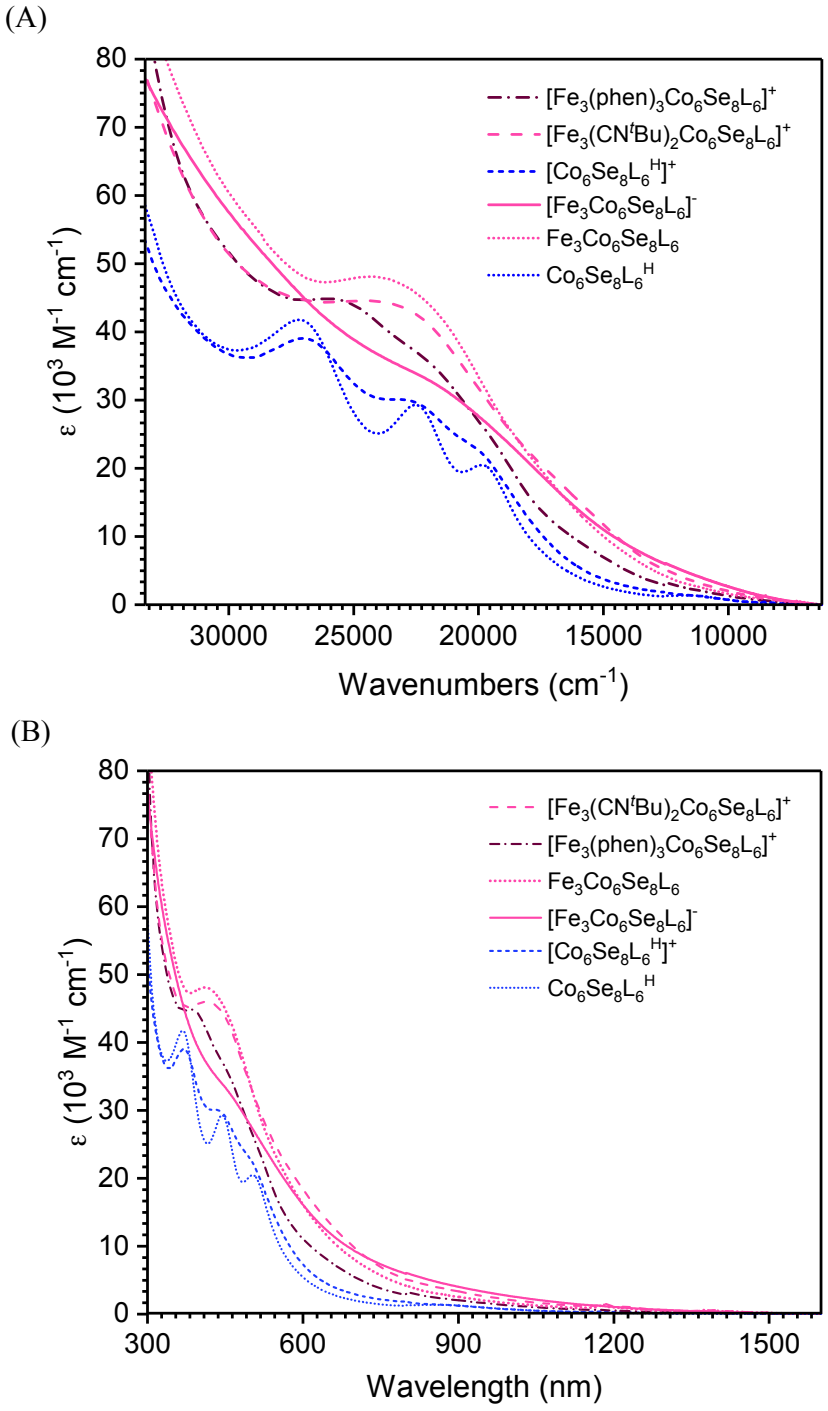


Figure 1.12. UV-vis-*n*IR absorption spectra of $Co_6Se_8L^{Tol,H}_6$ and $[Co_6Se_8L^{Tol,H}_6][OTf]$(blue lines); **Fe$_3$**, [Na(18-C-6)][**Fe$_3$**], and [**Fe$_3$**$(CN^tBu)_2][PF_6]$ (pink lines); and $[$**Fe$_3$**$(phen)_3][PF_6]$ (burgundy line) acquired in THF with extinction coefficient (ε) plotted *vs* wavenumber (A) or wavelength (B).

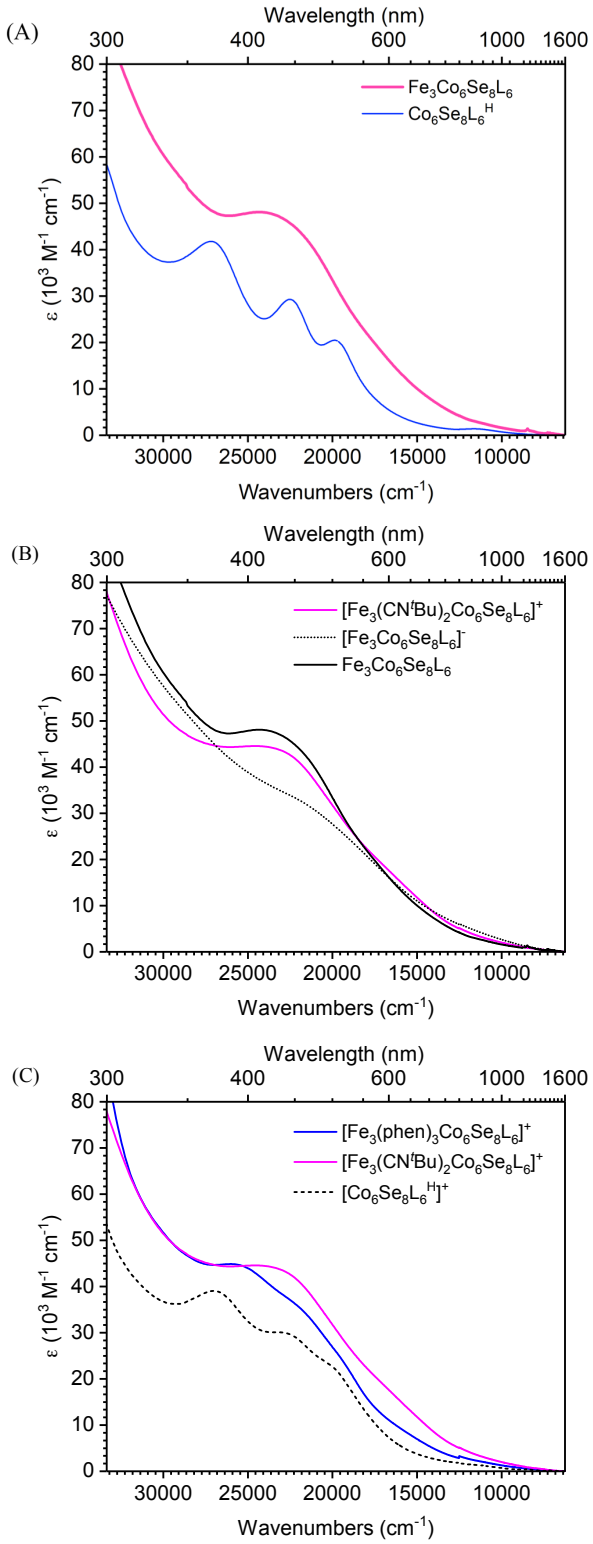


Figure 1.13. UV-vis-*n*IR absorption spectra of (A) $Co_6Se_8L^{Tol,H}_6$ and **Fe$_3$**; (B) **Fe$_3$**, [**Fe$_3$**(CN^tBu)$_2$][PF_6], and [Na(18-C-6)][**Fe$_3$**$Co_6Se_8L_6$]; and (C) [$Co_6Se_8L^{Tol,H}_6$][OTf], [**Fe$_3$**(CN^tBu)$_2$][PF_6], and [**Fe$_3$**(phen)$_3$][PF_6].

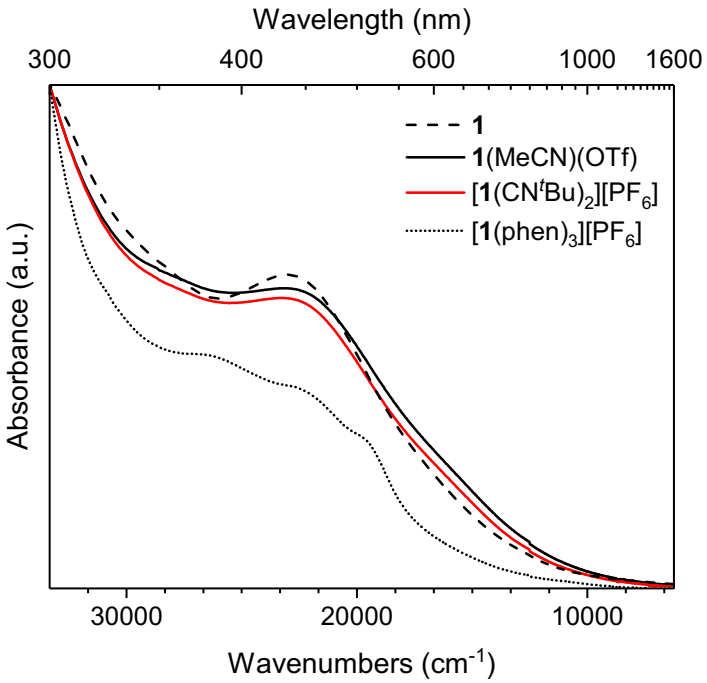


Figure 1.14. Normalized electronic absorption spectra of **Fe$_3$**, **Fe$_3$**(MeCN)(OTf), [**Fe$_3$**(CN^{t}Bu)$_2$][PF$_6$], and [**Fe$_3$**(phen)$_3$][PF$_6$] recorded in DCM at 25 °C. Here, the triiron cluster **Fe$_3$** is denoted as **1**.

1.3.13 *Determination of CN^{t}Bu Binding Constants*

General Comments on Binding Constant Analysis: The *tert*-butyl isocyanide binding strength was studied for the redox series [**Fe$_3$**(CN^{t}Bu)$_2$][PF$_6$], **Fe$_3$**, and [(^{n}Bu)$_4$N][**Fe$_3$**] using ^{1}H NMR spectroscopy. From a qualitative analysis of the NMR spectra recorded after sequential additions of CN^{t}Bu to the tri-iron clusters in their various redox states, several conclusions can be drawn: 1) The chemical shift values of the neutral species, **Fe$_3$**, prepared free of coordinating ligands, undergo several inflection points as CN^{t}Bu is added, suggesting that the irons are non-equivalent and that association of isocyanide with one Fe site has a steric or electronic impact on the other Fe sites. 2) The chemical shifts of the oxidized species, prepared with two Fe sites bound by CN^{t}Bu, exhibits no inflection points, and requires a great excess of CN^{t}Bu to reach a final chemical shift value, suggesting weak association at the third iron site. 3) Finally, the reduced species, [(^{n}Bu)$_4$N][**Fe$_3$**], exhibits no change in chemical shift upon addition of CN^{t}Bu. When taken into consideration together, these observations indicate that as the oxidation state of the compound is

lowered, the Co_6Se_8 core can support more direct Fe-Se contacts, ultimately allowing the Se ligands to outcompete CN^{t}Bu in the reduced state.

The binding event of one isocyanide (L) to an Fe center is described by the equilibrium constant:[59,60]

$$K_{eq} = \frac{[FeL]}{[Fe][L]}$$

and, for a known total concentration of $Fe_3Co_6Se_8L_6$, $[Fe^{tot}] = [Fe] + [FeL]$ and L, $[L^{tot}] = [L] + [FeL]$, the equilibrium constant can be defined as:

$$K_{eq} = \frac{[FeL]}{([Fe^{tot}] - [FeL])([L^{tot}] - [FeL])}$$

It is then possible to fit the equilibrium constant to the ^{1}H NMR data obtained by treating $Fe_3Co_6Se_8L_6$ with increasing amounts of L. This utilizes the ability to treat the chemical shift, δ, of a peak from these spectra as a weighted average of the chemical shift of that peak in the absence of L, δ_0, and in the presence of an infinite excess of L, δ_{max} such that:

$$\delta = \frac{[Fe]\delta_0 + [FeL]\delta_{max}}{[Fe^{tot}]}$$

After substituting the known concentrations, the concentration of the bound species [FeL] is obtained as a function of the initial $Fe_3Co_6Se_8L_6$ concentration and chemical shift.

$$[FeL] = [Fe^{tot}]\frac{\delta - \delta_0}{\delta_{max} - \delta_0}$$

In practice, it is also necessary to fit δ_{max}, as it is not possible to achieve an infinite excess of L.

Table 1.1. A compilation of the *tert*-butyl isocyanide binding constants for the neutral, oxidized and reduced tri-iron clusters **Fe$_3$**, [**Fe$_3$**(CN^{t}Bu)$_2$][PF$_6$], and [^{n}Bu$_4$N][**Fe$_3$**].

Equilibrium	K_{eq} (M^{-1})
Fe$_3$ ⇌ **Fe$_3$**(CN^{t}Bu)	1290
Fe$_3$(CN^{t}Bu) ⇌ **Fe$_3$**(CN^{t}Bu)$_2$	196
Fe$_3$(CN^{t}Bu)$_2$ ⇌ **Fe$_3$**(CN^{t}Bu)$_3$	19
[**Fe$_3$**(CN^{t}Bu)$_2$][PF$_6$] ⇌ [**Fe$_3$**(CN^{t}Bu)$_3$][PF$_6$]	24
[^{n}Bu$_4$N][**Fe$_3$**] ⇌ [^{n}Bu$_4$N][**Fe$_3$**(CN^{t}Bu)]	no binding observed

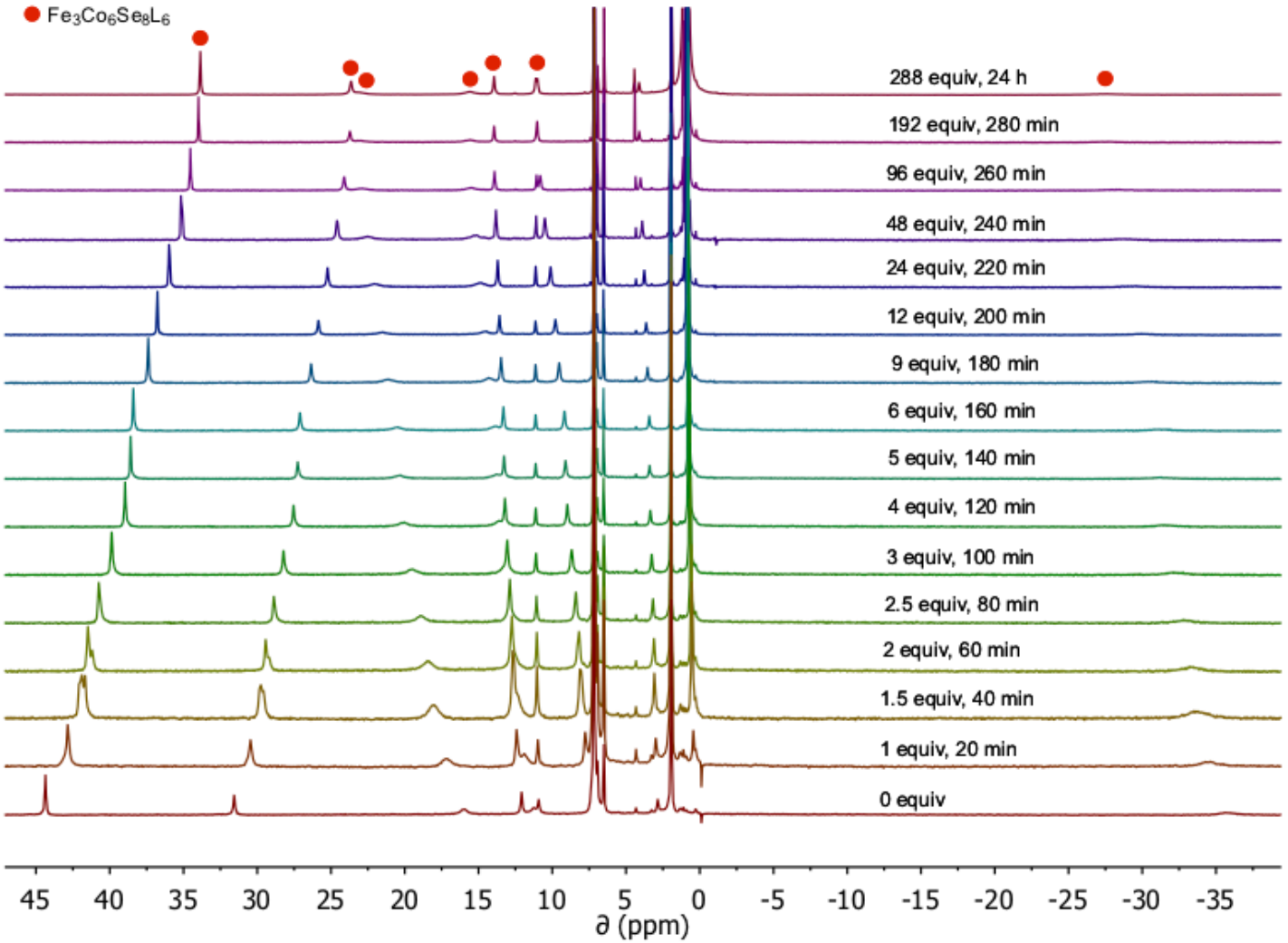


Figure 1.15. ^{1}H NMR (C_6D_6, 25 °C, 300 MHz) spectra of $Fe_3Co_6Se_8L_6$ (**Fe$_3$**) with varying equivalents of CN^{t}Bu, increasing from the bottom to the top spectrum as indicated. The binding constants were calculated based on the change in the farthest downfield chemical shift at each inflection point (1.5 and 5 equiv) and the starting and ending chemical shift values (0 and 288 equiv).

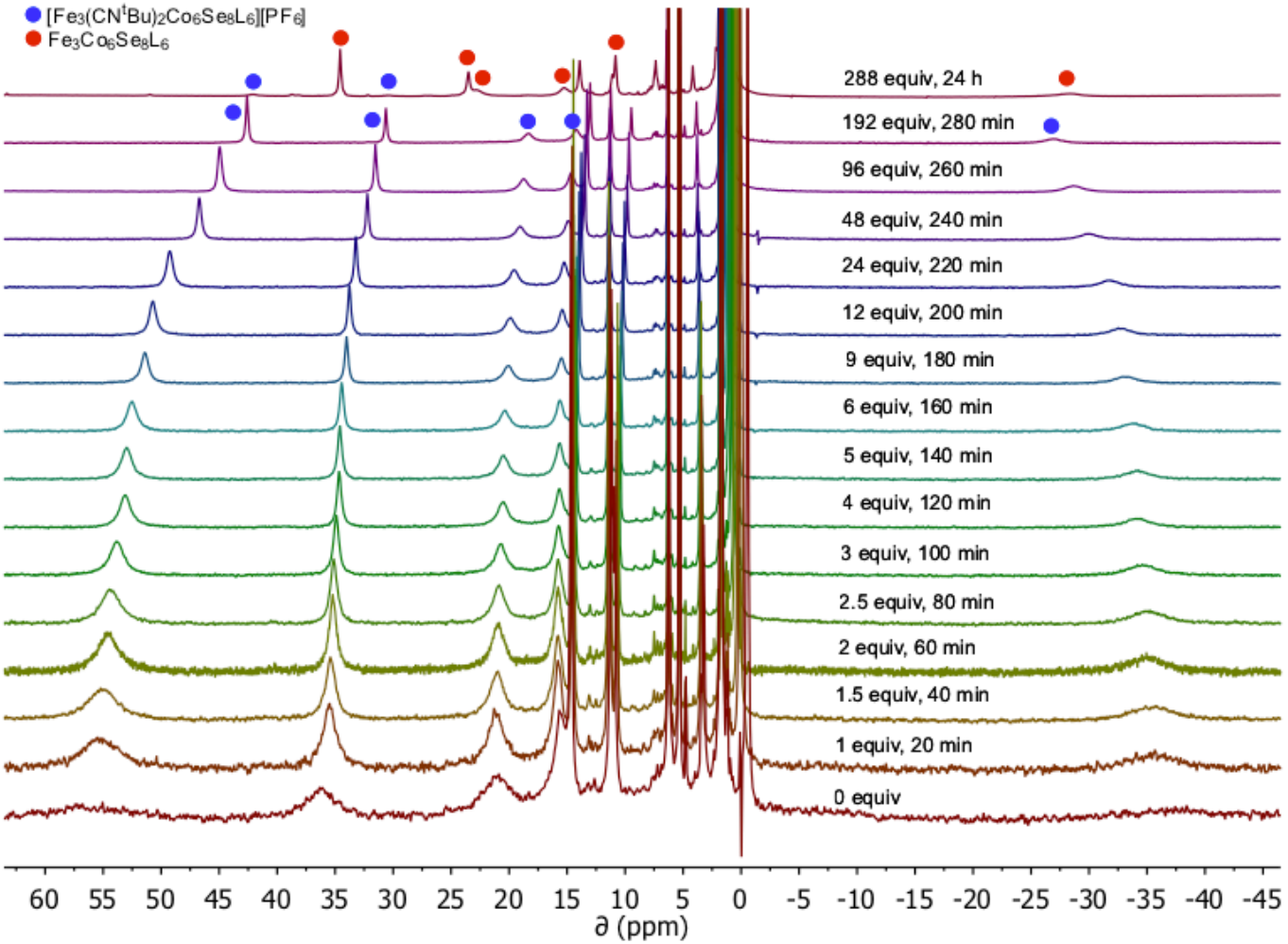


Figure 1.16. ^{1}H NMR (CD_2Cl_2, 25 °C, 300 MHz) spectra of $[Fe_3(CN^tBu)_2Co_6Se_8L_6][PF_6]$ ($[\mathbf{Fe_3}(CN^tBu)_2][PF_6]$) with varying equivalents of CN^tBu, increasing from the bottom to the top spectrum as indicated. The binding constant was calculated based on the change in chemical shift of the far downfield signal (~57 ppm, 0 equiv CN^tBu). Note that after adding 288 equiv of CN^tBu and allowing the sample to sit for ~24 h at 25 °C, the analyte appears to have been reduced to yield fully coordinated $\mathbf{Fe_3}$.

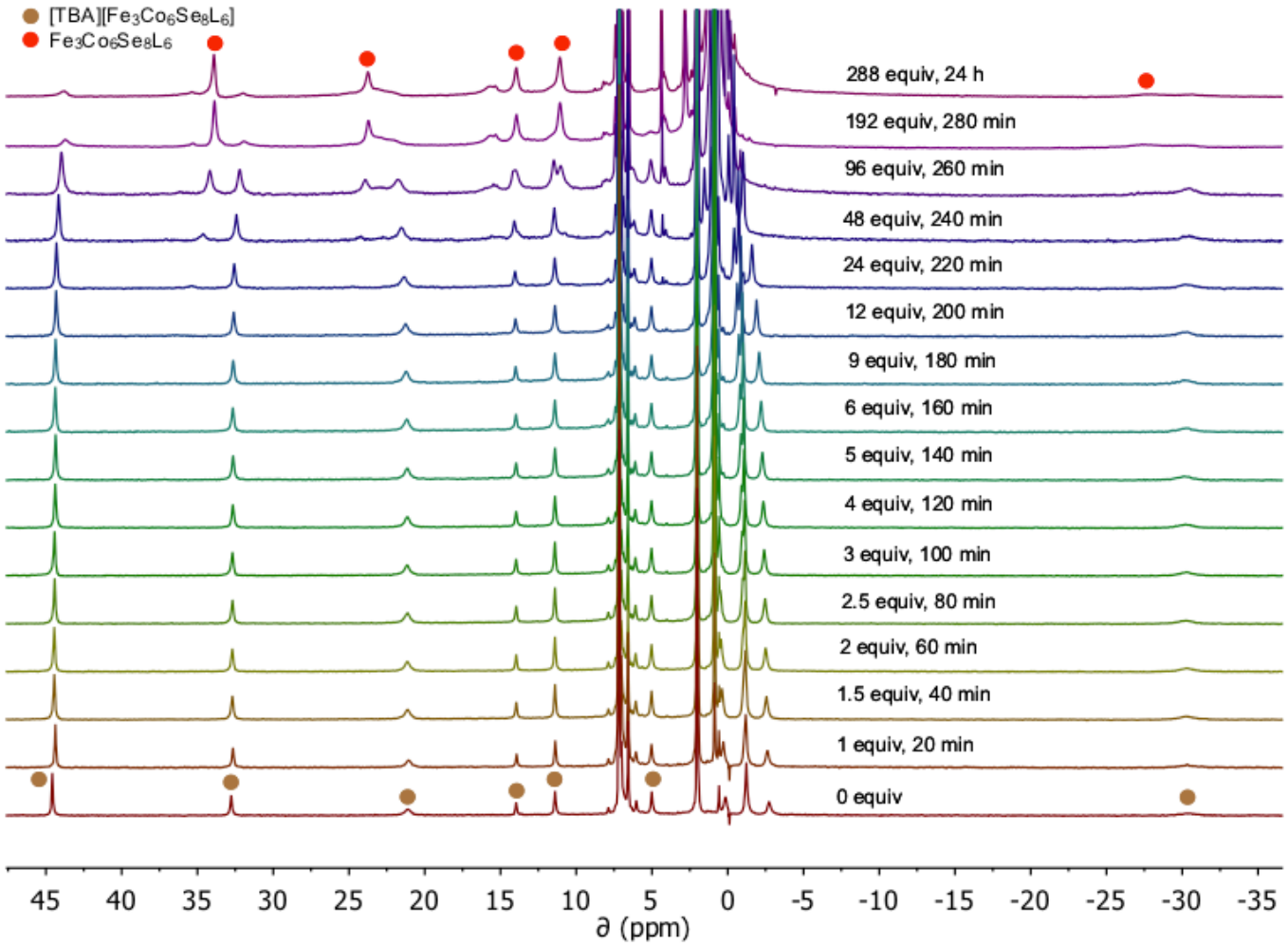


Figure 1.17. ^{1}H NMR (C_6D_6, 25 °C, 300 MHz) spectra of [^{n}Bu$_4$N][**Fe$_3$**] with varying equivalents of CN^{t}Bu that are increasing from the bottom to the top spectrum as indicated. A binding constant was not calculated as it appears that CN^{t}Bu does not coordinate to the mono-reduced species, suggesting that the Fe-Se interaction is more robust for the mono-anionic species. Note that as the excess of CN^{t}Bu increases the mono-reduced undergoes oxidation to produce neutral CN^{t}Bu-bound **Fe$_3$**.

1.3.14 *^{1}H NMR Response to Solvation*

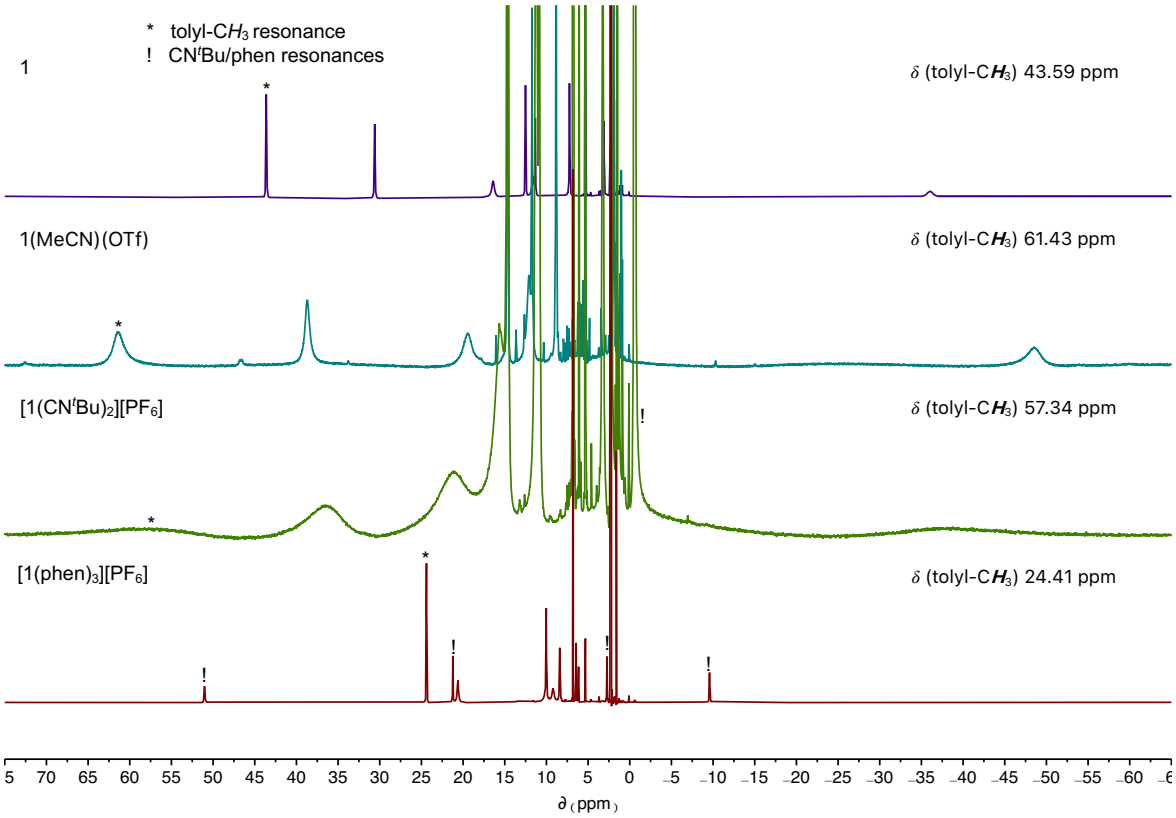


Figure 1.18. ^{1}H NMR (CD_2Cl_2, 25 °C, 500 MHz) spectra of crude **Fe$_3$**, **Fe$_3$**(MeCN)(OTf), [**Fe$_3$**CN^{t}Bu)$_2$][PF$_6$], and [**Fe$_3$**(phen)$_3$][PF$_6$], highlighting variation of the tolyl-CH_3 and ancillary ligand-based resonances. Here, **1** is used as an abbreviation for **Fe$_3$.**

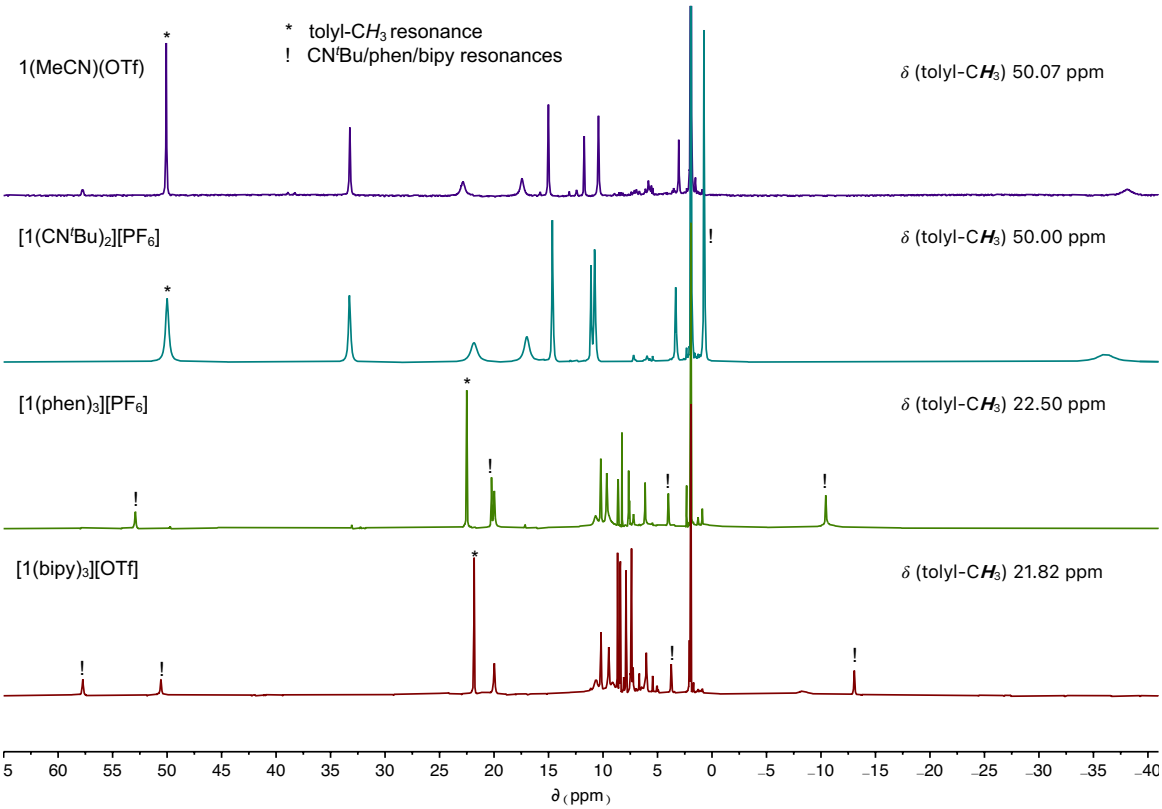


Figure 1.19. ^{1}H NMR (CD_3CN, 25 °C, 500 MHz) spectra of crude **Fe$_3$**(MeCN)(OTf), [**Fe$_3$**(CN^{t}Bu)$_2$][PF_6], [**Fe$_3$**(phen)$_3$[PF_6], and [**Fe$_3$**(bipy)$_3$][PF_6] highlighting variation of the tolyl-C*H*$_3$ and ligand-based resonances. Note that the similarities between the spectra obtained for **Fe$_3$**(MeCN)(OTf) and [**Fe$_3$**(CN^{t}Bu)$_2$][PF_6] are consistent with displacement of the surface ligands MeCN and by the coordinating CD_3CN solvent. Here, **1** is used as an abbreviation for **Fe$_3$.**

1.3.15 *Evans Method Determination of Solution-phase Magnetic Moment*

The solution-phase magnetic moments of **Fe$_3$** and [**Fe$_3$**(CN^{t}Bu)$_2$][PF_6] were determined using the Evans method.[61] A carefully measured mass of each compound was dissolved in a known mass of –35 °C CD_2Cl_2 spiked with mesitylene (1% v/v). The solution was passed through a pipet filter into a J. Young NMR tube equipped with a 1% mesitylene CD_2Cl_2 capillary. The samples were measured at six temperatures ranging between 188 and 297.3 K. The absolute temperature was determined from the separation between methanol signals for a CH_3OH/CD_3OD standard. ^{1}H NMR spectra were recorded for **Fe$_3$** and [**Fe$_3$**(CN^{t}Bu)$_2$][PF_6] and magnetic moments were calculated from the peak separation between the Mes-*CH*$_3$ signals of the capillary and bulk

solution. Diamagnetic correction values of –0.00145 and –0.00155 emu were calculated for **Fe$_3$** and [**Fe$_3$**(CN^{t}Bu)$_2$][PF$_6$], respectively, using Pascal's constants.[62]

Fe$_3$ and [**Fe$_3$**(CN^{t}Bu)$_2$][PF$_6$] exhibit solution-phase magnetic moments of 8.94 and 9.98 μB at 25 °C, respectively, which is consistent with three isolated S=2 Fe(II) sites. The slight increase observed for [**Fe$_3$**(CN^{t}Bu)$_2$][PF$_6$] can be attributed to the formation of a S=1/2 $[Co_6Se_8]^+$ core upon oxidation.

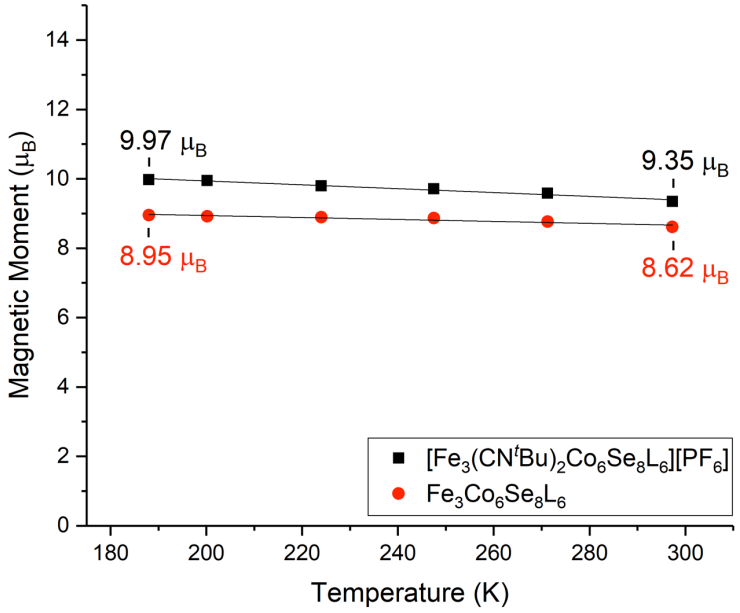


Figure 1.20. The solution-phase magnetic moments of **Fe$_3$** and [**Fe$_3$**(CN^{t}Bu)$_2$][PF$_6$] as determined using the Evans Method in dichloromethane-d_2 between 188 and 297 K.

1.3.16 *Electrochemical Analysis*

Large peak-to-peak separation potentials (ΔE_p) indicate that all of these redox processes are quasi-reversible. To gauge the chemical reversibility of these electrochemical transformations, cyclic voltammograms were recorded at several scan rates between 50 and 500 mV s^{-1}. For a chemically reversible process, peak anodic and cathodic currents should exhibit a linear dependence on the square root of the scan rate.[40] This is demonstrated by fitting the electrochemical data to the Randles–Sevcik equation:

$$j_p = 269000 n_e^{3/2} D_0^{1/2} C_0 v^{1/2}$$

where j_p is the current density in A/cm^2, n_e is the number of electron equivalents transferred in the redox process, D_0 is the diffusion coefficient in cm^2/s, C_0 is the bulk concentration in mol/cm^3, and

v is the potential scan rate in V/s. We found that the peak current densities exhibit a linear dependence on the square root of scan rate for $Co_6Se_8L^{Tol,H}{}_6$, **Fe$_3$**, and [**Fe$_3$**(CN^{t}Bu)$_2$][PF$_6$], consistent with diffusion limited reversible electron transfer.

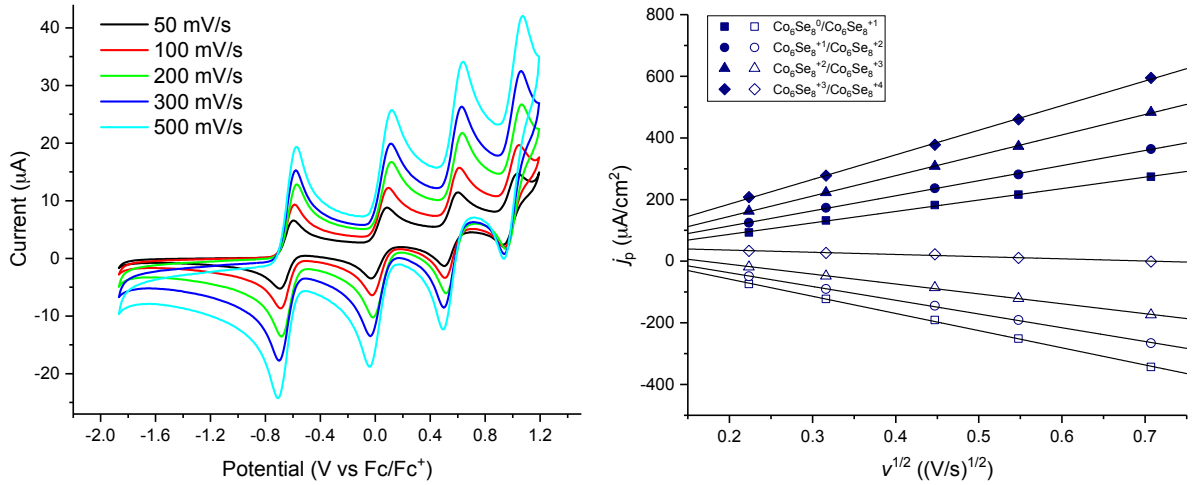


Figure 1.21. Cyclic voltammograms of $Co_6Se_8L^{Tol,H}{}_6$ recorded between 50 and 500 mV s^{-1} in 0.1 M [^{n}Bu$_4$N][PF$_6$] DCM and referenced to ferrocene (left) and a plot of current density (j_p) versus the square root of scan rate ($v^{1/2}$) with linear fits used to model the data with the Randles–Sevcik equation (right).

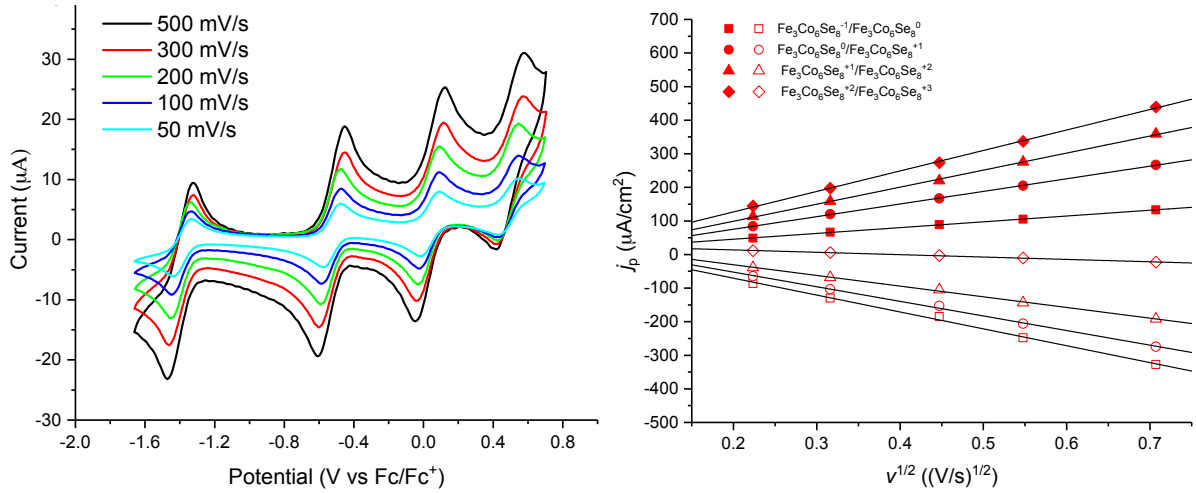


Figure 1.22. Cyclic voltammograms of **Fe$_3$** recorded between 50 and 500 mV s^{-1} in 0.1 M [^{n}Bu$_4$N][PF$_6$] DCM and referenced to ferrocene (left) and a plot of current density (j_p) versus the square root of scan rate ($v^{1/2}$) with linear fits used to model the data with the Randles–Sevcik equation (right).

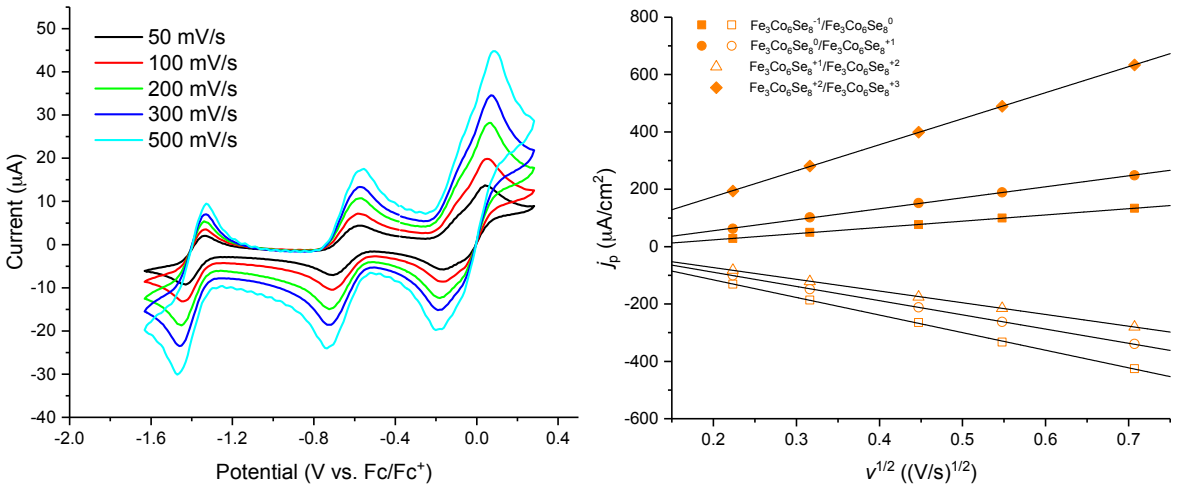


Figure 1.23. Cyclic voltammograms of [**Fe$_3$**(CN^{t}Bu)$_2$][PF$_6$] recorded between 50 and 500 mV s^{-1} in 0.1 M [^{n}Bu$_4$N][PF$_6$] DCM and referenced to ferrocene (left) and a plot of current density (j_p) versus the square root of scan rate ($v^{1/2}$) with linear fits used to model the data with the Randles–Sevcik equation (right).

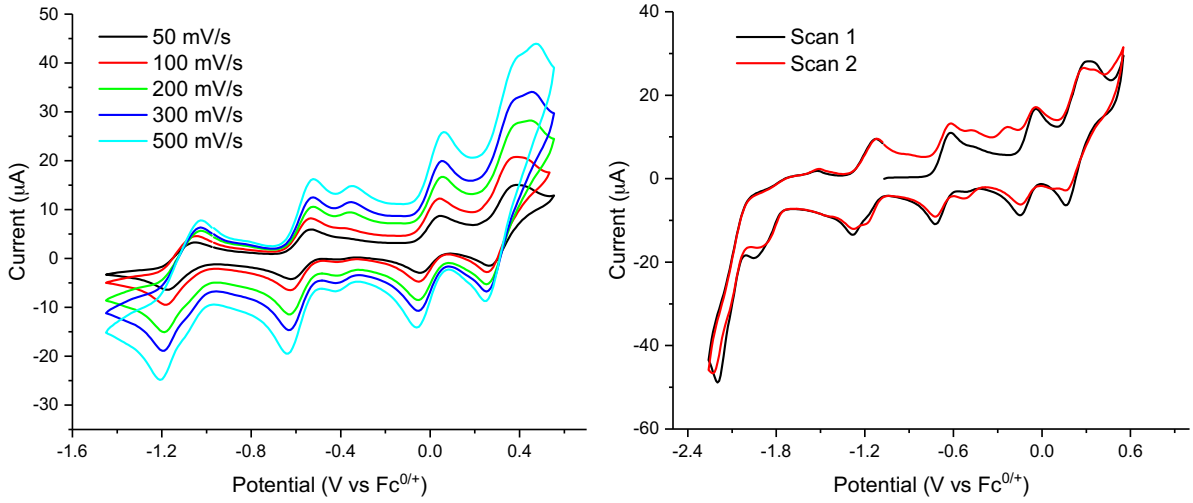


Figure 1.24. Cyclic voltammograms of [**Fe$_3$**(phen)$_3$][PF$_6$] recorded at scan rates (left) between 50 and 500 mV s^{-1}, (right) of 200 mV/s with a wider potential window, in 0.1 M [^{n}Bu$_4$N][PF$_6$] DCM and referenced to ferrocene.

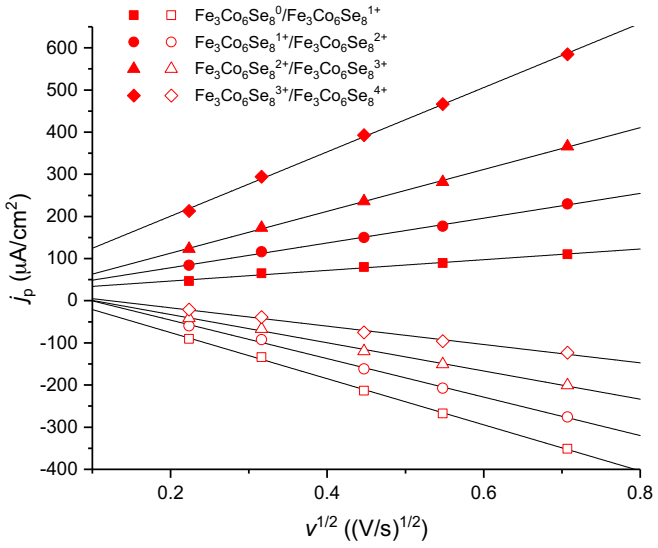


Figure 1.25. Plot of current density (j_p) versus the square root of scan rate ($v^{1/2}$) derived from cyclic voltammograms of [**Fe$_3$**(phen)$_3$][PF$_6$] in in 0.1 M [^{n}Bu$_4$N][PF$_6$] DCM. Linear fits used to model the data with the Randles–Sevcik equation.

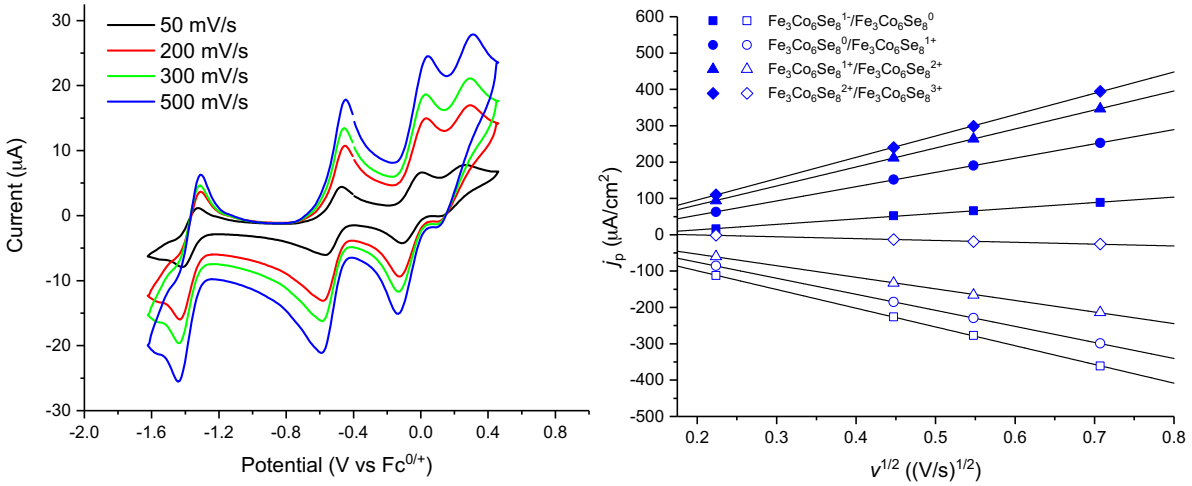


Figure 1.26. Cyclic voltammograms of **Fe$_3$**(MeCN)(OTf) recorded between 50 and 500 mV s^{-1} in 0.1 M [^{n}Bu$_4$N][PF$_6$] DCM and referenced to ferrocene (left) and plot of current density (j_p) versus the square root of scan rate ($v^{1/2}$) with linear fits used to model the data with the Randles-Sevcik equation (right).

Table 1.2. Half-wave potentials ($E_{1/2}$) and peak-to-peak separation potentials (ΔE_p) of **Fe$_3$**, **Fe$_3$**(MeCN)(OTf), [**Fe$_3$**(CN^{t}Bu)$_2$][PF_6], and [**Fe$_3$**(phen)$_3$][PF_6] recorded in 0.1 M [^{n}Bu$_4$N][PF_6] DCM (or THF) solutions at a scan rate of 200 mV/s.

redox couple (n_{red}/n_{ox})	$E_{1/2}$ (V vs $Fc^{0/+}$); ΔE_p (mV)			
	Fe$_3$	**Fe$_3$**(MeCN)(OTf)	[**Fe$_3$**(CN^{t}Bu)$_2$][PF_6]	[**Fe$_3$**(phen)$_3$][PF_6]
4+/3+	--	--	--	0.33; 130
2+/3+	0.48 (0.23); 130 (242)	0.21 (0.04); 181 (211)	0.05[a]	0.00; 100
1+/2+	–0.03 (–0.20); 120 (222)	–0.04 (–0.37); 161 (192)	–0.12[a] (–0.30); (151)	–0.58 (–0.61); 91 (131)
0/1+	–0.53 (–0.72); 111 (222)	–0.52 (–0.78); 141 (172)	–0.64 (–0.80); 111 (161)	–1.11 (–1.21); 131 (131)
1–/0	–1.39 (–1.50); 111 (221)	–1.37 (–1.56); 121 (181)	–1.39 (–1.57); 111 (151)	--
2–/1–	(–2.11); (211)	(–2.09); 141	(–2.16); (151)	--
OCP (V vs $Fc^{0/+}$)	–1.13 (–1.39)	–0.39 (–0.51)	–0.38 (–0.53)	–0.98 (–1.14)

[a]Due to overlap between the 1+/2+ and 2+/3+ redox couples, these values were approximated based on the location of the shoulders generated by the 1+/2+ anodic and 2+/3+ cathodic currents.

Table 1.3. Diffusion coefficients (D_0) obtained by applying the Randles–Sevcik equation assuming n_e=1 for various oxidation states determined from cyclic voltammograms of **Fe$_3$**, **Fe$_3$**(MeCN)(OTf), [**Fe$_3$**(CN^{t}Bu)$_2$][PF_6], and [**Fe$_3$**(phen)$_3$][PF_6] recorded in 0.1 M [^{n}Bu$_4$N][PF_6] DCM.

Oxidation state (n)	D_0 (10^{-5} cm^2/s)[a]			
	Fe$_3$	**Fe$_3$**(MeCN)(OTf)	[**Fe$_3$**(CN^{t}Bu)$_2$][PF_6]	[**Fe$_3$**(phen)$_3$][PF_6]
4+	--	--	--	(0.13)
3+	(0.003)	(0.004)	--	4.55 (0.35)
2+	1.23 (0.17)	1.13 (0.34)	1.74 (0.33)	1.63 (0.67)
1+	0.80 (0.38)	0.87 (0.66)	(0.49)	0.69 (1.22)
0	0.45 (0.58)	0.44 (1.00)	0.24 (0.79)	0.19
1–	0.13	0.05	0.06	--
2–	--		--	--

[a] Diffusion coefficients were calculated for each anodic and cathodic peak current density for scan rates ranging between 50 and 500 mV/s, then averaged for all scan rates to obtain the listed values. Values shown with and without parentheses were calculated from cathodic or anodic current densities, respectively.

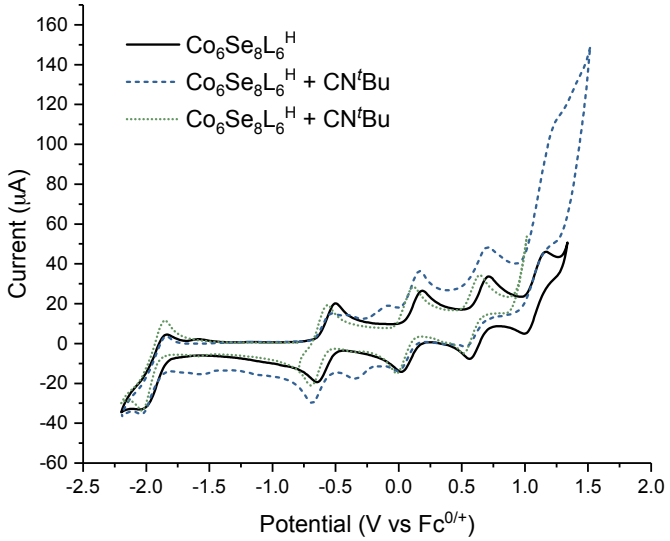


Figure 1.27. Cyclic voltammograms of $Co_6Se_8L^{Tol,H}_6$ (1.1 mM) recorded before (black) and after (blue/green) addition of CN^{t}Bu (8 equiv, 8.8 mM) in 0.1 M [^{n}Bu$_4$N][PF$_6$] DCM. Importantly, the 2+/3+ redox couple does not shift to lower potentials in the presence of excess CN^{t}Bu. Note that irreversible events are introduced if the 3+/4+ transition is accessed in the presence of CN^{t}Bu, but that the first three oxidation events appear to be reversible.

Table 1.4. Half-wave potentials ($E_{1/2}$), peak-to-peak separation potentials (ΔE_p), and open circuit potentials (OCP) of $Co_6Se_8L^{Tol,H}_6$ and **Fe$_3$** recorded in 0.1 M [^{n}Bu$_4$N][PF$_6$] DCM or (THF) with a scan rate of 200 mV/s.

redox couple (n_{red}/n_{ox})	$E_{1/2}$ (V vs $Fc^{0/+}$); ΔE_p (mV)	
	$Co_6Se_8L^{Tol,H}_6$	**Fe$_3$**
+3/+4	1.01; 110	-
+2/+3	0.57 (0.41); 110 (201)	0.48 (0.23); 130 (242)
+1/+2	0.05 (–0.08); 131 (201)	–0.03 (–0.20); 120 (222)
0/+1	–0.63 (–0.69); 110 (191)	–0.53 (–0.72); 111 (222)
–1/0	–1.98 (–2.13); 151 (313)	–1.39 (–1.50); 111 (221)
–2/–1	-	(–2.11); (211)
OCP (V vs $Fc^{0/+}$)	–0.87 (–0.88)	–0.85 (–1.39)

Table 1.5. Diffusion coefficients (D_0) obtained by applying the Randles–Sevcik equation assuming n_e=1 for various oxidation states determined from cyclic voltammograms of $Co_6Se_8L^{Tol,H}_6$, **Fe$_3$**, and [**Fe$_3$**$(CN^tBu)_2$][PF_6] recorded in 0.1 M [^{n}Bu$_4$N][PF_6] DCM.

redox couple n_{red}/n_{ox}	D_0 (10^{-5} cm^2/s)[a]		
	$Co_6Se_8L^{Tol,H}_6$	**Fe$_3$**	[**Fe$_3$**$(CN^tBu)_2$][PF_6]
+3/+4	2.39 (0.03)	--	--
+2/+3	1.54 (0.11)	1.23 (0.003)	1.74
+1/+2	0.90 (0.32)	0.80 (0.17)	(0.33)
0/+1	0.52 (0.56)	0.45 (0.38)	0.24 (0.49)
–1/0	--	0.12 (0.58)	0.06 (0.79)

[a] Diffusion coefficient calculated at each anodic and cathodic peak current density for scan rates between 50 and 500 mV/s and then averaged to obtain the listed values. Coefficients calculated from anodic and cathodic currents shown without and with parenthesis, respectively.

1.3.17 *^{57}Fe Mössbauer Spectroscopy*

Table 1.6. Zero-field ^{57}Fe Mössbauer parameters for [**Fe$_3$**(CN^{t}Bu)$_2$][PF$_6$], [**Fe$_3$**(phen)$_3$][PF$_6$], **Fe$_3$**(CN^{t}Bu)$_3$, **Fe$_3$**, and [^{n}Bu$_4$N][**Fe$_3$**Co$_6$Se$_8$L$_6$] collected at 90 K.

Compound	δ (mm/s)	$\lvert\Delta E_Q\rvert$ (mm/s)
oxidized		
[**Fe$_3$**(CN^{t}Bu)$_2$][PF$_6$]		
component 1 (60%)	0.61	1.23
component 2 (40%)	0.71	1.90
[**Fe$_3$**(phen)$_3$][PF$_6$]	0.94	1.55
neutral		
Fe$_3$(CN^{t}Bu)$_3$		
component 1 (89%)	0.84	1.43
component 2 (11%)[a]	0.42	1.16
Fe$_3$	0.65	0.66
reduced		
[^{n}Bu$_4$N][**Fe$_3$**]	0.64	0.69

[a] Component 2 stems from an unidentified impurity.

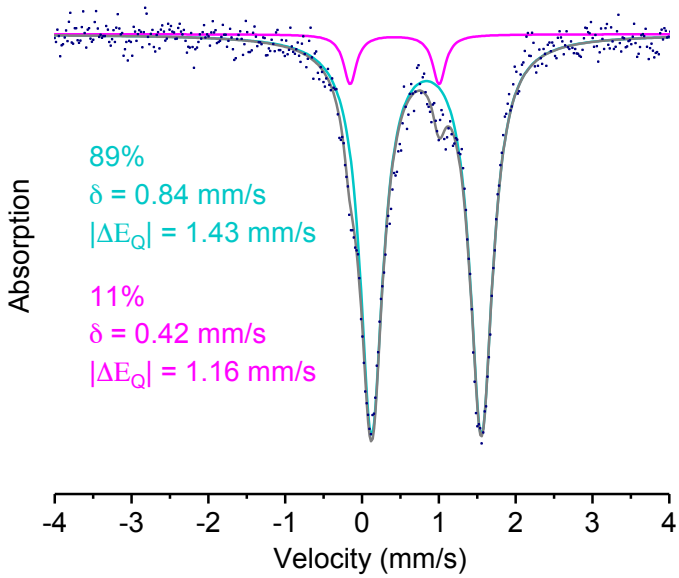


Figure 1.28. Zero-field ^{57}Fe Mössbauer spectrum (90 K) of **Fe$_3$**(CN^{t}Bu)$_3$. [δ, |ΔE$_Q$| (mm/s)]: component 1 (cyan fit): 0.84, 1.43, 89%; component 2 (magenta): 0.42, 1.16, 11%.

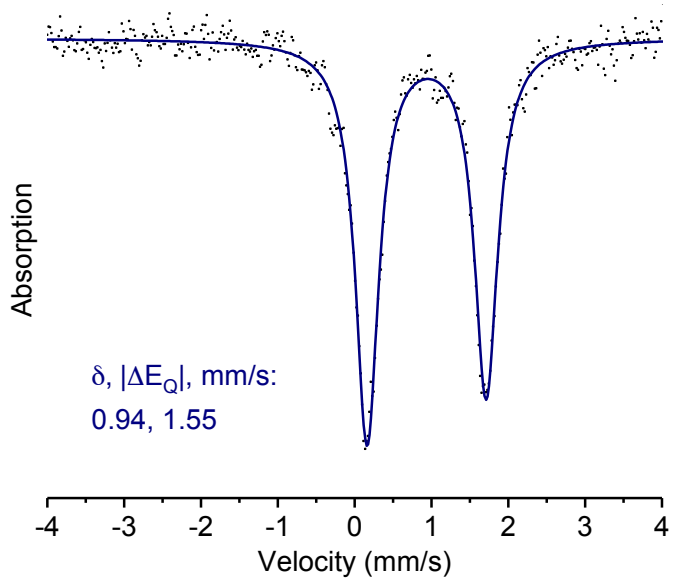


Figure 1.29. Zero-field ^{57}Fe Mössbauer spectrum (90 K) of [**Fe$_3$**(phen)$_3$][PF$_6$]. [δ, |ΔE$_Q$| (mm/s)]: component 1 (dark blue fit): 0.94, 1.55, 100%.

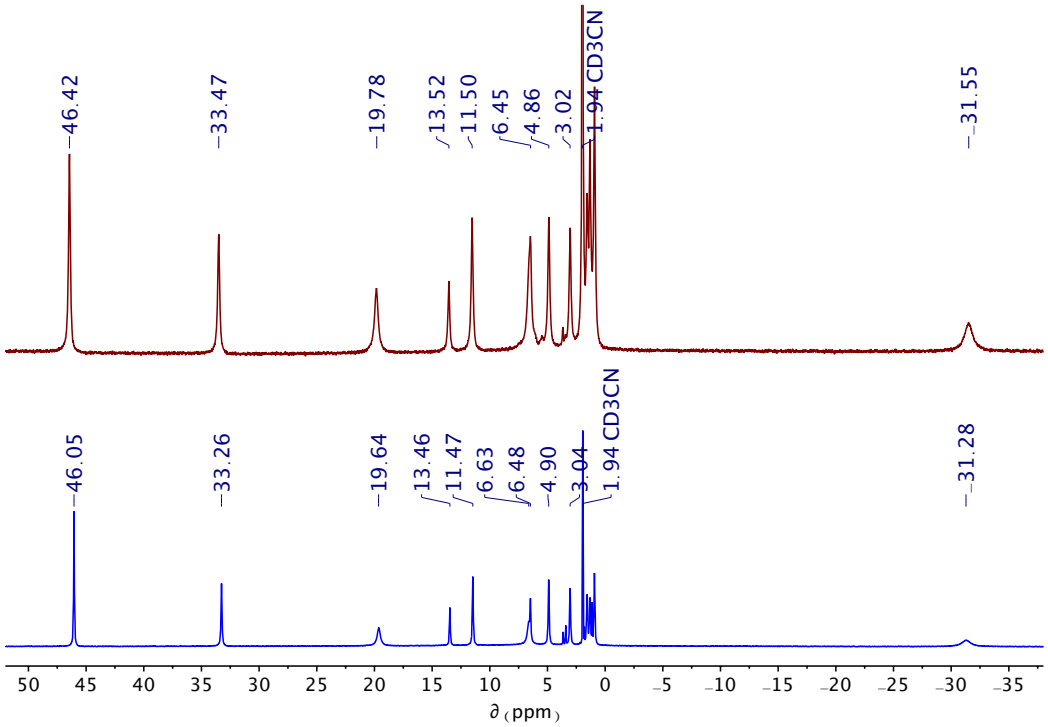


Figure 1.30. Given the similarity between the Mössbauer spectra obtained for **Fe$_3$** and [(^{n}Bu)$_4$N][**Fe$_3$**], ^{1}H NMR (CD$_3$CN, 25 °C, 300 MHz**)** spectra of [(^{n}Bu)$_4$N][**Fe$_3$**] were recorded before (bottom) and after (top) Mössbauer analysis.

1.3.18 *X-ray Structure Determination*

Single crystals suitable for X-ray analysis, grown according to methods detailed below, were coated in deoxygenated paratone oil and mounted on a 20 μm CryoLoop™ (Hampton Research, 18 mm mount, 0.2 to 0.3 mm loop diameter). Data was collected at –173 °C on a Bruker APEX II single crystal X-ray diffractometer, with a Mo source. Data was integrated and scaled using SAINT, SADABS within the APEX2 software package by Bruker.[64] Solution by direct methods (SHELXT[65] or SIR97[66,67]) produced a complete heavy atom phasing model consistent with the proposed structure. Structures were completed by difference Fourier synthesis with SHELXL.[68–70] Scattering factors are from Waasmair and Kirfel.[71] Hydrogen atoms were placed in geometrically idealized positions and constrained to ride on their parent atoms with C–H distances in the range 0.95–1.00 Å. Isotropic thermal parameters U_{eq} were fixed such that they were $1.2U_{eq}$ of their parent atom Ueq for CHs and $1.5U_{eq}$ of their parent atom U_{eq} in case of methyl groups. All non-hydrogen atoms were refined anisotropically by full-matrix least-squares.

1.3.18.1 $Co_6Se_8L^{Tol,H}{}_6$

Single crystals of $Co_6Se_8L^{Tol,H}{}_6$ of suitable quality for X-ray diffraction were grown by vapor diffusion of *n*-pentane into a saturated solution of $Co_6Se_8L^{Tol,H}{}_6$ in toluene at 25 °C over the course of 24 h. The asymmetric unit contains half of the molecule, with the molecule being thus rigorously C_s symmetric.

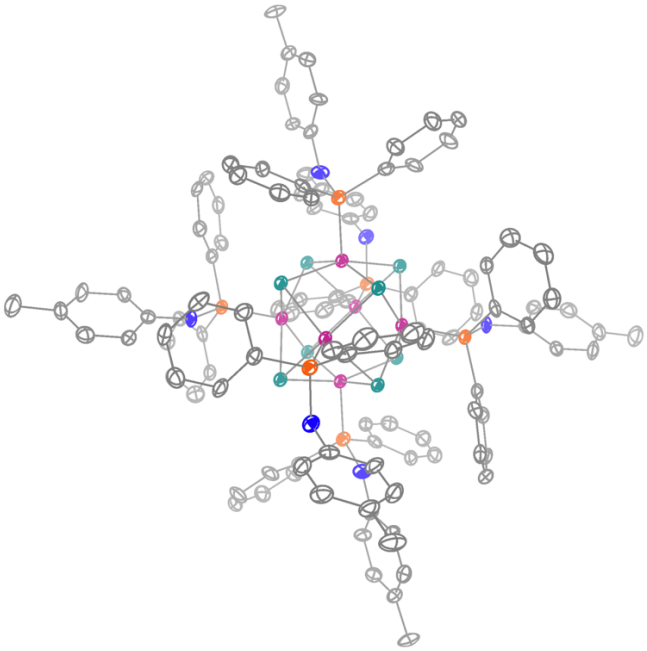


Figure 1.31. Solid-state structure of $Co_6Se_8L^{Tol,H}_6$ with thermal ellipsoids plotted at a 50% probability level. Hydrogen atoms have been omitted for clarity.

1.3.18.2 $[Co_6Se_8L^{Tol,H}_6][OTf]$

Single crystals of $[Co_6Se_8L^{Tol,H}_6][OTf]$ were grown *via* vapor diffusion of diethyl ether into a saturated solution of the product in THF at 25 °C over the course of 24 h. The compound crystallized in $P\bar{1}$. The asymmetric unit contains half of the cluster, one tetrahydrofuran molecule and half of a triflate anion (disordered by inversion at the median of the C-S bond.

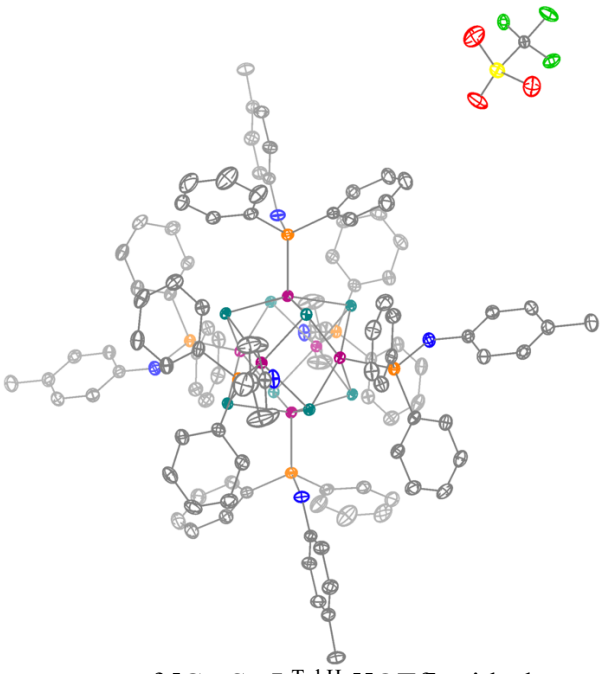


Figure 1.32. Solid-state structure of $[Co_6Se_8L^{Tol,H}_6][OTf]$ with thermal ellipsoids plotted at a 50% probability level. Hydrogen atoms have been omitted for clarity.

1.3.18.3 $\mathbf{Fe_3}(CN^tBu)_3$

Dark-red prismatic crystals were grown via vapor diffusion of *n*-pentane into a concentrated solution of $\mathbf{Fe_3}(CN^tBu)_3$ in toluene spiked with 4 equivalents of excess *tert*-butyl isocyanide. Attempts to grow high quality single crystals of $\mathbf{Fe_3}(CN^tBu)_3$ from THF, DCM and toluene solutions without excess isocyanide yielded polycrystalline material. The compound crystallized in the triclinic $P\bar{1}$ space group, and the asymmetric unit contains a single cluster with some highly disordered toluene and pentane solvent molecules inside of infinite channels along [111], which necessitated removal using SQUEEZE. The molecule exhibits multiple instances of toluene, phenyl and *tert*-butyl disorder.

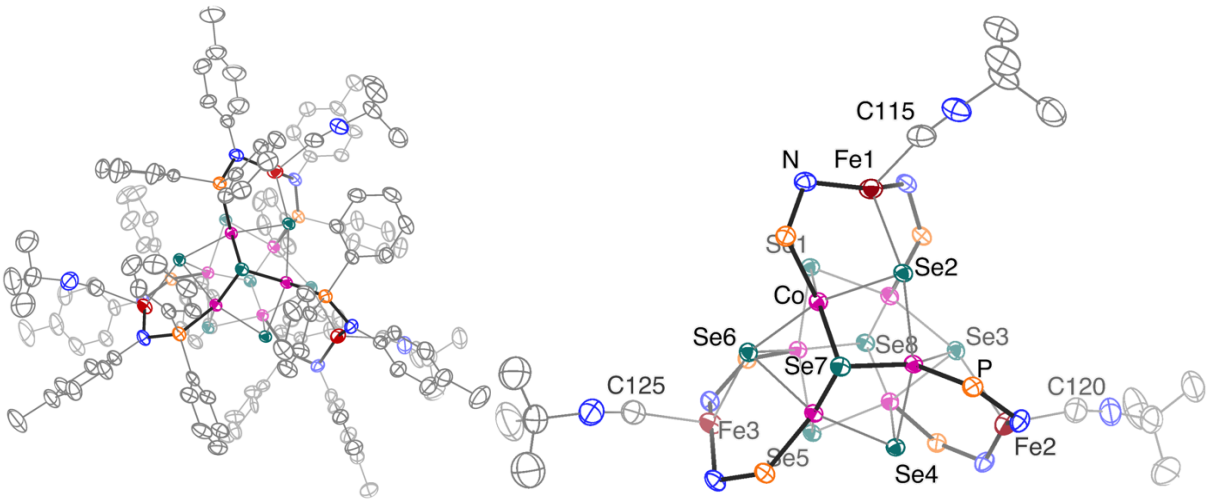


Figure 1.33. Molecular structure of **Fe$_3$**(CN^{t}Bu)$_3$ with thermal ellipsoids shown at a 50% probability level. All hydrogen atoms, disorder and co-crystallized solvent molecules are omitted for clarity. Selected interatomic distances (Å): Fe1-C115 2.126(5), Fe2-C120 2.127(5), Fe3-C125 2.140(4); Fe1-Se2 2.526(4), Fe2-Se3 2.488(4), Fe3-Se6 2.509(2); Se1…Se4 5.644(9), Se2…Se5 5.701(5), Se3…Se6 5.757(8), Se7…Se8 5.499(2).

1.3.18.4 [**Fe$_3$**(CN^{t}Bu)$_2$][PF$_6$]

Small prismatic crystals of [**Fe$_3$**(CN^{t}Bu)$_2$][PF$_6$] suitable for single crystal X-ray analysis were grown via vapor diffusion of *n*-pentane into a concentrated DCM solution at room temperature over the course of 72 h. The compound crystallized in the triclinic space group $P\bar{1}$ and the asymmetric unit contains a singular cluster, accompanied by a $[PF_6]^+$ counterion, and one DCM solvent molecule. The solid-state structure reveals that two Fe sites are bound by terminal CN^{t}Bu ligands, while the third iron site is bound κ^4 by the $Co_6Se_8L^{Tol}_6$ framework.

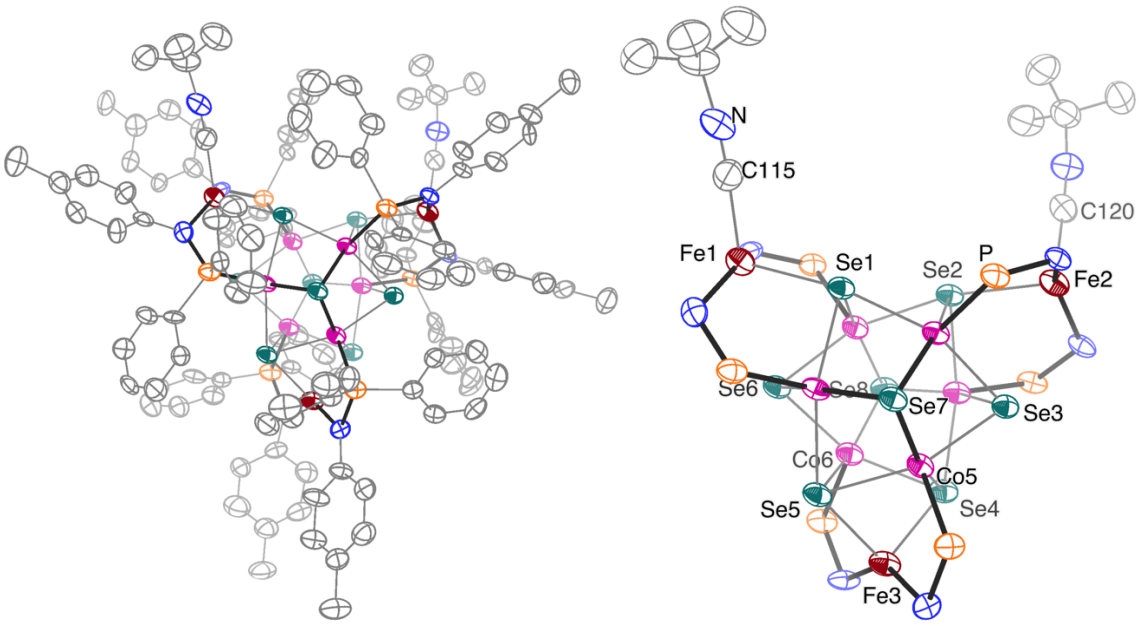


Figure 1.34. Molecular structure of [**Fe$_3$**(CN^{t}Bu)$_2$][PF$_6$] with thermal ellipsoids shown at a 50% probability level. All hydrogen atoms, disorder, the [PF$_6$]$^-$ counterion and co-crystallized solvent molecules are omitted for clarity. Selected interatomic distances (Å): Fe1-C115 2.04(2), Fe2-C120 2.08(2); Fe1-Se1 2.488(7), Fe2-Se2 2.546(7), Fe3-Se4 2.397(6), Fe3-Se5 2.433(5); Fe3-Co5 2.661(8), Fe3-Co6 2.853(7); Co5-Co6 2.800(7); Se7-Se8 5.486(3), Se1-Se4 5.734(8), Se2-Se5 5.83(1), Se3-Se6 5.58(2).

1.3.18.5 [**Fe$_3$**(phen)$_3$][PF$_6$]

X-ray quality dark-red platelets of [**Fe$_3$**(phen)$_3$][PF$_6$] were grown *via* vapor diffusion of diethyl ether into a saturated THF solution at 25 °C, over the course of 72 h. The compound crystallized in the orthorhombic space group Pca2$_1$, and the asymmetric unit contains two Fe$_3$ clusters, with both clusters accompanied by a [PF$_6$]$^-$ counterion and all Fe atoms bound by a 1,10-phenanthroline. The two clusters appear to be closely related by an inversion center; however, minute differences are observed and the [PF$_6$]$^-$ anions are not rigorously related by an inversion center. Only one of potentially several THF solvent molecules could be refined individually. Most of the solvent (3319 electrons, 23% of refined F$_{000}$ = 14408) appeared delocalized inside infinite channels along [0 1 0] and that contribution to the diffraction patterns was removed via SQUEEZE. Several global and individual restraints were applied to ensure convergence of the refinement. The space group is non-centrosymmetric, however, the Flack parameter of 0.5 indicates mirror twinning normal to the c-axis.

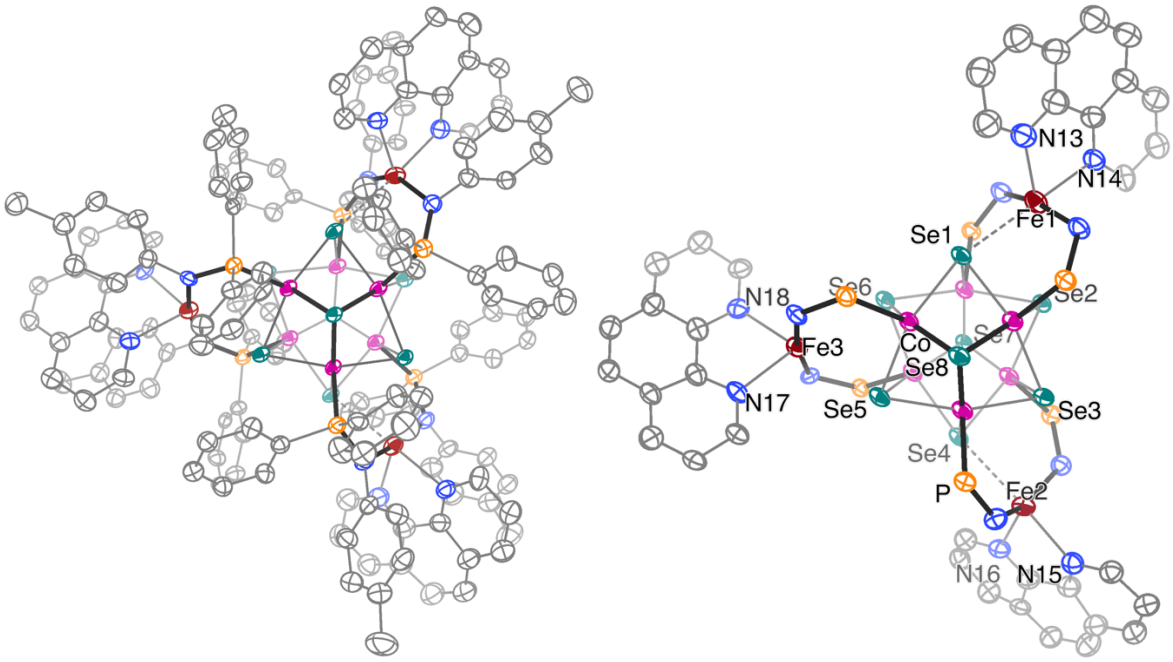


Figure 1.35. Molecular structure of [**Fe$_3$**(phen)$_3$][PF$_6$] with thermal ellipsoids plotted at a 50% probability level. Hydrogen atoms, disorder, co-crystallized solvent molecules, and the [PF$_6$]$^-$ counterion are omitted for clarity. One of two [**Fe$_3$**(phen)$_3$]$^+$ molecules in the asymmetric unit is displayed. Selected interatomic distances (Å): Fe1-Se1 2.780(6), Fe1…Se2 3.097(6), Fe2-Se4 2.815(9), Fe2…Se3 3.640(6), Fe3…Se5 2.99(1), Fe3…Se6 2.990(6); Fe1-N13 2.04(2), Fe1-N14 2.27(2), Fe2-N15 2.18(2), Fe2-N16 2.16(2), Fe3-N17 2.18(2), Fe3-N18 2.19(2); Se7…Se8 5.549(6), Se1…Se4 5.707(5), Se2…Se5 5.659(5), Se3…Se6 5.698(9).

1.3.18.6 [Na(18-C-6)(MeCN)$_2$][**Fe$_3$**]

X-ray quality dark-red platelets of [Na(18-C-6)(MeCN)$_2$][**Fe$_3$**] were grown at –35 °C *via* diffusion of diethyl ether into an acetonitrile concentrate, over the course of 2 weeks. The compound crystallized in the triclinic space group $P\bar{1}$, with the asymmetric unit containing two [Na(18-C-6)(MeCN)$_2$][**Fe$_3$**] pairs, and several diethyl ether and acetonitrile solvent molecules. The structure was pseudo-merohedrally twinned, thus multi-domain integration was not possible. The twin-law (2-fold rotation about the a-axis) was applied to the refinement instructions.

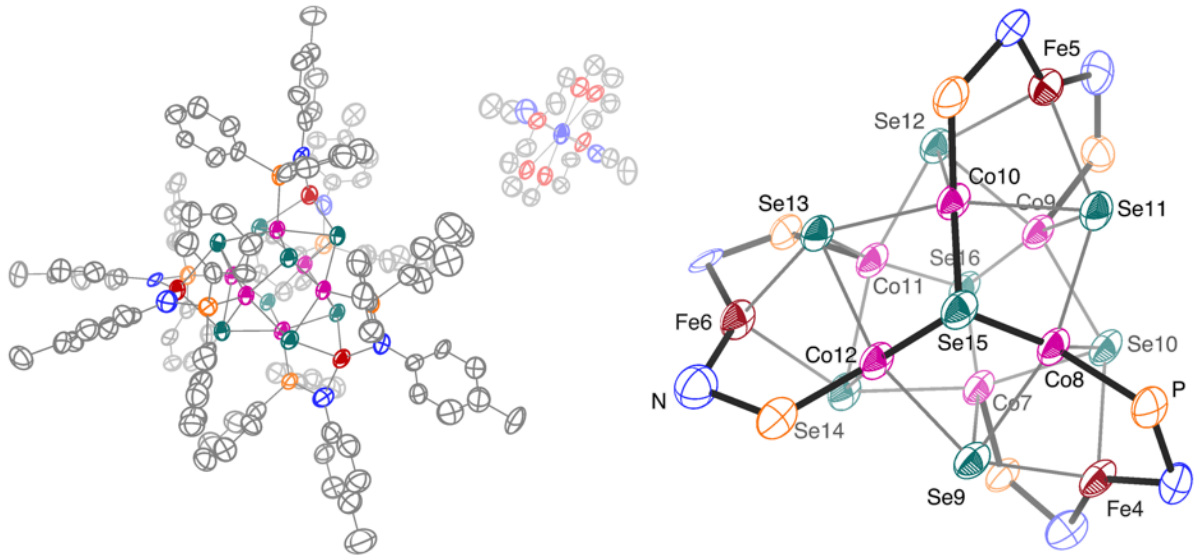


Figure 1.36. Molecular structure of [Na(18-C-6)][$\mathbf{Fe_3}$] with thermal ellipsoids shown at a 50% probability level. All hydrogen atoms, disorder and co-crystallized solvent molecules are omitted for clarity. One of two [$\mathbf{Fe_3}$]$^-$ molecules in the asymmetric unit is displayed. Selected interatomic distances (Å): Fe4-Se9 2.47(4), Fe4-Se10 2.46(1), Fe5-Se11 2.46(2), Fe5-Se12 2.46(3), Fe6-Se13 2.44(4), Fe6-Se14 2.47(3); Fe4…Co7 2.820(9), Fe4…Co8 2.80(2); Co7…Co8 2.78(3), Co7…Co12 2.94(5), Co7…Co11 3.00(3), Co8…Co10 3.01(3), Co8…Co9 2.94(3); Se15…Se16 5.34(7), Se9…Se12 5.79(5), Se10…Se3 5.87(9), Se11…Se14 5.92(8).

Table 1.7. Minimum and maximum values for select interatomic distances as determined by single crystal X-ray diffractometry.

Compound	**Interatomic Distance (Å)**						
	Co-Se	Co…Co	Fe…Co	Fe…Se	Co-P	Fe-N	P-N
oxidized							
[**Fe$_3$**(CN^{t}Bu)$_2$][PF$_6$]	2.304(4) - 2.424(6)	2.800(7) - 3.007(6)	2.661(8) - 3.551(9)	2.397(6) - 3.288(6)	2.163(6) - 2.178(7)	1.91(1) - 2.00(1)	1.65(1) - 1.70(1)
[**Fe$_3$**(phen)$_3$][PF$_6$]	2.284(5) - 2.389(9)	2.700(7) - 2.956(9)	3.503(7) - 3.862(8)	2.780(6) - 3.640(6)	2.13(1) - 2.18(1)	1.97(2) - 2.06(2)	1.61(3) - 1.70(3)
neutral							
Fe$_3$(CN^{t}Bu)$_3$	2.318(4) - 2.389(2)	2.846(5) - 2.991(5)	3.181(6) - 3.440(6)	2.488(4) - 3.102(5)	2.144(4) - 2.165(5)	1.986(3) - 2.018(4)	1.655(4) - 1.668(3)
reduced							
[Na(18-C-6)][**Fe$_3$**]	2.31(2) - 2.45(3)	2.77(3) - 3.04(4)	2.72(1) - 2.87(4)	2.42(2) - 2.48(2)	2.177(9) - 2.19(2)	1.98(2) - 2.00(2)	1.66(3) - 1.69(3)
unmetallated							
Co$_6$Se$_8$L$^{Tol,H}_6$	2.322(6) - 2.362(2)	2.917(7) - 2.974(4)	--	--	2.127(3) - 2.131(6)	--	1.676(6) - 1.716(7)
[Co$_6$Se$_8$L$^{Tol,H}_6$][OTf]	2.316(6) - 2.363(3)	2.852(3) - 2.958(3)	--	--	2.156(4) - 2.165(3)	--	1.679(4) - 1.683(3)

Table 1.8. Crystallographic information for $Co_6Se_8L^{Tol,H}_6$, $[Co_6Se_8L^{Tol,H}_6][OTf]$, and $\mathbf{Fe_3}(CN^tBu)_3$.

Compound	$Co_6Se_8L^{Tol,H}_6$	$[Co_6Se_8L^{Tol,H}_6][OTf]$	$\mathbf{Fe_3}(CN^tBu)_3$
Empirical formula	$C_{114}H_{108}Co_6N_6P_6Se_8$	$C_{123}H_{124}Co_6F_3N_6O_5P_6SSe_8$	$C_{129}H_{129}Co_6Fe_3N_9P_6Se_8$
CCDC Number	1968342	1968341	1968345
Formula weight	2733.14	3026.41	3144.03
Temperature (K)	100(2)	100(2)	100(2)
Wavelength (Å)	0.71073	0.71073	0.71073
Crystal system	Triclinic	Triclinic	Triclinic
Space group	$P\bar{1}$	$P\bar{1}$	$P\bar{1}$
a (Å)	13.2750(14)	13.6599(8)	17.2556(9)
b (Å)	14.0917(15)	14.6340(8)	17.8894(10)
c (Å)	15.9742(17)	16.5780(10)	24.1455(14)
α (°)	65.352(4)	65.320(3)	79.168(3)
β (°)	83.272(5)	77.241(3)	89.889(3)
γ (°)	73.800(5)	87.287(3)	81.934(3)
Volume (Å^3)	2608.1(5)	2933.1(3)	7246.0(7)
Z	1	1	2
ρ^{calc} (g cm^{-1})	1.740	1.713	1.441
Absorption coefficient (mm^{-1})	3.869	3.473	3.081
F(000)	1358	1511	3136
Crystal size (mm^3)	0.130 x 0.040 x 0.040	0.320 x 0.270 x 0.260	0.250 x 0.160 x 0.140
Theta range for data collection (°)	1.403 to 28.340	1.386 to 28.281	1.314 to 28.369
Index ranges	$-17\leq h\leq 17$, $-18\leq k\leq 18$, $-21\leq l\leq 21$	$-18\leq h\leq 18$, $-19\leq k\leq 19$, $-22\leq l\leq 22$	$-23\leq h\leq 23$, $-23\leq k\leq 23$, $-32\leq l\leq 32$
Reflections collected	25509	29082	344228
Independent reflections	12939 [R(int) = 0.0969]	14571 [R(int) = 0.0157]	36092 [R(int) = 0.0911]
Completeness to theta = 25.000°	99.8%	100%	100.0%
Data / restraints / parameters	12939 / 0 / 637	14571 / 84 / 776	36092 / 351 / 1526
Goodness-of-fit on F^2	0.940	1.034	1.011
Final R indices [I>2sigma(I)]	R1 = 0.0506, wR2 = 0.0835	R1 = 0.0228, wR2 = 0.0568	R1 = 0.0400, wR2 = 0.0802
R indices (all data)	R1 = 0.1221, wR2 = 0.1024	R1 = 0.0273, wR2 = 0.0595	R1 = 0.0832, wR2 = 0.0933
Largest diff. peak and hole (e$^-$Å^{-3})	1.292 and –0.907	1.420 and –1.315	0.862 and –0.739

Table 1.9. Crystallographic information for [**Fe$_3$**(phen)$_3$][PF$_6$], [Na(18-C-6)(MeCN)$_2$][**Fe$_3$**], and [**Fe$_3$**(CN^{t}Bu)$_2$][PF$_6$].

Compound	[**Fe$_3$**(phen)$_3$][PF$_6$]	[Na(18-C-6)(MeCN)$_2$][**Fe$_3$**]	[**Fe$_3$**(CN^{t}Bu)$_2$][PF$_6$]
Empirical formula	$C_{304}H_{260}Co_{12}F_{12}Fe_6N_{24}OP_{14}Se_{16}$	$C_{142}H_{158}Co_6Fe_3N_{10}NaO_8P_6Se_8$	$C_{125}H_{122}Cl_2Co_6F_6Fe_3N_8P_7Se_8$
CCCD Number	1968344	1968343	1968340
Formula weight	7232.54	3494.39	3290.80
Temperature (K)	100(2)	100(2)	100(2)
Wavelength (Å)	0.71073	0.71073	0.71073
Crystal system	Orthorhombic	Triclinic	Triclinic
Space group	$Pca2_1$	$P\bar{1}$	$P\bar{1}$
a (Å)	23.226(3)	19.258(11)	16.0879(11)
b (Å)	24.048(4)	23.136(12)	19.5198(14)
c (Å)	57.067(9)	34.819(15)	20.3718(16)
α (°)	90	101.566(19)	89.380(5)
β (°)	90	97.29(3)	82.032(5)
γ (°)	90	90.47(2)	89.052(4)
Volume (Å^3)	31873(8)	15067(13)	6334.5(8)
Z	4	4	2
ρ^{calc} (g cm^{-1})	1.507	1.540	1.725
Absorption coefficient (mm^{-1})	2.828	2.978	3.587
F(000)	14408	7028	3266
Crystal size (mm^3)	0.200 x 0.180 x 0.040	0.110 x 0.080 x 0.040	0.050 x 0.030 x 0.030
Theta range for data collection (°)	1.412 to 25.187	1.371 to 25.059	1.445 to 25.028
Index ranges	–22≤h≤22, –23≤k≤23, –54≤l≤54	–25≤h≤25, –30≤k≤30, –46≤l≤44	–18≤h≤19, –23≤k≤23, –24≤l≤24
Reflections collected	53108	52434	22129
Independent reflections	53108 [R(int) = 0.1600]	52434 [R(int) = 0.204]	22129 [R(int) = 0.177]
Completeness to theta = 25.000°	97.4%	98.3%	98.9%
Data / restraints / parameters	53108 / 7153 / 3005	52434 / 5996 / 2788	22129 / 762 / 1486
Goodness-of-fit on F^2	1.038	1.031	0.943
Final R indices [I>2sigma(I)]	R1 = 0.1282, wR2 = 0.3041	R1 = 0.1489, wR2 = 0.3466	R1 = 0.0842, wR2 = 0.1389
R indices (all data)	R1 = 0.1974, wR2 = 0.3369	R1 = 0.3381, wR2 = 0.4511	R1 = 0.2703, wR2 = 0.1964
Largest diff. peak and hole (e$^-$Å^{-3})	1.774 and –2.280	1.712 and –1.823	1.015 and –1.115

1.4 REFERENCES

(1) Alonso-Vante, N. *Chalcogenide Materials for Energy Conversion: Pathways to Oxygen and Hydrogen Reaction*, 2018th ed.; Springer, 2018.

(2) Zhang, Y.; Zhou, Q.; Zhu, J.; Yan, Q.; Dou, S. X.; Sun, W. Nanostructured Metal Chalcogenides for Energy Storage and Electrocatalysis. *Adv. Funct. Mater.* **2017**, *27* (35), 1702317. https://doi.org/10.1002/adfm.201702317.

(3) Asadi, M.; Kumar, B.; Behranginia, A.; Rosen, B. a; Baskin, A.; Repnin, N.; Pisasale, D.; Phillips, P.; Zhu, W.; Haasch, R.; Klie, R. F.; Král, P.; Abiade, J.; Salehi-Khojin, A. Robust Carbon Dioxide Reduction on Molybdenum Disulphide Edges. *Nature Communications* **2014**, *5*, 4470. https://doi.org/10.1038/ncomms5470.

(4) Hong, X.; Chan, K.; Tsai, C.; Nørskov, J. K. How Doped MoS $_2$ Breaks Transition-Metal Scaling Relations for CO_2 Electrochemical Reduction. *ACS Catal.* **2016**, *6* (7), 4428–4437. https://doi.org/10.1021/acscatal.6b00619.

(5) Nørskov, J. K.; Studt, F.; Abild-Pedersen, F.; Bligaard, T. *Fundamental Concepts in Heterogeneous Catalysis*; Wiley: Hoboken, New Jersey, 2015.

(6) Tributsch, H.; Pohlmann, L. Electron Transfer: Classical Approaches and New Frontiers. *Science* **1998**, *279* (5358), 1891–1895. https://doi.org/10.1126/science.279.5358.1891.

(7) Tributsch, H. Interfacial Processes Involving Strong Electronic Interactions in Solar Energy Conversion and Storage. *Journal of Photochemistry* **1985**, *29* (1), 89–113. https://doi.org/10.1016/0047-2670(85)87063-5.

(8) Vante, N. A.; Tributsch, H. Energy Conversion Catalysis Using Semiconducting Transition Metal Cluster Compounds. *Nature* **1986**, *323* (6087), 431–432. https://doi.org/10.1038/323431a0.

(9) Schubert, B.; Gocke, E.; Schöllhorn, R.; Alonso-Vante, N.; Tributsch, H. In Situ X-Ray-Electrochemical Studies on the Origin of H_2O_2 Production during Oxygen Reduction at Transition Metal Cluster Materials. *Electrochimica Acta* **1996**, *41* (9), 1471–1478. https://doi.org/10.1016/0013-4686(95)00396-7.

(10) Byskov, L. S.; Hammer, B.; Nørskov, J. K.; Clausen, B. S.; Topsøe, H. Sulfur Bonding in MoS_2 and Co-Mo-S Structures. *Catal. Letters* **1997**, *47* (3–4), 177–182. https://doi.org/10.1023/A:1019009105792.

(11) Li, J.; Guan, Q.; Wu, H.; Liu, W.; Lin, Y.; Sun, Z.; Ye, X.; Zheng, X.; Pan, H.; Zhu, J.; Chen, S.; Zhang, W.; Wei, S.; Lu, J. Highly Active and Stable Metal Single-Atom Catalysts Achieved by Strong Electronic Metal–Support Interactions. *J. Am. Chem. Soc.* **2019**. https://doi.org/10.1021/jacs.9b06482.

(12) Bruix, A.; Rodriguez, J. A.; Ramírez, P. J.; Senanayake, S. D.; Evans, J.; Park, J. B.; Stacchiola, D.; Liu, P.; Hrbek, J.; Illas, F. A New Type of Strong Metal–Support Interaction and the Production of H_2 through the Transformation of Water on $Pt/CeO_2(111)$ and $Pt/CeO_x/TiO_2(110)$ Catalysts. *J. Am. Chem. Soc.* **2012**, *134* (21), 8968–8974. https://doi.org/10.1021/ja302070k.

(13) Campbell, C. T. Catalyst–Support Interactions: Electronic Perturbations. *Nature Chemistry* **2012**, *4* (8), 597–598. https://doi.org/10.1038/nchem.1412.

(14) Chirik, P. J.; Wieghardt, K. Radical Ligands Confer Nobility on Base-Metal Catalysts. *Science* **2010**, *327* (5967), 794–795. https://doi.org/10.1126/science.1183281.

(15) Kaim, W.; Schwederski, B. Non-Innocent Ligands in Bioinorganic Chemistry-An Overview. *Coordination Chemistry Reviews* **2010**, *254* (13–14), 1580–1588. https://doi.org/10.1016/j.ccr.2010.01.009.

(16) Peters, J. W.; Stowell, M. H. B.; Soltis, S. M.; Finnegan, M. G.; Johnson, M. K.; Rees, D. C. Redox-Dependent Structural Changes in the Nitrogenase P-Cluster. *Biochemistry* **1997**, *36* (6), 1181–1187. https://doi.org/10.1021/bi9626665.

(17) Groysman, S.; Holm, R. H. Biomimetic Chemistry of Iron, Nickel, Molybdenum, and Tungsten in Sulfur-Ligated Protein Sites. *Biochemistry* **2009**, *48* (11), 2310–2320. https://doi.org/10.1021/bi900044e.

(18) Appel, A. M.; Bercaw, J. E.; Bocarsly, A. B.; Dobbek, H.; Dubois, D. L.; Dupuis, M.; Ferry, J. G.; Fujita, E.; Hille, R.; Kenis, P. J. A.; Kerfeld, C. A.; Morris, R. H.; Peden, C. H. F.; Portis, A. R.; Ragsdale, S. W.; Rauchfuss, T. B.; Reek, J. N. H.; Seefeldt, L. C.; Thauer, R. K.; Waldrop, G. L. Frontiers, Opportunities, and Challenges in Biochemical and Chemical Catalysis of CO_2 Fixation. *Chemical Reviews* **2013**, *113* (8), 6621–6658. https://doi.org/10.1021/cr300463y.

(19) Beinert, H.; Holm, R. H.; Münck, E. Iron-Sulfur Clusters: Nature's Modular, Multipurpose Structures. *Science* **1997**, *277* (5326), 653–659. https://doi.org/10.1126/science.277.5326.653.

(20) Lee, S. C.; Holm, R. H. The Clusters of Nitrogenase: Synthetic Methodology in the Construction of Weak-Field Clusters. *Chemical Reviews* **2004**, *104* (2), 1135–1157. https://doi.org/10.1021/cr0206216.

(21) Hernández Sánchez, R.; Zheng, S.-L.; Betley, T. A. Ligand Field Strength Mediates Electron Delocalization in Octahedral $[(^{H}L)_2Fe_6(L')_m]^{N+}$ Clusters. *J. Am. Chem. Soc.* **2015**, *137* (34), 11126–11143. https://doi.org/10.1021/jacs.5b06453.

(22) Hernández Sánchez, R.; Champsaur, A. M.; Choi, B.; Wang, S. G.; Bu, W.; Roy, X.; Chen, Y.-S.; Steigerwald, M. L.; Nuckolls, C.; Paley, D. W. Electron Cartography in Clusters. *Angew. Chem. Int. Ed.* **2018**, *57* (42), 13815–13820. https://doi.org/10.1002/anie.201806426.

(23) Li, F.; VanGelder, L. E.; Brennessel, W. W.; Matson, E. M. Self-Assembled, Iron-Functionalized Polyoxovanadate Alkoxide Clusters. *Inorg. Chem.* **2016**, *55* (15), 7332–7334. https://doi.org/10.1021/acs.inorgchem.6b01349.

(24) Petel, B. E.; Brennessel, W. W.; Matson, E. M. Oxygen-Atom Vacancy Formation at Polyoxovanadate Clusters: Homogeneous Models for Reducible Metal Oxides. *J. Am. Chem. Soc.* **2018**, *140* (27), 8424–8428. https://doi.org/10.1021/jacs.8b05298.

(25) De Ruiter, G.; Thompson, N. B.; Takase, M. K.; Agapie, T. Intramolecular C-H and C-F Bond Oxygenation Mediated by a Putative Terminal Oxo Species in Tetranuclear Iron Complexes. *J. Am. Chem. Soc.* **2016**, *138* (5), 1486–1489. https://doi.org/10.1021/jacs.5b12214.

(26) Reed, C. J.; Agapie, T. A Terminal FeIII–Oxo in a Tetranuclear Cluster: Effects of Distal Metal Centers on Structure and Reactivity. *J. Am. Chem. Soc.* **2019**, *141* (24), 9479–9484. https://doi.org/10.1021/jacs.9b03157.

(27) Arnett, C. H.; Chalkley, M. J.; Agapie, T. A Thermodynamic Model for Redox-Dependent Binding of Carbon Monoxide at Site-Differentiated, High Spin Iron Clusters. *J. Am. Chem. Soc.* **2018**, *140* (16), 5569–5578. https://doi.org/10.1021/jacs.8b01825.

(28) Pinkard, A.; Champsaur, A. M.; Roy, X. Molecular Clusters: Nanoscale Building Blocks for Solid-State Materials. *Acc. Chem. Res.* **2018**, *51* (4), 919–929. https://doi.org/10.1021/acs.accounts.8b00016.

(29) Stuczynski, S. M.; Kwon, Y.-U.; Steigerwald, M. L. The Use of Phosphine Chalcogenides in the Preparation of Cobalt Chalcogenides. *Journal of Organometallic Chemistry* **1993**, *449* (1–2), 167–172.

(30) Addison, A. W.; Rao, T. N.; Reedijk, J.; Rijn, J. van; Verschoor, G. C. Synthesis, Structure, and Spectroscopic Properties of Copper(II) Compounds Containing Nitrogen–Sulphur Donor Ligands; the Crystal and Molecular Structure of Aqua[1,7-Bis(N-Methylbenzimidazol-2′-Yl)-2,6-Dithiaheptane]Copper(II) Perchlorate. *J. Chem. Soc., Dalton Trans.* **1984**, No. 7, 1349–1356. https://doi.org/10.1039/DT9840001349.

(31) Brown, A. C.; Suess, D. L. M. Controlling Substrate Binding to Fe4S4 Clusters through Remote Steric Effects. *Inorg. Chem.* **2019**, *58* (8), 5273–5280. https://doi.org/10.1021/acs.inorgchem.9b00360.

(32) Esposito, V.; Solari, E.; Floriani, C.; Re, N.; Rizzoli, C.; Chiesi-Villa, A. Binding and Redox Properties of Iron(II) Bonded to an Oxo Surface Modeled by Calix[4]Arene. *Inorg. Chem.* **2000**, *39* (12), 2604–2613. https://doi.org/10.1021/ic991467h.

(33) Chiang, K. P.; Barrett, P. M.; Ding, F.; Smith, J. M.; Kingsley, S.; Brennessel, W. W.; Clark, M. M.; Lachicotte, R. J.; Holland, P. L. Ligand Dependence of Binding to Three-Coordinate Fe(II) Complexes. *Inorg. Chem.* **2009**, *48* (12), 5106–5116. https://doi.org/10.1021/ic802440h.

(34) de Ruiter, G.; Thompson, N. B.; Lionetti, D.; Agapie, T. Nitric Oxide Activation by Distal Redox Modulation in Tetranuclear Iron Nitrosyl Complexes. *J. Am. Chem. Soc.* **2015**, *137* (44), 14094–14106. https://doi.org/10.1021/jacs.5b07397.

(35) King, E. R.; Betley, T. A. Unusual Electronic Structure of First Row Transition Metal Complexes Featuring Redox-Active Dipyrromethane Ligands. *J. Am. Chem. Soc.* **2009**, *131* (40), 14374–14380. https://doi.org/10.1021/ja903997a.

(36) Dugan, T. R.; Bill, E.; MacLeod, K. C.; Brennessel, W. W.; Holland, P. L. Synthesis, Spectroscopy, and Hydrogen/Deuterium Exchange in High-Spin Iron(II) Hydride Complexes. *Inorg. Chem.* **2014**, *53* (5), 2370–2380. https://doi.org/10.1021/ic4013137.

(37) Pascualini, M. E.; Russo, N. V. D.; Thuijs, A. E.; Ozarowski, A.; Stoian, S. A.; Abboud, K. A.; Christou, G.; Veige, A. S. A High-Spin Square-Planar Fe(II) Complex Stabilized by a Trianionic Pincer-Type Ligand and Conclusive Evidence for Retention of Geometry and Spin State in Solution. *Chem. Sci.* **2014**, *6* (1), 608–612. https://doi.org/10.1039/C4SC02634A.

(38) Pinkert, D.; Demeshko, S.; Schax, F.; Braun, B.; Meyer, F.; Limberg, C. A Dinuclear Molecular Iron(II) Silicate with Two High-Spin Square-Planar FeO_4 Units. *Angew. Chem. Int. Ed.* **2013**, *52* (19), 5155–5158. https://doi.org/10.1002/anie.201209650.

(39) Turkiewicz, A.; Paley, D. W.; Besara, T.; Elbaz, G.; Pinkard, A.; Siegrist, T.; Roy, X. Assembling Hierarchical Cluster Solids with Atomic Precision. *J. Am. Chem. Soc.* **2014**, *136* (45), 15873–15876. https://doi.org/10.1021/ja508698w.

(40) Bard, A. J.; Faulkner, L. R. *Electrochemical Methods: Fundamentals and Applications*, 2nd Ed.; Wiley: New York, 2001.

(41) Glueck, D. S.; Hollander, F. J.; Bergman, R. G. Synthesis, Structure, and Reactivity of a Monomeric Pentamethylcyclopentadienyliridium(III) Imido Complex. *J. Am. Chem. Soc.* **1989**, *111* (7), 2719–2721. https://doi.org/10.1021/ja00189a059.

(42) Glueck, D. S.; Wu, J.; Hollander, F. J.; Bergman, R. G. Monomeric (Pentamethylcyclopentadienyl)Iridium Imido Compounds: Synthesis, Structure, and Reactivity. *J. Am. Chem. Soc.* **1991**, *113* (6), 2041–2054. https://doi.org/10.1021/ja00006a026.

(43) Mindiola, D.; L. Hillhouse, G. Isocyanate and Carbodiimide Synthesis by Nitrene-Group-Transfer from a Nickel(II) Imido Complex. *Chemical Communications* **2002**, *0* (17), 1840–1841. https://doi.org/10.1039/B204846A.

(44) Kogut, E.; Wiencko, H. L.; Zhang, L.; Cordeau, D. E.; Warren, T. H. A Terminal Ni(III)−Imide with Diverse Reactivity Pathways. *J. Am. Chem. Soc.* **2005**, *127* (32), 11248–11249. https://doi.org/10.1021/ja0533186.

(45) Dunn, S. C.; Hazari, N.; Cowley, A. R.; Green, J. C.; Mountford, P. Synthesis and Reactions of Group 4 Imido Complexes Supported by Cyclooctatetraene Ligands. *Organometallics* **2006**, *25* (7), 1755–1770. https://doi.org/10.1021/om0510526.

(46) Badiei, Y. M.; Krishnaswamy, A.; Melzer, M. M.; Warren, T. H. Transient Terminal Cu−Nitrene Intermediates from Discrete Dicopper Nitrenes. *J. Am. Chem. Soc.* **2006**, *128* (47), 15056–15057. https://doi.org/10.1021/ja065299l.

(47) Dai, Q. X.; Seino, H.; Mizobe, Y. Tungsten(II) Alkylimido Complexes from Insertion of Nitriles into Tungsten Hydride: Alkylideneamido Intermediate Stage and Nitrene Group Transfer to Isocyanide. *Organometallics* **2012**, *31* (14), 4933–4936. https://doi.org/10.1021/om3004338.

(48) Beaumier, E. P.; McGreal, M. E.; Pancoast, A. R.; Wilson, R. H.; Moore, J. T.; Graziano, B. J.; Goodpaster, J. D.; Tonks, I. A. Carbodiimide Synthesis via Ti-Catalyzed Nitrene Transfer from Diazenes to Isocyanides. *ACS Catal.* **2019**. https://doi.org/10.1021/acscatal.9b04107.

(49) Laskowski, C. A.; Hillhouse, G. L. Group-Transfer Reactions of Ni(II)-Ni(II) Bridging Imido Complexes. Catalytic Formation of Carbodiimides and Isocyanates via Nitrene Transfer from Organoazides. *Organometallics* **2009**, *28* (20), 6114–6120. https://doi.org/10.1021/om900783u.

(50) Saegusa, Takeo.; Ito, Yoshihiko.; Shimizu, Toyoji. Synthetic Reactions by Complex Catalysts. XVIII. Reaction of an Azide with Isocyanide Using an Iron Carbonyl Catalyst. New Route to Carbodiimide. *J. Org. Chem.* **1970**, *35* (11), 3995–3996. https://doi.org/10.1021/jo00836a105.

(51) Wiese, S.; Aguila, M. J. B.; Kogut, E.; Warren, T. H. β-Diketiminato Nickel Imides in Catalytic Nitrene Transfer to Isocyanides. *Organometallics* **2013**, *32* (8), 2300–2308. https://doi.org/10.1021/om300909n.

(52) Cowley, R. E.; Golder, M. R.; Eckert, N. A.; Al-Afyouni, M. H.; Holland, P. L. Mechanism of Catalytic Nitrene Transfer Using Iron(I)–Isocyanide Complexes. *Organometallics* **2013**, *32* (19), 5289–5298. https://doi.org/10.1021/om400379p.

(53) Kephart, J. A.; Mitchell, B. S.; Chirila, A.; Anderton, K. J.; Rogers, D.; Kaminsky, W.; Velian, A. Atomically Defined Nano-Propeller $Fe_3Co_6Se_8(Ph_2PNTol)_6$: Functional Model for the Electronic Metal-Support Interaction Effect, and High Catalytic Activity for Carbodiimide Formation. *J. Am. Chem. Soc.* **2019**, *141* (50), 19605–19610. https://doi.org/10.1021/jacs.9b12473.

(54) Arnett, C. H.; Kaiser, J. T.; Agapie, T. Remote Ligand Modifications Tune Electronic Distribution and Reactivity in Site-Differentiated, High-Spin Iron Clusters: Flipping Scaling Relationships. *Inorg. Chem.* **2019**, *58* (23), 15971–15982. https://doi.org/10.1021/acs.inorgchem.9b02470.

(55) Li, F.; Meyer, R. L.; Carpenter, S. H.; VanGelder, L. E.; Nichols, A. W.; Machan, C. W.; Neidig, M. L.; Matson, E. M. Nitric Oxide Activation Facilitated by Cooperative Multimetallic Electron Transfer within an Iron-Functionalized Polyoxovanadate–Alkoxide Cluster. *Chemical Science* **2018**, *9* (30), 6379–6389. https://doi.org/10.1039/C8SC00987B.

(56) Passarelli, V.; Benetollo, F. Reactivity of Novel N,N'-Diphosphino-Silanediamine-Based Rhodium(I) Derivatives. *Inorg. Chem.* **2011**, *50*, 9958–9967. https://doi.org/10.1021/ic2004408.

(57) Weiss, S.; Aguila, M. J. B.; Kogut, E.; Warren, T. H. β-Diketiminato Nickel Imides in Catalytic Nitrene Transfer to Isocyanides. *Organometallics* **2013**, *32* (8), 2300–2308.

(58) Sheff, J. T.; Lucius, A. L.; Owens, S. B.; Gray, G. M. Generally Applicable NMR Titration Methods for the Determination of Equilibrium Constants for Coordination Complexes: Syntheses and Characterizations of Metallacrown Ethers with α,ω-Bis(Phosphite)-Polyether Ligands and Determination of Equilibrium Binding. *Organometallics* **2011**, *30* (21), 5695–5709. https://doi.org/10.1021/om200580t.

(59) Hirose, K. Determination of Binding Constants. In *Analytical Methods in Supramolecular Chemistry*; Wiley-VCH Verlag GmbH & Co. KGaA: Weinheim, Germany, 2007; pp 17–54. https://doi.org/10.1002/9783527610273.ch2.

(60) Evans, D. F. 400. The Determination of the Paramagnetic Susceptibility of Substances in Solution by Nuclear Magnetic Resonance. *J. Chem. Soc. (Resumed)* **1959**, 2003. https://doi.org/10.1039/jr9590002003.

(61) Bain, G. A.; Berry, J. F. Diamagnetic Corrections and Pascal's Constants. *J. Chem. Ed.* **2008**, *85* (4), 532. https://doi.org/10.1021/ed085p532.

(62) Bruker APEX2 (Version 2.1-4), SAINT (Version 7.34A), SADABS (Version 2007/4)*,* **2007** *BrukerAXS Inc*, Madison, Wisconsin, USA.

(63) Sheldrick, G.M. *Acta Cryst.* **2015** *A71*, 3-8.

(64) Altomare, A.; Burla, C.; Camalli, M.; Cascarano, G. L.; Giacovazzo, C.; Guagliardi, A.; Moliterni, A.G.G.; Polidori, G.; Spagna, R. *J. Appl. Crystallogr.,* **1999***, 32,* 115-119.

(65) Altomare, A.; Cascarano, G. L.; Giacovazzo, C.; Guagliardi, A. *J. Appl. Crystallogr.*, **1993**, *26*, 343-350.

(66) Sheldrick, G. M. *SHELXL-97, Program for the Refinement of Crystal Structures*, **1997**, University of Göttingen, Germany.

(67) Sheldrick, G. M. *Acta Cryst.* **2015**, *C71*, 3–8.

(68) Mackay, S.; Edwards, C.; Henderson, A.; Gilmore, C.; Stewart, N.; Shankland, K.; Donald, A. *MaXus: A Computer Program for the Solution and Refinement of Crystal Structures from Diffraction Data*, **1997**, University of Glasgow, Scotland.

(69) Waasmaier, D.; Kirfel, A. *Acta Cryst.*, **1995**, *51*, 416-430.

CHAPTER 2.

INORGANIC CLUSTERS AS METALLOLIGANDS: LIGAND EFFECTS ON THE SYNTHESIS AND PROPERTIES OF TERNARY NANOPROPELLER CLUSTERS

2.1 ABSTRACT

Redox-active multimetallic platforms with synthetically addressable and hemilabile active sites are attractive synthetic targets for mimicking the reactivity of enzymatic co-factors toward multielectron transformations. To this end, a family of ternary clusters featuring three edge metal sites anchored on a Co_6Se_8 multimetallic support via amidophosphine ligands are a promising platform. In this report, we explore how small changes in the stereoelectronic properties of these ligands alter Co_6Se_8 metalloligand formation, but also substrate binding affinity and strength of the edge/support interaction in two new ternary clusters, $M_3Co_6Se_8L^{iPr}_6$ (**M$_3$**^{iPr}, M = Zn, Fe; L^{iPr} = $Ph_2PN^{(-)}{}^{i}Pr$). These clusters are characterized extensively using a range of methods, including single crystal X-ray diffraction, electronic absorption spectroscopy and cyclic voltammetry. Substrate binding studies reveal that **Fe$_3$**^{iPr} resists coordination of larger ligands like pyridine or tetrahydrofuran but binds the linear monodentate ligand CN^{t}Bu. Additionally, investigations into the synthesis of new Co_6Se_8 metalloligands using two aminophosphines, $Ph_2PN(H)^iPr$ ($L^{iPr,H}$) and $^iPr_2PN(H)^iPr$, led to the synthesis and characterization of $Co_6Se_8L^{iPr,H}_6$, as well as the smaller clusters $Co_4Se_2(CO)_6(L^{iPr,H})_4$ (**Co$_4$Se$_2$**), $Co_3Se(\mu_2\text{-}PPh_2)(CO)_4(L^{iPr,H})_3$ (**Co$_3$Se**), and $[Co(CO)_3(^iPr_2PN(H)^iPr)]_2$. Cumulatively, this study expands our understanding on the effect of the stereoelectronic properties of aminophosphine ligands in the synthesis of cobalt chalcogenide clusters, and, importantly on modulating the push–pull dynamic between the Co_6Se_8 support, the edge metals and incoming coordinating ligands in ternary M/Co/Se clusters.

Adapted in part with permission from:
1. Kephart, J. A.; Boggiano, A. C.; Kaminsky, W.; Velian, A. *Dalton Trans.* **2020**, *49*, 16464-16473. Copywrite 2020 Royal Society of Chemistry.

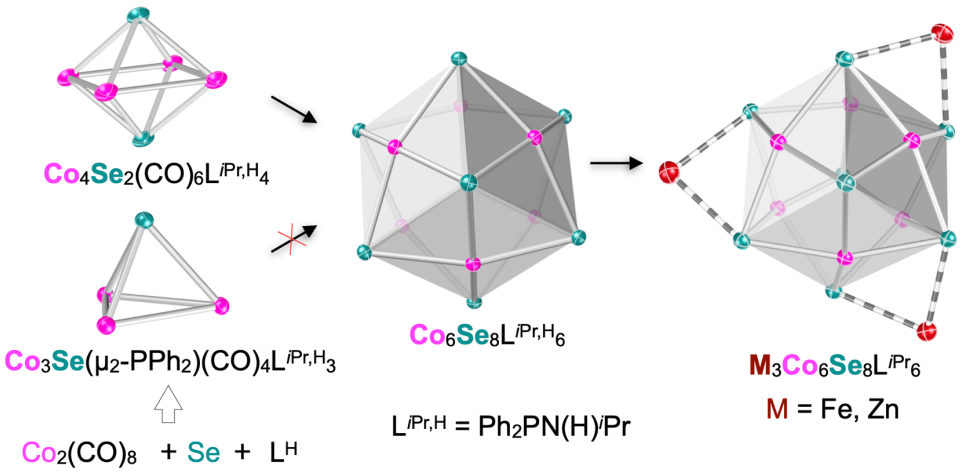


Figure 2.1. Capping phosphine ligands affect the speciation of intermediates formed en route to $Co_6Se_8L^{iPr,H}_6$, which can support three κ^4-bound surface metals.

2.2 Introduction

Multimetallic clusters play a critical role in many enzymatic transformations, including nitrogen fixation and oxygen evolution, among other challenging multielectron catalytic sequences.[1] Key features that enable their reactivity include their overall structural plasticity, which allows flexible active site conformations, and intracluster intermetallic cooperativity to facilitate multielectron processes.[2,3] Replicating enzymatic reactivity in synthetic clusters has been an area of intense research, and numerous synthetic platforms have been explored to achieve this. Figure 2.2a displays a selection of site differentiated clusters, including the heterocubane $[Mo(L_2)Fe_3S_4Cl_3]^{2-}$ (L_2^{2-} = tetrachlorocatecholate),[4] the polyoxovanadate $FeV_5O_6(OCH_3)_{12}$,[5] and the tetrametallic oxo cluster $MnFe_3(\mu_4\text{-}O)L_3L'$ (L = phenylpyrazolate; L′ = 1,3,5-triarylbenzene based ligand).[6] These platforms illustrate instances in which the active site is rigidly embedded in a redox-active poly- metallic framework that modulates its stoichiometric and even catalytic reactivity.

Alternatively, an active site bound in a hemilabile fashion to a polymetallic framework might better replicate the structural plasticity of enzymatic clusters and lead to improved reactivity, but achieving this requires synthetic innovations. Successful strategies to install a "dangler" metal on an inorganic cluster have been developed, especially in the context of modelling the oxygen evolving complex.[7–10] Figure 2.2b includes such an example, the heterocubane $Co_4MnO_4(OAc)_6(py)_3(NO_3)$ (Ac = acetate) featuring a dangling Co(II) subsite.[7] Our group

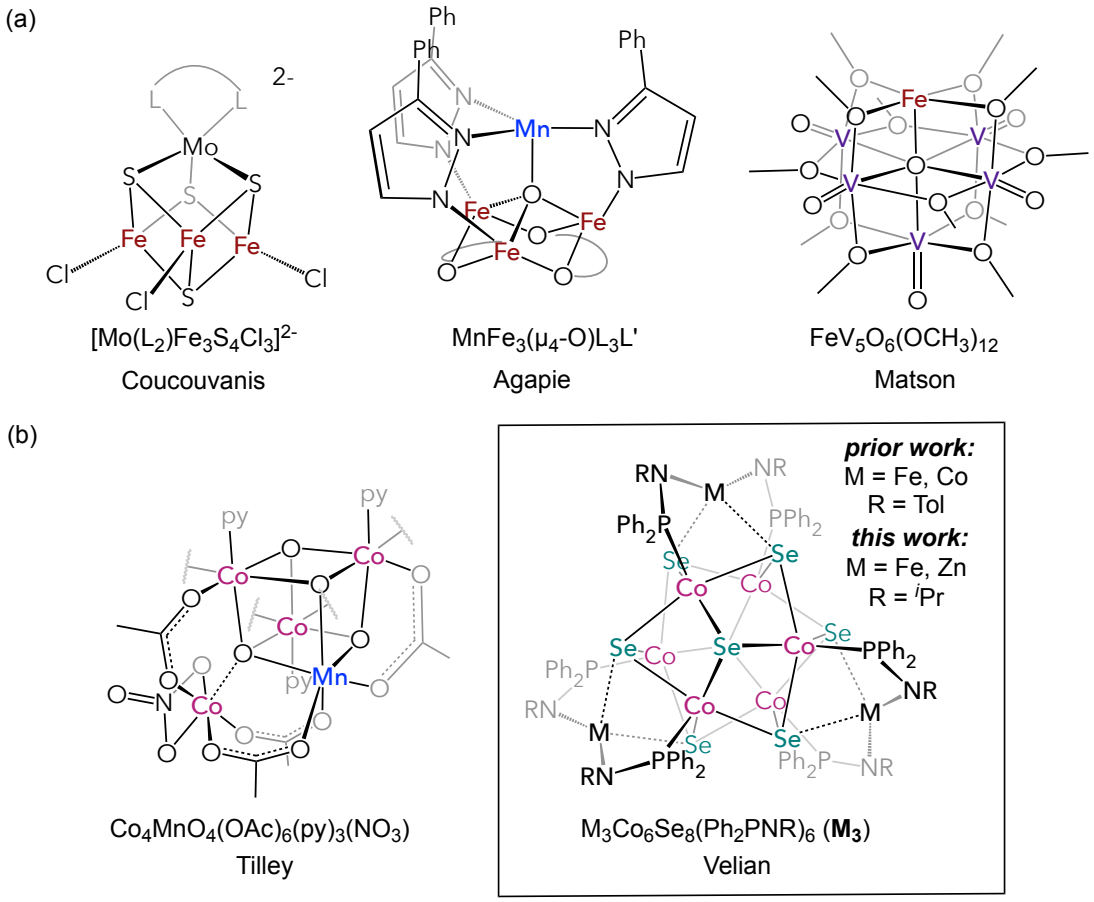


Figure 2.2. Heterometallic clusters featuring (a) active sites rigidly embedded within the polymetallic framework, (b) dangler sites tethered at the cluster surface.

recently introduced a modular strategy to install active sites that interact in a hemilabile fashion with a redox-active multimetallic platform, and demonstrated that these designer clusters are catalytically competent.[11,12] The ternary nanocluster $Fe_3Co_6Se_8L^{Tol}_6$ (**Fe$_3$**, Figure 2.2) features three Fe edge sites, each anchored to a [Co_6Se_8] cluster core by two amides and two hemilabile Fe···Se interactions. This cluster concept is highly modular, as the surface binding sites are poised to host other metals (e.g. cobalt),[12] and the stereoelectronic properties of the amidophosphine ligands can be easily tuned.[13]

2.3 Ligand Effects in the Synthesis of M/Co/Se Clusters

In our initial report,[11] we discovered that the strength of the Fe···Se interaction is redox-modulated. For example, mono-reduction of **Fe$_3$**, which effectively localizes an extra electron on the polymetallic cobalt core, increases the Fe···Se interaction strength and lowers the edge metal's

affinity for ligands to zero. We set out to explore this push–pull relation between the cluster support, the edge metals, and the incoming ligands further by probing how the nature of the edge/core interaction changes when ligand coordination is sterically blocked at the edge sites. To achieve this, we chose two aminophosphine ligands that are slightly bulkier and also more electron rich than $Ph_2PN(H)Tol$, namely $^{i}Pr_2PN(H)^{i}Pr$ and $Ph_2PN(H)^{i}Pr$.[14,15] To our surprise, we found that subtle changes in stereoelectronic properties of the aminophosphine not only affect ligand coordination at the edge sites and the electronic structure of the ternary clusters, but have long ranging consequences in the synthesis of the targeted $[Co_6Se_8L_6]^{(6-)}$ metalloligands, altering optimal reaction conditions and even favoring formation of smaller clusters. We report here our detailed findings on both fronts, including the synthesis and characterization of the two ternary clusters $M_3Co_6Se_8L^{iPr}_6$ (**M_3**^{i}**Pr**; M = Zn, Fe; $L^{iPr,H} = Ph_2PN^{(-)i}Pr$), the metalloligand $Co_6Se_8L^{iPr,H}_6$, as well as the smaller clusters $Co_4Se_2(CO)_6(L^{iPr,H})_4$ (**Co_4Se_2**), $Co_3Se(\mu_2\text{-}PPh_2)(CO)_4(L^{iPr,H})_3$ (**Co_3Se**), and $[Co(CO)_3(^{i}Pr_2PN(H)^{i}Pr)]_2$ (**Co_2**).

Several protocols are available to synthesize molecular cobalt chalcogenide Chevrel-type clusters. The first reported syntheses of $Co_6Q_8L_6$ (Q = S, Se; L = PPh_3) clusters relied on the use of silylated or anionic chalcogen sources, such as $Se(SiMe_3)_2$ and Na_2S, in conjunction with the phosphine-bound cobalt halide precursor, $CoCl_2(PPh_3)_2$.[16–18] A more convenient synthetic route that circumvents the experimental challenges associated with manipulating reactive chalcogen sources involves using instead a Co(0) source, elemental chalcogen, and phosphine ligands in different ratios.[19–21] For example, to produce $Co_6Q_8L_6$ clusters, stoichiometric $Co_2(CO)_8$ is treated with excess of both the chalcogen and the phosphine (≥12 equiv.),[20–23] whereas stoichiometric tellurium and excess phosphine are used to synthesize the more electron rich $Co_6Te_8L_6$ variants.[19,20,24] Empirically, it has been found that using excess chalcogen alone shifts the distribution of products toward the formation of partially carbonylated clusters $Co_6Se_8(CO)_xL^{iPr,H}_{6-x}$.[25]

While the details of the mechanism by which Chevrel-type clusters assemble are not well understood, the phosphine is proposed to play a critical role in their synthesis. In addition to binding to Co, the phosphine effectively functions as a chalcogen transfer reagent.[24] Empirically, we note the identity of the phosphine has a pronounced influence over the cluster for- mation process. For example, replacing a single ethyl group in PEt_3 with a bulkier and less electron rich group (i.e. 4-bromo-phenyl or 9-ethynyl phenanthroline) results in significantly longer reaction

times.[20–22] The stereoelectronic nature of the phosphine stands to alter the numerous equilibria involved in the formation of [Co_6Se_8] clusters, impacting both the rates of formation of different intermediates and the final distribution of products. Steric bulk considerations seem an especially important factor: while no $Co_6Se_8L_6$ clusters have been reported to form with bulkier phosphines (i.e. P^{i}Pr$_3$), phosphines of very different donor–acceptor properties (e.g. PEt_3 and PPh_3)[26] have been successfully used to produce them.

In our synthetic investigations, we have found that the aminophosphine $Ph_2PN(H)^iPr$ yields the Co_6Se_8 cluster $Co_6Se_8L^{iPr,H}_6$, whereas the related ligand $^iPr_2PN(H)^iPr$, completely inhibits the formation of Co/Se clusters, halting the reaction to yield the dimer $[Co(CO)_3(^iPr_2PN(H)^iPr)]_2$ (**Co$_2$**). Comparing strictly the relative steric bulk for PPh_3, PEt_3, Ph_2PCH_2Ph and $^iPr_2PCH_2Ph$ (the latter two serving as proxies for $L^{iPr,H}$ and $^iPr_2PN(H)^iPr$) using the Tolman cone angles in octahedral coordination environments, we find they steadily increase in the series from 152.0°, 157.8°, 165.5°, to 172.7°, respectively.[14,27] A similar trend in steric profiles is obtained using the percent buried volume method, which estimates values for this parameter between 27.6% and 29.1% for PPh_3, $L^{iPr,H}$ and $L^{Tol,H}$, and slightly larger for $^iPr_2PN(H)^iPr$, at 31.5%.[15]

2.3.1 *Aminophosphine $^iPr_2PN(H)^iPr$ halts cluster formation to Co dimer **Co$_2$***

The stoichiometric reaction of $Co_2(CO)_8$ (3 equiv), Se (8 equiv), and $^iPr_2PN(H)^iPr$ (6 equiv) produced only the Co(0) dimer complex **Co$_2$** (38% isolated yield), and no other observable cobalt products (Scheme 2.1). The UV-vis-*n*IR spectrum of this dimer features an absorption band at 377 nm, and infrared analysis reveals the presence of a terminal CO ligand (ν_{CO} = 1943 cm^{-1}). X-ray quality red-orange prismatic crystals of **Co$_2$** were grown from diethyl ether at −35 °C, allowing for its structural characterization in the solid state. The compound features a long unsupported Co–Co bond (2.6731(6) Å; formal shortness ratio, r_{fs} = 1.16),[28,29] with each Co(0) atom bound by three terminal CO groups and one $^iPr_2PN(H)^iPr$ aminophosphine in an overall trigonal bipyramidal geometry (Figure 2.3).[30] Similar $[Co(CO)_3(PR_3)]_2$ dimers equipped with a variety of phosphine ligands have been previously isolated, and used as pre-catalysts for the hydroformylation of alkenes.[31,32] **Co$_2$** is thermally robust, and does not undergo further chemical transformation upon treatment with $Se{=}P(^iPr)_2N(H)^iPr$ or with elemental selenium in refluxing toluene.

Scheme 2.1. Attempted cluster synthesis with the aminophosphine $^{i}Pr_2PN(H)^{i}Pr$ leads to formation of dimer **Co₂**, with no other detectable products.

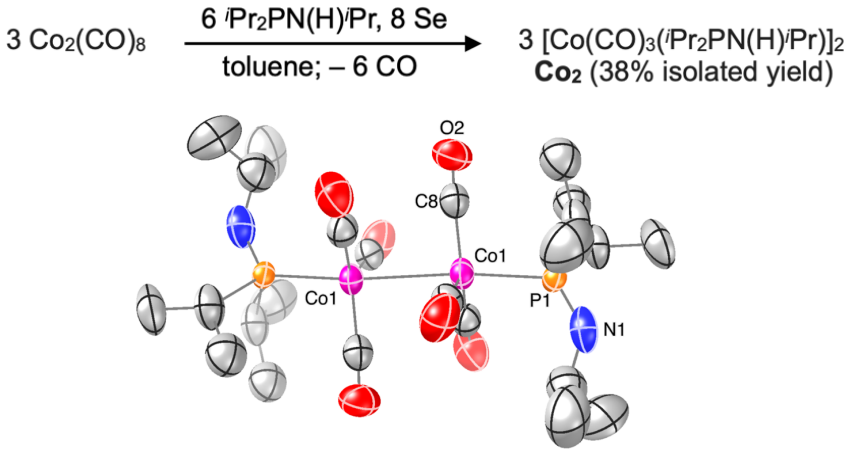
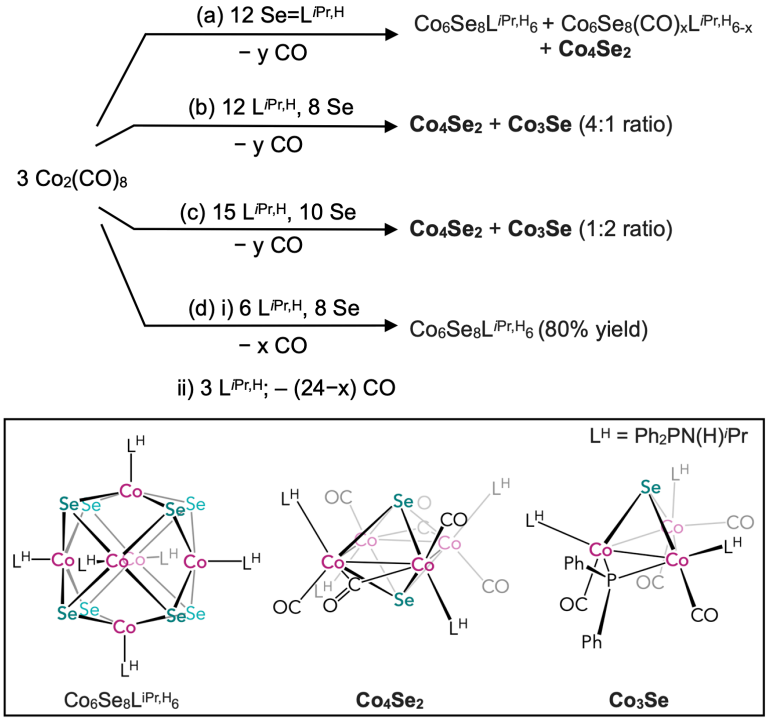


Figure 2.3. Solid-state structure of **Co₂** with thermal ellipsoids shown at a 50% probability level. All hydrogen atoms and three-fold rotational disorder have been omitted for clarity. Selected interatomic distances (Å): Co1-Co1 2.6731(6); Co1-P1 2.19(1); P1-N1 1.47(2).

2.3.2 *Aminophosphine $L^{iPr,H}$ alters optimal reagent stoichiometry*

Having quickly discovered that the all-isopropyl aminophosphine, $^{i}Pr_2PN(H)^{i}Pr$, does not lead to formation of the [Co_6Se_8] cluster under the experimental conditions we sampled, we turned to a closer variant of aminophosphine $L^{Tol,H}$, namely $L^{iPr,H}$, with a slightly bulkier and more electron rich N-isopropyl substituent that is spatially removed from the Co_6Se_8-binding phosphorus center at the PPh_2 terminus. To identify a synthetic protocol to prepare $Co_6Se_8L^{iPr,H}_6$, we investigated a range of conditions, including stoichiometric reagent ratios, excess $L^{iPr,H}$, and excess Se=$L^{iPr,H}$, with each variation yielding a different mixture of products (Scheme 2.2). Refluxing $Co_2(CO)_8$ with excess Se=$L^{iPr,H}$ (12 equiv.), a protocol successfully yielding a range of $Co_6Se_8(PR_3)_6$ clusters,[20–23] produced instead a mixture of partially carbonylated $Co_6Se_8(CO)_xL^{iPr,H}_{6-x}$ clusters and the [4,2] cluster **Co₄Se₂** (Scheme 2.2a). Refluxing stoichiometric $Co_2(CO)_8$ and Se with excess $L^{iPr,H}$ (12 equiv.), a strategy used to prepare $Co_6Te_8(PEt_3)_6$,[20] completely halted the formation of the [Co_6Se_8] cluster, forming instead a mixture of **Co₄Se₂** and **Co₃Se** (Scheme 2.2b). Empirically, we found that increasing both the concentration of the reagents and the amounts of phosphine and selenium favored formation of **Co₃Se**, allowing its isolation and characterization (Scheme 2.2c). Ultimately, the optimized synthetic protocol for $Co_6Se_8L^{iPr,H}_6$ entails refluxing a stoichiometric ratio of $Co_2(CO)_8$, Se, and $L^{iPr,H}$, followed by addition of excess

Scheme 2.2. Effects of the stoichiometry of reagents on the nuclearity and ratio of the cobalt selenide clusters produced in the reaction of $Co_2(CO)_8$, Se, $L^{iPr,H}$ or $Se{=}L^{iPr,H}$ in refluxing toluene.



$L^{iPr,H}$ under continued reflux to convert partially carbonylated intermediates, $Co_6Se_8(CO)_xL^{iPr,H}{}_{6-x}$, to the homoleptic product, $Co_6Se_8L^{iPr,H}{}_6$ (Scheme 2.2d). For experimental details regarding the effect of stoichiometry on cluster product distribution refer to Section 2.5.12.

2.3.3 *Square-capped [4,2] cluster $Co_4Se_2(CO)_6(L^{iPr,H})_4$ and its conversion to $Co_6Se_8L^{iPr,H}{}_6$*

Having discovered that the presence of excess phosphine at the onset of the synthesis halts the cluster assembly reaction, mainly to the [4,2] cluster **Co_4Se_2** (Scheme 2.2b), we proceeded to isolate it pure. NMR spectroscopy analysis of the crude mixture revealed the presence of unreacted $Se{=}L^{iPr,H}$ and $L^{iPr,H}$. Following their removal using *n*-pentane, **Co_4Se_2** was isolated pure as a dark green solid by extraction in toluene and subsequent crystallization from THF/*n*-pentane (0.219 g, 24% yield of first crop). The single set of diamagnetic ^1H NMR resonances associated with the aminophosphine ligand are accompanied by a broad singlet in the ^{31}P NMR (82 ppm, $\nu_{1/2}$ = 320

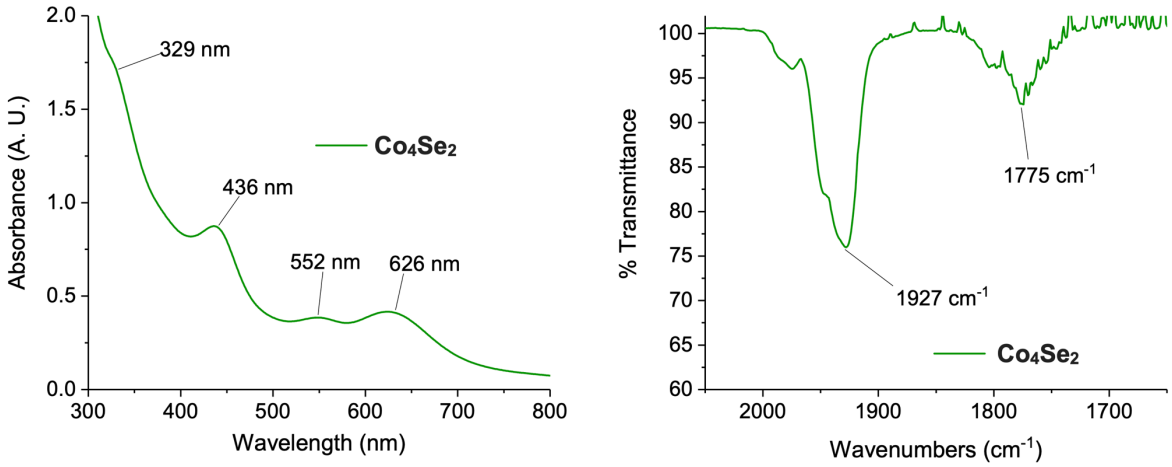


Figure 2.4. UV-visible absorption (in toluene; left) and ATR-FTIR (carbonyl region; right) spectra of **Co_4Se**.

Hz), suggestive of the high symmetry of the complex. UV-vis spectroscopy analysis revealed four broad electronic absorption bands between 329 and 626 nm (Figure 2.4), closely matching those of previously reported $Co_4Se_2(CO)_6(P^nBu_3)_4$,[20] and distinct from those of $[Co_6Se_8]$ clusters. The presence of terminal and bridging carbonyl ligands is evident in the infrared spectrum of the main product, with CO stretches at 1927 and 1775 cm^{-1}.

While the combination of spectroscopic characterizations indirectly pointed to the formation of a partially carbonylated $[Co_4Se_2]$ cluster as the main product of the reaction,[24,33] its identity as **Co_4Se_2** was confirmed using single crystal X-ray diffraction (Figure 2.5). Related bi-capped, rectangular $[Co_4Se_2]$ clusters, such as $Co_4Se_2(CO)_{10}$ or $Co_4Se_2(CO)_6(P^nBu)_4$, have been previously isolated from the reaction of $Co_2(CO)_8$ with either the more soluble red selenium (1 : 1 mole ratio), or with a mixture of Se and P^nBu_3 (1 : 1 : 4 mole ratio).[20,34] **Co_4Se_2** is only the second $[Co_4Se_2]$ cluster to be structurally characterized, with Co···Co and Co···Se distances closely matching its predecessor, $Co_4Se_2(CO)_{10}$.[35] The cluster core features a rectangular plane of Co(I) metals, that is capped on both faces by μ_4-Se ligands (Figure 2.5). Interatomic Co···Co distances are observed between 2.54(1) and 2.746(1) Å, indicative of weak Co–Co bonds (r_{fs} = 1.09, and 1.19, respectively),[28,29] and Co–Se bond lengths average 2.38 Å. The two shortened Co–Co contacts are supported by bridging CO ligands, as indicated by the presence of a 1775 cm^{-1} infrared feature. Each Co metal vertex is also bound by one $L^{iPr,H}$ ligand and one terminal CO. The up/down orientation of these ligands with respect to the plane of the metal ring alternates at each corner of the rectangle, enforcing the overall C_{2v} symmetry of the inorganic unit.

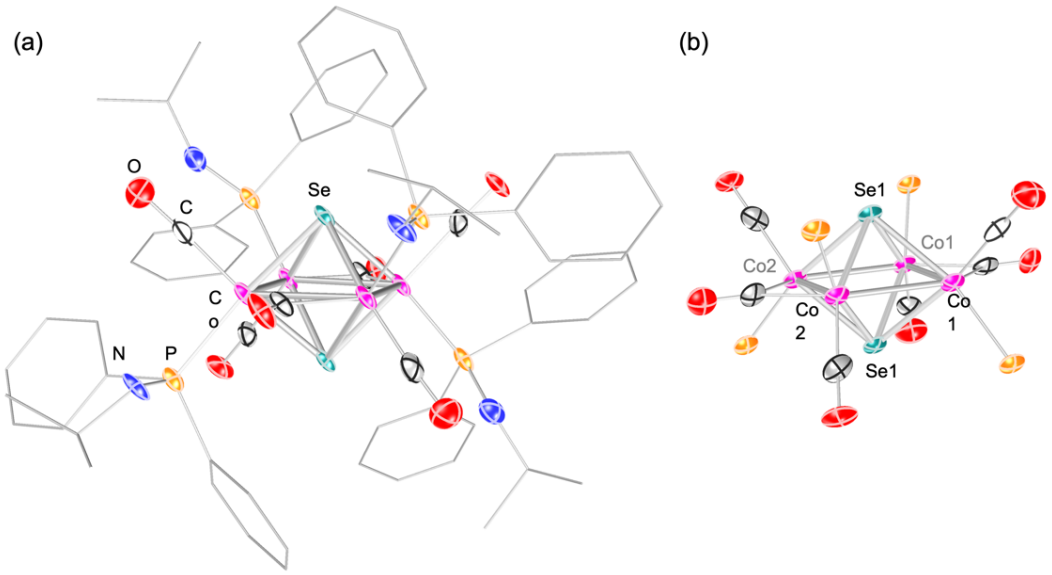


Figure 2.5. Single crystal X-ray diffraction structure of **Co_4Se_2** depicted (a) in full and (b) trimmed to only the inorganic core and the immediate coordination sphere. Selected interatomic distances(Å): Co1–Co1 2.54(1), Co1–Co2 2.746(1), Co2–Co2 2.51(1); Co1–Se1 2.386(5), Co2–Se1 2.405(2). Thermal ellipsoids are plotted at 50% probability level. All hydrogen atoms are omitted, and the aminophosphine carbon atoms are plotted as wireframes for clarity.

Analogous [Co_4Se_2] clusters, such as $Co_4Se_2(CO)_6(P^nBu_3)_4$ or $Co_4Te_2(CO)_6(PEt_3)_4$, have been shown to thermally convert to the corresponding [Co_6Se_8] clusters in the presence of excess phosphine and chalcogen.[20,24] To test if **Co_4Se_2** is a competent precursor to $Co_6Se_8L^{iPr,H}_6$, a mixture of **Co_4Se_2** (1 equiv.), $L^{iPr,H}$ (12 equiv) and selenium powder (6 equiv) was refluxed in toluene. Mild effervescence and a gradual color change from deep green to red-brown accompanied the reaction (Figure 2.6). ^{1}H NMR analysis of the crude reaction mixture revealed the clean conversion of the [Co_4Se_2] starting material to $Co_6Se_8L^{iPr,H}_6$ (Figure 2.7). The UV-vis absorption spectrum of this mixture bears the tell-tale signs of a [Co_6Se_8] cluster with three strong absorption features at 365, 444 and 505 nm. While excess $L^{iPr,H}$ was found to halt the self-assembly process to the formation of **Co_4Se_2**, excess phosphine and Se are necessary to convert this intermediate to the desired species $Co_6Se_8L^{iPr,H}_6$.

2.3.4 *Isolation of a trapped [Co_3Se] intermediate cluster $Co_3Se(\mu_2\text{-}PPh_2)(CO)_4(L^{iPr,H})_3$*

Empirically, we discovered that altering the stoichiometry of the reagents to a molar ratio of 3 $Co_2(CO)_8$: 10 Se : 15 $L^{iPr,H}$ and increasing the concentration of the reagents led to the preferential formation of the [Co_3Se] cluster **Co_3Se** over **Co_4Se_2** (Scheme 2.2c). After a solvent

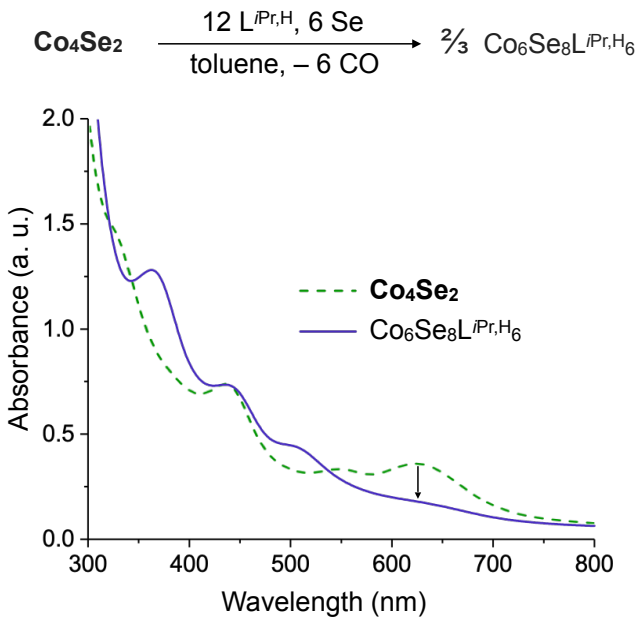


Figure 2.6. Thermal conversion of **Co_4Se_2** to $Co_6Se_8L^{iPr,H}_6$ in the presence of excess $L^{iPr,H}$ and Se. UV-vis absorption analysis of the reaction mixture before and after the thermal conversion, revealing a clear transition to the absorption profile characteristic of [Co_6Se_8] clusters.

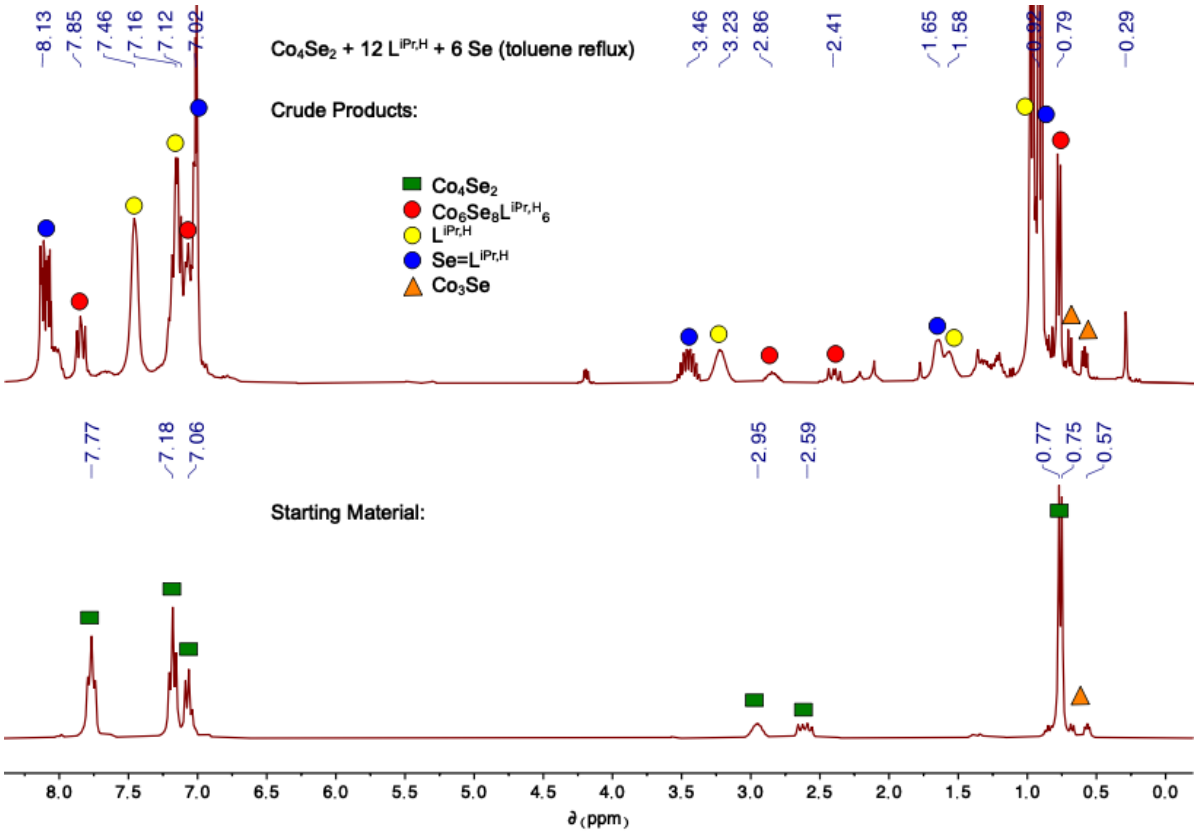


Figure 2.7. ^{1}H NMR (C_6D_6, 25 °C, 300 MHz) spectra of the starting material and crude products in the thermal conversion of **Co_4Se_2** to $Co_6Se_8L^{iPr,H}_6$.

workup, the new cluster could be isolated pure as a deep red solid by crystallization from a mixture of toluene and *n*-pentane (35% yield). Analysis by ^{31}P NMR spectroscopy revealed that the product is desymmetrized, featuring three broad resonances in a 2 : 1 : 1 ratio at 82, 89 and 165 ppm ($\nu_{1/2}$ ≈ 370–400 Hz) (Figure 2.8). The signal at 165 ppm is shifted downfield significantly from Co-bound L$^{i\text{Pr,H}}$, providing a first clue of the fragmentation incurred by the aminophosphine. This signal is located within a spectral region typical for bridging cobalt phosphido ligands. For

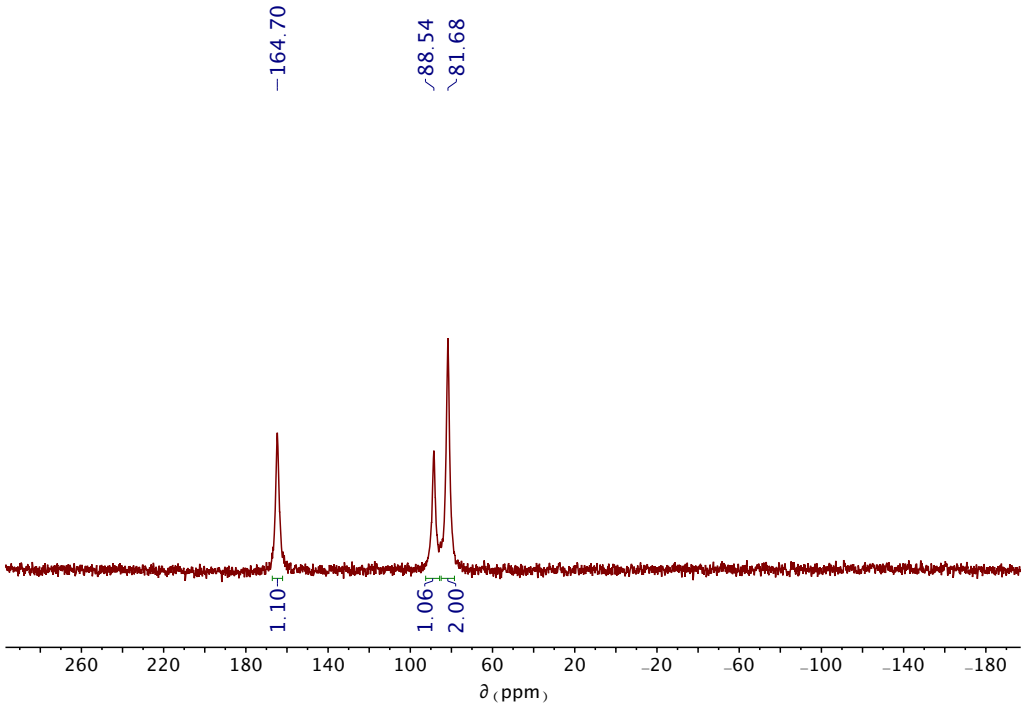


Figure 2.8. ^{31}P NMR (C_6D_6, 25 °C, 300 MHz) spectrum of **Co_3Se**.

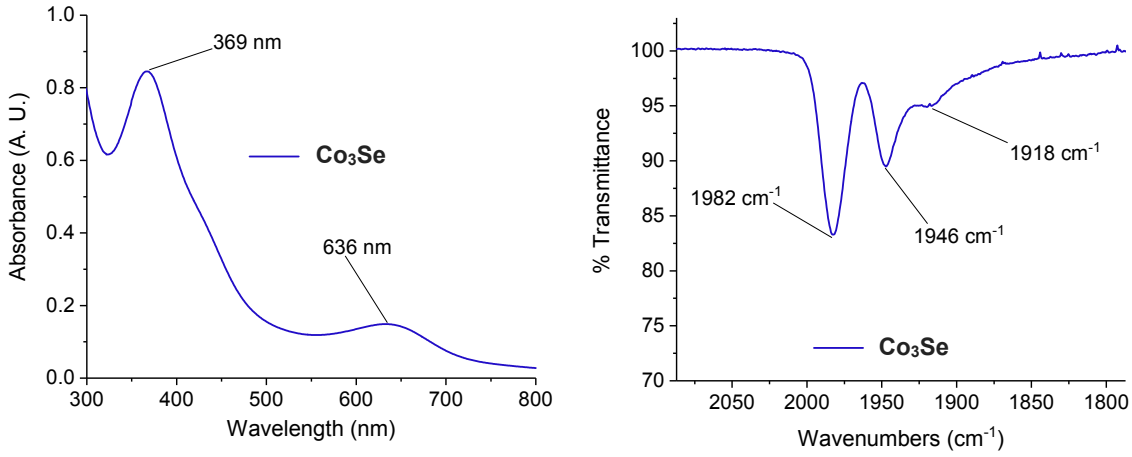


Figure 2.9. UV-visible absorption (in toluene; left) and ATR-FTIR (carbonyl region; right) spectra of **Co_3Se**.

example, $Co_2(\mu\text{-}PPh_2)_2(CO)_2(PEt_2Ph)_2$ and $Co_3(\mu_2\text{-}PPh_2)_3(CO)_5(PEt_2Ph)$ exhibit phosphido ^{31}P signals at 176, 199, and 275 ppm, respectively.[36] ^{1}H and ^{13}C NMR spectroscopy analysis indicates the presence of two $L^{iPr,H}$ environments in a 2 : 1 ratio, along with a separate set of PPh_2 aromatic resonances that corroborate the fragmentation of the P–N bond (see Section 2.5.6). Infrared spectroscopy confirmed the presence of only terminal carbonyl ligands, with three CO stretches observed between 1982 and 1918 cm^{-1}. Finally, the UV-vis spectrum contains two broad absorption bands at 369 and 636 nm, which is distinct from which is typical of $[Co_6Se_8]$ or $[Co_4Se_2]$ clusters (Figure 2.9).

The product was identified as the novel $[Co_3Se]$ cluster **Co_3Se** using single crystal X-ray diffraction (Figure 2.10). Red needle-shaped crystals were grown via vapor diffusion of diethyl ether into a concentrated THF solution of the compound at 25 °C. The Co_3Se core consists of a triangular Co_3 unit capped on one face by a μ_3-Se atom. The interatomic Co–Co distances, ranging between 2.47(1) and 2.62(1) Å, are again indicative of weak metal–metal bonding interactions (r_{fs} = 1.07, 1.11, 1.13). A diphenylphosphido ligand, μ_2-PPh_2, formed ostensibly via fragmentation of the aminophosphine P–N bond, bridges between two of the cobalt atoms. The asymmetry of the cluster detected in the IR and NMR spectra is also reflected in the distribution of the terminal ligands. While each cobalt is hexacoordinate, Co2 and Co3 are terminally bound to one $L^{iPr,H}$ and

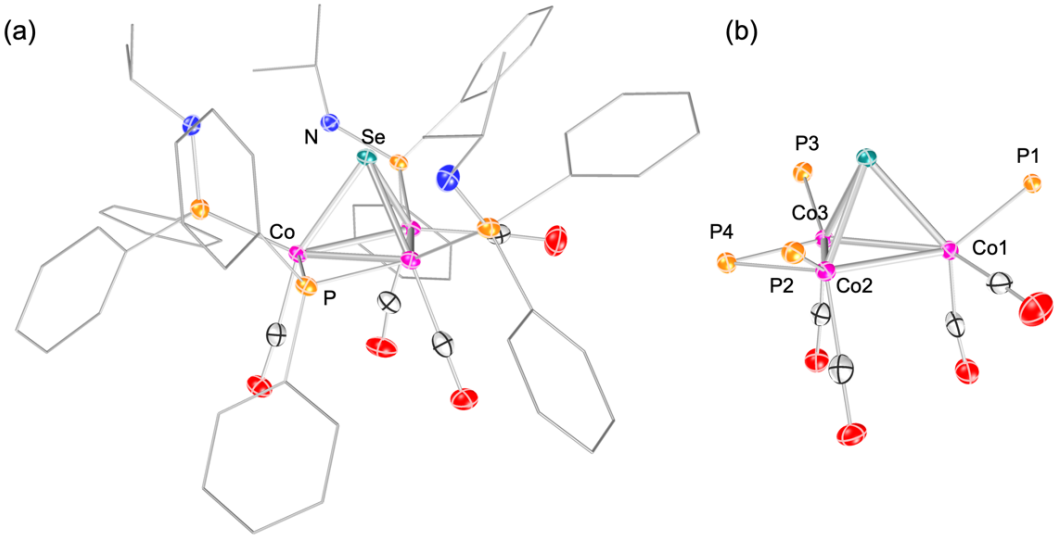


Figure 2.10. Single crystal X-ray diffraction structure of **Co_3Se** in full (a), and trimmed to only the inorganic core (b). Selected interatomic distances(Å): Co1–Co2 2.57(2), Co1–Co3 2.62(1), Co2–Co3 2.47(1); Co1–Se1 2.29(1), Co2–Se1 2.30(2), Co3–Se1 2.314(9); Co2–P4 2.179(9), Co3–P4 2.19(1). Thermal ellipsoids are plotted at 50% probability level. All hydrogen atoms and co-crystallizing solvent molecules are omitted. The aminophosphine carbon atoms are plotted as wireframes for clarity.

one CO, whereas the third metal, Co1, is coordinated by an aminophosphine and two CO ligands (Figure 2.10b).

The structural similarity of this [Co_3Se] complex with the $Co_3(\mu_3\text{-}Se)$ corners of the [Co_6Se_8] core suggests they might be intermediates in the formation of Chevrel-type clusters. Inspecting the literature, we find that [Co_3Se] clusters bound exclusively by L-type ligands[37] are unstable with respect to isolation. For example, $Co_3Se(CO)_9$ decomposes unless stored under carbon monoxide.[34] Molecular orbital considerations have attributed the high reactivity of $Co_3Se(CO)_9$ to the half-occupancy of a tricobalt antibonding orbital.[38] Typically, the inherent instability of such 27 electron, S = 1/2 [Co_3Se] clusters is overcome upon formal mono-oxidation to a 26 electron, diamagnetic cluster by introducing an anionic X-type ligand in the coordination environment of the metal ring.[39] Indeed, there is a plenitude of [Co_3Q] clusters that contain an X-type ligand, such as $Co_3SePh(CO)_8$ or $Co_3S(\mu_2\text{-}S^tBu)(CO)_7$.[39,40] While **$Co_3Se$** is the first selenide-capped [Co_3Q] cluster bound by a bridging phosphido, a close sulfide-based variant, $Co_3S(\mu_2\text{-}PPh_2)(CO)_6(PPh_3)$, has been previously reported. Interestingly, this species forms in the reaction between $Co_2(CO)_8$ with Ph_2PSPh, effectively via the fragmentation of the thiophosphine P–S bond.[41] Here, we hypothesize that if a putative 27 electron [Co_3Se] cluster $Co_3Se(CO)_{9-x}L^{iPr,H}_x$ is formed in the presence of excess aminophosphine, it favors conversion to the more stable 26 electron species **Co_3Se** via activation of the aminophosphine P–N bond and incorporation of the bridging phosphide. The relative susceptibility of the P–N bond toward fragmentation (compared to less reactive P–C bonds), allows here the observation and trapping of an otherwise elusive [Co_3Se] cluster intermediate.

2.3.5 *Homoleptic cluster $Co_6Se_8L^{iPr,H}_6$ and its chemical mono-oxidation*

Prepared by adding excess $L^{iPr,H}$ (3 equiv.) to a refluxing a stoichiometric mixture of $Co_2(CO)_8$, Se, and $L^{iPr,H}$ in toluene (Scheme 2d), $Co_6Se_8L^{iPr,H}_6$ is isolated pure in good yield (11.2 g, 80% yield) as a dark red, microcrystalline solid. In solution, $Co_6Se_8L^{iPr,H}_6$ exhibits a single set of ^1H NMR resonances for the six aminophosphine ligands, and a broad singlet in the ^{31}P NMR spectrum at 98 ppm. UV-vis absorption analysis in toluene reveals the diagnostic absorption profile anticipated for [Co_6Se_8] clusters, with three broad absorption bands cascading from higher to lower intensity at 365, 444, and 505 nm, respectively (see Figure 2.24).

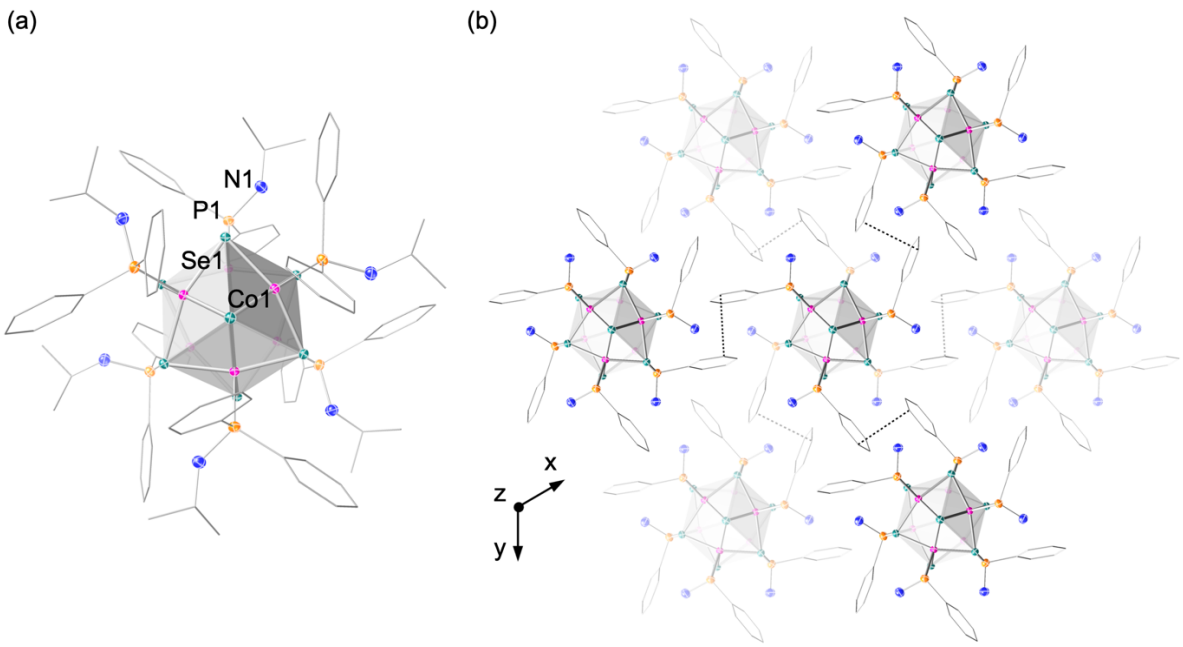
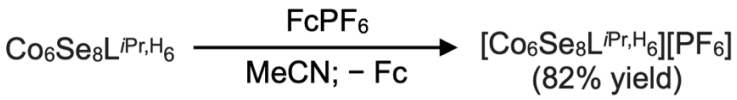


Figure 2.11. Single crystal X-ray diffraction structure of (a) neutral cluster $Co_6Se_8L^{iPr,H}_6$ and (b) its packing in the lattice governed by π-π stacking of phenyl rings.

The homoleptic cluster $Co_6Se_8L^{iPr,H}_6$ crystallizes in the trigonal space group $R\bar{3}$ and features a Co_6Se_8 core with pseudo-octahedral symmetry (Figure 2.11a). All eight trigonal facets of the distorted Co_6 octahedron are capped by μ_3-Se ligands, with Co–Se bond lengths of 2.34 Å (avg.). Each Co metal is bound in a square pyramidal geometry via four μ_3-Se atoms and an aminophosphine ligand. This mixed-valent, formally $(Co^{III})_4(Co^{II})_2$, cluster features nearly equivalent interatomic Co···Co distances, ranging from 2.9390(5) to 2.9961(6) Å.[42] In contrast to the more reduced $[Co_3Se]$ and $[Co_4Se_2]$ congeners, these elongated Co···Co distances indicate the absence of metal–metal bonding interactions (r_{fs} = 1.29), which is the norm for $Co_6Se_8L_6$ clusters.

Notably, in contrast to the tolyl congener, $Co_6Se_8L^{Tol,H}_6$, and other reported $[Co_6Se_8]$ clusters, the isopropyl derivative $Co_6Se_8L^{iPr,H}_6$ has extremely poor solubility in conventional organic solvents post-purification. In fact, dissolving it requires stirring in chlorobenzene (PhCl) at temperatures exceeding 120 °C for at least 1 h. Single crystal X-ray characterization of $Co_6Se_8L^{iPr,H}_6$ sheds light on the root cause of its low solubility, revealing that upon crystallization an intermolecular network of π–π interactions is formed (Figure 2.11b). Each cluster organizes around it a supramolecular octahedron of clusters by engaging one phenyl substituent of each of its aminophosphine ligands in π–π interactions with a phenyl group of a neighboring cluster.[43] Interestingly, the Co_6Se_8 core is compressed along the z-axis, with axial and equatorial Se···Se

Scheme 2.3. Chemical oxidation of the homoleptic [Co_6Se_8] cluster, $Co_6Se_8L^{iPr,H}_6$.



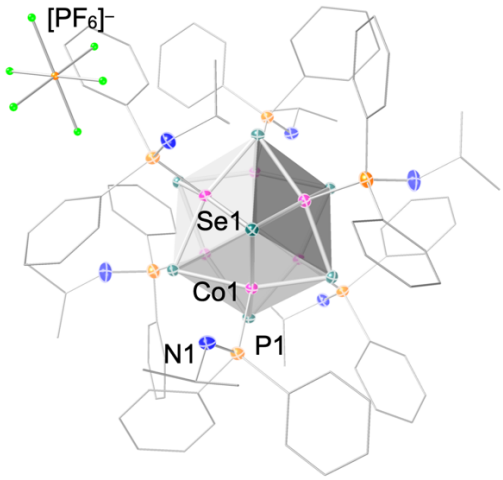


Figure 2.12. Single crystal X-ray structure of the mono-oxidized cluster, $[Co_6Se_8L^{iPr,H}_6][PF_6]$.

distances of 5.5081(9) and 5.6655(7) Å, respectively. While this core compression is intriguing, $Co_6Se_8L^{Tol,H}_6$ exhibits a similar trend in its Se···Se diagonals, which range between 5.56(2) and 5.716(7) Å, despite the absence of similar π–π packing effects.

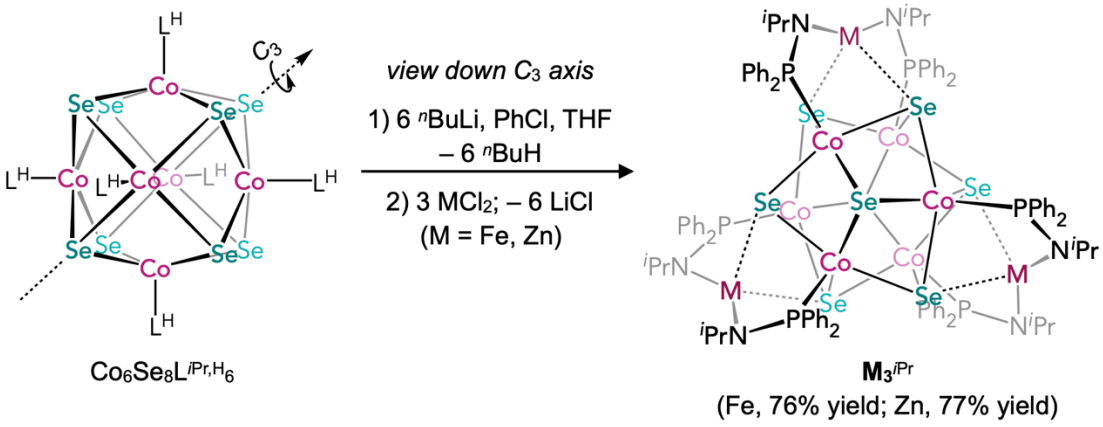
Chemical mono-oxidation of $Co_6Se_8L^{iPr,H}_6$ disrupts the π–π network and increases its solubility (Scheme 2.3). [Co_6Se_8] clusters are known to exhibit very rich redox profiles, undergoing up to four reversible single-electron oxidations.[44] Treating a slurry of $Co_6Se_8L^{iPr,H}_6$ in THF with [Fc][PF_6] (1 equiv.) causes an immediate dissolution of the suspended solids, and is associated with a simultaneous change in color from the dark red-brown adopts deeper red-orange hue. The mixture was stirred for 1 h before volatiles were removed *in vacuo*, and the resulting solids were slurried in toluene to remove the neutral ferrocene co-product. The dark red oxidized cluster, $[Co_6Se_8L^{iPr,H}_6][PF_6]$ (82% yield), now highly soluble in more polar solvents like acetonitrile, THF or DCM, can be easily crystallized from a mixture of THF and diethyl ether. Its ^{1}H NMR profile, recorded in d_3-acetonitrile, is comparable to that observed for $Co_6Se_8L^{iPr,H}_6$, although both the N*H* and C*H*(CH_3)$_2$ proton resonances are slightly broadened due the presence of a S = 1/2 $Co_6Se_8^{(+)}$ core. Single crystal X-ray diffraction analysis confirms mono-oxidation (Figure 2.12). In addition to the presence of the $[PF_6]^-$ counterion, we note changes in bond lengths that are diagnostic of cluster mono-oxidation.[21] For example, as the intracore *trans*-Co···Co distances

contract by ~0.08 Å from 4.197 to 4.120 Å (avg.), the Co–P bonds elongate by ~0.03 Å from 2.13 to 2.16 Å (avg.).

2.3.6 *Ternary nanopropeller clusters $M_3Co_6Se_8L^{iPr}{}_6$ (M = Fe, Zn)*

To trimetallate $Co_6Se_8L^{iPr,H}{}_6$, we adapted the previously reported protocol (Scheme 2.4).[11] To ensure the quantitative hexadeprotonation of $Co_6Se_8L^{iPr,H}{}_6$, a solvent mixture of PhCl and THF (5 : 1) and excess ^{n}BuLi (8 equiv.) were used. ^{31}P NMR analysis indicates that complete deprotonation is associated with a 10 ppm upfield shift in the signal of the amidophosphine phosphorus, to 89 ppm. In contrast to the tolyl derivative, $Co_6Se_8L^{Tol,H}{}_6$, the hexalithiated species, tentatively identified as $Li_6(THF)_xCo_6Se_8L^{iPr}{}_6$ (**Li$_6$**^{iPr}(THF)$_x$) does not precipitate from the PhCl solution, yet aliquots collected from the deprotonation mixture could not be redissolved in benzene-d_6 after removal of solvent. Intrigued at the possibility to access the putative zwitterion [**Li$_6$**^{iPr}(THF)$_x$][PF_6], we found that the hexadeprotonation of the mono-oxidized cluster $[Co_6Se_8L^{iPr,H}{}_6][PF_6]$ produces a mixture of species instead. Among them, a major component is neutral $Co_6Se_8L^{iPr,H}{}_6$, presumably formed by chemical reduction of $[Co_6Se_8L^{iPr,H}{}_6][PF_6]$ by ^{n}BuLi. Trimetallation was achieved *in situ* in the stoichiometric reaction between the hexalithiated complex **Li$_6$**(THF)$_x$ and MCl_2 (M = Fe, Zn; Scheme 2.4). For both metal salts, crude NMR spectroscopy analysis indicated the formation of a one major product, $M_3Co_6Se_8L^{iPr}{}_6$ (**M$_3$**^{iPr}). Significantly more soluble than their parent metalloligand, the **M$_3$**^{iPr} clusters can be isolated pure in good yields by crystallization (76 and 77% yield for Fe and Zn, respectively). Compared to the

Scheme 2.4. Synthesis of trimetallated nanopropellers **Fe$_3$**^{iPr} and **Zn$_3$**^{iPr}.



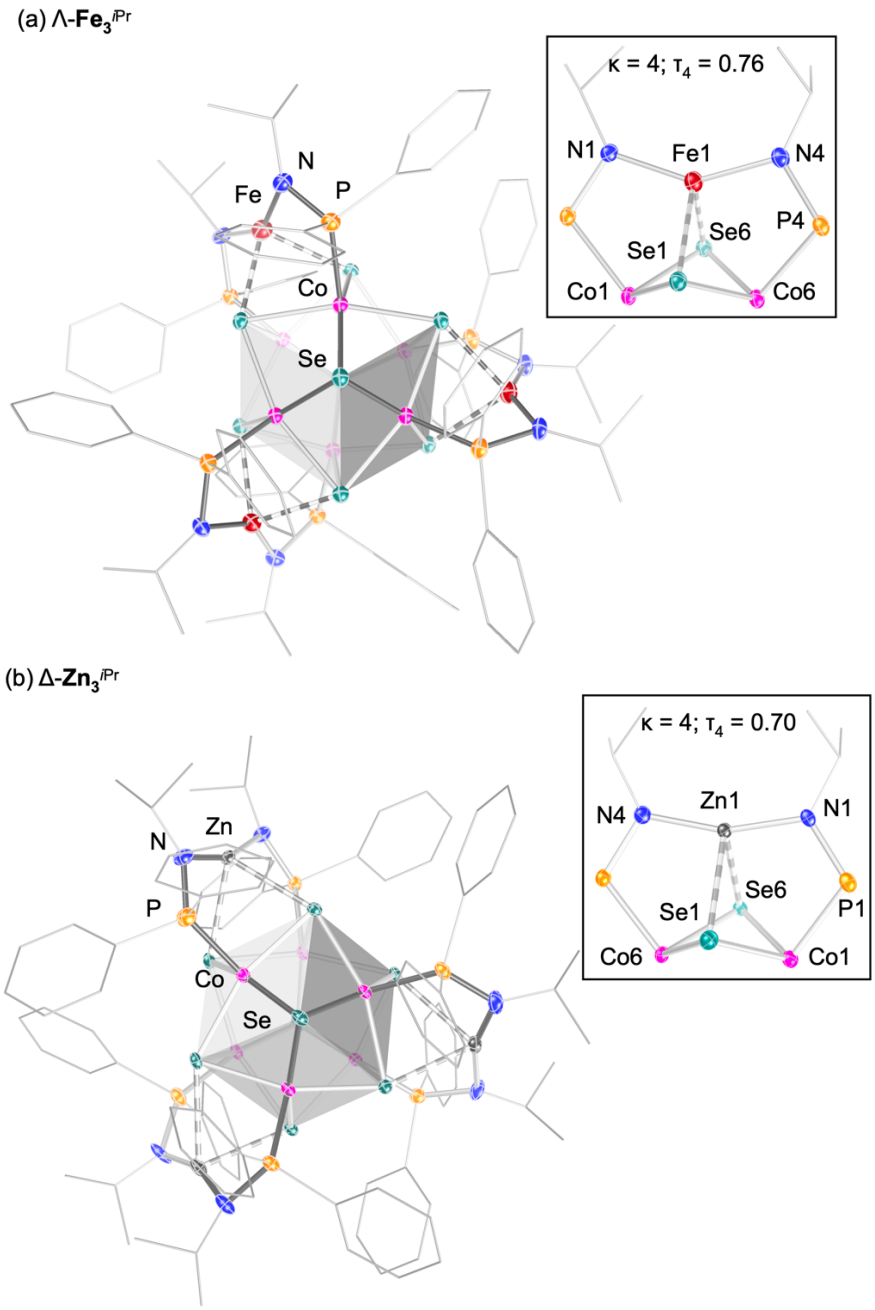


Figure 2.13. Single crystal X-ray structures of the nanopropeller clusters, Λ-**Fe**$_3$$^{i\text{Pr}}$ (a) and Δ-**Zn**$_3$$^{i\text{Pr}}$ (b), with insets highlighting the κ^4-bound edge sites. (a) Selected interatomic distances (Å): (a) Fe1–Se1 2.5360(2), Fe1–Se6 2.496(2), Fe1–N1 1.962(2), Fe1–N4 1.952(4), Fe1–Co1 2.885(1), Fe1–Co6 2.831(2), Co1–Co6 2.780(5), Co1–Se1 2.373(2), Co6–Se6 2.401(2), Co6–P4 2.171(2), P4–N4 1.6512(6); (b) Zn1–Se1 2.711(2), Zn1–Se6 2.660(5), Zn1–N1 1.882(7), Zn1–N4 1.888(8), Zn1–Co1 3.181(4), Zn1–Co6 3.181(3), Co1–Co6 2.910(4), Co1–Se1 2.369(2), Co6–Se6 2.385(1), N1–P1 1.648(8), Co1–P1 2.163(3). For **Zn**$_3$$^{i\text{Pr}}$, plotted is only the major component (88% occupancy), omitting for clarity the co-crystallizing $Co_6Se_8L^{i\text{Pr,H}}_6$ (12% occupancy; see Figure 2.36). Thermal ellipsoids plotted at 50% probability. Hydrogen atoms, co-crystallizing solvent, and disorder are omitted. All carbon atoms are displayed as wireframes for clarity.

tolyl derivative **Fe$_3$**, the isopropyl-capped clusters **M$_3$**$^{i\text{Pr}}$ are highly water sensitive, forming $Co_6Se_8L^{i\text{Pr,H}}_6$ or a mixture of mono- and dimetallated clusters in the presence of even trace water.

Single crystal X-ray analysis of the trimetallated clusters **Fe$_3$**$^{i\text{Pr}}$ and **Zn$_3$**$^{i\text{Pr}}$ reveals that they crystallize with no solvents coordinated to the edge sites (Figure 2.13), in contrast to the tolyl analogue **Fe$_3$** which was only obtained in single crystal form only as a tris(isocyanide) adduct.[11] As a result of the κ^4 chelation of each edge metal by the metalloligand, the inorganic $M_3Co_6Se_8$ cores of **Fe$_3$**$^{i\text{Pr}}$ and **Zn$_3$**$^{i\text{Pr}}$ exhibit near-perfect D_3 symmetry. Structurally, this most closely resembles the previously reported monoreduced triiron cluster [**Fe$_3$**]$^-$, isolated and characterized in the solid state free of bound surface ligands.[11] As was observed for [**Fe$_3$**]$^-$, the $M_3Co_6Se_8$ units of **M$_3$**$^{i\text{Pr}}$ can be deconstructed into three (μ_4-Se)-bicapped trinuclear $FeCo_2$ subunits interconnected along their Co···Co edge by two apical, non-M-binding μ_3-Se atoms, which also define the principle C_3 rotational axis of the cluster. As was the case for the tolyl derivatives, **Fe$_3$**$^{i\text{Pr}}$ and **Zn$_3$**$^{i\text{Pr}}$ crystallize as racemic mixtures of helical (Δ/Λ)-enantiomers.

In **Fe$_3$**$^{i\text{Pr}}$, each Fe edge site is bound κ^4 by the metalloligand via two isopropyl-amides and two μ_4-Se atoms, giving rise to a distorted-tetrahedral coordination at iron (τ_4 = 0.76; Figure 2.13).[45] The six Fe–Se bonds range between 2.496(2) and 2.5360(2) Å,[46] and cause pronounced structural distortions within the Co_6Se_8 cluster core. For example, the Co–(μ_4-Se) distances of 2.38 Å (avg.) are significantly longer than the Co–(μ_3-Se) bonds of 2.33 Å (avg.). This elongation effectively compresses the Co_6Se_8 cube toward the equatorial plane defined by the edge sites. This distortion can be quantified by the differences between the axial (along the C_3 axis) and equatorial Se···Se diagonal distances of the Co_6Se_8 core, of 5.412(8) and 5.77 (avg.) Å, respectively. Additionally, the Fe···Co and Co···Co interatomic distances within the $FeCo_2$ subunits average 2.87 and 2.80 Å, respectively, whereas the Co···Co distances that separate these triangles average 3.00 Å. These trends are like those observed for [**Fe$_3$**]$^-$, although in **Fe$_3$**$^{i\text{Pr}}$ the Fe–Se contacts are slightly longer (2.52 vs. 2.46 Å, avg.), and the core distortions are slightly less pronounced. While a direct comparison of bonding metrics with the tolyl cluster **Fe$_3$** cluster cannot be made since the latter was crystallized only as the tris-adduct **Fe$_3$**$(CN^tBu)_3$, we note that the three Fe–Se bonds in this tris(isocyanide) adduct, averaging 2.51 Å, are comparable to 2.52 Å, the average value for the six Fe–Se bonds in **Fe$_3$**$^{i\text{Pr}}$.[11]

The trizinc variant **Zn$_3$**$^{i\text{Pr}}$ exhibits a similar structure, except the Zn(II) sites coordinate in a geometry better described as distorted seesaw than tetrahedral ($\theta_{N–Zn–N} \approx 161°$; τ_4 = 0.70).

Compared to **Fe$_3$**$^{i\text{Pr}}$, the edge-support interactions in **Zn$_3$**$^{i\text{Pr}}$ are weaker, as reflected by weak Zn–Se bonds, ranging in length between 2.648(2) and 2.780(4) Å.[47] Consequently, the structural distortion of the Co_6Se_8 core is also less pronounced, with roughly equivalent axial and equatorial Se···Se diagonals of 5.613(4) and 5.66 (avg.) Å, respectively.

2.4 Electronic Influence of Surface Ligands

The electronic changes brought about by replacing the tolyl substituents with isopropyl ones in **Fe$_3$**$^{i\text{Pr}}$ and **Zn$_3$**$^{i\text{Pr}}$ was probed in solution using UV-vis-*n*IR absorption spectroscopy and cyclic voltammetry (Figure 2.14). A comparison of the electronic absorption profile of **Fe$_3$**$^{i\text{Pr}}$ with that of **Fe$_3$**, collected in a non-coordinative solvent (toluene), where no surface ligands are bound to either of the two clusters, reveals the main absorption feature of the isopropyl derivative is blue-shifted by 16 nm, and slightly less intense than that of the tolyl derivative (Figure 2.14a). We also note that while trimetallation with Fe significantly perturbs the characteristic absorption features of the metalloligand, this is less pronounced in the Zn derivative, empirically related to the degree of structural distortion observed within the Co_6Se_8 core. While the three absorption bands of **Zn$_3$**$^{i\text{Pr}}$ are red-shifted and broadened relative to those of $Co_6Se_8L^{i\text{Pr,H}}_6$, they are centered at a similar energy to the broad feature of **Fe$_3$**$^{i\text{Pr}}$.

Cyclic voltammetry reveals that both ternary **M$_3$**$^{i\text{Pr}}$ clusters feature a total of five pseudo-reversible one-electron redox processes, spanning oxidation states between −2 and +3 (Figure 2.14b). We note that the HOMO–LUMO gap, approximated as the separation between the (−1/0) and (0/+1) redox couples in THF, is smaller for **Fe$_3$**$^{i\text{Pr}}$ (1.01 eV) compared to the zinc variant **Zn$_3$**$^{i\text{Pr}}$ (1.38 eV), in accordance with the relative strength of the edge-support interactions in the two species. A comparison between the electrochemical profiles of **Fe$_3$**$^{i\text{Pr}}$ and **Fe$_3$** carried out in a DCM, a non-coordinative solvent, reveals an overall shift of the redox events to more reducing potentials (Figure 2.14c).[11] This change is in line with the more electron rich character of the isopropyl groups of **Fe$_3$**$^{i\text{Pr}}$ compared to the tolyl substituents in **Fe$_3$**. Another difference is a widening of the HOMO/LUMO gap in the isopropyl derivative compared to the tolyl one (0.92 vs. 0.87 eV in DCM). The decreased stabilization of the LUMO level can be attributed to the diminished Lewis acidity of the Fe sites in **Fe$_3$**$^{i\text{Pr}}$, which is also corroborated by coordination studies with CN^{t}Bu (see below).

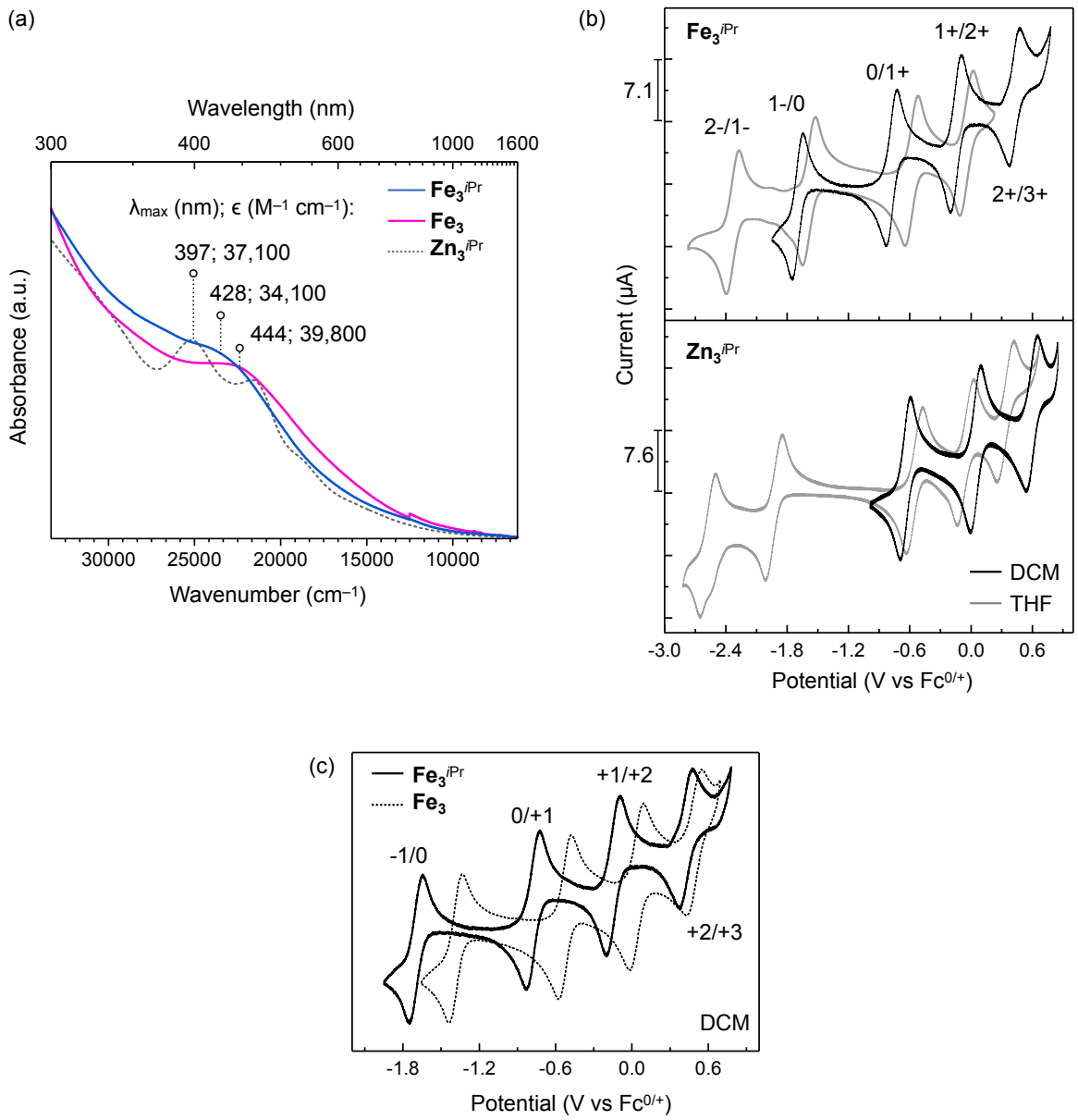


Figure 2.14. (a) UV-vis-*n*IR spectra including the λ_{max} (nm) and corresponding extinction coefficient ϵ (M^{-1} cm^{-1}) for $\mathbf{Fe_3}^{i\mathrm{Pr}}$ (428; 34100), $\mathbf{Fe_3}$ (444, 39800) and $\mathbf{Zn_3}^{i\mathrm{Pr}}$ (397; 37100), acquired in toluene. (b) Cyclic voltammograms of $\mathbf{Fe_3}^{i\mathrm{Pr}}$ and $\mathbf{Zn_3}^{i\mathrm{Pr}}$ recording in DCM or THF (0.1 M [^{n}Bu$_4$N][PF$_6$]) at 50 mV/s. (c) Comparison between the electrochemical profiles of $\mathbf{Fe_3}^{i\mathrm{Pr}}$ and $\mathbf{Fe_3}$, acquired in DCM (0.1 M [^{n}Bu$_4$N][PF$_6$]) at 50 mV/s.

In solution, NMR analysis reveals that the free rotation of the isopropyl substituents at the Fe and Zn edges is hindered. For example, $\mathbf{Fe_3}^{i\mathrm{Pr}}$ exhibits a total of eight paramagnetic proton resonances between 20 and −20 ppm, more than the five expected for a freely rotating ligand environment (Figure 2.20). As observed for the tolyl cluster $\mathbf{Fe_3}$, the ligand framework in $\mathbf{Fe_3}^{i\mathrm{Pr}}$ and $\mathbf{Zn_3}^{i\mathrm{Pr}}$ is structurally locked, both in the solid-state and in solution, in a helical conformation

such that two phenyl groups of each phosphine adopt either an axial or equatorial orientation, giving rise to two separate sets of NMR resonances. However, ^{1}H integrations for **Fe$_3$**$^{i\text{Pr}}$ suggest that the ^{i}Pr-C*H*$_3$ groups are also resolved under D_3 symmetry, indicating that the isopropyl substituents are sterically locked in place at the edge sites. In contrast, the tolyl substituents in **Fe$_3$** rotate freely even in a non-coordinative solvent, as is reflected by the singular set of tolyl resonances in its ^{1}H NMR profile.[11] Notably, solution-phase magnetic measurements carried out using the Evans method[48] confirm the iron edge sites remain high spin (S = 2) in **Fe$_3$**$^{i\text{Pr}}$ (μ_{eff} = 9.4 μ_B), as was observed for **Fe$_3$**.[11] In the trizinc variant, **Zn$_3$**$^{i\text{Pr}}$ the desymmetrization associated with the hindered rotation is reflected in both its ^{1}H and ^{13}C NMR spectra, for example by the presence of additional proton features in the aromatic region, and two nearly overlapping sets of ^{i}Pr-C*H*$_3$ and ^{i}Pr-C*H* resonances (see Section 2.5.9).

Comparison of space filling models for **Fe$_3$**$^{i\text{Pr}}$ and [**Fe$_3$**]$^-$, both of which feature Fe edge sites coordinated κ^4 by the cluster-ligand, reveals the presence of the required space to allow the rotation of the tolyl groups, whereas the increased steric bulk of the isopropyl substituents appears

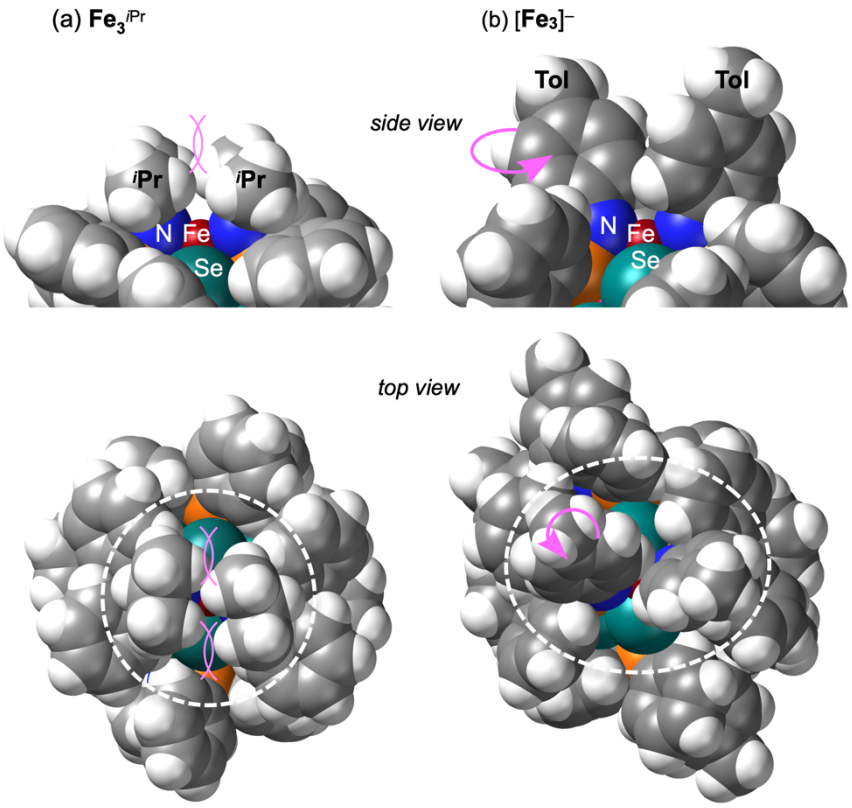


Figure 2.15. Space filling models for a single κ^4–Fe edge site in (a) **Fe$_3$**$^{i\text{Pr}}$ and (b) [**Fe$_3$**]$^-$, including a zoom-in on the side view, highlighting the isolated edge site, and the full cluster viewed from the top of the outlined edge site.

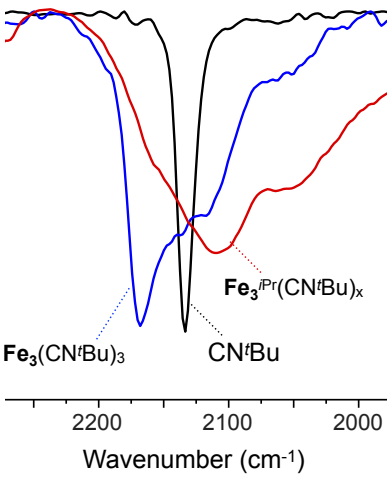


Figure 2.16. Comparison of CN infrared stretches of free CN^{t}Bu (black), **Fe$_3$**(CN^{t}Bu)$_3$ (blue) and **Fe$_3$**$^{i\text{Pr}}$(CN^{t}Bu)$_x$ (red).

to keep them locked in **Fe$_3$**$^{i\text{Pr}}$ (Figure 2.15). An important implication of the increased steric bulk at the edge Fe sites is that it might be a leading factor in preventing coordination of sufficiently large ligands. We set out to probe the affinity for ligands of the edge sites in **Fe$_3$**$^{i\text{Pr}}$, and compare it to those in **Fe$_3$**. Treatment of **Fe$_3$**$^{i\text{Pr}}$ with THF, or excess pyridine (15 equiv.) in benzene-d_6 revealed little-to-no changes in its paramagnetic ^{1}H resonances, consistent with no binding interactions (Figure 2.21). This resembles the behavior of the edge sites in the monoreduced cluster [**Fe$_3$**]$^-$, but stands in contrast to the neutral **Fe$_3$** which coordinates in solution to both.[11] To probe if the zero affinity of **Fe$_3$**$^{i\text{Pr}}$ for these solvents is sterically enforced, we turned to the linear monodentate ligand CN^{t}Bu, which was shown to bind to **Fe$_3$** but not to the monoreduced cluster [**Fe$_3$**]$^-$. Treatment of **Fe$_3$**$^{i\text{Pr}}$ with CN^{t}Bu (15 equiv.) elicited subtle, but noticeable changes in its proton chemical shifts, suggesting coordinative interactions. The isocyanide infrared CN stretch of the coordinated isocyanide (ν_{CN} = 2104 cm^{-1}), acquired after removal of the unbound excess ligand, is red-shifted compared to both free CN^{t}Bu and **Fe$_3$**(CN^{t}Bu)$_3$ (ν_{CN} = 2167, 2141 cm^{-1}, respectively; Figure 2.16). In contrast to the neutral **Fe$_3$,** where the electron deficient Fe sites not only do not activate the isocyanide but form one of the most deactivated adducts reported to date,[11] in **Fe$_3$**$^{i\text{Pr}}$ the edge sites are sufficiently electron rich to participate in π-backbonding with this π-acceptor, ostensibly due to the increased donor strength of the isopropyl amido ligands.

The ternary **M$_3$**$^{i\text{Pr}}$ clusters introduced by our group provide a new strategy to access redox-active multimetallic platforms with synthetically addressable, and hemilabile active sites. In previous work we demonstrated that not only the oxidation state of the overall cluster, but also the

chemical identity of the edge sites[12] provides a mechanism to tune their affinity to bind additional ligands (e.g. pyridine or CN^{t}Bu). In this report we probed the effects of small alterations in the stereoelectronic properties of the aminophosphine ligands, and found they significantly alter the [Co_6Se_8] cluster formation process, in addition to their affinity for external ligands and the strength of the edge-support interaction in **M3**$^{i\text{Pr}}$. While a slight increase in the steric bulk of the substituents of the amido groups that anchor the edge metals on the inorganic cobalt core appears to be the primary factor modulating ligand coordination, their increased donor strength was found to also contribute to the resulting electronic properties of the ternary clusters. In conclusion, we demonstrate how small modifications in the ligand framework of the ternary nanopropeller M/Co/Se clusters can result in pronounced impacts on their chemical and physical properties, altering the push–pull dynamic between the Co_6Se_8 support, the edge metal and external coordinating ligands.

2.5 Experimental Details

2.5.1 *General Considerations*

All syntheses were conducted under a dinitrogen atmosphere using a standard Schlenk line or an LC Technology Solutions glovebox equipped with a freezer set to −35 °C. All glassware was dried at 160 °C for a minimum of 12 h prior to use.

Solvents were purchased from Fischer Scientific and degassed, dried and purified using solvent purification columns housed in a stainless-steel cabinet and dispensed by a stainless-steel Schlenk line manufactured by JC Meyer Solvent Systems. Tetrahydrofuran (THF), diethyl ether (Et_2O), acetonitrile (MeCN), and methylene chloride (DCM) are passed through two packed columns of neutral alumina. *n*-Pentane and toluene are passed through a column packed with alumina, and one containing Q5 reactant, a copper(II) oxide oxygen scavenger. All solvents were passed through an in-line, 2 μm filter, then stored over activated 3Å molecular sieves in the glovebox. 3Å molecular sieves were purchased from Sigma Aldrich and activated under vacuum at 300 °C for 48 h. Anhydrous pyridine (99.8%) and anhydrous chlorobenzene (PhCl, 99.8%) were purchased from Sigma Aldrich and stored over activated 3Å molecular sieves for 72 h prior to use. Deuterated solvents ($CDCl_3$, C_6D_6, CD_2Cl_2, CD_3CN) were purchased from Sigma Aldrich, degassed and dried over activated 3Å molecular sieves in the glovebox for a minimum of 72 h.

$FeCl_2$ (98+%, Strem Chemicals, Inc.) was dried under vacuum at 150 °C for 24 h prior to use. $ZnCl_2$ (99.99%-Zn, anhydrous, PURATREM, Strem Chemicals, Inc.) was used without further purification. $Co_2(CO)_8$ (stabilized with 2-5% hexanes, Strem Chemicals, Inc.) was stored in the glovebox freezer, and used as received. Chlorodiphenylphosphine (97%, Alfa Aesar), chlorodiisopropylphosphine (≥96%, Acros Organics), isopropylamine (99%, Sigma Aldrich), selenium (99.5%, powder, 200 mesh, Sigma Aldrich) and *n*-butyl lithium (2.5 M in hexanes, Sigma Aldrich) were used as received. Ferrocenium hexafluorophosphate (97%, Sigma Aldrich) was purified by crystallization from dry acetone and diethyl ether, followed by drying *in vacuo* for 12 h prior to use. *Tert*-butyl isocyanide (CN^tBu, 98%) was purchased from Sigma Aldrich, degassed, and stored over activated 3 Å molecular sieves in the glovebox for a minimum of 72 h prior to use. The aminophosphines $Ph_2PN(H)^iPr$ (L^H) and $^iPr_2PN(H)^iPr$ (Ph = phenyl, ^{i}Pr = isopropyl) and $Fe_3Co_6Se_8(Ph_2PNTol)_6$ (Tol = 4-tolyl) were prepared according to the literature.[11,13,49]

UV-vis-*n*IR absorption spectra were acquired using a Varian Cary 5000 UV-Vis-*n*IR spectrophotometer, in *n*IR quartz cuvettes (Spectrocell Inc., 10 mm path length, 220–3500 nm spectral window). Attenuated total reflectance infrared (ATR-IR) spectra were recorded on a Bruker Alpha IR instrument equipped with a Platinum ATR accessory housed within a nitrogen glovebox. NMR spectra were acquired at 25 °C on Bruker AV300, AV301, or DRX499 spectrometers. ^{1}H NMR spectra were referenced to residual deuterated solvent peaks, ^{31}P NMR spectra were externally referenced to phosphoric acid. Solution magnetic susceptibilities were determined by the Evans method in CD_2Cl_2 using 1% (by volume) mesitylene as an internal standard.[48]

Samples were prepared for elemental analysis by crushing single crystalline material into a powder and then removing volatiles under reduced pressure for 12 h. Zn, Co, Se, P elemental analysis was conducted using a Perkin-Elmer Nexion 2000B inductively-coupled plasma mass spectrometer (ICP-MS). Fe elemental analysis was not performed as calibration data of sufficient quality could not be obtained for this element. Prior to ICP-MS analysis, samples were digested in neat nitric acid (Fisher Scientific, ICP-MS grade) at 50 °C. Note: combustion analysis to determine C,H,N percentages was not conducted, as it cannot discriminate between $M_3Co_6Se_8L_6$ (M = Fe, Zn) and possible contaminants, such as partly metallated clusters $M_2Co_6Se_8L_5L^H$ or $M_2Co_6Se_8L_4L^H_2$.

Cyclic voltammetry was conducted using an Interface 1010B potentiostat by Gamry. A three-electrode cell setup was used with a glassy carbon disk working electrode, a platinum wire counter electrode, and a silver-wire pseudo-reference electrode. All potentials were referenced to the $Fc^{0/+}$ redox couple by adding a small amount of ferrocene after each measurement. All electrochemical measurements were conducted under a dinitrogen atmosphere, at 25 °C.

2.5.2 *Synthesis and Isolation of $Co_6Se_8(Ph_2P(H)N^iPr)_6$, $Co_6Se_8L^{iPr,H}_6$*

Inside the glovebox, a Schlenk flask was loaded with $Co_2(CO)_8$ (5.84 g, 17.2 mmol, 3 equiv) and selenium powder (0.89 g, 11.3 mmol, 2 equiv), capped with a Suba Seal and transferred to the Schlenk line where toluene (24 mL) was syringed in. In parallel, inside the glovebox, $Se{=}PPh_2N(H)^iPr$ ($Se{=}L^{iPr,H}$) was prepared *in situ* by heating $L^{iPr,H}$ (8.32 g, 34.0 mmol, 6 equiv) and selenium powder (2.68 g, 34.0 mmol, 6 equiv) in toluene (13 mL) at 60 °C, until the mixture became homogeneous. The $Se{=}L^{iPr,H}$ solution was allowed to cool to room temperature, and then was added via syringe to the Schlenk flask, inducing the rapid evolution of carbon monoxide gas. After ca. 5 minutes of mixing the reagents, the reaction flask was immersed in a pre-heated oil bath (110 °C) and stirred vigorously for 15 h. To ensure conversion of partial carbonylated [6,8] clusters to the desired product, a second portion of $L^{iPr,H}$ (4.16 g, 17.0 mmol, 3 equiv) was added to the reaction flask as a solution in toluene (2 mL). After refluxing the reaction mixture for an additional 24 h, during which time the CO infrared stretch at 1970 cm^{-1} decreased in intensity, volatiles were removed under reduced pressure. The oily residue was subjected to a solvent workup, using successive portions of *n*-pentane (3 x 30 mL), diethyl ether (3 x 30 mL), and toluene (3 x 10 mL) to extract the material. The residue obtained after the toluene extraction was collected as a dark red microcrystalline solid on a fine-porosity fritted glass funnel and was subsequently identified as $Co_6Se_8L^{iPr,H}_6$ (11.21 g, 4.7 mmol, 80%).

UV-vis-*n*IR (toluene, 25 °C) λ: 365 (ϵ = 49400 M^{-1} cm^{-1}), 443 (ϵ = 29600 M^{-1} cm^{-1}), 505 (ϵ = 19600 M^{-1} cm^{-1}) nm. ^{1}H NMR (C_6D_6, 500 MHz) δ: 7.84 (t, 24H, J = 8.9 Hz, PPh_2 m-Ar*H*); 7.19 (m, 36H, PPh_2 o- and p-Ar*H*); 2.84 (m, 6H, $NCH(CH_3)_2$); 2.40 (dd, 6H, $^2J_{PH}$ = 15.7 Hz, J_{HH} = 10.0 Hz, N*H*); 0.77 (d, 36 H, 6.76 Hz, $NCH(CH_3)_2$) ppm. ^{13}C NMR (PhCl, 125 MHz) δ: 142.42 (d, $^1J_{PC}$ = 50.2 Hz, *i*-PPh_2); 132.42 (d, J_{PC} = 9.7 Hz, *o*-PPh_2); 128.17 (s, *p*-PPh_2); 126.86 (d, J_{PC} = 9.7 Hz, *m*-PPh_2); 46.43 (d, $^2J_{PC}$ = 10.4 Hz, $NCH(CH_3)_2$); 25.58 (s, $NCH(CH_3)_2$) ppm. ^{31}P NMR (C_6D_6, 283

MHz) δ: +90.7 ($\nu_{1/2}$ = 383 Hz) ppm. Elemental analysis found (calc.) for $Co_6Se_8L^{iPr,H}_6$ (Formula: $C_{90}H_{108}Co_6N_6P_6Se_8$): Co 15.12 (14.46), Se 26.10 (25.83), P 7.24 (7.60).

2.5.3 *Synthesis and Isolation of $[Co_6Se_8L^{iPr,H}_6][PF_6]$; $[Co_6Se_8L^{iPr,H}_6]^+$*

A slurry of $Co_6Se_8L^{iPr,H}_6$ (1.000 g, 0.4 mmol, 1 equiv) in THF (25 mL) was treated with ferrocenium hexafluorophosphate (0.135 g, 0.4 mmol, 1 equiv), yielding a red-orange solution. The mixture was stirred for 1 h at 25 °C before volatiles were removed under reduced pressure. After evaporation of volatiles, the crude products were washed with toluene (3 x 10 mL) to remove ferrocene. The product was then dissolved in THF (30 mL) and filtered through a plug of Celite on a medium-porosity fritted glass funnel. This filtrate was concentrated to 10 mL, layered with 50 mL of diethyl ether and cooled to –35 °C for 24 hours to yield dark red crystals of $[Co_6Se_8L^{iPr,H}_6][PF_6]$ (0.876 g, 0.338 mmol, 82%).

^{1}H NMR (CD_3CN, 300 MHz) δ: 7.70 (t, 12H, 7.40 Hz, PPh_2 p-Ar*H*); 7.31 (d, 24H, 7.3 Hz, PPh_2 o-Ar*H*); 6.91 (t, 24H, 7.3 Hz, PPh_2 m-Ar*H*); 2.56 (m, 6H, NC*H*$(CH_3)_2$); 0.83 (d, 6H, 8.4 Hz, N*H*); 0.49 (d, 36 H, 6.2 Hz, NCH(C*H*$_3)_2$) ppm. Elemental analysis found (calc.) for $[Co_6Se_8L^{iPr,H}_6][PF_6]$ (Formula: $C_{90}H_{108}Co_6F_6N_6P_7Se_8$): Co 13.99 (13.65), Se 24.43 (24.39), P 7.05 (8.37).

2.5.4 *Synthesis and Isolation of $Co_4Se_2(CO)_6L^{iPr,H}_6$,* ***$Co_4Se_2$***

Inside the glovebox, a Schlenk flask was charged with $Co_2(CO)_8$ (0.403 g, 1.18 mmol, 3 equiv) and a magnetic stir bar, then it was transferred to the Schlenk line where toluene (12 mL) was syringed in. In parallel, inside the glovebox, a mixture of $Se{=}L^{iPr,H}$ and $L^{iPr,H}$ was prepared in toluene by heating $L^{iPr,H}$ (1.145 g, 4.71 mmol, 12 equiv) and selenium powder (0.248 g, 3.14 mmol, 8 equiv) in toluene (28 mL) at 60 °C. The resulting solution was allowed to cool to room temperature, then transferred using a syringe to the Schlenk flask inducing the rapid evolution of carbon monoxide gas. The reaction mixture was stirred at room temperature for 5 min, before being transferred to a preheated oil bath (113 °C). After 16 h, the volatiles were removed under reduced pressure. The oily residue was triturated with *n*-pentane (3 x 10 mL), then subjected to a solvent workup that used successive portions of *n*-pentane (3 x 30 mL), diethyl ether (3 x 30 mL), and toluene (3 x 10 mL) to extract the material. The toluene extracts were concentrated and layered

with *n*-pentane for bulk crystallization. Dark green prismatic crystals formed and were identified as **Co_4Se_2** (0.219 g, 0.143 mmol, 24%).

UV-vis-*n*IR (toluene, 25 °C) λ: 329, 436, 552, 626 nm. ATR-FTIR (dropcast in toluene) ν_{CO}: 1927, 1775 cm^{-1}. ^1H NMR (CD_2Cl_2, 500 MHz) δ: 7.50 (m, 16H, PPh_2 m-Ar*H*); 7.34 (m, 24H, PPh_2 o-/*p*-Ar*H*); 2.94 (m, 4H, NC*H*(CH_3)$_2$); 2.23 (dd, 4H, $^2J_{PH}$ = 20.1 Hz, J_{HH} = 9.7 Hz, N*H*); 0.78 (d, 24H, 5.7 Hz, NCH(C*H*$_3$)$_2$) ppm. ^1H NMR (C_6D_6, 300 MHz) δ: 7.77 (t, 16H, *J* = 8.4 Hz, PPh_2 m-Ar*H*); 7.20 (d, 16H, *J* = 7.4 Hz, PPh_2 o-Ar*H*); 7.07 (t, 8H, *J* = 7.4 Hz, PPh_2 p-Ar*H*); 2.96 (m, 4H, NC*H*(CH_3)$_2$); 2.61 (dd, 4H, $^2J_{PH}$ = 19.7 Hz, J_{HH} = 10.0 Hz, N*H*); 0.77 (d, 24H, 6.4 Hz, NCH(C*H*$_3$)$_2$) ppm. ^{13}C NMR (CD_2Cl_2, 125 MHz) δ: 136.48 (d, $^1J_{PC}$ = 43.2 Hz, *i*-PPh_2); 132.29 (s, *o*-PPh_2); 129.10 (s, *p*-PPh_2); 127.56 (s, *m*-PPh_2); 99.98 (s, μ$_2$-*C*O); 46.16 (s, N*C*H(CH_3)$_2$); 25.14 (s, NCH(*C*H$_3$)$_2$); 13.82 (s, μ$_1$-*C*O). ^{31}P NMR (C_6D_6, 283 MHz) δ: +81.9 ($\nu_{1/2}$ = 320 Hz) ppm. Elemental analysis found (calc.) for **Co_4Se_2** (Formula: $C_{66}H_{72}Co_4N_4O_6P_4Se_2$): Co 15.15 (15.36), Se 10.27 (10.29), P 8.37 (8.07).

2.5.5 *Thermal Conversion of **Co_4Se_2** to $Co_6Se_8L^{iPr,H}_6$*

Inside the glovebox, a 10 mL Schlenk flask equipped with a magnetic stir bar was loaded with **Co_4Se_2** (0.063 g, 0.041 mmol, 1 equiv), $L^{iPr,H}$ (0.120 g, 0.490 mmol, 12 equiv), selenium powder (0.020 g, 0.245 mmol, 6 equiv) and toluene (2 mL) and sealed with a Suba Seal. The flask was transferred to the Schlenk line and immersed in a preheated oil bath (115 °C) for 18 h, with vigorous stirring. Volatiles were removed under reduced pressure, and the crude solids were triturated with *n*-pentane (2 x 5 mL). A small portion of the resulting solids was completely dissolved in benzene-d_6 and the resulting solution was analyzed by ^1H NMR spectroscopy, confirming a clean conversion to $Co_6Se_8L^{iPr,H}_6$. An isolated yield was not measured for this transformation.

2.5.6 *Synthesis of $Co_3Se(\mu_2\text{-}PPh_2)(CO)_4L^{iPr,H}_3$, **$Co_3Se$***

Inside the glovebox, a 25 mL Schlenk flask equipped with a magnetic stir bar was loaded with $L^{iPr,H}$ (1.435 g, 5.9 mmol, 15 equiv), Se powder (0.310 g, 3.9 mmol, 10 equiv) and toluene (1 mL). The flask was capped with a Suba Seal, and transferred to the Schlenk line where it was heated with vigorous stirring to 60 °C, until it became homogeneous. A solution of $Co_2(CO)_8$ (0.403 g,

1.2 mmol, 3 equiv) in toluene (7 mL) was rapidly added to the Schlenk flask using a syringe, causing the rapid evolution of carbon monoxide gas. The reaction flask was then immersed in a pre-heated oil bath (110 °C), and stirred for 24 h before the volatiles were removed under reduced pressure. The oily residue was stirred in *n*-pentane for 2 h, then brought to constant mass under vacuum. The resulting solids were extracted with successive portions of *n*-pentane (3 x 20 mL), diethyl ether (3 x 20 mL), and toluene (3 x 10 mL). The toluene extracts were concentrated to ~3 mL and layered with *n*-pentane to yield **Co_3Se** as a dark red-brown precipitate (0.344 g, 0.268 mmol, 35%).

UV-vis-*n*IR (toluene, 25 °C) λ: 369, 636 nm. ATR-FTIR (dropcast in toluene) ν_{CO}: 1982, 1946, 1918 cm^{-1}. ^{1}H NMR (C_6D_6, 500 MHz) δ: 8.01 (t, 4H, 8.8 Hz, m-Ar*H*); 7.82 (t, 2H, 8.8 Hz, PPh_2 p-Ar*H*); 7.67 (m, 8H, m-Ar*H*); 7.19 (m, 6H, Ar*H*); 7.08 (m, 14H, Ar*H*); 6.96 (m, 4H, Ar*H*); 6.79 (m, 2H, μ_2-PPh_2 p-Ar*H*); 3.16 (m, 1H, NC*H*$(CH_3)_3$); 2.82 (m, 2H, NC*H*$(CH_3)_2$); 2.46 (dd, 2H, $^{2}J_{PH}$ = 22.8 Hz, $^{2}J_{HH}$ = 11.3 Hz, N*H*); 1.86 (dd, 1H, $^{2}J_{PH}$ = 17.5 Hz, $^{2}J_{HH}$ = 11.3 Hz, N*H*); 0.70 (d, 6H, 6.0 Hz, NCH(C*H*$_3)_2$); 0.59 (m, 12H, NCH(C*H*$_3)_2$) ppm. ^{13}C NMR (C_6D_6, 125 MHz) δ: 148.36 (s, *C*O); 142.85 (d, J_{PC} = 13.1 Hz, *p*-(μ_2-PPh_2)); 141.0 (d, $^{1}J_{PC}$ = 44.4 Hz, $L^{iPr,H}$ *i*-PPh_2); 140.26 (d, $^{1}J_{PC}$ = 44.4 Hz, $L^{iPr,H}$ *i*-PPh_2); 139.52 (d, $^{1}J_{PC}$ = 40.6 Hz, *i*-(μ_2-PPh_2)); 133.82 (d, J_{PC} = 9.8 Hz, $L^{iPr,H}$ *o*-PPh_2); 133.26 (d, J_{PC} = 11.6 Hz, $L^{iPr,H}$ *o*-PPh_2); 132.89 (d, J_{PC} = 9.8 Hz, $L^{iPr,H}$ *m*-PPh_2); 132.54 (d, J_{PC} = 11.6 Hz, $L^{iPr,H}$ *m*-PPh_2); 133.21 (d, J_{PC} = 11.2 Hz, $L^{iPr,H}$ *p*-PPh_2); 129.46 (s, *o*-(μ_2-PPh_2)); 129.17 (s, *m*-(μ_2-PPh_2); 46.71 (d, $^{2}J_{PC}$ = 9.7 Hz, NCH$(CH_3)_2$); 46.31 (d, $^{2}J_{PC}$ = 9.8 Hz, NCH$(CH_3)_2$); 25.75 (s, NCH(C*H*$_3)_2$); 25.65 (s, NCH(***C***H$_3)_2$). ^{31}P NMR (C_6D_6, 283 MHz) δ: +164.7 (1P, $\nu_{1/2}$ = 408 Hz, μ_2-*P*Ph_2); +88.5 (1P, $\nu_{1/2}$ = 385 Hz, *P*Ph_2); +81.7 (2P, $\nu_{1/2}$ = 374 Hz; *P*Ph_2) ppm. Elemental analysis found (calc.) for **Co_3Se** (Formula: $C_{61}H_{64}Co_3N_3O_4P_4Se$): Co 13.91 (13.78), Se 6.14 (6.16), P 11.48 (9.66).

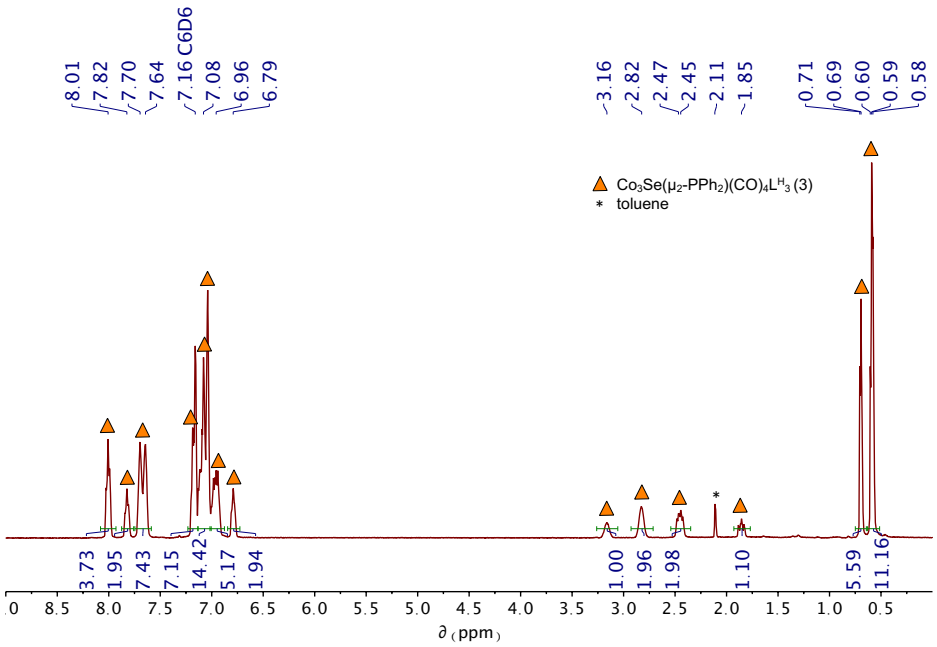


Figure 2.17. ^{1}H NMR (C_6D_6, 25 °C, 500 MHz) spectrum of $Co_3Se(\mu_2\text{-}PPh_2)(CO)_4L^H_3$.

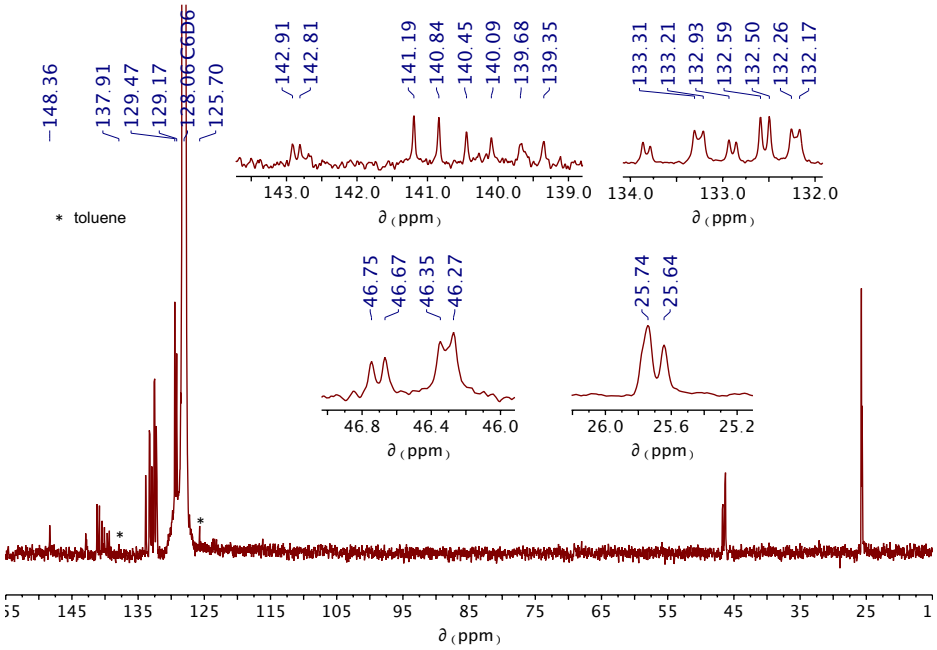


Figure 2.18. ^{13}C NMR (C_6D_6, 25 °C, 125 MHz) spectrum of $Co_3Se(\mu_2\text{-}PPh_2)(CO)_4L^H_3$.

2.5.7 *Synthesis and Isolation of $[Co(CO)_3(^iPr_2PN(H)^iPr)]_2$,* ***Co₂***

Inside the glovebox, a 100 mL Schlenk tube equipped with a magnetic stir bar was loaded with $Co_2(CO)_8$ (0.730 g, 2.1 mmol, 3 equiv) and selenium powder (0.449 g, 5.7 mmol, 8 equiv), then capped with a Suba Seal and transferred to the Schlenk line. Toluene (20 mL) were added via

syringe injection, then a solution of $^{i}Pr_2PN(H)^{i}Pr$ (0.748 g, 4.3 mmol, 6 equiv) in toluene (10 mL), the latter inducing the rapid evolution of carbon monoxide gas. The Schlenk flask was then immersed in a preheated oil bath (110 °C) and stirred for 14 h. Volatiles were removed under reduced pressure, and the crude products were triturated with *n*-pentane (3 x 10 mL). The crude solids were extracted with *n*-pentane (2 x 10 mL), and the residue dissolved in diethyl ether and passed through a plug of Celite, on a medium porosity glass fritted funnel. The filtrate was brought to constant mass *in vacuo* to yield a crop of orange-red solids, subsequently identified as $[Co(CO)_3(^{i}Pr_2PN(H)^{i}Pr)]_2$ (**Co_2**, 0.5121 g, 0.805 mmol, 38% based on $Co_2(CO)_8$).

UV-vis-*n*IR (toluene, 25 °C) λ: 377 nm. ATR-FTIR (dropcast in toluene) ν_{CO}: 1943 cm^{-1}. ^{1}H NMR (C_6D_6, 300 MHz) δ: 3.56 (m, 2H, NC*H*$(CH_3)_2$); 1.80 (dh, 4H, $^{2}J_{PH}$ = 6.9 Hz, $^{2}J_{HH}$ = 7.4 Hz, PC*H*$(CH_3)_2$); 1.08 (m, 24H, PCH(C*H*$_3)_2$); 0.94 (d, 12H, 6.5 Hz, NCH(C*H*$_3)_2$); 0.75 (d, 2H, 10.2 Hz, N*H*) ppm. ^{13}C NMR (C_6D_6, 125 MHz) *δ*: 204.61 (s, *C*O); 46.31 (s, N*C*H$(CH_3)_2$); 32.66 (d, $^{1}J_{PC}$ = 28.3 Hz, P*C*H$(CH_3)_2$); 26.41 (s, NCH(*C*H$_3)_2$); 18.15 (d, $^{2}J_{PC}$ = 19.4 Hz, PCH(*C*H$_3)_2$). ^{31}P NMR (C_6D_6, 283 MHz) δ: +129.3 ($\nu_{1/2}$ = 82.2 Hz) ppm. Elemental analysis found (calc.) for $[Co(CO)_3(^{i}Pr_2PN(H)^{i}Pr)]_2$ (Formula: $C_{24}H_{44}Co_2N_2O_6P_2$): Co 18.48 (18.52), P 9.72 (9.73).

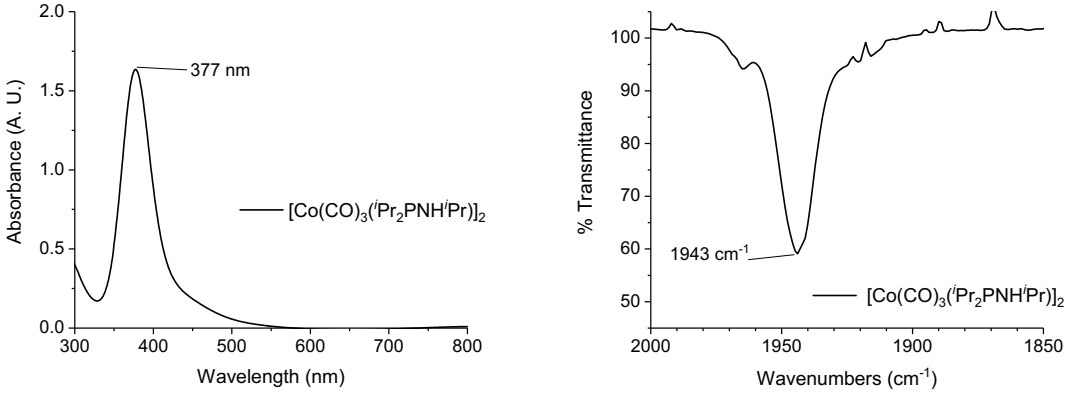


Figure 2.19. UV-vis absorption (in toluene; left) and ATR-FTIR (solids; carbonyl region; right) spectra of $[Co(CO)_3(^{i}Pr_2PN(H)^{i}Pr)]_2$.

2.5.8 *Synthesis and Isolation of $Fe_3Co_6Se_8L^{iPr}{}_6$, **Fe_3^{iPr}***

$Co_6Se_8L^{iPr,H}{}_6$ (200 mg, 0.082 mmol, 1 equiv) was dissolved in chlorobenzene (12 mL) by stirring the sample at 130 °C for 1 h. The resulting deep red solution was cooled to room temperature before adding THF (2 mL) and freezing the mixture in the glovebox cold well. A solution of ^{n}BuLi

(2.5 M in hexanes; 262 µL, 0.654 mmol, 8 equiv) was added dropwise to the thawing mixture, which was then allowed to warm to room temperature. After 16 h, the reaction mixture was frozen once again, and upon thawing, solid $FeCl_2$ (31 mg, 0.245 mmol, 3 equiv) was added portion-wise to the stirring solution. The mixture was warmed to room temperature, and stirred for 4 h, during which time it became homogeneous and took on a darker red color. Volatiles were removed *in vacuo*, and the resulting solids were triturated thoroughly with diethyl ether (3 x 10 mL), extracted with *n*-pentane (3 x 15 mL), and then with toluene (10 mL). The toluene extract was passed through a plug of Celite on a fritted glass funnel. The filtrate was then concentrated *in vacuo*, diluted with *n*-pentane, and cooled to –35 °C for 24 h to yield dark red crystals of **Fe$_3$**$^{i\text{Pr}}$ (0.1621 g, 0.062 mmol, 76%).

UV-vis-*n*IR (toluene, 25 °C) λ: 428 (ϵ = 34100 M^{-1} cm^{-1}) nm. ^{1}H NMR (CD_2Cl_2, 500 MHz) δ: 19.17 (s, 12H, $\nu_{1/2}$ = 140 Hz); 16.00 (s, 12H, $\nu_{1/2}$ = 19 Hz); 14.08 (s, 12H, $\nu_{1/2}$ = 162 Hz); 11.00 (s, 6H, $\nu_{1/2}$ = 17 Hz); 8.85 (s, 12H, $\nu_{1/2}$ = 27 Hz); 1.88 (s, 6H, $\nu_{1/2}$ = 17 Hz); –18.51 (s, 18H, $\nu_{1/2}$ = 277 Hz, NCH(C*H*$_3$)$_2$); –19.39 (s, 18H, $\nu_{1/2}$ = 290 Hz, NCH(C*H*$_3$)$_2$) ppm. μ_{eff} (Evans method, CD_2Cl_2, 298 K) 9.4 μ_B. Elemental analysis found (calc.) for **Fe$_3$**$^{i\text{Pr}}$ (Formula: $C_{90}H_{102}Co_6Fe_3N_6P_6Se_8$): Co 13.95 (13.57), Se 24.00 (24.24), P 6.49 (7.13).

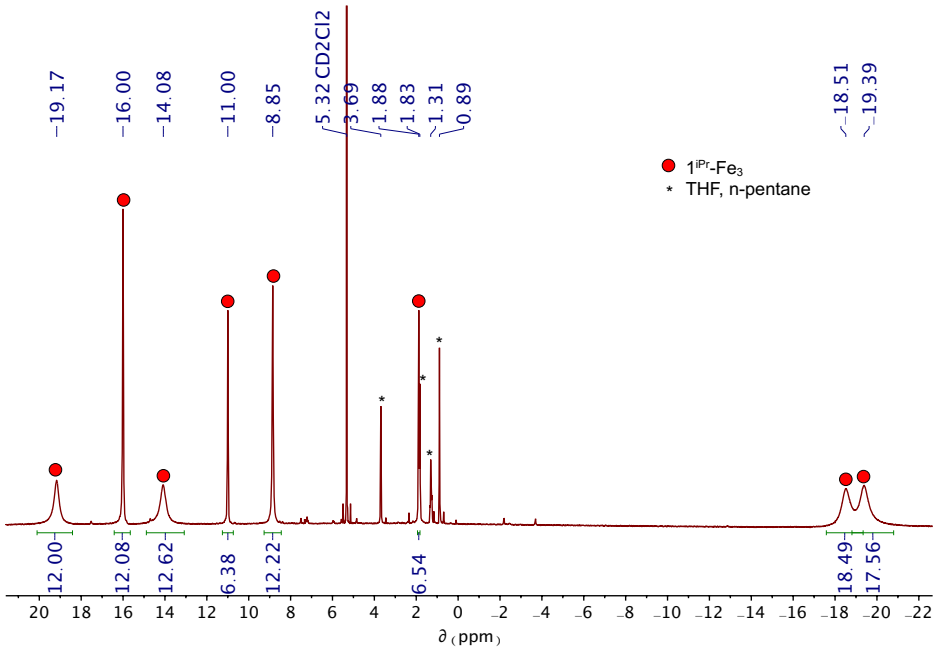


Figure 2.20. ^{1}H NMR (CD_2Cl_2, 25 °C, 500 MHz) spectrum of **Fe$_3$**$^{i\text{Pr}}$. Here, **Fe$_3$**$^{i\text{Pr}}$ is abbreviated as **1**$^{i\text{Pr}}$-Fe_3.

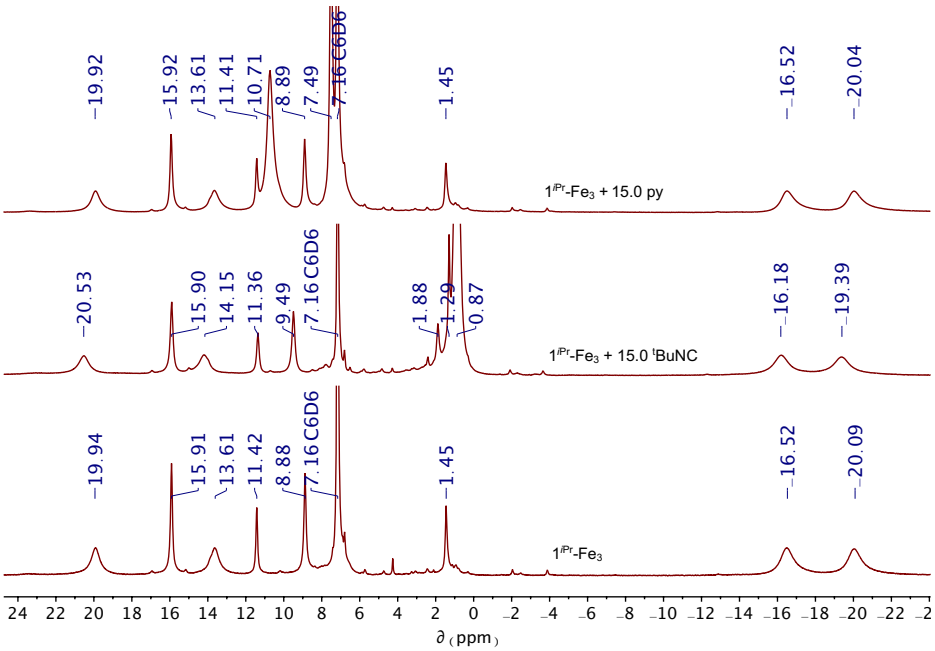


Figure 2.21. ^{1}H NMR (C_6D_6, 25 °C, 300 MHz) spectra **Fe$_3$**^{iPr} (0.012 M, 1 equiv) without ligand (bottom), and in the presence of either *tert*-butyl isocyanide (0.18 M, 15 equiv) or pyridine (0.18 M, 15 equiv). Here, **Fe$_3$**^{iPr} is abbreviated as **1**^{iPr}-Fe$_3$.

2.5.9 *Synthesis and Isolation of $Zn_3Co_6Se_8L^{iPr}{}_6$, **Zn$_3$**^{iPr}*

A 20 mL scintillation vial equipped with a magnetic stir bar was loaded with $Co_6Se_8L^{iPr,H}{}_6$ (0.200 g, 0.082 mmol, 1 equiv) and chlorobenzene (12 mL). The reaction mixture was heated at 130 °C in an aluminum heating block with vigorous stirring for 1h, until it became homogeneous. The solution was then cooled to room temperature and THF (1 mL) was added, and mixture was frozen in the glovebox cold well. Upon thawing, a solution of ^{n}BuLi (2.5 M in hexanes; 262 µL, 0.654 mmol, 8 equiv) was added dropwise. The mixture was allowed to warm to room temperature, and after 16 h of stirring it was cooled to –35 °C in the glovebox freezer. Solid $ZnCl_2$ (0.033 g, 0.245 mmol, 3 equiv) was added potion-wise to the cold, stirring solution, which was then allowed to warm up to room temperature, and stirred for an additional 4 h. Volatiles were removed *in vacuo*, and the crude solids were triturated with diethyl ether (3 x 5 mL), before extraction with *n*-pentane (3 x 5 mL), followed by extraction with toluene (3 x 3 mL). The toluene fraction was passed through a plug of Celite, and the resulting filtrate was concentrated to a volume of ~3 mL under reduced pressure, layered with *n*-pentane (15 mL) and kept still at 25 °C. After 48 h, a crop of dark red prismatic crystals were collected, and identified as **Zn$_3$**^{iPr} (0.167 g, 0.063 mmol, 77%).

UV-vis-*n*IR (toluene, 25 °C) λ: 397 (ϵ = 37120 M^{-1} cm^{-1}), 461 (ϵ = 29650 M^{-1} cm^{-1}), 546 (ϵ = 13210 M^{-1} cm^{-1}) nm. ^{1}H NMR (CD_2Cl_2, 500 MHz) δ: 7.43 (m, 24H, Ar*H*); 7.39 (t, 12H, 8.5 Hz, Ar*H*); 7.24 (t, 6H, 6.2 Hz, Ar*H*); 7.16 (t, 7.1 Hz, 24H, Ar*H*); 2.89 (m, 6H, NC*H*$(CH_3)_2$); 0.67 (d, 18H, 4.7 Hz, NCH(C*H*$_3)_2$); 0.64 (d, 18H, 4.7 Hz, NCH(C*H*$_3)_2$) ppm. ^{13}C NMR (CD_2Cl_2, 125 MHz) *δ*: 142.70 (d, $^{1}J_{PC}$ = 43.8 Hz, *i*-PPh_2); 132.67 (d, J_{PC} = 10.4 Hz, *o*-PPh_2); 132.58 (d, J_{PC} = 10.4 Hz, *o*-PPh_2); 128.74 (s, *p*-PPh_2); 128.7 (s, *p*-PPh_2); 127.46 (d, J_{PC} = 9.7 Hz, *m*-PPh_2); 126.85 (d, J_{PC} = 9.7 Hz, *m*-PPh_2); 51.45 (d, $^{2}J_{PC}$ = 12.5 Hz, N*C*H$(CH_3)_2$); 28.53 (d, J_{PC} = 6.5 Hz, NCH(*C*H$_3)_2$); 28.17 (d, J_{PC} = 4.6 Hz, NCH(*C*H$_3)_2$) ppm. ^{31}P NMR (C_6D_6, 283 MHz) δ: +90.6 ($\nu_{1/2}$ = 635 Hz) ppm. Elemental analysis found (calc.) for **Zn$_3^{i\text{Pr}}$** (Formula: $C_{90}H_{102}Co_6Zn_3N_6P_6Se_8$): Zn 7.68 (7.44), Co 13.21 (13.42), Se 23.19 (23.97), P 6.99 (7.05).

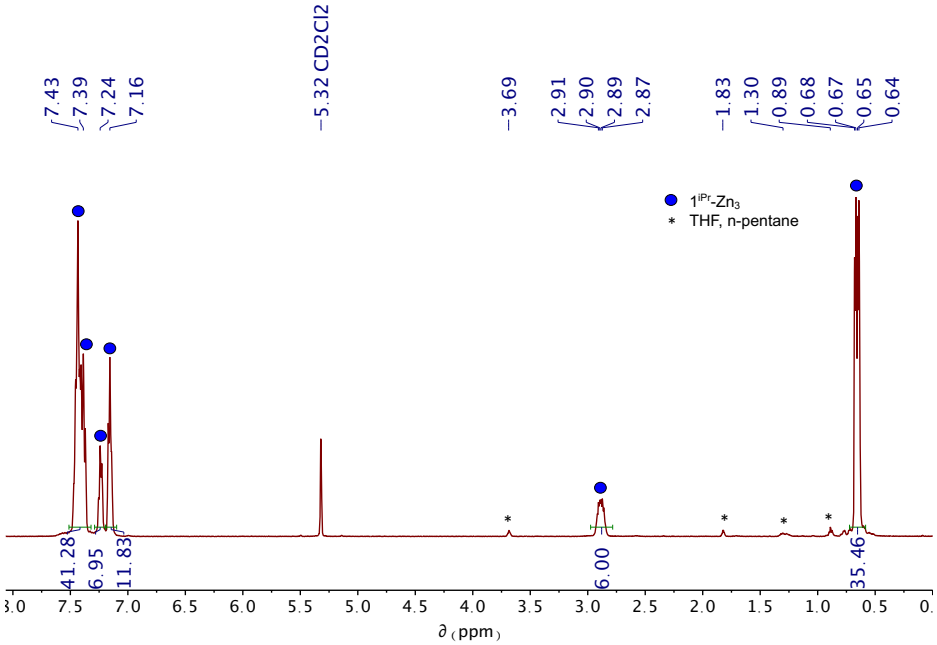


Figure 2.22. ^{1}H NMR (CD_2Cl_2, 25 °C, 500 MHz) spectrum of **Zn$_3^{i\text{Pr}}$**. Here, **Zn$_3^{i\text{Pr}}$** is abbreviated as **1**$^{i\text{Pr}}$-Zn_3.

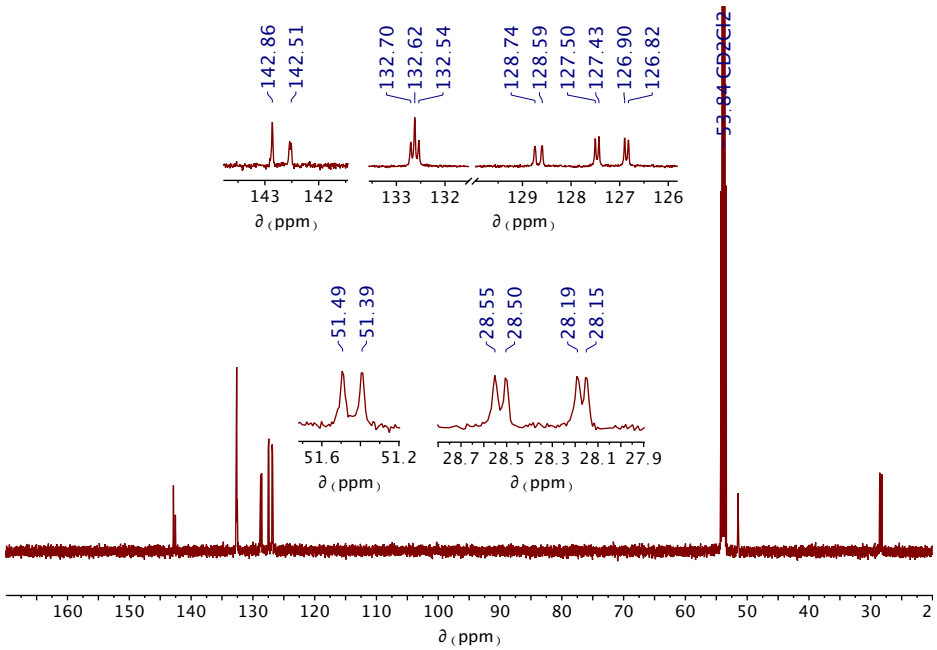


Figure 2.23. ^{13}C NMR (CD_2Cl_2, 25 °C, 125 MHz) spectrum of **Zn$_3$**$^{i\text{Pr}}$.

2.5.10 *Electronic Absorption Spectra*

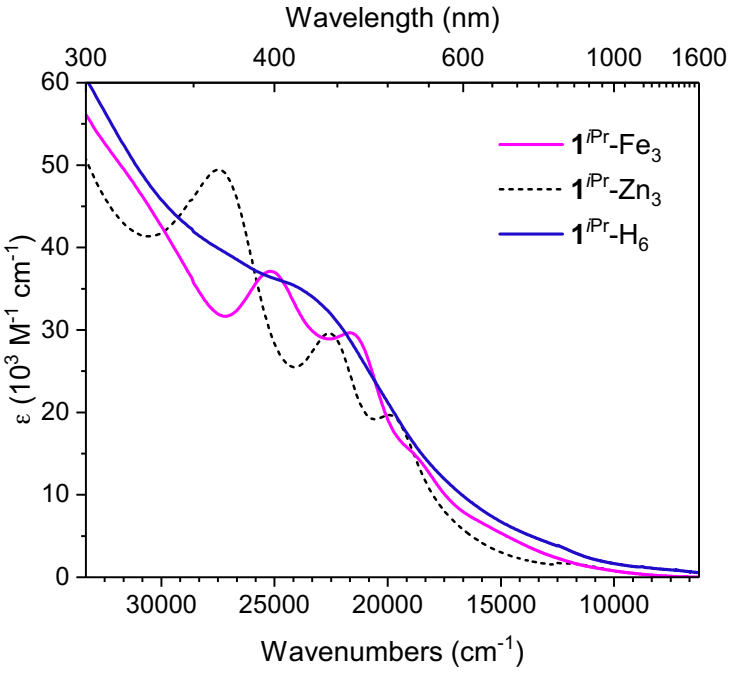


Figure 2.24. UV-vis-*n*IR spectra of **Fe$_3$**$^{i\text{Pr}}$, **Zn$_3$**$^{i\text{Pr}}$, and $Co_6Se_8L^{i\text{Pr,H}}_6$, recorded in toluene. Here, **Fe$_3$**$^{i\text{Pr}}$, **Zn$_3$**$^{i\text{Pr}}$, and $Co_6Se_8L^{i\text{Pr,H}}_6$ are abbreviated as **1**$^{i\text{Pr}}$-Fe$_3$, **1**$^{i\text{Pr}}$-Zn$_3$, and **1**$^{i\text{Pr}}$-H$_6$, respectively.

2.5.11 *Electrochemical Analysis*

Table 2.1. Half-wave potentials ($E_{1/2}$) and open circuit potentials (OCP) of **Zn$_3$**$^{i\text{Pr}}$ and **Fe$_3$**$^{i\text{Pr}}$ recorded in 0.1 M [^{n}Bu$_4$N][PF$_6$] THF or (DCM) at 50 mV/s.

redox couple (n_{red}/n_{ox})	$E_{1/2}$ (V vs $Fc^{0/+}$)	
	Zn$_3$ $^{i\text{Pr}}$	**Fe$_3$**$^{i\text{Pr}}$
–2/–1	–2.58	–2.34
–1/0	–1.93	–1.59 (–1.70)
0/+1	–0.55 (–0.65)	–0.58 (–0.78)
+1/+2	–0.06 (0.04)	–0.05 (–0.15)
+2/+3	0.34 (0.60)	(0.43)
OCP (V vs $Fc^{0/+}$)	–0.85 (–0.84)	–1.26 (–0.98)

2.5.12 *Effect of Reagent Stoichiometry in the Synthesis of $Co_6Se_8L^{iPr,H}{}_6$*

2.5.12.1 Treatment of $Co_2(CO)_8$ with Se=L$^{i\text{Pr,H}}$ (3:12 molar ratio)

Inside the glovebox, a 100 mL Schlenk flask equipped with a magnetic stir bar was charged with $Co_2(CO)_8$ (0.318 g, 0.92 mmol, 3 equiv). The flask was capped with a Suba Seal, moved to the Schlenk line and placed under a nitrogen flow before syringing in toluene (28 mL). In parallel, in the glovebox, a 20 mL scintillation vial was loaded with selenium (0.291 g, 3.7 mmol, 12 equiv), L$^{i\text{Pr,H}}$ (0.895 g, 3.7 mmol, 12 equiv) and toluene (12 mL). This mixture was stirred at 70 °C until it became homogeneous, cooled to room temperature, and transferred using a syringe to the Schlenk flask, promoting the rapid evolution of CO gas. The Schlenk flask was then immersed in a pre-heated oil bath (115 °C), and stirred for 24 h. Volatiles were removed under reduced pressure[1] and the crude solids were analyzed by ^{1}H NMR spectroscopy, which revealed the presence of a mixture of $Co_6Se_8L^{i\text{Pr,H}}{}_6$, $Co_4Se_2(CO)_6L^{i\text{Pr,H}}{}_4$, and $Co_6Se_8(CO)_xL^{i\text{Pr,H}}{}_{6-x}$. IR analysis reveals the presence of two broad features at 1966 and 1813 cm^{-1}, which we attribute to terminal and bridging CO groups, respectively.

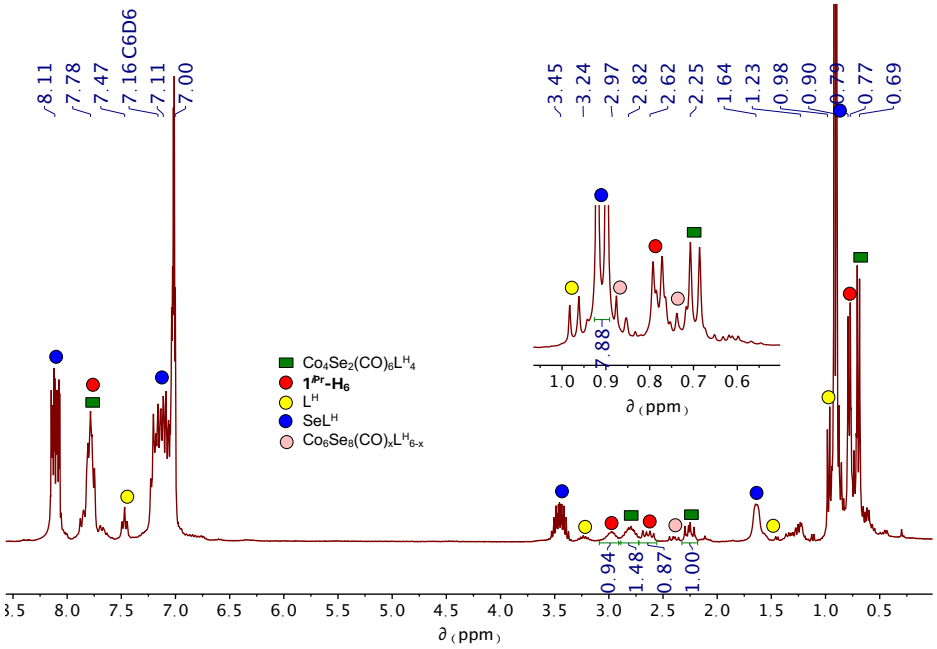


Figure 2.25. ^{1}H NMR (C_6D_6, 25 °C, 300 MHz) spectrum of the crude mixture obtained in the reaction of $Co_2(CO)_8$ (3 equiv) with Se=$L^{iPr,H}$ (12 equiv). Here, $Co_6Se_8L^{iPr,H}_6$ and $L^{iPr,H}$ are abbreviated as **1**$^{i\text{Pr}}$-H_6 and L^{H}, respectively.

2.5.12.2 Treatment of $Co_2(CO)_8$ with Se and $L^{iPr,H}$ (3:8:6 molar ratio)

A 25 mL Schlenk flask equipped with a small magnetic stir bar was charged with $Co_2(CO)_8$ (0.729 g, 2.13 mmol, 3 equiv), Se powder (0.449 g, 5.7 mmol, 8 equiv), and $L^{iPr,H}$ (1.04 g, 4.26 mmol, 6 equiv). Toluene (6 mL) was added to this mixture under a flow of nitrogen, via syringe injection. The mixture was heated to 115 °C, and stirred for 14 h. Volatiles were removed under reduced pressure and the crude mixture was analyzed by ^{1}H NMR spectroscopy, revealing the presence of $Co_6Se_8L^{iPr,H}_6$ with additional CH(C***H***$_3$)$_2$ and N***H*** resonances that we attribute to $Co_6Se_8(CO)_xL^{iPr,H}_{6-x}$. IR analysis of this mixture revealed a singular CO stretch at 1970 cm^{-1}.

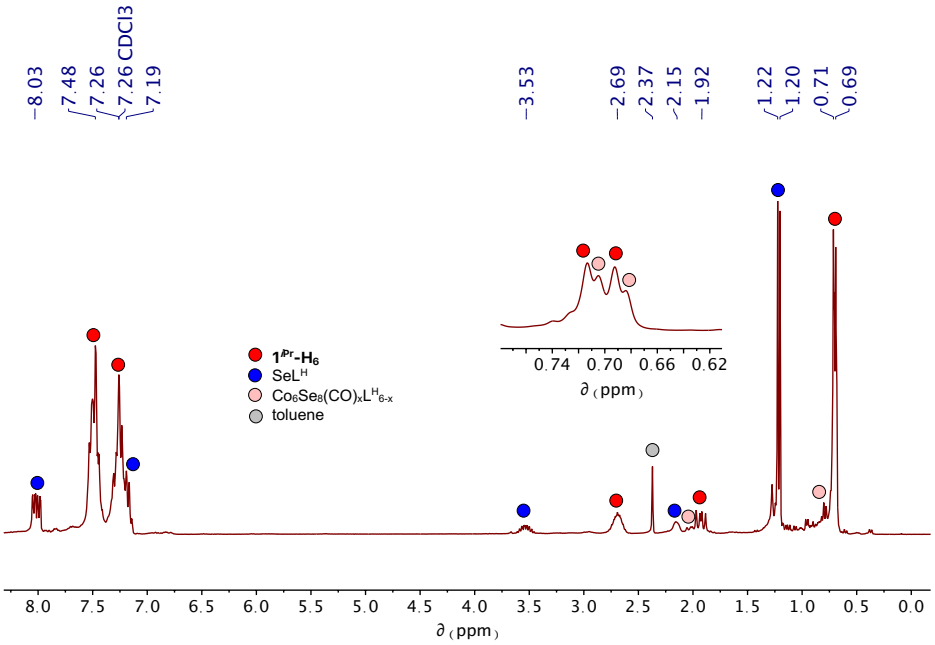


Figure 2.26. ^{1}H NMR ($CDCl_3$, 25 °C, 300 MHz) spectrum of the crude mixture obtained in the reaction of $Co_2(CO)_8$ (3 equiv) with Se (8 equiv) and $L^{iPr,H}$ (6 equiv). Here, $Co_6Se_8L^{iPr,H}_6$ and $L^{iPr,H}$ are abbreviated as $\mathbf{1}^{iPr}$-H_6 and L^{H}, respectively.

2.5.12.3 Treatment of $Co_2(CO)_8$ with Se and $L^{iPr,H}$ (3:8:12 molar ratio)

Inside the glovebox, a 100 mL Schlenk flask equipped with a magnetic stir bar was loaded with $Co_2(CO)_8$ (0.402 g, 1.18 mmol, 3 equiv). The flask was capped with a Suba-Seal septum, moved to the Schlenk line and placed under a nitrogen flow before syringing in toluene (28 mL). In parallel, in the glovebox, a 20 mL scintillation vial equipped with a magnetic stir bar was loaded with $L^{iPr,H}$ (1.145 g, 4.7 mmol, 12 equiv), selenium (0.248 g, 3.14 mmol, 8 equiv), and toluene (12 mL). This mixture was stirred until it became homogeneous (ca. 10 min), and transferred using a syringe to the Schlenk flask, promoting the rapid evolution of CO. The reaction flask was then transferred to a pre-heated oil bath (113 °C), and stirred for 16 h. Volatiles were removed under reduced pressure, and the crude solids were analyzed by ^{1}H NMR spectroscopy, which revealed the presence of $Co_4Se_2(CO)_6L^{iPr,H}_4$ and $Co_3Se(\mu_2\text{-}PPh_2)(CO)_4L^{iPr,H}_3$. IR analysis revealed the presence of broad terminal and bridging CO stretches located at 1932 cm^{-1} and 1770 cm^{-1}.

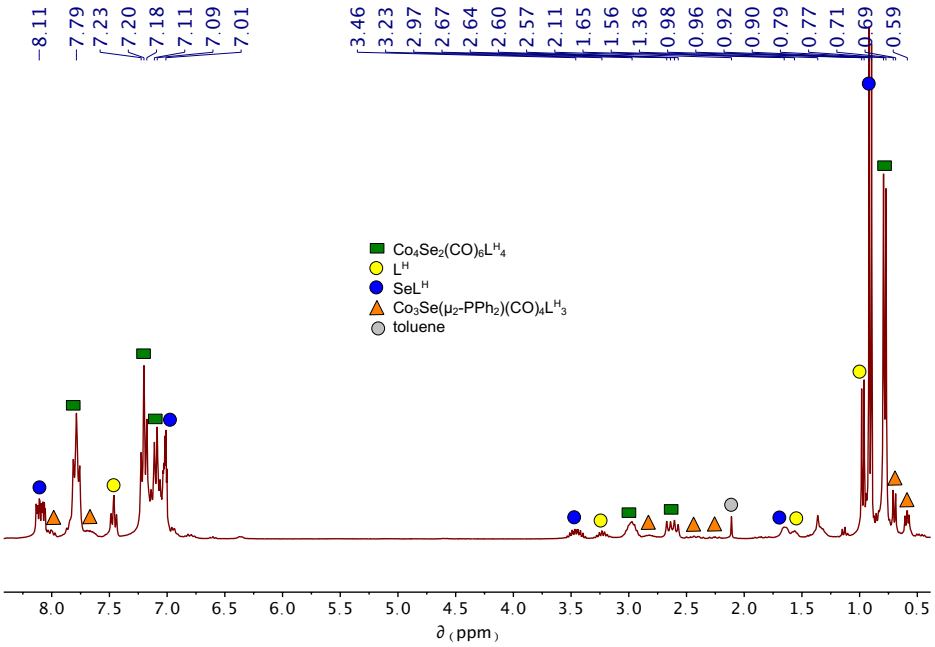


Figure 2.27. ^{1}H NMR (C_6D_6, 25 °C, 300 MHz) spectrum of the crude mixture obtained in the reaction of $Co_2(CO)_8$ (3 equiv) with Se (8 equiv) and $L^{iPr,H}$ (12 equiv). Here, $Co_6Se_8L^{iPr,H}_6$ and $L^{iPr,H}$ are abbreviated as $\mathbf{1}^{iPr}$-H_6 and L^{H}, respectively.

2.5.12.4 Treatment of $Co_2(CO)_8$ with Se and $L^{iPr,H}$ (3:10:15 molar ratio)

Inside the glovebox, a 25 mL Schlenk flask equipped with a magnetic stir bar was loaded with $Co_2(CO)_8$ (0.400 g, 1.18 mmol, 3 equiv). The flask was capped with a Suba-Seal septum, moved to the Schlenk line and placed under a nitrogen flow, before syringing in toluene (3 mL). In parallel, in the glovebox, a 20 mL scintillation vial was loaded with $L^{iPr,H}$ (1.435 g, 5.9 mmol, 15 equiv), Se (0.310 g, 3.9 mmol, 10 equiv), and toluene (5 mL). This mixture was stirred until it became homogeneous (ca. 10 min), and transferred using a syringe to the Schlenk flask, promoting the rapid evolution of CO. The reaction flask was then transferred to a pre-heated oil bath (113 °C), and stirred for 24 h. Volatiles were removed under reduced pressure and the crude solids were analyzed by ^{1}H NMR spectroscopy, revealing a mixture of $Co_3Se(\mu_2\text{-}PPh_2)(CO)_4L^{iPr,H}_3$ and $Co_4Se_2(CO)_6L^{iPr,H}_4$.

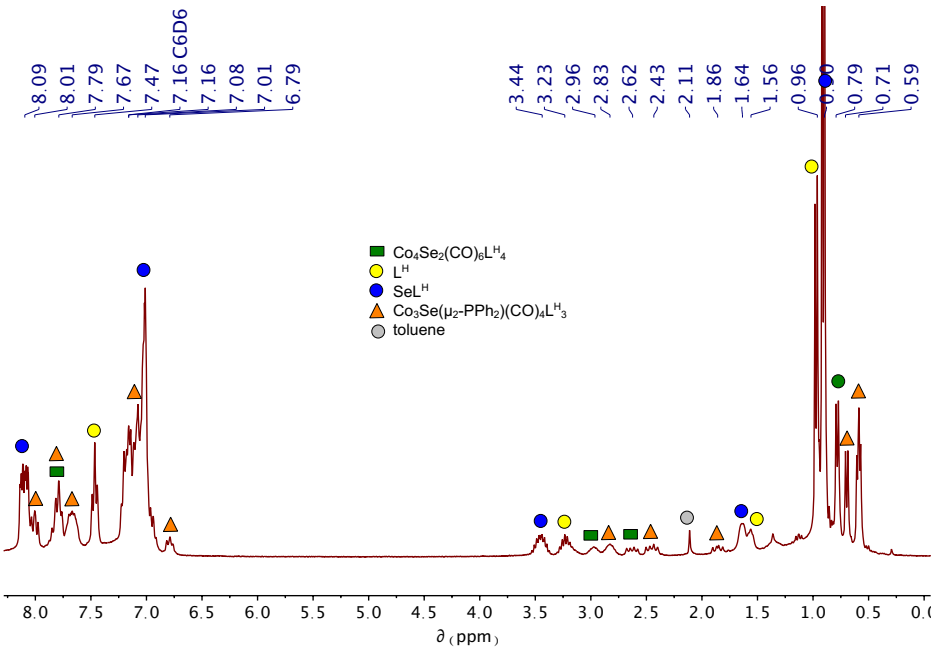


Figure 2.28. ^{1}H NMR (C_6D_6, 25 °C, 300 MHz) spectrum of the crude reaction mixture obtained in the reaction of $Co_2(CO)_8$ (3 equiv) with Se (10 equiv) and $L^{i\mathrm{Pr,H}}$ (15 equiv). Here, $Co_6Se_8L^{i\mathrm{Pr,H}}{}_6$ and $L^{i\mathrm{Pr,H}}$ are abbreviated as $\mathbf{1}^{i\mathrm{Pr}}$-$H_6$ and L^{H}, respectively.

2.5.13 *X-ray Structure Determination*

Single crystals suitable for X-ray analysis, grown according to methods detailed below, were coated in deoxygenated paratone oil and mounted on a 20 µm CryoLoop™ (Hampton Research, 18 mm mount, 0.2 to 0.3 mm loop diameter). Data was collected at –173 °C on a Bruker APEX II single crystal X-ray diffractometer, with a Mo source. Data was integrated and scaled using SAINT, SADABS within the APEX2 software package by Bruker.[50] Solution by direct methods (SHELXT[51] or SIR97[52,53]) produced a complete heavy atom phasing model consistent with the proposed structure. Structures were completed by difference Fourier synthesis with SHELXL.[54–56] Scattering factors are from Waasmair and Kirfel. [57] Hydrogen atoms were placed in geometrically idealized positions and constrained to ride on their parent atoms with C–H distances in the range 0.95–1.00 Å. Isotropic thermal parameters U_{eq} were fixed such that they were 1.2U_{eq} of their parent atom Ueq for CHs and 1.5U_{eq} of their parent atom U_{eq} in case of methyl groups. All non-hydrogen atoms were refined anisotropically by full-matrix least-squares.

2.5.13.1 $Co_6Se_8L^{iPr,H}{}_6$

Dark red prismatic crystals of $Co_6Se_8L^{iPr,H}{}_6$ suitable for single crystal X-ray diffraction analysis were grown via vapor diffusion of *n*-pentane into a saturated solution of the cluster in toluene at 25 °C over the course of 24 h. The compound crystallizes in the trigonal space group $R\bar{3}$, and the asymmetric unit features a single cluster molecule. The refinement was routine. Interestingly, in the solid state, the cluster assembles into an 3D octahedral network due to π-π stacking between the PPh_2 groups of neighboring clusters.

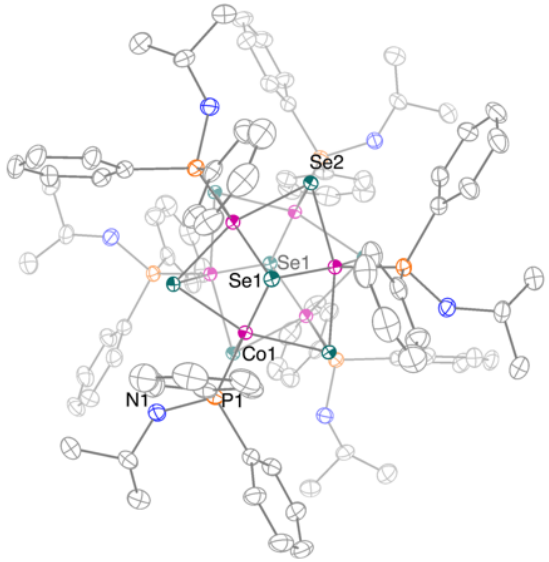


Figure 2.29. Solid-state structure of $Co_6Se_8L^{iPr,H}{}_6$. Thermal ellipsoids displayed at a 50% probability level. All hydrogen atoms are omitted for clarity. Selected interatomic distances (Å): Co1-Se1 2.3334(5), Co1-Se2 2.3448(5); Co1…Co1 2.9390(5); Se1…Se1 5.5081(9), Se2…Se2 5.6655(7); Co1…P1 2.1354(9).

2.5.13.2 $[Co_6Se_8L^{iPr,H}{}_6][PF_6]$

Dark red prismatic crystals of $[Co_6Se_8L^{iPr,H}{}_6][PF_6]$ suitable quality for single crystal X-ray diffraction analysis were grown from a concentrated solution of the cluster THF that was layered with diethyl ether and stored at –35 °C for 16 h. The compound crystallizes in triclinic $P\bar{1}$ with the asymmetric unit containing a singular cluster molecule and one $[PF_6]^-$ counterion. The $[PF_6]^-$ counterion exhibits rotational disorder. Inversion symmetry relates one half of the cluster and the $[PF_6]^-$ counterion.

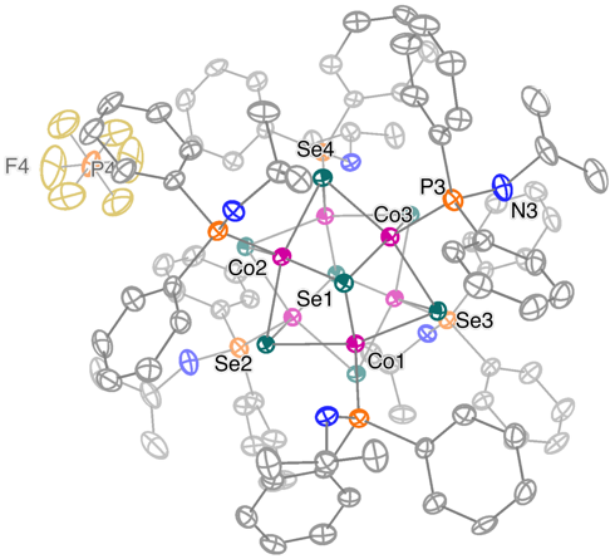


Figure 2.30. Molecular structure of $[Co_6Se_8L^{iPr,H}_6][PF_6]$ with thermal ellipsoids shown at a 50% probability level. All hydrogen atoms and disorder in the $[PF_6]^-$ counterion are omitted for clarity. Selected interatomic distances (Å): Co1-Se1 2.349(2), Co1-Se3 2.343(8), Co1-Se2 2.343(4), Co1-Se4 2.336(2); Se1…Se1 5.633(3), Se2…Se2 5.53(2), Se3…Se3 5.657(5), Se4…Se4 5.710(3); Co3-P3 2.163(4).

2.5.13.3 **Co_4Se_2**

Dark green prismatic crystals of **Co_4Se_2**, suitable for single crystal X-ray diffraction analysis, were grown via vapor diffusion of *n*-pentane into a saturated solution of the cluster in THF at 25 °C over the course of 24 h. The compound crystallizes in the monoclinic space group C2/c, and the asymmetric unit contains a singular cluster molecule. The refinement was routine. The cluster contains a two-fold rotational symmetry axis that passes through the bridging μ_2-CO ligands C32-O2 and C34-O4.

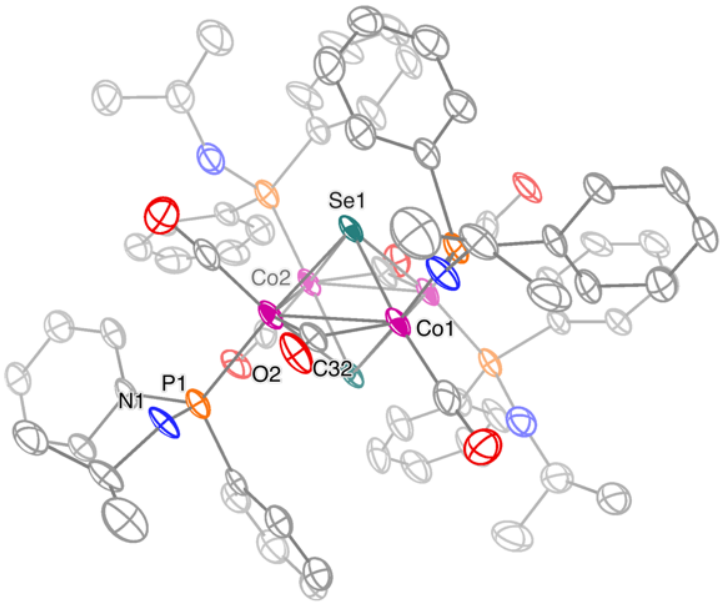


Figure 2.31. Molecular structure of **Co_4Se_2** with thermal ellipsoids shown at a 50% probability level. All hydrogen atoms are omitted for clarity. Selected interatomic distances (Å): Co1-Co1 2.54(1), Co1-Co2 2.746(1), Co2-Co2 2.51(1); Co1-Se1 2.387(5), Co2-Se1 2.361(5).

2.5.13.4 **Co_3Se**

Red needle-like crystals of **Co_3Se**, suitable for single crystal X-ray diffraction analysis, were grown via vapor diffusion of diethyl ether into a saturated solution of the cluster in THF at 25 °C over the course of 24 h. The compound crystallizes in the triclinic space group $P\bar{1}$, and the asymmetric unit contains a single cluster molecule and one diethyl ether molecule. The refinement was routine.

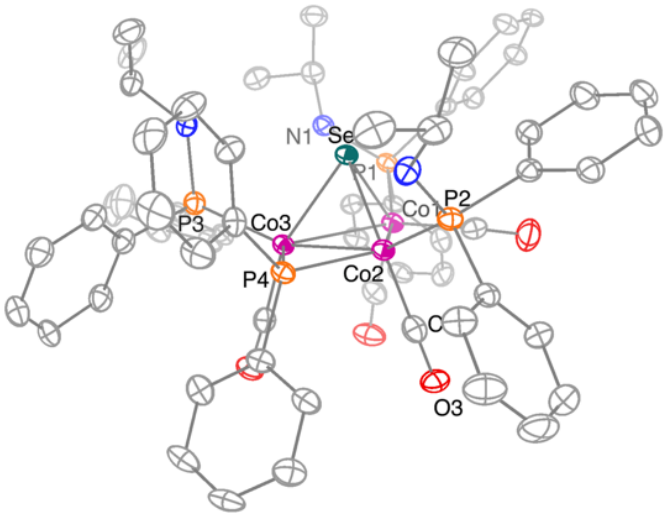


Figure 2.32. Molecular structure of **Co_3Se** with thermal ellipsoids shown at a 50% probability level. All hydrogen atoms and a co-crystallizing solvent molecule are omitted for clarity. Selected interatomic distances (Å): Co1-Co2 2.57(2), Co1-Co3 2.62(1), Co2-Co3 2.47(1); Co1-Se1 2.29(1), Co2-Se1 2.30(2), Co3-Se1 2.314(9); Co2-P4 2.179(9), Co3-P4 2.19(1); Co1-P1 2.20(1), Co2-P2 2.173(4), Co3-P3 2.17(1).

2.5.13.5 **Co_2**

Red prismatic crystals of **Co_2**, suitable for single crystal X-ray diffraction analysis, were grown from a saturated solution of the dimer in diethyl ether at –35 °C over the course of 48 h. The compound crystallizes in the cubic space group $Pa\bar{3}$ with one half of the dimer contained within the asymmetric unit. The dimer exhibits three-fold rotational disorder, and as a result all of the ligand substituents were modeled over three positions. One half of the dimer is related to the other via inversion. As such, restraints were placed on some distances and displacement parameters during refinement in order to produce a stable model.

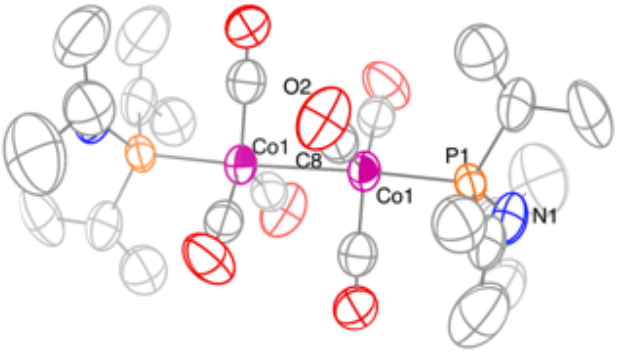


Figure 2.33. Solid-state structure of **Co$_2$** with thermal ellipsoids shown at a 50% probability level. All hydrogen atoms and three-fold rotational disorder have been omitted for clarity. Selected interatomic distances (Å): Co1-Co1 2.6731(6); Co1-P1 2.19(1); P1-N1 1.47(2).

2.5.13.6 **Fe$_3$**$^{i\text{Pr}}$

Dark red prismatic crystals of **Fe$_3$**$^{i\text{Pr}}$, suitable for single crystal X-ray diffraction analysis, were grown via vapor diffusion of *n*-pentane into a saturated solution of the cluster in toluene at 25 °C over the course of 4 days. The compound crystallizes in the monoclinic space group P 2_1/c, and the asymmetric unit contains a single cluster molecule in addition to three disordered toluene molecules and one disordered *n*-pentane molecule, all of which were modeled over two positions. Fe1 refines freely at 94%, Fe3 refines freely at 95%, and Fe2 to only 90%, ostensibly due to co-crystallization of trace protonated cluster, $Co_6Se_8L^{i\text{Pr,H}}_6$. The population of the protonated species was insufficient to produce a chemical disorder model based on percent occupancies. Accordingly, the Fe atom thermal displacement parameters were slightly higher than those observed for neighboring atoms (e.g. Co or Se), however, there is no evidence that any element other than Fe is present at the three edge sites.

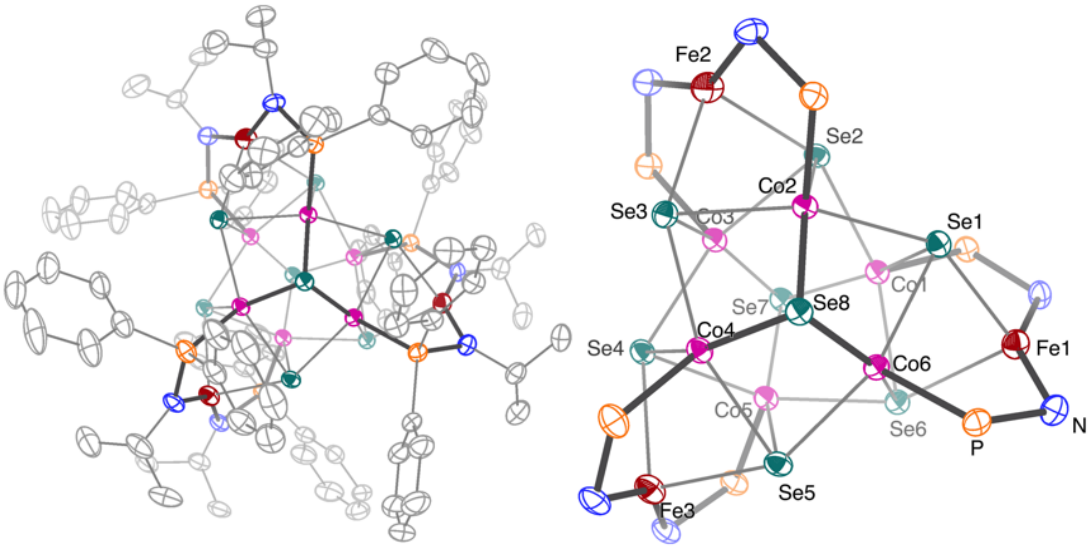


Figure 2.34. Molecular structure of **Fe$_3$**$^{i\text{Pr}}$ with thermal ellipsoids shown at a 50% probability level. All hydrogen atoms and co-crystallizing solvent molecules are omitted for clarity. Selected interatomic distances (Å): Fe1-Se1 2.5360(2), Fe1-Se6 2.492(2), Fe2-Se2 2.5193(5), Fe2-Se3 2.5304(9), Fe3-Se4 2.534(2), Fe3-Se5 2.519(2); Fe1…Co1 2.885(1), Fe1…Co6 2.831(2); Co1…Co6 2.780(5), Co1…Co2 2.959(1), Co1…Co3 2.989(2); Se7…Se8 5.412(8), Se1…Se4 5.800(6), Se2…Se5 5.756(3), Se3…Se6 5.7607(7).

2.5.13.7 **Zn$_3$**$^{i\text{Pr}}$

Dark red prismatic crystals of **Zn$_3$**$^{i\text{Pr}}$, suitable for single crystal X-ray diffraction analysis, were grown from a concentrated toluene solution that was layered with *n*-pentane and kept still for 48 h. The compound crystallizes in the monoclinic space group, Pn, and the asymmetric unit contains two full cluster molecules with minor structural differences. The structure exhibits chemical disorder with non-stoichiometric occupancy of Zn at the edge metal sites. Specifically, the refinement was stabilized considering 88% occupancy of **Zn$_3$**$^{i\text{Pr}}$ co-crystallized with 12% $Co_6Se_8L^{i\text{Pr,H}}{}_6$, of just enough abundance to develop a complete chemical disorder model. In the protonated form, the aminophosphine ligands exhibit the same orientation as those that are bound to zinc, causing no positional disorder in the ligand framework.

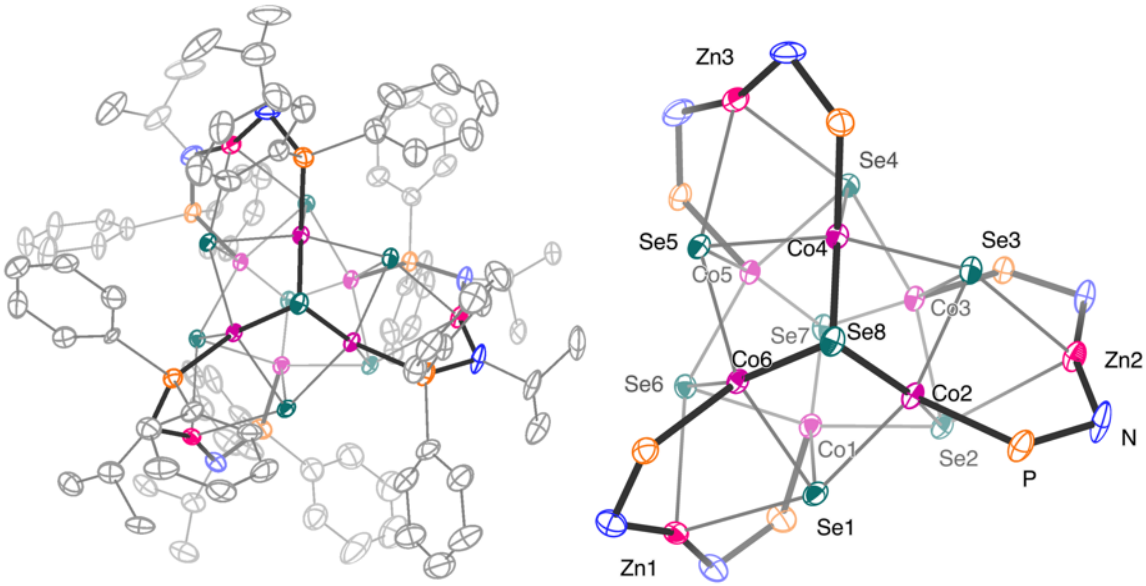


Figure 2.35. Molecular structure of **Zn$_3$**$^{i\text{Pr}}$ with thermal ellipsoids shown at a 50% probability level. All co-crystallizing solvent molecules and disorder have been omitted for clarity. Selected interatomic distances (Å): Zn1-Se1 2.711(2), Zn1-Se6 2.660(5), Zn2-Se2 2.733(2), Zn2-Se3 2.658(2), Zn3-Se4 2.648(2), Zn3-Se5 2.780(4); Co1…Co6 2.910(4), Co1…Co2 3.036(2), Co1…Co3 2.949(2); Se7…Se8 5.613(3), Se1…Se4 5.642(9), Se2…Se5 5.685(2), Se3…Se6 5.671(3).

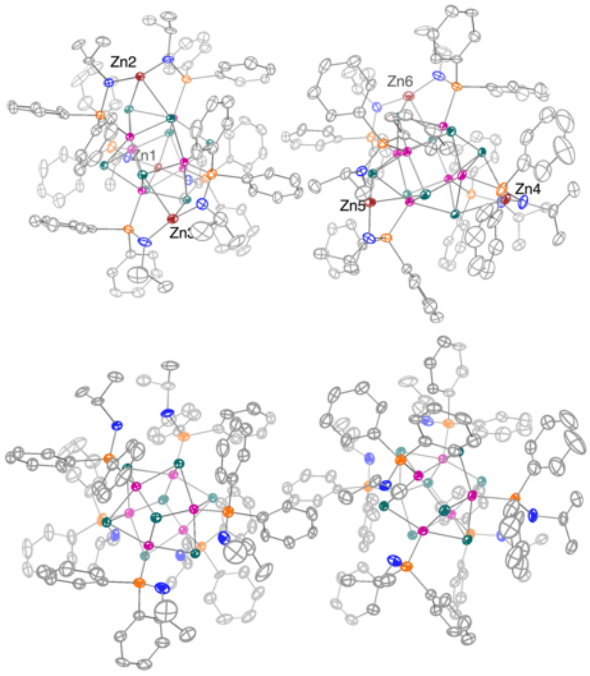


Figure 2.36. (top) The major component of the asymmetric unit consisting of a racemic pair of **Zn$_3$**$^{i\text{Pr}}$ clusters with Zn(II) ions occupying each of the metal binding edge sites. (bottom) The minor component of the asymmetric unit, consisting of two molecules of $Co_6Se_8L^{i\text{Pr,H}}{}_6$. All hydrogen atoms omitted for clarity. Thermal ellipsoids plotted at a 50% probability level.

2.5.14 *X-ray Tables*

Table 2.2. Crystallographic information for $Co_6Se_8L^{iPr,H}_6$, $[Co_6Se_8L^{iPr,H}_6][PF_6]$.

Compound	$Co_6Se_8L^{iPr,H}_6$	$[Co_6Se_8L^{iPr,H}_6][PF_6]$
Empirical formula	$C_{90}H_{108}Co_6N_6P_6Se_8$	$C_{90}H_{108}Co_6F_6N_6P_7Se_8$
CCDC Number	2014424	2014429
Formula weight	2444.90	2589.87
Temperature (K)	100(2)	100(2)
Wavelength (Å)	0.71073	0.71073
Crystal system	Trigonal	Triclinic
Space group	$R\bar{3}$	$P\bar{1}$
a (Å)	21.5360(10)	14.2628(8)
b (Å)	21.5360(10)	14.2802(9)
c (Å)	17.0203(17)	15.0757(9)
α (°)	90	112.912(3)
β (°)	90	112.532(3)
γ (°)	120	99.092(3)
Volume (Å^3)	6836.4(9)	2436.1(3)
Z	3	1
ρ^{calc} (g cm^{-1})	1.782	1.765
Absorption coefficient (mm^{-1})	4.415	4.160
F(000)	3642	1283
Crystal size (mm^3)	0.350 x 0.180 x 0.150	0.160 x 0.130 x 0.070
Theta range for data collection (°)	1.620 to 28.386	1.658 to 28.340
Index ranges	$-28\leq h\leq 28$, $-28\leq k\leq 28$, $-22\leq l\leq 22$	$-19\leq h\leq 19$, $-18\leq k\leq 19$, $-20\leq l\leq 20$
Reflections collected	22311	23511
Independent reflections	3814 [R(int) = 0.0859]	12050 [R(int) = 0.0447]
Completeness to theta = 25.000°	99.9%	99.8%
Data / restraints / parameters	3814 / 0 / 177	12050 / 0 / 581
Goodness-of-fit on F^2	1.068	0.993
Final R indices [I>2sigma(I)]	R1 = 0.0294, wR2 = 0.0564	R1 = 0.0410, wR2 = 0.0786
R indices (all data)	R1 = 0.0577, wR2 = 0.0675	R1 = 0.0713, wR2 = 0.0861
Largest diff. peak and hole (e$^-$Å^{-3})	0.668 and –0.546	0.702 and –0.793

Table 2.3. Crystallographic information for **Co_4Se_2**, **Co_3Se**, and **Co_2**.

Compound	Co_4Se_2	Co_3Se	Co_2
Empirical formula	$C_{66}H_{72}Co_4N_4O_6P_4Se_2$	$C_{65}H_{74}Co_3N_3O_5P_4Se$	$C_{12}H_{22}CoNO_3P$
CCDC Number	2014423	2014425	2014422
Formula weight	1534.79	1356.90	318.20
Temperature (K)	100(2)	100(2)	100(2)
Wavelength (Å)	0.71073	0.71073	0.71073
Crystal system	Monoclinic	Triclinic	Cubic
Space group	C 2/c	$P\bar{1}$	$Pa\bar{3}$
a (Å)	22.463(3)	10.968(2)	14.6369(9)
b (Å)	16.532(3)	11.693(3)	14.6369(9)
c (Å)	19.790(3)	25.670(5)	14.6369(9)
α (°)	90	3183.7(11)	90
β (°)	96.43(1)	85.582(11)	90
γ (°)	90	78.460(11)	90
Volume ($Å^3$)	7302.9(19)	81.148(11)	3135.8(6)
Z	4	2	8
ρ^{calc} (g cm^{-1})	1.396	1.415	1.348
Absorption coefficient (mm^{-1})	2.025	1.495	1.196
F(000)	3120	1400	1336
Crystal size (mm^3)	0.160 x 0.120 x 0.100	0.280 x 0.120 x 0.100	0.070 x 0.050 x 0.040
Theta range for data collection (°)	1.533 to 26.483	1.621 to 26.890	2.410 to 28.328
Index ranges	$-28\leq h\leq 27$, $-20\leq k\leq 20$, $-24\leq l\leq 24$	$-13\leq h\leq 13$, $-14\leq k\leq 14$, $-32\leq l\leq 31$	$-13\leq h\leq 13$, $-13\leq k\leq 13$, $-19\leq l\leq 19$
Reflections collected	14728	93316	2470
Independent reflections	7522 [R(int) = 0.0932]	13254 [R(int) = 0.1055]	1306 [R(int) = 0.0539]
Completeness to theta = 25.000°	100.0%	99.7%	98.9%
Data / restraints / parameters	7522 / 18 / 394	13254 / 0 / 738	1306 / 95 / 139
Goodness-of-fit on F^2	0.963	1.012	1.014
Final R indices [I>2sigma(I)]	R1 = 0.0595, wR2 = 0.1402	R1 = 0.0475, wR2 = 0.0940	R1 = 0.0414, wR2 = 0.0983
R indices (all data)	R1 = 0.1276, wR2 = 0.1756	R1 = 0.0896, wR2 = 0.1097	R1 = 0.1349, wR2 = 0.1479
Largest diff. peak and hole ($e^-Å^{-3}$)	2.243 and –1.275	0.732 and –0.875	0.341 and –0.260

Table 2.4. Crystallographic information for **Fe$_3$**$^{i\text{Pr}}$, **Zn$_3$**$^{i\text{Pr}}$.

Compound	**Fe$_3$**$^{i\text{Pr}}$	**Zn$_3$**$^{i\text{Pr}}$
Empirical formula	$C_{105.75}H_{125.50}Co_6Fe_3N_6P_6Se_8$	$C_{90}H_{102.68}Co_6N_6P_6Se_8Zn_{2.66}$
CCDC Number	2014426	2014427
Formula weight	2819.27	2613.58
Temperature (K)	100(2)	100(2)
Wavelength (Å)	0.71073	0.71073
Crystal system	Monoclinic	Monoclinic
Space group	P 2_1/c	Pn
a (Å)	29.1239(18)	18.8172(15)
b (Å)	14.1669(10)	22.3972(16)
c (Å)	26.9352(18)	25.035(2)
α (°)	90	90
β (°)	102.301(3)	92.286(4)
γ (°)	90	90
Volume (Å^3)	10858.2(13)	10542.8(14)
Z	4	4
ρ^{calc} (g cm^{-1})	1.725	1.647
Absorption coefficient (mm^{-1})	4.099	4.409
F(000)	5616	5154
Crystal size (mm^3)	0.140 x 0.130 x 0.100	0.150 x 0.100 x 0.100
Theta range for data collection (°)	1.431 to 28.343	1.329 to 28.328
Index ranges	$-38\leq h\leq 38$, $-18\leq k\leq 18$, $-35\leq l\leq 35$	$-25\leq h\leq 25$, $-29\leq k\leq 29$, $-33\leq l\leq 33$
Reflections collected	52954	51744
Independent reflections	27038 [R(int) = 0.0622]	51716 [R(int) = 0.0083]
Completeness to theta = 25.000°	100.0%	99.9%
Data / restraints / parameters	27038 / 56 / 1235	51716 / 163 / 2168
Goodness-of-fit on F^2	1.002	1.018
Final R indices [I>2sigma(I)]	R1 = 0.0416, wR2 = 0.0817	R1 = 0.0379, wR2 = 0.0703
R indices (all data)	R1 = 0.0948, wR2 = 0.0981	R1 = 0.0656, wR2 = 0.0786
Largest diff. peak and hole (e$^-$Å^{-3})	1.107 and –1.471	0.758 and –0.620

2.6 REFERENCES

(1) *Biological Inorganic Chemistry: Structure and Reactivity*; Bertini, I., Ed.; University Science Books: Sausalito, Calif, 2007.

(2) Cox, N.; Retegan, M.; Neese, F.; Pantazis, D. A.; Boussac, A.; Lubitz, W. Electronic Structure of the Oxygen-Evolving Complex in Photosystem II Prior to O-O Bond Formation. *Science* **2014**, *345* (6198), 804–808. https://doi.org/10.1126/science.1254910.

(3) Bullock, R. M.; Chen, J. G.; Gagliardi, L.; Chirik, P. J.; Farha, O. K.; Hendon, C. H.; Jones, C. W.; Keith, J. A.; Klosin, J.; Minteer, S. D.; Morris, R. H.; Radosevich, A. T.; Rauchfuss, T. B.; Strotman, N. A.; Vojvodic, A.; Ward, T. R.; Yang, J. Y.; Surendranath, Y. Using Nature's Blueprint to Expand Catalysis with Earth-Abundant Metals. *Science* **2020**, *369* (6505), eabc3183. https://doi.org/10.1126/science.abc3183.

(4) Coucouvanis, D.; Mosier, P. E.; Demadis, K. D.; Patton, S.; Malinak, S. M.; Kim, C. G.; Tyson, M. A. The Catalytic Reduction of Hydrazine to Ammonia by the $MoFe_3S_4$ Cubanes and Implications Regarding the Function of Nitrogenase. Evidence for Direct Involvement of the Molybdenum Atom in Substrate Reduction. *J. Am. Chem. Soc.* **1993**, *115* (25), 12193–12194. https://doi.org/10.1021/ja00078a079.

(5) Li, F.; L. Meyer, R.; H. Carpenter, S.; E. VanGelder, L.; W. Nichols, A.; W. Machan, C.; L. Neidig, M.; M. Matson, E. Nitric Oxide Activation Facilitated by Cooperative Multimetallic Electron Transfer within an Iron-Functionalized Polyoxovanadate–Alkoxide Cluster. *Chemical Science* **2018**, *9* (30), 6379–6389. https://doi.org/10.1039/C8SC00987B.

(6) de Ruiter, G.; Carsch, K. M.; Gul, S.; Chatterjee, R.; Thompson, N. B.; Takase, M. K.; Yano, J.; Agapie, T. Accelerated Oxygen Atom Transfer and C−H Bond Oxygenation by Remote Redox Changes in Fe_3 Mn-Iodosobenzene Adducts. *Angew. Chem.* **2017**, *129* (17), 4850–4854. https://doi.org/10.1002/ange.201701319.

(7) Nguyen, A. I.; Darago, L. E.; Balcells, D.; Tilley, T. D. Influence of a "Dangling" Co(II) Ion Bound to a $[MnCo_3O_4]$ Oxo Cubane. *J. Am. Chem. Soc.* **2018**, *140* (29), 9030–9033. https://doi.org/10.1021/jacs.8b04065.

(8) Kanady, J. S.; Lin, P.-H.; Carsch, K. M.; Nielsen, R. J.; Takase, M. K.; Goddard, W. A.; Agapie, T. Toward Models for the Full Oxygen-Evolving Complex of Photosystem II by Ligand Coordination To Lower the Symmetry of the Mn_3CaO_4 Cubane: Demonstration That Electronic Effects Facilitate Binding of a Fifth Metal. *J. Am. Chem. Soc.* **2014**, *136* (41), 14373–14376. https://doi.org/10.1021/ja508160x.

(9) Mukherjee, S.; Stull, J. A.; Yano, J.; Stamatatos, T. C.; Pringouri, K.; Stich, T. A.; Abboud, K. A.; Britt, R. D.; Yachandra, V. K.; Christou, G. Synthetic Model of the Asymmetric $[Mn_3CaO_4]$ Cubane Core of the Oxygen-Evolving Complex of Photosystem II. *Proceedings of the National Academy of Sciences* **2012**, *109* (7), 2257–2262. https://doi.org/10.1073/pnas.1115290109.

(10) Zhang, C.; Chen, C.; Dong, H.; Shen, J.-R.; Dau, H.; Zhao, J. A Synthetic Mn4Ca-Cluster Mimicking the Oxygen-Evolving Center of Photosynthesis. *Science* **2015**, *348* (6235), 690–693. https://doi.org/10.1126/science.aaa6550.

(11) Kephart, J. A.; Mitchell, B. S.; Chirila, A.; Anderton, K. J.; Rogers, D.; Kaminsky, W.; Velian, A. Atomically Defined Nano-Propeller $Fe_3Co_6Se_8(Ph_2PNTol)_6$: Functional Model for the Electronic Metal-Support Interaction Effect, and High Catalytic Activity for Carbodiimide Formation. *J. Am. Chem. Soc.* **2019**, *141* (50), 19605–19610. https://doi.org/10.1021/jacs.9b12473.

(12) Kephart, J. A.; Romero, C. G.; Tseng, C.-C.; Anderton, K. J.; Yankowitz, M.; Kaminsky, W.; Velian, A. Hierarchical Nanosheets Built from Superatomic Clusters: Properties, Exfoliation and Single-Crystal-to-Single-Crystal Intercalation. *Chem. Sci.* **2020**, *11* (39), 10744–10751. https://doi.org/10.1039/D0SC03506H.

(13) Greenwood, B. P.; Forman, S. I.; Rowe, G. T.; Chen, C.-H.; Foxman, B. M.; Thomas, C. M. Multielectron Redox Activity Facilitated by Metal-Metal Interactions in Early/Late Heterobimetallics: Co/Zr Complexes Supported by Phosphinoamide Ligands. *Inorg. Chem* **2009**, *48*, 6251–6260. https://doi.org/10.1021/ic900552b.

(14) Tolman, C. A. Steric Effects of Phosphorus Ligands in Organometallic Chemistry and Homogeneous Catalysis. *Chem. Rev.* **1977**, *77* (3), 313–348. https://doi.org/10.1021/cr60307a002.

(15) Falivene, L.; Cao, Z.; Petta, A.; Serra, L.; Poater, A.; Oliva, R.; Scarano, V.; Cavallo, L. Towards the Online Computer-Aided Design of Catalytic Pockets. *Nat. Chem.* **2019**, *11* (10), 872–879. https://doi.org/10.1038/s41557-019-0319-5.

(16) Fenske, D.; Hachgenei, J.; Ohmer, J. Novel Cobalt- and Nickel-Clusters with S and PPh3 as Ligands; Crystal Structures of $[Co_7S_6(PPh_3)_5Cl_2]$, $[Co_6S_8(PPh_3)_6]^+[CoCl_3(THF)]^-$, $[Ni_8S_6Cl_2(PPh_3)_6]$, and $[Ni_8S_5(PPh_3)_7]$. *Angew. Chem. Int. Ed.* **1985**, *24* (8), 706–709. https://doi.org/10.1002/anie.198507061.

(17) Fenske, D.; Ohmer, J.; Hachgenei, J. New Co and Ni Clusters with Se and PPh3 as Ligands:$[Co_4(\mu_3\text{-}Se)_4(PPh_3)_4]$,$[Co_6(\mu_3\text{-}Se)_8(PPh_3)_6]$,$[Co_9(\mu_4\text{-}Se)_3(\mu_3\text{-}Se)_8(PPh_3)_6]$, and $[Ni_{34}(\mu_5\text{-}Se)_2(\mu_4\text{-}Se)_{20}(PPh_3)_{10}]$. *Angew. Chem. Int. Ed.* **1985**, *24* (11), 993–995. https://doi.org/10.1002/anie.198509931.

(18) Fenske, D.; Ohmer, J.; Merzweiler, K. Darstellung Und Kristallstrukturen von $[Co_6Se_8(PPh_3)_6]^+[CoCl_3(THF)]^-$, $[Co_8Se_8(PPh_3)_6][Co_6Se_8(PPh_3)_6]$ Und $[Co_8Se_8(PPh_3)_6]^+[CoCl_3(PPh_3)]^-$. *Zeitschrift für Naturforschung B* **1987**, *42* (7), 803–809. https://doi.org/10.1515/znb-1987-0701.

(19) Steigerwald, M. L.; Siegrist, T.; Stuczynski, S. M. Octatelluridohexakis(Triethylphosphine)Hexacobalt and a Connection between Chevrel Clusters and the NiAs Structure. *Inorg. Chem.* **1991**, *30* (10), 2256–2257. https://doi.org/10.1021/ic00010a005.

(20) Stuczynski, S. M.; Kwon, Y. U.; Steigerwald, M. L. The Use of Phosphine Chalcogenides in the Preparation of Cobalt Chalcogenides. *Journal of Organometallic Chemistry* **1993**, *449*, 167–172.

(21) Choi, B.; Yu, J.; Paley, D. W.; Trinh, M. T.; Paley, M. V.; Karch, J. M.; Crowther, A. C.; Lee, C.-H.; Lalancette, R. A.; Zhu, X.; Kim, P.; Steigerwald, M. L.; Nuckolls, C.; Roy, X. Van Der Waals Solids from Self-Assembled Nanoscale Building Blocks. *Nano Lett.* **2016**, *16* (2), 1445–1449. https://doi.org/10.1021/acs.nanolett.5b05049.

(22) Champsaur, A. M.; Yu, J.; Roy, X.; Paley, D. W.; Steigerwald, M. L.; Nuckolls, C.; Bejger, C. M. Two-Dimensional Nanosheets from Redox-Active Superatoms. *ACS Cent. Sci.* **2017**, *3* (9), 1050–1055. https://doi.org/10.1021/acscentsci.7b00328.

(23) Roy, X.; Schenck, C. L.; Ahn, S.; Lalancette, R. A.; Venkataraman, L.; Nuckolls, C.; Steigerwald, M. L. Quantum Soldering of Individual Quantum Dots. *Angew. Chem. Int. Ed.* **2012**, *51* (50), 12473–12476. https://doi.org/10.1002/anie.201206301.

(24) Steigerwald, M. L.; Siegrist, T.; Stuczynski, S. M. Initial Stages in the Molecule-Based Growth of the Solid-State Compound Cobalt Telluride (CoTe). *Inorg. Chem.* **1991**, *30* (26), 4940–4945. https://doi.org/10.1021/ic00026a018.

(25) Champsaur, A. M.; Velian, A.; Paley, D. W.; Choi, B.; Roy, X.; Steigerwald, M. L.; Nuckolls, C. Building Diatomic and Triatomic Superatom Molecules. *Nano Lett.* **2016**, *16* (8), 5273–5277. https://doi.org/10.1021/acs.nanolett.6b02471.

(26) Tolman, C. A. Electron Donor-Acceptor Properties of Phosphorus Ligands. Substituent Additivity. *J. Am. Chem. Soc.* **1970**, *92* (10), 2953–2956. https://doi.org/10.1021/ja00713a006.

(27) Jover, J.; Cirera, J. Computational Assessment on the Tolman Cone Angles for P-Ligands. *Dalton Trans.* **2019**, *48* (40), 15036–15048. https://doi.org/10.1039/C9DT02876E.

(28) *Multiple Bonds Between Metal Atoms*; Cotton, F. A., Murillo, C. A., Walton, R. A., Eds.; Springer-Verlag: New York, 2005. https://doi.org/10.1007/b136230.

(29) Pauling, L. Atomic Radii and Interatomic Distances in Metals. *J. Am. Chem. Soc.* **1947**, *69* (3), 542–553. https://doi.org/10.1021/ja01195a024.

(30) Casati, N.; Macchi, P.; Sironi, A. Staggered to Eclipsed Conformational Rearrangement of $[Co_2(CO)_6(PPh_3)_2]$ in the Solid State: An X-ray Diffraction Study at High Pressure and Low Temperature. *Angew. Chem.* **2005**, *117* (47), 7914–7917. https://doi.org/10.1002/ange.200502241.

(31) Bungu, P. N.; Otto, S. Evaluation of Ligand Effects in the Modified Cobalt Hydroformylation of 1-Octene. Crystal Structures of $[Co(L)(CO)_3]_2$ (L = PA–C5, PCy_3 and $PCyp_3$). *Dalton Trans.* **2011**, *40* (36), 9238. https://doi.org/10.1039/c1dt10581g.

(32) Birbeck, J. M.; Haynes, A.; Adams, H.; Damoense, L.; Otto, S. Ligand Effects on Reactivity of Cobalt Acyl Complexes. *ACS Catal.* **2012**, *2* (12), 2512–2523. https://doi.org/10.1021/cs300589n.

(33) Markó, L.; Bor, G.; Klumpp, E.; Markó, B.; Almásy, G. Schwefelhaltige Metallcarbonyle, III. Die Reaktion zwischen Kobaltcarbonylen und Schwefel. *Chem. Ber.* **1963**, *96* (4), 955–964. https://doi.org/10.1002/cber.19630960406.

(34) Gervasio, G.; Kettle, S. F. A.; Musso, F.; Rossetti, R.; Stanghellini, P. L. Synthesis and Characterization of Three Novel Selenidohexacobalt Carbonyl Clusters. Crystal Structures of $[(\mu_3\text{-}Se)Co_3(CO)_7]_2\mu_4\text{-}(Se_2)$ and $Co_6(\mu_3\text{-}Se)_8(CO)_6$. *Inorg. Chem.* **1995**, *34* (1), 298–305. https://doi.org/10.1021/ic00105a047.

(35) Gervasio, G.; Rossetti, R.; Stanghellini, P. L.; Braga, D.; Kettle, S. F. A. Crystal Structure of $Co_4(CO)_{10}S_2$ and $Co_4(CO)_{10}Se_2$; ν(CO) Vibrations of a Model Cluster Molecule: $Co_4(CO)_{10}S_2$. *Journal of Crystallographic and Spectroscopic Research* **1993**, *23* (4), 255–264. https://doi.org/10.1007/BF01263584.

(36) Harley, A. D.; Guskey, G. J.; Geoffroy, G. L. Interconversion of Phosphido-Bridged Polynuclear Cobalt Carbonyl Complexes. Cleavage of the Phosphido Bridge during Hydroformylation Catalysis. *Organometallics* **1983**, *2* (1), 53–59. https://doi.org/10.1021/om00073a011.

(37) Green, M. L. H. A New Approach to the Formal Classification of Covalent Compounds of the Elements. *Journal of Organometallic Chemistry* **1995**, *500* (1), 127–148. https://doi.org/10.1016/0022-328X(95)00508-N.

(38) Strouse, C. E.; Dahl, L. F. Organometallic Chalcogen Complexes. XXII. Syntheses and Structural Analyses by x-Ray Diffraction and Electron Spin Resonance Single-Crystal Methods of $Co_3(CO)_9Se$, $FeCo_2(CO)_9Se$, and $FeCo_2(CO)_9Te$. Antibonding Metallic Nature of an Unpaired Electron in an Organometallic Cluster System. *J. Am. Chem. Soc.* **1971**, *93* (23), 6032–6041. https://doi.org/10.1021/ja00752a012.

(39) Vastag, S.; Gervasio, G.; Marabello, D.; Szalontai, G.; Markó, L. Chemistry of the Paramagnetic $Co_3(CO)_9(\mu_3\text{-}S)$ Cluster. Rational Synthesis of $Co_3(CO)_7(\mu\text{-}X)(\mu_3\text{-}S)$ Complexes. *Organometallics* **1998**, *17* (19), 4218–4225. https://doi.org/10.1021/om980147n.

(40) Davies, J. E.; Mays, M. J.; Raithby, P. R.; Sarveswaran, V.; Shields, G. P. Nature of Previously Reported Thermally Unstable Products Derived from the Reaction of $[Co_2(CO)_8]$ with PhSSPh, EtSSEt or PhSeSePh and of the Reactions of These Products with Alkynes or Isocyanides. *J. Chem. Soc., Dalton Trans.* **1998**, No. 5, 775–780. https://doi.org/10.1039/a707709b.

(41) Edwards, A. J.; Martían, A.; Mays, M. J.; Nazar, D.; Raithby, P. R.; Solan, G. A. Synthesis and Reactions with Alkynes of Complexes Containing Both Phosphorus and Sulfur Bridging Ligands: Crystal and Molecular Structures of $[Mn_2(\mu\text{-}PPh_2)(\mu\text{-}SPh)(CO)_8]$, $[Co_3(\mu_3\text{-}S)(\mu\text{-}PPh_2)(CO)_6(PPh_3)]$ and $[Co_3(\mu_3\text{-}S)(\mu\text{-}PPh_2CHCPh)(CO)_6(PPh_3)]$. *J. Chem. Soc., Dalton Trans.* **1993**, No. 3, 355–363. https://doi.org/10.1039/DT9930000355.

(42) Hernández Sánchez, R.; Champsaur, A. M.; Choi, B.; Wang, S. G.; Bu, W.; Roy, X.; Chen, Y.; Steigerwald, M. L.; Nuckolls, C.; Paley, D. W. Electron Cartography in Clusters. *Angew. Chem. Int. Ed.* **2018**, *57* (42), 13815–13820. https://doi.org/10.1002/anie.201806426.

(43) Yao, Z.-F.; Wang, J.-Y.; Pei, J. Control of π–π Stacking via Crystal Engineering in Organic Conjugated Small Molecule Crystals. *Crystal Growth & Design* **2018**, *18* (1), 7–15. https://doi.org/10.1021/acs.cgd.7b01385.

(44) Turkiewicz, A.; Paley, D. W.; Besara, T.; Elbaz, G.; Pinkard, A.; Siegrist, T.; Roy, X. Assembling Hierarchical Cluster Solids with Atomic Precision. *J. Am. Chem. Soc.* **2014**, *136* (45), 15873–15876. https://doi.org/10.1021/ja508698w.

(45) Yang, L.; Powell, D. R.; Houser, R. P. Structural Variation in Copper(I) Complexes with Pyridylmethylamide Ligands: Structural Analysis with a New Four-Coordinate Geometry Index, τ_4. *Dalton Trans.* **2007**, No. 9, 955–964. https://doi.org/10.1039/B617136B.

(46) *A Search for All Fe...Se Bond Lengths in the Cambridge Structural Database (Updated June 2020) Yielded 591 Hits between 2.142 and 2.949 Å (Mean 2.39(6) Å).*

(47) *A Search for All Zn...Se Bond Lengths in the Cambridge Structural Database (Updated June 2020) Yielded 140 Hits between 2.289 and 2.949 Å (Mean 2.47(7) Å).*

(48) Evans, D. F. 400. The Determination of the Paramagnetic Susceptibility of Substances in Solution by Nuclear Magnetic Resonance. *J. Chem. Soc.* **1959**, 2003. https://doi.org/10.1039/jr9590002003.

(49) Poetschke, N.; Nieger, M.; Khan, M. A.; Niecke, E.; Ashby, M. T. Synthesis and Crystal Structures of Lithium Salts of New Iminophosphide/Phosphinoamide Anions. *Inorg. Chem.* **1997**, *36* (18), 4087–4093. https://doi.org/10.1021/ic9700720.

(50) Bruker APEX2 (Version 2.1-4), SAINT (Version 7.34A), SADABS (Version 2007/4), **2007** *BrukerAXS Inc*, Madison, Wisconsin, USA.

(51) Sheldrick, G.M. *Acta Cryst.* **2015**, *A71*, 3-8.

(52) Altomare, A.; Burla, C.; Camalli, M.; Cascarano, G. L.; Giacovazzo, C.; Guagliardi, A.; Moliterni, A.G.G.; Polidori, G.; Spagna, R. *J. Appl. Crystallogr.,* **1999**, *32*, 115-119.

(53) Altomare, A.; Cascarano, G. L.; Giacovazzo, C.; Guagliardi, A. *J. Appl. Crystallogr.*, **1993**, *26*, 343-350.

(54) Sheldrick, G. M. *SHELXL-97, Program for the Refinement of Crystal Structures*, **1997**, University of Göttingen, Germany.

(55) Sheldrick, G. M. *Acta Cryst.* **2015**, *C71*, 3–8.

(56) Mackay, S.; Edwards, C.; Henderson, A.; Gilmore, C.; Stewart, N.; Shankland, K.; Donald, A. *MaXus: A Computer Program for the Solution and Refinement of Crystal Structures from Diffraction Data,* **1997**, University of Glasgow, Scotland.

(57) Waasmaier, D.; Kirfel, A. *Acta Cryst*., **1995**, *51*, 416-430.



Submitted for consideration for the Dalton Transactions cover: Nanopropeller ternary clusters take flight from the Velian lab at the University of Washington. In this work we uncover how steric bulk modulates the synthesis and push-pull dynamic between the cluster support, edge sites and substrates in atomically precise ternary clusters $M_3Co_6Se_8L^{iPr}_6$ (M = Fe, Zn; L^{iPr} = $Ph_2PN^{(-)}iPr$).

CHAPTER 3.

CAUGHT IN THE ACT OF SUBSTITUTION: INTER-ADSORBATE EFFECTS ON AN ATOMICALLY PRECISE FE/CO/SE NANOCLUSTER WITH MULTIPLE ACTIVE SITES

3.1 ABSTRACT

Just as directing groups guide substitution patterns in organic synthesis, ligands bound to exposed active sites of an inorganic material encode surface reactivity patterns via the inter-adsorbate effect. However, owing to the limitations of surface analysis there is little opportunity to resolve these effects on the atomic scale. Here, we explore an atomically defined nanocluster $[Fe_3Co_6Se_8L^{Tol}_6]^+$ ($[\mathbf{Fe_3}]^+$; $L^{Tol} = Ph_2PN^{(-)}Tol$, Ph = phenyl, Tol = 4-tolyl) where the inter-adsorbate effect is self-apparent, manifesting in the site-differentiated of three Fe surface sites to afford bis-ligated $[\mathbf{1}(L)_2]^+$ adducts (L = CN^{t}Bu, THF, MeCN). Using a combination of spectroscopic techniques and single-crystal X-ray diffractometry, we find that ligation of the "naked" Fe site in $[\mathbf{Fe_3}(CN^tBu)_2]^+$ sets off a domino effect wherein allosteric through-cluster interactions promote the dissociation of CN^{t}Bu at a neighboring active site. In the solid-state, we find that allosteric ligand substitution proceeds with complete regioselectivity, as computational analysis suggests the frontier orbitals reorganize to interconnect the active sites via delocalized Fe···Co···Se covalent interactions.

3.2 CAPTURING INTER-ADSORBATE DYNAMICS

Substrate adsorption is an elementary step in any surface-based chemical transformation[1] and can dramatically alter electronic properties[2,3] or invoke surface restructuring within the lattice.[4–9] However, even the simplest of coordinative processes become enormously complex when considered at an inorganic surface, where an ensemble of interconnected "active sites" compete for substrate binding.[10] At these interfaces, chemically degenerate surface sites are differentiated upon ligand binding, as steric[11] and inductive[12] effects give rise to inter-adsorbate interactions that promote long-range substrate ordering[13,14] and modulate catalytic activity.[15–17] In effect, these

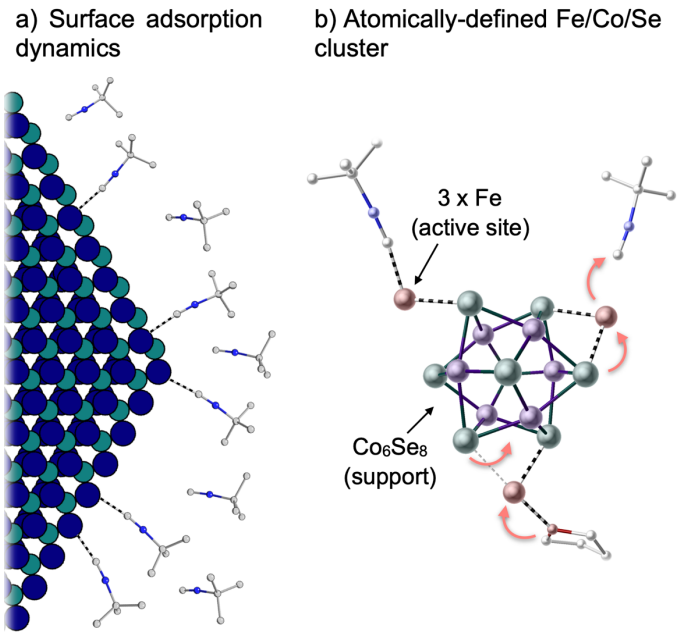


Figure 3.1. Atomically precise M/Co/Se nanoclusters with multiple active sites enable probing inter-adsorbate interactions at neighboring active sites. Red arrows illustrate the correlated reactivity of neighboring active sites.

inter-adsorbate forces guide the reactivity of neighboring surface sites, just as directing groups guide substitution patterns in organic synthesis. Furthermore, during the course of a catalytic transformation, adsorption-induced structural dynamics can lead to metastable surface phases with reactive properties distinct from the thermodynamic phase.[10,18,19] Understanding how inter-adsorbate effects manifest to facilitate active site speciation and guide surface reactivity is fundamental to the design and implementation of new catalysts.[20] However, these multi-active site dynamics are difficult to resolve experimentally, relying primarily on advanced surface analysis techniques and computational methods.[21]

Molecular nanoclusters provide ideal models to study the electronic properties and reactivity of transition metal oxide[22–24] and chalcogenide[25,26] materials.[27] In these atomically defined systems, ligand adsorption at a substrate-accessible metal site has been demonstrated to invoke a redistribution of charges within a remote polymetallic support.[28–31] Further, nanoclusters also provide a platform to study the regiochemical aspects of surface substitution reactions when there are multiple reactive surface sites available, as was first explored in C_{60} fullerenes.[32] Indeed, several instances of site-specific ligand-exchange reactivity have been reported in metal chalcogenide (M_6Se_8, M = Co, Re)[33,34] and metallic Au nanoclusters.[35,36] Still, there are few

nanocluster frameworks that suitably model the interactions between multiple discrete active sites through a supporting lattice.

Our group has introduced a family of atomically precise ternary nanoclusters, $M_3Co_6Se_8L_6$ (M = Cr, Fe, Co, Zn; L = $Ph_2PN^{(-)}Tol$; Ph = phenyl, Tol = *p*-tolyl), that enable probing the interplay of multiple active sites dispersed on an inorganic support with molecular characterization techniques.[37–41] These clusters feature three low-coordinate edge metals that interact directly with a Co_6Se_8 support via hemilabile M–Se bonds. With its well-defined metal-support architecture, this system has granted key insights into the electronic and coordinative aspects of the metal-support interaction, and enabled the direct measurement of multi-active site interactions.[37,42] Notably, we have shown the reactivity of neighboring active sites is intertwined via through-cluster allosteric effects, resulting in site-specific ligand binding and active site ordering for programmable self-assembly as well as the kinetic regulation of catalytic nitrene transfer catalysis.[38–40]

Here, a serendipitous discovery enables us to demonstrate the interconnected reactivity of the three edge sites and to propose a mechanism for how allosteric inter-adsorbate effects guide ligand substitution patterns on the surface of $Fe_3Co_6Se_8L^{Tol}_6$ (**Fe$_3$**;). Remarkably, we find that ligand binding sets off a cascade of stereoelectronic changes that propagate through the cluster to alter the ligand binding affinity of vicinal active sites. Computational analysis reveals that allosteric ligand substitution is guided by covalent Fe···Co···Se interactions that intertwine the reactivity of neighboring Fe centers to engender regioselective active site correlation.

3.3 Inter-Adsorbate Dynamics within Fe/Co/Se Clusters

3.3.1 *Ligand Binding Induces Stereoisomerism in **Fe$_3$** Clusters*

Taken in isolation, ligand binding to a single Fe edge site is simple to understand. Each Fe–L bond making event is associated with a Fe–Se bond breaking event, with the Fe centers retaining their pseudo-tetrahedral geometry throughout (Figure 3.2a). However, when considering the three active sites in aggregate, we note that the orientation of ligand binding defines a unique stereochemistry (Figure 3.2b). For example, upon binding to an Fe edge, a mono-dentate ligand, L, desymmetrizes the inorganic core such that each Fe–Se bond becomes α or β stereogenic, where α and β denote the equatorial Se atoms located on the top (α) or bottom (β) Co_3Se_4 hemispheres

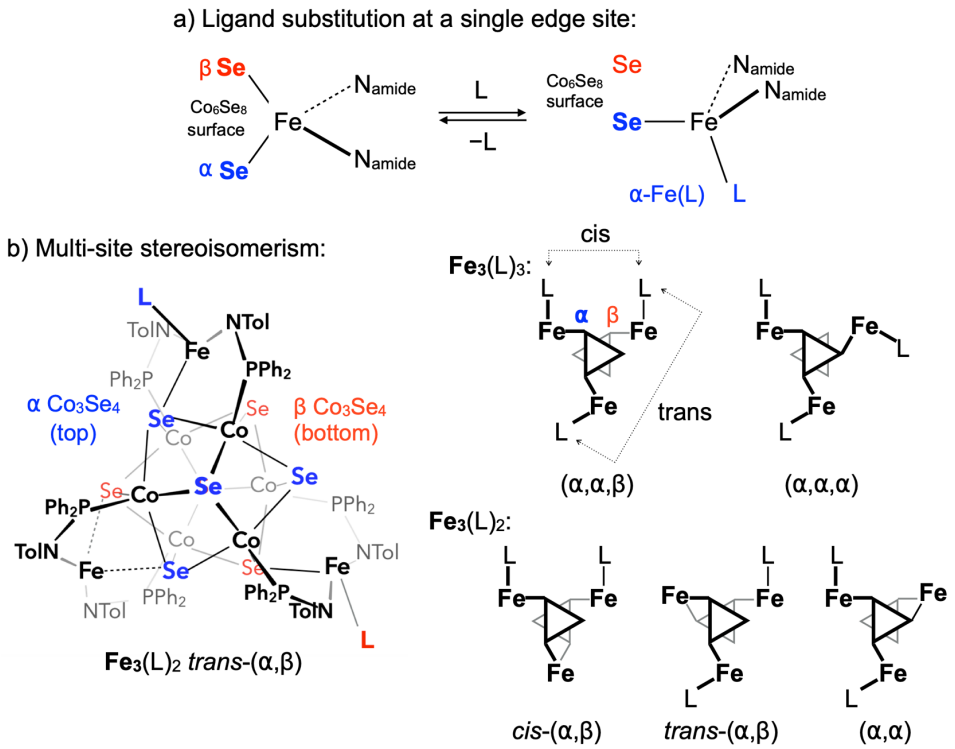


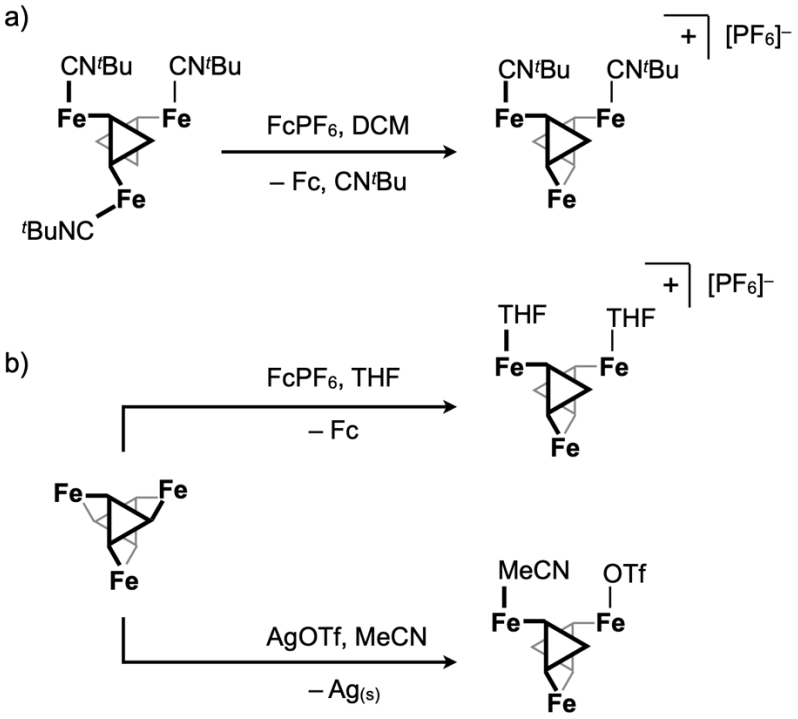
Figure 3.2. Changes in the coordination environment of a single Fe edge site in response to ligand binding at the edge metals of **Fe$_3$**, and b) the stereochemical implications of ligands binding at multiple Fe edge sites.

of the Co_6Se_8 cube. A tris-adduct **Fe$_3$**$(L)_3$, could therefore exist as either of two unique diastereomers, (α,α,α) or (α,α,β), depending on which Se atoms are displaced upon coordination of L. Similarly, three unique diastereomers are possible for a bis-adduct **Fe$_3$**$(L)_2$; (α,α), *cis*-(α,β) and *trans*-(α,β). Ultimately, we note that the stereochemical transitions of this system are reflective of an allosteric inter-adsorbate effect, wherein displacement of Fe–Se bonds liberates electron density to the Co_6Se_8 support and modulates Fe–Se bonding and ligand-binding affinity of neighboring active sites.

3.3.2 *Structural Trends in the Site-differentiation of [**Fe$_3$**]$^+$*

The inter-adsorbate effect is self-apparent for mono-oxidized derivatives of **Fe$_3$**, where we observe a uniform preference for the formation of bis-ligated adducts that feature one "naked" Fe site. For example, we previously showed chemical oxidation of the neutral tris(isocyanide) cluster, **Fe$_3$**$(CN^tBu)_3$, liberates isocyanide from one of the Fe edges to afford the site-differentiated product, [**Fe$_3$**$(CN^tBu)_2$][PF_6] (Scheme 3.1a).[37] This bis(isocyanide) adduct features one κ^4-Fe edge bound only to the cluster surface, and two κ^3-Fe(CN^tBu) edges in which the coordination of CN^tBu

Scheme 3.1. Chemical oxidation of **Fe$_3$** to yield a family of bis-ligated adducts.



disrupts one Fe–Se bond. Since this initial discovery, we have found that site-differentiation is generally favored among [**Fe$_3$**]$^+$ clusters, even in the presence of excess ligand. For example, both [**Fe$_3$**(THF)$_2$][PF$_6$] and **Fe$_3$**(MeCN)(OTf) exhibit the same site-differentiation with one κ^4-Fe edge free of surface ligands despite crystallization from neat THF or MeCN, respectively (Scheme 3.1b).

In the solid state, we find that the mono-oxidized clusters, [**Fe$_3$**(CN^{t}Bu)$_2$][PF$_6$], [**Fe$_3$**(THF)$_2$][PF$_6$], and **Fe$_3$**(MeCN)(OTf), all adopt a psuedo-C_2 symmetric *cis*-(α,β) conformation (Figure 3.3). Within these clusters, bond metrics vary even at Fe(CN^{t}Bu) and Fe(THF) edge sites exhibiting identical immediate coordination environments. For example, the Fe(CN^{t}Bu)–Se bonds in [**Fe$_3$**(CN^{t}Bu)$_2$]$^+$ range between 2.488(7) and 2.546(7) Å. This inequivalence is even more pronounced in [**Fe$_3$**(THF)$_2$]$^+$, where one Fe(THF) edge adopts a *pseudo*-κ^4 conformation. The κ^4-Fe site in each of these clusters is tightly bound by the Co$_6$Se$_8$ support, featuring two markedly contacted Fe–Se bonds. Empirically, this *cis*-(α,β) diastereomer is favored as it maximizes the separation of the Fe(L)–Se bonds away from the κ^4-Fe site, affording an optimal distribution of electron density within the Co$_6$Se$_8$ support. A comparison of the calculated energies for density functional theory (DFT) optimized diastereomers of [**Fe$_3$**(CNMe)$_2$]$^+$ reveals that the *cis*-(α,β)

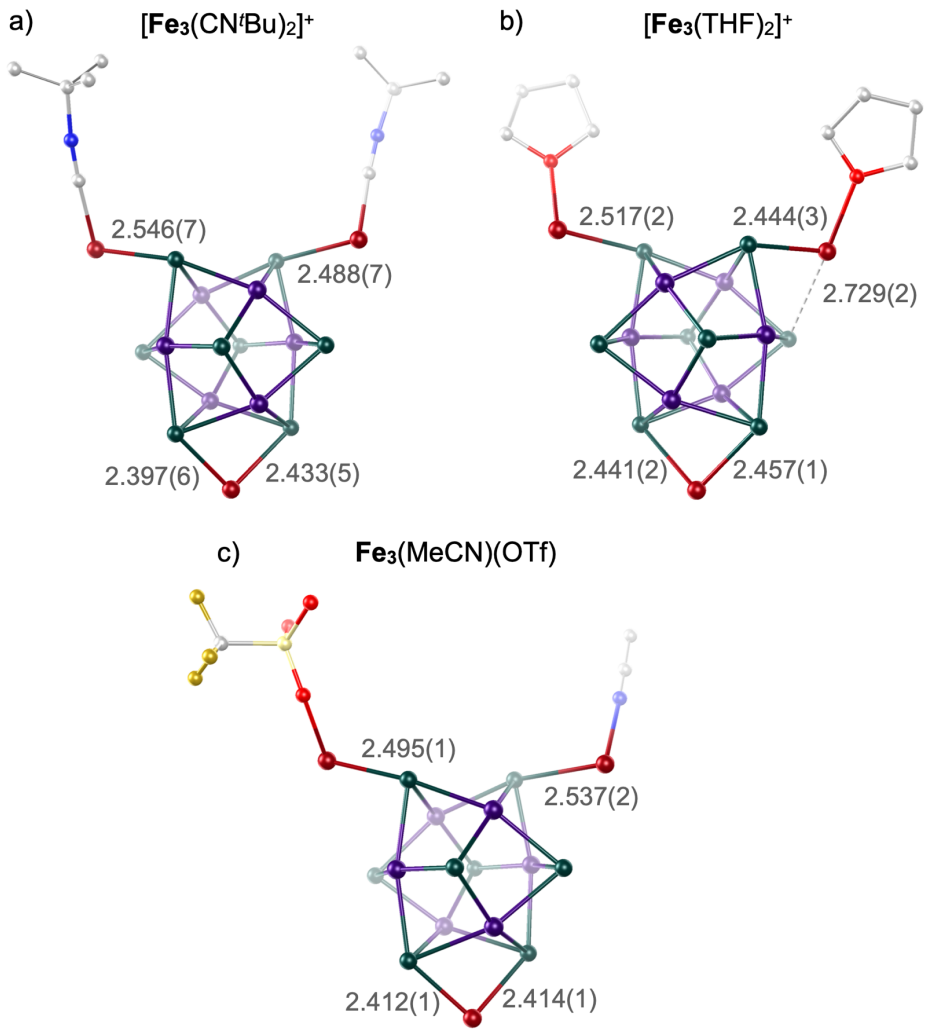


Figure 3.3. Single-crystal X-ray diffraction structures for a family of *cis*-(α,β) nanoclusters including a) [**Fe**$_3$(CN^{t}Bu)$_2$][PF$_6$], b) [**Fe**$_3$(THF)$_2$][PF$_6$], and c) **Fe**$_3$(MeCN)(OTf). Phosphinoamide ligands, chemical disorder and solvent molecules are omitted for clarity.

isomer is thermodynamically favored, lying 1.23 and 1.26 kcal/mol lower in energy than the (α,α) or *trans*-(α,β) congeners, respectively (see Section 3.8.8).

3.3.3 *Solution-phase Ligand Exchange with [**Fe**$_3$(CN^{t}Bu)$_2$]$^+$*

With a κ^4-Fe active site available for coordination of a third ligand and two Fe(CN^{t}Bu) edges equipped with isocyanide reporters for vibrational spectroscopy, we sought to investigate the ligand exchange dynamics at the surface of [**Fe**$_3$(CN^{t}Bu)$_2$][PF$_6$]. Despite the apparent preference to form a site-differentiated bis-adduct, we previously demonstrated that the κ^4-Fe site

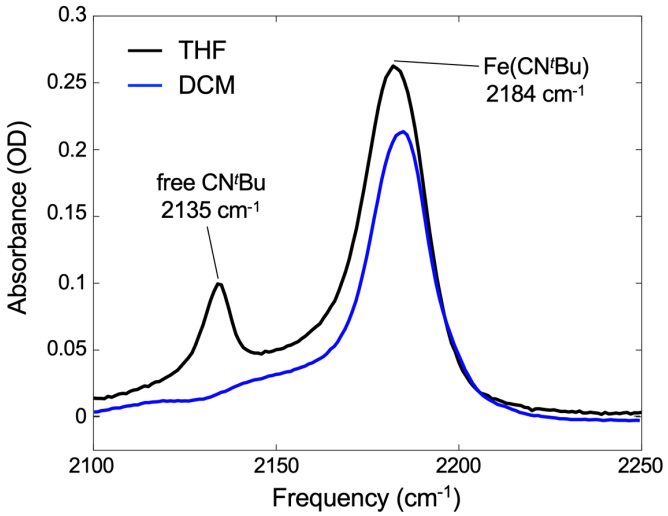


Figure 3.4. Solution-phase FTIR absorption (25 °C, 7.8 mM, 2 mm pathlength) spectra of [**Fe$_3$**(CN^{t}Bu)$_2$][PF$_6$] recorded in neat DCM or THF. Solvent contributions were accounted for via solvent subtraction.

exhibits a low, but appreciable, CN^{t}Bu binding affinity ($K_a \simeq 24$ M^{-1}), as determined by ^{1}H NMR spectroscopy.[53] However, we found that ligand exchange in the [**Fe$_3$**]$^+$ system cannot be resolved on the NMR timescale, turning instead to solution-phase infrared (IR) spectroscopy to more effectively resolve ligand binding dynamics. Solution-phase IR spectroscopy analysis of [**Fe$_3$**(CN^{t}Bu)$_2$][PF$_6$] in the coordinating solvent THF confirms the presence of ligand exchange with two isocyanide stretches at 2184 and 2135 cm^{-1} that can be attributed to bound Fe(CN^{t}Bu) and free CN^{t}Bu, respectively (Figure 3.4). Similar results are obtained upon titration of [**Fe$_3$**(THF)$_2$][PF$_6$] with CN^{t}Bu (0.1 – 2.0 equiv) in THF, confirming that a substitution equilibrium is rapidly established upon combining CN^{t}Bu and [**Fe$_3$**]$^+$ in THF. Integration of these peaks via curve fitting analysis reveals a ratio of 7.0:1.0 ± 0.3 for bound and unbound CN^{t}Bu, respectively (see Section 3.8.5). Conversely, no free CN^{t}Bu is detected when [**Fe$_3$**(CN^{t}Bu)$_2$][PF$_6$] is analyzed in DCM. These data suggest that THF coordination directly promotes the dissociation of CN^{t}Bu, giving rise to a ligand exchange equilibrium which may ultimately interconvert [**Fe$_3$**(CN^{t}Bu)$_2$]$^+$ and [**Fe$_3$**(THF)$_2$]$^+$ in solution.

3.3.4 *Single-crystal Resolution of the Inter-adsorbate Effect*

Fortuitously, we are able to detect two intermediates formed in this ligand exchange reaction crystallographically to directly resolve inter-adsorbate dynamics on the atomic-scale. Layering a THF solution of [**Fe$_3$**(CN^{t}Bu)$_2$][PF$_6$] with diethyl ether at 298 K affords dark-red

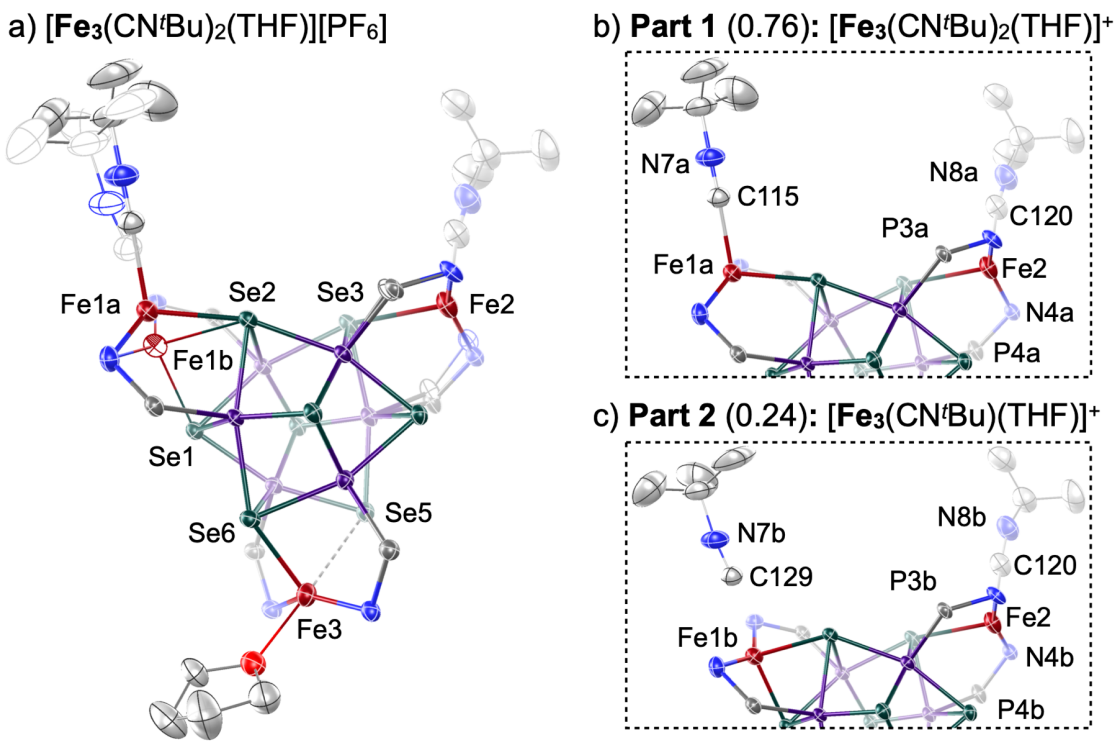


Figure 3.5. a) Solid-state structures of the co-crystallized intermediates (α,α,β)-[**Fe**$_3$(CN^{t}Bu)$_2$(THF)][PF$_6$] and *trans*-(α,β)-[**Fe**$_3$(CN^{t}Bu)(THF)][PF$_6$]. Thermal ellipsoids plotted at 50% probability. Insets included to highlight the dynamic exchange of isocyanide at the b) major and c) minor components of the crystal. All hydrogen atoms, phosphinoamide carbon atoms, and the [PF$_6$]$^-$ counterion have been omitted for clarity. Selected interatomic distances (Å): Fe1a-Se2 2.498(7), Fe1a-Se1 3.258(3), Fe1b-Se2 2.471(8), Fe1b-Se1 2.404(5), Fe2-Se3 2.541(7), Fe3-Se6 2.450(2), Fe3-Se5 2.699(3); Fe1a-C115 2.13(1); Fe1b-C129 2.41(3), Fe2-C120 2.11(3).

prismatic crystals containing a disordered mixture of the THF-bound tris-adduct, [**Fe**$_3$(CN^{t}Bu)$_2$(THF)][PF$_6$], and a new site-differentiated bis-adduct, [**Fe**$_3$(CN^{t}Bu)(THF)][PF$_6$], with a dissociated molecule of isocyanide hovering near the surface, co-crystallized in a 0.76/0.24 ratio (Figure 3.5). This chemical disorder reveals how the coordination of THF at the previously κ^4-bound Fe of [**Fe**$_3$(CN^{t}Bu)$_2$][PF$_6$] releases electron density to the Co$_6$Se$_8$ core, thereby inducing fluctional dissociation of CN^{t}Bu at Fe(1) with the formation of a new κ^4-Fe site. This leads us to draw a striking conclusion: the ligand-substitution reactivities of the three Fe active sites are intertwined via through-cluster allosteric interactions. Moreover, the displacement of isocyanide by Se at Fe(1) directly impacts the environment of the vicinal Fe(2) site, even as the Co$_6$Se$_8$ support remains structurally unaffected. As Fe(1) attaches itself to a second selenium atom, adopting κ^4-coordination by the Co$_6$Se$_8$ support, the lighter organic ligands at Fe(2) reorganize. Remarkably, the ratio of bound Fe(CN^{t}Bu) and free CN^{t}Bu observed here in the solid-state (~7:1) perfectly

matches that which we observe in solution, suggesting that this ligand exchange equilibrium may also be operative upon dissolution. Although initially an unexpected discovery, this disordered structure is easily reproduced by replicating these crystallization conditions, providing an atom level glimpse of the inter-adsorbate forces that guide ligand substitution on the cluster's surface.

The stereochemical changes incurred upon coordination of THF to the naked active site of $[\mathbf{Fe_3}(CN^tBu)_2]^+$ provide key insights into the interconnected reactivity of the three edge metals, revealing that this allosteric ligand exchange reaction proceeds with complete regioselectivity. Coordination of THF to the κ^4-Fe site of $[\mathbf{Fe_3}(CN^tBu)_2]^+$ breaks the C_2-symmetry of the Fe(CN^tBu) edges, giving rise to the tris-adduct (α,α,β)-$[\mathbf{Fe_3}(CN^tBu)_2(THF)]^+$ where these Fe(CN^tBu)–Se edges now occupy unique α and β positions. Careful inspection of the minor component of this crystal structure reveals α-oriented coordination of THF directs ligand dissociation at the α-oriented Fe(CN^tBu) edge to afford the *trans*-(α,β) diastereomer of $[\mathbf{Fe_3}(CN^tBu)(THF)]^+$ with complete selectivity. Notably, the dissociated isocyanide remains trapped near Fe1b, implying that these coordinative dynamics are reversible *in crystallo* and offer a true snapshot of the substitution process. That said, there is no bonding interaction between Fe1b and C129, which are separated by 2.41(3) Å. Moreover, this structural analysis indicates that within these site-differentiated $[\mathbf{Fe_3}(L)_2]^+$ clusters, allosteric inter-adsorbate forces guide ligand exchange with regioselectivity for Fe(L) active sites positioned on the same α or β cluster face.

3.4 ^{57}Fe Mössbauer Spectroscopy Analysis

The chemical disorder that we resolve crystallographically is also reflected in the zero-field ^{57}Fe Mössbauer spectrum obtained for bulk crystalline samples of this material (Figure 3.6). Comparison of the spectral parameters obtained for the disordered $[\mathbf{Fe_3}(CN^tBu)_2(THF)][PF_6]$/$[\mathbf{Fe_3}(CN^tBu)(THF)][PF_6]$ crystals with those of $[\mathbf{Fe_3}(CN^tBu)_2][PF_6]$ and $[\mathbf{Fe_3}(THF)_2][PF_6]$ confirms that the binding of THF occurs with concomitant release of CN^tBu and formation of a new κ^4-Fe edge site. For the disordered material, we note the presence of signals associated with both Fe(CN^tBu) and κ^4-Fe edge sites ($\partial, |\Delta E_Q|$ (mm/s): 0.71, 1.90; 0.61, 1.23, respectively) and the appearance of a new signal that can be attributed to the pseudo-κ^4-Fe(THF) edge ($\partial, |\Delta E_Q|$ (mm/s): 0.68, 1.08). The area ratio obtained from a best-fit analysis of these signals also matches the expected distribution of Fe edges based on the chemical disorder observed in the

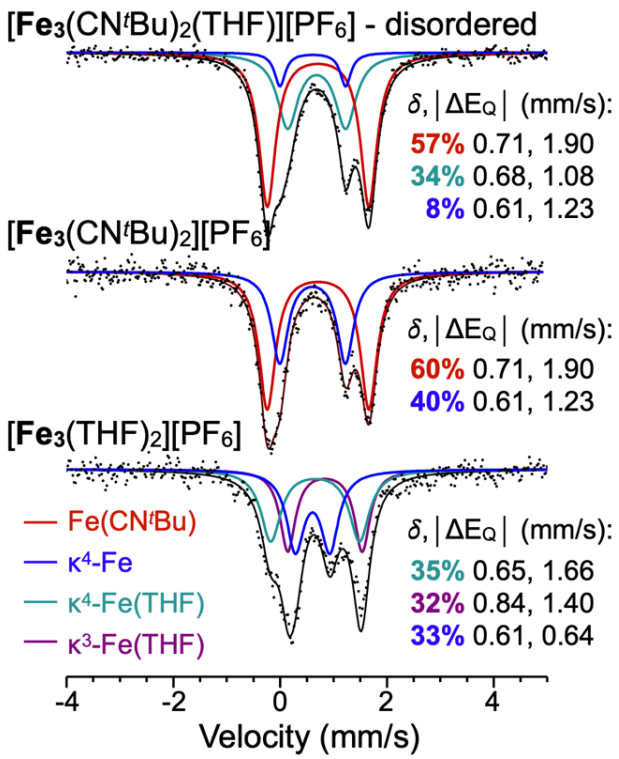


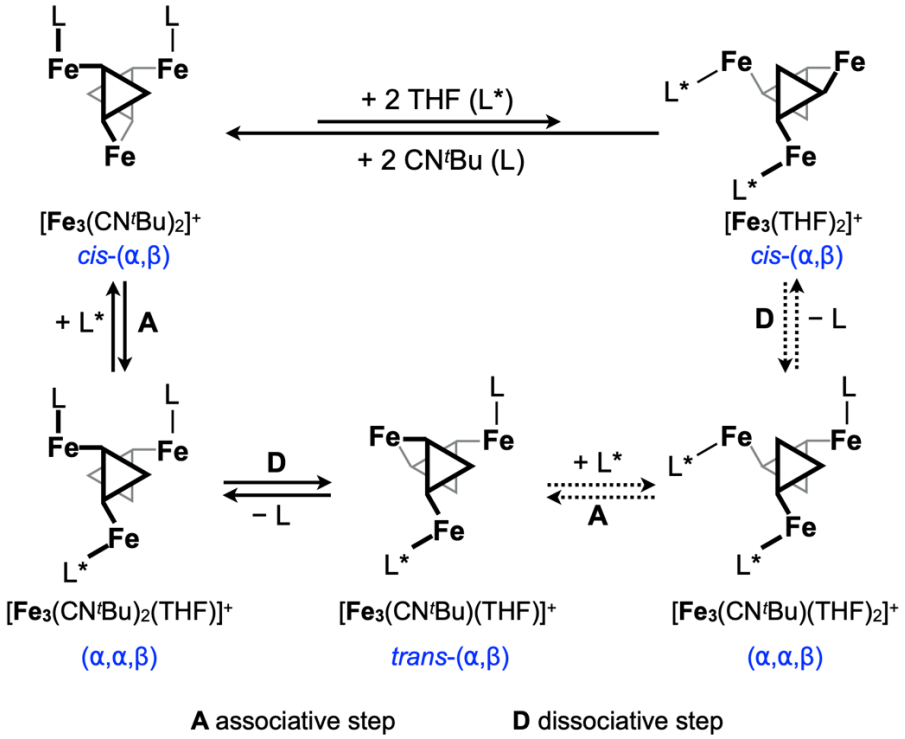
Figure 3.6. Zero-field ^{57}Fe Mössbauer spectra (90 K) collected on bulk solid samples of disordered [**Fe$_3$**(CN^{t}Bu)$_2$(THF)][PF$_6$], [**Fe$_3$**(CN^{t}Bu)$_2$][PF$_6$], and [**Fe$_3$**(THF)$_2$][PF$_6$], with quadrupole doublets tentatively assigned to distinct Fe environments.

solid-state. Notably, the Mössbauer spectrum collected for [**Fe$_3$**(THF)$_2$][PF$_6$] supports the presence of three unique high-spin Fe(II) environments (∂, $|\Delta E_Q|$ (mm/s): 0.61, 0.70; 0.66, 1.67; 0.86, 1.38) in a 1:1:1 area ratio. These signals can be tentatively attributed to the respective κ^4-Fe, pseudo-κ^4-Fe(THF), and κ^3-Fe(THF) edge sites that we observe crystallographically for this compound.

3.5 Multi-site Solvolysis Mechanism

In neat THF, we note that this allosteric ligand substitution mechanism could be extrapolated further to fully interconvert [**Fe$_3$**(CN^{t}Bu)$_2$]$^+$ and [**Fe$_3$**(THF)$_2$]$^+$ (Scheme 3.2). For example, β-oriented coordination of a second THF molecule to the κ^4-Fe site of *trans*-(α,β)-[**Fe$_3$**(CN^{t}Bu)(THF)]$^+$ would incite dissociation of the remaining β isocyanide to afford the thermodynamically favored *cis*-(α,β) isomer of [**Fe$_3$**(THF)$_2$]$^+$. Important insights surface when considering the alternative, unobserved scenario in the first dissociation step. If the β isocyanide was the leaving group from [**Fe$_3$**(CN^{t}Bu)$_2$(THF)]$^+$, the resulting (α,α) isomer of [**Fe$_3$**(CN^{t}Bu)(THF)]$^+$ would associate with a second THF ligand to yield either the (α,α,α) or

Scheme 3.2. Proposed multi-site mechanism for the interconversion of $[\mathbf{Fe_3}(CN^tBu)_2]^+$ and $[\mathbf{Fe_3}(THF)_2]^+$ via allosteric ligand substitution.



(α,α,β) isomers of $[\mathbf{Fe_3}(CN^tBu)(THF)_2]^+$. Isocyanide dissociation from these species would result in the formation of either the *trans*-(α,β) or the (α,α) isomer of the bis-adduct $[\mathbf{Fe_3}(THF)_2]^+$, which do not appear to be the thermodynamic stereoisomers.

Notably, this ligand exchange mechanism invokes for formation of a second tris-ligated intermediate, (α,α,β)-$[\mathbf{Fe_3}(CN^tBu)(THF)_2]^+$ *en route* to the bis(THF) adduct. Despite efforts to independently characterize this unobserved intermediate via crystallization of $[\mathbf{Fe_3}]^+$ in the presence of one equivalent of CN^tBu and THF, this compound has remained elusive. However, solution-phase IR measurements of this mixture reveal the presence of diagnostic bound and free isocyanide stretching frequencies, indicating that ligand exchange is active even when less than two equivalents of isocyanide are present. Interestingly, DFT calculations suggest that (α,α,β)-$[\mathbf{Fe_3}(CNMe)(THF)_2]^+$ exists as a transition state, with ground-state optimizations favoring dissociation of the β-oriented THF ligand to reproduce *trans*-(α,β)-$[\mathbf{Fe_3}(CNMe)(THF)]^+$.

3.5.1 *Computational Modelling of Multi-site Ligand Substitution.*

This multi-step ligand exchange process was modelled computationally using DFT to better understand the energetics of $[\mathbf{Fe_3}(CN^tBu)_2]^+$ and $[\mathbf{Fe_3}(THF)_2]^+$ interconversion as well as the electronic origins of the inter-adsorbate effect (Figure 3.7). The $[\mathbf{Fe_3}]^+$ clusters were optimized at the uBPV86/def2SVP level of theory using a minimally adapted phosphinoamide ligand platform, $Ph_2PN^{(-)}Ph$, and methyl isocyanide, CNMe. These changes were made to simplify the computational problem without significantly altering the electronic or steric traits of our system. Notably, analytical frequency calculations for these optimized structures reveal isocyanide

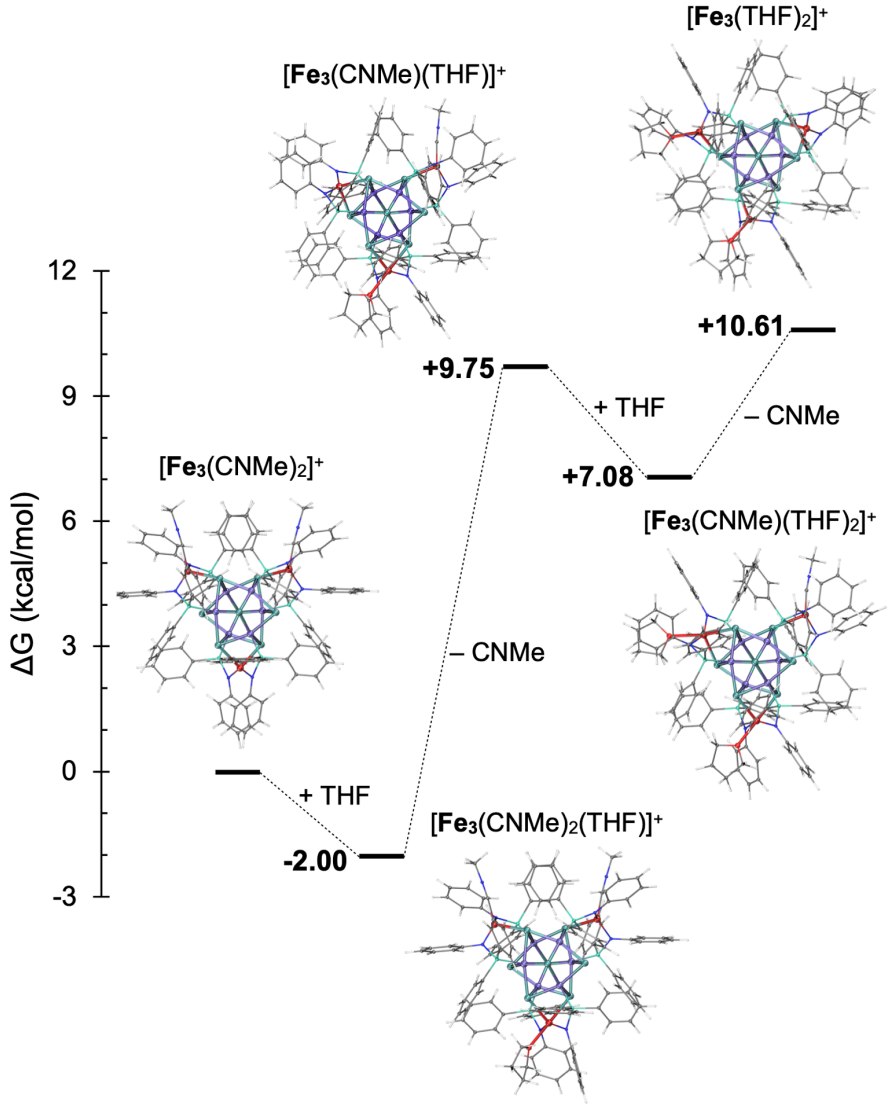


Figure 3.7. Calculated energetics and optimized geometries for the proposed ligand substitution reaction coordinate. Calculations were run at the uB3LYP+/cc-PVTZ level of theory.

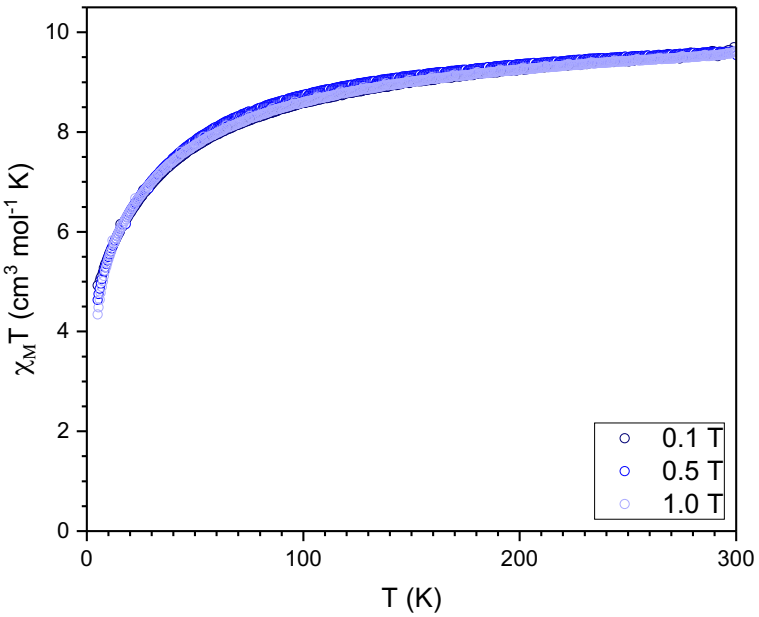


Figure 3.8. Variable-temperature *dc* magnetic susceptibility ($\chi_M T$, filled circles) data recorded for [**Fe$_3$**(CN^{t}Bu)$_2$][PF$_6$] upon warming from 5 to 300K under applied fields of 0.1, 0.5, and 1.0 T.

stretching frequencies ($\nu_{CN,calc}$ = 2169 – 2179 cm^{-1}) close to that observed experimentally (ν_{CN} = 2184 cm^{-1}). Single-point electronics were then calculated at the uB3LYP+/cc-pVTZ level of theory. Spin-multiplicity assignments for these calculations were informed by solid-state magnetometry data collected for [**Fe$_3$**(CN^{t}Bu)$_2$][PF$_6$], which exhibits a magnetic susceptibility of 9.5 cm^3 mol^{-1} K at 298 K (Figure 3.8). When taken into consideration with its corresponding ^{57}Fe Mössbauer spectrum, these data are indicative of a magnetic ground state with three s = 2 Fe(II) edge metals and a s = 1/2 [Co$_6$Se$_8$]$^+$ core (9.4 cm^3 mol^{-1} K, g = 2). For additional details regarding magnetometry, refer to Section 3.8.6.

Computational analysis reveals an overall energy landscape for the interconversion of [**Fe$_3$**(CNMe)$_2$]$^+$ and [**Fe$_3$**(THF)$_2$]$^+$ that favors the bis(isocyanide) derivative (ΔG_{calc} = +10.6 kcal/mol), which is perhaps unsurprising considering the relative binding strengths of CNMe and THF. Further, these calculations suggest the thermodynamic minimum of ligand exchange is [**Fe$_3$**(CNMe)$_2$(THF)]$^+$, which is in line with our observation that the tris-adduct [**1**(CN^{t}Bu)$_2$(THF)]$^+$ is present as the major species upon crystallization from neat THF. The free energy values calculated for each reaction step vary within a range comparable to that of a

cyclohexane chair-flip (11.7 vs 10.8 kcal/mol), suggesting that ligand exchange may proceed rapidly at room temperature to interconvert derivatives of $[\mathbf{Fe_3}(CN^tBu)_2]^+$ and $[\mathbf{Fe_3}(THF)_2]^+$.

3.5.2 *Electronic Origins of the Inter-adsorbate Effect*

Our computational analysis also provides a conceptual foundation for the electronic factors that underpin allosteric ligand substitution and guide the observed α/α-regioselectivity. Owing to the sheer multitude of electronic states present in this system as well as the complexity of bonding due to a high degree of Fe/Co/Se covalency, the overarching electronic structure and relative contributions of the edge and support atoms are most easily visualized by plotting a density of states. Partial density of states (*p*-DOS) plots for the crystallographically observable ligand exchange participants, *cis*-(α,β)-$[\mathbf{Fe_3}(CNMe)_2]^+$, (α,α,β)-$[\mathbf{Fe_3}(CNMe)_2(THF)]^+$ and *trans*-(α,β)-$[\mathbf{Fe_3}(CNMe)(THF)]^+$, including Co 3d, Se 4p, and Fe 3d orbital contributions, are provided in Figure 3.9a. The 3d orbital contributions of each Fe center are plotted individually, which enables the resolution of the changes in electronic structure at each active site during ligand substitution. The highest-lying filled states of $[\mathbf{Fe_3}(CNMe)_2]^+$ are primarily composed of Se 4p character, whereas the lowest-lying empty states are primarily localized on the κ^4-Fe center. The coordination of THF to form $[\mathbf{Fe_3}(CNMe)_2(THF)]^+$ causes minimal change in the filled states, with Fe 3d contributions of each Fe(CNMe) edge remaining nearly identical and the frontier states maintaining Se 4p character. Further, the lowest empty orbitals maintain primarily Fe(THF) 3d orbital character. Interestingly, in the formation of $[\mathbf{Fe_3}(CNMe)(THF)]^+$, isocyanide dissociation is accompanied by a reorganization of the frontier states. This occurs as the highest filled states adopt to the Fe(THF) 3d orbital character and the lowest unfilled states adopt κ^4-Fe 3d character. This electronic reorganization is accompanied by redistribution of charges amongst the edge sites, as Hirshfeld charge analysis reveals the migration of partial positive charge from one κ^4-Fe to the next (Table S7). This *p*-DOS analysis reveals that ligand substitution entails more than meets the eye, driving a reorganization of the frontier electronic states and a redistribution of partial charges at the Fe active sites. However, in order to rationalize the observed allosteric regioselectivity one must consider the contributions of individual molecular orbitals.

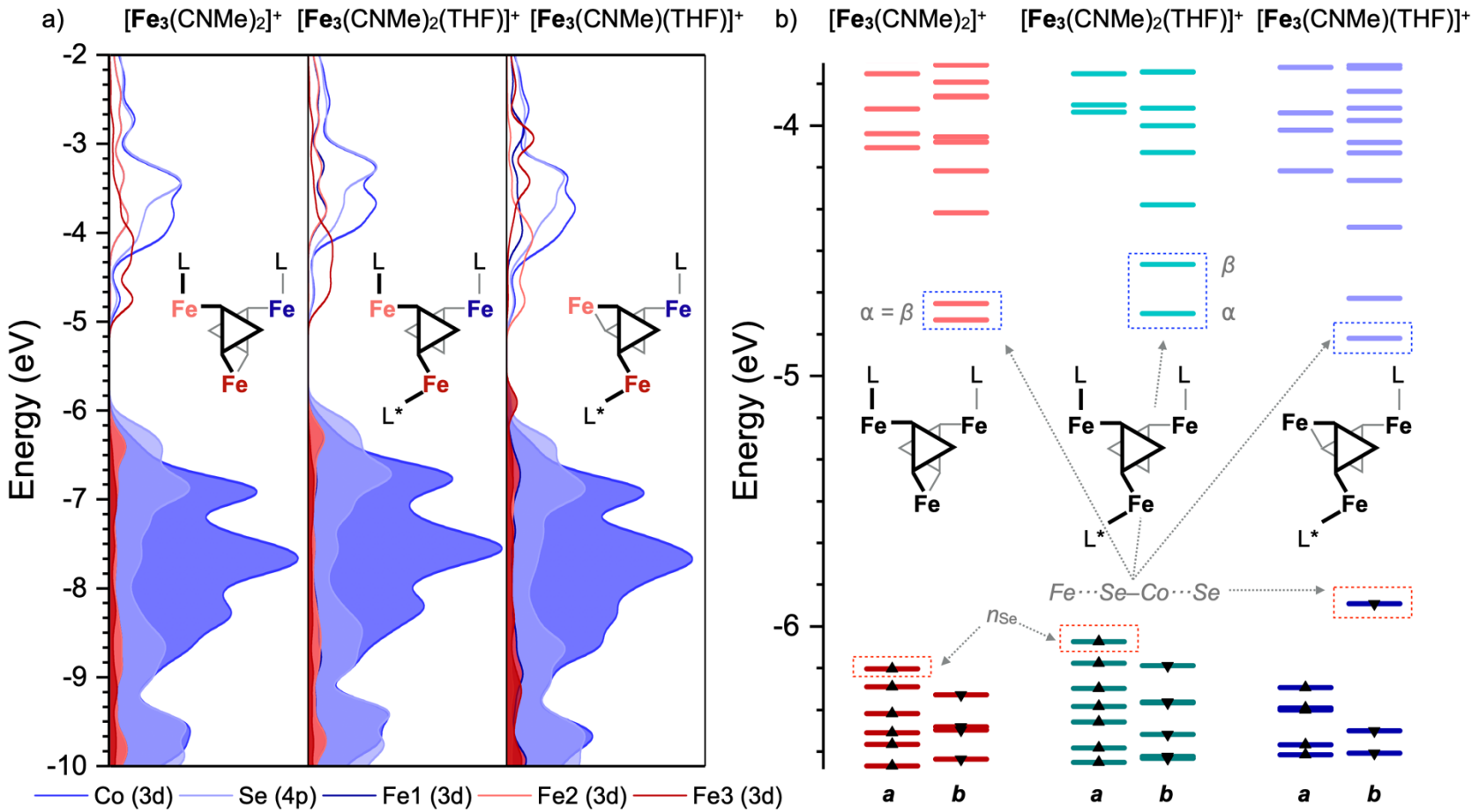


Figure 3.9. Partial density of states plots and b) molecular orbital diagrams of the crystallographically resolved [**Fe$_3$**]$^+$ ligand exchange series, *cis*-(α,β)-[**Fe$_3$**(CNMe)$_2$]$^+$, (α,α,β)-[**Fe$_3$**(CNMe)$_2$(THF)]$^+$ and *trans*-(α,β)-[**Fe$_3$**(CNMe)(THF)]$^+$. Here, *a* and *b* are used to abbreviate the up and down spin-manifolds. Calculations were run at the uB3LYP+/cc-PVTZ level of theory.

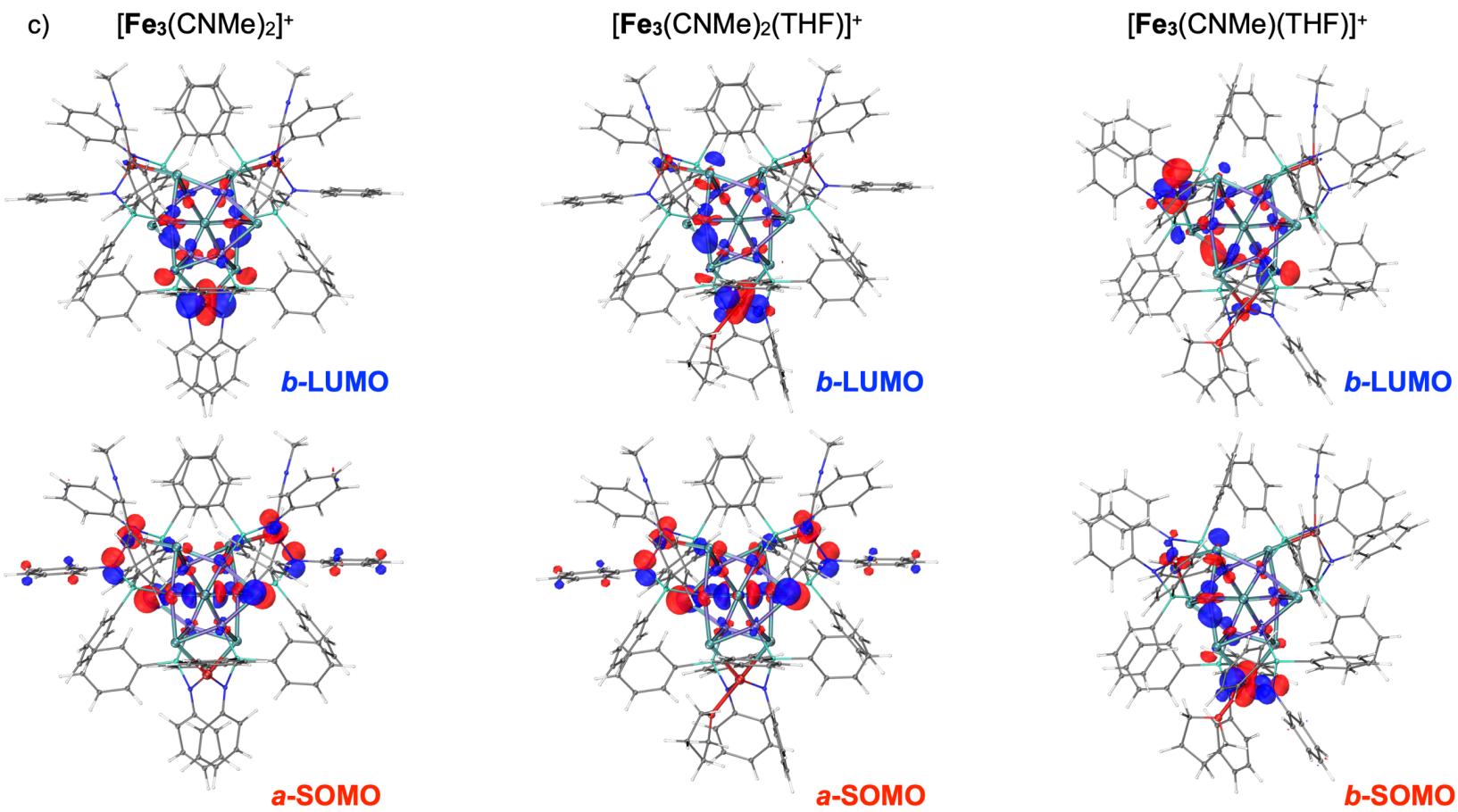


Figure 3.10. Isosurface plots are provided for select frontier orbitals of *cis*-(α,β)-[**Fe**$_3$(CNMe)$_2$]$^+$, (α,α,β)-[**Fe**$_3$(CNMe)$_2$(THF)]$^+$ and *trans*-(α,β)-[**Fe**$_3$(CNMe)(THF)]$^+$ (bottom, 0.04 au). Here, *a* and *b* are used to abbreviate the up and down spin-manifolds. Calculations were run at the uB3LYP+/cc-PVTZ level of theory.

The frontier orbitals are responsive to THF-induced desymmetrization of the Fe(CN^{t}Bu) edges and interconnect the reactivity of active sites positioned on the same α or β cluster face. Molecular orbital diagrams for *cis*-(α,β)-[**Fe$_3$**(CNMe)$_2$]$^+$, (α,α,β)-[**Fe$_3$**(CNMe)$_2$(THF)]$^+$ and *trans*-(α,β)-[**Fe$_3$**(CNMe)(THF)]$^+$ are provided in Figure 3.9b, and select isosurface plots for molecular orbitals are provided in Figure 3.10. As noted in our *p*-DOS analysis, we observe two nearly-degenerate low-lying unfilled orbitals in the *b*-spin manifold of [**Fe$_3$**(CNMe)$_2$]$^+$. These orbitals propagate from the κ^4-Fe edge into the Co_6Se_8 support with equal contributions from the α or β cluster halves with *Fe···Se–Co···Se* antibonding topology, where dashed and solid lines indicate bonding or antibonding interactions between adjacent atoms. The delocalization of these orbitals confirms electronic overlap between appended Fe edge sites and the Co_6Se_8 support, which is in line with the high covalency anticipated for metal-chalcogenides.[25,43,44] Furthermore, the *Fe···Se* antibonding character of the LUMO/LUMO+1 orbitals explains the observed preference to form site-differentiated *cis*-(α,β)-[**Fe$_3$**(L)$_2$]$^+$ bis-adducts, as chemical oxidation would depopulate this edge-support antibonding orbital to reinforce edge-support Fe···Se bonding at the κ^4-Fe site.

Just as the α-coordination of THF breaks the symmetry of Fe(CNMe) edge sites within (α,α,β)-[**Fe$_3$**(CNMe)$_2$(THF)]$^+$, it also disrupts the degeneracy of the LUMO and LUMO+1 orbitals to afford *Fe···Se–Co···Se* orbitals with primary contributions from Co/Se atoms on the α or β cluster halves, respectively. This reveals how the ligand binding impacts the orientation of delocalized orbitals to direct the edge-support binding interactions. Notably, the *a*-SOMO is largely unaffected by the coordination of THF and maintains primarily non-bonding Se 4p lone pair character, poised to participate in Fe–Se binding with one of the Fe(CNMe) edges. Interestingly, the dissociation of the α-oriented CNMe to form *trans*-(α,β)-[**Fe$_3$**(CNMe)(THF)]$^+$ occurs with the population of the *Fe···Se–Co···Se b*-LUMO to afford a *b*-SOMO of the same phase as the previous non-bonding Se *a*-HOMO is buried due to Fe···Se bond formation at the new κ^4-Fe edge. In this process, a new *b*-LUMO is introduced that is primarily localized to the new κ^4-Fe edge with *Fe···Se–Co···Se* antibonding character oriented back toward the weak-field Fe(THF) edge site. This is intriguing in that it suggests α-oriented ligand-binding is favored at this new κ^4-Fe edge and would promote dissociation of the weaker THF ligand. This orbital analysis reveals how α/β-oriented ligand binding perturbs delocalized *Fe···Co/Se* frontier orbitals to promote directional edge-support binding interactions that encode regioselective ligand substitution patterns.

3.6 Chemical Disorder in Solid-State Structure of $\mathbf{Fe_3}(py)_3$

The inter-adsorbate effect is not only observed in the case of mono-oxidized $[\mathbf{Fe_3}]^+$, but it can also be resolved for its neutral analogues. Our above analysis demonstrates how $[\mathbf{Fe_3}]^+$ clusters favor formation of *cis*-(α,β)-$[\mathbf{Fe_3}(L)_2]^+$ adducts, ostensibly owing to the depopulation of a low-lying Fe–Se antibonding orbital (*Fe···Se–Co···Se*) upon chemical oxidation, which would in turn reinforce Fe–Se bonding to produce a κ^4-Fe edge site. Owing to the depopulation of this *Fe···Se–Co···Se*, the coordination of ligands (i.e. THF above) at this naked edge site, promotes migration of κ4-Fe binding to a neighboring, α-oriented edge. Similar trends are observed in the case of the tris(pyridyl) cluster, $\mathbf{Fe_3}(py)_3$, where in the solid state we observe fluctional κ^4-binding at one Fe edge. Single crystals of $\mathbf{Fe_3}(py)_x$ (x = 2, 3) were grown in the presence of excess pyridine (~30 equiv) to yield a disordered mixture of the tris-adduct (α,α,β)-$\mathbf{Fe_3}(py)_3$ (54%) and a bis-adduct *cis*-(α,β)-$\mathbf{Fe_3}(py)_2$ (46%).

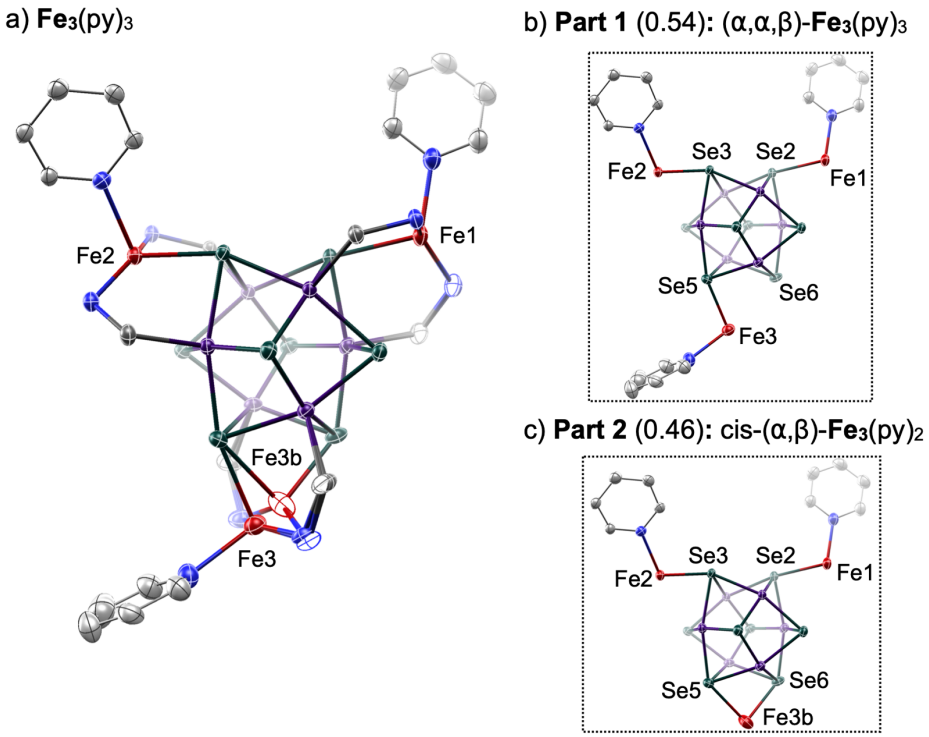


Figure 3.11. a) Solid-state structure of neutral $\mathbf{Fe_3}(py)_x$ (x = 2, 3) containing major and minor components of (α,α,β)-$\mathbf{Fe_3}(py)_3$ and *cis*-(α,β)-$\mathbf{Fe_3}(py)_2$, respectively. All phosphinoamide carbon atoms and hydrogen atoms are omitted for clarity. Thermal ellipsoids are plotted with 50% probability. Select interatomic distances (Å): Fe2-Se3 2.555(5), Fe1-Se2 2.507(5), Fe3-Se5 2.487(4), Fe3b-Se5 2.544(6), Fe3b-Se6 2.353(7).

3.7 Molecular Formalism for the Inter-adsorbate Dynamics

At solid-liquid interfaces, chemically equivalent surface metals are distinguished as they compete for substrate-binding and activation, their reactivities intertwined through a supporting lattice. Here, we show that interfacial metal-support interactions are responsive to substrate binding and promote regiospecific through-cluster ligand substitution dynamics at the active sites of a Fe/Co/Se nanocluster. This provides an unprecedented atom-scale glimpse into the inter-adsorbate forces that guide reactive heterogenous surfaces. Utilizing a combined spectroscopic, crystallographic and computational analysis, we explore the electronic origins of 1) the site-differentiated bis-ligation observed for $[\mathbf{Fe_3}]^+$ clusters, and 2) the regioselectivity observed in allosteric ligand substitution. Ultimately, this work introduces a molecular formalism to investigate the inter-adsorbate effect, which we anticipate to vary as a function of edge site/support composition as well as the edge site/substrate interaction strength.

3.8 Experimental Details

3.8.1 *General Considerations*

All syntheses were conducted under a dinitrogen atmosphere using a standard Schlenk line or an LC Technology Solutions glovebox equipped with a freezer set to –35 °C. All glassware was dried at 160 °C for a minimum of 12 h prior to use. Solvents were purchased from Fischer Scientific and degassed, dried and purified using solvent purification columns housed in a stainless-steel cabinet and dispensed by a stainless-steel Schlenk line manufactured by JC Meyer Solvent Systems. Tetrahydrofuran (THF), diethyl ether (Et_2O), acetonitrile (MeCN), and methylene chloride (DCM) are passed through two packed columns of neutral alumina. *n*-Pentane and toluene are passed through a column packed with alumina, and one containing Q5 reactant, a copper(II) oxide oxygen scavenger. All solvents were passed through an in-line, 2 μm filter, then stored over activated 3Å molecular sieves in the glovebox. 3Å molecular sieves were purchased from Sigma Aldrich and activated under vacuum at 300 °C for 48 h.

Deuterated solvents (C_6D_6, CD_2Cl_2, CD_3CN) were purchased from Cambridge Isotope Laboratories, Inc., degassed and dried over activated 3Å molecular sieves in the glovebox for a minimum of 72 h. $FeCl_2$ (anhydrous, 98+%) was purchased from Strem Chemicals, Inc. and dried

under vacuum at 120 °C for 24 h prior to use. $Co_2(CO)_8$ (stabilized with 2-5% hexanes; Strem Chemicals, Inc.) was stored in the glovebox freezer and used as received. The aminophosphine $Ph_2PN(H)Tol$ (Ph = phenyl, Tol = 4-tolyl), $Co_6Se_8L^H{}_6$, $Li_6(py)_6Co_6Se_8L_6$, $Fe_3Co_6Se_8L_6$, and $[Fe_3(CN^tBu)_2Co_6Se_8L_6][PF_6]$ were prepared according to the literature.[37,45] Chlorodiphenylphosphine (97%) and p-toluidine (99+%) were purchased from Alfa Aesar and used without further purification. Selenium (99.5%, powder, 200 mesh) and n-butyl lithium (2.5 M in hexanes) were purchased from Sigma Aldrich and used without further purification. *Tert*-butyl isocyanide (CN^tBu, 98%) was purchased from Sigma Aldrich and stored over activated 3Å molecular sieves in the glovebox for 72 h prior to use. Ferrocenium hexafluorophosphate (97%) was purchased from Sigma Aldrich and recrystallized from dry acetone and diethyl ether prior to use. Silver triflate (≥99%) was purchased from Sigma Aldrich and used without further purification. Tetra(*n*-butyl)ammonium hexafluorophosphate ($[^nBu_4N][PF_6]$, 98%) was purchased from Sigma Aldrich and recrystallized from ethanol upon cooling from 78 to –35 °C three times followed by removal of volatiles under reduced pressure at 110 °C for 24 h prior to its use.

Solution-phase FTIR spectra were recorded at 298 K on a Perkin Elmer Frontier FTIR spectrometer with a spectral resolution of 0.5 cm^{-1} equipped with a solution-cell holder. UV-vis-*n*IR absorption spectra were acquired using a Varian Cary 5000 UV-Vis-*n*IR spectrometer in *n*IR quartz cuvettes (Spectrocell Inc., 10 mm path length, 220–3500 nm spectral window). Extinction coefficients were collected in triplicate for each compound and reported as an average. NMR spectra were acquired at 25 °C on Bruker 300 or 500 MHz spectrometers, as indicated. ^1H and ^{13}C NMR spectra were referenced to residual deuterated solvent peaks. ^{31}P NMR spectra were externally referenced to phosphoric acid, and ^{19}F NMR spectra were referenced externally to CCl_3F.

3.8.2 *Synthesis and Isolation of $[Fe_3(MeCN)Co_6Se_8L^{Tol}{}_6][OTf]$, **$Fe_3(MeCN)(OTf)$***

A 100 mL round bottom flask equipped with a magnetic stir bar was loaded with **Fe_3** (0.600 g, 0.207 mmol, 1 equiv), AgOTf (0.053 g, 0.207 mmol, 1 equiv), acetonitrile (2 mL) and DCM (50 mL). The mixture was stirred at 25 °C for 2 h, and then passed through a plug of Celite in a fritted-glass funnel to remove silver triflate and silver metal. The filtrate was evaporated to dryness under reduced pressure, and the product was extracted in acetonitrile (10 mL). The acetonitrile extracts were layered with diethyl ether and stored at –35 °C for 24 h to yield black needles. These were

collected on a fritted-glass filter and volatiles were removed under reduced pressure to yield **Fe$_3$**(MeCN)(OTf) (0.331 g, 0.107 mmol, 48%).

UV-vis-*n*IR (DCM, 25 °C) λ: 431 (ϵ = 38500 M^{-1} cm^{-1}) nm. ^{1}H NMR (CD_3CN, 300 MHz) δ: 50.07 (s, 18 H, $\nu_{1/2}$ = 31 Hz, tolyl-C*H*$_3$); 32.23 (s, 12H, $\nu_{1/2}$ = 51 Hz); 22.76 (s, 12H, $\nu_{1/2}$ = 225 Hz), 17.38 (s, 12H, $\nu_{1/2}$ = 183 Hz); 15.01 (s, 12H, $\nu_{1/2}$ = 39 Hz); 11.72 (s, 6H, $\nu_{1/2}$ = 27 Hz); 10.41 (s, 12H, $\nu_{1/2}$ =42 Hz); 3.05 (s, 6H, $\nu_{1/2}$ = 31.5 Hz); –38.12 (s, 12H, $\nu_{1/2}$ = 471 Hz) ppm. ^{1}H NMR (CD_2Cl_2, 300 MHz) δ: 61.41 (s, $\nu_{1/2}$ = 1140 Hz, tolyl-C*H*$_3$); 38.66 (s, $\nu_{1/2}$ = 474 Hz); 19.33 (s, $\nu_{1/2}$ = 902 Hz), 14.66 (s, 12H, $\nu_{1/2}$ = 55 Hz); 12.10 (s, $\nu_{1/2}$ = 390 Hz); 11.73 (s, $\nu_{1/2}$ = 59 Hz); 8.84 (s, $\nu_{1/2}$ = 59 Hz); 1.91 (s, $\nu_{1/2}$ = 37 Hz); 1.82 (s, $\nu_{1/2}$ = 52 Hz, MeCN-C*H*$_3$); –48.56 (s, $\nu_{1/2}$ = 1414 Hz) ppm. ^{19}F NMR (CD_3CN, 471 MHz) δ: –79.11 (s, $\nu_{1/2}$ = 272 Hz) ppm; (C_6D_6, 471 MHz) δ: +6.47 (s, $\nu_{1/2}$ = 258 Hz) ppm; (CD_2Cl_2, 471 MHz) δ: –63.00 (s, $\nu_{1/2}$ = 787 Hz) ppm. μ_{eff} (Evans Method, CD_2Cl_2, 298K): 8.8(3) μ_B. Elemental analysis found (calc.) for **Fe$_3$**(MeCN)(OTf) (Formula: $C_{117}H_{105}Co_6F_3Fe_3N_7O_3P_6SSe_8$): Co 11.32 (11.46), Se 20.30 (20.48), P 5.91 (6.02).

3.8.3 *Synthesis and Isolation of [Fe$_3$(THF)$_2$Co$_6$Se$_8$L$^{Tol}_6$][PF$_6$], [**Fe$_3$**(THF)$_2$][PF$_6$]*

A 50 mL Schlenk flask equipped with a Teflon valve and magnetic stir bar was loaded with **Fe$_3$** (1.000 g, 0.345 mmol, 1 equiv) and THF (25 mL). The dark red-brown slurry was stirred at room temperature and DCM (8 mL) was added until the mixture was homogeneous. The solution was then cooled to –35 °C and ferrocenium hexafluorophosphate (0.115 g, 0.345 mmol, 1 equiv) was added portion wise with rapid stirring. The solution was brought to room temperature and stirred for 1 h, over the course of this time the solution adopted a dark red-purple color. The solution was passed through a plug of Celite on a fritted glass funnel and the filtrate was layered with *n*-pentane for bulk crystallization. The solution was kept still at room temperature for 16 hours, affording a crop of large, dark red prismatic crystals which collected on a fritted glass funnel and washed with additional pentane (3 x 6 mL). After removal of volatiles from these solids *in vacuo*, this process afforded [**Fe$_3$**(THF)$_2$][PF_6] as an analytically pure, crystalline solid (0.977 g, 0.307 mmol, 89%).

^{1}H NMR (CD_3CN, 300 MHz) δ: 50.16 (s, 18 H, $\nu_{1/2}$ = 65 Hz, tolyl-C*H*$_3$); 33.27 (s, 12H, $\nu_{1/2}$ = 69 Hz); 22.94 (s, 12H, $\nu_{1/2}$ = 247 Hz), 17.45 (s, 12H, $\nu_{1/2}$ = 208 Hz); 15.03 (s, 12H, $\nu_{1/2}$ = 55 Hz); 11.75 (s, 6H, $\nu_{1/2}$ = 40 Hz); 10.42 (s, 12H, $\nu_{1/2}$ = 62 Hz); 3.64 (s, 6H, $\nu_{1/2}$ = 36 Hz); 13.08 (s, 8H, $\nu_{1/2}$ = 44

Hz); 1.80 (s, 8H, $\nu_{1/2}$ = 40 Hz); –38.25 (s, $\nu_{1/2}$ = 550 Hz) ppm. ^{1}H NMR (CD_2Cl_2, 300 MHz) δ: ppm. ^{19}F NMR (CD_3CN, 471 MHz) δ: ppm. μ_{eff} (Evans Method, CD_2Cl_2, 298K): 9.5(3) μ_B. Elemental analysis found (calc.) for [**Fe$_3$**(THF)$_2$][PF_6] (Formula: $C_{122}H_{118}Co_6F_6Fe_3N_6O_2P_7Se_8$): Co 11.05 (11.11), Se 20.01 (19.84), P 6.85 (6.81).

3.8.4 *Adapted Synthesis of [Fe$_3$(CN^{t}Bu)$_2$Co$_6$Se$_8$L$^{Tol}_6$][PF$_6$], [**Fe$_3$**(CN^{t}Bu)$_2$][PF$_6$]*

A 50 mL Schlenk flask equipped with a Teflon valve and magnetic stir bar was loaded with **Fe$_3$** (1.000 g, 0.345 mmol, 1 equiv) and DCM (25 mL). The dark red-brown solution was stirred at room temperature until the mixture was homogeneous. The solution was then spiked with neat CN^{t}Bu (78 μL, 0.69 mmol, 2 equiv) and cooled to –35 °C before solid ferrocenium hexafluorophosphate (0.115 g, 0.345 mmol, 1 equiv) was added portion wise with rapid stirring. This mixture was warmed to room temperature and stirred for 1 h. Over the course of this time the solution adopted a dark red-purple color. The solution was passed through a plug of Celite on a fritted glass funnel and the filtrate was layered with *n*-pentane (~120 mL) for bulk crystallization. The layered mixture was kept still at room temperature for 16 hours, affording a crop of large, dark red prismatic crystals, which were collected on a fritted glass funnel and washed with additional pentane (3 x 6 mL). This material was recrystallized once more to remove trace paramagnetic impurities. Volatiles were removed from these solids *in vacuo* to afford [**Fe$_3$**(CN^{t}Bu)$_2$][PF_6] as an analytically pure, crystalline solid (0.952 g, 0.297 mmol, 86%).

UV-vis-*n*IR (DCM, 25 °C) λ: 430 (ϵ = 38400 M^{-1} cm^{-1}) nm. ^{1}H NMR (CD_2Cl_2, 300 MHz) δ: 57.70 (s, $\nu_{1/2}$ = ~6000 Hz); 36.46 (s, $\nu_{1/2}$ = 2500 Hz); 21.28 (s, $\nu_{1/2}$ = 2430 Hz), 15.52 (s, $\nu_{1/2}$ = 660 Hz); 14.64 (s, $\nu_{1/2}$ = 65 Hz); 11.23 (s, 6H, $\nu_{1/2}$ = 112 Hz); 10.86 (s, $\nu_{1/2}$ = 99 Hz); 3.24 (s, $\nu_{1/2}$ = 85 Hz); –0.58 (s, $\nu_{1/2}$ = 41 Hz); –37.85 (s, $\nu_{1/2}$ = ~8000 Hz) ppm. ^{1}H NMR (CD_3CN, 300 MHz) δ: 49.82 (s, 18H, $\nu_{1/2}$ = 102 Hz, tolyl-C*H*$_3$); 33.22 (s, 12H, $\nu_{1/2}$ = 65 Hz); 21.52 (s, 12H, $\nu_{1/2}$ = 211 Hz), 16.90 (s, 12H, $\nu_{1/2}$ = 173 Hz); 14.52 (s, 12H, $\nu_{1/2}$ = 34 Hz); 10.89 (s, 20H, $\nu_{1/2}$ = 34 Hz); 3.42 (s, 6H, $\nu_{1/2}$ = 31 Hz); 0.54 (s, 18H, $\nu_{1/2}$ = 24 Hz, CN^{t}Bu-C*H*$_3$); –35.22 (s, $\nu_{1/2}$ = 500 Hz) ppm. ^{19}F NMR (CD_3CN, 471 MHz) δ: –72.96 (*d*, $^{1}J_{PF}$ = 718 Hz) ppm. μ_{eff} (Evans Method, CD_2Cl_2, 298K): 9.9(3) μ_B. Elemental analysis found (calc.) for [**Fe$_3$**(CN^{t}Bu)$_2$][PF_6] (Formula: $C_{124}H_{120}Co_6F_6Fe_3N_8P_7Se_8$): Co 11.06 (11.03), Se 19.89 (19.71), P 6.90 (6.76).

3.8.5 *Solution-phase Fourier Transform Infrared Spectroscopy*

The solution-phase ligand substitution dynamics of $[\mathbf{Fe_3}]^+$ with *tert*-butyl isocyanide (CN^tBu) were studied by monitoring the isocyanide stretching frequency (ν_{CN}) using a Fourier transform infrared spectroscopy (FTIR). Solutions of $[\mathbf{Fe_3}(THF)_2][PF_6]$ (7.8 mM in THF or DCM) were treated with varying amounts of CN^tBu (0.1–2.0 equiv; added via microsyringe as a 0.5 M THF or DCM stock solution). Separate spectra were recorded for $[\mathbf{Fe_3}(CN^tBu)_2][PF_6]$ dissolved in neat THF or DCM, and for neat THF or DCM for solvent subtraction. All samples were stirred until homogeneous and transferred to an air-free 2 mm pathlength solution IR cell with CaF_2 windows. All FTIR spectra were collected at room temperature (~298 K). Each spectrum was background corrected to account for atmospheric contributions to the IR absorption pattern followed by a subtraction of a pure solvent spectrum.

In neat THF solutions two major CN stretching are resolved in these spectra at 2184 and 2135 cm^{-1}, corresponding to bound $Fe(CN^tBu)$ and free CN^tBu, respectively. These CN stretching frequencies are slightly blue-shifted in DCM solutions (2185 and 2140 cm^{-1}), and analysis of $[\mathbf{Fe_3}(CN^tBu)_2][PF_6]$ in DCM reveals a single major peak at 2185 cm^{-1}, with no appreciable amount of free CN^tBu. To assess the relative concentrations of free and bound CN^tBu, these peaks were fit to a series of four gaussian curves, accounting for the contribution of minor overtone bands at ~2160 and 2118 cm^{-1}, which reliably reproduced the recorded line shape with a low residual. The major peaks for bound $Fe(CN^tBu)$ and free CN^tBu were integrated and the ratio of their areas was used to calculate concentrations via relation to the known total concentrations of CN^tBu and $[\mathbf{Fe_3}]^+$.

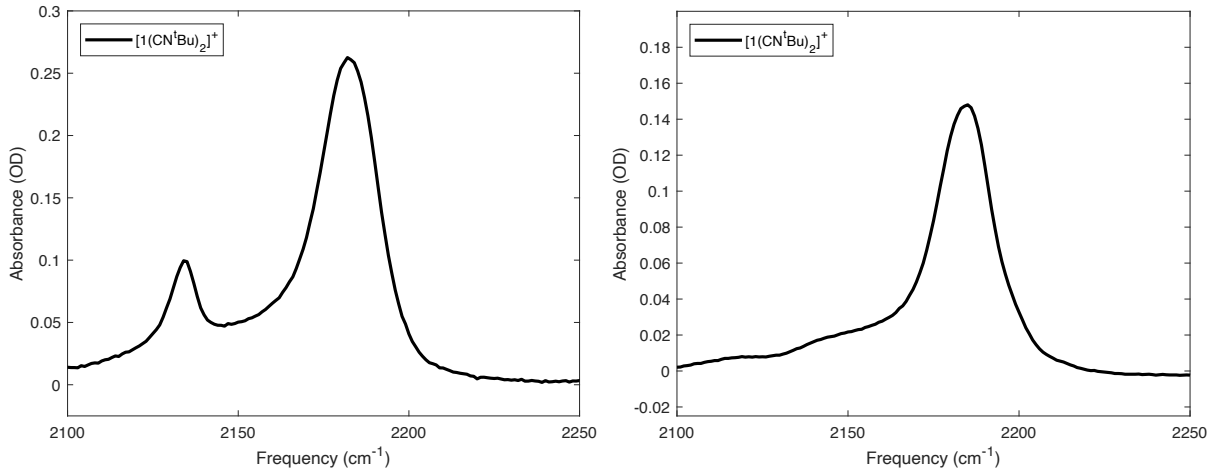


Figure 3.12. FTIR absorption spectra for [**Fe$_3$**(CN^{t}Bu)$_2$][PF$_6$] collected in neat THF (left) and DCM (right).

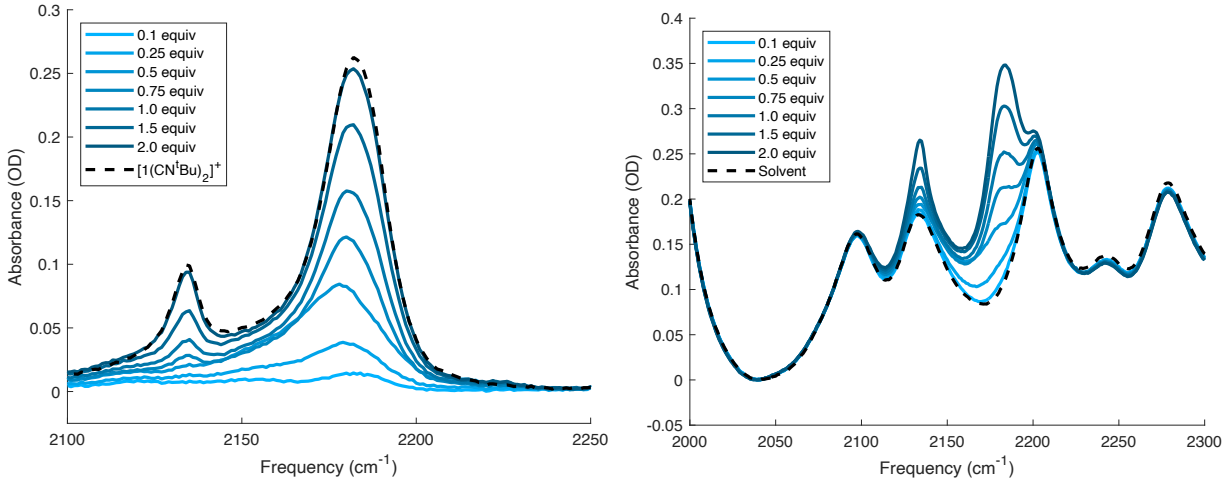


Figure 3.13. FTIR absorption spectra recorded for [**Fe$_3$**(THF)$_2$][PF$_6$] upon titration with varying equivalents of CN^{t}Bu in neat THF both after (left) and before solvent subtraction (right).

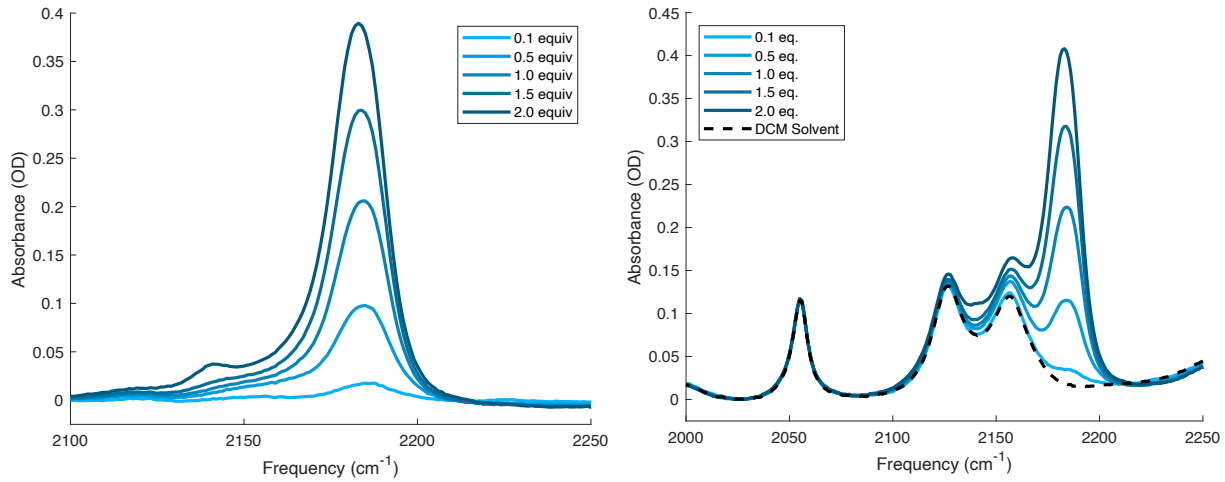


Figure 3.14. FTIR absorption spectra recorded for [**Fe$_3$**(THF)$_2$][PF$_6$] upon titration with varying equivalents of CN^{t}Bu in neat DCM after (left) and before solvent subtraction (right).

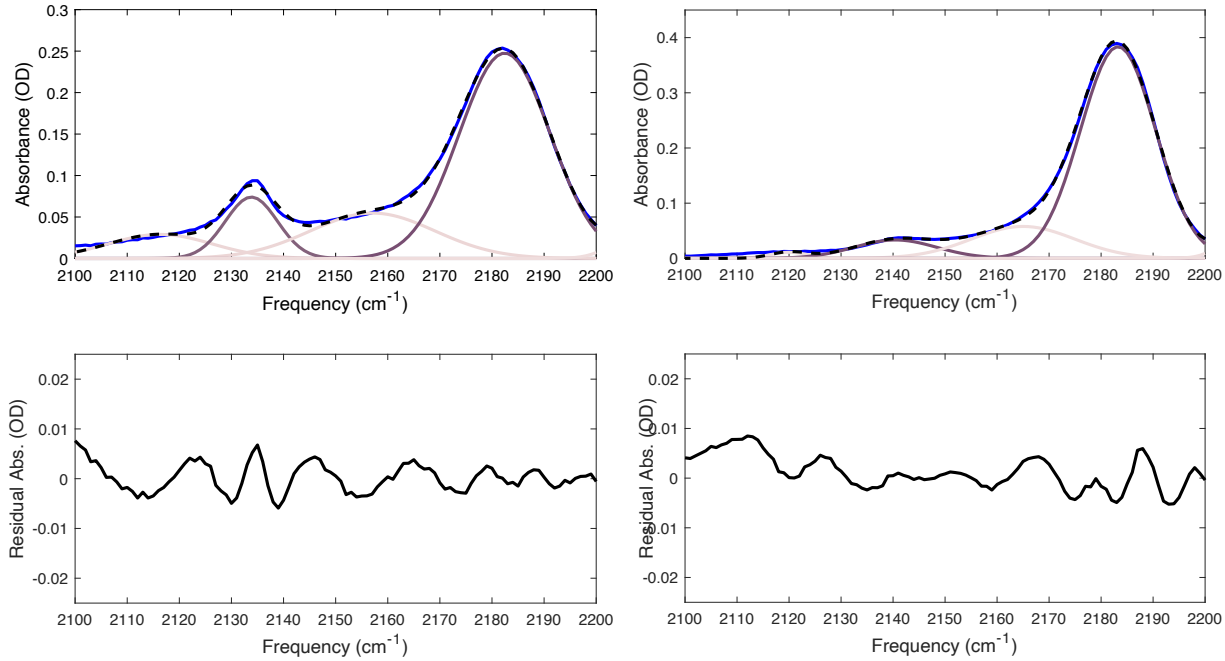


Figure 3.15. Representative gaussian fits used to assess the concentrations of bound and free CN^{t}Bu (dark gray curves) in both THF (left) and DCM (right). Light grey curves are attributed to overtone bands and were necessary to achieve a good fit to the line shape for the major CN^{t}Bu stretches.

3.8.6 *Magnetic Characterization of [**Fe$_3$**(CN^{t}Bu)$_2$][PF$_6$]*

dc Magnetic susceptibility data for [**Fe$_3$**(CN^{t}Bu)$_2$][PF$_6$] were collected on warming from 5 to 300 K under applied fields of 0.1, 0.5, and 1 T using a Quantum Design Inc. PPMS DynaCool

equipped with a 14 T magnet. To prepare these samples, polycrystalline material was loaded within a VSM powder sample holder (P125E, Quantum Design Inc.) that was carefully sealed with a thin loop of epoxy. Crushed crystalline material placed under vacuum at 60 °C for 2 hours prior to analysis. All magnetic susceptibility data was corrected for diamagnetic contributions from the analyte calculated using Pascal's constants,[46] as well as for the susceptibility of the capsule and sample holder. Magnetization data was recorded at 50 K between –14 and 14 T to confirm the absence of any ferromagnetic impurities. Further, variable-temperature *dc* magnetic susceptibility does not decrease with increasing field strength, providing further support that the samples are free of ferromagnetic impurities. Susceptibility data (0.5 T applied field) for [**Fe$_3$**(CN^{t}Bu)$_2$][PF$_6$] provides a reasonable value for a 3 x Fe(II) (s = 2), 1 x $Co_6Se_8^{1+}$ (s = ½) spin system, with S_{Tot} = 13. This data was modeled using PHI in order to extract the g-value (g = 2.03, R^2 = 1.18), but a quantitative model was not developed due to the complexity of the system.[47] Variable-temperature variable-field reduced magnetization data supports the presence of a high-spin ground state, but magnetic saturation is not reached under applied fields of up to 7 T and temperatures down to 2.5 K. Accordingly, the selected spin multiplicity for DFT analysis was assigned based on the observed magnetic susceptibility at 298 K.

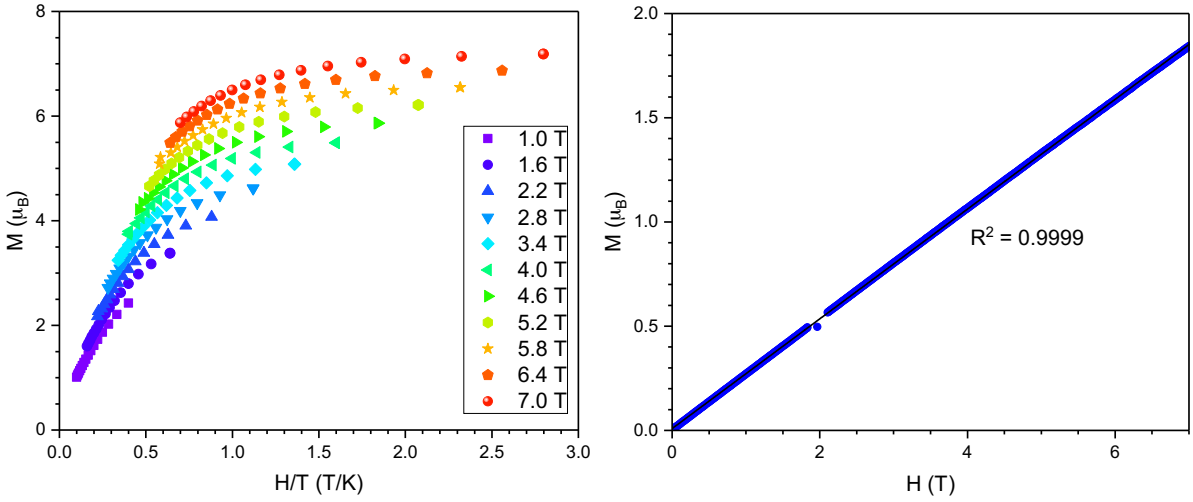


Figure 3.16. (left) Variable-temperature, variable-field reduced magnetization data for [**Fe$_3$**(CN^{t}Bu)$_2$][PF$_6$], collected upon warming from 2.5 to 10 K at each applied field. This plot confirms the presence of a high-spin ground state, but the sample resists magnetic saturation under applied magnetic fields up to 7.0 T. (right) Magnetization of [**Fe$_3$**(CN^{t}Bu)$_2$][PF$_6$] recorded on sweeping the applied field from 0 and 7 T at 50 K. This plot confirms the absence of ferromagnetic impurities.

3.8.7 *X-ray Structure Determination*

Single crystals suitable for X-ray analysis, grown according to methods detailed below, were coated in deoxygenated paratone oil and mounted on a 20 μm CryoLoop™ (Hampton Research, 18 mm mount, 0.2 to 0.3 mm loop diameter). Data was collected at –173 °C on a Bruker APEX II single crystal X-ray diffractometer, with a Mo source. Data was integrated and scaled using SAINT, SADABS within the APEX2 software package by Bruker.[48] Solution by direct methods (SHELXT[49] or SIR97[50,51]) produced a complete heavy atom phasing model consistent with the proposed structure. Structures were completed by difference Fourier synthesis with SHELXL.[52–54] Scattering factors are from Waasmair and Kirfel.[55] Hydrogen atoms were placed in geometrically idealized positions and constrained to ride on their parent atoms with C–H distances in the range 0.95–1.00 Å. Isotropic thermal parameters U_{eq} were fixed such that they were $1.2U_{eq}$ of their parent atom Ueq for CHs and $1.5U_{eq}$ of their parent atom U_{eq} in case of methyl groups. All non-hydrogen atoms were refined anisotropically by full-matrix least-squares.

3.8.7.1 [**Fe$_3$**(THF)$_2$][PF$_6$]

Dark red, prismatic crystals of [**Fe$_3$**(THF)$_2$][PF$_6$] suitable for single-crystal X-ray analysis were grown by vapor diffusion of diethyl ether into a solution of **Fe$_3$** (1 equiv) and [Fc][PF$_6$] (1 equiv) in THF at 25 °C. The compound crystallizes in the monoclinic space group P 21/c, with an asymmetric unit consisting of a singular [**Fe$_3$**(THF)$_2$]$^+$ cluster accompanied by a [PF$_6$]$^-$ counterion. One of the amidophosphine phenyl groups as well as one *p*-tolyl substituent exhibit rotational disorder and as a result they were modeled over two positions.

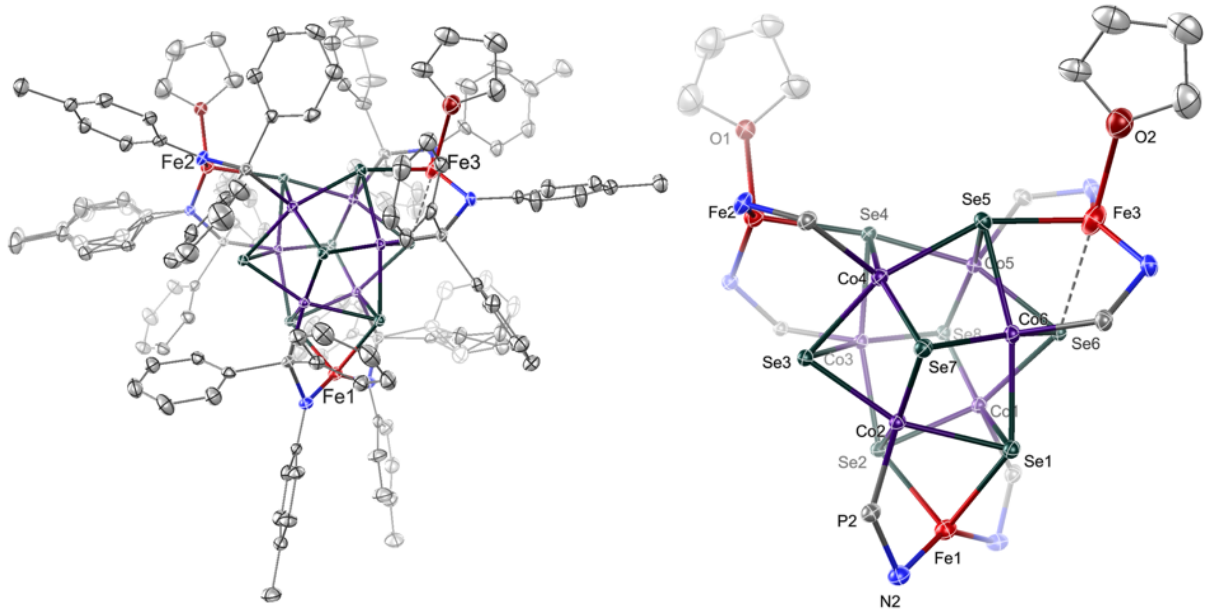


Figure 3.17. Single-crystal X-ray structure of [**Fe$_3$**(THF)$_2$][PF$_6$] (thermal ellipsoids plotted at 50% probability). Disordered amidophosphine substituents are plotted over two positions. All hydrogen atoms have been omitted for clarity.

3.8.7.1 **Fe$_3$**(MeCN)(OTf)

Long, dark-red needles suitable for single crystal X-ray analysis were grown via vapor diffusion of diethyl ether into a concentrated acetonitrile solution at –35 °C over the course of 72 h. The compound crystallizes in the orthorhombic Pbca space group, and the asymmetric unit contains a single cluster, the triflate counterion, and two unbound diethyl ether molecules, one of which is disordered and was modeled over two positions. In the solid state, each of the three iron atoms exhibit a distinct coordination environment: one with a bound, rotationally disordered triflate anion (modeled over two positions), another with an acetonitrile molecule coordinated, and a third iron bound κ^4 to the $[Co_6Se_8L_6]^{6-}$ ligand framework.

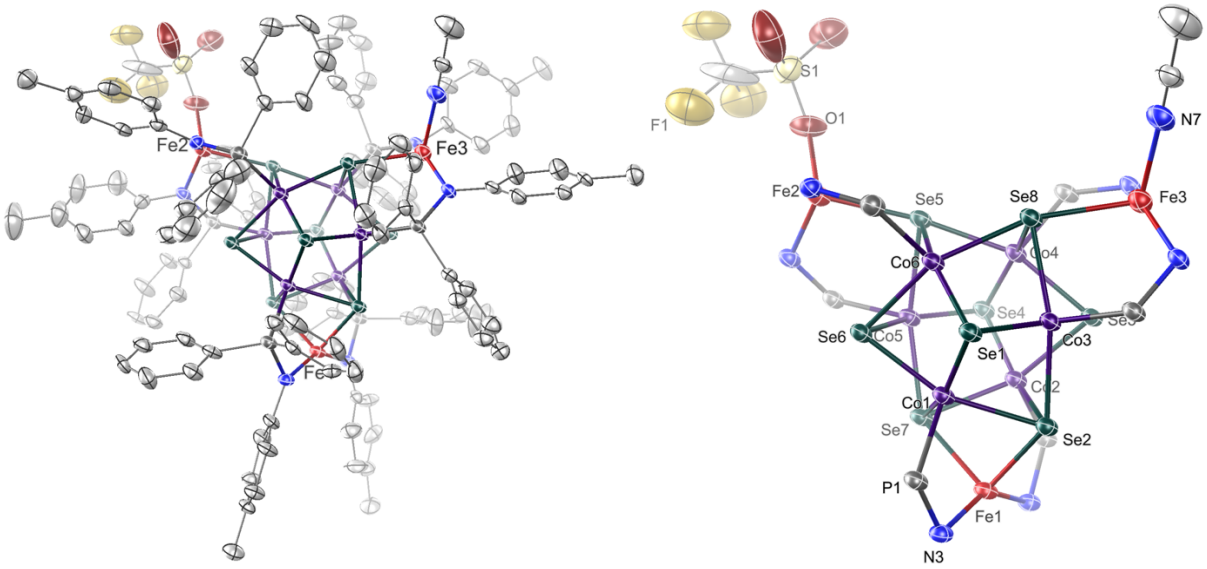


Figure 3.18. Single-crystal X-ray structure of **Fe$_3$**(MeCN)(OTf) with thermal ellipsoids plotted at 50% probability. All hydrogen atoms, the disordered triflate fragment and two co-crystallizing diethyl ether molecules have been omitted for clarity.

3.8.7.2 Disordered [**Fe$_3$**(CN^{t}Bu)$_2$(THF)][PF$_6$] (1st measurement)

Dark red, prismatic crystals of [**Fe$_3$**(CN^{t}Bu)$_2$(THF)][PF$_6$] were grown via slow diffusion of diethyl ether into a solution of [**Fe$_3$**(CN^{t}Bu)$_2$][PF$_6$] in THF at 25 °C. The compound crystallizes in the triclinic space group $P\bar{1}$, and the asymmetric unit contains a singular [**Fe$_3$**(CN^{t}Bu)$_2$(THF)]$^+$ cluster accompanied by a [PF$_6$]$^-$ counterion. Although the refinement is of high quality, the structure exhibits multiple instances of positional disorder, which necessitated the implementation of numerous restraints. The [PF$_6$]$^-$ counterion exhibits rotational disorder, and as a result it needed to be modeled over two positions. With a THF ligand bound to Fe3, the coordination of CN^{t}Bu to Fe1 is fluctional in the solid-state, causing Fe1 to oscillate between κ^3 and κ^4 binding. Further, both CN^{t}Bu ligands exhibit positional disorder and were modeled over two positions, one of which oscillates between a bound and unbound positions. Finally, two of the amidophosphines exhibit positional disorder and as a result were modeled over two positions. Taking all of these instances of disorder into consideration, the structure was modeled as a co-crystallizing mixture of [**Fe$_3$**(CN^{t}Bu)$_2$(THF)]$^+$ and [**Fe$_3$**(CN^{t}Bu)(THF)]$^+$ with 0.76 and 0.24 relative contributions, respectively. Crystals were grown in this manner in triplicate with each diffraction measurement revealed the presence of the same chemical disorder.

Elemental analysis found (calc.) for crystalline [**Fe$_3$**(CN^{t}Bu)$_2$(THF)][PF$_6$] (Formula: $C_{128}H_{128}Co_6F_6Fe_3N_8OP_7Se_8$): Co 10.82 (10.79), Se 19.49 (19.27), P 6.63 (6.61).

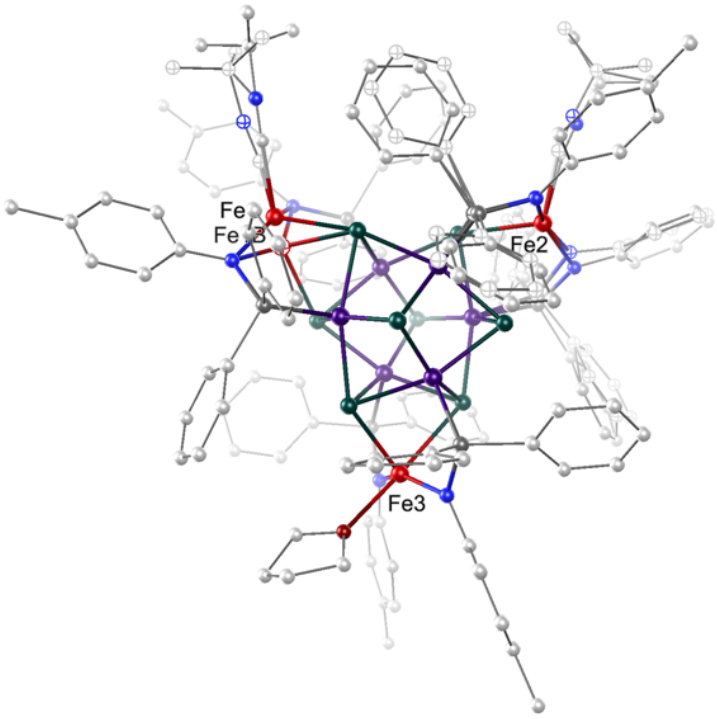


Figure 3.19. Solid-state structure of co-crystallized [**Fe$_3$**(CN^{t}Bu)$_2$(THF)]$^+$ and *trans*-(α,β)-[**Fe$_3$**(CN^{t}Bu)(THF)]$^+$ plotting both disordered components, which are present in a 76:24 ratio, respectively. Atoms associated only with the secondary component, *trans*-(α,β)-[**Fe$_3$**(CN^{t}Bu)(THF)]$^+$ are depicted as hollow spheres. All hydrogen atoms and the rotationally disordered [PF$_6$]$^-$ counterion have been omitted for clarity.

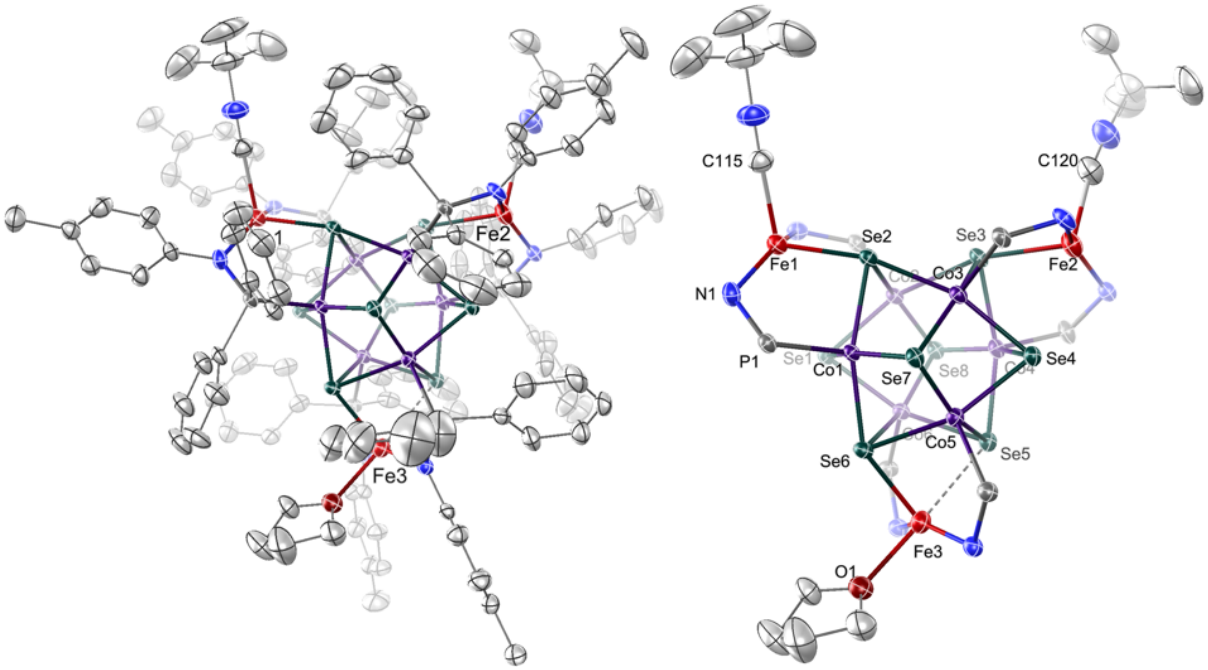


Figure 3.20. Single-crystal X-ray structure of (α,α,β)-[**Fe$_3$**(CN^{t}Bu)$_2$(THF)][PF$_6$] with thermal ellipsoids plotted at 50% probability. All hydrogen atoms and the rotationally disordered [PF$_6$]$^-$ counterion have been omitted for clarity.

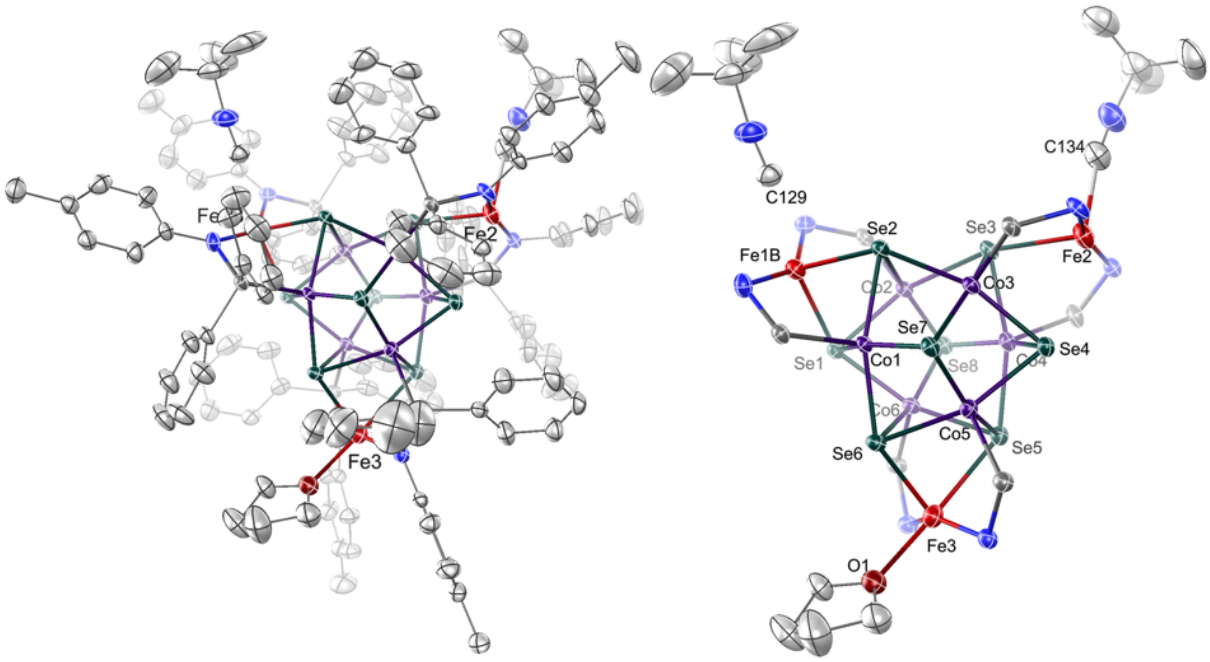


Figure 3.21. Single-crystal X-ray structure of *trans*-(α,β)-[**Fe$_3$**(CN^{t}Bu)(THF)]$^+$ including a dissociated CN^{t}Bu molecule proximal to Fe1B. Thermal ellipsoids are plotted at 50% probability. All hydrogen atoms and the rotationally disordered [PF$_6$]$^-$ counterion have been omitted for clarity.

3.8.7.3 Disordered [**Fe$_3$**(CN^{t}Bu)$_2$(THF)][PF$_6$] (2nd measurement)

As demonstration of the reproducibility of the chemical disorder we observe in the solid-state, multiple structures were determined for single crystalline samples of the disordered crystals. Dark red, prismatic crystals of [**Fe$_3$**(CN^{t}Bu)$_2$(THF)][PF$_6$] were grown via slow diffusion of a 1:7 mixture of diethyl ether and pentane into a solution of [**Fe$_3$**(CN^{t}Bu)$_2$][PF$_6$] in THF at 25 °C. The compound crystallizes in the triclinic space group $P\bar{1}$, and the asymmetric unit contains a singular [**Fe$_3$**(CN^{t}Bu)$_2$(THF)]$^+$ cluster accompanied by a [PF$_6$]$^-$ counterion. Refinement is of high quality and the structure exhibits positional disorder similar to previous measurements. However, for this structure the co-crystallizing mixture of [**Fe$_3$**(CN^{t}Bu)$_2$(THF)]$^+$ and [**Fe$_3$**(CN^{t}Bu)(THF)]$^+$ exhibit slightly different relative contributions of 0.85 and 0.15, respectively.

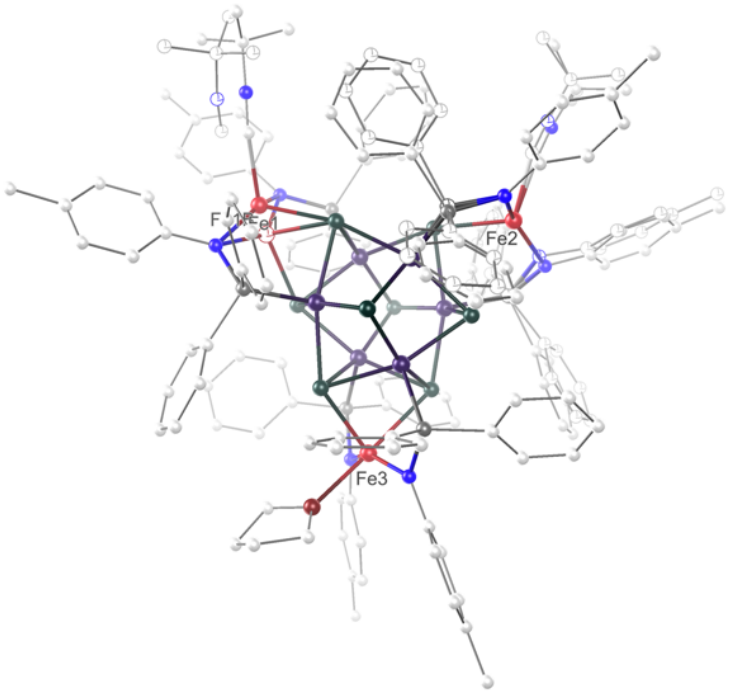


Figure 3.22. (2nd Measurement) Solid-state structure of co-crystallized [**Fe$_3$**(CN^{t}Bu)$_2$(THF)]$^+$ and *trans*-(α,β)-[**Fe$_3$**(CN^{t}Bu)(THF)]$^+$ plotting both disordered components, which are present in a 85:15 ratio, respectively. Atoms associated only with the secondary component, *trans*-(α,β)-[**Fe$_3$**(CN^{t}Bu)(THF)]$^+$ are depicted as hollow spheres. All hydrogen atoms and the rotationally disordered [PF$_6$]$^-$ counterion have been omitted for clarity.

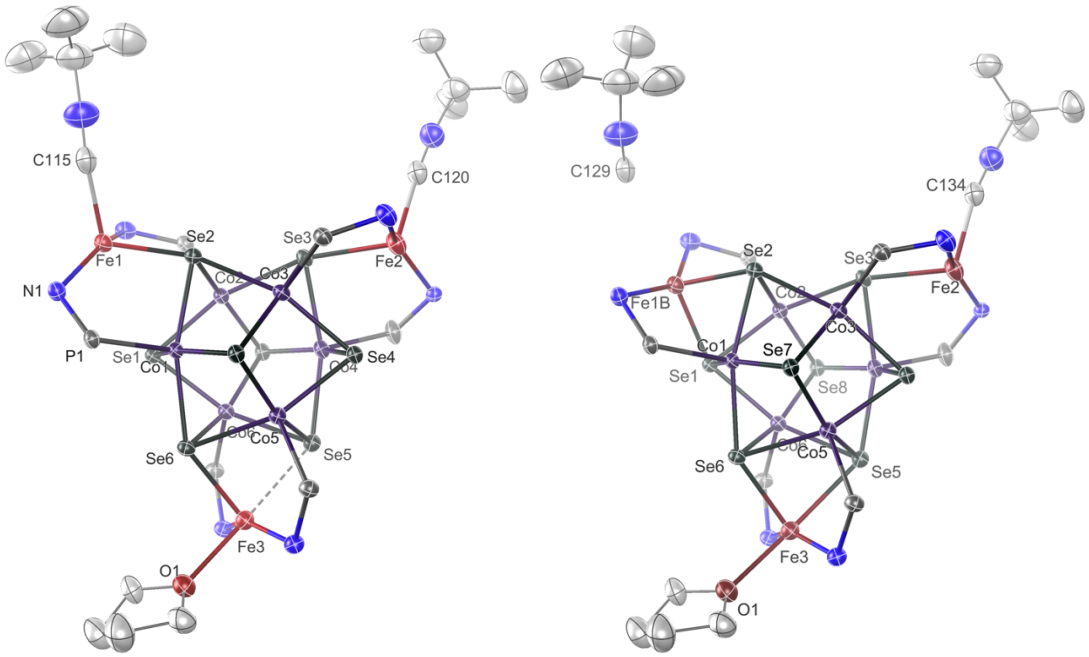


Figure 3.23. (2nd Measurement) Single-crystal X-ray structure of the two components of the disordered crystal structure: (α,α,β)-[**Fe$_3$**(CN^{t}Bu)$_2$(THF)][PF$_6$] (85%) and *trans*-(α,β)-[**Fe$_3$**(CN^{t}Bu)(THF)]$^+$ (15%). Thermal ellipsoids plotted at 50% probability. All hydrogen atoms and the rotationally disordered [PF$_6$]$^-$ counterion have been omitted for clarity.

Dark red prismatic crystals containing a disordered mixture of pyridyl-bound clusters, Fe$_3$(py)$_x$Co$_6$Se$_8$L$_6$ (**Fe$_3$**(py)$_x$, x = 2, 3) suitable for single crystal X-ray analysis were grown via vapor diffusion of *n*-pentane into a saturated toluene solution of **Fe$_3$** in the presence of excess pyridine (30 equiv) at 25 °C over the course of 48 hours. The compound crystallizes in the triclinic space group $P\bar{1}$, and the asymmetric unit contains a singular triiron cluster. Although the structure is of high quality, there are several instances of disorder. Three of the phosphinoamide ligands are disordered and as a result they were modeled over two positions. Due to the low affinity of the Fe edge site for surface ligands, the compound crystallizes as a 1:1 mixture of the bis- and tris-pyridine adducts, 1(py)$_3$ and 1(py)$_2$. Accordingly, Fe3 exhibits positional disorder, and was modeled as a mixture of κ^3 bound Fe with a pyridine bound and κ^4 bound Fe with no ancillary ligands with 0.544 and 0.456 relative contributions, respectively.

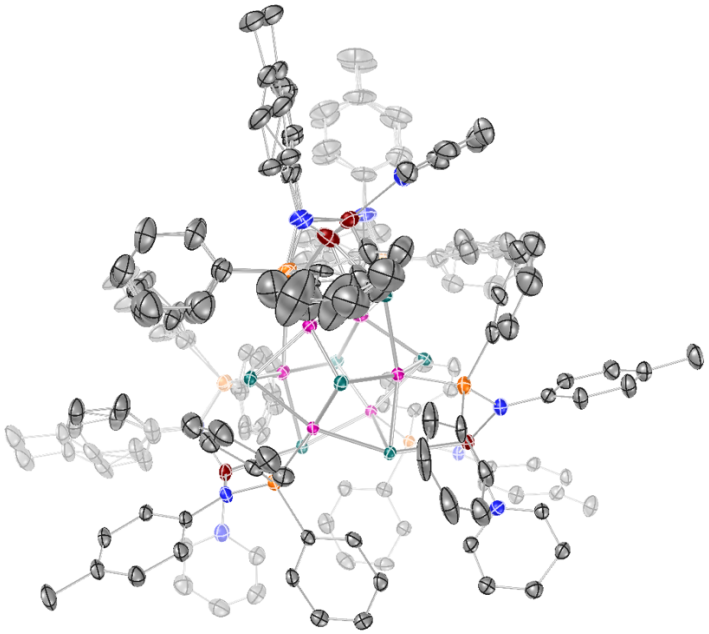


Figure 3.24. Single-crystal X-ray structure of **Fe$_3$**(py)$_x$ (x = 2, 3) (thermal ellipsoids plotted at 50% probability) with all disorder included. Three amidophosphine ligands and one Fe center are plotted over two positions. All hydrogen atoms have been omitted for clarity.

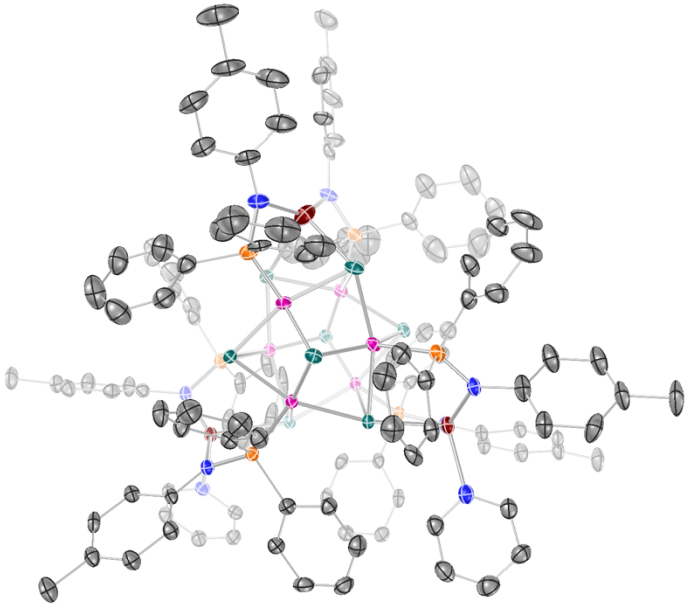


Figure 3.25. Single-crystal X-ray structure of **Fe$_3$**(py)$_2$ (46% abundance) (thermal ellipsoids plotted at 50% probability), which co-crystallizes with **Fe$_3$**(py)$_3$ (54% abundance). All hydrogen atoms and disorder have been omitted for clarity.

3.8.7.1 X-ray Tables

Table 3.1. Select interatomic distances for **Fe$_3$**(MeCN)(OTf), [**Fe$_3$**(CN^{t}Bu)$_2$][PF$_6$], and [**Fe$_3$**(phen)$_3$][PF$_6$]. Bonding parameters involving Fe centers as well as τ4 values are listed for Fe1, Fe2, and Fe3 from top to bottom.

Compound	Interatomic Distance (Å)						
	Fe…Se	Fe…Co	Co–P	*trans*-Co…Co	Co–Se	Fe–N^{Tol}	τ_4
Fe$_3$(MeCN)(OTf)	2.412(1) 2.414(1) 2.495(2) 3.483(2) 2.574(1) 3.194(2)	2.766(1) 2.785(2) 3.426(2) 3.652(2) 3.429(2) 3.453(2)	2.169(2) – 2.188(2)	4.151(1) 4.082(1) 4.132(2)	2.315(1) – 2.435(1) Avg. 2.35 ∑ 56.34	1.945(6) 1.956(6) 1.982(6) 1.980(6) 1.955(6) 1.980(6) Avg. 1.97	0.79 0.80 0.82
[**Fe$_3$**(CN^{t}Bu)$_2$][PF$_6$]	2.488(7) 3.288(6) 2.546(7) 3.254(8) 2.397(6) 2.433(5)	3.372(8) 3.458(6) 3.321(5) 3.551(9) 2.661(8) 2.853(7)	2.164(5) – 2.178(5)	4.044(9) 4.11(1) 4.18(1)	2.304(3) – 2.424(3) Avg. 2.35 ∑ 56.43	1.996(12) 1.972(13) 2.003(12) 1.996(12) 1.960(12) 1.914(12) Avg. 2.01	0.80 0.81 0.77
Fe$_3$(py)$_3$	2.507(5) 3.349(7) 2.555(5) 2.891(4) 2.487(4) 3.229(9)	3.404(8) 3.52(1) 3.212(5) 3.271(8) 3.335(5) 3.394(8)	2.14(3) – 2.18(2)	4.093(4) 4.175(8) 4.195(8)	2.3102(9) – 2.4073(8) Avg. 2.35 ∑ 56.43	2.01(2) 1.993(4) 2.017(4) 2.003(4) 1.93(2) 1.97(2) Avg. 1.97	0.81 0.75 0.75

Table 3.2. Select interatomic distances for [**Fe$_3$**(THF)$_2$][PF$_6$] and both measurements of [**Fe$_3$**(CN^{t}Bu)$_2$(THF)]/*trans*-(α,β)-[**Fe$_3$**(CN^{t}Bu)(THF)][PF$_6$]. Parameters involving Fe centers as well as τ4 values are listed for Fe1, Fe2, and Fe3 from top to bottom.

Compound	Interatomic Distance (Å)						
	Fe…Se	Fe…Co	Co–P	*trans*-Co…Co	Co–Se	Fe–N^{Tol}	τ_4
[**Fe$_3$**(THF)$_2$][PF$_6$]	2.4410(7) 2.4566(7) 2.5172(7) 3.388(8) 2.4441(8) 2.7294(8)	2.880(2) 2.755(3) 3.594(4) 3.395(2) 2.997(1) 3.049(4)	2.168(1) – 2.186(1)	4.130(3) 4.204(4) 4.0900(6)	2.3027(6) – 2.4274(6) Avg. 2.36 ∑ 56.55	1.970(3) 1.955(3) 1.982(3) 1.980(3) 1.964(3) 1.949(3) Avg. 1.97	0.75 0.81 0.75 0.58[a]
[**Fe$_3$**(CN^{t}Bu)$_2$(THF)]$^+$/*trans*-(α,β)-[**Fe$_3$**(CN^{t}Bu)(THF)]$^+$ (1)	2.403(4)[b] 2.471(4)[b] 2.498(1) 3.258(3) 2.541(1) 3.042(4) 2.450(1) 2.699(1)	2.853(4)[b] 2.888(4)[b] 3.370(4) 3.427(6) 3.216(6) 3.411(4) 2.981(1) 3.031(3)	2.162(2) – 2.194(9)	4.101(7) 4.113(8) 4.113(6)	2.3146(9) – 2.3928(9) Avg. 2.35 ∑ 56.45	1.966(6)[b] 2.023(5)[b] 2.010(5) 1.965(4) 2.011(5) 2.054(8) 2.002(4) 2.020(5) Avg. 1.99 Å	0.76 0.76[b] 0.73 0.74 0.46[a]
[**Fe$_3$**(CN^{t}Bu)$_2$(THF)]$^+$/*trans*-(α,β)-[**Fe$_3$**(CN^{t}Bu)(THF)]$^+$ (2)	2.37(1)[b] 2.46(1)[b] 2.512(7) 3.248(4) 2.537(7) 3.056(4) 2.436(3) 2.648(3)	2.84(1)[b] 2.86(1)[b] 3.374(5) 3.442(6) 3.216(6) 3.430(5) 2.963(6) 3.005(4)	2.15(2) – 2.18(1)	4.077(8) 4.117(8) 4.122(6)	2.309(2) – 2.396(2) Avg. 2.35 ∑ 56.43	1.99(1)[b] 2.04(1)[b] 2.015(6) 1.969(6) 2.033(7) 2.11(1) 2.012(6) 2.030(6) Avg. 2.02 Å	0.75 0.78[b] 0.73 0.74 0.24[a]

[a]Calculated τ_5 value for Fe3 taking the weakly associated Se atom into account for the κ^4-bound Fe sites.

[b]Parameters corresponding to the minor component, the κ^4-bound Fe1b of *trans*-(α,β)-[**Fe$_3$**(CN^{t}Bu)(THF)][PF$_6$].

Table 3.3. Crystallographic data for duplicate measurements of disordered [**Fe$_3$**(CN^{t}Bu)$_2$(THF)]/*trans*-(α,β)-[**Fe$_3$**(CN^{t}Bu)(THF)][PF$_6$]. Separate measurements denoted at (1) or (2).

Compound	[**Fe$_3$**(CN^{t}Bu)$_2$(THF)][PF$_6$] (1)	[**Fe$_3$**(CN^{t}Bu)$_2$(THF)][PF$_6$] (2)
Empirical formula	$C_{128}H_{128}Co_6F_6Fe_3N_8OP_7Se_8$	$C_{128}H_{128}Co_6F_6Fe_3N_8OP_7Se_8$
CCDC Number	2097609	
Formula weight	3277.98	3277.98
Temperature (K)	100(2)	100(2)
Wavelength (Å)	0.71073	0.71073
Crystal system	Triclinic	Triclinic
Space group	$P\bar{1}$	$P\bar{1}$
a (Å)	19.480(2)	19.480(2)
b (Å)	19.724(2)	19.724(2)
c (Å)	20.296(2)	20.296(2)
α (°)	89.548(3)	89.548(3)
β (°)	71.860(3)	71.860(3)
γ (°)	72.506(3)	72.506(3)
Volume (Å^3)	7036.4(13)	7036.4(13)
Z	2	2
ρ^{calc} (g cm^{-1})	1.547	1.547
Absorption coefficient (mm^{-1})	3.193	3.193
F(000)	3262	3262
Crystal size (mm^3)	0.600 x 0.420 x 0.090	0.600 x 0.420 x 0.090
Theta range for data collection (°)	1.445 to 28.339	1.293 to 28.282
Index ranges	–26≤h≤25, –26≤k≤26, –27≤l≤27	–25≤h≤25, –26≤k≤26, –27≤l≤27
Reflections collected	69531	228082
Independent reflections	34926 [R(int) = 0.0472]	60498 [R(int) = 0.0579]
Completeness to theta = 25.000°	99.8%	96.0
Data / restraints / parameters	34926 / 441 / 1671	60498 / 2829 / 1631
Goodness-of-fit on F^2	1.019	1.063
Final R indices [I>2sigma(I)]	R1 = 0.0605, wR2 = 0.1452	R1 = 0.0836, wR2 = 0.1546
R indices (all data)	R1 = 0.0964, wR2 = 0.1621	R1 = 0.1587, wR2 = 0.1887
Largest diff. peak and hole (e$^-$Å^{-3})	3.033 and –1.036	2.345 and –1.265

Table 3.4. Crystallographic data for [**Fe$_3$**(THF)$_2$][PF$_6$], **Fe$_3$**(MeCN)(OTf), and **Fe$_3$**(py)$_x$ (x = 2, 3).

Compound	[**Fe$_3$**(THF)$_2$][PF$_6$]	**Fe$_3$**(MeCN)(OTf)	**Fe$_3$**(py)$_x$ (x = 2, 3)
Empirical formula	$C_{122}H_{118}Co_6F_6Fe_3N_6O_2P_7Se_8$	$C_{123.32}H_{120.79}Co_6F_3Fe_3N_7O_{4.58}P_6SSe_8$	$C_{253}H_{229}Co_{12}Fe_6N_{17}P_{12}Se_{16}$
CCDC Number	2097608	2090142	2090143
Formula weight	3183.82	3201.83	6184.80
Temperature (K)	100(2)	100(2)	100(2)
Wavelength (Å)	0.71073	0.71073	0.71073
Crystal system	Monoclinic	Orthorhombic	Triclinic
Space group	P 21/c	Pbca	$P\bar{1}$
a (Å)	22.4240(12)	a = 19.4968(13)	15.3074(10)
b (Å)	19.6456(9)	b = 29.070(2)	16.5873(11)
c (Å)	28.5568(15)	c = 43.890(3)	26.5962(17)
α (°)	90	90	87.821(4)
β (°)	100.843(3)	90	81.706(4)
γ (°)	90	90	67.787(3)
Volume (Å^3)	12355.6(11)	24875(3)	6185.4(7)
Z	4	8	1
ρ^{calc} (g cm^{-1})	1.712	1.710	1.660
Absorption coefficient (mm^{-1})	3.634	3.613	3.607
F(000)	6316	12731	3070
Crystal size (mm^3)	0.770 x 0.080 x 0.070	0.320 x 0.050 x 0.040	0.380 x 0.210 x 0.050
Theta range for data collection (°)	1.389 to 28.333	1.340 to 28.343	1.451 to 28.435
Index ranges	$-29\leq h\leq 29$, $-26\leq k\leq 26$, $-38\leq l\leq 38$	$-26\leq h\leq 26$, $-38\leq k\leq 38$, $-58\leq l\leq 58$	$-20\leq h\leq 20$, $-22\leq k\leq 22$, $-35\leq l\leq 35$
Reflections collected	60651	59854	60289
Independent reflections	30778 [R(int) = 0.0465]	30874 [R(int) = 0.1428]	30747 [R(int) = 0.0565]
Completeness to theta = 25.000°	100.0%	99.9 %	99.7%
Data / restraints / parameters	30778 / 45 / 1489	30874 / 130 / 1561	30747 / 231 / 1662
Goodness-of-fit on F^2	1.000	1.005	1.021
Final R indices [I>2sigma(I)]	R1 = 0.0373, wR2 = 0.0736	R1 = 0.0654, wR2 = 0.1222	R1 = 0.0562, wR2 = 0.1138
R indices (all data)	R1 = 0.0802, wR2 = 0.0882	R1 = 0.1963, wR2 = 0.1625	R1 = 0.1100, wR2 = 0.1346
Largest diff. peak and hole (e$^-$Å^{-3})	2.190 and –2.013	1.212 and –1.055	2.743 and –1.569

3.8.8 *DFT Calculations*

All calculations were performed using Gaussian 16, Revision B.01 quantum chemistry program package for the Linux operating system.[56] The initial starting point geometries were adapted from the corresponding crystallographically obtained structures and optimized to a stationary point, followed by analytical frequency calculations (Hessian) to confirm that no imaginary frequencies were present. The geometry optimizations were performed using DFT calculations at a pure GGA functional level using Becke's 1988 gradient-corrected exchange functional[57] and Perdew's 1986 electron correlation functional[58] (BPV86) and def2SVP[59,60] as a basis set. Using the optimized geometries, single point calculations were conducted using B3LYP+[61–64] as a functional and the correlation consistent basis set, cc-pVTZ.[65–69] These single point calculations were used to generate density of states plots, orbital energy diagrams, and spin density calculations. Multiwfn was used to generate partial density of states plots.[70] To reduce calculation time, geometry optimizations and frequency calculations were run over multiple nodes using an interactive batch file, which requires the use of %LindaWorker and %usessh commands. Further, to aid in the identification of a stationary point, a quadratic convergence algorithm was applied to the self-consistent field should the first-order SCF convergence fail (e.g. scf=(xqc,maxconventional=256)). Optimization of *trans*-(α,β)-[**Fe$_3$**(CNMe)(THF)]$^+$, (α,α,β)-[**Fe$_3$**(CNMe)$_2$(THF)]$^+$, and *cis*-(α,β)-[**Fe$_3$**(THF)$_2$]$^+$ proved to be challenging and required the implementation of a fragmented initial guess (see example input below). Despite fragmentation of the initial guess, these calculations yielded structural and electronic parameters highly similar to the non-fragmented counterpart, *cis*-(α,β)-[**Fe$_3$**(CNMe)$_2$]$^+$, as illustrated by Hirshfeld spin-density values provided below. Interestingly, free optimization of the experimentally unobserved intermediate (α,α,β)-[**Fe$_3$**(CNMe)(THF)$_2$]$^+$ resulted in dissociation of one THF molecule to yield *trans*-(α,β)-[**Fe$_3$**(CNMe)(THF)]$^+$. Accordingly, this species was optimized as a transition state using the input file described below, with frequency calculations confirming the presence of a singular negative eigenvalue. Optimized atomic coordinates for all calculated [**Fe$_3$**]$^+$ clusters are provided in Appendix A.

Table 3.5. Comparison of bond metrics of the DFT optimized structures of [**Fe$_3$**(CNMe)$_2$]$^+$ and [**Fe$_3$**(CNMe)$_2$(THF)]$^+$ and those of the related single-crystal X-ray diffraction structures of [**Fe$_3$**(CN^{t}Bu)$_2$][PF$_6$] and [**Fe$_3$**(CN^{t}Bu)$_2$(THF)][PF$_6$].

Compound	**Interatomic Distance (Å)**				
	Fe…Se	Fe–L	Co–Se (avg.)	Co–P (avg.)	Fe–N^{Tol} (avg.)
[**Fe$_3$**(CN^{t}Bu)$_2$][PF$_6$]	2.488(7)[a] 2.546(7)[a] 2.397(6)[c] 2.433(5)[c]	2.04(2)[a] 2.08(2)[a] --	2.35	2.17	2.01
[**Fe$_3$**(CNMe)$_2$]$^+$ (calc.)	2.441[a] 2.441[a] 2.426[c] 2.426[c]	1.998[a] 1.998[a] --	2.36	2.18	1.98
[**Fe$_3$**(CN^{t}Bu)$_2$(THF)][PF$_6$]	2.498(1)[a] 2.541(1)[a] 2.450(1)[b] 2.699(3)[b]	2.12(1)[a] 2.11(3)[a] 2.237(5)[b]	2.35	2.16	1.99
[**Fe$_3$**(CNMe)$_2$(THF)]$^+$ (calc.)	2.439[a] 2.453[a] 2.449[b] 2.588[b]	2.001[a] 1.993[a] 2.355[b]	2.36	2.17	1.99

[a]Fe(CNMe/CN^{t}Bu) edge site; [b]Fe(THF) edge site; [c]κ^4-Fe edge site.

Table 3.6. Comparison of bond metrics of the DFT optimized structures of *trans*-(α,β)-[**Fe$_3$**(CNMe)(THF)]$^+$ and *cis*-(α,β)-[**Fe$_3$**(THF)$_2$] and those of the related single-crystal X-ray diffraction structures of *trans*-(α,β)-[**Fe$_3$**(CN^{t}Bu)(THF)][PF$_6$] and *cis*-(α,β)-[**Fe$_3$**(THF)$_2$][PF$_6$].

Compound	Interatomic Distance (Å)				
	Fe…Se	Fe–L	Co–Se (avg.)	Co–P (avg.)	Fe–N^{Tol} (avg.)
[**Fe$_3$**(CN^{t}Bu)(THF)][PF$_6$]	2.541(7)^a 2.450(2)^b 2.699(3)^b 2.404(5)^c 2.471(7)^c	2.1(1)^a 2.237(5)^b --	2.35	2.15	1.97
[**Fe$_3$**(CNMe)(THF)]$^+$ (calc.)	2.5082^a 2.489^b 2.594^b 2.407^c 2.458^c	1.966^a 2.391^b --	2.37	2.18	1.97
[**Fe$_3$**(THF)$_2$][PF$_6$]	2.4441(8)^b 2.7294(8)^b 2.5172(7)^b 2.4410(7)^c 2.4566(7)^c	2.201(4)^b 2.081(3)^b --	2.36	2.18	1.97
[**Fe$_3$**(THF)$_2$]$^+$ (calc.)	2.422^b 3.197^b 2.423^b 3.198^b 2.425^c 2.425^c	2.182^b 2.182^b --	2.37	2.18	1.97
[**Fe$_3$**(CNMe)(THF)$_2$]$^+$ (calc.)	2.479^b 2.582^b 2.504^a 2.485^b 2.515^b	2.418^b 1.969^a 2.666^b	2.37	2.17	1.98

^{a}Fe(CNMe/CN^{t}Bu) edge site; ^{b}Fe(THF) edge site; $^c\kappa^4$-Fe edge site.

Table 3.7. Total energies calculated for *cis*-(α,β)-[**Fe$_3$**(CNMe)$_2$]$^+$, [**Fe$_3$**(CNMe)$_2$(THF)]$^+$, [**Fe$_3$**(CNMe)(THF)]$^+$, [**Fe$_3$**(CNMe)(THF)$_2$]$^+$, [**Fe$_3$**(THF)$_2$]$^+$, *trans*-(α,β)-[**Fe$_3$**(CNMe)$_2$]$^+$, and (α,α)-[**Fe$_3$**(CNMe)$_2$]$^+$ at the B3LYP+/cc-pVTZ level of theory.

Compound	**Total Energy (eV)**
cis-(α,β)-[**Fe$_3$**(CNMe)$_2$]$^+$	-1034471.565
[**Fe$_3$**(CNMe)$_2$(THF)]$^+$	-1040756.003
[**Fe$_3$**(CNMe)(THF)]$^+$	-1037167.03
[**Fe$_3$**(CNMe)(THF)$_2$]$^+$	-1043452.074
[**Fe$_3$**(THF)$_2$]$^+$	-1039862.882
trans-(α,β)-[**Fe$_3$**(CNMe)$_2$]$^+$	-1034472.083
(α,α)-[**Fe$_3$**(CNMe)$_2$]$^+$	-1034472.081

[a]Fe(CNMe) edge site; [b]Fe(THF) edge site; [c]κ^4-Fe edge site.

Table 3.8. Hirshfeld spin-density values calculated for [**Fe$_3$**(CNMe)$_2$]$^+$, [**Fe$_3$**(CNMe)$_2$(THF)]$^+$, [**Fe$_3$**(CNMe)(THF)]$^+$, [**Fe$_3$**(CNMe)(THF)$_2$]$^+$, and [**Fe$_3$**(THF)$_2$]$^+$ at the B3LYP+/cc-pVTZ level of theory.

Compound	**Hirshfeld Spin-density**						
	Fe1	Fe2	Fe3	Co_6Se_8 core	Total Spin	% on Fe edges	% on Co_6Se_8
[**Fe$_3$**(CNMe)$_2$]$^+$	3.37[a]	3.37[a]	3.65[c]	1.15	13	79.9	8.8
[**Fe$_3$**(CNMe)$_2$(THF)]$^+$	3.37[a]	3.37[a]	3.70[b]	1.06	13	80.3	8.2
[**Fe$_3$**(CNMe)(THF)]$^+$	3.34[a]	3.48[b]	3.59[c]	1.07	13	80.1	8.2
[**Fe$_3$**(CNMe)(THF)$_2$]$^+$	3.35[a]	3.46[b]	3.67[b]	1.08	13	80.6	8.3
[**Fe$_3$**(THF)$_2$]$^+$	3.45[b]	3.45[b]	3.59[c]	1.15	13	80.7	8.8

[a]Fe(CNMe) edge site; [b]Fe(THF) edge site; [c]κ^4-Fe edge site.

Table 3.9. Hirshfeld charges calculated for $[\mathbf{Fe_3}(CNMe)_2]^+$, $[\mathbf{Fe_3}(CNMe)_2(THF)]^+$, $[\mathbf{Fe_3}(CNMe)(THF)]^+$, $[\mathbf{Fe_3}(CNMe)(THF)_2]^+$, and $[\mathbf{Fe_3}(THF)_2]^+$ at the B3LYP+/cc-pVTZ level of theory.

Compound	**Hirshfeld Charge (a.u.)**		
	Fe1	Fe2	Fe3
$[\mathbf{Fe_3}(CNMe)_2]^+$	+0.25[c]	+0.19[a]	+0.19[a]
$[\mathbf{Fe_3}(CNMe)_2(THF)]^+$	+0.29[b]	+0.19[a]	+0.19[a]
$[\mathbf{Fe_3}(CNMe)(THF)]^+$	+0.22[b]	+0.25[c]	+0.19[a]
$[\mathbf{Fe_3}(CNMe)(THF)_2]^+$	+0.22[b]	+0.29[b]	+0.19[a]
$[\mathbf{Fe_3}(THF)_2]^+$	+0.22[b]	+0.22[b]	+0.25[c]

[a]Fe(CNMe) edge site; [b]Fe(THF) edge site; [c]κ^4-Fe edge site.

3.9 REFERENCES

(1) Nørskov, J. K.; Studt, F.; Abild-Pedersen, F.; Bligaard, T. *Fundamental Concepts in Heterogeneous Catalysis*; Wiley: Hoboken, New Jersey, 2015.

(2) Syres, K. L.; Thomas, A. G.; Flavell, W. R.; Spencer, B. F.; Bondino, F.; Malvestuto, M.; Preobrajenski, A.; Grätzel, M. Adsorbate-Induced Modification of Surface Electronic Structure: Pyrocatechol Adsorption on the Anatase TiO_2(101) and Rutile TiO_2(110) Surfaces. *J. Phys. Chem. C* **2012**, *116* (44), 23515–23525. https://doi.org/10.1021/jp308614k.

(3) Nowakowska, S.; Mazzola, F.; Alberti, M. N.; Song, F.; Voigt, T.; Nowakowski, J.; Wäckerlin, A.; Wäckerlin, C.; Wiss, J.; Schweizer, W. B.; Broszio, M.; Polley, C.; Leandersson, M.; Fatayer, S.; Ivas, T.; Baljozovic, M.; Mousavi, S. F.; Ahsan, A.; Nijs, T.; Popova, O.; Zhang, J.; Muntwiler, M.; Thilgen, C.; Stöhr, M.; Pasti, I. A.; Skorodumova, N. V.; Diederich, F.; Wells, J.; Jung, T. A. Adsorbate-Induced Modification of the Confining Barriers in a Quantum Box Array. *ACS Nano* **2018**, *12* (1), 768–778. https://doi.org/10.1021/acsnano.7b07989.

(4) Somorjai, G. A.; Van Hove, M. A. Adsorbate-Induced Restructuring of Surfaces. *Progress in Surface Science* **1989**, *30* (3–4), 201–231. https://doi.org/10.1016/0079-6816(89)90009-9.

(5) Zhang, Z.; Wei, Z.; Sautet, P.; Alexandrova, A. N. Hydrogen-Induced Restructuring of a Cu(100) Electrode in Electroreduction Conditions. *J. Am. Chem. Soc.* **2022**, *144* (42), 19284–19293. https://doi.org/10.1021/jacs.2c06188.

(6) Min, B. K.; Deng, X.; Pinnaduwage, D.; Schalek, R.; Friend, C. M. Oxygen-Induced Restructuring with Release of Gold Atoms from Au(111). *Phys. Rev. B* **2005**, *72* (12), 121410. https://doi.org/10.1103/PhysRevB.72.121410.

(7) Eren, B.; Zherebetskyy, D.; Patera, L. L.; Wu, C. H.; Bluhm, H.; Africh, C.; Wang, L.-W.; Somorjai, G. A.; Salmeron, M. Activation of Cu(111) Surface by Decomposition into Nanoclusters Driven by CO Adsorption. *Science* **2016**, *351* (6272), 475–478. https://doi.org/10.1126/science.aad8868.

(8) Klust, A.; Madix, R. J. Mesoscopic Restructuring and Mass Transport of Metal Atoms during Reduction of the Ag(111)-p(4×4)-O Surface with CO. *The Journal of Chemical Physics* **2007**, *126* (8), 084707. https://doi.org/10.1063/1.2483919.

(9) Tissot, H.; Wang, C.; Stenlid, J. H.; Panahi, M.; Kaya, S.; Soldemo, M.; Ghadami Yazdi, M.; Brinck, T.; Weissenrieder, J. Interaction of Atomic Hydrogen with the Cu_2O(100) and (111) Surfaces. *J. Phys. Chem. C* **2019**, *123* (36), 22172–22180. https://doi.org/10.1021/acs.jpcc.9b03888.

(10) Vogt, C.; Weckhuysen, B. M. The Concept of Active Site in Heterogeneous Catalysis. *Nat Rev Chem* **2022**, *6* (2), 89–111. https://doi.org/10.1038/s41570-021-00340-y.

(11) Nadeem, I. M.; Hargreaves, L.; Harrison, G. T.; Idriss, H.; Shluger, A. L.; Thornton, G. Carboxylate Adsorption on Rutile TiO_2(100): Role of Coulomb Repulsion, Relaxation, and Steric Hindrance. *J. Phys. Chem. C* **2021**, *125* (25), 13770–13779. https://doi.org/10.1021/acs.jpcc.1c00892.

(12) Krishnamoorthy, A.; Yildiz, B. Quantifying the Origin of Inter-Adsorbate Interactions on Reactive Surfaces for Catalyst Screening and Design. *Phys. Chem. Chem. Phys.* **2015**, *17* (34), 22227–22234. https://doi.org/10.1039/C5CP03143E.

(13) Shong, B.; Bent, S. F. One-Dimensional Pattern Formation of Adsorbed Molecules on the Ge(100)-2 × 1 Surface Driven by Nearest-Neighbor Effects. *J. Phys. Chem. C* **2013**, *117* (2), 949–955. https://doi.org/10.1021/jp3078503.

(14) Lousada, C. M.; Johansson, A. J.; Korzhavyi, P. A. Adsorption of Hydrogen Sulfide, Hydrosulfide and Sulfide at Cu(110) - Polarizability and Cooperativity Effects. First Stages of Formation of a Sulfide Layer. *ChemPhysChem* **2018**, *19* (17), 2159–2168. https://doi.org/10.1002/cphc.201800246.

(15) Zonnevylle, M. C.; Hoffmann, R. Coadsorbate Interactions: Sulfur and Carbon Monoxide on Nickel(100). *Langmuir* **1987**, *3* (4), 452–459. https://doi.org/10.1021/la00076a003.

(16) Qi, L.; Li, J. Adsorbate Interactions on Surface Lead to a Flattened Sabatier Volcano Plot in Reduction of Oxygen. *Journal of Catalysis* **2012**, *295*, 59–69. https://doi.org/10.1016/j.jcat.2012.07.019.

(17) Deng, X.; Min, B. K.; Guloy, A.; Friend, C. M. Enhancement of O_2 Dissociation on Au(111) by Adsorbed Oxygen: Implications for Oxidation Catalysis. *J. Am. Chem. Soc.* **2005**, *127* (25), 9267–9270. https://doi.org/10.1021/ja050144j.

(18) Ertl, G. Oscillatory Kinetics and Spatio-Temporal Self-Organization in Reactions at Solid Surfaces. *Science* **1991**, *254* (5039), 1750–1755. https://doi.org/10.1126/science.254.5039.1750.

(19) Zhang, Z.; Zandkarimi, B.; Alexandrova, A. N. Ensembles of Metastable States Govern Heterogeneous Catalysis on Dynamic Interfaces. *Acc. Chem. Res.* **2020**, *53* (2), 447–458. https://doi.org/10.1021/acs.accounts.9b00531.

(20) Seh, Z. W.; Kibsgaard, J.; Dickens, C. F.; Chorkendorff, I.; Nørskov, J. K.; Jaramillo, T. F. Combining Theory and Experiment in Electrocatalysis: Insights into Materials Design. *Science* **2017**, *355* (6321), eaad4998. https://doi.org/10.1126/science.aad4998.

(21) Montemore, M. M.; van Spronsen, M. A.; Madix, R. J.; Friend, C. M. O_2 Activation by Metal Surfaces: Implications for Bonding and Reactivity on Heterogeneous Catalysts. *Chem. Rev.* **2018**, *118* (5), 2816–2862. https://doi.org/10.1021/acs.chemrev.7b00217.

(22) Fan, X.; Wang, J.; Wu, K.; Zhang, L.; Zhang, J. Isomerism in Titanium-Oxo Clusters: Molecular Anatase Model with Atomic Structure and Improved Photocatalytic Activity. *Angew. Chem. Int. Ed.* **2019**, *58* (5), 1320–1323. https://doi.org/10.1002/anie.201809961.

(23) Song, F.; Moré, R.; Schilling, M.; Smolentsev, G.; Azzaroli, N.; Fox, T.; Luber, S.; Patzke, G. R. $\{Co_4O_4\}$ and $\{Co_xNi_{4-x}O_4\}$ Cubane Water Oxidation Catalysts as Surface Cut-Outs of Cobalt Oxides. *J. Am. Chem. Soc.* **2017**, *139* (40), 14198–14208. https://doi.org/10.1021/jacs.7b07361.

(24) Schreiber, E.; Petel, B. E.; Matson, E. M. Acid-Induced, Oxygen-Atom Defect Formation in Reduced Polyoxovanadate-Alkoxide Clusters. *J. Am. Chem. Soc.* **2020**, *142* (22), 9915–9919. https://doi.org/10.1021/jacs.0c03864.

(25) Dornsiepen, E.; Pieck, F.; Tonner, R.; Dehnen, S. $[\{(PhSn)_3SnS_6\}\{(MCp)_3S_4\}]$ (M = W, Mo): Minimal Molecular Models of the Covalent Attachment of Metal Chalcogenide Clusters on

Doped Transition Metal Dichalcogenide Layers. *J. Am. Chem. Soc.* **2019**, *141* (41), 16494–16500. https://doi.org/10.1021/jacs.9b09209.

(26) Kibsgaard, J.; Jaramillo, T. F.; Besenbacher, F. Building an Appropriate Active-Site Motif into a Hydrogen-Evolution Catalyst with Thiomolybdate $[Mo_3S_{13}]^{2-}$ Clusters. *Nat. Chem.* **2014**, *6* (3), 248–253. https://doi.org/10.1038/nchem.1853.

(27) Muetterties, E. L.; Rhodin, T. N.; Band, Elliot.; Brucker, C. F.; Pretzer, W. R. Clusters and Surfaces. *Chem. Rev.* **1979**, *79* (2), 91–137. https://doi.org/10.1021/cr60318a001.

(28) Brown, A. C.; Thompson, N. B.; Suess, D. L. M. Evidence for Low-Valent Electronic Configurations in Iron–Sulfur Clusters. *J. Am. Chem. Soc.* **2022**, *144* (20), 9066–9073. https://doi.org/10.1021/jacs.2c01872.

(29) Brown, A. C.; Suess, D. L. M. Valence Localization in Alkyne and Alkene Adducts of Synthetic $[Fe_4S_4]^+$ Clusters. *Inorg. Chem.* **2022**. https://doi.org/10.1021/acs.inorgchem.2c01353.

(30) Arnett, C. H.; Chalkley, M. J.; Agapie, T. A Thermodynamic Model for Redox-Dependent Binding of Carbon Monoxide at Site-Differentiated, High Spin Iron Clusters. *J. Am. Chem. Soc.* **2018**, *140* (16), 5569–5578. https://doi.org/10.1021/jacs.8b01825.

(31) Hernández Sánchez, R.; Champsaur, A. M.; Choi, B.; Wang, S. G.; Bu, W.; Roy, X.; Chen, Y.; Steigerwald, M. L.; Nuckolls, C.; Paley, D. W. Electron Cartography in Clusters. *Angew. Chem. Int. Ed.* **2018**, *57* (42), 13815–13820. https://doi.org/10.1002/anie.201806426.

(32) Hirsch, A.; Lamparth, I.; Groesser, T.; Karfunkel, H. R. Regiochemistry of Multiple Additions to the Fullerene Core: Synthesis of a Th-Symmetric Hexakis Adduct of C_{60} with Bis(Ethoxycarbonyl)Methylene. *J. Am. Chem. Soc.* **1994**, *116* (20), 9385–9386. https://doi.org/10.1021/ja00099a088.

(33) Champsaur, A. M.; Velian, A.; Paley, D. W.; Choi, B.; Roy, X.; Steigerwald, M. L.; Nuckolls, C. Building Diatomic and Triatomic Superatom Molecules. *Nano Lett.* **2016**, *16* (8), 5273–5277. https://doi.org/10.1021/acs.nanolett.6b02471.

(34) Gray, T. G.; Holm, R. H. Site-Differentiated Hexanuclear Rhenium(III) Cyanide Clusters $[Re_6Se_8(PEt_3)_n(CN)_{6-n}]^{n-4}$ (n = 4, 5) and Kinetics of Solvate Ligand Exchange on the Cubic $[Re_6Se_8]^{2+}$ Core. *Inorg. Chem.* **2002**, *41* (16), 4211–4216. https://doi.org/10.1021/ic020214c.

(35) Guo, R.; Song, Y.; Wang, G.; Murray, R. W. Does Core Size Matter in the Kinetics of Ligand Exchanges of Monolayer-Protected Au Clusters? *J. Am. Chem. Soc.* **2005**, *127* (8), 2752–2757. https://doi.org/10.1021/ja044638c.

(36) Hosier, C. A.; Ackerson, C. J. Regiochemistry of Thiolate for Selenolate Ligand Exchange on Gold Clusters. *J. Am. Chem. Soc.* **2019**, *141* (1), 309–314. https://doi.org/10.1021/jacs.8b10013.

(37) Kephart, J. A.; Mitchell, B. S.; Chirila, A.; Anderton, K. J.; Rogers, D.; Kaminsky, W.; Velian, A. Atomically Defined Nano-Propeller $Fe_3Co_6Se_8(Ph_2PNTol)_6$: Functional Model for the Electronic Metal-Support Interaction Effect, and High Catalytic Activity for Carbodiimide Formation. *J. Am. Chem. Soc.* **2019**, *141* (50), 19605–19610. https://doi.org/10.1021/jacs.9b12473.

(38) Kephart, J. A.; Mitchell, B. S.; Kaminsky, W.; Velian, A. Multi-Active Site Dynamics on a Molecular Cr/Co/Se Cluster Catalyst. *J. Am. Chem. Soc.* **2022**, *144* (21), 9206–9211. https://doi.org/10.1021/jacs.2c00234.

(39) Mitchell, B. S.; Krajewski, S. M.; Kephart, J. A.; Rogers, D.; Kaminsky, W.; Velian, A. Redox-Switchable Allosteric Effects in Molecular Clusters. *JACS Au* **2022**, *2* (1), 92–96. https://doi.org/10.1021/jacsau.1c00491.

(40) Kephart, J. A.; Romero, C. G.; Tseng, C.-C.; Anderton, K. J.; Yankowitz, M.; Kaminsky, W.; Velian, A. Hierarchical Nanosheets Built from Superatomic Clusters: Properties, Exfoliation and Single-Crystal-to-Single-Crystal Intercalation. *Chem. Sci.* **2020**, *11* (39), 10744–10751. https://doi.org/10.1039/D0SC03506H.

(41) Kephart, J. A.; Boggiano, A. C.; Kaminsky, W.; Velian, A. Inorganic Clusters as Metalloligands: Ligand Effects on the Synthesis and Properties of Ternary Nanopropeller Clusters. *Dalton Trans.* **2020**, *49* (45), 16464–16473. https://doi.org/10.1039/D0DT02416C.

(42) Mitchell, B. S.; Chirila, A.; Kephart, J. A.; Boggiano, A. C.; Krajewski, S. M.; Rogers, D.; Kaminsky, W.; Velian, A. Metal–Support Interactions in Molecular Single-Site Cluster Catalysts. *J. Am. Chem. Soc.* **2022**, *144* (40), 18459–18469. https://doi.org/10.1021/jacs.2c07033.

(43) Dey, A.; Glaser, T.; Couture, M. M.-J.; Eltis, L. D.; Holm, R. H.; Hedman, B.; Hodgson, K. O.; Solomon, E. I. Ligand K-Edge X-Ray Absorption Spectroscopy of $[Fe_4S_4]^{1+,2+,3+}$ Clusters: Changes in Bonding and Electronic Relaxation upon Redox. *J. Am. Chem. Soc.* **2004**, *126* (26), 8320–8328. https://doi.org/10.1021/ja0484956.

(44) Bista, D.; Aydt, A. P.; Anderton, K. J.; Paley, D. W.; Betley, T. A.; Reber, A. C.; Chauhan, V.; Bartholomew, A. K.; Roy, X.; Khanna, S. N. High-Spin Superatom Stabilized by Dual Subshell Filling. *J. Am. Chem. Soc.* **2022**, *144* (11), 5172–5179. https://doi.org/10.1021/jacs.2c00731.

(45) Greenwood, B. P.; Forman, S. I.; Rowe, G. T.; Chen, C.-H.; Foxman, B. M.; Thomas, C. M. Multielectron Redox Activity Facilitated by Metal-Metal Interactions in Early/Late Heterobimetallics: Co/Zr Complexes Supported by Phosphinoamide Ligands. *Inorg. Chem* **2009**, *48*, 6251–6260. https://doi.org/10.1021/ic900552b.

(46) Bain, G. A.; Berry, J. F. Diamagnetic Corrections and Pascal's Constants. *Journal of Chemical Education* **2008**, *85* (4), 532. https://doi.org/10.1021/ed085p532.

(47) Chilton, N. F.; Anderson, R. P.; Turner, L. D.; Soncini, A.; Murray, K. S. PHI: A Powerful New Program for the Analysis of Anisotropic Monomeric and Exchange-Coupled Polynuclear *d*- and *f*-Block Complexes. *J. Comput. Chem.* **2013**, *34* (13), 1164–1175. https://doi.org/10.1002/jcc.23234.

(48) Bruker APEX2 (Version 2.1-4), SAINT (Version 7.34A), SADABS (Version 2007/4), **2007** *BrukerAXS Inc*, Madison, Wisconsin, USA.

(49) Sheldrick, G.M. *Acta Cryst.* **2015** *A71*, 3-8.

(50) Altomare, A.; Burla, C.; Camalli, M.; Cascarano, G. L.; Giacovazzo, C.; Guagliardi, A.; Moliterni, A.G.G.; Polidori, G.; Spagna, R. *J. Appl. Crystallogr.,* **1999**, *32*, 115-119.

(51) Altomare, A.; Cascarano, G. L.; Giacovazzo, C.; Guagliardi, A. *J. Appl. Crystallogr*., **1993**, *26*, 343-350.

(52) Sheldrick, G. M. *SHELXL-97, Program for the Refinement of Crystal Structures,* **1997***,* University of Göttingen, Germany.

(53) Sheldrick, G. M. *Acta Cryst.* **2015**, *C71*, 3–8.

(54) Mackay, S.; Edwards, C.; Henderson, A.; Gilmore, C.; Stewart, N.; Shankland, K.; Donald, A. *MaXus: A Computer Program for the Solution and Refinement of Crystal Structures from Diffraction Data,* **1997**, University of Glasgow, Scotland.

(55) Waasmaier, D.; Kirfel, A. *Acta Cryst.,* **1995**, *51*, 416-430.

(56) Frisch, M. J.; Trucks, G. W.; Schlegel, H. B.; Scuseria, G. E.; Robb, M. A.; Cheeseman, J. R.; Scalmani, G.; Barone, V.; Petersson, G. A.; Nakatsuji, H.; Li, X.; Caricato, M.; Marenich, A. V.; Bloino, J.; Janesko, B. G.; Gomperts, R.; Mennucci, B.; Hratchian, H. P.; Ortiz, J. V.; Izmaylov, A. F.; Sonnenberg, J. L.; Williams; Ding, F.; Lipparini, F.; Egidi, F.; Goings, J.; Peng, B.; Petrone, A.; Henderson, T.; Ranasinghe, D.; Zakrzewski, V. G.; Gao, J.; Rega, N.; Zheng, G.; Liang, W.; Hada, M.; Ehara, M.; Toyota, K.; Fukuda, R.; Hasegawa, J.; Ishida, M.; Nakajima, T.; Honda, Y.; Kitao, O.; Nakai, H.; Vreven, T.; Throssell, K.; Montgomery Jr., J. A.; Peralta, J. E.; Ogliaro, F.; Bearpark, M. J.; Heyd, J. J.; Brothers, E. N.; Kudin, K. N.; Staroverov, V. N.; Keith, T. A.; Kobayashi, R.; Normand, J.; Raghavachari, K.; Rendell, A. P.; Burant, J. C.; Iyengar, S. S.; Tomasi, J.; Cossi, M.; Millam, J. M.; Klene, M.; Adamo, C.; Cammi, R.; Ochterski, J. W.; Martin, R. L.; Morokuma, K.; Farkas, O.; Foresman, J. B.; Fox, D. J. *Gaussian 16 Rev. A.03*; Wallingford, CT, 2016.

(57) Becke, A. D. Density-Functional Exchange-Energy Approximation with Correct Asymptotic Behavior. *Phys. Rev. A* **1988**, *38* (6), 3098–3100. https://doi.org/10.1103/PhysRevA.38.3098.

(58) Perdew, J. P. Density-Functional Approximation for the Correlation Energy of the Inhomogeneous Electron Gas. *Phys. Rev. B* **1986**, *33* (12), 8822–8824. https://doi.org/10.1103/PhysRevB.33.8822.

(59) Weigend, F.; Ahlrichs, R. Balanced Basis Sets of Split Valence, Triple Zeta Valence and Quadruple Zeta Valence Quality for H to Rn: Design and Assessment of Accuracy. *Phys. Chem. Chem. Phys.* **2005**, *7* (18), 3297. https://doi.org/10.1039/b508541a.

(60) Weigend, F. Accurate Coulomb-Fitting Basis Sets for H to Rn. *Phys. Chem. Chem. Phys.* **2006**, *8* (9), 1057. https://doi.org/10.1039/b515623h.

(61) Becke, A. D. Density-functional Thermochemistry. III. The Role of Exact Exchange. *The Journal of Chemical Physics* **1993**, *98* (7), 5648–5652. https://doi.org/10.1063/1.464913.

(62) Miehlich, B.; Savin, A.; Stoll, H.; Preuss, H. Results Obtained with the Correlation Energy Density Functionals of Becke and Lee, Yang and Parr. *Chemical Physics Letters* **1989**, *157* (3), 200–206. https://doi.org/10.1016/0009-2614(89)87234-3.

(63) Lee, C.; Yang, W.; Parr, R. G. Development of the Colle-Salvetti Correlation-Energy Formula into a Functional of the Electron Density. *Phys. Rev. B* **1988**, *37* (2), 785–789. https://doi.org/10.1103/PhysRevB.37.785.

(64) Yanai, T.; Tew, D. P.; Handy, N. C. A New Hybrid Exchange–Correlation Functional Using the Coulomb-Attenuating Method (CAM-B3LYP). *Chemical Physics Letters* **2004**, *393* (1–3), 51–57. https://doi.org/10.1016/j.cplett.2004.06.011.

(65) Dunning, T. H. Gaussian Basis Sets for Use in Correlated Molecular Calculations. I. The Atoms Boron through Neon and Hydrogen. *The Journal of Chemical Physics* **1989**, *90* (2), 1007–1023. https://doi.org/10.1063/1.456153.

(66) Woon, D. E.; Dunning, T. H. Gaussian Basis Sets for Use in Correlated Molecular Calculations. III. The Atoms Aluminum through Argon. *The Journal of Chemical Physics* **1993**, *98* (2), 1358–1371. https://doi.org/10.1063/1.464303.

(67) Wilson, A. K.; van Mourik, T.; Dunning, T. H. Gaussian Basis Sets for Use in Correlated Molecular Calculations. VI. Sextuple Zeta Correlation Consistent Basis Sets for Boron through Neon. *Journal of Molecular Structure: THEOCHEM* **1996**, *388*, 339–349. https://doi.org/10.1016/S0166-1280(96)80048-0.

(68) Peterson, K. A.; Woon, D. E.; Dunning, T. H. Benchmark Calculations with Correlated Molecular Wave Functions. IV. The Classical Barrier Height of the H+H_2 →H_2 +H Reaction. *The Journal of Chemical Physics* **1994**, *100* (10), 7410–7415. https://doi.org/10.1063/1.466884.

(69) Kendall, R. A.; Dunning, T. H.; Harrison, R. J. Electron Affinities of the First-row Atoms Revisited. Systematic Basis Sets and Wave Functions. *The Journal of Chemical Physics* **1992**, *96* (9), 6796–6806. https://doi.org/10.1063/1.462569.

(70) Lu, T.; Chen, F. Multiwfn: A Multifunctional Wavefunction Analyzer. *Journal of Computational Chemistry* **2012**, *33* (5), 580–592. https://doi.org/10.1002/jcc.22885.

CHAPTER 4.

HIERARCHICAL NANOSHEETS BUILT FROM SUPERATOMIC CLUSTERS: PROPERTIES, EXFOLIATION AND SINGLE-CRYSTAL-TO-SINGLE-CRYSTAL INTERCALATION

4.1 ABSTRACT

Tuning the properties of atomic crystals in the two-dimensional (2D) limit is synthetically challenging, but critical to unlock their potential in fundamental research and nanotechnology alike. 2D crystals assembled using superatomic blocks could provide a route to encrypt desirable functionality, yet strategies to link the inorganic blocks together in predetermined dimensionality or symmetry are scarce. Here, we describe the synthesis of anisotropic van der Waals crystalline frameworks using the designer superatomic nanocluster $Co_3(py)_3Co_6Se_8L^{Tol}_6$ (**Co_3**$(py)_3$ py = pyridine, L^{Tol} = $Ph_2PN^{(-)}Tol$), and ditopic linkers. Post-synthetically, the 3D crystals can be mechanically exfoliated into ultrathin flakes (8 to 60 nm), or intercalated with the redox-active guest tetracyanoethylene in a single-crystal-to-single-crystal transformation. Extensive characterization, including by single-crystal X-ray diffraction, reveals how intrinsic features of the nanocluster, such as its structure, chirality, redox-activity, and magnetic profile, predetermine key properties of the emerging 2D structures. Within the nanosheets, the strict and unusual stereoselectivity of the nanocluster's Co edges for the low-symmetry (α,α,β) isomer gives rise to in-plane structural anisotropy, while the helically chiral nanoclusters self-organize into alternating Δ- and Λ-homochiral rows. The nanocluster's high-spin Co edges, and its rich redox profile make the nanosheets both magnetically and electrochemically active, as revealed by solid-state magnetic and cyclic voltammetry studies. The length and flexibility of the ditopic linker was varied and found to have a secondary effect on the structure and stacking of the nanosheets within the 3D

Adapted in part with permission from:
1. Kephart, J. A.; Romero, C. G.; Tseng, C.-C.; Anderton, K. J.; Yankowitz, M.; Kaminsky, W.; Velian, A. *Chem. Sci.*, **2020**, *11*, 10744-10751. Copyright 2020 The Royal Society of Chemistry.

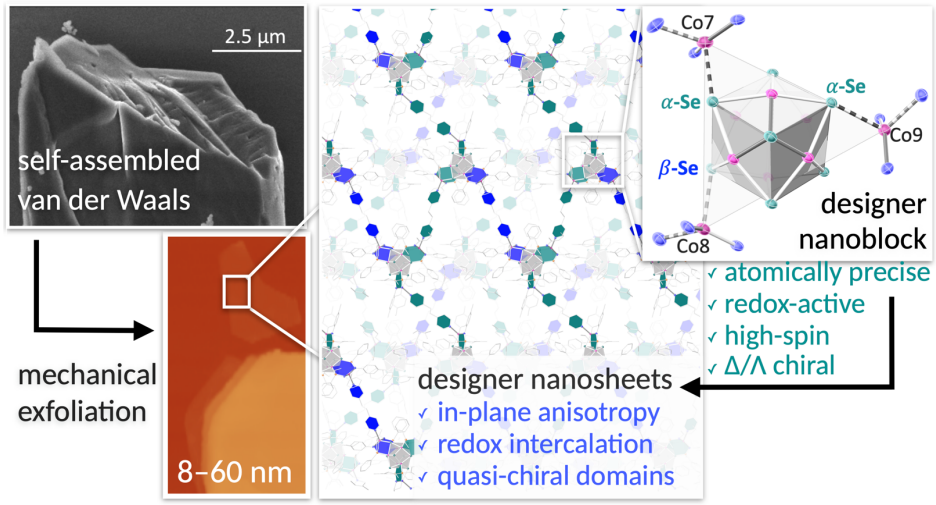


Figure 4.1. Pre-formed inorganic Co/Se/Co clusters serve as templated building blocks to guide the self-assembly of two-dimensional nanosheets.

crystals. With these results we introduce a deterministic and versatile synthetic entry to programmable functionality and symmetry in 2D superatomic crystals.

4.2 Introduction

The dimensionality of a material is a key determinant of its properties, as demonstrated especially over the past two decades with the isolation of two-dimensional (2D) atomic crystals.[1] These materials have opened new frontiers in exotic physics,[2] catalysis[3] and nanotechnology,[4] yet they face several limitations including relatively low chemical addressability, and difficulty to access high quality flakes at scale.[5] An attractive route to circumvent these challenges is to prepare "programmable" 2D hierarchical crystals using superatomic building blocks of predetermined structural and physicochemical properties.[5–12] Examples of solid-state 2D hierarchical materials exist, for example the semiconductor $Re_6Se_8Cl_2$, formed of layers of interlinked Chevrel-like cluster units,[13,14] yet only a handful of reports of cluster-assembled 2D superatomic crystals have been synthesized thus far via a bottom-up approach.[12,15–19]

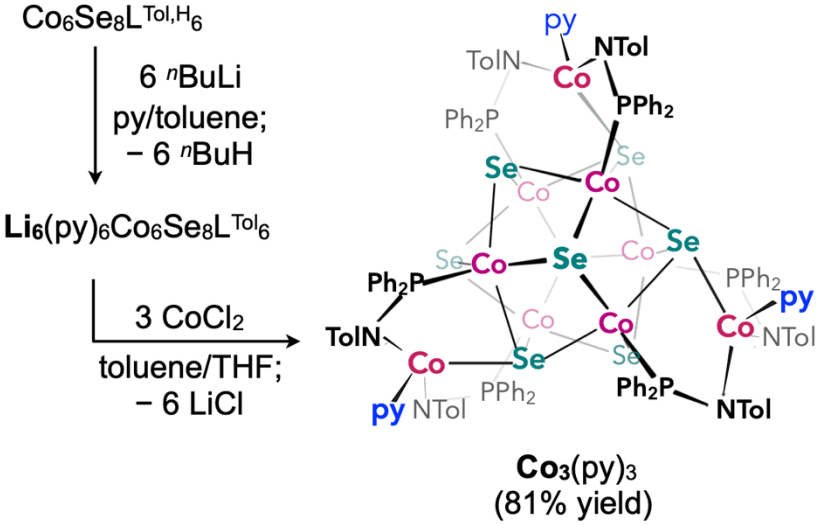
Although wide libraries of atomically precise inorganic clusters of different sizes, compositions and properties are available,[20,21] there are critical synthetic challenges to using them as superatomic building blocks. For example, access to 2D cluster-assembled materials is inhibited by the intrinsic high symmetry of the cluster cores. Typically prepared under thermodynamic control in one-pot syntheses, inorganic clusters have many chemically indistinguishable surface sites. Upon assembly, these degenerate surface sites bind indiscriminately to linkers and give rise

to three dimensional structures.[22–26] Synthetic strategies to deliberately lower the symmetry of the nanocluster blocks could address this challenge.[25,27] For example, site-differentiation, achieved empirically under stoichiometric control, has enabled the synthesis of the low-symmetry linear *trans*-$Co_6Se_8(PEt_3)_4(CNC_6H_4NC)_2$ cluster, which in turn seeded the growth of 1D chains.[16,28] More commonly though dimensional control is obtained serendipitously.[18,19] For example, equipping the degenerate capping ligands with functional groups designed to interlink clusters via coordinative, π-π or H-bonding, has produced 2D cluster frameworks.[9,15,17]

These strategies, however, are either not deterministic or they lack versatility, and rely heavily on using the organic capping ligands as linkers, limiting further the potential to tailor the structural and electronic properties of cluster-assembled materials. For example, in-plane anisotropy, found in many inorganic solid-state van der Waals materials, is a highly desirable structural feature as it provides distinct in-plane pathways for electronic and thermal transport.[29] Still, deterministically encoding it in atomically precise materials remains a synthetic challenge. Most commonly, in reticular materials, in-plane anisotropy occurs serendipitously as the inorganic nodes self-assemble in situ, but it can be deliberate when using asymmetric, or mixtures of organic linkers.[18,30–32] Directing in-plane anisotropy by relying on structural features of the inorganic nodes instead is desirable, but requires access to preformed blocks with distinct low-symmetries. This strategy has been successfully demonstrated using anisotropic colloidal nanoparticles,[33,34] but not for atomically precise inorganic clusters. This work represents, to the best of our knowledge, the first such example.

Our group developed a generalizable strategy to deliberately lower the symmetry of existing nanoclusters by decorating their inorganic cores with addressable linker-binding sites. Specifically, we recently introduced the synthesis of the helically chiral nanocluster, $Fe_3Co_6Se_8L^{Tol}_6$ (L^{Tol} = $Ph_2PN^{(-)}Tol$), Ph = phenyl, Tol = 4-tolyl), obtained by functionalizing the surface of the Chevrel-type cluster $Co_6Se_8L^{Tol,H}_6$ ($L^{Tol,H}$ = $Ph_2PN(H)Tol$) with three Fe edges.[35] Oriented at the vertices of a triangle, the iron sites are poised to function as linker-attachment points that would impose 2D growth upon assembly with linear linkers. A quick evaluation of $Fe_3Co_6Se_8L_6$ as a building block for self-assembly reveals a critical limitation: the Fe edges have very low affinities for external ligands. Here, we find that simply replacing the Fe with Co, the edge sites become not only competent attachment points for linear ditopic linkers, but also unusual inorganic stereocenters with strict stereoselectivity for a low-symmetry isomer. The 2D cluster-

Scheme 4.1. Synthesis of tritopic nanocluster building block, **Co$_3$**(py)$_3$; L^{Tol,H} = Ph$_2$PN(H)Tol; py = pyridine.



assembled materials obtained from these nanoclusters represent exceedingly rare examples where preformed building blocks encode their key structural and physical properties, including in-plane anisotropy, quasi-chiral domains as well as rich redox activity and magnetism. Remarkably, these synthetic 2D superatomic crystals are amenable to post-synthetic manipulations, including exfoliation to ultrathin flakes, and intercalation with guest molecules in a single-crystal-to-single-crystal transformation that highlights their rich, and robust redox profile.

4.3 Synthesis and Characterization of Co/Se/Co Nanoblock

We illustrate the unprecedented versatility of our synthetic strategy to program nanoclusters through the facile synthesis of the tricobalt variant, prepared similarly to $Fe_3Co_6Se_8L_6$.[35] With increased affinity of the edge sites for external ligands, the tricobalt nanopropeller is isolated exclusively as the tris-pyridine adduct $Co_3(py)_3Co_6Se_8L_6$ (**Co$_3$**(py)$_3$, 81% yield, Scheme 4.1). As was observed in the case of **Fe$_3$**, the UV-vis-*n*IR absorption profile of **Co$_3$**(py)$_3$ reveals how trimetallation with cobalt invokes a stark red-shift in λ_{max}, with a general broadening of adsorption features and increase in absorptivity relative to $Co_6Se_8L^{Tol,H}_6$ (Figure 4.2). Single-crystal X-ray analysis reveals that within **Co$_3$**(py)$_3$, each Co edge is capped by a pyridine ligand and anchored κ^3 to the cluster core via two amides, and one surface selenium pseudo-tetrahedral geometry (Figure 4.3).

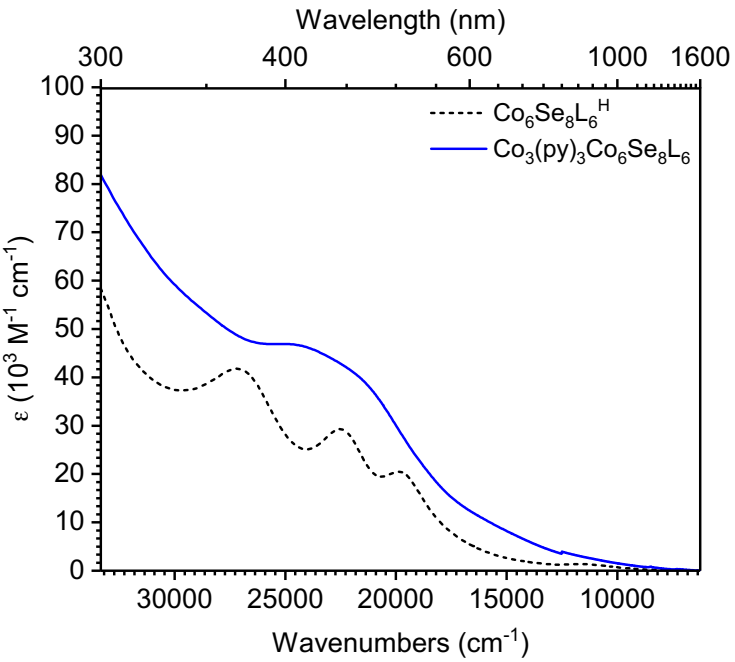


Figure 4.2. UV-vis-*n*IR absorption spectra of $Co_3(py)_3Co_6Se_8L_6$ (**Co_3**$(py)_3$) and $Co_6Se_8L^{Tol,H}{}_6$ recorded in THF.

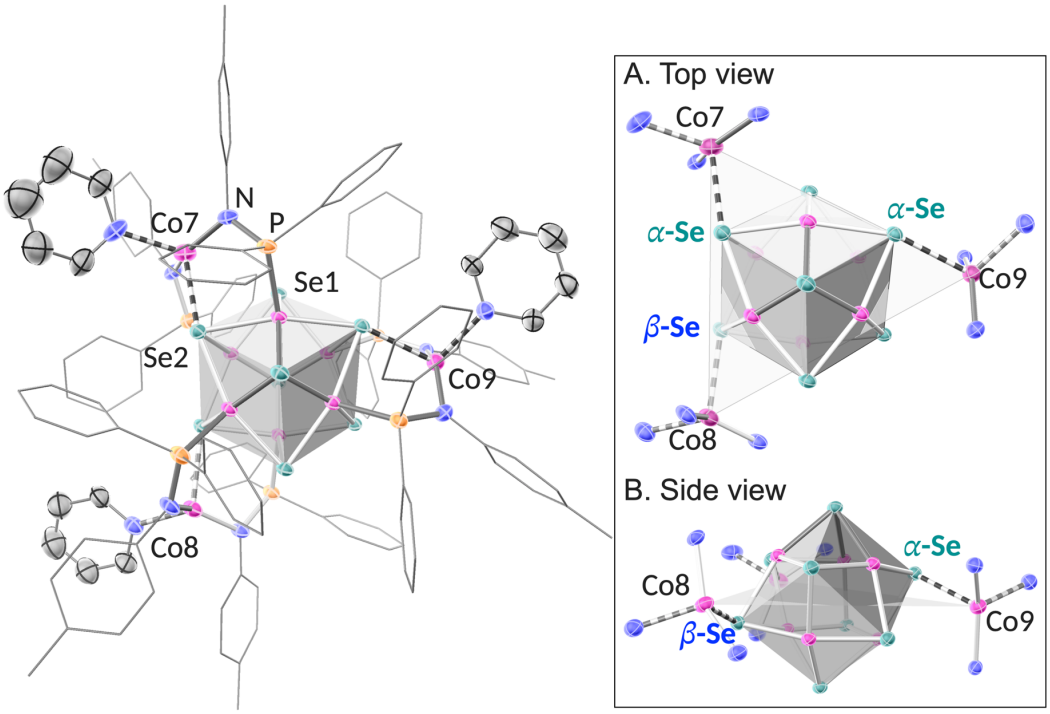


Figure 4.3. Single-crystal X-ray structure of the Λ enantiomer of **Co_3**$(py)_3$, with selected interatomic distances (Å): Co7–Se2 2.534(1), Co7…Se1 3.200(2), Co8–Se3 2.524(1), Co9–Se6 2.573(2). Thermal ellipsoids plotted at 50%. Disordered ligands, solvent and hydrogen atoms hidden for clarity. Inset: top (a) and side (b) view of **Co_3**$(py)_3$ illustrating (α,α,β) orientation with respect to the plane of the Co edge sites, with two Se bound above this triangle (α) and one below(β).

Nanocluster **Co$_3$**(py)$_3$ contains two distinct Co environments: three exposed tetrahedral Co "edge" sites doubling as linker-attachment points, and six square pyramidal Co "core" sites. X-ray diffraction analysis reveals two distinctive structural features, consequential to using **Co$_3$**(py)$_3$ as a pre-templated inorganic building block for nanomaterials. One is the intrinsic helicity of **Co$_3$**(py)$_3$, isolated as a (Δ/Λ) racemic pair, stemming from the propeller geometry of its inorganic core.[35] The other is the stereogenic nature of the Co edge sites. The stereoisomerism of **Co$_3$**(py)$_3$ is easiest understood by analogy to isomerism in 1,2,3-trisubstituted cyclopropanes, where the three substituents are either all oriented on the same face of the ring, or one points to the opposite side from the other two. Similarly, the three edge Co atoms define a triangle that separates two Co_3Se_4 hemispheres of the Co_6Se_8 nanocube, with each edge-binding site containing an above-the-plane (α-Se) and beneath-the-plane (β-Se) selenium atom (Figures 1). Upon coordination, pyridine formally displaces one of these Se atoms from a κ^4-bound Co edge site, to yield an α- or a β-bound edge site. Each Co surface site effectively discriminates between the two structurally equivalent α, β selenium atoms, and creates three discrete edge Co stereocenters. In turn, these stereocenters orient the bound pyridine above or beneath the plane of the Co edge sites, akin to the isomers of 1,2,3-trisubstituted cyclopropane.

Remarkably, in the solid state, **Co$_3$**(py)$_3$ is completely stereoselective for the formation of the low-symmetry (α,α,β) diastereomer. Searching the literature for examples of stereoisomerism in trinuclear clusters, we find they overwhelmingly favor the formation of the high symmetry isomer (α,α,α).[36–38] Low-symmetry isomers could only be isolated as adducts with bulky metal electrophiles that sterically enforce the (α,α,β) orientation of the ring substituents. For example, treating the (α,α,α) isomer of the indenyl complex $Ir_3(CO)_3(\eta^5\text{-}C_9H_7)_3$ with the electrophile $[Au(PPh_3)][PF_6]$ allows the isolation of the (α,α,β) isomer as the $\{Ir_3[Au(PPh_3)](CO)_3(\eta^5\text{-}C_9H_7)_3\}[PF_6]$ adduct.[39] While different structural phases of the same elemental composition are prevalent in both extended and molecular inorganic materials, such well-defined, localized isomerism is typically associated with organic structures; **Co$_3$**(py)$_3$ represents an unusual and rare example of stereoisomerism within a well-defined inorganic cluster core.[40–42]

Investigating the origin of the stereoselectivity guiding the interaction of the edge-Co with the Co_6Se_8 surface in **Co$_3$**(py)$_3$, we note an analogy with how metal adatoms discriminate between different surface sites of inorganic supports, preferentially adsorbing to minimize adsorption-induced strain.[43,44] In **Co$_3$**(py)$_3$, the Co_6Se_8 support behaves as an electron reservoir, donating

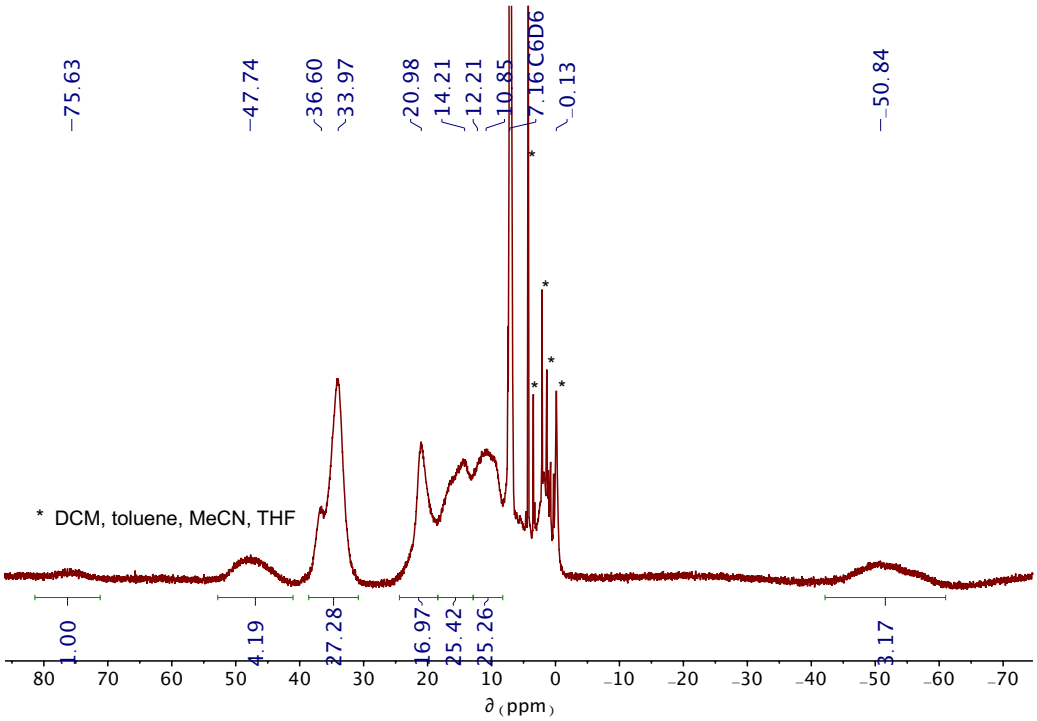


Figure 4.4. ^{1}H NMR (benzene-d_6, 25 °C, 300 MHz) spectrum of **Co$_3$**(py)$_3$.

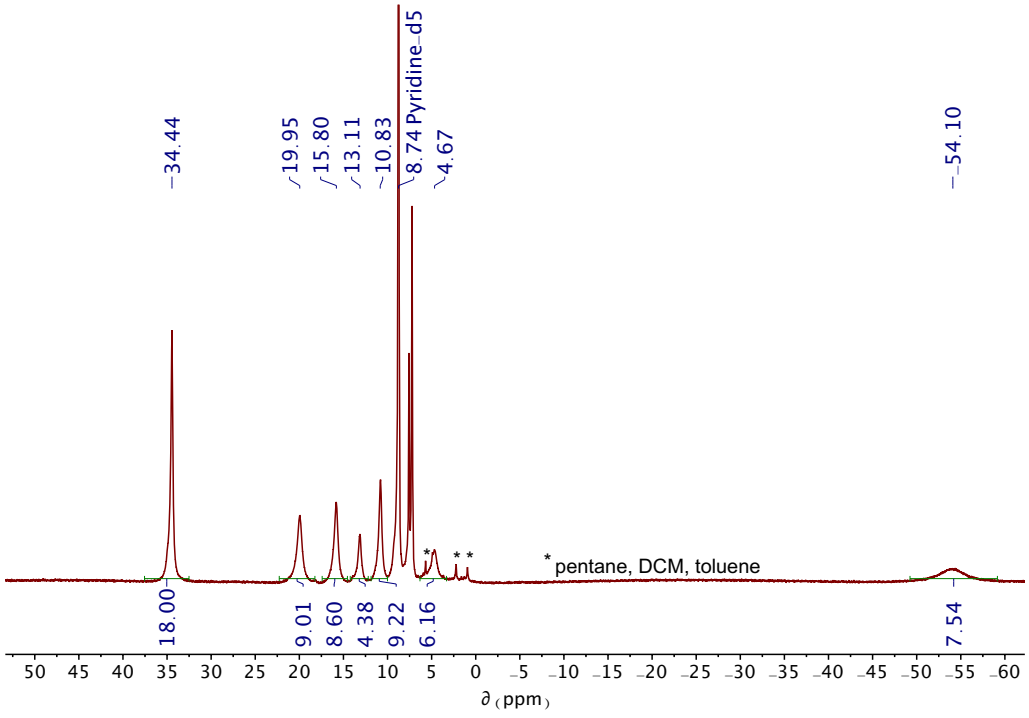


Figure 4.5. ^{1}H NMR (pyridine-d_5, 25 °C, 300 MHz) spectrum of **Co$_3$**(py)$_3$.

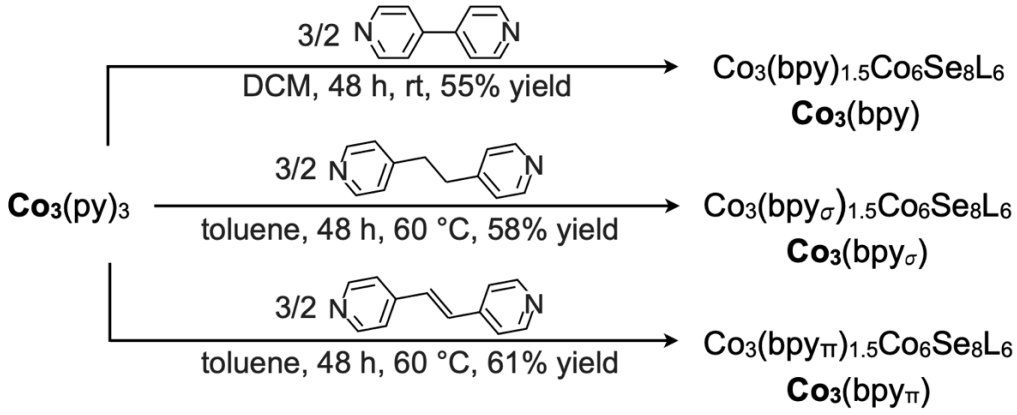
electron density to the Lewis-acidic edge sites through Co–Se interactions.[35] In turn, these core–edge contacts induce steric distortions and electron density redistribution within the Co_6Se_8 core. As Se lone pairs engage in bonding interactions with the edge Co sites, their corresponding bonds to the core Co elongate from an average of 2.33 Å to 2.38 Å. The unobserved (α,α,α) isomer would place all elongated intracore Co–Se bonds in the same cluster hemisphere, compounding the structural and electronic polarization effects brought about by the distortions. In contrast, the (α,α,β) isomer distributes the edge Co–Se bonds between the two cluster hemispheres, minimizing strain and dispersing electron density more evenly within the inorganic core.

The low symmetry of the Co/Se/Co core is also detected in solution via NMR spectroscopy when **Co$_3$**(py)$_3$ is dissolved in a non-coordinating solvent. The slow exchange of the surface-bound pyridines in benzene-d_6, and the resultant lower symmetry of the nanocluster are reflected in a very broad ^{1}H NMR spectrum (Figure 4.4). Dissolution in pyridine-d_5 dramatically speeds up ligand exchange, giving rise to seven, comparatively sharper phosphinoamide ^{1}H signals (Figure 4.5), suggestive of the pseudo-D_3 symmetry of a Co/Se/Co core where the edge metals are rapidly reorganizing between α/β orientations. This provides another instance of the choreography of the three edge metals dancing through the Co_6Se_8 support.

4.4 Self-Assembly of Anisotropic Nanosheets

We hypothesized that while the presence of trigonally disposed attachment points on the nanocluster surface would give rise to a 2D material upon assembly with linear ditopic linkers, the (α,α,β) stereoselectivity would ensure in-plane structural anisotropy. To investigate the potential offered by **Co$_3$**(py)$_3$ as a building block, we selected a family of ditopic, linear linkers of increasing length and structural flexibility: bpy, bpy$_\pi$ and bpy$_\sigma$ (4,4'-bipyridine, 1,2-di(4-pyridyl)ethylene and 1,2-bi(4-pyridyl)ethane, respectively). We found that mixing the linkers with **Co$_3$**(py)$_3$ in a non-coordinating solvent induced the formation of dark red crystals (Scheme 4.2). Each of the emerging materials, $Co_3(bpy)_{1.5}Co_6Se_8L_6$ (**Co$_3$**(bpy)), $Co_3(bpy_\sigma)_{1.5}Co_6Se_8L_6$ (**Co$_3$**(bpy$_\sigma$)) and $Co_3(bpy_\pi)_{1.5}Co_6Se_8L_6$ (**Co$_3$**(bpy$_\pi$)), were isolated in good yields after 48 h (55–61%). Inspecting their single crystal X-ray structures, we discovered in each case the formation of anisotropic nanosheets that are layered to form superatomic van der Waals solids (Figure 4.6). The three laminar materials are structurally similar, with slight variations in the structure, morphology and stacking of the nanosheets in the 3D crystal, in accordance with the length and flexibility of the

Scheme 4.2. Self-assembly of van der Waals nanosheets, **Co3**(bpy), **Co3**(bpy$_\sigma$), and **Co3**(bpy$_\pi$), from tritopic nanoblock **Co3**(py)$_3$ and pyridyl-based ditopic linkers.



linkers. Each nanosheet is constructed of fused six-sided polygons in a chair-like conformation, with nanocluster vertices interconnected by linkers. Upon assembly, the inorganic nodes retain the (α,α,β) stereoisomerism of **Co3**(py)$_3$, successfully engendering in-plane structural anisotropy.

The smoothness, thickness and orientation of individual layers in the 3D crystal depend on the organic linker. Within each layer, the nanopropeller nodes are tilted in unison with respect to the plane of the nanosheet, causing the formation of periodic ripples (Figure 4.6a). The amplitude of the ripples is determined by the length and flexibility of the linker. With an amplitude of 1.31 Å, the ripples are most pronounced for **Co3**(bpy$_\pi$), which is built using a long and rigid linker. In contrast, **Co3**(bpy$_\sigma$), which contains the more flexible ethane-spaced linker, exhibits a smoother nanosheet surface with a ripple amplitude of only 0.14 Å. Notably, the intersheet distance of 0.92 nm in **Co3**(bpy$_\sigma$) is significantly smaller than the 1.29 nm layer thickness. Inspecting the structure of this derivative closer, we discover that neighboring sheets interdigitate to allow pairs of Co_9Se_8 vertices in each polygon to rest within the valley found at the center of polygons belonging to above and beneath layers. Further, the nanosheets in **Co3**(bpy$_\sigma$) propagate along a 2_1 screw axis that runs parallel to a primary crystal facet, making this material amenable to mechanical exfoliation. In contrast, **Co3**(bpy) and **Co3**(bpy$_\pi$), built of more rigid linkers, contain nanosheets packed along diagonal lattice planes, and their layers are significantly more separated, by 1.40 and 1.33 nm, respectively.

Within the nanosheets, the racemic mixture of helical nanopropellers undergoes quasi-chiral phase separation within the nanosheets, segregating into alternating Δ- and Λ-homochiral rows (Figure 4.6b). This phenomenon, wherein a racemic mixture of enantiomers spontaneously

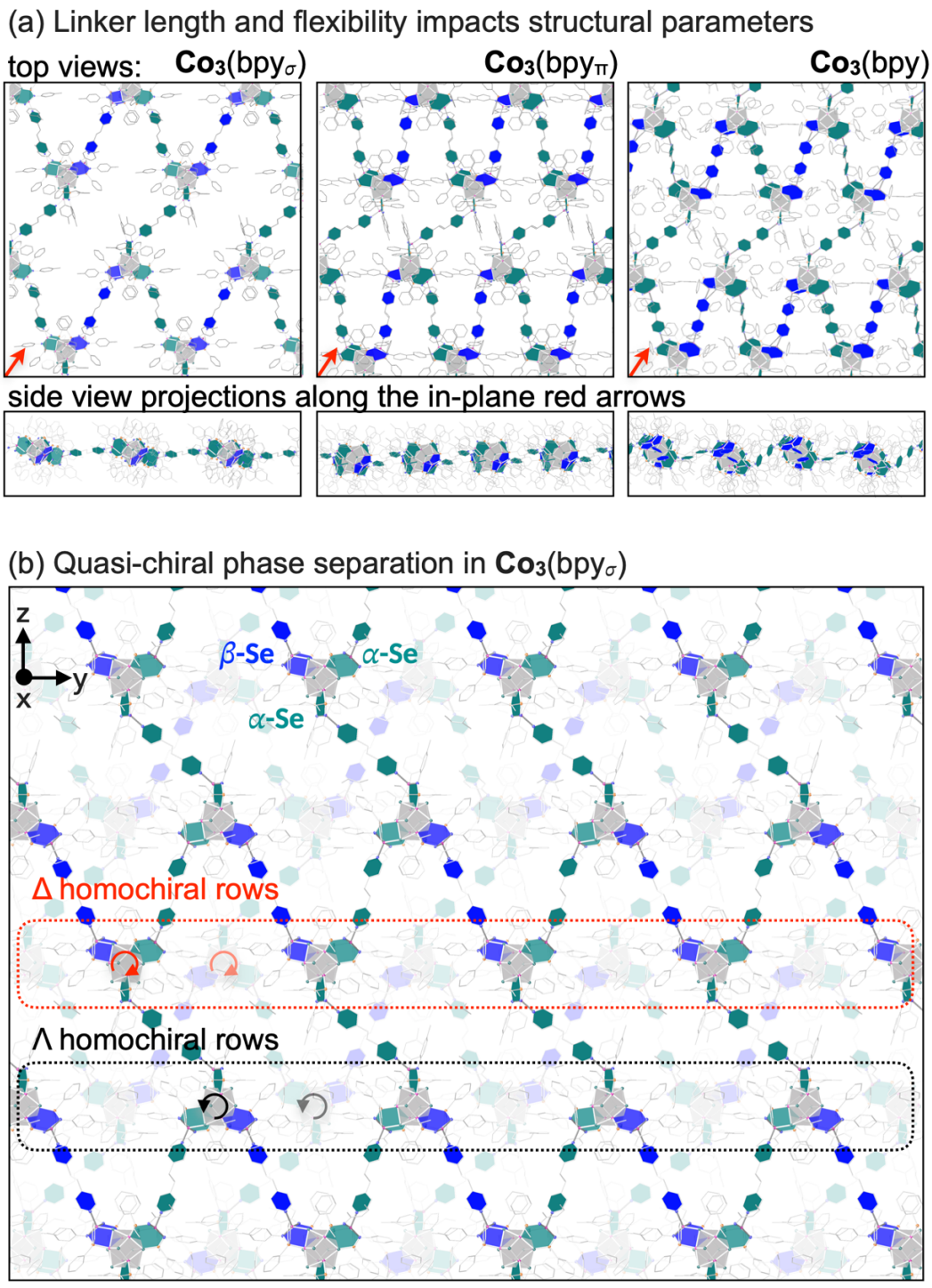


Figure 4.6. (a) Single crystal X-ray structure for single layers of **Co3**(bpy), **Co3**(bpy$_\sigma$) and **Co3**(bpy$_\pi$) (top and side views), illustrating the variations in tile sizes and layer corrugation. (b) In-plane anisotropy and quasi-chiral phase separation in **Co3**(bpy$_\sigma$). Linkers and nanopropeller blades are colored blue when linked to β-Se, and teal when associated with α-Se sites.

separates into enantiomerically pure domains upon assembly, was first observed in monolayers of chiral organic molecules deposited on surfaces,[45,46] and more recently also in 3D frameworks.[47] **Co$_3$**(bpy), **Co$_3$**(bpy$_\sigma$), and **Co$_3$**(bpy$_\pi$) represent examples where quasi-chiral separation is a guiding force in the self-assembly of 2D frameworks. Notably, the homochiral rows are also aligned vertically in the 3D lattice of **Co$_3$**(bpy$_\sigma$), opening intriguing possibilities for harnessing emerging optoelectronic properties associated with the individual homochiral domains within the 3D crystals.

4.5 Solid-state Magnetic Analysis

One trait that distinguishes **Co$_3$**(py)$_3$ from other reported superatomic building blocks is the high-spin electronic configuration of the Co edge sites. Here, we find that within the nanosheets, the individual magnetic properties of the nanoblock **Co$_3$**(py)$_3$ are unaltered. This is illustrated in Figure 4.7a, which depicts the virtually identical magnetic responses of nanoblock **Co$_3$**(py)$_3$ and nanosheet **Co$_3$**(bpy$_\pi$). Similar results are observed for the other two derivatives, **Co$_3$**(bpy) and **Co$_3$**(bpy$_\sigma$), with minor deviations at high temperatures for the latter (Figure 4.12). Given the similarity between the magnetic response of the nanosheets with the monomeric precursor, we focused our interpretation of these properties on those of **Co$_3$**(py)$_3$. Featuring a triangle of high-spin Co(II) sites that inscribes a hexametallic Co_6Se_8 core, formally $(Co^{III})_4(Co^{II})_2$, nanopropeller **Co$_3$**(py)$_3$ offers a rare opportunity to study the magnetic interaction between paramagnetic ions mediated through a well-defined inorganic support.[48] Within the nanoblock **Co$_3$**(py)$_3$, the magnetic properties are dominated by the three S = 3/2 Co(II) edge sites. Above 150 K, the magnetic susceptibility of **Co$_3$**(py)$_3$ is greater than expected for three non-interacting Co(II) ions (7.2 vs 5.6 $cm^3\ mol^{-1}$ K, g = 2.0). This discrepancy is expected for the distorted-tetrahedral Co(II) edges, and stems from unquenched orbital angular momentum contributions to the spin-only susceptibility (g = 2.28).[49,50] Reduced magnetization data, which resists saturation up to a maximum field of 7 T at 1.8 K, corroborates this interpretation and confirms the presence of a high-spin ground state (Figure 4.7b). Below 150 K, the magnetic susceptibility decreases steadily, reaching a minimum of 2.9 $cm^3\ mol^{-1}$ K at 2 K. We interpret this behavior to be a combined result of weak antiferromagnetic exchange between the three Co edge sites, also reflected in the negative Weiss constant (θ = –10.5 K),[51] and localized anisotropy of the Co(II) edges. As intra- and intermolecular edge site Co…Co distances are prohibitively long for through-space magnetic

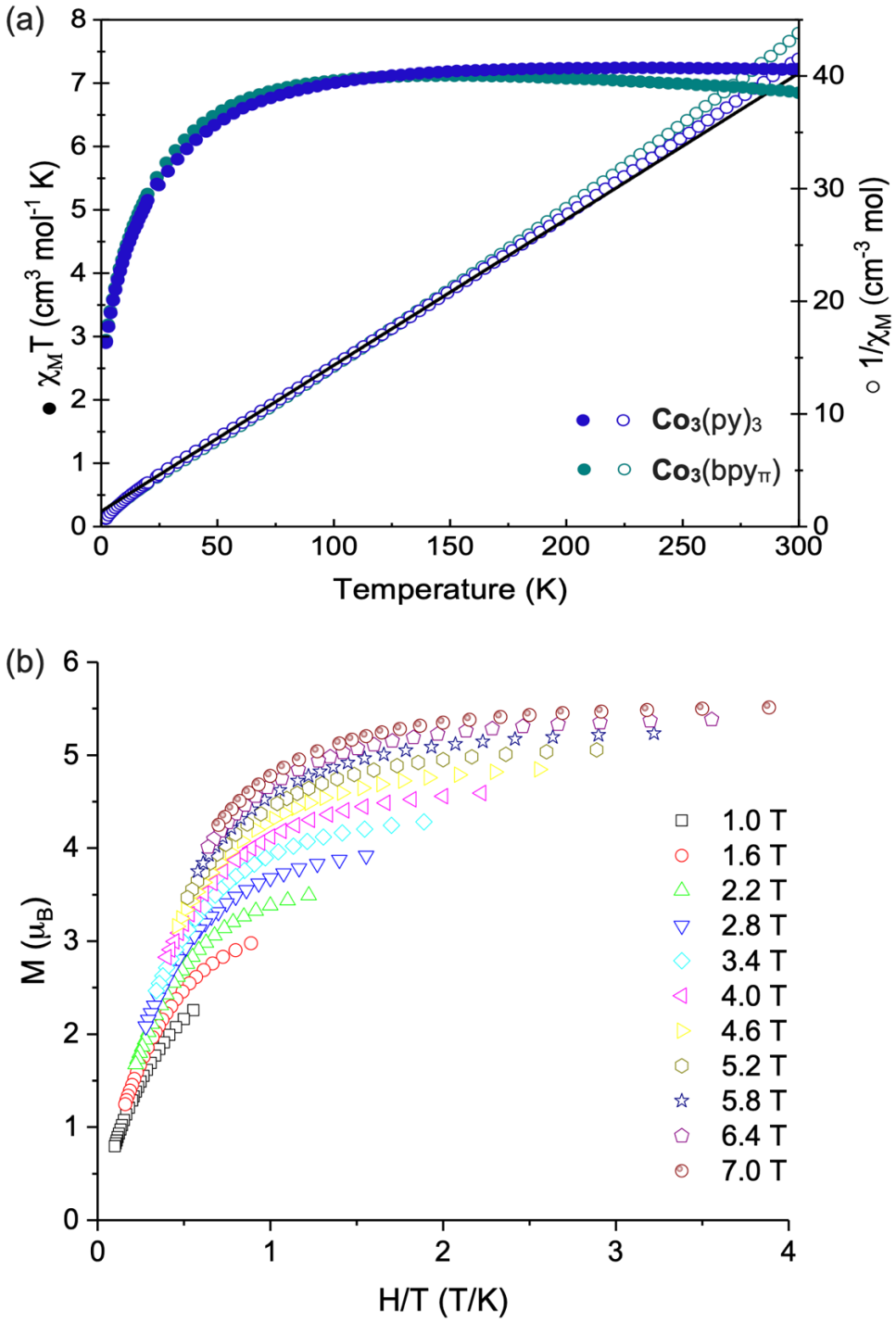


Figure 4.7. Post-assembly, **Co$_3$**(py)$_3$ preserves its individual magnetic properties within the nanosheets. (a) Plotted are the variable-temperature *dc* magnetic susceptibility ($\chi_M T$, filled circles), the reciprocal molar susceptibility ($1/\chi_M$, hollow circles) data for nanoblock **Co$_3$**(py)$_3$ (blue) and nanosheet **Co$_3$**(bpy$_\pi$) (teal), collected between 2 to 300 K, at 0.1 T, and the linear fit (25 to 150 K) used to obtain the Weiss constant. (b) Variable-temperature, variable-field reduced magnetization data for **Co$_3$**(py)$_3$, collected upon warming from 1.8 to 10 K at each applied field.

exchange (> 9 Å),[52] we propose the antiferromagnetic coupling is mediated through the diamagnetic Co_6Se_8 core.[53] Considering that the previously reported [Re_5OsSe_8] cluster core, diamagnetic and isostructural with Co_6Se_8, has been shown to prevent the magnetic interaction between surface bound S = 1/2 Cu(II) ions, antiferromagnetic coupling between the edge S = 3/2 Co in **Co$_3$**(py)$_3$ was initially surprising. The different behavior observed in **Co$_3$**(py)$_3$ may stem in part from the increased spin response of the Co(II) ions. We propose that the high-spin Co(II) sites interact through low-lying Van Vleck paramagnetic spin states within the Co_6Se_8 core, which resemble magnetic interactions reported in Co_6Te_8 and Ni_9Te_6 clusters.[54] Alternatively, the edge Co may interact with the core via intervalence charge transfer processes that may be enabled at low temperature.

4.6 Redox-Active Hybrid Nanosheets

4.6.1 *Electrochemical Characterization of Co/Se/Co Nanosheets*

Nanocluster **Co$_3$**(py)$_3$ exhibits a total of five quasi-reversible one-electron redox events spanning 2.5 V and six oxidation states, between 2– and 3+ (Figure 4.8). Randles-Sevcik analysis confirms that each redox process is chemically reversible within the diffusion-limit.[35,55,56] Interestingly, the robust binding of pyridine to the Co edge sites is reflected in an electrochemical profile completely insensitive to the presence of a coordinating solvent. The first two oxidation events in **Co$_3$**(py)$_3$ occur at similar potentials to those observed for **Fe$_3$** and the parent cluster $Co_6Se_8L^{Tol,H}{}_6$, indicating these remain localized on the Co_6Se_8 core, and do not involve the edge Co sites. Additionally, in **Fe$_3$** we determined that the LUMO, estimated electrochemically as the first reduction event, was localized on the Co_6Se_8 core and stabilized relative to $Co_6Se_8L^{Tol,H}{}_6$. We attributed this stabilization to the Lewis acidity of the edge sites that withdraw electron density from the core through the binding Se. In **Co$_3$**(py)$_3$, donation from the electron rich pyridine ligands effectively decreases the Lewis acidity of the Co edge sites, which in turn leads to a larger HOMO–LUMO gap than that of the Fe derivative (1.01 vs 0.79 eV), but still markedly smaller than that of parent cluster (1.44 eV).

To probe the electronic states of the assembled nanosheets, we dropcast crystalline material on a glassy carbon working electrode. Figure 4.8 depicts the comparison between the electrochemical profile of the nanocluster **Co$_3$**(py)$_3$, acquired in solution, and that of the **Co$_3$**(bpy$_\sigma$)

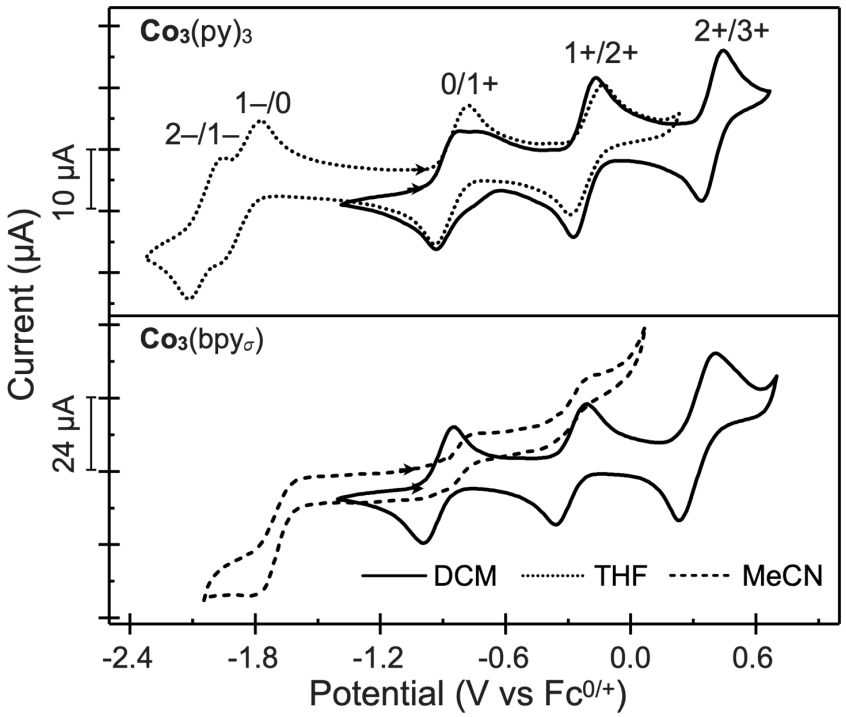


Figure 4.8. Solution and solid-state cyclic voltammograms of **Co3**(py)3 and **Co3**(bpy$_\sigma$), respectively, recorded in DCM (solid lines), THF (dotted lines) or MeCN (dashed lines) solutions of [^{n}Bu$_4$N][PF$_6$] (0.1 M), at a scan rate of 200 mV/s. The data for **Co3**(bpy$_\sigma$) was recorded by dropcasting a slurry of crystalline **Co3**(bpy$_\sigma$) in toluene on a glassy carbon disk electrode.

nanosheets. We discover that the rich redox behavior of the nanopropeller nodes is preserved upon assembly, and the nanosheets exhibit three well-resolved oxidation processes and one irreversible reduction event, all at potentials effectively coinciding with those of nanocluster **Co3**(py)3. The irreversibility of the –1/0 event is not surprising, and we attribute it to the decrease in the Co edge binding affinity for the pyridyl linker, which in turn would be associated with the dissolution of the nanosheet. A similar redox-state controlled affinity for ligands was observed for the triiron nanocluster $Fe_3Co_6Se_8L_6$. Finally, we found the linker has a minimal impact on the electrochemical behavior of the cluster nodes. **Co3**(bpy) and **Co3**(bpy$_\pi$) exhibit similar redox profiles to that of **Co3**(bpy$_\sigma$), though slight variations in the half-wave potentials, peak-to-peak separation and reversibility of peaks are observed (see Section 4.9.8 for supplementary electrochemical characterization).

4.6.2 *Single-crystal-to-single-crystal Redox Intercalation*

Redox intercalation into layered materials is a powerful strategy to post-synthetically alter structural, electronic, or magnetic properties.[57] For example, ion intercalation has been used to switch between insulating and semiconductor behaviors in a 2D metal-organic framework,[58] or to tune the conductive properties of the cluster-assembled donor-acceptor solid.[59] Testing our ability to predictably introduce dopants via nondestructive post-synthetic techniques, we investigated the intercalation of redox-active tetracyanoethylene (TCNE) guest molecules into the lattice of **Co$_3$**(bpy$_\sigma$) (Figure 6a).

A crop of crystals of **Co$_3$**(bpy$_\sigma$) (1 equiv) were immersed in a solution of TCNE (5 equiv) in *n*-pentane/toluene for 24 h. Before collecting the product (41 mg, 95%), excess TCNE was removed by repeatedly soaking the crystals in toluene (3 x 3 mL) and *n*-pentane (3 x 3 mL) and volatiles were removed under reduced pressure. Infrared vibrational analysis revealed the crystals exhibit only CN stretching frequencies diagnostic of the mono-reduced $[TCNE]^{\cdot-}$ anion (ν_{CN} = 2182, 2142 cm^{-1}),[60] indicating the redox reaction had occurred (Figure 6b). Thermodynamic considerations derived from the electrochemical analysis of **Co$_3$**(bpy$_\sigma$) (Figure 4) indicate excess TCNE will lead to the dioxidation of each cluster node, as $TCNE^{-/0}$ = –0.27 V vs $Fc^{0/+}$; this is indeed verified by solid state analysis. The change in oxidation state from neutral is also reflected in the ^{1}H NMR spectrum of the nanoclusters, obtained by dissolving the intercalated nanosheets in d_5-pyridine.

Single crystal X-ray analysis of the intercalated nanosheets revealed the crystallinity of the parent material was preserved, the reaction proceeding via a single-crystal-to-single-crystal transformation. Identified as [**Co$_3$**(bpy$_\sigma$)][TCNE]$_2$, we draw attention to the 1:2 ratio of $[Co_9Se_8L_6]^{2+}$ nodes and $[TCNE]^{\cdot-}$ guest molecules (Figure 6c). The oxidized product is largely isostructural with the neutral starting material, maintaining the P 2_1/n space group, but it does have an increased interlayer distance, from 9.2 to 9.6 Å. Two pairs of crystallographically distinct $[TCNE]^{\cdot-}$ anions occupy each pore of the nanosheet. We note that upon dioxidation, the Co(edge)–Se interaction weakens, elongating by 0.05 Å (avg), while the linker-Co(edge) bonds strengthen, contracting by 0.05 Å (avg). Other structural changes that occur within the inner core of the nodes upon oxidation include a contraction of the *trans*-Co…Co interatomic distances within the Co_6Se_8 unit from 4.12 to 3.99 Å (avg.), and an elongation of the Co–P average bond lengths from 2.14 to

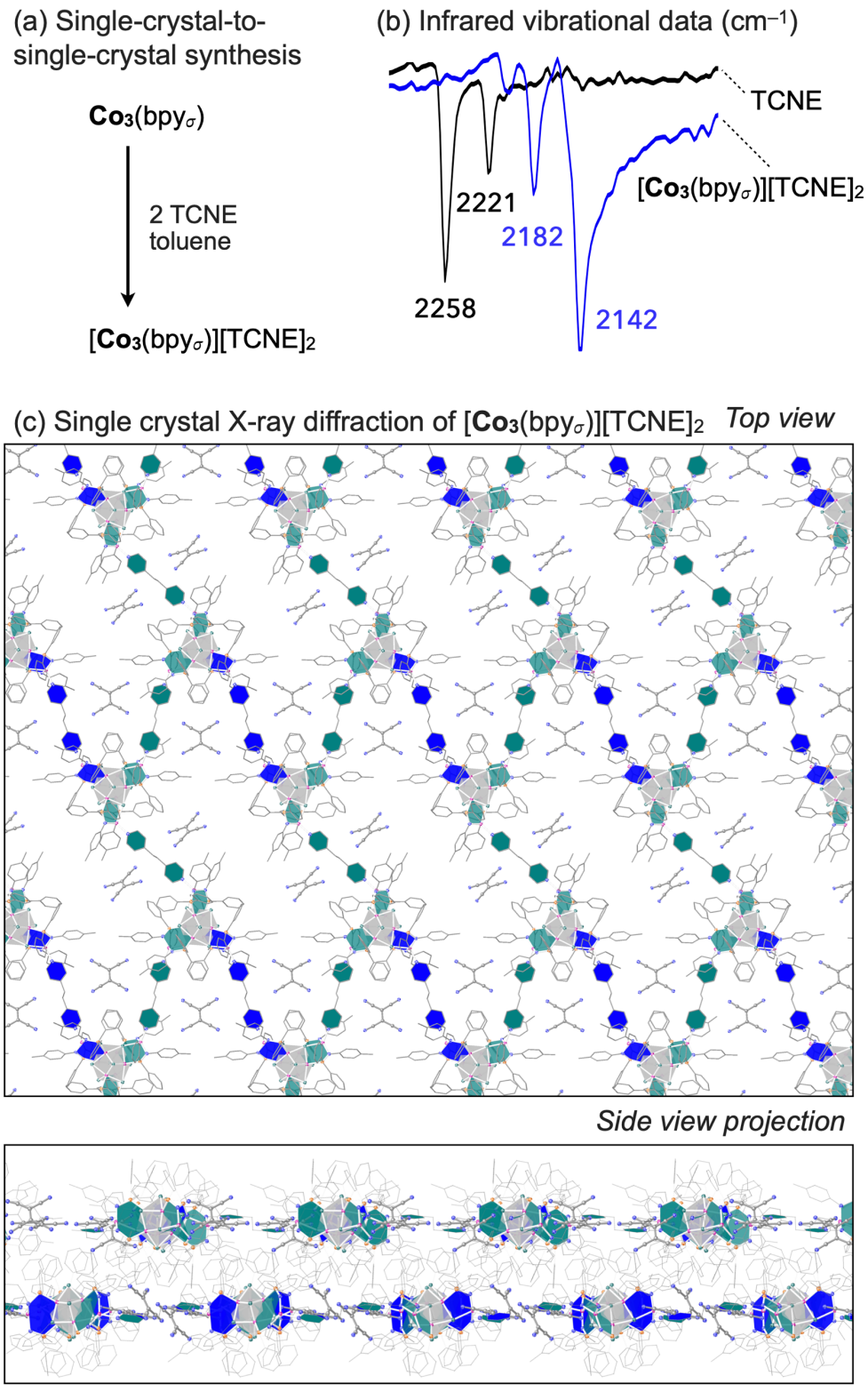


Figure 4.9. a) Single-crystal-to-single-crystal synthesis of $[\mathbf{Co_3}(bpy_\sigma)][TCNE]_2$ via redox intercalation. b) ATR-FTIR analysis of $[\mathbf{Co_3}(bpy_\sigma)][TCNE]_2$ and TCNE, highlighting the CN stretching region. c) Single crystal X-ray structure of $[\mathbf{Co_3}(bpy_\sigma)][TCNE]_2$ (top and side views).

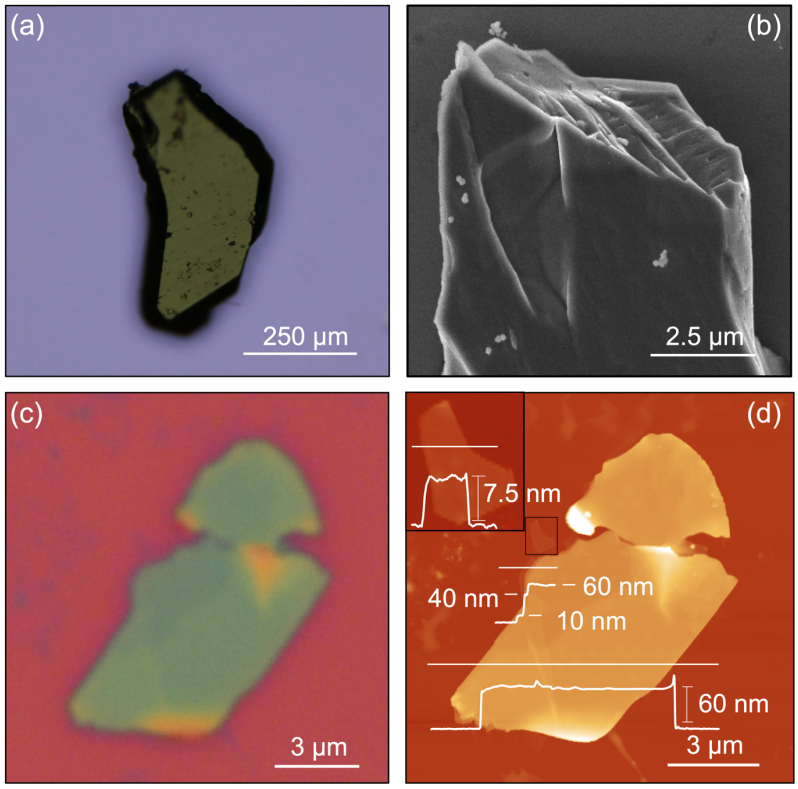


Figure 4.10. The laminar structure of **Co3**(bpy$_\sigma$) revealed by imaging pre- and post-mechanical exfoliation of a single crystal. (a) Optical microscopy image of a bulk single crystal. (b) Scanning electron microscopy image focused on laminar edge of the bulk crystal. (c) Optical microscopy of a mechanically exfoliated flake. (d) Atomic force microscopy characterization of the exfoliated flake, including height profiles and a zoom-in inset of a thin flake.

2.19 Å, both of which are tell-tale structural changes incurred upon oxidation of Co_6Se_8 clusters.[59,61]

4.7 Mechanical Exfoliation of **Co3**(bpy$_\sigma$) into Ultrathin Nanosheets

The individual nanosheets assembled from nanocluster **Co3**(py)$_3$ are structurally robust, and can be isolated as ultrathin atomic crystals, behaving akin to solid-state inorganic van der Waals 2D materials. Indeed, **Co3**(bpy$_\sigma$) can be successfully exfoliated using the Scotch tape method (Figure 4.10).[62] Optical microscopy imaging of the exfoliated crystals reveals its layered structure, along with a well-defined, thickness-dependent color contrast. Atomic force microscopy analysis shows the exfoliated flakes depicted in Figure 4.10d have large lateral dimensions (6-15 µm), flat surfaces, and a well-defined lamellar structure with steps ranging between 10 and 30 nm. The

thickness of these flakes ranges from 60 nm to as low as 8 nm (ca. 8 layers). Examples of bottom-up assembled 2D materials that could be exfoliated or prepared as few or mono-layers primarily include organic[63,64] or hybrid[65–67] reticular frameworks. However, 2D cluster-assembled materials—attractive for their promise of function programmability—that have been successfully exfoliated are exceedingly scarce. In addition to **Co$_3$**(bpy$_\sigma$), there are only two other examples, a 2D framework interconnected through the capping ligands by zinc-carboxylate nodes, and a hybrid nanosheet in which individual clusters are sandwiched between sheets of photopolymerized C_{60}.[15,17]

4.8 Conclusions

With this report we introduce a deterministic and modular synthetic strategy to access anisotropic 2D superatomic crystals, and demonstrate these are post-synthetically addressable for further engineering their physical and chemical properties. Our unique strategy to circumvent the pervasive synthetic limitations to interlink clusters relies on equipping the inorganic surface of the nanocluster with three chemically accessible linker-attachment sites. The intrinsic features of the resulting designer nanocluster block predetermine the key structural and physical properties of the emergent materials, including dimensionality, in-plane anisotropy, quasi-chiral domains, magnetism and redox-activity. Notably, the rich redox profile and layered structure uniquely poises this new class of cluster-assembled materials for use as atomically defined anodes in battery materials.[68] The ease of mechanical exfoliation to ultrathin superatomic crystals, and single-crystal-to-single-crystal intercalation with TCNE demonstrates the emerging nanosheets are structurally and chemically robust, providing a potent strategy to encrypt desired functionality in superatomic 2D materials.

4.9 Experimental Details

4.9.1 *General Considerations*

All syntheses were conducted under a dinitrogen atmosphere using standard Schlenk or glovebox techniques (LC Technology Solutions glovebox equipped with a freezer set to −35 °C). All glassware was dried at 160 °C for a minimum of 12 h and cooled in an evacuated antechamber prior to use in the glovebox.

Solvents were purchased from Fischer Scientific and degassed, dried and purified using solvent purification columns housed in a stainless-steel cabinet and dispensed by a stainless-steel Schlenk line manufactured by JC Meyer Solvent Systems. Tetrahydrofuran (THF), diethyl ether, acetonitrile (MeCN), and methylene chloride (DCM) are passed through two packed columns of neutral alumina. In the cases of *n*-pentane and toluene, one of the columns is alumina and the other is Q5 reactant, a copper(II) oxide oxygen scavenger. All solvents were passed through an in-line, 2 μm filter, then stored over activated 3Å molecular sieves in the glovebox for a minimum of 72 h. 3Å molecular sieves were purchased from Sigma Aldrich and activated under vacuum at 300 °C for 48 h. Anhydrous pyridine (99.8%) was purchased from Sigma Aldrich and stored over activated 3Å molecular sieves for 72 h prior to use.

Deuterated solvents ($CDCl_3$, C_6D_6, CD_2Cl_2, CD_3CN) were purchased from Cambridge Isotope Laboratories, Inc. degassed and dried over activated 3Å molecular sieves in the glovebox for a minimum of 72 h. $CoCl_2$ (98+%) was purchased from Strem Chemicals, Inc. and dried under vacuum at 120 °C for 24 h prior to use. $Co_2(CO)_8$ (stabilized with 2-5% hexanes) was purchased from Strem Chemicals, Inc. stored in the glovebox freezer and used as received without further purification. The aminophosphine $Ph_2PN(H)Tol$ (Ph = phenyl, Tol = 4-tolyl; $L^{Tol,H}$) was prepared according to the literature.[69] $Co_6Se_8L^{Tol,H}_6$ and $\mathbf{Li_6}(py)_6Co_6Se_8L_6$ were prepared according to methods reported in the literature.[35] Chlorodiphenylphosphine (97%) and *p*-Toluidine (99+%) were purchased from Alfa Aesar and used without further purification. Selenium (99.5%, powder, 200 mesh) and *n*-butyl lithium (2.5 M in hexanes) were purchased from Sigma Aldrich and used without further purification. 4,4'-bipyridine (bpy) (98%), 1,2-bis(4-pyridyl)ethane (bpy_σ) (99%), and 1,2-di(4-pyridyl)ethylene (bpy_π) (97%) were purchased from Sigma Aldrich and used without further purification. Tetracyanoethylene (TCNE, 98%) was purchased from Sigma Aldrich, purified by sublimation, and sheltered from ambient light at –35 °C prior to its use.

Atomic force microscopy (AFM) images were acquired on a Bruker Dimension Icon housed within an MBRAUN LABstar argon glovebox. AFM samples were prepared via mechanical exfoliation of bulk crystalline material. The exfoliated flakes were deposited and analyzed on freshly plasma-cleaned 285 nm SiO_2/Si wafers. Thin flakes of $\mathbf{Co_3}(bpy_\sigma)$ were first identified by optical microscopy, and then their thickness was determined by AFM. Throughout the exfoliation process, flakes were prepared, handled, and imaged in an argon atmosphere.

Cyclic voltammetry was conducted using a μAutolabIII/FRA2 potentiostat by Metrohm. A three-electrode cell setup was used with a glassy carbon disk working electrode, a platinum wire counter electrode, and a silver-wire pseudo-reference electrode. All potentials were referenced to the Fc/Fc^+ redox couple by adding a small amount of ferrocene after each measurement. All electrochemical measurements were conducted under a dinitrogen atmosphere at 25 °C. Samples were prepared for elemental analysis by crushing single crystalline material into a powder and then drying under reduced pressure for 12 h. Co, Se, P elemental analysis was conducted using a Perkin-Elmer Nexion 2000B inductively-coupled plasma mass spectrometer (ICP-MS). Prior to ICP-MS analysis, samples were digested in neat nitric acid (Fisher Scientific, ICP-MS grade) at 50 °C. Scanning electron microscopy (SEM) imaging was performed using a Sirion FEI XL30 at 5 kV for crystalline material dropcast on a 285 nm SiO_2/Si wafer. UV-vis-*n*IR absorption spectra were acquired using a Varian Cary 5000 UV-Vis-*n*IR spectrophotometer, in *n*IR quartz cuvettes (Spectrocell Inc., 10 mm path length, 220–3500 nm spectral window). NMR spectra were acquired at 25 °C on Bruker AV300 or AV500 spectrometers. ^{1}H NMR spectra were referenced to residual deuterated solvent peaks.

4.9.2 *Synthesis and Isolation of $Co_3(py)_3Co_6Se_8L^{Tol}_6$, $\mathbf{Co_3(py)_3}$*

A 350 mL Schlenk tube equipped with a Teflon valve and a large magnetic stir bar was loaded with $\mathbf{Li_6}(py)_6$ (4.000 g, 1.232 mmol, 1 equiv), toluene (144 mL), and THF (6 mL). The sample was partially frozen within the glovebox coldwell. Solid $CoCl_2$ (0.480 g, 3.70 mmol, 3.0 equiv) was added portion wise to the thawing, stirring slurry. The flask was sealed, slowly warmed to 25 °C, and then heated at 60 °C for 14 h. Over the course of this time, the initially red-brown slurry homogenized to yield a deep-red solution. Volatiles were removed under reduced pressure, and the sample was triturated with diethyl ether (3 x 20 mL), thoroughly drying *in vacuo* between each trituration to remove excess THF and pyridine. The product was dissolved in DCM (40 mL) and passed through a plug of Celite on a fritted glass funnel. Volatiles were removed from the DCM filtrate under reduced pressure. The solids were triturated once more with diethyl ether (15 mL), and then stirred in acetonitrile (30 mL). The solids were collected on a fine-porosity fritted glass funnel, washed with additional acetonitrile (2 x 20 mL), then a small amount of diethyl ether (10 mL). The collected solids were then dissolved in THF (50 mL), and this solution was filtered before the filtrate was layered with diethyl ether (50 mL) and *n*-pentane (100 mL). This layered

mixture was kept still at 25 °C for 48 h to yield a crop of large prismatic crystals. The crystals were collected on a fine porosity fritted glass funnel, and the filtrate was layered with additional pentane (50 mL) to produce a second crop of crystals. The separate crops of crystals were combined, and volatiles were removed *in vacuo* to yield **Co$_3$**(py)$_3$ (3.1256 g, 0.995 mmol, 81%) as a dark red, crystalline solid.

^{1}H NMR (C_6D_6, 300 MHz) δ: 75.63 (s, $\nu_{1/2}$ = 1288 Hz); 47.74 (s, $\nu_{1/2}$ = 1935 Hz); 36.72 (s, $\nu_{1/2}$ = 476 Hz), 34.07 (s, 12H, $\nu_{1/2}$ = 722 Hz); 20.87 (s, 12H, $\nu_{1/2}$ = 748 Hz); 14.42 (s, $\nu_{1/2}$ = 1774 Hz); 10.85 (s, $\nu_{1/2}$ = 1402 Hz); –0.13 (s, $\nu_{1/2}$ = 124 Hz); –50.57 (s, $\nu_{1/2}$ = 2993 Hz) ppm. ^{1}H NMR (d_5-pyr, 300 MHz) δ: 34.45 (s, $\nu_{1/2}$ = 83 Hz); 19.96 (s, $\nu_{1/2}$ = 194 Hz); 15.80 (s, $\nu_{1/2}$ = 153 Hz), 13.11 (s, 12H, $\nu_{1/2}$ = 136 Hz); 10.83 (s, $\nu_{1/2}$ = 117 Hz); 4.67 (s, $\nu_{1/2}$ = 211 Hz); –54.10 (s, $\nu_{1/2}$ = 1081 Hz) ppm. μ_{eff} (Evans Method, CD_2Cl_2, 300K): 7.5 μ_B. Elemental analysis found (calc.) for **Co$_3$**(py)$_3$ (Formula*:* $C_{129}H_{117}Co_9N_9P_6Se_8$)*:* Co 16.73 (16.88), Se 18.73 (20.11), P 7.30 (5.92).

4.9.3 *Synthesis and Isolation of Co$_3$(bpy)$_{1.5}$Co$_6$Se$_8$L$^{Tol}_6$,* ***Co$_3$(bpy)***

A 20 mL scintillation vial was loaded with **Co$_3$**(py)$_3$ (0.100 g, 0.032 mmol, 1 equiv) and DCM (8 mL). A separate 20 mL scintillation vial was loaded with 4,4'-bipyridine (bpy) (7.5 mg, 0.048 mmol, 1.5 equiv). The solution of **Co$_3$**(py)$_3$ was passed through a plug of Celite into the vial containing 4,4'-bipyridine. The filter cake was rinsed with DCM (2 mL) and then sample was kept still at 25 °C for 48 h. Dark prismatic crystals were deposited along the walls of the vial within 12 h, which continue to develop for a total of 48 h. The *mother liquor was decanted, and crystals were soaked in DCM (5 x 3 mL; 15 minutes each cycle), decanting the supernatant after each treatment. Volatiles were removed under reduced pressure at 90 °C for 12 h* to yield **Co$_3$**(bpy) (0.0549 g, 0.018 mmol, 55%) as a dark red crystalline solid. The crystals are insoluble in DCM and toluene, although they can be dissolved in coordinating solvents such as d_5-pyridine for ^{1}H NMR analysis, which reveals the clean conversion to **Co$_3$**(py)$_3$.

4.9.4 *Synthesis and Isolation of Co$_3$(bpy$_\pi$)$_{1.5}$Co$_6$Se$_8$L$^{Tol}_6$,* ***Co$_3$(bpy$_\pi$)***

A 20 mL scintillation vial was loaded with **Co$_3$**(py)$_3$ (0.100 g, 0.032 mmol, 1 equiv) and toluene (8 mL). A separate 20 mL scintillation vial was loaded with 1,2-di(4-pyridyl)ethylene (bpy$_\pi$) (0.0146 g, 0.080 mmol, 2.5 equiv). The solution of **Co$_3$**(py)$_3$ was rapidly passed through a plug of

Celite on a pipet filter into the vial containing bpy_{π}. The filter cake was rinsed with toluene (2 mL) and the solution was kept still at 60 °C for 48 h. Within 12 h, a crop of dark red prismatic crystals had deposited along the walls of the vial, which continued to develop for a total of 48 h. The mother liquor was decanted, and crystals were soaked in toluene (5 x 3 mL; 15 minutes each cycle), decanting the supernatant after each treatment. Volatiles were then removed under reduced pressure *at 90 °C for 12 h* to yield $\mathbf{Co_3}(bpy_{\pi})_{1.5}Co_6Se_8L^{Tol}_6$ ($\mathbf{Co_3}(bpy_{\pi})$) (0.0617 g, 0.020 mmol, 61%) as a dark red crystalline solid. The crystals are insoluble in DCM and toluene, although they can be dissolved in coordinating solvents such as d_5-pyridine for ^{1}H NMR analysis, which reveals a clean conversion back to $\mathbf{Co_3}(py)_3$ with displacement of the bpy_{π} linker.
[NMR Spectra?]

4.9.5 *Synthesis and Isolation of $Co_3(bpy_{\sigma})_{1.5}Co_6Se_8L^{Tol}_6$, $\mathbf{Co_3}(bpy_{\sigma})$*

A 20 mL scintillation vial was loaded with $Co_3(py)_3Co_6Se_8L_6$ (0.100 g, 0.032 mmol, 1 equiv) and toluene (8 mL). A separate 20 mL scintillation vial was loaded with 1,2-bi(4-pyridyl)ethane (bpy_{σ}) (0.0146 g, 0.080 mmol, 2.5 equiv). The solution of $\mathbf{Co_3}(py)_3$ was rapidly passed through a plug of Celite on a pipet filter into the vial containing bpy_{σ}. The vial and filter cake were rinsed with toluene (2 mL). The vial was then kept still and heated at 60 °C for 48 h. A layer of dark red prismatic crystals was deposited along the walls of the vial within 12 h, which continued to develop in size and quantity for a total of 48 h. The mother liquor was decanted, and the crystals were soaked in toluene (5 x 3 mL; 15 minutes each cycle), decanting the supernatant between each wash. Volatiles were then removed under reduced pressure at 90 °C for 12 h to yield $Co_3(bpy_{\sigma})_{1.5}Co_6Se_8L^{Tol}_6$ ($\mathbf{Co_3}(bpy_{\sigma})$) (0.0588 g, 0.019 mmol, 58%) as a dark red, crystalline solid. The crystals are insoluble in DCM and toluene, although they can be dissolved in coordinating solvents such as d_5-pyridine for ^{1}H NMR analysis, which revealed a clean conversion back to $\mathbf{Co_3}(py)_3$ with displacement of the bpy_{σ} linker.

4.9.6 *Synthesis and Isolation of $[Co_3(bpy_{\sigma})_{1.5}Co_6Se_8L^{Tol}_6][TCNE]_2$, $[\mathbf{Co_3}(bpy_{\sigma})][TCNE]_2$*

A 20 mL scintillation vial was loaded with $\mathbf{Co_3}(bpy_{\sigma})$ (0.0414 g, 0.013 mmol, 1 equiv) and toluene (1 mL). A separate 20 mL scintillation vial was loaded with TCNE (0.0083 g, 0.065 mmol, 5 equiv), toluene (1 mL) and *n*-pentane (7 mL). The solution of TCNE was passed through a plug of

Celite on a pipet filter into the slurry of **Co$_3$**(bpy$_\sigma$). The filter cake was rinsed with *n*-pentane (1 mL). The mixture was kept still at 25 °C for 24 hours. The supernatant was decanted and the solids were soaked in toluene (3 x 3 mL; 15 minutes each cycle) followed by *n*-pentane (3 x 3 mL; 15 minutes each cycle) before volatiles were removed under reduced pressure to yield [Co$_3$(bpy$_\sigma$)$_{1.5}$Co$_6$Se$_8$L$^{Tol}_6$][TCNE]$_2$ ([**Co$_3$**(bpy$_\sigma$)][TCNE]$_2$) as a dark red crystalline solid (0.0408 g, 0.012 mmol, 95%).

^{1}H NMR (d_5-pyr, 300 MHz) δ: 31.96 (s, $\nu_{1/2}$ = 54 Hz); 18.32 (s, $\nu_{1/2}$ = 70 Hz); 15.21 (s, $\nu_{1/2}$ = 51 Hz), 13.03 (s, $\nu_{1/2}$ = 60 Hz); 11.83 (s, $\nu_{1/2}$ = 50 Hz); 5.92 (s, $\nu_{1/2}$ = 84 Hz); –52.11 (s, $\nu_{1/2}$ = 621 Hz) ppm. ATR-FTIR (powder): ν_{CN} = 2184 (s), 2145 (s) cm^{-1}.

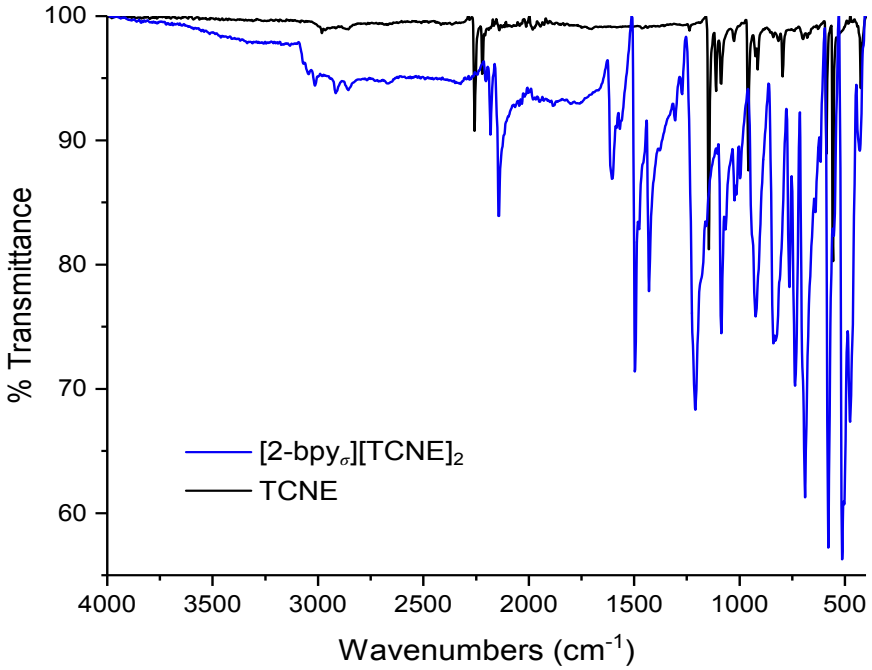


Figure 4.11. ATR-FTIR spectra of [**Co$_3$**(bpy$_\sigma$)][TCNE]$_2$ (blue) and neutral TCNE (black), displaying the full spectral window acquired (zoom in included in Figure 4.9). In this figure, [**Co$_3$**(bpy$_\sigma$)][TCNE]$_2$ is denoted as **[2-bpy$_\sigma$]**[TCNE]$_2$.

4.9.7 *Magnetic Measurements*

Direct current (dc) magnetic susceptibility data for **Co$_3$**(py)$_3$ and **Co$_3$**(bpy$_\pi$) were collected on warming from 2 to 300 K with applied fields of 0.1, 0.5 and 1 T using a Quantum Design MPMS3 Evercool SQUID Magnetometer. These samples were prepared by loading a gelatin capsule (size #4) with polycrystalline material followed by molten eicosane. dc magnetic

susceptibility data for **Co$_3$**(bpy) and **Co$_3$**(bpy$_\sigma$) were collected on warming from 5 to 300 K under applied fields of 0.1, 0.5, and 1 T using a Quantum Design PPMS DynaCool equipped with a 14 T magnet. To prepare these samples, polycrystalline material was loaded within a gelatin capsule sealed with Kapton tape. In each case, crushed crystalline material was dried *in vacuo* at 90 °C prior to analysis. All magnetic susceptibility data was corrected for the diamagnetic contributions from the analyte, calculated using Pascal's constants,[70] as well as the susceptibility of the capsule, sample holder and eicosane. Magnetization data was recorded at 100 K between 0 and 7 T to confirm the absence of any ferromagnetic impurities. Magnetic susceptibility data recorded under different applied fields does not decrease with increasing field strength, indicating that the samples are free of any ferromagnetic impurities. Reduced magnetization data were collected for **Co$_3$**(py)$_3$ between 1.8 and 10 K under applied fields between 1.0 and 7.0 T. Susceptibility data for **Co$_3$**(py)$_3$ were modeled using PHI in order to extract the g-value, although a quantitative model was not developed due to the complexity of the system.[71]

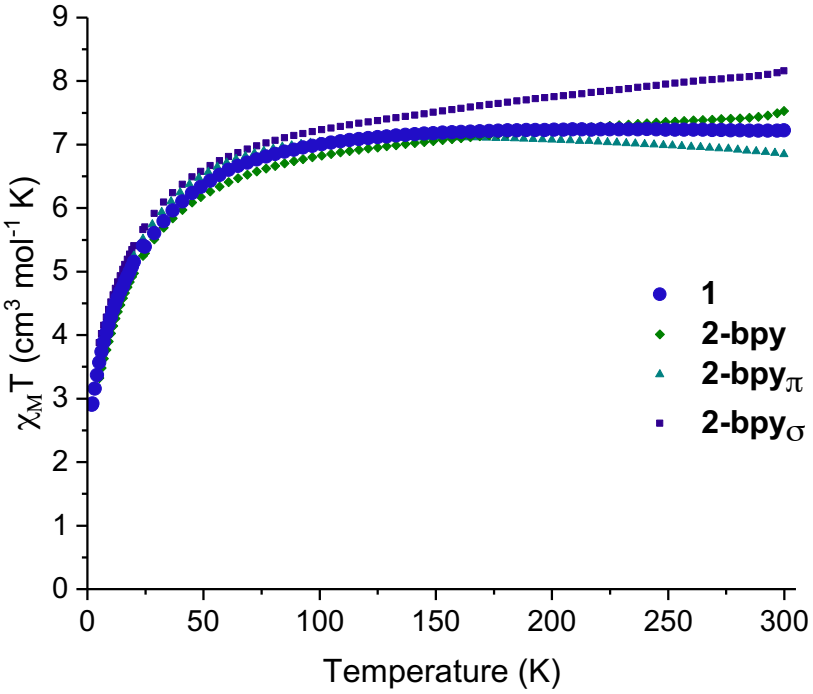


Figure 4.12. A comparison of the variable-temperature dc magnetic susceptibility of **Co$_3$**(py)$_3$, **Co$_3$**(bpy), **Co$_3$**(bpy$_\pi$), and **Co$_3$**(bpy$_\sigma$) recorded at 0.1 T. We attribute the slight deviation in the data recorded for **Co$_3$**(bpy$_\sigma$) to a small amount of an unidentified impurity. In these figures, **Co$_3$**(py)$_3$, **Co$_3$**(bpy), **Co$_3$**(bpy$_\pi$), and **Co$_3$**(bpy$_\sigma$) are denoted as **1**, **2-bpy**, **2-bpy$_\pi$**, and **2-bpy$_\sigma$**, respectively.

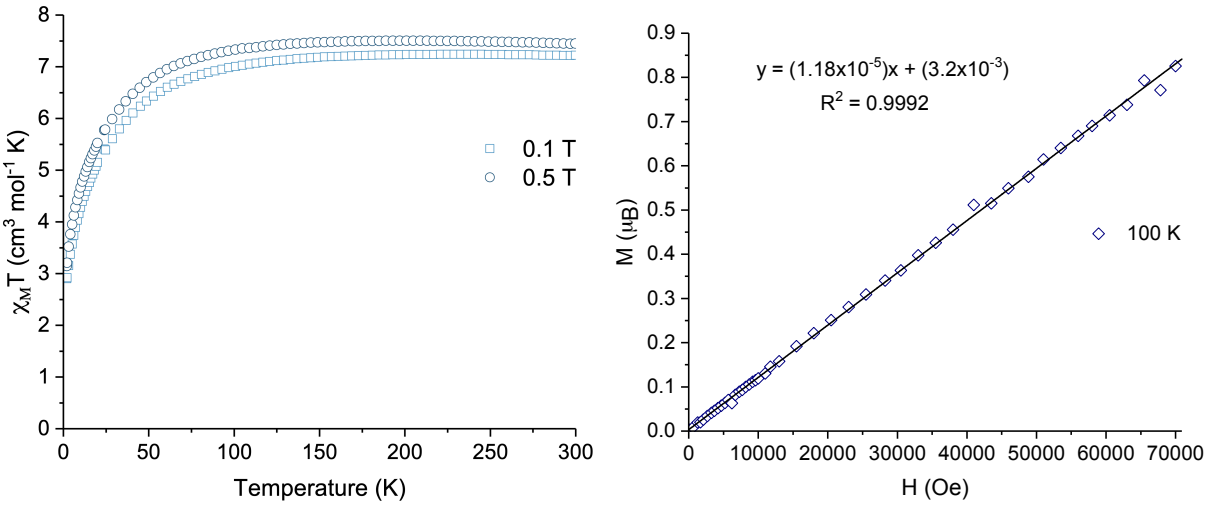


Figure 4.13. (left) Variable-temperature dc magnetic susceptibility of **Co3**(py)3 recorded at 0.1 and 0.5 T, upon warming from 2 to 300 K. (right) Magnetization of **Co3**(py)3 recorded between 0 and 7 T at 100 K. These plots indicate that the sample is free of ferromagnetic impurities.

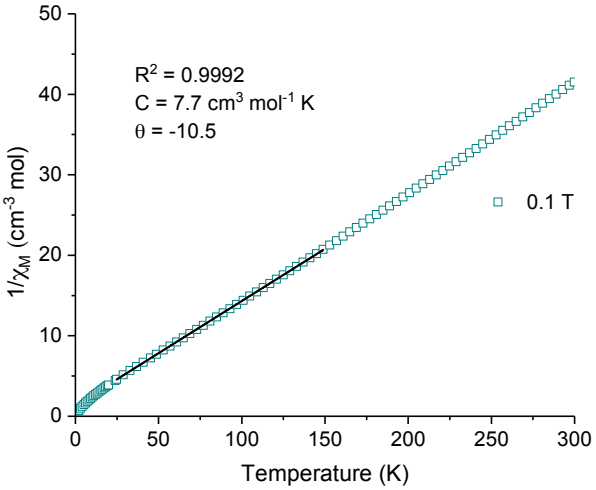


Figure 4.14. Inverse molar susceptibility of **Co3**(py)3 recorded upon warming from 2 to 300 K at 0.1 T. A linear fit to the data between 25 and 150 K, which was used to calculate Curie (C) and Weiss (θ) constants.

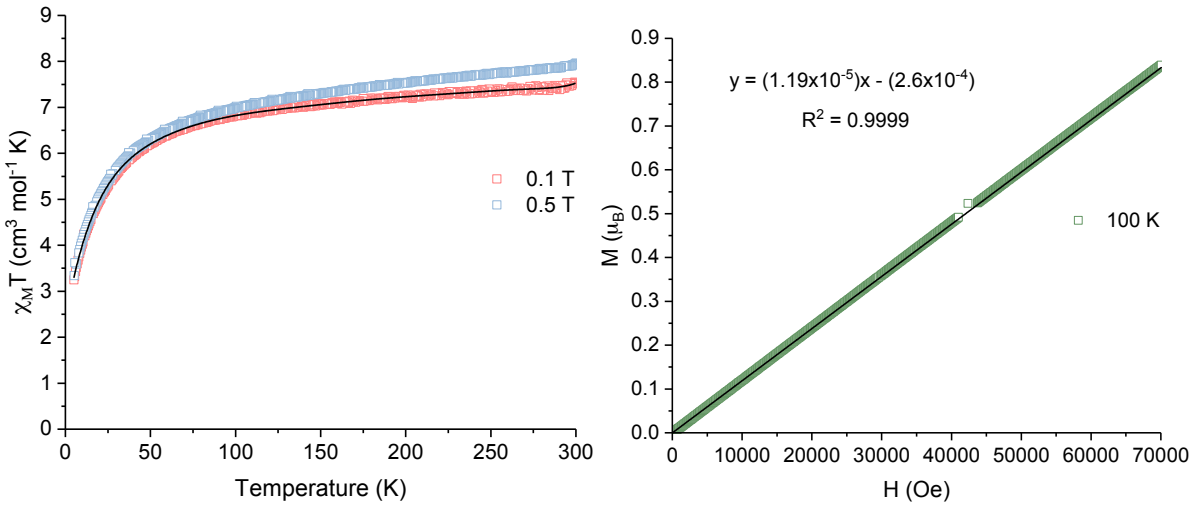


Figure 4.15. (left) Variable-temperature dc magnetic susceptibility of **Co$_3$**(bpy) recorded at 0.1 and 0.5 T upon warming from 5 to 300 K. The polynomial fit (R^2 = 0.9999) to the data recorded at 0.1 T was used to generate a truncated data set for the susceptibility of **Co$_3$**(bpy) shown above. (right) Magnetization of **Co$_3$**(bpy) recorded at 100 K between 0 and 7 T. These plots indicate the absence of ferromagnetic impurities.

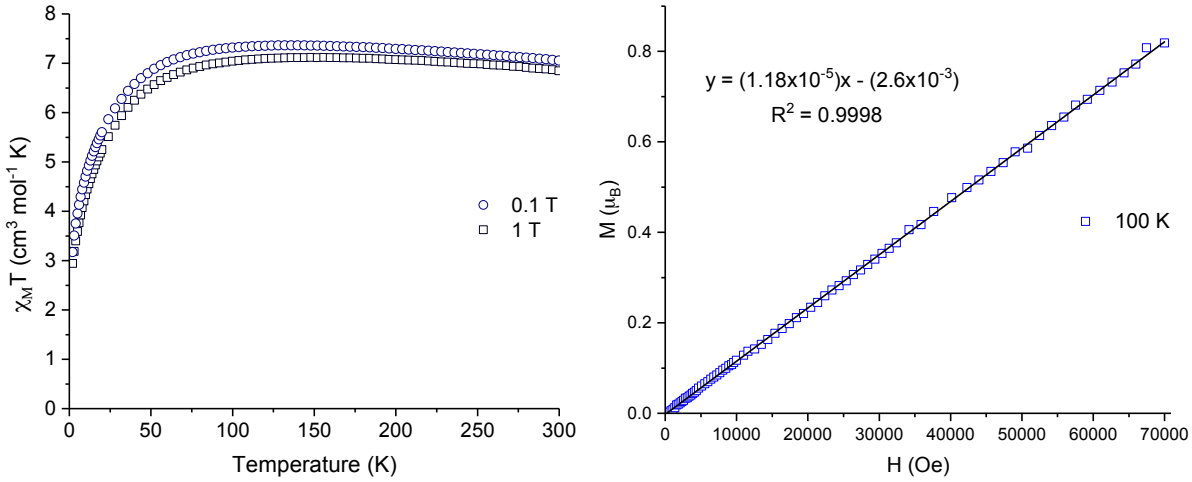


Figure 4.16. (left) Variable-temperature dc magnetic susceptibility of **Co$_3$**(bpy$_\pi$) recorded at 0.1 and 1 T upon warming from 2 to 300 K. (right) Magnetization of **Co$_3$**(bpy$_\pi$) recorded between 0 and 7 T at 100 K. These plots confirm the absence of ferromagnetic impurities.

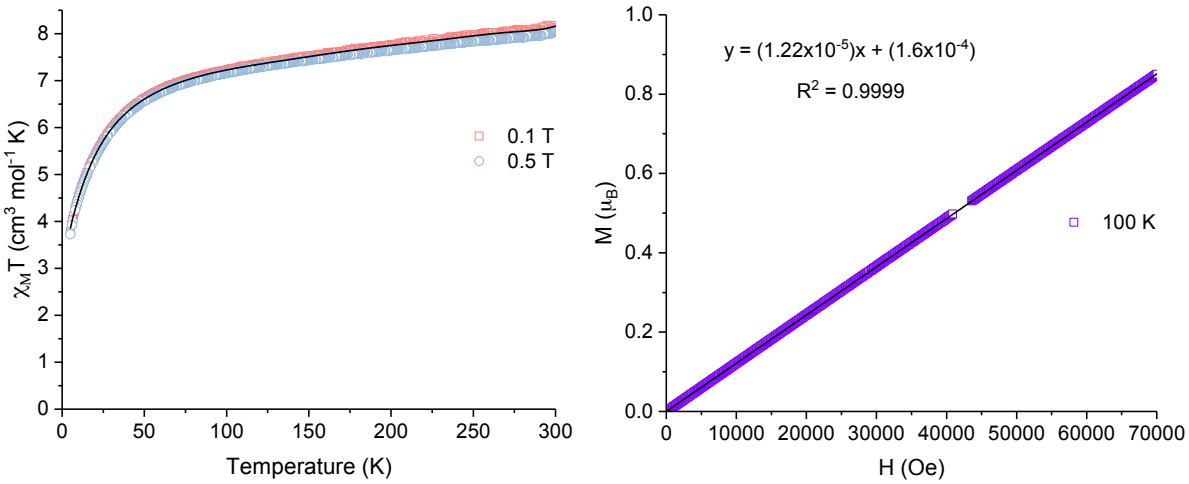


Figure 4.17. (left) Variable-temperature dc magnetic susceptibility of **Co3**(bpy$_\sigma$) recorded at 0.1 and 0.5 T, upon warming from 5 to 300 K. The polynomial fit to the data ($R^2 = 0.9999$) recorded at 0.1 T was used to generate the truncated data set for the susceptibility of **Co3**(bpy$_\sigma$) shown above. (right) Magnetization of **Co3**(bpy$_\sigma$) recorded between 0 and 7 T at 100 K. Both plots indicate the absence of ferromagnetic impurities.

4.9.8 *Electrochemical Measurements*

Large peak-to-peak separation potentials (ΔE_p) indicate that all of these redox processes are quasi-reversible. To gauge the chemical reversibility of these electrochemical transformations, cyclic voltammograms were recorded at several scan rates between 20 and 500 mV s^{-1}. For a chemically reversible process, peak anodic and cathodic currents should exhibit a linear dependence on the square root of the scan rate.[55] This is demonstrated by fitting the electrochemical data to the Randles–Sevcik equation:

$$j_p = 269000 n_e^{3/2} D_0^{1/2} C_0 v^{1/2}$$

, where j_p is the current density in A/cm^2, n_e is the number of electron equivalents transferred in the redox process, D_0 is the diffusion coefficient in cm^2/s, C_0 is the bulk concentration in mol/cm^3, and v is the potential scan rate in V/s.

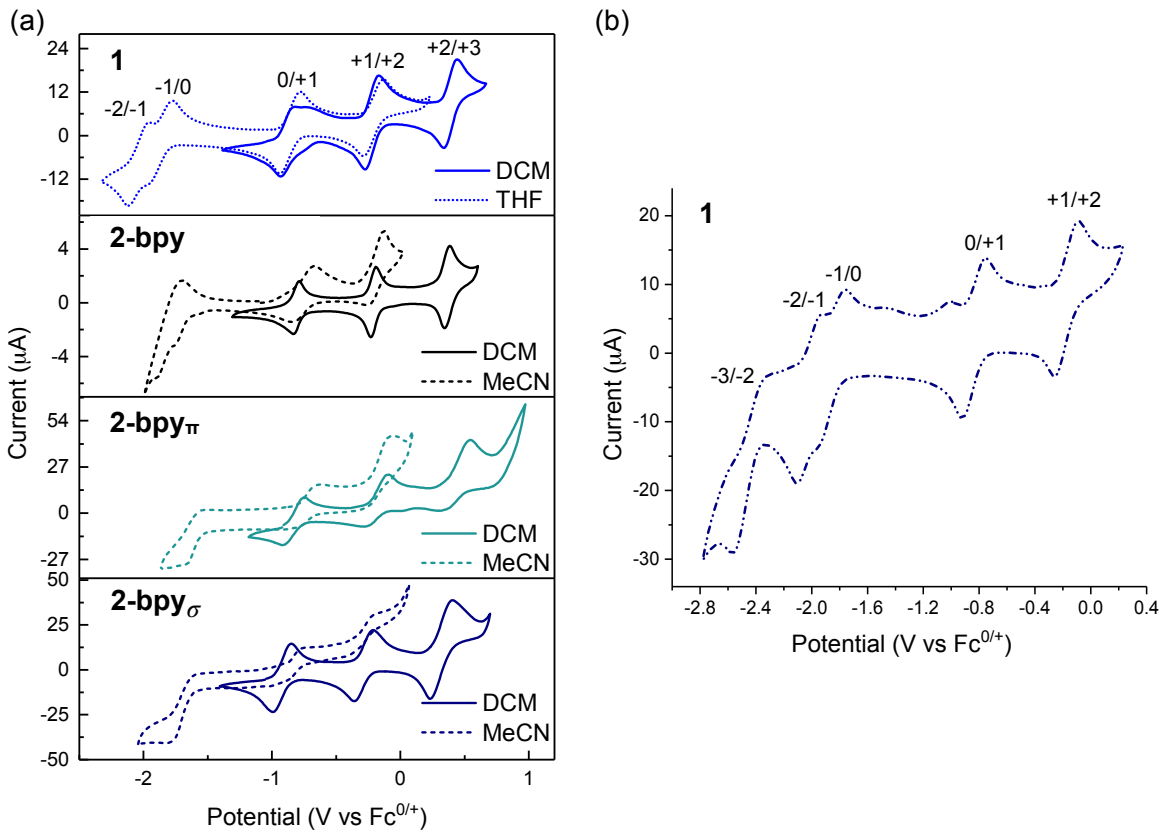


Figure 4.18. (a) A comparison of the solution-phase cyclic voltammograms recorded for $\mathbf{Co_3}(py)_3$ to the solid-state cyclic voltammograms recorded for $\mathbf{Co_3}(bpy)$, $\mathbf{Co_3}(bpy_\pi)$, and $\mathbf{Co_3}(bpy_\sigma)$ in THF, DCM, or MeCN solutions with 0.1 M $TBAPF_6$ electrolyte. The solid-state voltammograms for $\mathbf{Co_3}(bpy)$, $\mathbf{Co_3}(bpy_\pi)$, and $\mathbf{Co_3}(bpy_\sigma)$ were obtained by first dropcasting crystalline material on a glassy carbon working electrode. (b) A cyclic voltammogram of **1** in 0.1 M $TBAPF_6$ THF, revealing a third, irreversible reduction event (n_{red}/n_{ox} = –3/–2) at –2.45 V. All voltammograms were recorded with a scan rate of 200 mV/s. In these figures, $\mathbf{Co_3}(py)_3$, $\mathbf{Co_3}(bpy)$, $\mathbf{Co_3}(bpy_\pi)$, and $\mathbf{Co_3}(bpy_\sigma)$ are denoted as **1**, **2-bpy**, **2-bpy$_\pi$**, and **2-bpy$_\sigma$**, respectively.

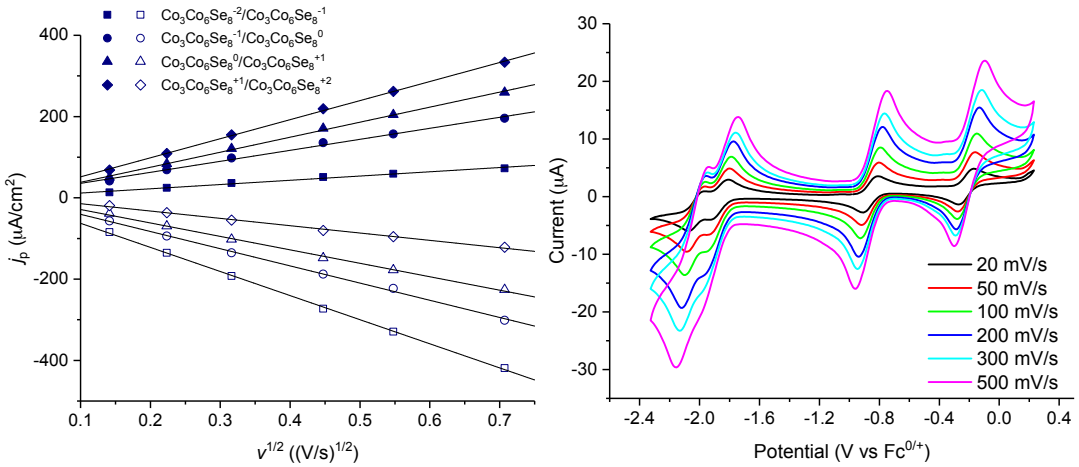


Figure 4.19. (left) A plot of current density (j_p) versus the square root of scan rate ($v^{1/2}$) for **Co3**(py)$_3$ in 0.1 M [^{n}Bu$_4$N][PF$_6$] THF. Linear fits were used to extract diffusion coefficients using the Randles-Sevcik equation. (right) Cyclic voltammograms of **Co3**(py)$_3$ recorded in 0.1 M [^{n}Bu$_4$N][PF$_6$] THF.

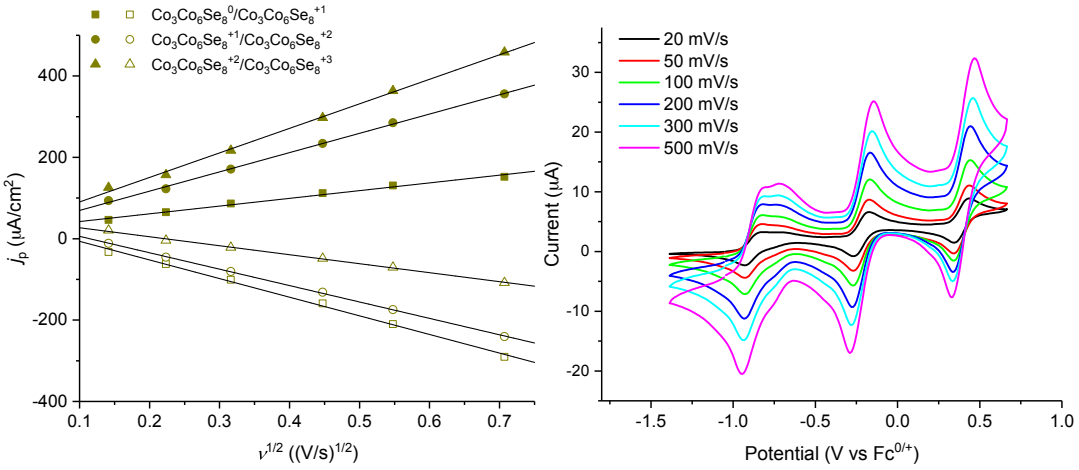


Figure 4.20. (left) A plot of current density (j_p) versus the square root of scan rate ($v^{1/2}$) for **Co3**(py)$_3$ in 0.1 M [^{n}Bu$_4$N][PF$_6$] DCM. Linear fits were used to extract diffusion coefficients using the Randles-Sevcik equation. (right) Cyclic voltammograms of **Co3**(py)$_3$ recorded in 0.1 M [^{n}Bu$_4$N][PF$_6$] DCM.

Table 4.1. Half-wave potentials ($E_{1/2}$), peak-to-peak separation potentials (ΔE_p), and open circuit potentials (OCP) of **Co$_3$**(py)$_3$ recorded in 0.1 M [^{n}Bu$_4$N][PF$_6$] DCM or (THF) at 200 mV/s.

redox couple (n_{red}/n_{ox})	$E_{1/2}$ (V vs $Fc^{0/+}$); ΔE_p (mV)
	Co$_3$(py)$_3$
+2/+3	0.39; 111
+1/+2	–0.22 (–0.21); 111 (162)
0/+1	–0.84 (–0.86); 192 (161)
–1/0	(–1.86); (181)[a]
–1/–2	(–2.03); (163)[a]
OCP (V vs $Fc^{0/+}$)	–1.04 (–0.976)

[a]Due to overlap between the –2/–1 and –1/0 redox couples, these values were approximated based on the location of the shoulders generated by the –2/–1 anodic and –1/0 cathodic currents.

Table 4.2. Diffusion coefficients (D_0) obtained by applying the Randles–Sevcik equation assuming n_e=1 for various oxidation states determined from cyclic voltammograms of **Co$_3$**(py)$_3$ recorded in 0.1 M [^{n}Bu$_4$N][PF$_6$] DCM or (THF).

oxidation state (n)	D_0 (10^{-6} cm^2/s)[a]
	Co$_3$(py)$_3$
+3	(0.29)[b]
+2	11.1[b] (0.61)
+1	5.10 (2.16)
0	3.02 (3.79)
–1	1.92 (7.91)
–2	0.25

[a] Diffusion coefficients calculated for each anodic and cathodic peak current density for scan rates ranging between 20 and 500 mV/s, then averaged for all scan rates to obtain the listed values. [b]Calculated using the anodic or cathodic current densities for the (+2/+3) redox couple as measured in 0.1 M [^{n}Bu$_4$N][PF$_6$] DCM. Values shown with and without parentheses were calculated from cathodic or anodic current densities, respectively.

Table 4.3. Half-wave potentials ($E_{1/2}$), peak-to-peak separation potentials (ΔE_p), and open circuit potentials (OCP) of **Co$_3$**(bpy), **Co$_3$**(bpy$_\pi$), and **Co$_3$**(bpy$_\sigma$) recorded in 0.1 M [^{n}Bu$_4$N][PF$_6$] DCM or (MeCN) at 200 mV/s.

redox couple (n_{red}/n_{ox})	$E_{1/2}$ (V vs $Fc^{0/+}$); ΔE_p (mV)		
	Co$_3$(bpy)	**Co$_3$**(bpy$_\pi$)	**Co$_3$**(bpy$_\sigma$)
+2/+3	0.36; 41	0.43; 242	0.32; 165
+1/+2	–0.21 (–0.19); 40 (131)	–0.19 (–0.18); 192 (242)	–0.28 (–0.29); 151 (190)
0/+1	–0.81 (–0.76); 50 (171)	–0.83 (–0.74); 171 (243)	–0.92 (–0.86); 143 (211)
–1/0	(–1.74); (71)	(–1.59); (172)	(–1.69); (201)
–1/–2	--	--	--
OCP (V vs $Fc^{0/+}$)	–1.10 (–1.08)	–0.91 (–0.88)	–1.04 (–0.89)

4.9.9 *X-ray Structure Determination*

Single crystals suitable for X-ray analysis, grown according to methods detailed below, were coated in deoxygenated paratone oil and mounted on a 20 μm CryoLoop™ (Hampton Research, 18 mm mount, 0.2 to 0.3 mm loop diameter). Data was collected at –173 °C on a Bruker APEX II single crystal X-ray diffractometer, with a Mo source. Data was integrated and scaled using SAINT, SADABS within the APEX2 software package by Bruker.[72] Solution by direct methods (SHELXT[73] or SIR97[74,75]) produced a complete heavy atom phasing model consistent with the proposed structure. Structures were completed by difference Fourier synthesis with SHELXL.[76–78] Scattering factors are from Waasmair and Kirfel.[79] Hydrogen atoms were placed in geometrically idealized positions and constrained to ride on their parent atoms with C–H distances in the range 0.95–1.00 Å. Isotropic thermal parameters U_{eq} were fixed such that they were $1.2U_{eq}$ of their parent atom Ueq for CHs and $1.5U_{eq}$ of their parent atom U_{eq} in case of methyl groups. All non-hydrogen atoms were refined anisotropically by full-matrix least-squares.

4.9.9.1 **Co$_3$**(py)$_3$

Dark-red prismatic crystals of **Co$_3$**(py)$_3$ suitable for single-crystal X-ray diffraction analysis, were grown from a saturated THF solution (3 mL) layered with a mixture of diethyl ether (9 mL) and *n*-pentane (1 mL) over the course of 24 hours at 25 °C. The compound crystallizes in the monoclinic space group $P2_1/c$, and the asymmetric unit contains a singular **Co$_3$**(py)$_3$ cluster. Each surface Co atom is coordinated by one molecule of pyridine, and also exhibits κ^3 coordination by the $[Co_6Se_8L_6]^{6-}$ framework. One of three coordinating pyridine molecules is disordered over two positions.

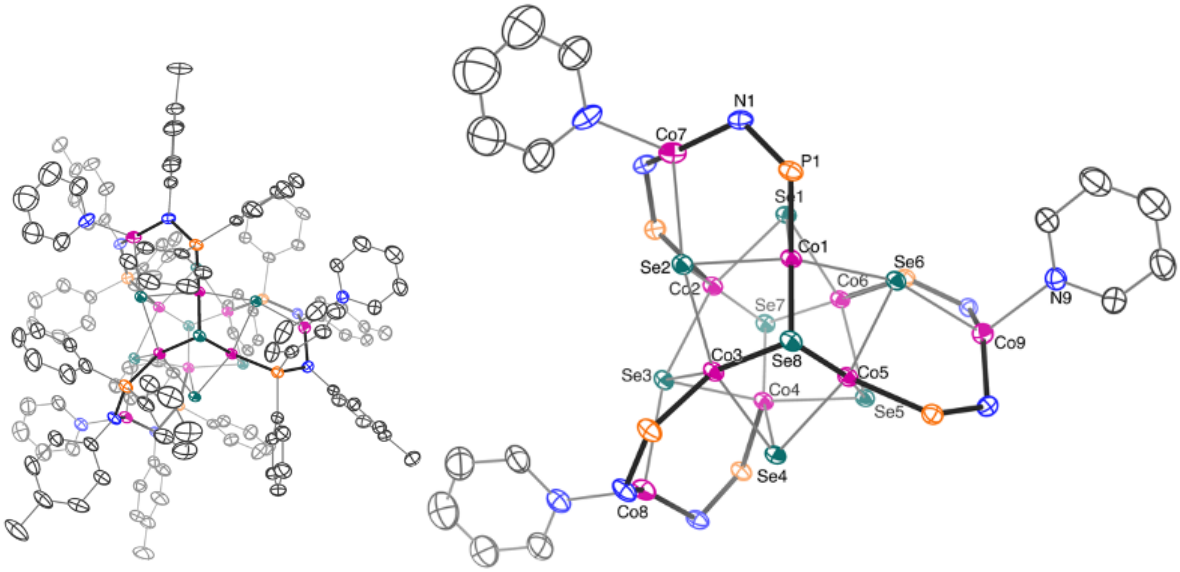


Figure 4.21. Solid-state structure of **Co$_3$**(py)$_3$ with thermal ellipsoids plotted at a 50% probability level. All hydrogen atoms are omitted for clarity. Selected interatomic distances (Å): Co(7)-Se(2) 2.534(1), Co(7)-Se(1) 3.200(2), Co(8)-Se(3) 2.524(1), Co(8)-Se(4) 3.243(2), Co(9)-Se(6) 2.573(2), Co(9)-Se(5) 3.147(1), Co(1)-Se(8) 2.334(1), Co(1)-Se(2) 2.347(2), Co(9)-N(9) 2.101(2), Co(7)-N(1) 1.941(2), Se(1)-Se(4) 5.587(2), Se(2)-Se(5) 5.657(3), Se(7)-Se(8) 5.5524(8), Se(3)-Se(6) 5.830(3), Co(1)-Co(2) 2.868(1), Co(3)-Co(4) 2.8383(6), Co(5)-Co(6) 2.831(1), Co(1)-Co(6) 2.8934(6), Co(2)-Co(3) 2.922(1), Co(4)-Co(5) 2.954(1), N(1)-P(1) 1.673(3).

4.9.9.2 **Co$_3$**(bpy)

Small dark red, prismatic crystals of **Co$_3$**(bpy) of sufficient quality for single-crystal X-ray diffractometry were grown using the synthetic methods described above. The material crystallizes as a 2D, layered reticular solid in the triclinic space group $P\bar{1}$, and the asymmetric unit contains two **Co$_3$** clusters, one (R) and one (S) enantiomer. The asymmetric unit also contains one whole bpy molecule and four half bpy molecules. Each bpy molecule is bound to a surface Co(II) atom. The contribution of disordered CH_2Cl_2 solvent to the diffraction pattern was removed with SQUEEZE.

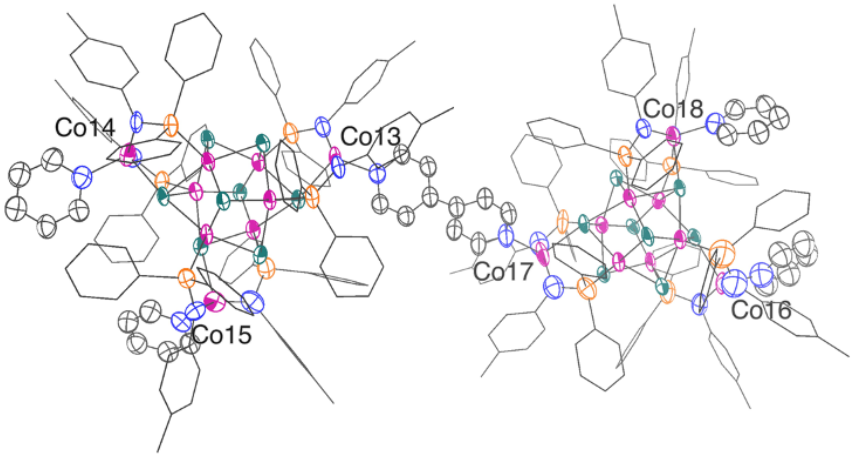


Figure 4.22. The asymmetric unit of **Co3**(bpy) with thermal ellipsoids plotted at a 50% probability level. All hydrogen atoms are omitted and phosphinoamide carbon atoms are plotted as wireframes for clarity.

4.9.9.3 **Co3**(bpy_{π})

Dark red prismatic crystals of **Co3**(bpy_{π}) of sufficient quality for single-crystal X-ray analysis were grown using the synthetic methods described above. The material crystallizes in the triclinic space group $P\bar{1}$. The asymmetric unit contains a single **Co3** cluster with each surface Co(II) site bound by half of a bpy_{π} molecule. Each cluster is interlinked with three neighboring clusters to produce a 2D layered structure. The contribution of disordered toluene solvent (7 per asymmetric unit) to the diffraction pattern was removed with SQUEEZE.

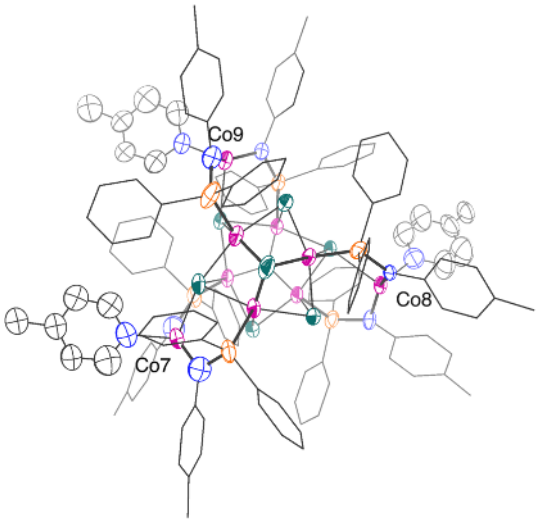


Figure 4.23. The asymmetric unit of **Co3**(bpy_{π}) with thermal ellipsoids plotted at a 50% probability level. All hydrogen atoms are omitted and phosphinoamide carbon atoms are plotted as wireframes for clarity.

4.9.9.4 **Co3**(bpy$_\sigma$)

Dark red prismatic crystals of $Co_3(bpy_\sigma)_{1.5}Co_6Se_8L_6$ (**Co3**(bpy$_\sigma$) of sufficient quality for single-crystal X-ray analysis were grown using the synthetic methods described above. The material crystallizes in the monoclinic space group P 2_1/n. The asymmetric unit contains a single $Co_9Se_8L^{Tol}_6$ cluster with each surface Co(II) site bound by half of a bpy$_\sigma$ molecule. Each cluster is interlinked with three neighboring clusters to produce a 2D layered structure. The contribution of disordered toluene solvent (3 per asymmetric unit) to the diffraction pattern was removed with SQUEEZE.

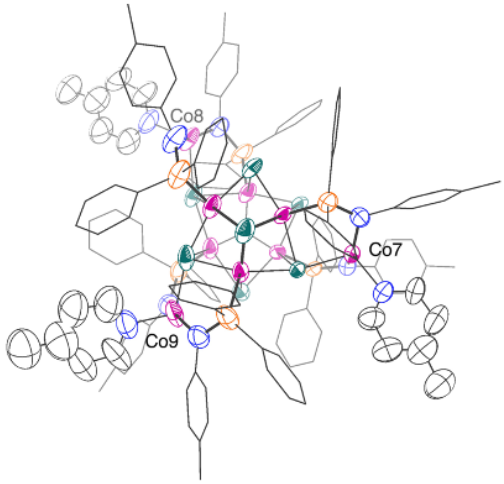


Figure 4.24. The asymmetric unit of **Co3**(bpy$_\sigma$) with thermal ellipsoids plotted at a 50% probability level. All hydrogen atoms are omitted and phosphinoamide carbon atoms are plotted as wireframes for clarity.

4.9.9.5 [**Co3**(bpy$_\sigma$)][TCNE]$_2$

Dark red crystals of $[Co_3(bpy_\sigma)_{1.5}Co_6Se_8L_6][TCNE]_2$ ([**Co3**(bpy$_\sigma$)][TCNE]$_2$) of sufficient quality for single-crystal X-ray analysis were produced upon treatment of single-crystalline **Co3**(bpy$_\sigma$) with excess TCNE in a mixture of toluene and n-pentane. The intercalated crystals maintain the space group of their precursor, monoclinic P 21/n. The asymmetric unit contains a single $Co_9Se_8L^{Tol}_6$ cluster with each Co edge site bound by half of a bpy$_\sigma$ molecule, as well as four molecules of toluene and two $[TCNE]^-$ molecules. Each cluster is interlinked with three neighboring clusters to produce a 2D layered structure. The two TCNE molecules insert within the pores of the nanosheet. A small amount of twinning was observed and accounted for during the refinement. Several 4-tolyl substituents of the aminophosphine ligand framework exhibit disorder

and were modeled over two positions. The contributions of all but one of the intercalated toluene molecules (4 per asymmetric unit) to the diffraction pattern were removed with SQUEEZE.

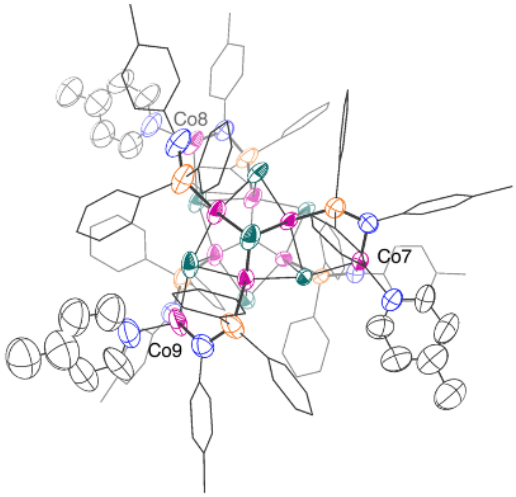


Figure 4.25. The asymmetric unit of **Co$_3$**(bpy$_\sigma$) with thermal ellipsoids plotted at a 50% probability level. All hydrogen atoms are omitted and phosphinoamide carbon atoms are plotted as wireframes for clarity.

4.9.9.6 X-ray Tables

Table 4.4. Crystallographic information for **Co_3**(py)$_3$ and **Co_3**(bpy).

Compound	**Co_3**(py)$_3$	**Co_3**(bpy)
Empirical formula	$C_{129}H_{117}Co_9N_9P_6Se_8$	$C_{258}H_{228}Co_{18}N_{18}P_{12}Se_{16}$
CCDC Number	2012111	2012112
Formula weight	3141.18	6276.31
Temperature (K)	100(2)	100(2)
Wavelength (Å)	0.71073	0.71073
Crystal system	Monoclinic	Triclinic
Space group	$P2_1/c$	$P\bar{1}$
a (Å)	30.1353(8)	19.0473(13)
b (Å)	15.1296(5)	28.0304(18)
c (Å)	33.4288(10)	30.824(3)
α (°)	90	109.902(5)
β (°)	116.5790(10)	97.084(5)
γ (°)	90	102.271(4)
Volume (Å^3)	13630.6(7)	14773.8(19)
Z	4	2
ρ^{calc} (g/cm^3)	1.531	1.411
Absorption coefficient (mm^{-1})	3.321	3.064
F(000)	6236	6224
Crystal size (mm^3)	0.150 x 0.140 x 0.090	0.180 x 0.060 x 0.050
Theta range for data collection (°)	1.362 to 28.339	1.353 to 25.545
Index ranges	$-40\leq h\leq 40$, $-20\leq k\leq 20$, $-44\leq l\leq 44$	$-22\leq h\leq 21$, $-33\leq k\leq 34$, $-36\leq l\leq 37$
Reflections collected	66442	87290
Independent reflections	33870 [R(int) = 0.0379]	48703 [R(int) = 0.3504]
Completeness to theta = 25.000°	100.0%	91.1%
Data / restraints / parameters	33870 / 75 / 1474	48703 / 6251 / 2407
Goodness-of-fit on F^2	1.022	1.116
Final R indices [I>2sigma(I)]	R1 = 0.0341, wR2 = 0.0670	R1 = 0.1683, wR2 = 0.3907
R indices (all data)	R1 = 0.0589, wR2 = 0.0729	R1 = 0.4204, wR2 = 0.5253
Largest diff. peak and hole (e$^-$Å^{-3})	1.622 and –0.875	2.629 and –1.813

Table 4.5. Crystallographic information for **Co$_3$**(bpy$_\pi$), **Co$_3$**(bpy$_\sigma$), and [**Co$_3$**(bpy$_\sigma$)][TCNE]$_2$.

Compound	**Co$_3$**(bpy$_\pi$)	**Co$_3$**(bpy$_\sigma$)	[**Co$_3$**(bpy$_\sigma$)][TCNE]$_2$
Empirical formula	$C_{181}H_{173}Co_9N_9P_6Se_8$	$C_{153}H_{144}Co_9N_9P_6Se_8$	$C_{172}H_{152}Co_9N_{17}P_6Se_8$
CCDC Number	2012109	2012110	2012108
Formula weight	3822.45	3456.91	3804.97
Temperature (K)	100(2)	100(2)	100(2)
Wavelength (Å)	0.71073	0.71073	0.71073
Crystal system	Triclinic	Monoclinic	Monoclinic
Space group	$P\bar{1}$	P 2_1/n	P 2_1/n
a (Å)	15.3355(14)	18.3156(16)	19.2673(10)
b (Å)	17.8362(17)	24.1602(18)	23.5145(10)
c (Å)	29.564(3)	35.255(3)	35.6971(18)
α (°)	87.013(6)	90	90
β (°)	87.701(5)	92.120(4)	92.434(3)
γ (°)	82.900(5)	90	90
Volume (Å^3)	8008.9(13)	15590(2)	16158.4(14)
Z	2	4	4
ρ^{calc} (g/cm^3)	1.318	1.355	1.564
Absorption coefficient (mm^{-1})	2.827	2.904	2.818
F(000)	3154	6320	7632
Crystal size (mm^3)	0.130 x 0.080 x 0.060	0.150 x 0.120 x 0.030	0.150 x 0.080 x 0.070
Theta range for data collection (°)	1.314 to 25.091	1.396 to 24.995	1.367 to 25.027
Index ranges	$-14\leq h\leq 14$, $-17\leq k\leq 17$, $-28\leq l\leq 28$	$-21\leq h\leq 21$, $-28\leq k\leq 28$, $0\leq l\leq 41$	$-22\leq h\leq 22$, $-27\leq k\leq 27$, $-42\leq l\leq 42$
Reflections collected	28506	53839	56717
Independent reflections	28506 [R(int) = 0.2693]	27385 [R(int) = 0.1850]	28523 [R(int) = 0.1691]
Completeness to theta = 25.000°	100.0%	99.8%	99.9%
Data / restraints / parameters	28506 / 1772 / 1274	27385 / 2752 / 1308	28523 / 1577 / 1546
Goodness-of-fit on F^2	0.803	1.042	1.087
Final R indices [I>2sigma(I)]	R1 = 0.0856, wR2 = 0.1839	R1 = 0.1364, wR2 = 0.3424	R1 = 0.1854, wR2 = 0.3438
R indices (all data)	R1 = 0.2913, wR2 = 0.2380	R1 = 0.2844, wR2 = 0.3990	R1 = 0.3094, wR2 = 0.3969
Largest diff. peak and hole (e$^-$Å^{-3})	0.817 and –0.649	1.276 and –1.481	2.381 and –1.674

4.10 REFERENCES

(1) Novoselov, K. S.; Jiang, D.; Schedin, F.; Booth, T. J.; Khotkevich, V. V.; Morozov, S. V.; Geim, A. K. Two-Dimensional Atomic Crystals. *Proceedings of the National Academy of Sciences* **2005**, *102* (30), 10451–10453. https://doi.org/10.1073/pnas.0502848102.

(2) Yankowitz, M.; Chen, S.; Polshyn, H.; Zhang, Y.; Watanabe, K.; Taniguchi, T.; Graf, D.; Young, A. F.; Dean, C. R. Tuning Superconductivity in Twisted Bilayer Graphene. *Science* **2019**, *363* (6431), 1059–1064. https://doi.org/10.1126/science.aav1910.

(3) Deng, D.; Novoselov, K. S.; Fu, Q.; Zheng, N.; Tian, Z.; Bao, X. Catalysis with Two-Dimensional Materials and Their Heterostructures. *Nat. Nanotech.* **2016**, *11* (3), 218–230. https://doi.org/10.1038/nnano.2015.340.

(4) Fiori, G.; Bonaccorso, F.; Iannaccone, G.; Palacios, T.; Neumaier, D.; Seabaugh, A.; Banerjee, S. K.; Colombo, L. Electronics Based on Two-Dimensional Materials. *Nat. Nanotech.* **2014**, *9* (10), 768–779. https://doi.org/10.1038/nnano.2014.207.

(5) Alivisatos, P.; Barbara, P. F.; Castleman, A. W.; Chang, J.; Dixon, D. A.; Klein, M. L.; McLendon, G. L.; Miller, J. S.; Ratner, M. A.; Rossky, P. J.; Stupp, S. I.; Thompson, M. E. From Molecules to Materials: Current Trends and Future Directions. *Advanced Materials* **1998**, *10* (16), 1297–1336. https://doi.org/10.1002/(SICI)1521-4095(199811)10:16<1297::AID-ADMA1297>3.0.CO;2-7.

(6) Doud, E. A.; Voevodin, A.; Hochuli, T. J.; Champsaur, A. M.; Nuckolls, C.; Roy, X. Superatoms in Materials Science. *Nat. Rev. Mater.* **2020**, *5* (5), 371–387. https://doi.org/10.1038/s41578-019-0175-3.

(7) Ji, Z.; Trickett, C.; Pei, X.; Yaghi, O. M. Linking Molybdenum–Sulfur Clusters for Electrocatalytic Hydrogen Evolution. *J. Am. Chem. Soc.* **2018**, *140* (42), 13618–13622. https://doi.org/10.1021/jacs.8b09807.

(8) Horwitz, N. E.; Xie, J.; Filatov, A. S.; Papoular, R. J.; Shepard, W. E.; Zee, D. Z.; Grahn, M. P.; Gilder, C.; Anderson, J. S. Redox-Active 1D Coordination Polymers of Iron–Sulfur Clusters. *J. Am. Chem. Soc.* **2019**, *141* (9), 3940–3951. https://doi.org/10.1021/jacs.8b12339.

(9) Baudron, S. A.; Batail, P.; Coulon, C.; Clérac, R.; Canadell, E.; Laukhin, V.; Melzi, R.; Wzietek, P.; Jérome, D.; Auban-Senzier, P.; Ravy, S. (EDT-TTF-$CONH_2$)$_6$[$Re_6Se_8(CN)_6$], a Metallic Kagome-Type Organic−Inorganic Hybrid Compound: Electronic Instability, Molecular Motion, and Charge Localization. *J. Am. Chem. Soc.* **2005**, *127* (33), 11785–11797. https://doi.org/10.1021/ja0523385.

(10) Yuhas, B. D.; Smeigh, A. L.; Samuel, A. P. S.; Shim, Y.; Bag, S.; Douvalis, A. P.; Wasielewski, M. R.; Kanatzidis, M. G. Biomimetic Multifunctional Porous Chalcogels as Solar Fuel Catalysts. *J. Am. Chem. Soc.* **2011**, *133*, 7252–7255. https://doi.org/10.1021/ja111275t.

(11) Turo, M. J.; Chen, L.; Moore, C. E.; Schimpf, A. M. Co^{2+}-Linked $[NaP_5W_{30}O_{110}]^{14-}$: A Redox-Active Metal Oxide Framework with High Electron Density. *J. Am. Chem. Soc.* **2019**, *141* (11), 4553–4557. https://doi.org/10.1021/jacs.9b00866.

(12) Beauvais, L. G.; Shores, M. P.; Long, J. R. Cyano-Bridged Re_6Q_8 (Q = S, Se) Cluster-Metal Framework Solids: A New Class of Porous Materials. *Chemistry of Materials* **1998**, *10* (12), 3783–3786. https://doi.org/10.1021/cm980564q.

(13) Choi, B.; Lee, K.; Voevodin, A.; Wang, J.; Steigerwald, M. L.; Batail, P.; Zhu, X.; Roy, X. Two-Dimensional Hierarchical Semiconductor with Addressable Surfaces. *J. Am. Chem. Soc.* **2018**, *140* (30), 9369–9373. https://doi.org/10.1021/jacs.8b05010.

(14) Telford, E. J.; Russell, J. C.; Swann, J. R.; Fowler, B.; Wang, X.; Lee, K.; Zangiabadi, A.; Watanabe, K.; Taniguchi, T.; Nuckolls, C.; Batail, P.; Zhu, X.; Malen, J. A.; Dean, C. R.; Roy, X. Doping-Induced Superconductivity in the van Der Waals Superatomic Crystal $Re_6Se_8Cl_2$. *Nano Lett.* **2020**, *20* (3), 1718–1724. https://doi.org/10.1021/acs.nanolett.9b04891.

(15) Champsaur, A. M.; Yu, J.; Roy, X.; Paley, D. W.; Steigerwald, M. L.; Nuckolls, C.; Bejger, C. M. Two-Dimensional Nanosheets from Redox-Active Superatoms. *ACS Cent. Sci.* **2017**, *3* (9), 1050–1055. https://doi.org/10.1021/acscentsci.7b00328.

(16) Champsaur, A. M.; Mézière, C.; Allain, M.; Paley, D. W.; Steigerwald, M. L.; Nuckolls, C.; Batail, P. Weaving Nanoscale Cloth through Electrostatic Templating. *J. Am. Chem. Soc.* **2017**, *139* (34), 11718–11721. https://doi.org/10.1021/jacs.7b07279.

(17) Lee, K.; Choi, B.; Plante, I. J.-L.; Paley, M. V.; Zhong, X.; Crowther, A. C.; Owen, J. S.; Zhu, X.; Roy, X. Two-Dimensional Fullerene Assembly from an Exfoliated van Der Waals Template. *Angew. Chem. Int. Ed.* **2018**, *57* (21), 6125–6129. https://doi.org/10.1002/anie.201800953.

(18) Alhilaly, M. J.; Huang, R.-W.; Naphade, R.; Alamer, B.; Hedhili, M. N.; Emwas, A.-H.; Maity, P.; Yin, J.; Shkurenko, A.; Mohammed, O. F.; Eddaoudi, M.; Bakr, O. M. Assembly of Atomically Precise Silver Nanoclusters into Nanocluster-Based Frameworks. *J. Am. Chem. Soc.* **2019**, *141* (24), 9585–9592. https://doi.org/10.1021/jacs.9b02486.

(19) Huang, R.-W.; Dong, X.-Y.; Yan, B.-J.; Du, X.-S.; Wei, D.-H.; Zang, S.-Q.; Mak, T. C. W. Tandem Silver Cluster Isomerism and Mixed Linkers to Modulate the Photoluminescence of Cluster-Assembled Materials. *Angew. Chem. Int. Ed.* **2018**, *57* (28), 8560–8566. https://doi.org/10.1002/anie.201804059.

(20) Claridge, S. A.; Castleman, A. W.; Khanna, S. N.; Murray, C. B.; Sen, A.; Weiss, P. S. Cluster-Assembled Materials. *ACS Nano* **2009**, *3* (2), 244–255. https://doi.org/10.1021/nn800820e.

(21) Cook, A. W.; Hayton, T. W. Case Studies in Nanocluster Synthesis and Characterization: Challenges and Opportunities. *Acc. Chem. Res.* **2018**, *51* (10), 2456–2464. https://doi.org/10.1021/acs.accounts.8b00329.

(22) Wu, T.; Khazhakyan, R.; Wang, L.; Bu, X.; Zheng, S.-T.; Chau, V.; Feng, P. Three-Dimensional Covalent Co-Assembly between Inorganic Supertetrahedral Clusters and Imidazolates. *Angew. Chem. Int. Ed.* **2011**, *50* (11), 2536–2539. https://doi.org/10.1002/anie.201006531.

(23) Shores, M. P.; Beauvais, L. G.; Long, J. R. Cluster-Expanded Prussian Blue Analogues. *J. Am. Chem. Soc.* **1999**, *121* (4), 775–779. https://doi.org/10.1021/ja983530s.

(24) Jin, S.; DiSalvo, F. J. 3-D Coordination Network Structures Constructed from $[W_6S_8(CN)_6]^{6-}$ Anions. *Chem. Mater.* **2002**, *14* (8), 3448–3457. https://doi.org/10.1021/cm020103b.

(25) Wang, Z.-Y.; Wang, M.-Q.; Li, Y.-L.; Luo, P.; Jia, T.-T.; Huang, R.-W.; Zang, S.-Q.; Mak, T. C. W. Atomically Precise Site-Specific Tailoring and Directional Assembly of Superatomic Silver Nanoclusters. *J. Am. Chem. Soc.* **2018**, *140* (3), 1069–1076. https://doi.org/10.1021/jacs.7b11338.

(26) Huang, R.-W.; Wei, Y.-S.; Dong, X.-Y.; Wu, X.-H.; Du, C.-X.; Zang, S.-Q.; Mak, T. C. W. Hypersensitive Dual-Function Luminescence Switching of a Silver-Chalcogenolate Cluster-Based Metal–Organic Framework. *Nat. Chem.* **2017**, *9* (7), 689–697. https://doi.org/10.1038/nchem.2718.

(27) Zheng, N.; Bu, X.; Lu, H.; Chen, L.; Feng, P. One-Dimensional Assembly of Chalcogenide Nanoclusters with Bifunctional Covalent Linkers. *J. Am. Chem. Soc.* **2005**, *127* (43), 14990–14991. https://doi.org/10.1021/ja055376x.

(28) Champsaur, A. M.; Velian, A.; Paley, D. W.; Choi, B.; Roy, X.; Steigerwald, M. L.; Nuckolls, C. Building Diatomic and Triatomic Superatom Molecules. *Nano. Lett.* **2016**, *16* (8), 5273–5277. https://doi.org/10.1021/acs.nanolett.6b02471.

(29) Wang, C.; Zhang, G.; Huang, S.; Xie, Y.; Yan, H. The Optical Properties and Plasmonics of Anisotropic 2D Materials. *Advanced Optical Materials* **2020**, *8* (5), 1900996. https://doi.org/10.1002/adom.201900996.

(30) Huang, N.; Zhai, L.; Coupry, D. E.; Addicoat, M. A.; Okushita, K.; Nishimura, K.; Heine, T.; Jiang, D. Multiple-Component Covalent Organic Frameworks. *Nat. Comm.* **2016**, *7* (1), 12325. https://doi.org/10.1038/ncomms12325.

(31) Papaefstathiou, G. S.; Friščić, T.; MacGillivray, L. R. Design and Construction of a 2D Metal Organic Framework with Multiple Cavities: A Nonregular Net with a Paracyclophane That Codes for Multiply Fused Nodes. *J. Am. Chem. Soc.* **2005**, *127* (41), 14160–14161. https://doi.org/10.1021/ja054841n.

(32) Bu, X.-H.; Weng, W.; Li, J.-R.; Chen, W.; Zhang, R.-H. Novel Five-Connected Lanthanide(III)−Bis(Sulfinyl) Coordination Polymers Forming a Unique Two-Dimensional (3/4, 5) Network. *Inorg. Chem.* **2002**, *41* (2), 413–415. https://doi.org/10.1021/ic010605b.

(33) Glotzer, S. C.; Solomon, M. J. Anisotropy of Building Blocks and Their Assembly into Complex Structures. *Nat. Mater.* **2007**, *6* (8), 557–562. https://doi.org/10.1038/nmat1949.

(34) Liu, Y.; Deng, K.; Yang, J.; Wu, X.; Fan, X.; Tang, M.; Quan, Z. Shape-Directed Self-Assembly of Nanodumbbells into Superstructure Polymorphs. *Chem. Sci.* **2020**, *11*, 4065–4073. https://doi.org/10.1039/D0SC00592D.

(35) Kephart, J. A.; Mitchell, B. S.; Chirila, A.; Anderton, K. J.; Rogers, D.; Kaminsky, W.; Velian, A. Atomically Defined Nano-Propeller $Fe_3Co_6Se_8(Ph_2PNTol)_6$: Functional Model for the Electronic Metal-Support Interaction Effect, and High Catalytic Activity for Carbodiimide Formation. *J. Am. Chem. Soc.* **2019**, *141* (50), 19605–19610. https://doi.org/10.1021/jacs.9b12473.

(36) Cotton, F. A.; Llusar, R.; Eagle, C. T. Triangular Trinuclear Cluster Compounds: Molybdenum and Tungsten Complexes of the Type $[M_3S_4(Diphos)_3X_3]^+$ with X = Cl and H. *J. Am. Chem. Soc.* **1989**, *111* (12), 4332–4338. https://doi.org/10.1021/ja00194a027.

(37) Robben, M. P.; Rieger, P. H.; Geiger, W. E. Geometric Preferences of Tricobalt Clusters Having 47−49 Valence Electron Counts: Deceptively Simple Cyclic Voltammetric Responses and EPR Evidence for Exchange-Coupled Dimers in Frozen Solutions. *J. Am. Chem. Soc.* **1999**, *121* (2), 367–375. https://doi.org/10.1021/ja983341%2B.

(38) Park, B. K.; Lee, C. Y.; Jung, J.; Lim, J. H.; Han, Y.-K.; Hong, C. S.; Park, J. T. $[Os_3(CO)_6(PMe_3)_3](\mu_3\text{-}H_2\text{:}H_2\text{:}H_2\text{-}C_{60})[Re_3(\mu\text{-}H)_3(CO)_9]$: A Fullerene[60] Coordinated to Two Different Trinuclear Clusters. *Angew. Chem. Int. Ed.* **2007**, *46* (9), 1436–1439. https://doi.org/10.1002/anie.200603882.

(39) Comstock, M. C.; Prussak-Wieckowska, T.; Wilson, S. R.; Shapley, J. R. Complexes of $Ir_3(CO)_3(H_5\text{-}C_9H_7)_3$ with Metal Fragment Electrophiles. *Organometallics* **1997**, *16* (19), 4033–4040. https://doi.org/10.1021/om960460u.

(40) Fan, X.; Wang, J.; Wu, K.; Zhang, L.; Zhang, J. Isomerism in Titanium-Oxo Clusters: Molecular Anatase Model with Atomic Structure and Improved Photocatalytic Activity. *Angew. Chem. Int. Ed.* **2019**, *58* (5), 1320–1323. https://doi.org/10.1002/anie.201809961.

(41) Williamson, C. B.; Nevers, D. R.; Nelson, A.; Hadar, I.; Banin, U.; Hanrath, T.; Robinson, R. D. Chemically Reversible Isomerization of Inorganic Clusters. *Science* **2019**, *363* (6428), 731–735. https://doi.org/10.1126/science.aau9464.

(42) Chen, Y.; Liu, C.; Tang, Q.; Zeng, C.; Higaki, T.; Das, A.; Jiang, D.-E.; Rosi, N. L.; Jin, R. Isomerism in $Au_{28}(SR)_{20}$ Nanocluster and Stable Structures. *J. Am. Chem. Soc.* **2016**, *138* (5), 1482–1485. https://doi.org/10.1021/jacs.5b12094.

(43) Nilius, N.; Rienks, E. D. L.; Rust, H.-P.; Freund, H.-J. Self-Organization of Gold Atoms on a Polar FeO(111) Surface. *Phys. Rev. Lett.* **2005**, *95* (6), 066101. https://doi.org/10.1103/PhysRevLett.95.066101.

(44) Xu, W.; Adams, J. B. W Adatom-Adatom Interactions on the W(110) Surface. *Surface Science* **1995**, *339* (3), 241–246. https://doi.org/10.1016/0039-6028(95)00653-2.

(45) Cai, Y.; Bernasek, S. L. Chiral Pair Monolayer Adsorption of Iodine-Substituted Octadecanol Molecules on Graphite. *J. Am. Chem. Soc.* **2003**, *125* (6), 1655–1659. https://doi.org/10.1021/ja0285619.

(46) Huang, T.; Hu, Z.; Zhao, A.; Wang, H.; Wang, B.; Yang, J.; Hou, J. G. Quasi Chiral Phase Separation in a Two-Dimensional Orientationally Disordered System: 6-Nitrospiropyran on Au(111). *J. Am. Chem. Soc.* **2007**, *129* (13), 3857–3862. https://doi.org/10.1021/ja066521p.

(47) Zhang, F.; Yajima, T.; Li, Y.-Z.; Xu, G.-Z.; Chen, H.-L.; Liu, Q.-T.; Yamauchi, O. Iodine-Assisted Assembly of Helical Coordination Polymers of Cucurbituril and Asymmetric Copper(II) Complexes. *Angew. Chem. Int. Ed.* **2005**, *44* (22), 3402–3407. https://doi.org/10.1002/anie.200463071.

(48) Tulsky, E. G.; Crawford, N. R. M.; Baudron, S. A.; Batail, P.; Long, J. R. Cluster-to-Metal Magnetic Coupling: Synthesis and Characterization of 25-Electron $[Re_6\text{-}NOsnSe8(CN)6]$ (5-n)-

(n = 1, 2) Clusters and {Re6-NOsnSe 8[CNCu(Me6tren)]6}9+ (n = 0, 1, 2) Assemblies. *J. Am. Chem. Soc.* **2003**, *125* (50), 15543–15553. https://doi.org/10.1021/ja037444q.

(49) Pilbrow, J. R. Effective g Values for S = 3/2 and S = 5/2. *Journal of Magnetic Resonance* **1978**, *31* (3), 479–490. https://doi.org/10.1016/S0022-2364(78)80015-8.

(50) Sottini, S.; Poneti, G.; Ciattini, S.; Levesanos, N.; Ferentinos, E.; Krzystek, J.; Sorace, L.; Kyritsis, P. Magnetic Anisotropy of Tetrahedral Co II Single-Ion Magnets: Solid-State Effects. *Inorg. Chem.* **2016**, *55* (19), 9537–9548. https://doi.org/10.1021/acs.inorgchem.6b00508.

(51) Carlin, R. L. *Magnetochemistry*; Springer Berlin Heidelberg: Berlin, Heidelberg, 1986. https://doi.org/10.1007/978-3-642-70733-9.

(52) Mochizuki, T.; Nogami, T.; Ishida, T. Ferromagnetic Superexchange Coupling through a Diamagnetic Iron(II) Ion in a Mixed-Valent Iron(III, II, III) Meso -Helicate. *Inorganic Chemistry* **2009**, *48* (5), 2254–2259. https://doi.org/10.1021/ic8020589.

(53) Fenske, D.; Ohmer, J.; Hachgenei, J. New Co and Ni Clusters with Se and PPh3 as Ligands: $[Co_4(\mu_3\text{-}Se)_4(PPh_3)_4]$,$[Co_6(\mu_3\text{-}Se)_8(PPh_3)_6]$, $[Co_9(\mu_4\text{-}Se)_3(\mu_3\text{-}Se)_8(PPh_3)_6]$, and$[Ni_{34}(\mu_5\text{-}Se)_2(\mu_4\text{-}Se)_{20}(PPh_3)_{10}]$. *Angew. Chem. Int. Ed.* **1985**, *24* (11), 993–995. https://doi.org/10.1002/anie.198509931.

(54) Palstra, T. T. M.; Steigerwald, M. L.; Ramirez, A. P.; Kwon, Y.-U.; Stuczynski, S. M.; Schneemeyer, L. F.; Waszczak, J. V.; Zaanen, J. Electron Correlations on a Mesoscopic Scale: Magnetic Properties of Transition Metal Telluride Cluster Compounds. *Phys. Rev. Lett.* **1993**, *71* (11), 1768–1771. https://doi.org/10.1103/PhysRevLett.71.1768.

(55) Bard, A. J.; Faulkner, L. R. *Electrochemical Methods: Fundamentals and Applications*, 2nd ed.; Wiley: New York, 2001.

(56) Sánchez, R. H.; Willis, A. M.; Zheng, S.-L.; Betley, T. A. Synthesis of Well-Defined Bicapped Octahedral Iron Clusters $[(^{tren}L)_2Fe_8(PMe_2Ph)_2]^n$ (n = 0, −1). *Angew. Chem. Int. Ed.* **2015**, *54* (41), 12009–12013. https://doi.org/10.1002/anie.201505671.

(57) Wan, J.; Lacey, S. D.; Dai, J.; Bao, W.; Fuhrer, M. S.; Hu, L. Tuning Two-Dimensional Nanomaterials by Intercalation: Materials, Properties and Applications. *Chem. Soc. Rev.* **2016**, *45* (24), 6742–6765. https://doi.org/10.1039/C5CS00758E.

(58) Ogihara, N.; Ohba, N.; Kishida, Y. On/off Switchable Electronic Conduction in Intercalated Metal-Organic Frameworks. *Sci. Adv.* **2017**, *3* (8), e1603103. https://doi.org/10.1126/sciadv.1603103.

(59) O'Brien, E. S.; Trinh, M. T.; Kann, R. L.; Chen, J.; Elbaz, G. A.; Masurkar, A.; Atallah, T. L.; Paley, M. V.; Patel, N.; Paley, D. W.; Kymissis, I.; Crowther, A. C.; Millis, A. J.; Reichman, D. R.; Zhu, X.-Y.; Roy, X. Single-Crystal-to-Single-Crystal Intercalation of a Low-Bandgap Superatomic Crystal. *Nat. Chem.* **2017**, *9* (12), 1170–1174. https://doi.org/10.1038/nchem.2844.

(60) Miller, J. S. Tetracyanoethylene (TCNE): The Characteristic Geometries and Vibrational Absorptions of Its Numerous Structures. *Angew. Chem. Int. Ed.* **2006**, *45* (16), 2508–2525. https://doi.org/10.1002/anie.200503277.

(61) Choi, B.; Yu, J.; Paley, D. W.; Trinh, M. T.; Paley, M. V.; Karch, J. M.; Crowther, A. C.; Lee, C.-H.; Lalancette, R. A.; Zhu, X.; Kim, P.; Steigerwald, M. L.; Nuckolls, C.; Roy, X. Van

Der Waals Solids from Self-Assembled Nanoscale Building Blocks. *Nano Lett.* **2016**, *16* (2), 1445–1449. https://doi.org/10.1021/acs.nanolett.5b05049.

(62) Tan, C.; Cao, X.; Wu, X.-J.; He, Q.; Yang, J.; Zhang, X.; Chen, J.; Zhao, W.; Han, S.; Nam, G.-H.; Sindoro, M.; Zhang, H. Recent Advances in Ultrathin Two-Dimensional Nanomaterials. *Chem. Rev.* **2017**, *117* (9), 6225–6331. https://doi.org/10.1021/acs.chemrev.6b00558.

(63) Colson, J. W.; Woll, A. R.; Mukherjee, A.; Levendorf, M. P.; Spitler, E. L.; Shields, V. B.; Spencer, M. G.; Park, J.; Dichtel, W. R. Oriented 2D Covalent Organic Framework Thin Films on Single-Layer Graphene. *Science* **2011**, *332* (6026), 228–231. https://doi.org/10.1126/science.1202747.

(64) Kissel, P.; Murray, D. J.; Wulftange, W. J.; Catalano, V. J.; King, B. T. A Nanoporous Two-Dimensional Polymer by Single-Crystal-to-Single-Crystal Photopolymerization. *Nat. Chem.* **2014**, *6* (9), 774–778. https://doi.org/10.1038/nchem.2008.

(65) Zhao, M.; Huang, Y.; Peng, Y.; Huang, Z.; Ma, Q.; Zhang, H. Two-Dimensional Metal–Organic Framework Nanosheets: Synthesis and Applications. *Chem. Soc. Rev.* **2018**, *47* (16), 6267–6295. https://doi.org/10.1039/C8CS00268A.

(66) Zhang, R.; Liu, J.; Gao, Y.; Hua, M.; Xia, B.; Knecht, P.; Papageorgiou, A. C.; Reichert, J.; Barth, J. V.; Xu, H.; Huang, L.; Lin, N. On-Surface Synthesis of a Semiconducting 2D Metal-Organic Framework $Cu_3(C_6O_6)$ Exhibiting Dispersive Electronic Bands. *Angew. Chem. Int. Ed.* **2020**, *59* (7), 2669–2673. https://doi.org/10.1002/anie.201913698.

(67) Quan, Y.; Lan, G.; Fan, Y.; Shi, W.; You, E.; Lin, W. Metal–Organic Layers for Synergistic Lewis Acid and Photoredox Catalysis. *J. Am. Chem. Soc.* **2020**, *142* (4), 1746–1751. https://doi.org/10.1021/jacs.9b12593.

(68) Aydt, A. P.; Qie, B.; Pinkard, A.; Yang, L.; Cheng, Q.; Billinge, S. J. L.; Yang, Y.; Roy, X. Microporous Battery Electrodes from Molecular Cluster Precursors. *ACS Applied Materials & Interfaces* **2019**, *11* (12), 11292–11297. https://doi.org/10.1021/acsami.8b18149.

(69) Passarelli, V.; Benetollo, F. Reactivity of Novel N,N'-Diphosphino-Silanediamine-Based Rhodium(I) Derivatives. *Inorg. Chem.* **2011**, *50*, 9958–9967. https://doi.org/10.1021/ic2004408.

(70) Bain, G. A.; Berry, J. F. Diamagnetic Corrections and Pascal's Constants. *J. Chem. Ed.* **2008**, *85* (4), 532. https://doi.org/10.1021/ed085p532.

(71) Chilton, N. F.; Anderson, R. P.; Turner, L. D.; Soncini, A.; Murray, K. S. PHI: A Powerful New Program for the Analysis of Anisotropic Monomeric and Exchange-Coupled Polynuclear *d* - and *f* -Block Complexes. *J. Comput. Chem.* **2013**, *34* (13), 1164–1175. https://doi.org/10.1002/jcc.23234.

(72) Bruker APEX2 (Version 2.1-4), SAINT (Version 7.34A), SADABS (Version 2007/4), **2007** *BrukerAXS Inc*, Madison, Wisconsin, USA.

(73) Sheldrick, G.M. *Acta Cryst.* **2015**, *A71*, 3-8.

(74) Altomare, A.; Burla, C.; Camalli, M.; Cascarano, G. L.; Giacovazzo, C.; Guagliardi, A.; Moliterni, A.G.G.; Polidori, G.; Spagna, R. *J. Appl. Crystallogr.,* **1999***, 32,* 115-119.

(75) Altomare, A.; Cascarano, G. L.; Giacovazzo, C.; Guagliardi, A. *J. Appl. Crystallogr*., **1993**, *26*, 343-350.

(76) Sheldrick, G. M. *SHELXL-97, Program for the Refinement of Crystal Structures*, **1997**, University of Göttingen, Germany.

(77) Sheldrick, G. M. *Acta Cryst.* **2015**, *C71*, 3–8.

(78) Mackay, S.; Edwards, C.; Henderson, A.; Gilmore, C.; Stewart, N.; Shankland, K.; Donald, A. *MaXus: A Computer Program for the Solution and Refinement of Crystal Structures from Diffraction Data*, **1997**, University of Glasgow, Scotland.

(79) Waasmaier, D.; Kirfel, A. *Acta Cryst.*, **1995**, *51*, 416-430.

CHAPTER 5.

MULTI-ACTIVE SITE DYNAMICS ON A MOLECULAR CR/CO/SE CLUSTER CATALYST

5.1 ABSTRACT

This study uncovers the interconnected reactivity of the three catalytically active sites of an atomically precise nanocluster $Cr_3(py)_3Co_6Se_8L^{Tol}_6$ (**Cr$_3$**$(py)_3$, $L^{Tol} = Ph_2PN^{(-)}Tol$, Ph = phenyl, Tol = 4-tolyl). Catalytic and stoichiometric studies into tosyl azide activation and carbodiimide formation enabled the isolation and crystallographic characterization of key catalytically competent metal-imido intermediates, including the tris(imido) cluster **Cr$_3$**$(NTs)_3$, the catalytic resting state **Cr$_3$**$(NTs)_3(CN^tBu)_3$, and the site-differentiated mono(imido) cluster **Cr$_3$**$(NTs)(CN^tBu)_2$. Their isolation reveals that nitrene transfer proceeds via a stepwise mechanism in the stoichiometric regime, with the three active sites engaging sequentially to produce carbodiimide. Moreover, the chemical state of neighboring active sites was found to regulate the

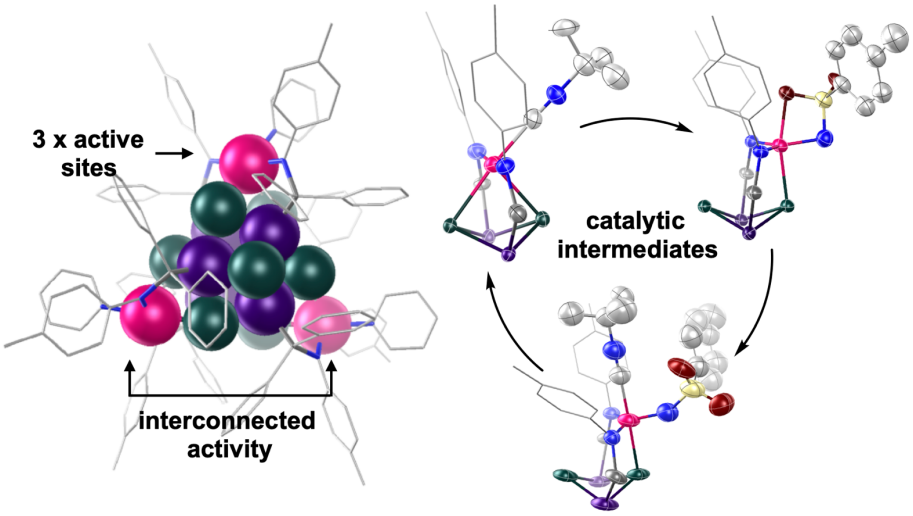


Figure 5.1. The Cr/Co/Se nanocluster grants enhanced stability to key intermediates formed upon azide activation and nitrene transfer, enabling their isolation and single-crystal X-ray characterization.

Adapted in part with permission from:
1. Kephart, J. A.; Mitchell, B. S.; Kaminsky, W.; Velian, A. *J. Am. Chem. Soc.* **2022**, *144* (21), 9206-9211.
Copyright 2022 American Chemical Society.

affinity for substrates of an individual Cr-imido edge site, as revealed by comparative structural analysis and CN′Bu binding studies.

5.2 Introduction

Understanding and controlling catalytically active sites is the holy grail of nanoscale catalysis,[1–3] promising to unlock fundamental insights into their mechanism and facilitate the creation of catalysts designed for specific transformations. The concept of "active sites" in heterogeneous catalysis was first introduced by Taylor nearly a century ago,[4] but their identity as low-coordinate surface sites was not experimentally verified until decades later by Ertl.[5] To date, identifying active sites experimentally and elucidating their mechanism of action remains exceedingly difficult. Although surface characterization techniques can provide atomic level understanding of the identity, location, and even mechanism of active sites in well-defined surfaces,[5–8] they withhold critical details into bonding and electronic structure that are more easily accessed using the myriad strategies available to molecular chemists. Atomically precise nanoclusters could enable incorporating molecular precision in the design and mechanistic study of active sites.[2,3] Relative to their bulk counterparts, these platforms exhibit large surface-to-core ratios, which maximizes the number of possible active, and their catalytic selectivity and performance can be systematically tuned by altering size,[6,9] morphology,[10] or composition.[7,11–13] However, in order to unlock their potential for catalysis, synthetic innovations are required to prepare monodisperse clusters at scale and to exercise precise control over their surface chemistry and composition.

A large library of molecular ligand-stabilized transition metal nanoclusters exists, which are solution processable and have discrete chemical compositions.[14–16] Although the vast majority are not catalytically competent, some shed light on the physicochemical processes that underpin the catalytic interface between active site and multimetallic support. Select examples that provide these fundamental insights include clusters with inorganic $[Fe_4(\mu_4\text{-}O)]$,[17] $[RuCo_3(\mu_3\text{-}O)_4]$,[18] and $[Fe_4(\mu_3\text{-}S)_4]$[19] cores, wherein metal-bound oxo and imido substituents are stabilized by coordinative and electronic participation of a polymetallic support, and a series of trinuclear $[Fe_3]$ and $[Cr_3]$ clusters in which electronic coupling between the metal centers facilitates cooperative, multi-site reactivity.[20,21] Catalytically active chalcogenide clusters are scarce, including $[Mo_3S_{13}]^{2-}$ and $[MoFe_3(\mu_3\text{-}S)_4]$, for hydrogen evolution and hydrazine reduction,[22,23] respectively,

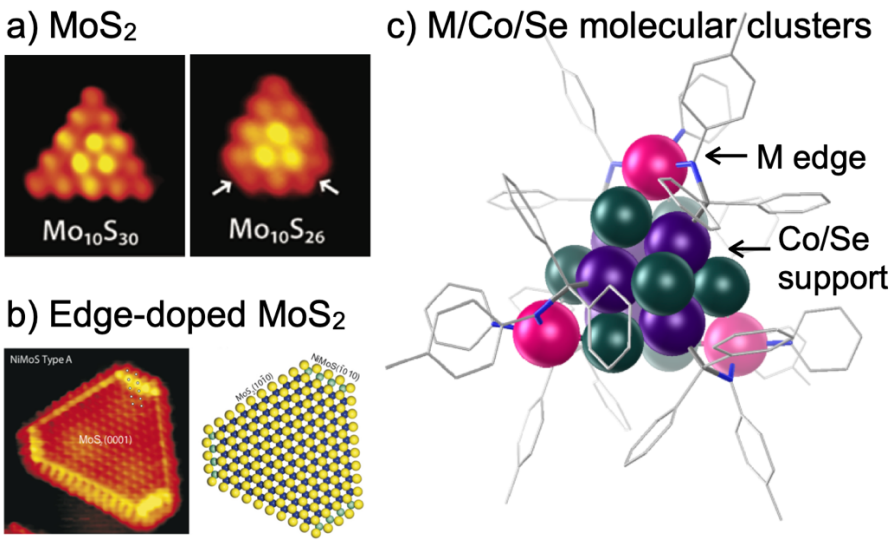


Figure 5.2. Structural resemblance between a) MoS_2, b) edge-doped MoS_2, and c) M/Co/Se nanoclusters. Image a) reproduced from Besenbacher *et al*. *ACS Nano* **2010**, *4*, 4677–4682. Copyright 2010 American Chemical Society. Image b) reproduced with permission from Besenbacher *et al*. *J. Catal.* **2007**, *249*, 220–233. Copyright 2007 Elsevier.

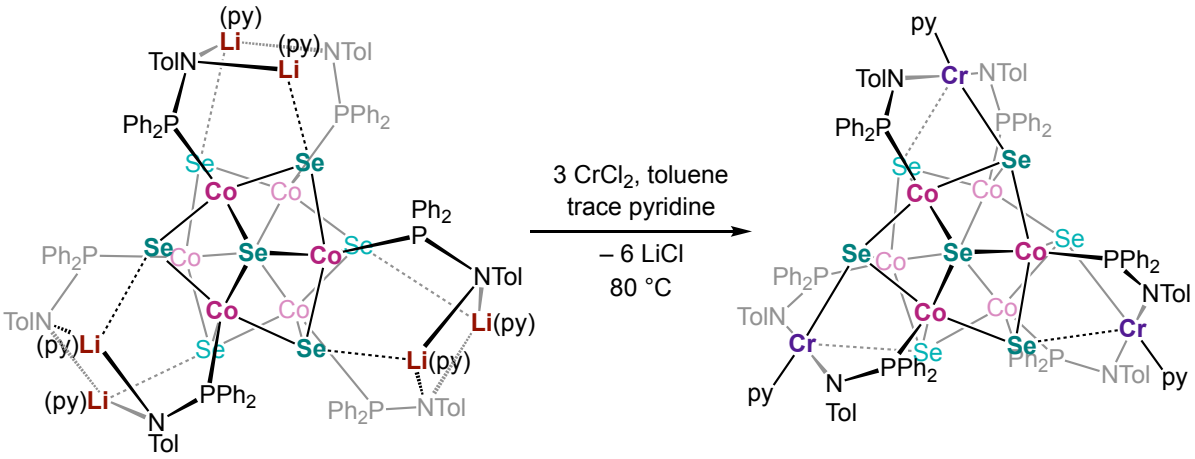
whereas metallic or metal oxide molecular clusters have been shown to catalyze a wider range of reactions.[24–28] However, the elucidation of catalytic intermediates remains challenging across these platforms and relies heavily on computational modeling as opposed to direct experimental observation.[29,30]

Combining molecular precision and scalability with catalytic competence, we introduced a family of molecular clusters $M_3Co_6Se_8L^{Tol}_6$ (M = Fe, Co, Zn, Sn; L^{Tol} = $Ph_2PN^{(-)}Tol$) that incorporate three chemically addressable edge sites (M) on the surface of a Co/Se cluster core.[31–35] This synthetic construct is reminiscent of a broad class of catalytically active edge-doped transition metal dichalcogenide nanomaterials (Figure 5.2).[6,7,11] Hemilabile edge–support interactions stabilize the three edge sites in protected low-coordinate states,[31] positioning them to function as catalytically active sites and enabling the systematic study of electronic metal–support interactions,[36] as well as allosteric effects[35] and multi-site dynamics on the cluster surface. Previously, we discovered that $Fe_3Co_6Se_8L^{Tol}_6$ (**Fe$_3$**) is an excellent catalyst for activating an organic azide and forming CN bonds[37,38] upon transferring the nitrene to *tert*-butyl isocyanide. However, the role of the Fe edges as the catalytically active sites has not been demonstrated.[31]

5.3 Synthesis of a Catalytically Active Cr/Co/Se Nanopropeller

We hypothesized that an earlier transition metal might stabilize the high valent metal-imido intermediates formed in this transformation by localizing oxidation to the edge metals and circumventing the electronic involvement of the Co_6Se_8 support.[31] Leveraging the synthetic versatility of the M/Co/Se construct, a trichromium variant $Cr_3(py)_3Co_6Se_8L_6$ (**Cr$_3$**(py)$_3$, 94% isolated yield; Scheme 5.1) was prepared from the hexalithiated salt **Li$_6$**(py)$_6$ and $CrCl_2$.[39] Single crystal X-ray diffraction reveals that the 14 e$^-$ square pyramidal Cr(py) edges (Figure 3a) expose open axial coordination sites for binding substrates at the cluster surface. The three Cr(py) edge sites form one equatorial Cr–Se bond (ranging between 2.581(2) and 2.647(2) Å), and one weak axial Cr–Se bond (ranging between 2.703(2) and 2.726(2) Å), with two tolyl-amido groups and a pyridyl ligand occupying the remainder of the equatorial coordination sites. Once again, the edge sites within **Cr$_3$**(py)$_3$ adopt a low-symmetry (α,α,β) arrangement on the cluster core, which seemingly constitutes a ubiquitous structural trait of the edge-support bonding. However, in contrast to the tricobalt cluster **Co$_3$**(py)$_3$, the pyridyl ligands of **Cr$_3$**(py)$_3$ appear to exchange in non-coordinating solvents, as ^{1}H NMR analysis in benzene-d_6 reveals a highly symmetrical species.

Scheme 5.1. Synthesis of the Cr/Co/Se nanocluster, **Cr$_3$**(py)$_3$.



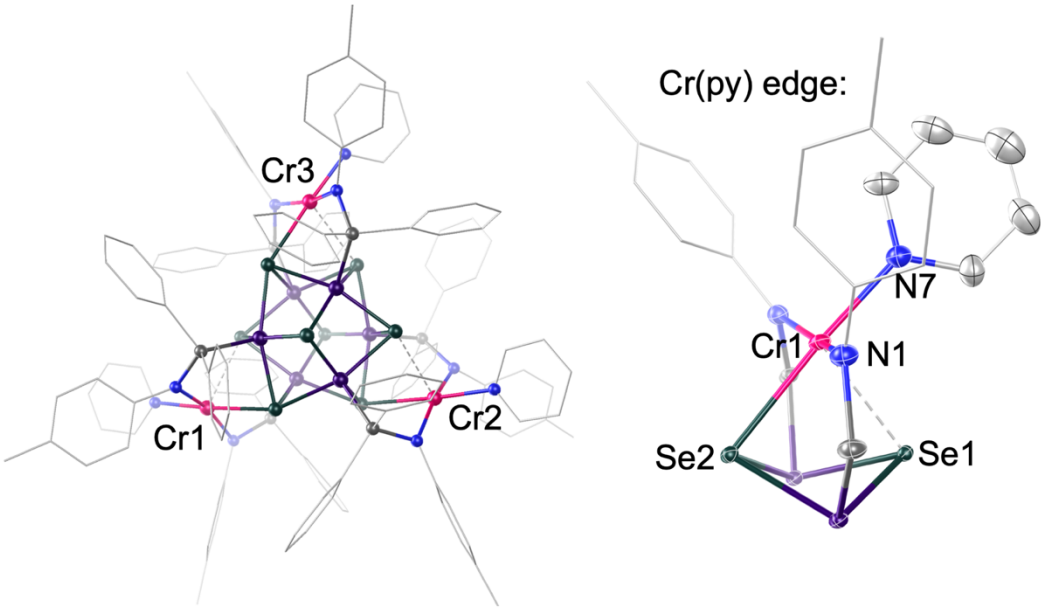


Figure 5.3. Single crystal X-ray diffraction structure of **Cr$_3$**(py)$_3$, including an inset to highlight the Cr(py) edge coordination environment. Select interatomic distances (Å): Cr1-Se2 2.581(2), Cr1-Se1 2.726(7), Cr1-N1 2.022(9), Cr1-N7 2.101(8). Thermal ellipsoids plotted at 50% probability. All hydrogen atoms and co-crystallizing solvent molecules omitted for clarity.

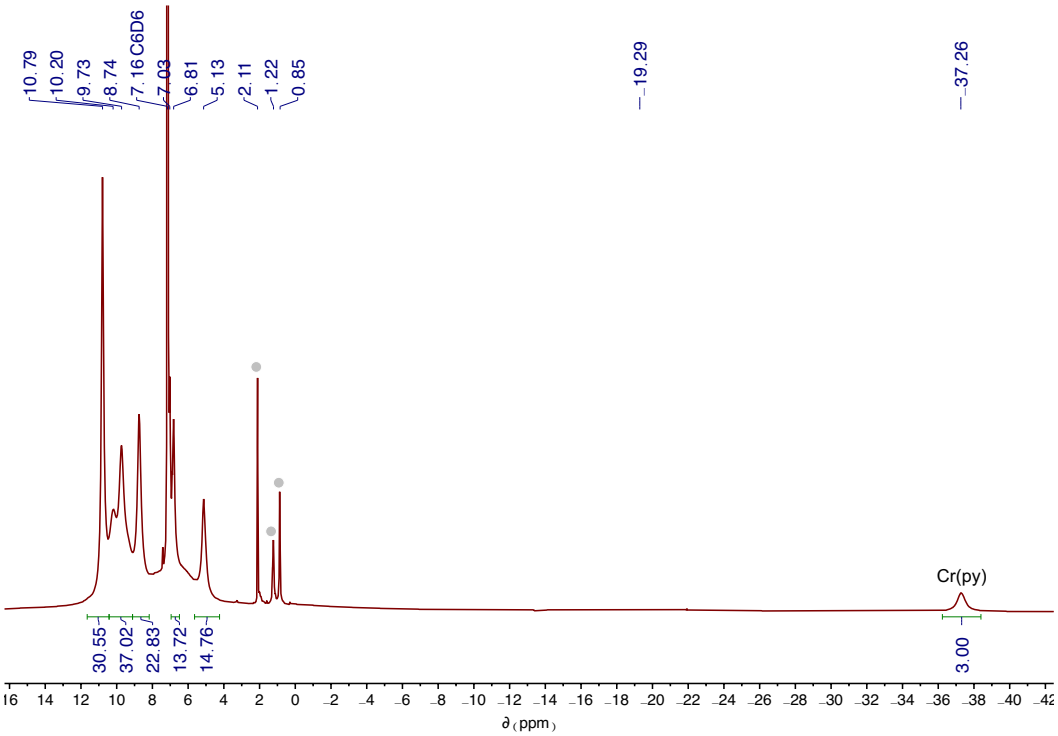


Figure 5.4. ^{1}H NMR (benzene-d_6, 25 °C, 300 MHz) spectrum of **Cr$_3$**(py)$_3$. Gray dots indicate toluene/*n*-pentane resonances.

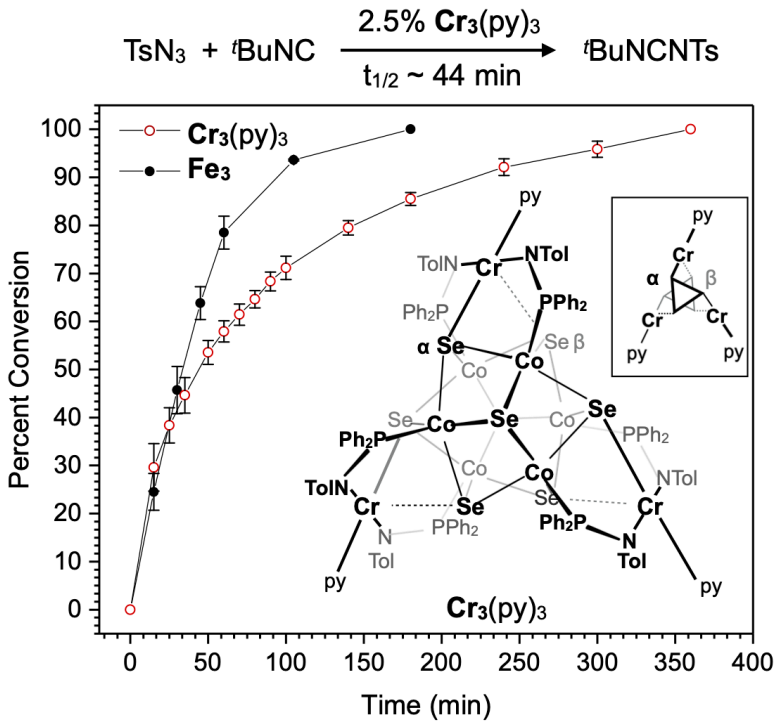


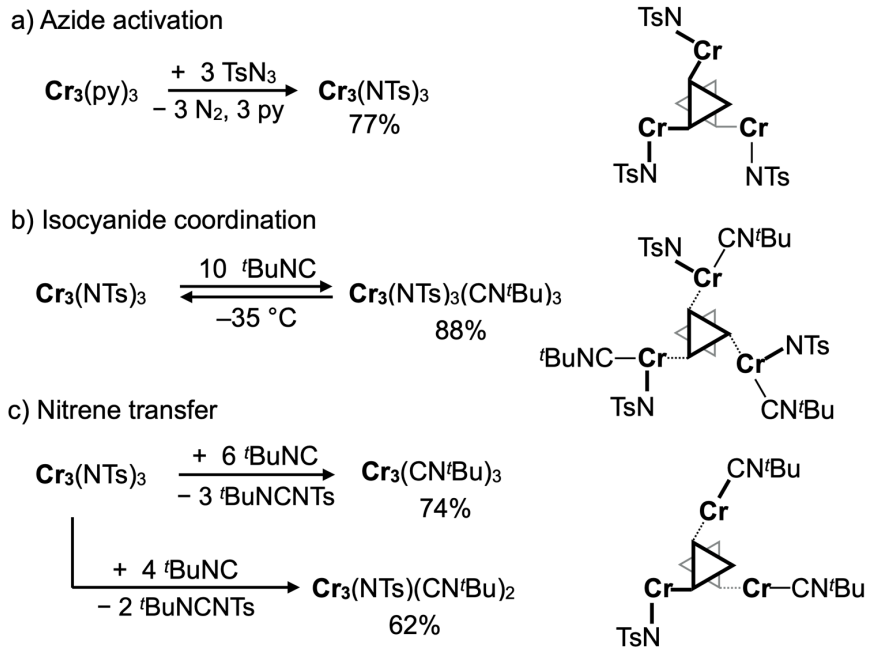
Figure 5.5. Catalytic carbodiimide formation using nanoclusters **Cr$_3$**(py)$_3$ and **Fe$_3$**, including kinetic monitoring by ^{1}H NMR spectroscopy.

Like the iron congener, **Cr$_3$**(py)$_3$ is an excellent catalyst for carbodiimide formation (Figure 5.5).[40] The conversion of tosyl azide (100 equiv) and *tert*-butyl isocyanide (165 equiv) to carbodiimide TsNCN^{t}Bu is completed at room temperature within 6 h of adding the **Cr$_3$**(py)$_3$ (2.5 mol%, 2.8 mM; TOF at $t_{1/2}$ = 27 h^{-1}), slightly slower than in the case of **Fe$_3$** (TOF at $t_{1/2}$ = 34 h^{-1}). The decrease in catalytic rate was taken as a good indication that, indeed, installation of Cr(II) edge sites somewhat tames the reactivity of catalytic intermediates.

5.4 Isolation of a Catalytically Competent Tris(Imido) Nanocluster

We set out to probe the reactivity of our Cr(py) edge sites by conducting stoichiometric azide activation experiments. Indeed, each Cr edge of the **Cr$_3$**(py)$_3$ cluster rapidly activates tosyl azide, forming three stable Cr-imido units at the cluster surface. In the absence of isocyanide, **Cr$_3$**(NTs)$_3$ (77% isolated yield) is obtained as the sole product within just 15 minutes of mixing **Cr$_3$**(py)$_3$ with TsN$_3$ (3 equiv; Scheme 5.2a, see also Section 5.6.10.1). In the solid-state, the Cr(IV) edges adopt a distorted trigonal bipyramidal geometry, with the imido group oriented equatorially (Figure 5.6).[41] Each tosyl-imido binds to Cr by N/O-chelation,[42] and as a result the ∠Cr–N$_{Ts}$–S

Scheme 5.2. Stoichiometric syntheses and isolated yields of catalytically competent azide activation and nitrene transfer intermediates.



angles are significantly bent (avg. 96°), and the Cr–N_{Ts} double bonds are elongated (avg. 1.82 Å).[43] There is only one other structurally characterized Cr(NTs) complex in the literature,[44] others eluding isolation due to rapid C–H or C–C bond activation.[45,46]

Although the three Cr(NTs) edges have identical first coordination spheres, they are chemically inequivalent due to their (α,α,β) orientation on the Co_6Se_8 surface. Here α and β designate equatorial Se atoms from the top and bottom Co_3Se_4 halves of the cubic Co_6Se_8 support, respectively, as illustrated in the inset of Figure 2.[33] Small variations in the TsN/Cr/Co_6Se_8 bonding interactions structurally distinguish the three edge sites, most notable when comparing the Cr–Se bond lengths of Cr1 with either of Cr2 or Cr3. In solution, the Cr(NTs) edges remain locked in chemically inequivalent orientations even at elevated temperatures, giving rise to multiple N-tosyl ^{1}H NMR environments (Figure 5.7; see also Section 5.6.3). Generally, the low-symmetry (α,α,β) orientation of the edge sites appears to be favored over the previously unobserved (α,α,α) isomer in these nanoclusters.[31,33] To a first approximation, we have proposed that this structural preference reflects the intrinsic preference of the nanocluster to evenly distribute electron density between the three electron deficient edge centers on the Co_6Se_8 support, and hypothesize this force guides the formation of (α,α,β)-**Cr$_3$**(NTs)$_3$ as the sole isomer upon reaction of **Cr$_3$**(py)$_3$ with azide. Intent on demonstrating that the Cr edges are viable active sites not only for azide activation but also for

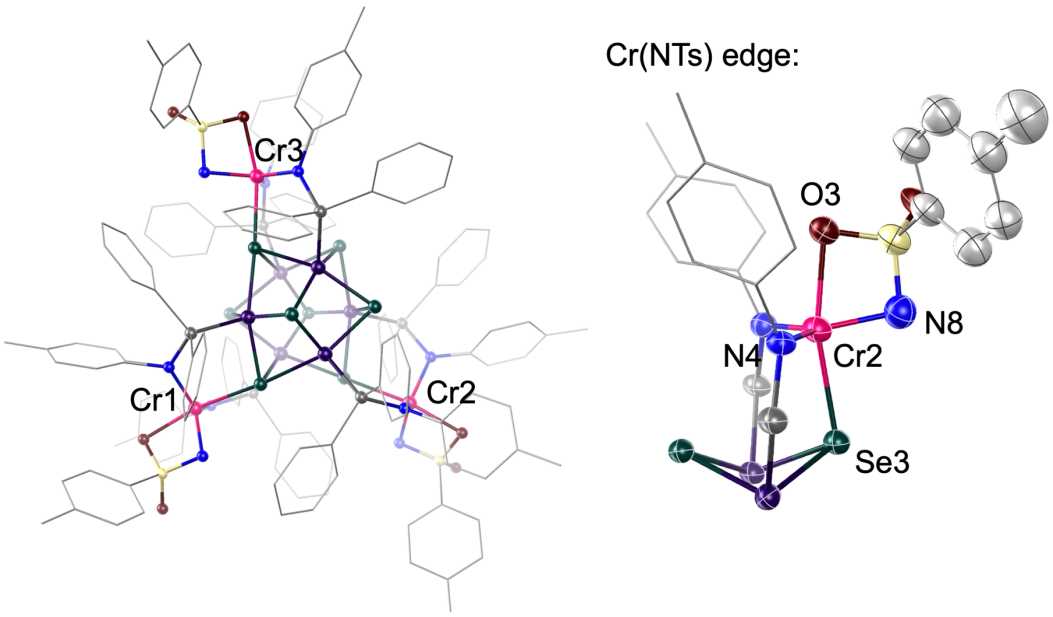


Figure 5.6. Single crystal X-ray diffraction structure of **Cr$_3$**(NTs)$_3$, including an inset to highlight the Cr(NTs) edge coordination environment. Select interatomic distances (Å): Cr2-Se3 2.475(7), Cr2-N8 1.83(1), Cr2-N4 1.90(2), Cr2-O3 2.12(1). Thermal ellipsoids plotted at 50% probability. All hydrogen atoms and co-crystallizing solvent molecules omitted for clarity.

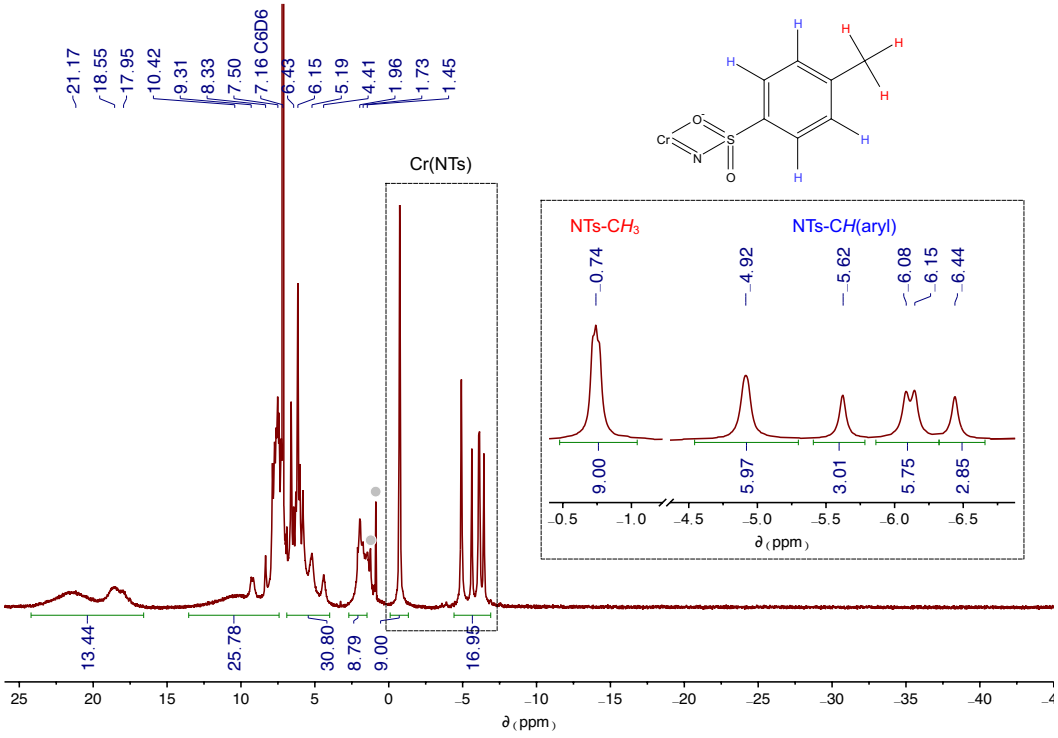


Figure 5.7. ^{1}H NMR (benzene-d_6, 25 °C, 300 MHz) spectrum of **Cr$_3$**(NTs)$_3$. The C_1 symmetry is reflected in solution, where we observe a highly desymmetrized NMR profile with a range of different ^{1}H resonances. Gray dots indicate toluene/*n*-pentane resonances.

nitrene transfer, we tested the catalytic competence of the tris(imido) as a pre-catalyst. Remarkably, the tris(imido) nanocluster **Cr$_3$**(NTs)$_3$ catalyzes carbodiimide formation similarly to **Cr$_3$**(py)$_3$ (see Section 5.6.9).

5.5 Isolation of Nitrene Transfer Intermediates

Stoichiometric studies confirm that each of the three edge sites in **Cr$_3$**(NTs)$_3$ can transfer the nitrene group to isocyanide, cementing their viability as catalytically active sites (Scheme 5.2c). Two equivalents of isocyanide per Cr(NTs) edge (6 equiv total) are required to complete the nitrene transfer from **Cr$_3$**(NTs)$_3$, forming quantitatively the tris(isocyanide) adduct **Cr$_3$**(CN^{t}Bu)$_3$ (74% isolated yield) and the carbodiimide product, TsNCN^{t}Bu (3 equiv). *In situ* ^{1}H NMR monitoring of this reaction reveals that this transformation unfolds via a stepwise mechanism (see Figure 5.8 and Figure 5.9). The edge sites engage sequentially to produce carbodiimide, giving rise in the process to two major observable intermediates, which were isolated independently. The first, **Cr$_3$**(NTs)$_3$(CN^{t}Bu)$_3$, forms upon isocyanide binding at **Cr$_3$**(NTs)$_3$ and was identified as the resting state of the nanocluster under catalytic conditions (Figure 5.10). This species is consumed over the course of 4 h at room temperature, generating a second, site-differentiated intermediate **Cr$_3$**(NTs)(CN^{t}Bu)$_2$ and substoichiometric carbodiimide (2 equiv). Under these conditions, the last equivalent of carbodiimide is released slowly (> 48 h at 60 °C) alongside **Cr$_3$**(CN^{t}Bu)$_3$.

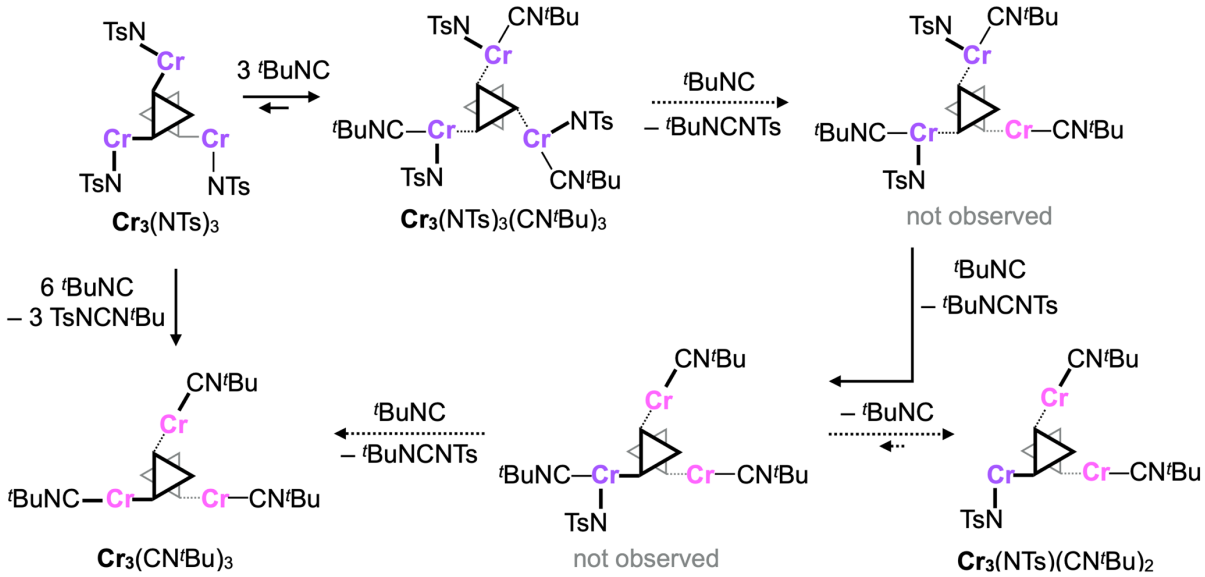


Figure 5.8. Step-wise nitrene transfer mechanism wherein the reactivity of Cr(NTs) edges is differentiated under stoichiometric conditions.

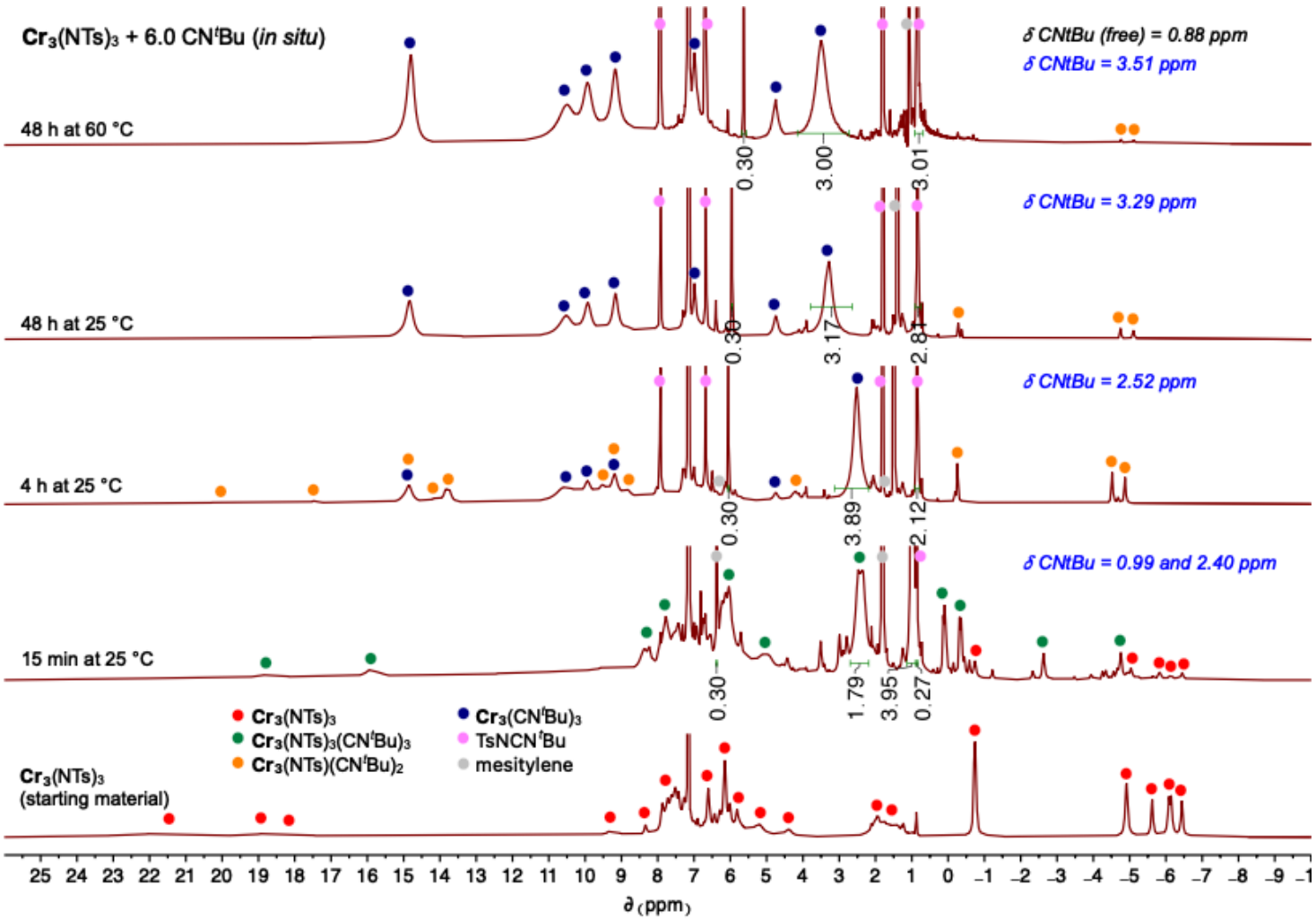


Figure 5.9. ^{1}H NMR (benzene-d_6, 25 °C, 500 MHz) spectra of the *in situ* reaction mixture of **Cr$_3$**(NTs)$_3$ with CN^{t}Bu (6 equiv) recorded after 15 min and 4 h at 25 °C, and after an additional 48 h at 60 °C. The C(C*H*$_3$)$_3$ resonances of Cr(CN^{t}Bu) (reagent) and TsNCN^{t}Bu (product) are integrated against the internal standard mesitylene to track the reactions progress (see Section 5.6.10 for more details).

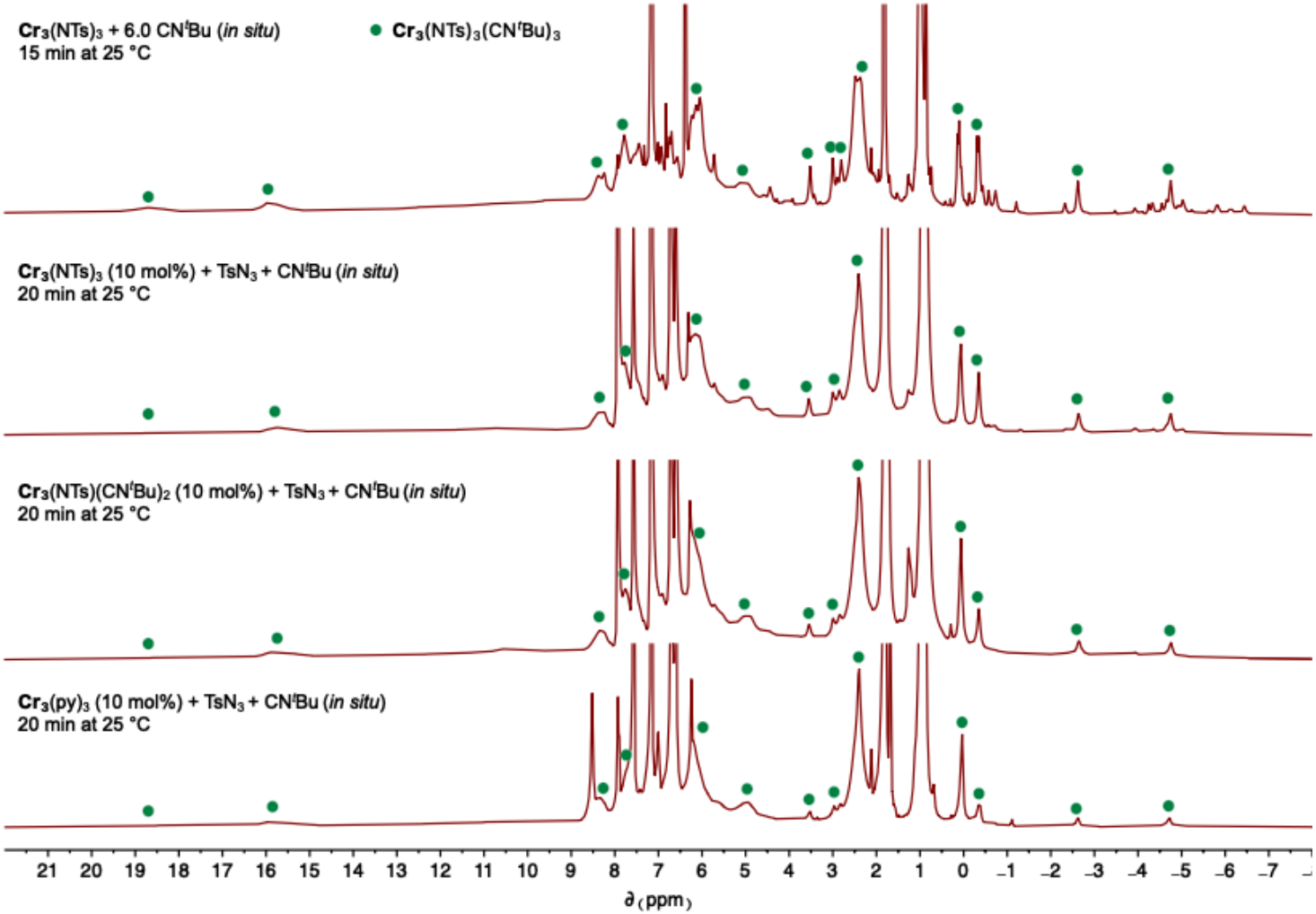


Figure 5.10. *In situ* ^{1}H NMR (benzene-d_6, 25 °C, 300 MHz) spectra collected for the catalytic reaction mixture formed using either **Cr$_3$**(py)$_3$, **Cr$_3$**(NTs)(CN^{t}Bu)$_2$, or **Cr$_3$**(NTs)$_3$ (10 mol%) as a pre-catalyst 20 min after the addition of TsN_3, plotted in comparison to the spectrum obtained 15 min after stoichiometric treatment of **Cr$_3$**(NTs)$_3$ with CN^{t}Bu (6 equiv) (top).

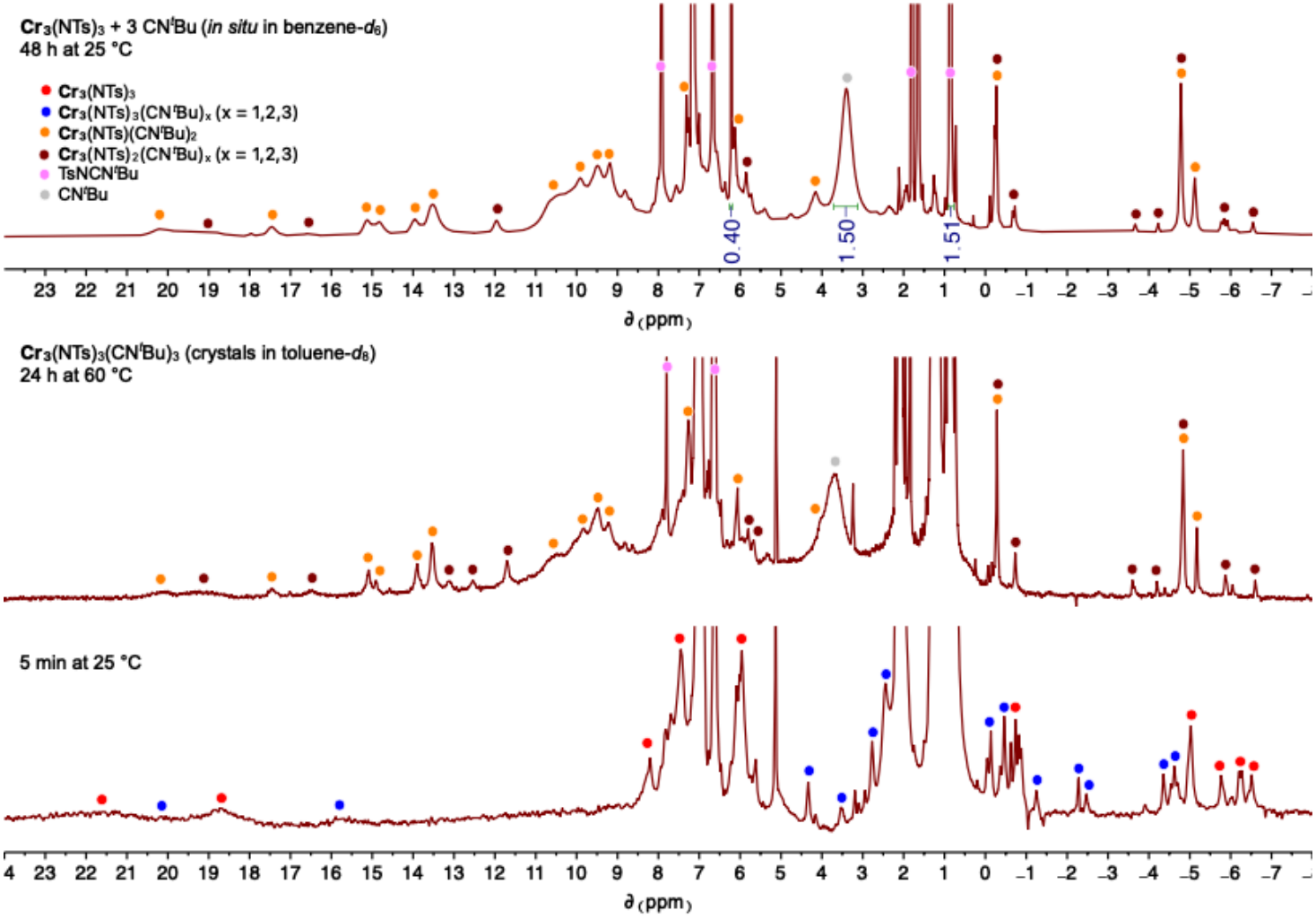


Figure 5.11. *In situ* ^{1}H NMR (benzene-d_6, 25 °C, 500 MHz) reaction monitoring of **Cr$_3$**(NTs)$_3$ treated with CN^{t}Bu (3 equiv) recorded after 48 h at 25 °C. The C(CH_3)$_3$ resonances of CN^{t}Bu (reagent) and TsNCN^{t}Bu (product) are integrated to reveal the ~1:1 distribution of Cr(CN^{t}Bu) and TsNCN^{t}Bu. This spectrum is plotted in comparison to *in situ* ^{1}H NMR (toluene-d_8, 25 °C, 500 MHz) spectra monitoring the reactivity of crystalline **Cr$_3$**(NTs)$_3$(CN^{t}Bu)$_3$ upon dissolution after 5 min at 25 °C (bottom) and 24 h at 60 °C (middle). *For the latter spectra, overlap between toluene-d_8 and TsNCN^{t}Bu CH_3 resonances makes Cr(CN^{t}Bu) and TsNCN^{t}Bu integration challenging.

5.5.1 *Isolation of the Catalyst Resting State,* ***Cr*****$_3$***(NTs)$_3$(CN^{t}Bu)$_3$*

Immediately after the addition of isocyanide, we observe the formation of a new, more symmetrical species in solution prior to the evolution of any carbodiimide product (denoted in green within Figure 5.9). To independently isolate this first intermediate and unveil the identity of the catalytic resting state, **Cr$_3$**(NTs)$_3$ was treated with CN^{t}Bu (10 equiv) at a temperature sufficiently low to prevent the evolution of carbodiimide (–35 °C). Over the course of 24 h, dark red prismatic crystals of the tris(isocyanide)-tris(imido) cluster **Cr$_3$**(NTs)$_3$(CN^{t}Bu)$_3$ formed quantitatively (88% isolated yield, Scheme 5.2b). Single crystal X-ray diffraction reveals how CN^{t}Bu binds the Cr(NTs) edge site axially, breaking N/O-chelation of the N-tosyl group observed in **Cr$_3$**(NTs)$_3$ to afford a monodentate tosyl imido substituent (Figure 5.12). Isocyanide binding at the Cr(NTs) edge strengthens the substrate-edge interactions and weakens the edge-support contacts, trends marked by contracted Cr–NTs bonds (avg. 1.75 vs 1.82 Å) and elongated Cr–Se bonds (avg. 2.61 Å vs 2.48 Å), respectively. We propose that the weakening of edge–support bonding interactions depolarizes the Co_6Se_8 core and provides the necessary structural flexibility

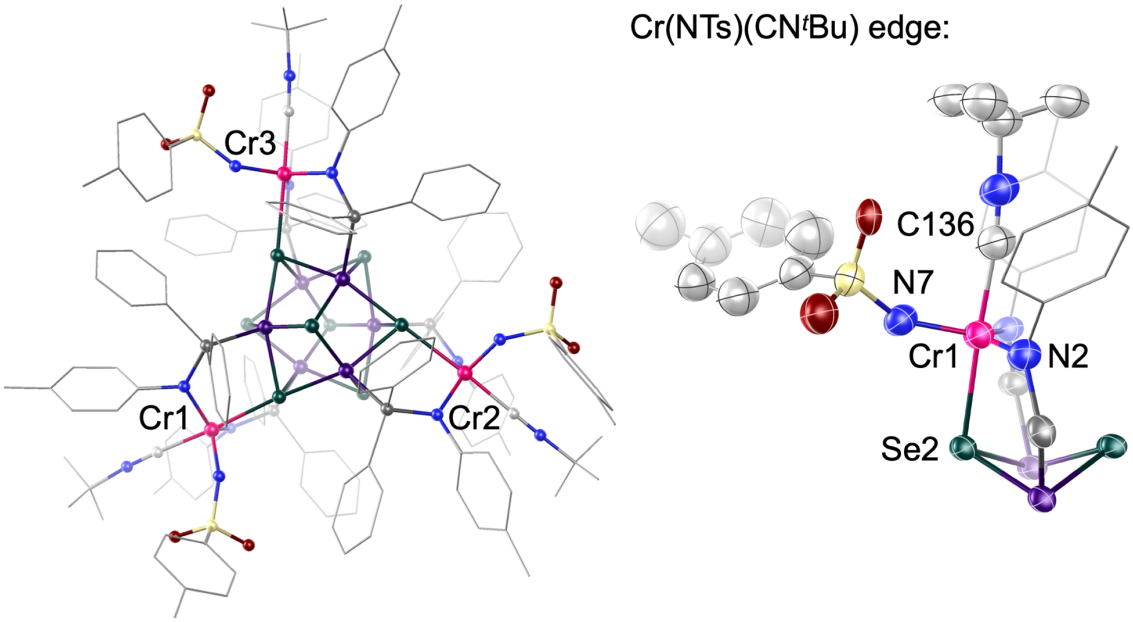


Figure 5.12. Single crystal X-ray diffraction structure of **Cr$_3$**(NTs)$_3$(CN^{t}Bu)$_3$, including an inset to highlight the Cr(NTs)(CN^{t}Bu) edge coordination environment. Select interatomic distances (Å): Cr1-Se2 2.574(4), Cr1-N7 1.75(1), Cr1-N2 1.916(9), Cr1-C136 2.07(1). Thermal ellipsoids plotted at 50% probability. All hydrogen atoms and co-crystallizing solvent molecules omitted for clarity.

for the Cr–Se contacts to reorganize from (α,α,β) in **Cr$_3$**(NTs)$_3$ to the (α,α,α) configuration in **Cr$_3$**(NTs)$_3$(CN^{t}Bu)$_3$ in which all edge sites are identical. This unusual behavior constitutes a rare molecular example of surface restructuring, and the first to our knowledge that transpires over the course of a catalytic transformation.[47] Notably, these structural dynamics are of paramount importance in heterogeneous catalysis, where catalytic reactions can give rise to meta-stable surface phases.[48–52] Finally, to our knowledge, this is the first structurally characterized Cr^{IV}(CN^{t}Bu) complex in the literature, and it exhibits a massively blue-shifted isocyanide stretch (ν_{CN} = 2218 cm^{-1}) (Figure 5.13).

Cr$_3$(NTs)$_3$(CN^{t}Bu)$_3$ is thermally unstable, and readily produces carbodiimide upon dissolution in benzene-d_6. However, as this reaction proceeds, Cr^{II}(CN^{t}Bu) edges scavenge isocyanide from solution to afford cluster products with a mixture of Cr(NTs) and Cr(CN^{t}Bu) edge sites. To test this reactivity and further verify this compound's identity as a tris(imido)-tris(isocyanide) cluster, its solution-phase reactivity was monitored by ^{1}H NMR spectroscopy in toluene-d_8 (Figure 5.11). Immediately after dissolution of crystalline **Cr$_3$**(NTs)$_3$(CN^{t}Bu)$_3$, we observe the generation of an isocyanide binding equilibrium to yield a mixture of **Cr$_3$**(NTs)$_3$ and **Cr$_3$**(NTs)$_3$(CN^{t}Bu)$_x$ (x = 1, 2, 3) clusters. After heating this mixture at 60 °C for 24h, the reaction is halted with the same product mixture, featuring clusters with a mixture of Cr(NTs) and

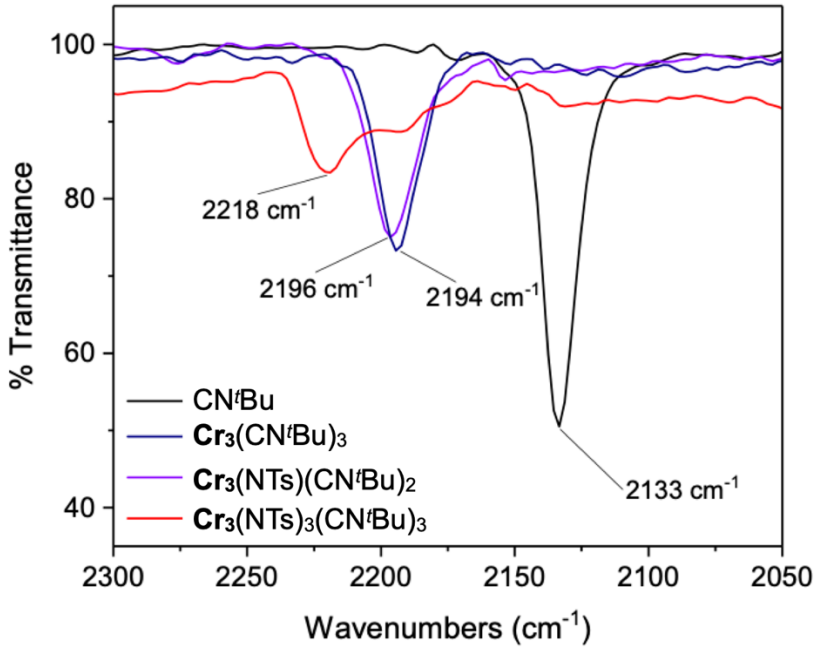


Figure 5.13. ATR-FTIR spectra of crystalline **Cr$_3$**(CN^{t}Bu)$_3$, **Cr$_3$**(NTs)(CN^{t}Bu)$_2$, **Cr$_3$**(NTs)$_3$(CN^{t}Bu)$_3$, and neat CN^{t}Bu, highlighting the isocyanide CN stretching frequencies.

Cr(CN^{t}Bu) edges, that is obtained upon treatment of **Cr$_3$**(NTs)$_3$ with just three equivalents of CN^{t}Bu (see Section 5.6.10.2).

5.5.2 *Isolation of a Site-differentiated Cr(NTs)/Cr(CN^{t}Bu) Intermediate*

Returning now to the reaction of **Cr$_3$**(NTs)$_3$ with six equivalents of CN^{t}Bu, after generation of the catalytic resting state, in which all three Cr edges are loaded with both coupling substrates, we find that nitrene transfer is far from over. Rather than extruding three equivalents of carbodiimide, **Cr$_3$**(NTs)$_3$(CN^{t}Bu)$_3$ evolves to a second intermediate that contains a single Cr^{IV}(NTs) edge free of bound isocyanide (Figure 5.9). Its identity as **Cr$_3$**(NTs)(CN^{t}Bu)$_2$ was elucidated by independent synthesis (62% isolated yield) from **Cr$_3$**(NTs)$_3$ and substoichiometric CN^{t}Bu (4 equiv; Scheme 5.2c), and its catalytic competence demonstrated (see Section 5.6.9.2). Unlike **Cr$_3$**(NTs)$_3$(CN^{t}Bu)$_3$, the mono(imido) **Cr$_3$**(NTs)(CN^{t}Bu)$_2$ is indefinitely stable at room temperature, evidence of the high affinity for isocyanide of the two Cr(II) sites which do not release isocyanide that would otherwise strip the nitrene off the Cr(NTs) edge. Despite this high affinity, the Cr–CN^{t}Bu bonding interactions in **Cr$_3$**(NTs)(CN^{t}Bu)$_2$ are among the longest reported (avg.

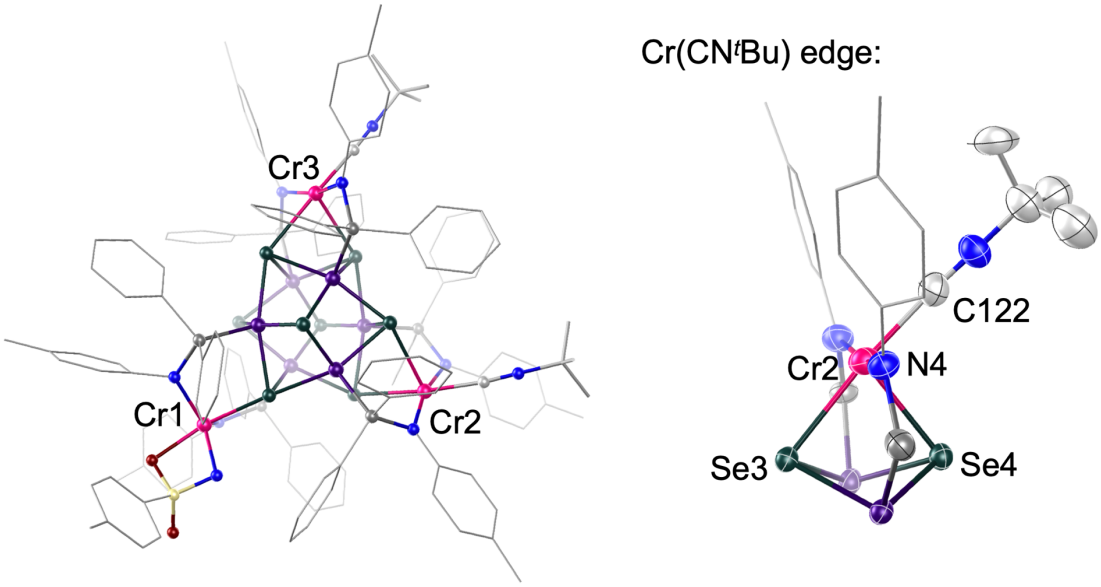


Figure 5.14. Single crystal X-ray diffraction structure of **Cr$_3$**(NTs)(CN^{t}Bu)$_2$, including an inset to highlight the Cr(CN^{t}Bu) edge coordination environment. Select interatomic distances (Å): Cr2-Se3 2.611(3), Cr2-Se4 2.663(4), Cr2-N4 2.04(1), Cr-C122 2.09(2). Thermal ellipsoids plotted at 50% probability. All hydrogen atoms and co-crystallizing solvent molecules omitted for clarity.

2.08 Å),[53] and the CN stretching frequency (ν_{CN} = 2196 cm^{-1}) is blue-shifted, a mark of the electron deficiency of these Cr centers which do not engage in π-backbonding (Figure 5.13).

Comparing the Cr(NTs) site in **Cr$_3$**(NTs)(CN^{t}Bu)$_2$ with those of **Cr$_3$**(NTs)$_3$ we discovered that the chemical state of the neighboring active sites on the cluster impact its structure and reactivity. Although of identical coordination environment to those in **Cr$_3$**(NTs)$_3$, the Cr(NTs) edge in **Cr$_3$**(NTs)(CN^{t}Bu)$_2$ features a strengthened Cr–Se interaction (2.444(2) vs 2.48 avg. Å), and an elongated Cr–N_{Ts} bond (1.862(9) vs 1.82 avg. Å; Figure 5.14) in the solid state. To probe if the strengthened edge–support interaction decreases nitrene transfer reactivity of the Cr(NTs) edge, the isocyanide binding affinities of **Cr$_3$**(NTs)$_3$ and **Cr$_3$**(NTs)(CN^{t}Bu)$_2$ were compared. Using ^{1}H NMR spectroscopy, the binding constant for isocyanide at the **Cr$_3$**(NTs)$_3$ cluster to produce **Cr$_3$**(NTs)$_3$(CN^{t}Bu)$_{1–3}$ adducts at room temperature is estimated to average 44(7) M^{-1} for the three sites, whereas there is no spectroscopic evidence of any isocyanide binding at the Cr(NTs) site in **Cr$_3$**(NTs)(CN^{t}Bu)$_2$ under identical conditions (for detailed CN^{t}Bu binding constant analysis see Section 5.5.4). We propose that structural differentiation with Cr^{II}(CN^{t}Bu) edge sites slows nitrene transfer kinetics at this third edge site, distinguishing its reactivity from that of the first Cr(NTs) edge. The strengthened edge–support interactions in **Cr$_3$**(NTs)(CN^{t}Bu)$_2$ are also associated with a reorganization back to (α,α,β) symmetry in the solid state. This rearrangement reinforces the hypothesis that α/β isomerism enables the Co_6Se_8 support to reversibly distribute electron density via structural changes in response to substrate binding events at the active sites.

Informed by the catalytic and stoichiometric reactivity of the trichromium nanoclusters, a catalytic cycle is proposed at a single edge site (Figure 4a). The cycle begins with a Cr^{II}L (L = py, CN^{t}Bu) site that quickly activates tosyl azide, producing a Cr^{IV}(NTs) species. Isocyanide binding to Cr^{IV}(NTs) disrupts the N/O-chelation of the N-tosyl group, and generates the catalytic resting state Cr^{IV}(NTs)(CN^{t}Bu). Although both coupling substrates are already bound at the Cr^{IV}(NTs)(CN^{t}Bu) edge, an additional equivalent of isocyanide is required for carbodiimide formation to occur. Extrusion of carbodiimide is the rate determining step and regenerates the Cr^{II}(CN^{t}Bu) site, which is ready to reengage with azide.

Electronic and structural differences distinguish the individual Cr edge sites of the nanocluster, leading to interdependent and sequential reactivity that is observable under stoichiometric conditions. The step-wise process of transferring the nitrene groups from **Cr$_3$**(NTs)$_3$ is detailed in Figure 5.8, informed by the observation and isolation of **Cr$_3$**(NTs)$_3$(CN^{t}Bu)$_3$ and

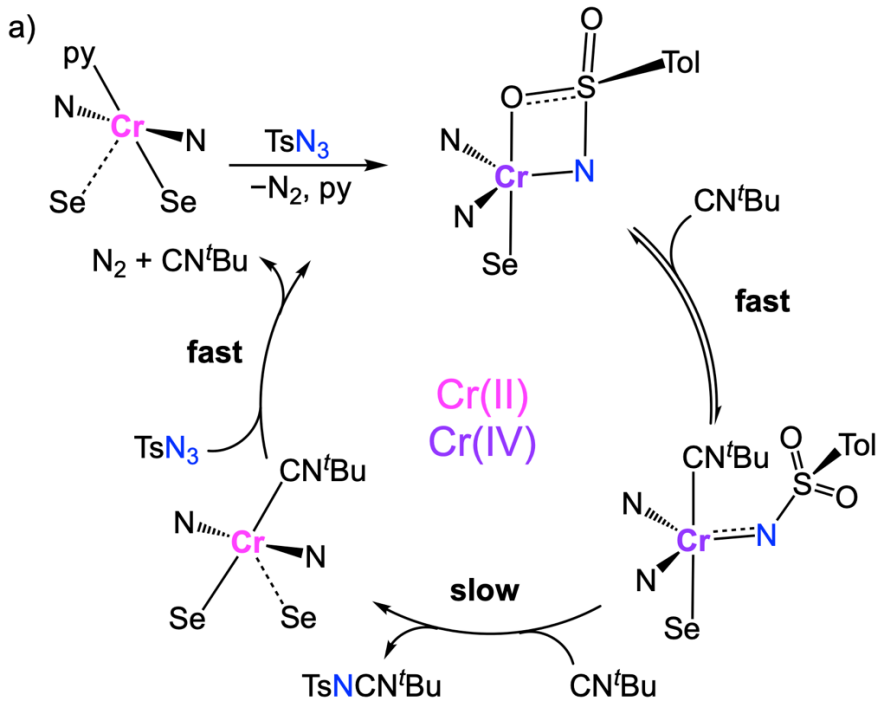


Figure 5.15. Proposed catalytic cycle for carbodiimide formation at an isolated Cr edge site, informed by the isolation of key reactive intermediates.

Cr$_3$(NTs)(CN^{t}Bu)$_2$. We propose that as the Cr^{II}(CN^{t}Bu) edges are regenerated on the nanocluster, they have a stabilizing effect on the neighboring Cr^{IV}(NTs) edges, deactivating them towards isocyanide binding and, consequently, nitrene transfer. Throughout the catalytic cycle, the inorganic Co/Se support is structurally responsive to substrate activation and transfer with hemilabile Cr–Se interactions enabling facile transitions between κ^3 and κ^4 binding to accommodate the Cr edge sites in diverse configurations.

5.5.3 *Conclusions*

The dichotomy between the stability of the Cr(NTs) edges in the Cr/Co/Se clusters towards isolation and their propensity to accomplish group transfer catalytically is unusual and uniquely positions the system for mechanistic investigations. Only two other imido-bound transition metal-chalcogenide clusters have been previously reported, the cubane-type Fe$_4$S$_4$(NR) and Mo$_4$S$_4$(NR)$_4$ clusters,[19,54] though neither have been shown to be catalytically competent or active towards stoichiometric group transfer chemistry. The Cr/Co/Se nanopropeller is not only a functional model for heterogeneous single-atom group transfer catalysis, but also a powerful platform to study the dynamics of neighboring active sites in heterogenous catalysts. While the push-pull

dynamic between the substrate/edge/support is central to completing a catalytic cycle at an isolated Cr edge site, a domino effect wherein electronic changes propagate through the Co_6Se_8 support intertwines the reactivity of neighboring active sites. Overall, this study sheds light on the mechanism of nitrene transfer at the surface of a well-defined nanocluster catalyst bearing three operational active sites, achieving a distinguished level of detail for nanocluster catalysis.

5.5.4 *CN^{t}Bu Binding Constant Determination*

The coordination of CN^{t}Bu to the Cr(NTs) edge sites of **Cr$_3$**(NTs)$_3$ gives rise to Cr(NTs)(CN^{t}Bu) edge sites exhibiting C(CH_3)$_3$ ^{1}H resonances with chemical shifts distinct from those of free CN^{t}Bu or exchanging Cr(CN^{t}Bu). The reversible coordination of CN^{t}Bu gives rise to the equilibrium depicted below, which precedes the formation of TsNCN^{t}Bu, and a Cr(CN^{t}Bu) edge (Figure 5.16). It is important to note that we observe three unique C(CH_3) resonances: 1) Cr^{IV}(NTs)(CN^{t}Bu) edges, 2) Cr^{II}(CN^{t}Bu) edges, and 3) TsNCN^{t}Bu, which can be integrated to determine their relative concentrations. Due to coordinative exchange that exceeds the NMR timescale, in all cases we do not observe a resonance for free CN^{t}Bu. Finally, although the binding constant at the three edge sites is expected to be differentiated, in this model it is assumed to be identical at all edge sites (See note below).

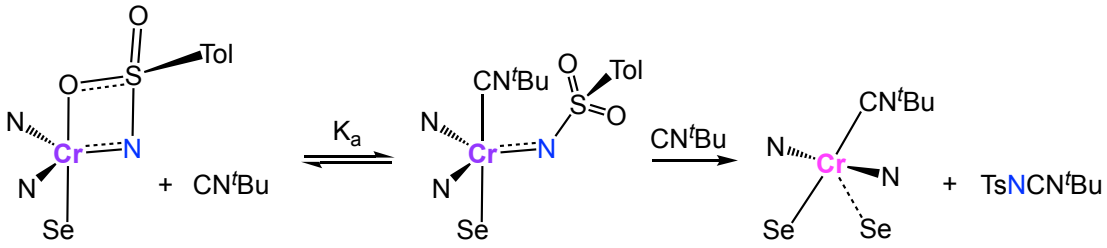


Figure 5.16. Partition of CN^{t}Bu as it engages in reversible coordinative at a Cr(NTs) edge, or undergoes migratory (1,2)-insert with the imido group to afford carbodiimide product.

This equilibrium is described by the binding constant:

$$K_a = \frac{[Cr(NTs)(CNtBu)]}{[Cr(NTs)][CNtBu]}$$

With predetermined initial concentrations of **Cr$_3$**(NTs)$_3$ and CN^{t}Bu ([Cr(NTs)]$_{init}$ and [CN^{t}Bu]$_{init}$), the total concentration of Cr(NTs) edge sites and free CN^{t}Bu ligand present in this equilibrium ([Cr(NTs)]$_{ex}$ and [CN^{t}Bu]$_{ex}$) can be calculated by correcting for the formation of TsNCN^{t}Bu and bound Cr(CN^{t}Bu) edge sites:

$$[Cr(NTs)]_{ex} = 3 * [\mathbf{Cr_3}(NTs)_3]_{init} - [TsNCNtBu]$$

$$[CNtBu]_{ex} = [CNtBu]_{init} - [TsNCNtBu] - [Cr(CNtBu)] = [CNtBu]_{init} - 2 * [TsNCNtBu]$$

The concentration of TsNCN^{t}Bu can be extracted from the ratio of its C(CH_3)$_3$ ^{1}H integration to the total integration of C(CH_3)$_3$ resonances from Cr(NTs)(CN^{t}Bu), Cr(CN^{t}Bu), free CN^{t}Bu, and TsNCN^{t}Bu.

$$[TsNCNtBu] = [CNtBu]_{init} * \frac{i_{TsNCNtBu}}{i_{TsNCNtBu} + i_{CNtBu} + i_{Cr(NTs)(CNtBu)}}$$

It should be noted that the C(CH_3)$_3$ resonances of free CN^{t}Bu and bound Cr(CN^{t}Bu) coalesce due to exchange. Accordingly, they are combined above in a singular term, i_{CN^tBu}. Recalling that the concentration of bound Cr(CN^{t}Bu) is equal to the concentration of TsNCN^{t}Bu, the contribution of bound Cr(CN^{t}Bu) accounted for by subtracting the integration of the carbodiimide:

$$i_{CNtBu} = i_{CNtBu(free)} + i_{Cr(CNtBu)} = i_{CNtBu(free)} + i_{TsNCNtBu}$$

$$i_{CNtBu(free)} = i_{CNtBu} - i_{TsNCNtBu}$$

The concentrations of free CN^{t}Bu and bound Cr(NTs)(CN^{t}Bu) can now be determined by multiplying the total concentration of exchanging isocyanide, [CN^{t}Bu]$_{ex}$, with the ratio of their respective (CH_3)$_3$ ^{1}H integrations to the total integration of exchanging CN^{t}Bu:

$$[CNtBu]_{free} = [CNtBu]_{ex} * \frac{i_{CNtBu(free)}}{i_{Cr(NTs)(CNtBu)} + i_{CNtBu(free)}}$$

$$[Cr(NTs)(CNtBu)] = [CNtBu]_{ex} * \frac{i_{Cr(NTs)(CNtBu)}}{i_{Cr(NTs)(CNtBu)} + i_{CNtBu(free)}}$$

Finally, the concentration of unbound Cr(NTs) sites is determined as:

$$[Cr(NTs)] = [Cr(NTs)]_{ex} - [Cr(NTs)(CNtBu)]$$

This calculation assumes the three Cr(NTs) edge sites of **Cr$_3$**(NTs)$_3$ exhibit equivalent affinities for CN^{t}Bu.

Note: In reality, it is likely that this is not the case, as the Cr(NTs) edges are (α,α,β) site-differentiated on the cluster's surface. Along these lines, **Cr$_3$**(NTs)$_3$(CN^{t}Bu)$_3$ is not formed as the only isocyanide adduct upon treatment of **Cr$_3$**(NTs)$_3$ with CN^{t}Bu, and we instead observe a mixture of **Cr$_3$**(NTs)$_3$(CN^{t}Bu)$_3$ and **Cr$_3$**(NTs)$_3$(CN^{t}Bu)$_x$ (x = 1, 2) (Figure 5.17). A definitive spectroscopic identification of these intermediate **Cr$_3$**(NTs)$_3$(CN^{t}Bu)$_x$ species is non-trivial due to

the sheer complexity of their NMR profiles. Further, the resolution of distinct binding constants for separate Cr(NTs) sites is precluded by the near coalescence of their Cr(NTs)(CN^{t}Bu) C(CH_3)$_3$ resonances (δ ~2.5-2.3 ppm).

Binding constants were calculated from *in situ* NMR spectra collected upon treatment of **Cr$_3$**(NTs)$_3$ (9.7-9.2 mM) with varying amounts of CN^{t}Bu (1, 2, 3, 4, 5, 6 equiv) by integrating the Cr(NTs)(CN^{t}Bu), CN^{t}Bu and TsNCN^{t}Bu -C(CH_3)$_3$ resonances (Figure 5.18). Isocyanide was added as a solution in benzene-d_6 (0.88 M) by microsyringe. In each case, we observe the formation of a mixture of nanoclusters bearing Cr(NTs)(CN^{t}Bu) edge sites. By contrast, Cr(NTs)(CN^{t}Bu) species are not detected in the *in situ* analysis of the reaction between **Cr$_3$**(NTs)(CN^{t}Bu)$_2$ with CN^{t}Bu (3 equiv), despite the slow production of TsNCN^{t}Bu and **Cr$_3$**(CN^{t}Bu)$_3$ (Figure 5.19).

Table 5.1. Binding constants collected for **Cr$_3$**(NTs)$_3$ and **Cr$_3$**(NTs)(CN^{t}Bu)$_2$ in the presence of varying equivalents of added isocyanide in benzene-d_6.

Cr$_3$(NTs)$_3$	
CN^{t}Bu (equiv)	K_a (M^{-1})
1	40
2	39
3	35
4	51
5	49
6	50
Avg:	44(7)
Cr$_3$(NTs)(CN^{t}Bu)$_2$	
CN^{t}Bu (equiv)	K_a (M^{-1})
3	no binding detected

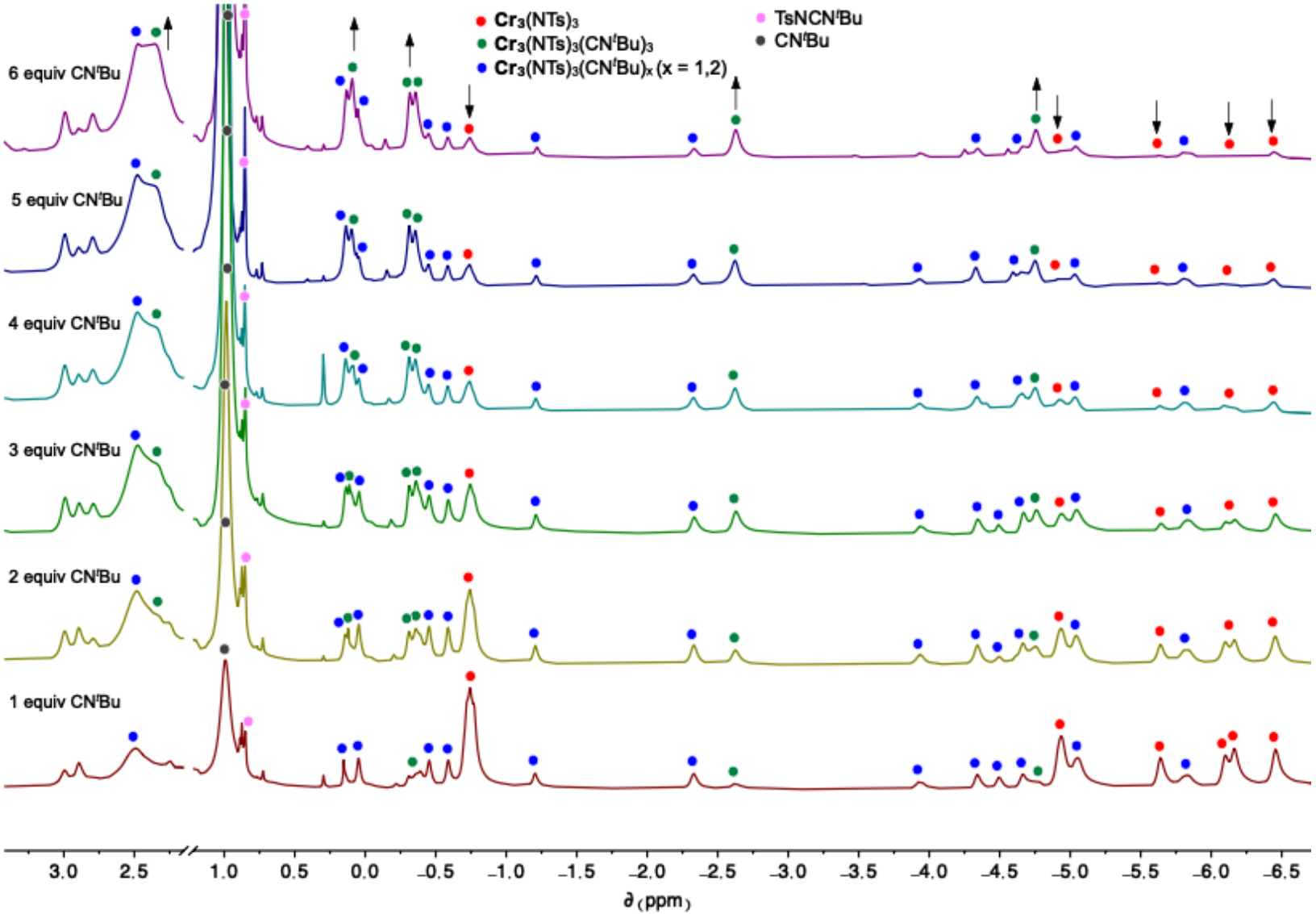


Figure 5.17. In situ ^{1}H NMR (benzene-d_6, 25 °C, 500 MHz) spectra recorded 15 min after treatment of **Cr$_3$**(NTs)$_3$ with varying amounts of CN^{t}Bu (1, 2, 3, 4, 5, 6 equiv) at 25 °C. Mesitylene CH_3 resonance (internal standard) at ~1.8 ppm omitted for clarity.

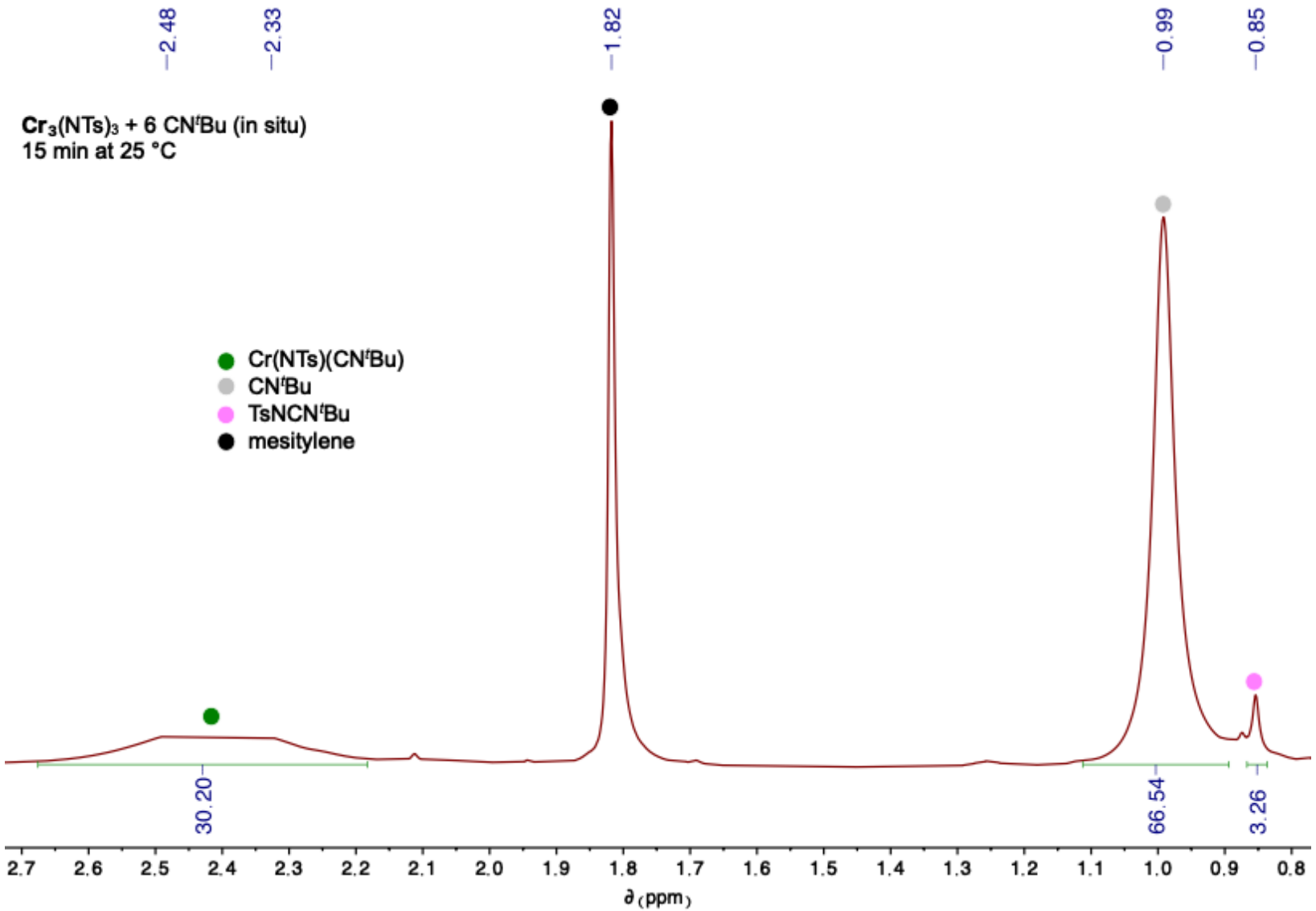


Figure 5.18. *In situ* ^{1}H NMR (benzene-d_6, 25 °C, 500 MHz) spectrum recorded 15 min after treatment of **Cr$_3$**(NTs)$_3$ with CN^{t}Bu (6 equiv) at 25 °C. Depicted integrations are representative of those used to calculate the isocyanide binding constant.

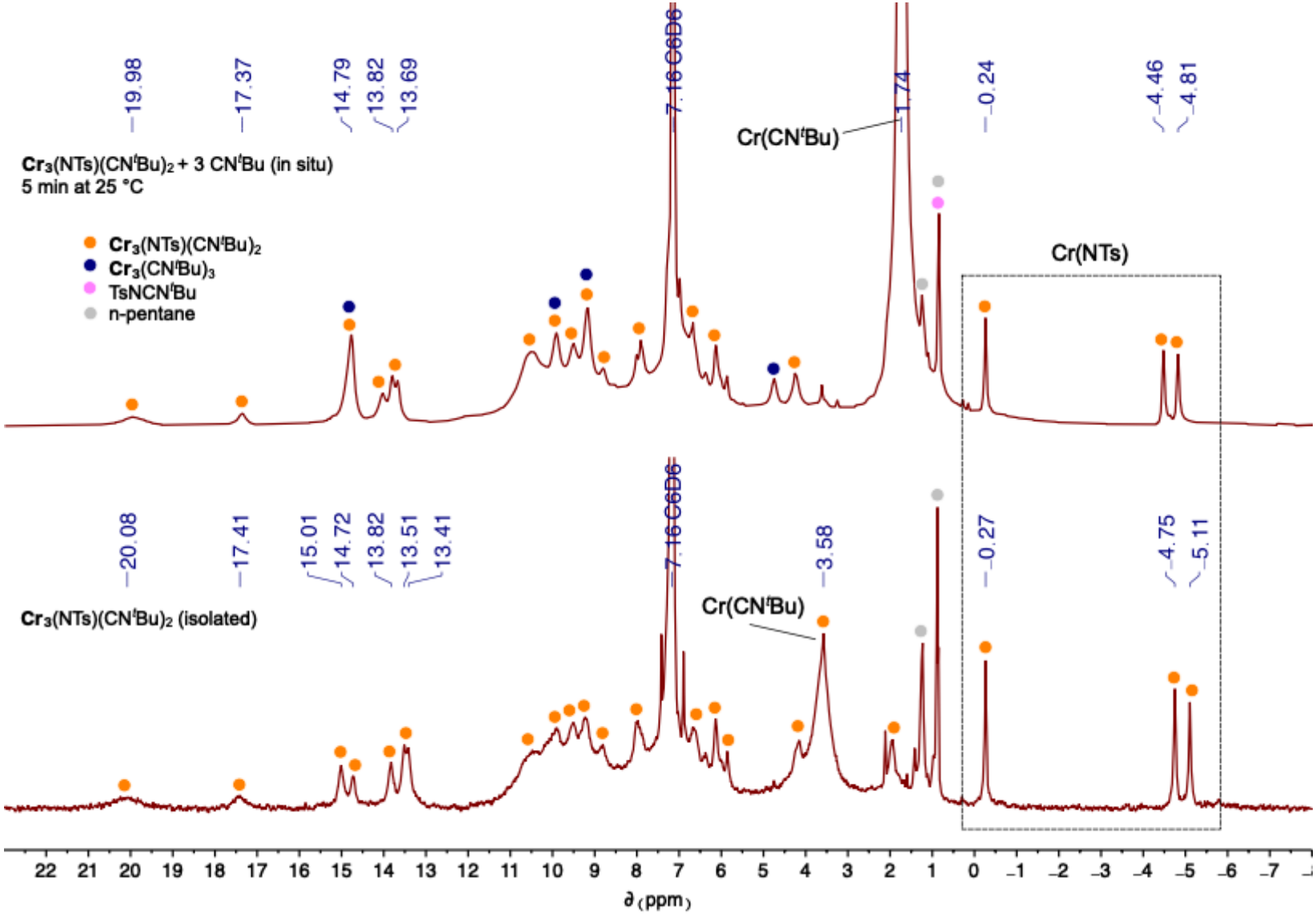


Figure 5.19. ^{1}H NMR (benzene-d_6, 25 °C, 500 MHz) spectra recorded in situ upon treatment of **Cr$_3$**(NTs)(CN^{t}Bu)$_2$ with CN^{t}Bu (3 equiv) at 25 °C (top), and of isolated **Cr$_3$**(NTs)(CN^{t}Bu)$_2$ (bottom).

5.6 EXPERIMENTAL DETAILS

5.6.1 *General Information*

All syntheses were conducted under a dinitrogen atmosphere using a standard Schlenk line or an LC Technology Solutions glovebox equipped with a freezer set to −35 °C. All glassware was dried at 160 °C for a minimum of 12 h prior to use.

Solvents were purchased from Fischer Scientific and degassed, dried and purified using solvent purification columns housed in a stainless-steel cabinet and dispensed by a stainless-steel Schlenk line manufactured by JC Meyer Solvent Systems. Tetrahydrofuran (THF), diethyl ether (Et_2O), and methylene chloride (DCM) are passed through two packed columns of neutral alumina. *n*-Pentane, benzene, and toluene are passed through a column packed with alumina, and one containing Q5 reactant, a copper(II) oxide oxygen scavenger. All solvents were passed through an in-line, 2 µm filter, then stored over activated 3Å molecular sieves in the glovebox. 3Å molecular sieves were purchased from Sigma Aldrich and activated under vacuum at 300 °C for 48 h. Anhydrous pyridine (99.8%) was purchased from Sigma Aldrich and stored over activated 3Å molecular sieves for 72 h prior to use.

Deuterated solvents (benzene-d_6, toluene-d_8, DCM-d_2) were purchased from Sigma Aldrich, degassed and dried over activated 3Å molecular sieves in the glovebox for a minimum of 72 h. $CrCl_2$ (anhydrous, 99.9%-Cr, Strem Chemicals, Inc.) was dried under vacuum at 180 °C for 24 h prior to use. $Co_2(CO)_8$ (stabilized with 2-5% hexanes, Strem Chemicals, Inc.) was stored in the glovebox freezer, and used as received. Chlorodiphenylphosphine (97%, Alfa Aesar), selenium (99.5%, powder, 200 mesh, Sigma Aldrich), and *n*-butyl lithium (2.5 M in hexanes, Sigma Aldrich) were used as received. Tosyl azide was synthesized according to a literature procedure,[55] and it was dried over activated 3Å molecular sieves in diethyl ether prior to use and stored at –35 °C. *Tert*-butyl isocyanide (CN^tBu, 98%) was purchased from Sigma Aldrich, degassed, and stored over activated 3 Å molecular sieves in the glovebox for a minimum of 72 h prior to use. $Ph_2PN(H)Tol$ (Ph = phenyl, Tol = 4-tolyl; $L^{Tol,H}$), $Co_6Se_8L^{Tol,H}_6$, $\mathbf{Li_6}(py)_6$, and $\mathbf{Fe_3}$ were prepared according to methods reported in the literature.[31,56]

UV-vis-*n*IR absorption spectra were acquired using a Varian Cary 5000 UV-Vis-*n*IR spectrophotometer, in *n*IR quartz cuvettes (Spectrocell Inc., 10 mm path length, 220–3500 nm

spectral window). Attenuated total reflectance infrared (ATR-IR) spectra were recorded on a Bruker Alpha IR instrument equipped with a Platinum ATR accessory housed within a nitrogen glovebox. NMR spectra were acquired at 25 °C unless indicated otherwise on Bruker 300, 500, or 700 MHz spectrometers. ^{1}H NMR spectra were referenced to residual deuterated solvent peaks. For variable-temperature NMR measurements, temperatures were calibrated using an 80% ethylene glycol/DMSO-d_6 external standard. Solution-phase magnetic susceptibilities were determined by the Evans method in benzene-d_6 using 5% (by volume) mesitylene in benzene-d_6 as an internal standard.[57]

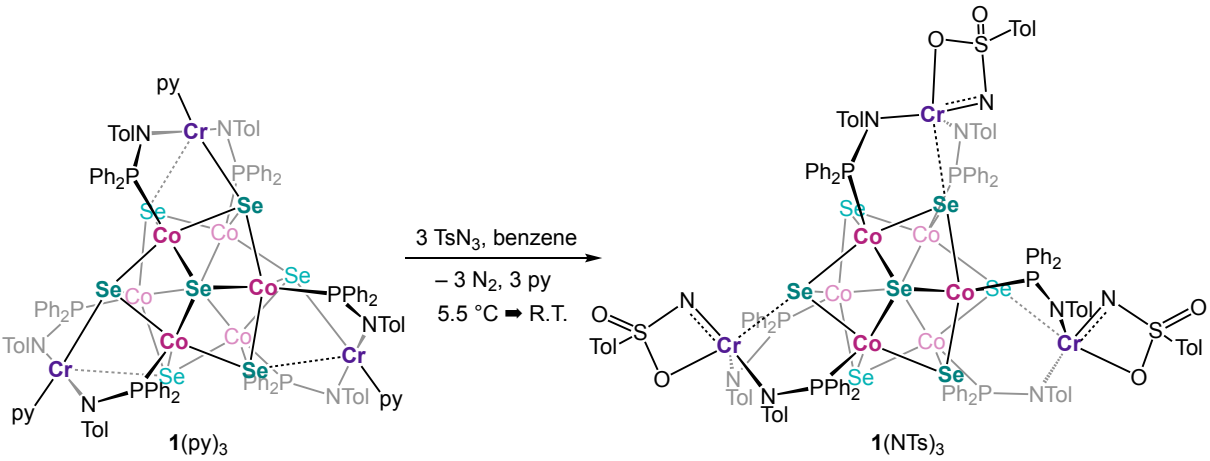
Samples were prepared for elemental analysis by crushing single-crystalline material into a powder and then removing volatiles under reduced pressure for 12 h. Co, Se, P elemental analysis was conducted using a Perkin-Elmer Nexion 2000B inductively-coupled plasma mass spectrometer (ICP-MS). Prior to ICP-MS analysis, samples were digested in neat nitric acid (Fisher Scientific, ICP-MS grade) at 50 °C, and serial dilutions were performed with Milli-Q reference water.

5.6.2 *Synthesis and Isolation of $Cr_3(py)_3Co_6Se_8L^{Tol}_6$, $\mathbf{Cr_3}(py)_3$*

Inside the glovebox, a 100 mL Schlenk tube equipped with a Teflon valve and magnetic stir bar was charged with $\mathbf{Li_6}(py)_6$ (2.000 g, 0.62 mmol, 1 equiv), toluene (60 mL), and five drops of pyridine. This slurry was partially frozen within the glovebox cold well. Solid $CrCl_2$ (0.235 g, 1.91 mmol, 3.1 equiv) was added portion-wise to the thawing, stirring mixture. The flask was then sealed, brought out of the glovebox and heated at 80 °C for 36 h, and over the course of this time, the mixture became homogenous and adopted a deep red-brown color. Volatiles were removed under reduced pressure and the flask was brought back into the glovebox. The solids were triturated with diethyl ether (3 x 15 mL) with thorough stirring and removal of volatiles at each addition. The product was then extracted in toluene (3 x 10 mL) through a plug of Celite on a fritted glass funnel, leaving a small amount of poorly soluble brown-gray solids, identified as a mixture of the hexalithiated starting material and lithium chloride. The toluene extracts were carefully layered with *n*-pentane (80 mL), and the sample was kept still at 25 °C for 24 h to yield a crop of large dark brown prismatic crystals, which were collected on a fritted glass funnel and washed with *n*-pentane before volatiles were removed *in vacuo* to yield analytically pure $\mathbf{Cr_3}(py)_3$ (1.816 g, 0.58 mmol, 94%).

UV-vis-*n*IR (toluene, 25 °C) λ: 426 (ϵ = 60,870 M^{-1} cm^{-1}) nm. ^{1}H NMR (benzene-d_6, 300 MHz) δ: 10.79 (s, $\nu_{1/2}$ = 37 Hz); 10.20 (s, $\nu_{1/2}$ = 177 Hz); 9.73 (s, $\nu_{1/2}$ = 120 Hz); 8.74 (s, $\nu_{1/2}$ = 64 Hz); 6.81 (s, $\nu_{1/2}$ = 40 Hz); 5.13 (s, $\nu_{1/2}$ = 73 Hz); –37.26 (s, $\nu_{1/2}$ = 151 Hz) ppm. ^{31}P NMR (benzene-d_6, 121 MHz): no peaks observed between ±2000 ppm. μ_{eff} (Evans method, benzene-d_6, 298 K) 8.3(3) μ_B. Elemental analysis found (calc.) for **Cr$_3$**(py)$_3$ (Formula: $C_{129}H_{117}Co_6Cr_3N_9P_6Se_8$): Co 11.28 (11.33), Se 20.18 (20.25), P 5.87 (5.96).

5.6.3 *Synthesis and Isolation of $Cr_3(NTs)_3Co_6Se_8L^{Tol}{}_6$, **Cr$_3$**(NTs)$_3$*



In the glovebox, a 100 mL Schlenk flask equipped with a magnetic stir bar and Teflon valve was loaded with **Cr$_3$**(py)$_3$ (0.500 g, 0.16 mmol, 1 equiv) and benzene (30 mL). The flask was sealed, and the sample was briefly stirred until homogeneous and then frozen within the glovebox freezer. Upon thawing, a freshly prepared solution of TsN_3 (0.96 M in benzene, 553 µL, 3.3 equiv) was added dropwise over the course of 2 minutes via syringe injection, prompting the evolution of nitrogen gas. The flask was degassed and stirred at 25 °C for 2 h. The resultant red-brown solution was passed through a plug of Celite on a fritted glass funnel, and the dark red filtrate was layered with *n*-pentane. The sample was kept still at 25 °C for 16 h to afford a crop of small dark brown crystals, which were collected on a fritted glass funnel and washed with *n*-pentane (3 x 5 mL). Volatiles were removed under reduced pressure to yield **Cr$_3$**(NTs)$_3$ as an analytically pure, dark brown solid (0.418 g, 0.13 mmol, 77%). This compound appears to be indefinitely stable as a solid at 25 °C, although for safe-keeping it was stored at –35 °C.

UV-vis-*n*IR (toluene, 25 °C) λ: 426 (ϵ = 48,700 M^{-1} cm^{-1}) nm. ^{1}H NMR (benzene-d_6, 300 MHz) δ: 21.17 (s, $\nu_{1/2}$ = 883 Hz); 18.55 (s, $\nu_{1/2}$ = 316 Hz); 18.01 (s, $\nu_{1/2}$ = 230 Hz); 10.42 (s, $\nu_{1/2}$ = 837 Hz); 9.31 (s, $\nu_{1/2}$ = 76 Hz); 9.15 (s, $\nu_{1/2}$ = 81 Hz); 8.33 (s, $\nu_{1/2}$ = 30 Hz); 7.87 (s, $\nu_{1/2}$ = 31 Hz); 7.72 (s, $\nu_{1/2}$ = 42 Hz); 7.62 (s, $\nu_{1/2}$ = 45 Hz); 7.51 (s, $\nu_{1/2}$ = 56 Hz); 7.42 (s, $\nu_{1/2}$ = 36 Hz); 7.27 (s, $\nu_{1/2}$ = 60 Hz); 6.60 (s, $\nu_{1/2}$ = 30 Hz); 6.43 (s, $\nu_{1/2}$ = 36 Hz); 6.29 (s, $\nu_{1/2}$ = 40 Hz); 6.15 (s, $\nu_{1/2}$ = 27 Hz); 6.02 (s, $\nu_{1/2}$ = 36 Hz); 5.81 (s, $\nu_{1/2}$ = 45 Hz); 5.19 (s, $\nu_{1/2}$ = 121 Hz); 4.41 (s, $\nu_{1/2}$ = 70 Hz); 1.96 (s, $\nu_{1/2}$ = 85 Hz); 1.73 (s, $\nu_{1/2}$ = 60 Hz); 1.45 (s, $\nu_{1/2}$ = 73 Hz); –0.74 (s, $\nu_{1/2}$ = 26 Hz); –4.92 (s, $\nu_{1/2}$ = 26 Hz); –5.63 (s, $\nu_{1/2}$ = 18 Hz); –6.09 (s, $\nu_{1/2}$ = 21 Hz); –6.15 (s, $\nu_{1/2}$ = 22 Hz); –6.44 (s, $\nu_{1/2}$ = 19 Hz) ppm. ^{31}P NMR (benzene-d_6, 121 MHz): no peaks observed between ±2000 ppm. μ_{eff} (Evans method, benzene-d_6, 298 K) 4.8(3) μ_B. Elemental analysis found (calc.) for **Cr$_3$**(NTs)$_3$ (Formula: $C_{135}H_{123}Co_6Cr_3N_9O_6S_3P_6Se_8$): Co 10.34 (10.43), Se 18.81 (18.63), P 5.67 (5.48).

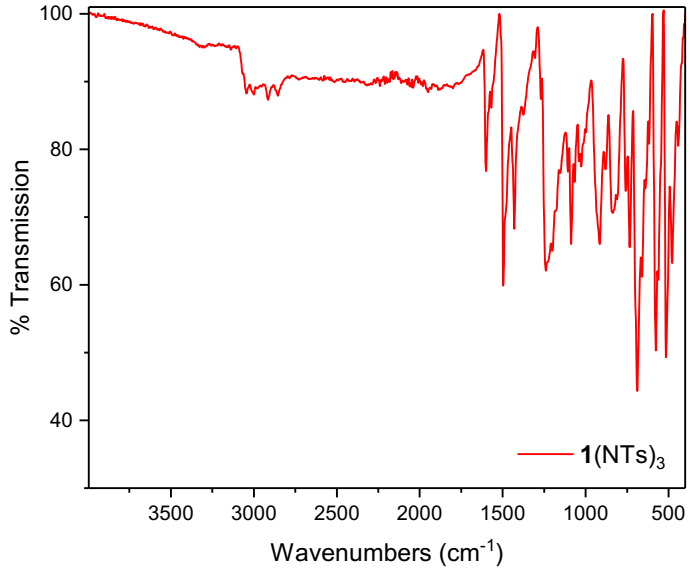


Figure 5.20. ATR-FTIR spectrum of **Cr$_3$**(NTs)$_3$ (solids). Here, the trichromium cluster **Cr$_3$** is denoted as **1**.

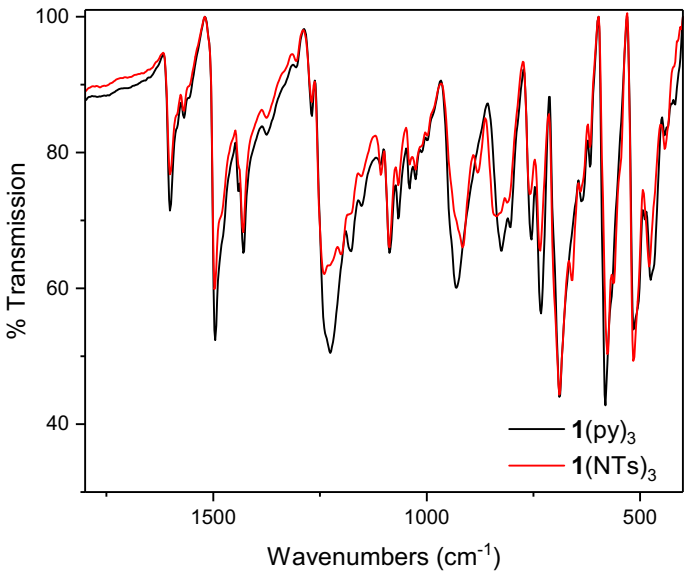


Figure 5.21. ATR-FTIR spectra of $\mathbf{Cr_3}(NTs)_3$ (red) and $\mathbf{Cr_3}(py)_3$ (black), highlighting the fingerprint region. Here, the trichromium cluster $\mathbf{Cr_3}$ is denoted as **1**.

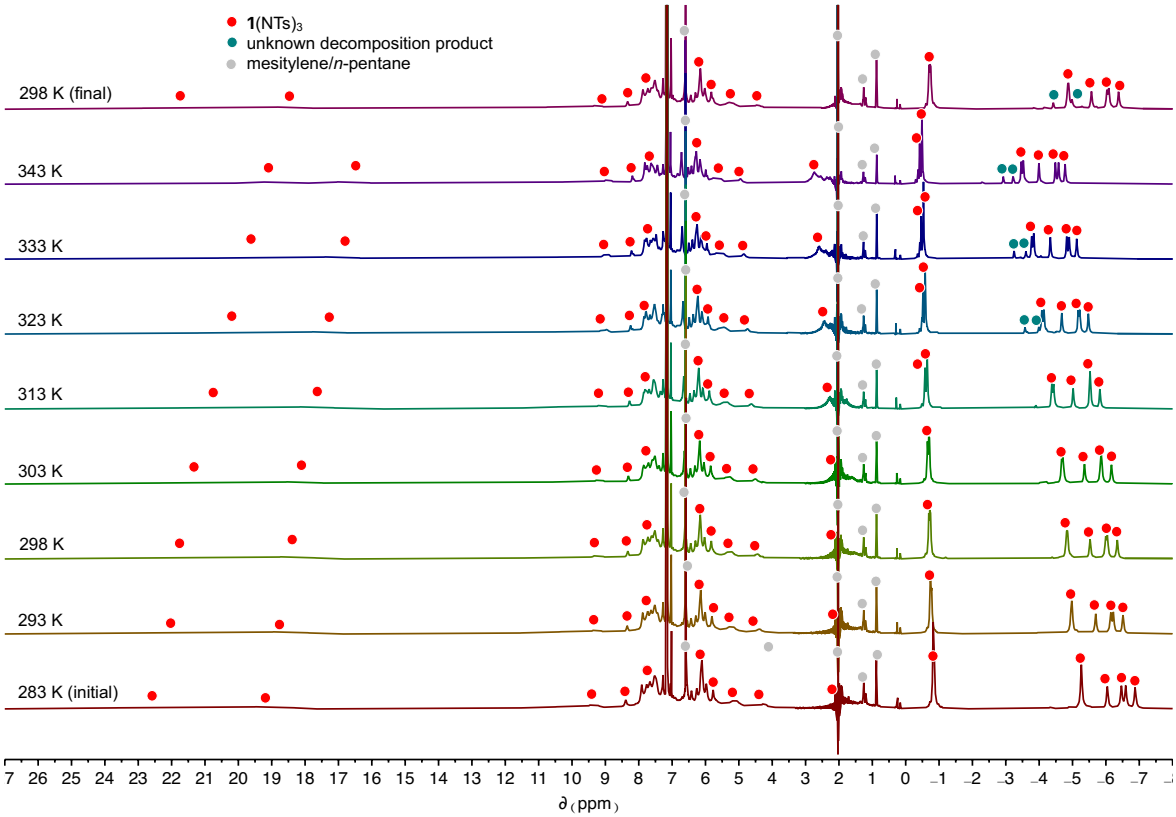


Figure 5.22. Variable-temperature ^{1}H NMR (benzene-d_6, 700 MHz) spectra collected for $\mathbf{Cr_3}(NTs)_3$. Spectra were recorded as the sample temperature was increased from 283 to 343 K, and then a final spectrum was collected upon cooling back to 298 K. These data indicate that $\mathbf{Cr_3}(NTs)_3$ remains locked in a low-symmetry (α,α,β) conformation in solution. Here, the trichromium cluster $\mathbf{Cr_3}$ is denoted as **1**.

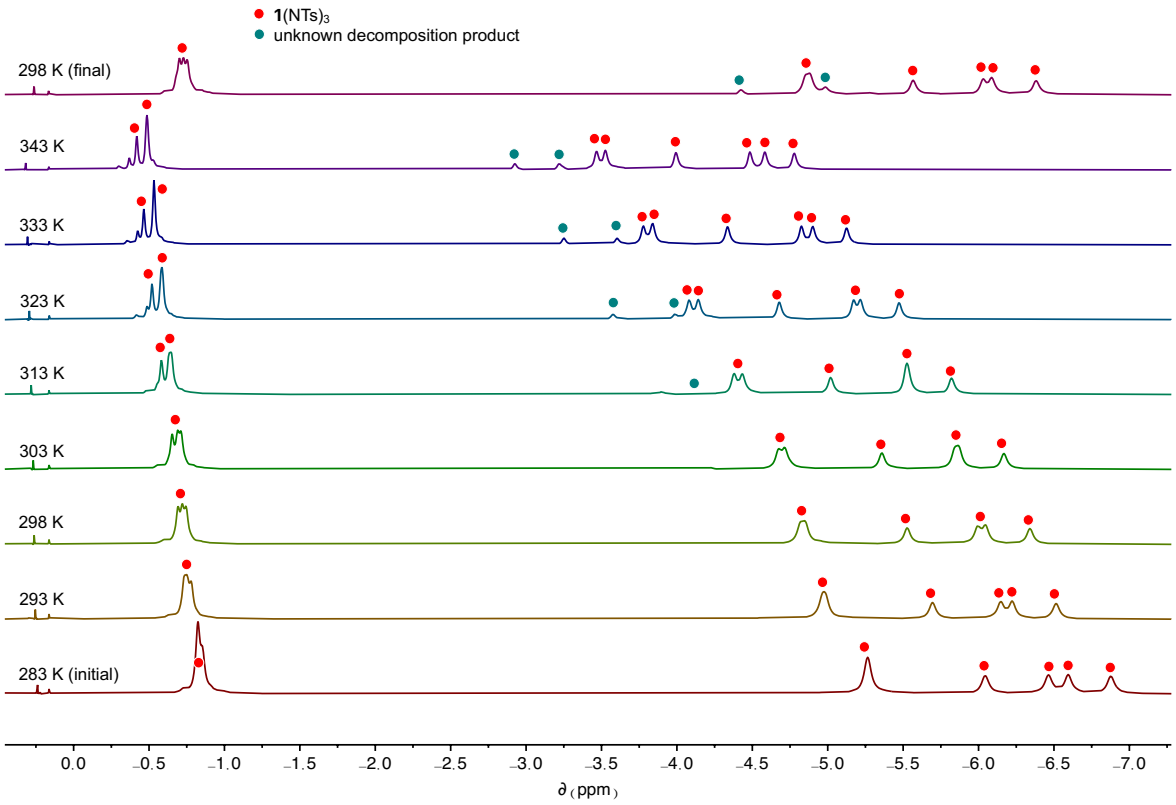
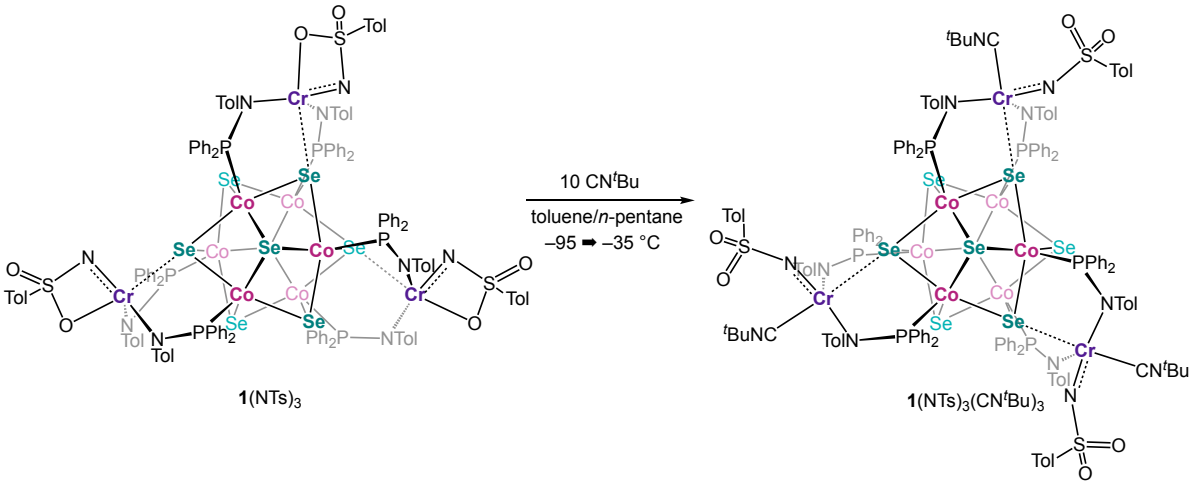


Figure 5.23. Variable-temperature ^{1}H NMR (benzene-d_6, 700 MHz) spectra collected for **Cr$_3$**(NTs)$_3$. Here, we highlight the diagnostic N-tosyl ^{1}H resonances between 0 and –8 ppm. Spectra were recorded as the sample temperature was increased from 283 to 343 K, and then a final spectrum was collected upon cooling back to 298 K. These data indicate that **Cr$_3$**(NTs)$_3$ remains locked in a low-symmetry (α,α,β) conformation in solution. Here, the trichromium cluster **Cr$_3$** is denoted as **1**.

5.6.4 *Synthesis and Isolation of $Cr_3(NTs)_3(CN^tBu)_3Co_6Se_8L^{Tol}{}_6$, $\mathbf{Cr_3}(NTs)_3(CN^tBu)_3$*



A 20 mL scintillation vial equipped with a magnetic stir bar was charged with $\mathbf{Cr_3}(NTs)_3$ (0.100 g, 29 µmol, 1 equiv) and toluene (8 mL). The sample was briefly stirred at 25 °C until homogeneous, and the deep red solution was frozen within the glovebox coldwell. Upon thawing, *tert*-butyl isocyanide (33 µL, 294 µmol, 10 equiv) was added dropwise to the cold, stirring solution using a microsyringe. The mixture was stirred for one minute before being frozen once again in the glovebox coldwell. The thawing solution was then quickly passed through a cold fritted glass funnel into a cold filter flask. The filtrate was layered with cold *n*-pentane (–35 °C, 12 mL) and kept still at –35 °C for 24 hours. This afforded a crop of large dark red prismatic crystals, which were collected on a cold fritted glass funnel, washed with cold *n*-pentane (–35 °C, 3 x 5 mL), and briefly dried *in vacuo* to yield analytically pure $\mathbf{Cr_3}(NTs)_3(CN^tBu)_3$ (0.093 g, 26 µmol, 88%). This compound slowly decomposes both as a solid and in solution if kept at room temperature, via the dissociation of CN^tBu and eventual evolution of carbodiimide, but single-crystals appear to be indefinitely stable when stored at –35 °C.

ATR-FTIR (solids): ν_{CN} = 2218 cm^{-1}. ^1H NMR (toluene-d_8, –35 °C, 500 MHz) δ: 21.71 (s, $\nu_{1/2}$ = 710 Hz); 18.07 (s, $\nu_{1/2}$ = 784 Hz); 10.14 (s, $\nu_{1/2}$ = 244 Hz); 9.67 (s, $\nu_{1/2}$ = 217 Hz); 8.00 (s, $\nu_{1/2}$ = 211 Hz); 6.64 (s, $\nu_{1/2}$ = 130 Hz); 5.92 (s, $\nu_{1/2}$ = 242 Hz); 5.39 (s, $\nu_{1/2}$ = 162 Hz); 4.96 (s, $\nu_{1/2}$ = 242 Hz); 4.42 (s, $\nu_{1/2}$ = 360 Hz); 2.84 (s, $\nu_{1/2}$ = 336 Hz); –0.10 (s, $\nu_{1/2}$ = 118 Hz); –0.88 (s, $\nu_{1/2}$ = 77 Hz); –4.14 (s, $\nu_{1/2}$ = 162 Hz); –6.71 (s, $\nu_{1/2}$ = 112 Hz) ppm. Elemental analysis found (calc.) for

Cr$_3$(NTs)$_3$(CN^{t}Bu)$_3$ (Formula: $C_{150}H_{153}Co_6Cr_3N_{12}O_6P_6S_3Se_8$): Co 9.69 (9.71), Se 17.50 (17.34), P 5.20 (5.10).

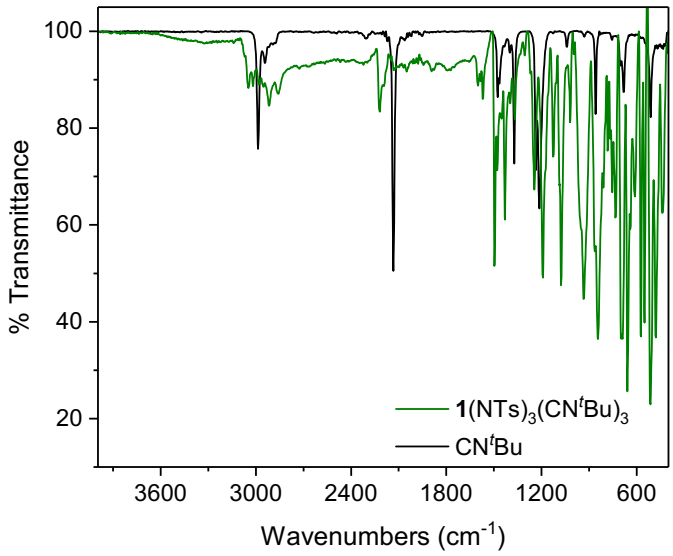
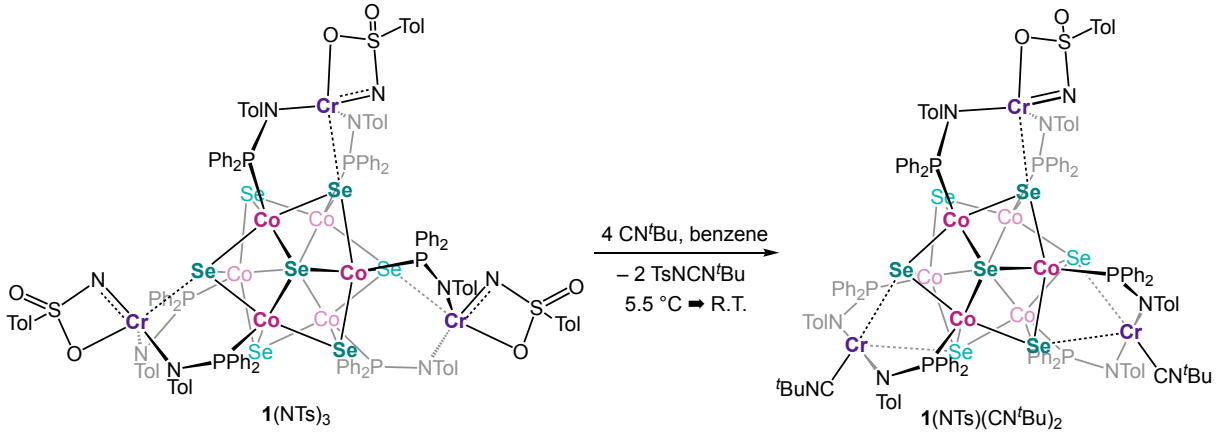


Figure 5.24. ATR-FTIR spectra of **Cr$_3$**(NTs)$_3$(CN^{t}Bu)$_3$ (solids, green) and neat CN^{t}Bu (dropcast, black). Here, the trichromium cluster **Cr$_3$** is denoted as **1**.

5.6.5 *Synthesis and Isolation of Cr$_3$(NTs)(CN^{t}Bu)$_2$Co$_6$Se$_8$L$^{Tol}_6$,* ***Cr$_3$****(NTs)(CN^{t}Bu)$_2$*



A 20 mL scintillation vial equipped with a magnetic stir bar was charged with **Cr$_3$**(NTs)$_3$ (0.200 g, 0.059 mmol, 1 equiv) and benzene (16 mL). The sample was stirred until homogeneous and frozen within a –35 °C glovebox freezer. Upon thawing, CN^{t}Bu (26.6 µL, 0.236 mmol, 4 equiv) was added dropwise to the cold stirring solution using a microsyringe. The sample was slowly warmed to room temperature and stirred for 24 h, before it was passed through a plug of Celite on a fritted glass funnel. The filter cake was washed with a small amount of benzene (~2 mL) and the

filtrate was layered with *n*-pentane (50 mL). The sample was kept still at room temperature for 48 hours to yield a crop of large dark red prismatic crystals. The mother liquor was decanted, and the crystals were washed with *n*-pentane (3 x 2 mL) to yield **Cr$_3$**(NTs)(CN^{t}Bu)$_2$ as an analytically pure red-brown crystalline solid (117 mg, 0.036 mmol, 62%).

ATR-FTIR (dropcast in benzene-d_6): ν_{CN} = 2196 cm^{-1}. ^{1}H NMR (benzene-d_6, 300 MHz) δ: 20.04 (s, $\nu_{1/2}$ = 283 Hz); 17.41 (s, $\nu_{1/2}$ = 100 Hz); 15.03 (s, $\nu_{1/2}$ = 48 Hz); 14.74 (s, $\nu_{1/2}$ = 37 Hz); 13.82 (s, $\nu_{1/2}$ = 46 Hz); 13.47 (s, $\nu_{1/2}$ = 39 Hz); 13.41 (s, $\nu_{1/2}$ = 39 Hz); 10.46 (s, $\nu_{1/2}$ = 223 Hz); 9.87 (s, $\nu_{1/2}$ = 130 Hz); 9.51 (s, $\nu_{1/2}$ = 1.46 Hz); 9.22 (s, $\nu_{1/2}$ = 100 Hz); 8.81 (s, $\nu_{1/2}$ = 124 Hz); 7.98 (s, $\nu_{1/2}$ = 105 Hz); 6.67 (s, $\nu_{1/2}$ = 87 Hz); 6.14 (s, $\nu_{1/2}$ = 41 Hz); 5.86 (s, $\nu_{1/2}$ = 34 Hz); 4.18 (s, $\nu_{1/2}$ = 80 Hz); 3.58 (s, $\nu_{1/2}$ = 111 Hz, CNC(C*H*$_3$)$_3$); 1.96 (s, $\nu_{1/2}$ = 50 Hz); –0.27 (s, $\nu_{1/2}$ = 15 Hz); –4.75 (s, $\nu_{1/2}$ = 20 Hz); –5.11 (s, $\nu_{1/2}$ = 18 Hz) ppm. ^{31}P NMR (benzene-d_6, 121 MHz): no peaks observed between ±2000 ppm. μ_{eff} (Evans method, benzene-d_6, 298 K) 6.8(3) μ_B. Elemental analysis found (calc.) for **Cr$_3$**(NTs)(CN^{t}Bu)$_2$ (Formula: $C_{131}H_{129}Co_6Cr_3N_9O_2SP_6Se_8$): Co 10.97 (10.98), Se 19.65 (19.62), P 5.77 (5.77).

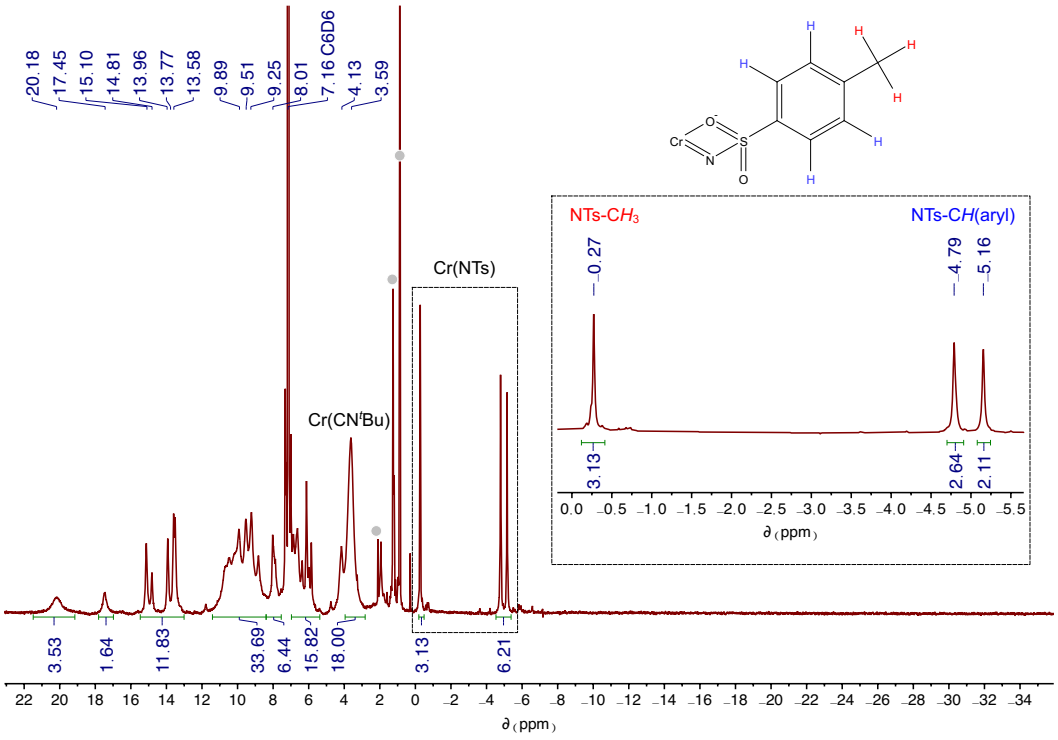


Figure 5.25. ^{1}H NMR (benzene-d_6, 25 °C, 300 MHz) spectrum of **Cr$_3$**(NTs)(CN^{t}Bu)$_2$. Gray dots indicate toluene/*n*-pentane resonances.

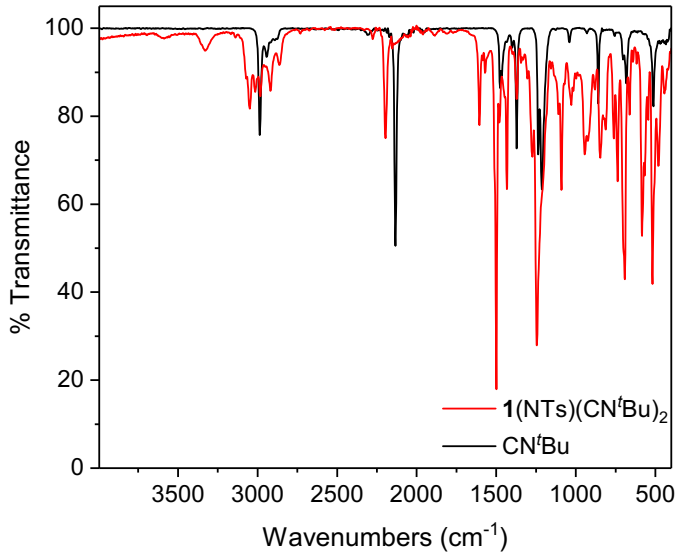
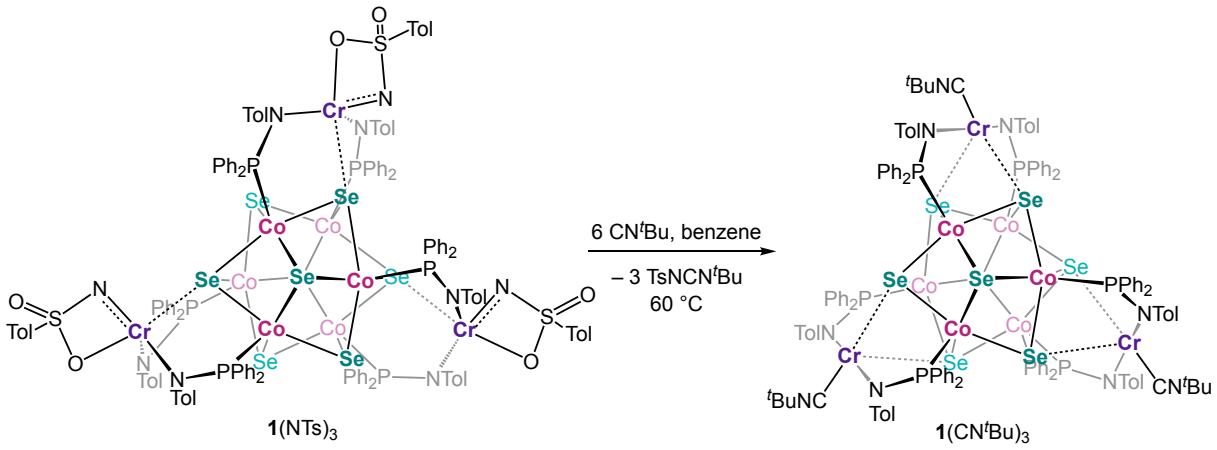


Figure 5.26. ATR-FTIR spectra of $\mathbf{Cr_3}(NTs)(CN^tBu)_2$ (dropcast, red) and neat CN^tBu (dropcast, black). Here, the trichromium cluster $\mathbf{Cr_3}$ is denoted as **1**.

5.6.6 *Synthesis and Isolation of $Cr_3(CN^tBu)_3Co_6Se_8L^{Tol}_6$, $\mathbf{Cr_3}(CN^tBu)_3$*



A 20 mL scintillation vial equipped with a magnetic stir bar was loaded with $\mathbf{Cr_3}(NTs)_3$ (0.050 g, 0.015 mmol, 1 equiv) and benzene (3 mL). The dark red-brown slurry was briefly stirred at room temperature and then frozen within a –35 °C freezer. Neat CN^tBu (10 µL, 88.5 µmol, 6 equiv) was added dropwise to the thawing, stirring mixture using a microsyringe. Upon addition of the isocyanide, the sample quickly became homogeneous. The mixture was slowly warmed to 60 °C and stirred for 24 h to yield a deep red solution, which was then passed through a plug of Celite on a pipet filter. The filtrate was layered with *n*-pentane (16 mL) and kept still at room temperature

for 24 h to yield a crop of opaque red needles, which were washed with additional *n*-pentane (3 x 5 mL) and identified as the tris(isocyanide) derivative, **Cr$_3$**(CN^{t}Bu)$_3$ (0.034 mg, 0.010 mmol, 74%).

ATR-FTIR (solids): ν_{CN} = 2194 cm^{-1}. ^{1}H NMR (benzene-d_6, 300 MHz) δ: 14.74 (s, $\nu_{1/2}$ = 37 Hz); 10.48 (s, $\nu_{1/2}$ = 146 Hz); 9.94 ($\nu_{1/2}$ = 108 Hz); 9.16 ($\nu_{1/2}$ = 72 Hz); 6.98 ($\nu_{1/2}$ = 52 Hz); 4.76 ($\nu_{1/2}$ = 50 Hz); 3.26 ($\nu_{1/2}$ = 103 Hz, CNC(C*H*$_3$)$_3$) ppm. ^{31}P NMR (benzene-d_6, 121 MHz): no peaks observed between ±2000 ppm. μ_{eff} (Evans method, benzene-d_6, 298 K) 8.0(3) μ_B. Elemental analysis found (calc.) for **Cr$_3$**(CN^{t}Bu)$_3$ (Formula: $C_{129}H_{132}Co_6Cr_3N_9P_6Se_8$): Co 11.27 (11.28), Se 20.09 (20.15), P 5.90 (5.93).

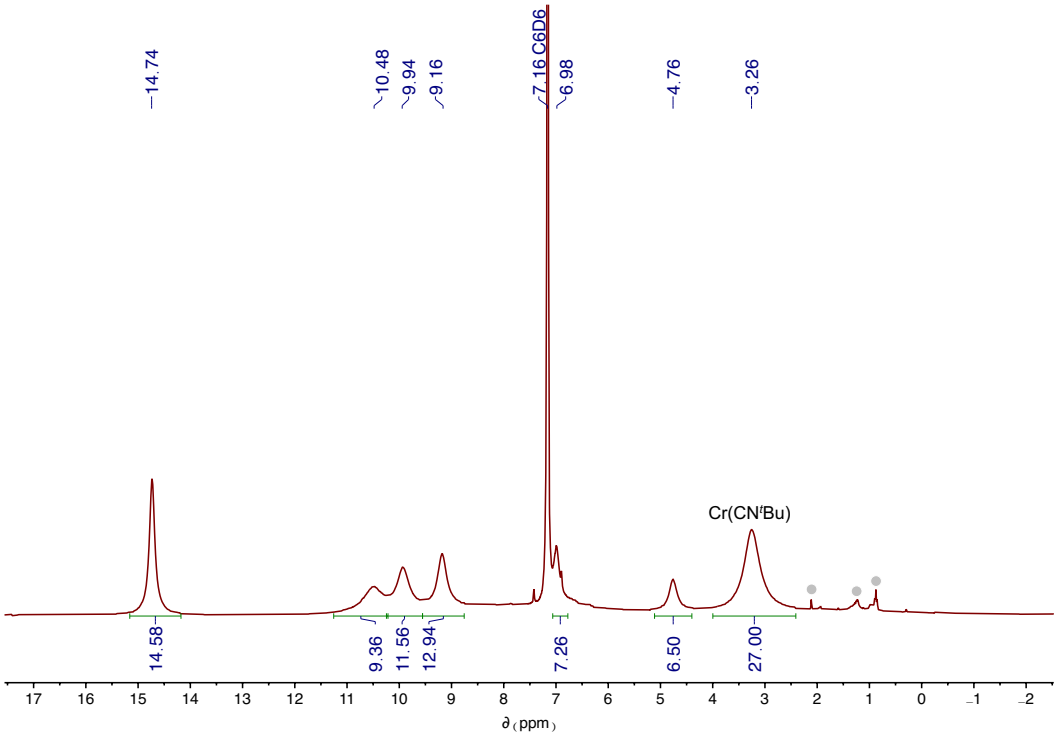


Figure 5.27. ^{1}H NMR (benzene-d_6, 25 °C, 300 MHz) spectrum of **Cr$_3$**(CN^{t}Bu)$_3$. Gray dots indicate toluene/*n*-pentane resonances.

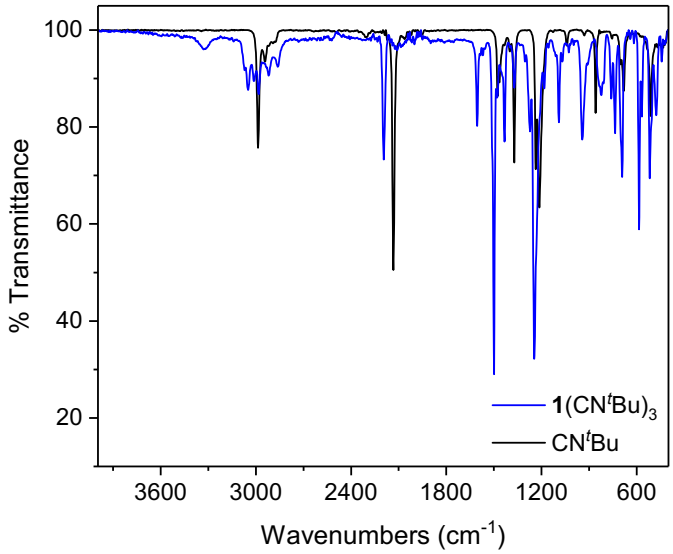


Figure 5.28. ATR-FTIR spectra of $\mathbf{Cr_3}(CN^tBu)_3$ (solids, blue) and neat CN^tBu (dropcast, black). Here, the trichromium cluster $\mathbf{Cr_3}$ is denoted as **1**.

5.6.7 *Electronic Absorption Spectra*

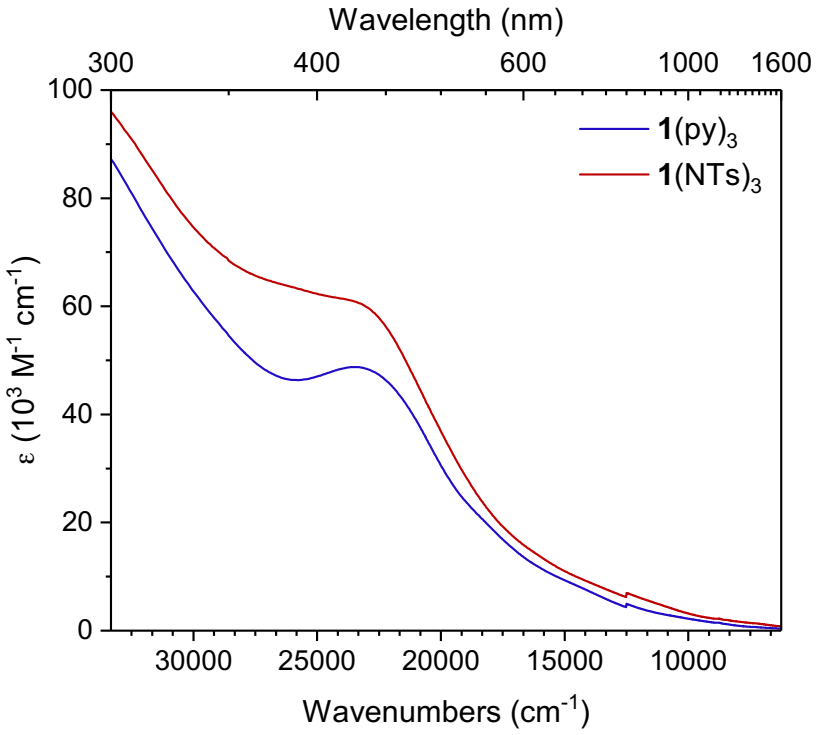


Figure 5.29. UV-vis-*n*IR Absorption Spectra of $\mathbf{Cr_3}(NTs)_3$ and $\mathbf{Cr_3}(py)_3$ recorded in toluene. Here, the trichromium cluster $\mathbf{Cr_3}$ is denoted as **1**.

5.6.8 *Nitrene Transfer Catalysis*

The catalyst **Cr$_3$**(py)$_3$ (5.3 mg, 1.7 μmol, 2.5 equiv) was dissolved in benzene-d_6 (0.517 mL), and CN^{t}Bu (12.7 μL, 112 μmol, 165 equiv) was added to this solution neat by microsyringe injection. The reaction mixture is frozen in the glovebox freezer at –35 °C. Upon thawing, TsN_3 (0.97 M in benzene-d_6, 70 μmol, 100 equiv) is added dropwise, to yield a solution totaling 0.6 mL in volume. The reaction mixture was left to warm to room temperature, passed through a pipet filter into a J. Young NMR tube, and monitored by ^{1}H NMR spectroscopy for 6 h with a mesitylene/benzene-d_6 (5% by volume) capillary as an internal standard to track the formation of the carbodiimide product, TsNCN^{t}Bu (100% spectroscopic yield).[58]

^{1}H NMR (benzene-d_6, 25 °C, 300 MHz) δ: 7.92 (d, J = 7.8 Hz, 2H, Ar), 6.72 (d, J = 7.6 Hz, 2H, Ar), 1.83 (s, 3H, Me), 0.87 (s, 9H, ^{t}Bu) ppm. GC-MS (temp program: initial temp = 60° C, 15.00° C/min, final temp = 300° C, hold time = 3.5 min) retention time = 12.78 min; m/z (intensity): 252 (11), 197 (48), 142 (88), 155 (60), 91 (100), 57 (86). ATR-FTIR (dropcast): 2155 ($\nu_{N=C=N}$), 1340 and 1160 (ν_{SO2}) cm^{-1}.

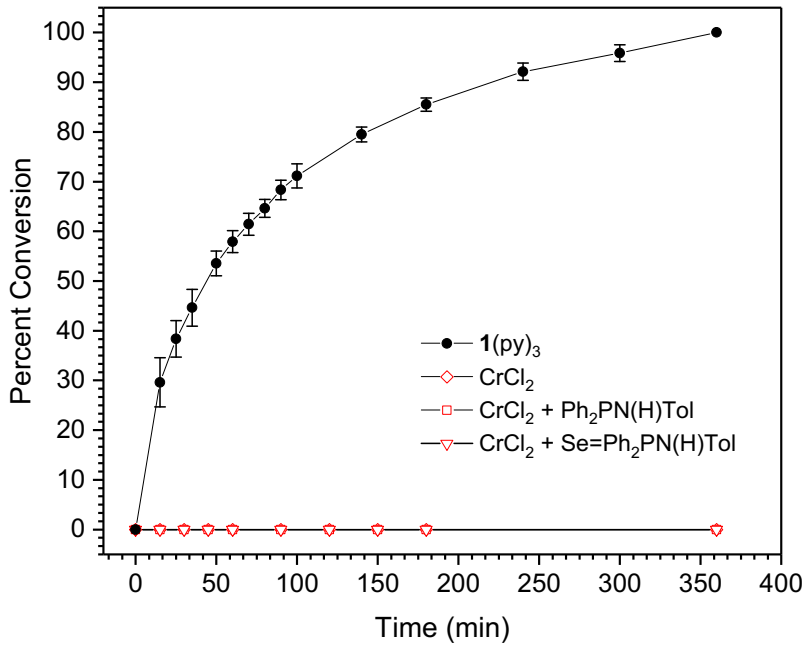


Figure 5.30. Monitoring the catalytic conversion of TsN_3 and CN^tBu to $TsNCN^tBu$ at 25 °C. CN^tBu (165 equiv), TsN_3 (100 equiv), and $\mathbf{Cr_3}(py)_3$ (2.8 mM, 2.5 equiv) in benzene-d_6. Data was collected in triplicate, and percent conversion was calculated based on ^1H NMR integrations of the reagents and products versus an internal mesitylene standard. Control experiments were run with 7.5 mol% loading of $CrCl_2$ with 15 mol% $Ph_2PN(H)Tol$ or $Se{=}Ph_2PN(H)Tol$ (2 equiv per $CrCl_2$). The control samples exhibit no reaction with TsN_3 or formation of the carbodiimide product. Here, the trichromium cluster $\mathbf{Cr_3}$ is denoted as **1**.

5.6.9 *In situ Reaction Monitoring with 10 mol% Catalyst Loading*

Catalytic carbodiimide formation was also performed with elevated concentrations of catalyst to enable the *in situ* observation of catalytic intermediates and to verify that this transformation proceeds without catalyst decomposition. Specifically, 10 mol% catalyst was used to ensure the visibility of the paramagnetic species present before, during and after catalysis. Additionally, the catalytic competence of $\mathbf{Cr_3}(NTs)_3$ and $\mathbf{Cr_3}(NTs)(CN^tBu)_2$ was independently tested and compared to that of $\mathbf{Cr_3}(py)_3$ under these conditions. For each pre-catalysts, ^1H NMR monitoring reveals the formation of the same well-defined resting state, $\mathbf{Cr_3}(NTs)_3(CN^tBu)_3$, and ultimately the quantitative formation of $TsNCN^tBu$ and $\mathbf{Cr_3}(CN^tBu)_3$. The differing reaction rates observed for these samples (detailed below) stems from variation of the effective concentration of isocyanide or pyridine in each sample: $\mathbf{Cr_3}(py)_3$ effectively introduces 3 equivalents of pyridine per equivalent of $\mathbf{Cr_3}$, whereas $\mathbf{Cr_3}(NTs)(CN^tBu)_2$ effectively introduces an extra equivalent of

nitrene and 2 equivalents of CN^{t}Bu per equivalent of **Cr$_3$**. In contrast, **Cr$_3$**(NTs)$_3$ effectively introduces three extra equivalents of nitrene with no extra equivalents of ligand, so at the end of catalysis there is only a small excess (5 equiv) of CN^{t}Bu remaining.

5.6.9.1 Catalytic monitoring with **Cr$_3$**(py)$_3$ (10 mol%)

A 20 mL scintillation vial equipped with a magnetic stir bar was loaded with **Cr$_3$**(py)$_3$ (21.1 mg, 6.8 μmol, 10 equiv) and benzene-d_6 (0.720 mL). The sample was briefly stirred at until homogeneous before CN^{t}Bu (12.7 μL, 112 μmol, 165 equiv) was added via microsyringe injection. Finally, TsN_3 (1.0 M in benzene-d_6, 68 μL, 67.6 μmol, 100 equiv) was added via microsyringe injection. The sample was briefly mixed before being passed through a pipet filter into a J. Young NMR tube equipped with a mesitylene/benzene-d_6 (5% by volume) capillary. The sample was kept at room temperature and monitored by ^{1}H NMR spectroscopy until complete.

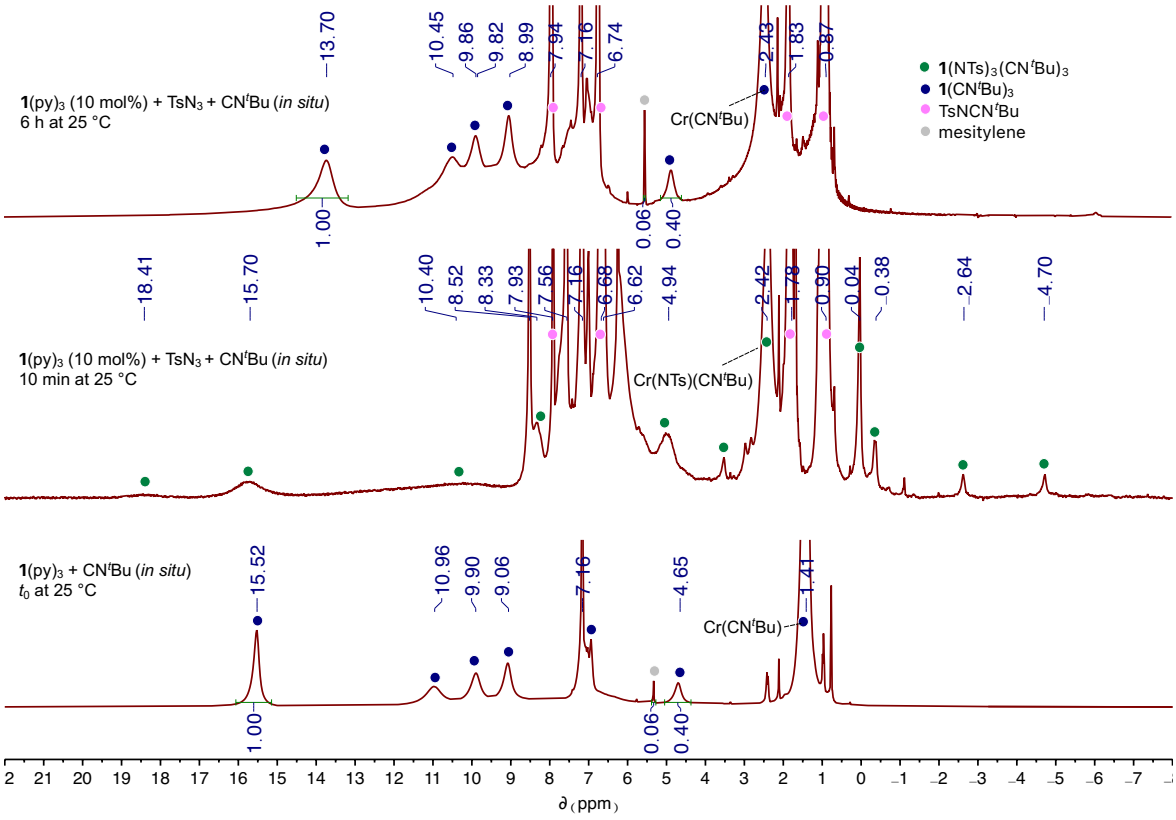


Figure 5.31. ^{1}H NMR (benzene-d_6, 25 °C, 300 MHz) spectra of the catalytic reaction mixture prior to the addition of TsN_3 (bottom), 10 min (middle) and 6 h (top) after the addition of TsN_3. A catalyst loading of 10 mol% **Cr$_3$**(py)$_3$ (0.0085 M, 10 equiv) was employed to increase the visibility of the paramagnetic species, and the reaction was performed in the presence of TsN_3 (100 equiv, 0.085 M) and CN^{t}Bu (165 equiv, 0.140 M). Here, the trichromium cluster **Cr$_3$** is denoted as **1**.

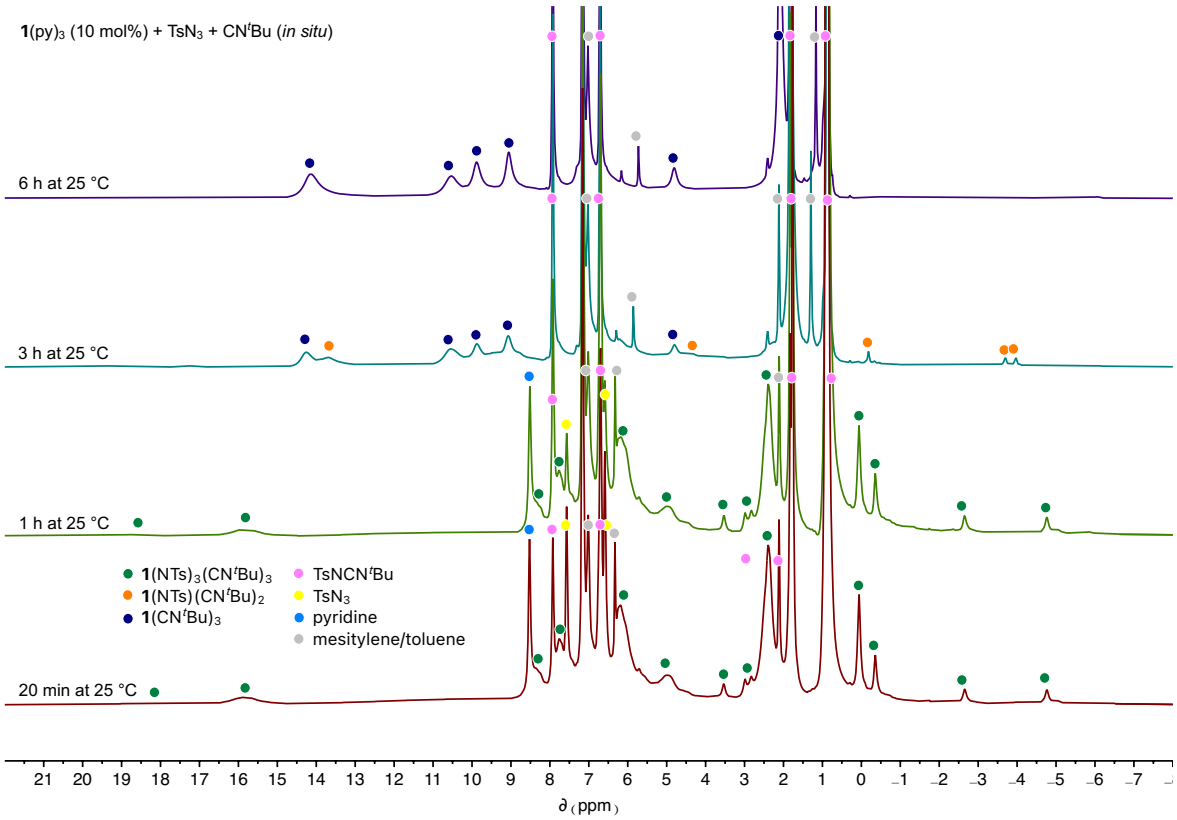


Figure 5.32. ^{1}H NMR (benzene-d_6, 25 °C, 500 MHz) spectra of the catalytic reaction upon mixing **Cr$_3$**(py)$_3$, TsN_3 and CN^{t}Bu. A catalyst loading of 10 mol% **Cr$_3$**(py)$_3$ (0.0085 M, 10 equiv) was employed to increase the visibility of the paramagnetic species, and the reaction was performed in the presence of TsN_3 (100 equiv, 0.085 M) and CN^{t}Bu (165 equiv, 0.140 M). Here, the trichromium cluster **Cr$_3$** is denoted as **1**.

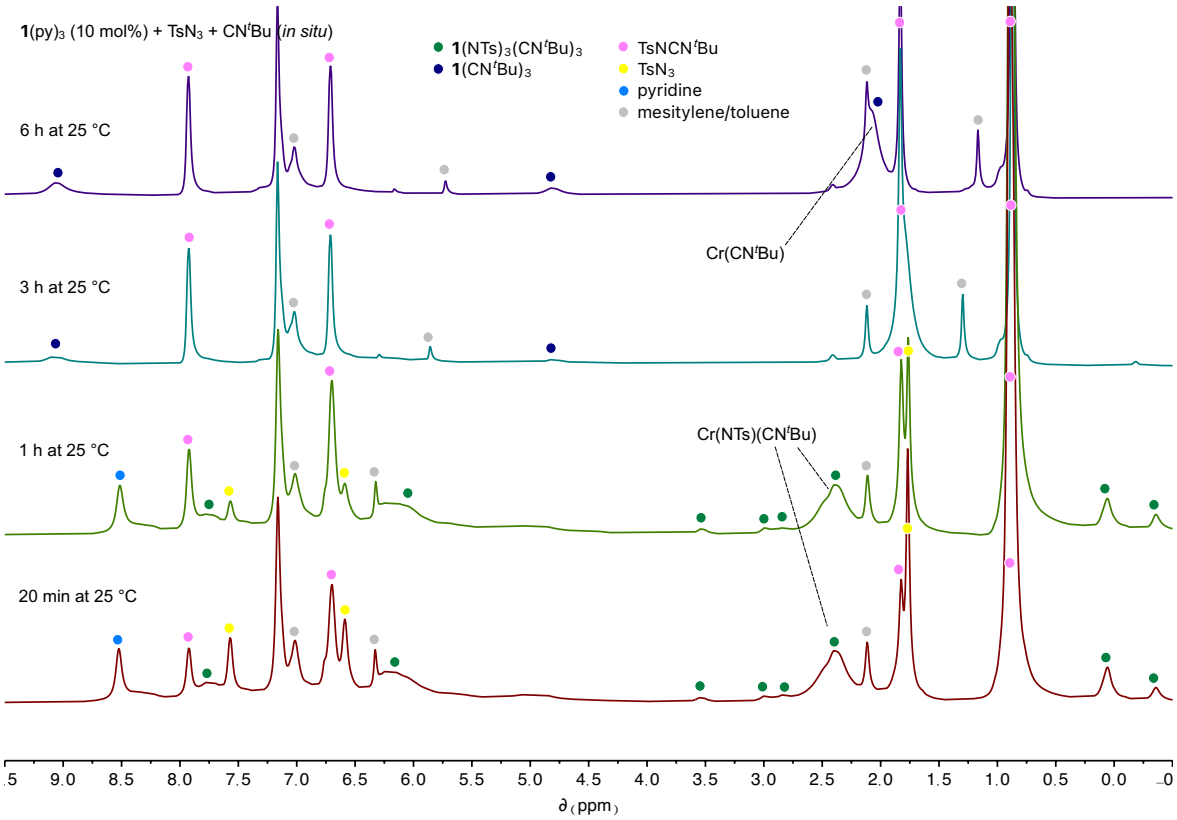


Figure 5.33. ^{1}H NMR (benzene-d_6, 25 °C, 500 MHz) spectra of the catalytic reaction upon mixing **Cr$_3$**(py)$_3$, TsN_3 and CN^{t}Bu, highlighting the diamagnetic region to show the clean conversion of tosyl azide to carbodiimide. A catalyst loading of 10 mol% **Cr$_3$**(py)$_3$ (0.0085 M, 10 equiv) was employed to increase the visibility of the paramagnetic species, and the reaction was performed in the presence of TsN_3 (100 equiv, 0.085 M) and CN^{t}Bu (165 equiv, 0.140 M). Here, the trichromium cluster **Cr$_3$** is denoted as **1**.

5.6.9.2 Catalytic monitoring with **Cr$_3$**(NTs)(CN^{t}Bu)$_2$ (10 mol%)

A 20 mL scintillation vial equipped with a magnetic stir bar was loaded with **Cr$_3$**(NTs)(CN^{t}Bu)$_2$ (21.8 mg, 6.8 µmol, 10 equiv) and benzene-d_6 (0.720 mL). The sample was briefly stirred at until homogeneous before CN^{t}Bu (12.7 µL, 112 µmol, 165 equiv) was added via microsyringe injection. Finally, TsN_3 (1.0 M in benzene-d_6, 68 µL, 67.6 µmol, 100 equiv) was added via microsyringe injection. The sample was briefly mixed before being passed through a pipet filter into a J. Young NMR tube equipped with a mesitylene/benzene-d_6 (5% by volume) capillary. The sample was kept at room temperature and monitored by ^{1}H NMR spectroscopy until complete.

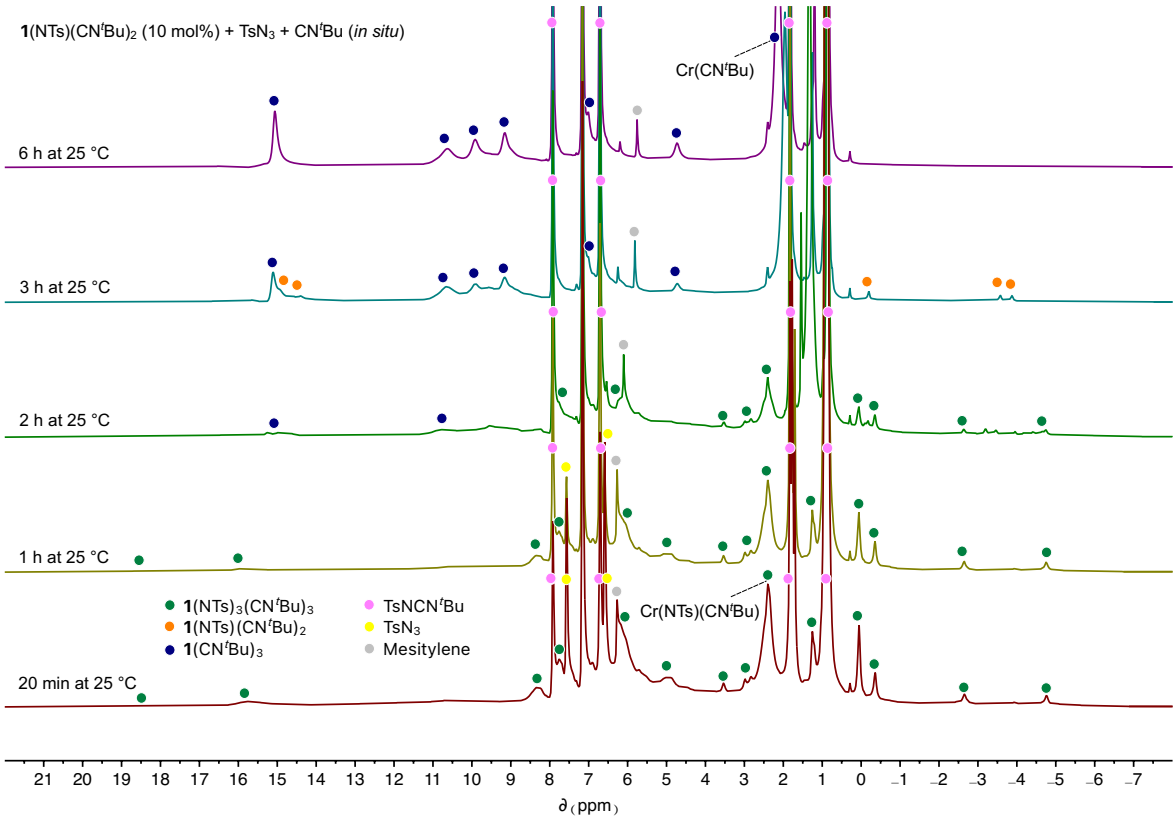


Figure 5.34. ^{1}H NMR (benzene-d_6, 25 °C, 500 MHz) spectra of the catalytic reaction upon mixing $\mathbf{Cr_3}$(NTs)(CN^{t}Bu)$_2$, TsN_3 and CN^{t}Bu. A catalyst loading of 10 mol% $\mathbf{Cr_3}$(NTs)(CN^{t}Bu)$_2$ (0.0085 M, 10 equiv) was employed to increase the visibility of the paramagnetic species, and the reaction was performed in the presence of TsN_3 (100 equiv, 0.085 M) and CN^{t}Bu (165 equiv, 0.140 M). Here, the trichromium cluster $\mathbf{Cr_3}$ is denoted as **1**.

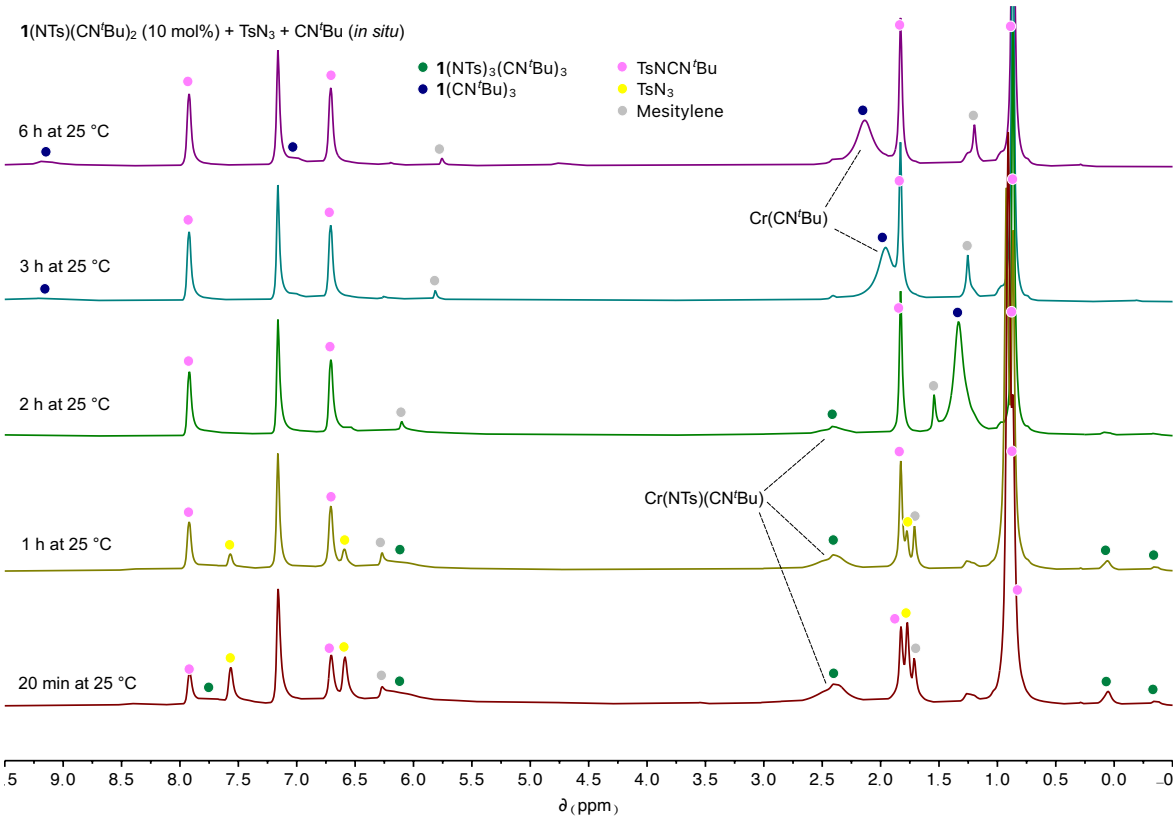


Figure 5.35. ^{1}H NMR (benzene-d_6, 25 °C, 500 MHz) spectra of the catalytic reaction upon mixing **Cr$_3$**(NTs)(CN^{t}Bu)$_2$, TsN$_3$ and CN^{t}Bu, highlighting the diamagnetic region to show the clean conversion of tosyl azide to carbodiimide. A catalyst loading of 10 mol% **Cr$_3$**(NTs)(CN^{t}Bu)$_2$ (0.0085 M, 10 equiv) was employed to increase the visibility of the paramagnetic species, and the reaction was performed in the presence of TsN$_3$ (100 equiv, 0.085 M) and CN^{t}Bu (165 equiv, 0.140 M). Here, the trichromium cluster **Cr$_3$** is denoted as **1**.

5.6.9.3 Catalytic Monitoring with **Cr$_3$**(NTs)$_3$ (10 mol%)

A 20 mL scintillation vial equipped with a magnetic stir bar was loaded with **Cr$_3$**(NTs)$_3$ (22.9 mg, 6.8 µmol, 10 equiv) and benzene-d_6 (0.720 mL). The sample was briefly stirred at until homogeneous before CN^{t}Bu (12.7 µL, 112 µmol, 165 equiv) was added via microsyringe injection. Finally, TsN$_3$ (1.0 M in benzene-d_6, 68 µL, 67.6 µmol, 100 equiv) was added via microsyringe injection. The sample was briefly mixed before being passed through a pipet filter into a J. Young NMR tube equipped with a mesitylene/benzene-d_6 (5% by volume) capillary. The sample was kept at room temperature and monitored by ^{1}H NMR spectroscopy. In this case, the reaction proceeded as expected until all observable TsN$_3$ was consumed. However, at the end of catalytic conversion, low concentrations of remaining CN^{t}Bu resulted in very slow nitrene transfer kinetics, and trace

amounts of **Cr$_3$**(NTs)(CN^{t}Bu)$_2$ were still observed after 16 hours. At this point, an additional portion of CN^{t}Bu (4.6 µL, 40.8 µmol, 60 equiv) was added to drive the reaction to completion, cleanly producing **Cr$_3$**(CN^{t}Bu)$_3$ and TsNCN^{t}Bu.

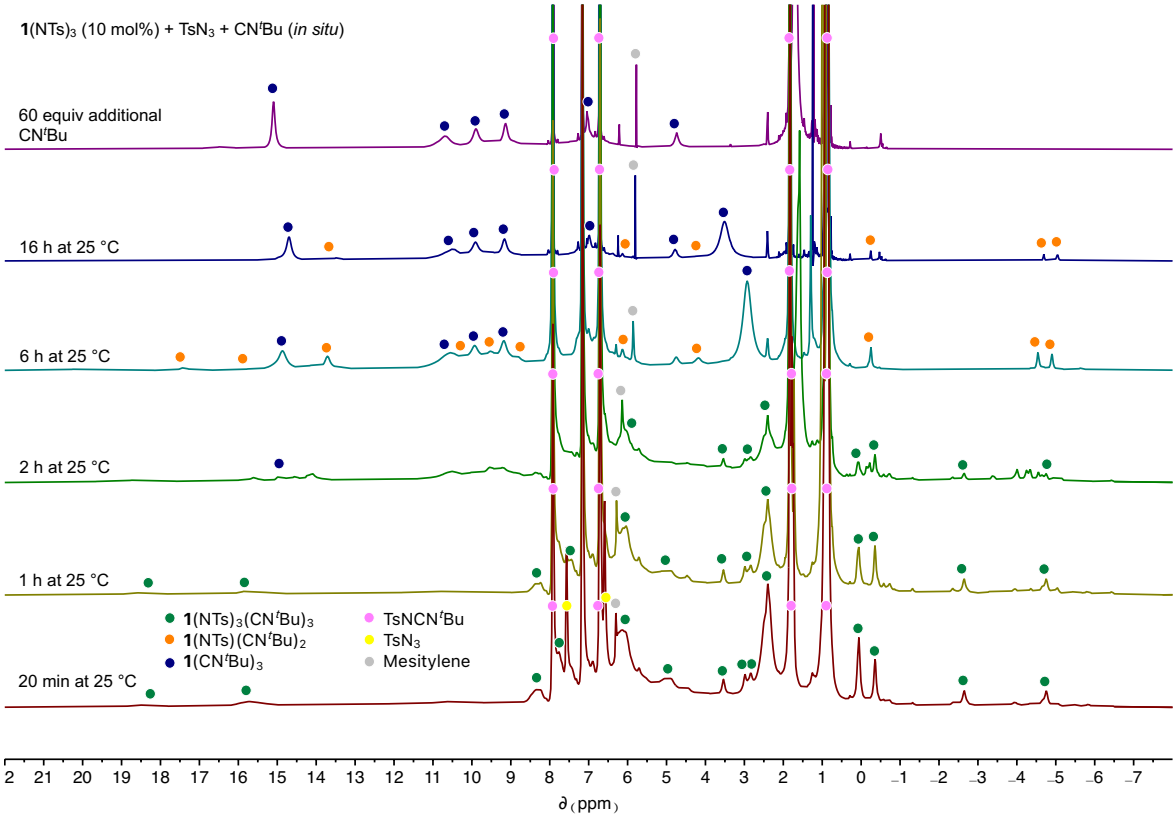


Figure 5.36. ^{1}H NMR (benzene-d_6, 25 °C, 500 MHz) spectra of the catalytic reaction upon mixing **Cr$_3$**(NTs)$_3$, TsN$_3$ and CN^{t}Bu. A catalyst loading of 10 mol% **Cr$_3$**(NTs)$_3$ (0.0085 M, 10 equiv) was employed to increase the visibility of the paramagnetic species, and the reaction was performed in the presence of TsN$_3$ (100 equiv, 0.085 M) and CN^{t}Bu (165 equiv, 0.140 M). Here, the trichromium cluster **Cr$_3$** is denoted as **1**.

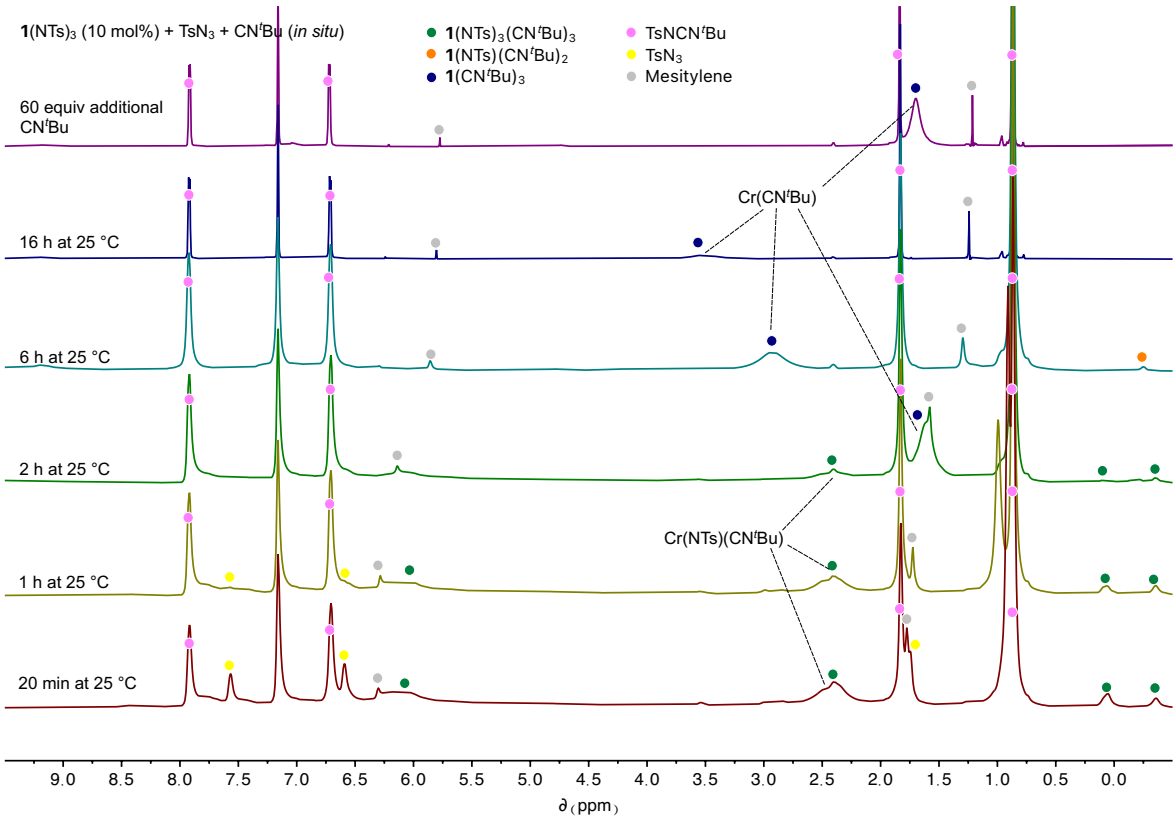


Figure 5.37. ^{1}H NMR (benzene-d_6, 25 °C, 500 MHz) spectra of the catalytic reaction upon mixing **Cr$_3$**(NTs)$_3$, TsN_3 and CN^{t}Bu, highlighting the diamagnetic region to show the clean conversion of tosyl azide to carbodiimide. A catalyst loading of 10 mol% **Cr$_3$**(NTs)$_3$ (0.0085 M, 10 equiv) was employed to increase the visibility of the paramagnetic species, and the reaction was performed in the presence of TsN_3 (100 equiv, 0.085 M) and CN^{t}Bu (165 equiv, 0.140 M). Here, the trichromium cluster **Cr$_3$** is denoted as **1**.

5.6.10 *Stoichiometric Azide Activation and Nitrene Transfer Experiments*

5.6.10.1 ^{1}H Reaction Monitoring: **Cr$_3$**(py)$_3$ + 3 equiv TsN_3

A 20 mL scintillation vial equipped with a magnetic stir bar was charged with **Cr$_3$**(py)$_3$ (10 mg, 3.2 µmol, 1 equiv) and benzene-d_6 (0.6 mL). The mixture was briefly stirred until homogeneous, and then frozen within a –35 °C glovebox freezer. A solution of TsN_3 in benzene-d_6 (0.994 M, 9.6 µL, 9.6 µmol, 3 equiv) was slowly added to the thawing, stirring solution by microsyringe. The sample was slowly brought to 25 °C and briefly stirred before being passed through a pipet filter into a J. Young NMR tube equipped with a mesitylene/benzene-d_6 (5% by volume) capillary. The sample was analyzed by ^{1}H NMR spectroscopy after 15, 30, and 70 min, although a comparison

of these spectra reveals that the reaction is complete after just 15 minutes, with **Cr$_3$**(NTs)$_3$ as the major product.

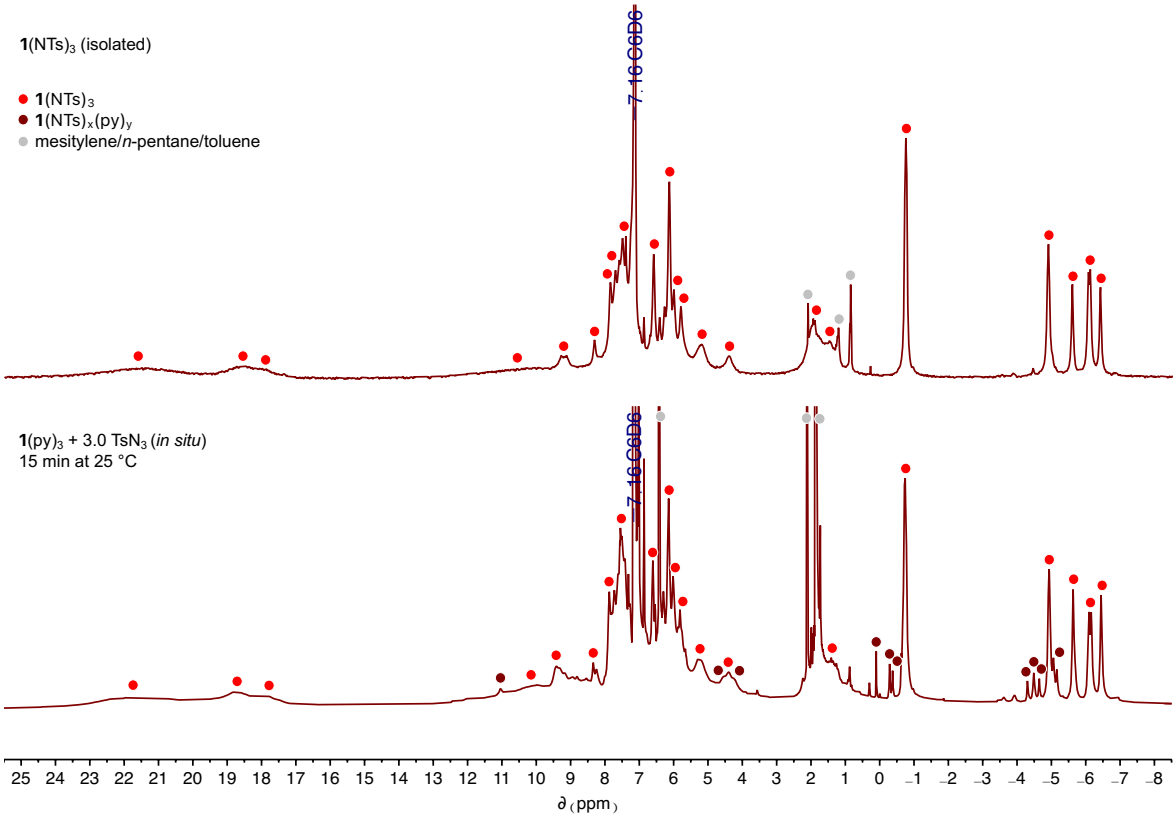


Figure 5.38. ^{1}H NMR (benzene-d_6, 25 °C, 500 MHz) spectra tracking the reaction of **Cr$_3$**(py)$_3$ with TsN_3 (3 equiv). The *in situ* reaction mixture after 15 min is plotted in comparison to that of isolated **Cr$_3$**(NTs)$_3$ in benzene-d_6. Here, the trichromium cluster **Cr$_3$** is denoted as **1**.

5.6.10.1 ^{1}H Reaction Monitoring: **Cr$_3$**(NTs)$_3$ + 6 equiv CN^{t}Bu

A 20 mL scintillation vial equipped with a magnetic stir bar was loaded with **Cr$_3$**(NTs)$_3$ (20 mg, 5.9 µmol, 1 equiv) and benzene-d_6 (0.6 mL). The mixture was stirred until homogeneous and then frozen at in a −35 °C freezer. Upon thawing CN^{t}Bu (0.88M in benzene-d_6; 39.9 µL, 35.4 µmol, 6 equiv) was added dropwise using a microsyringe. The sample was warmed to 25 °C with stirring, and then passed through a pipet filter into a J. Young NMR tube equipped with a mesitylene/benzene-d_6 (5% by volume) capillary. ^{1}H NMR spectra were collected after 15 min, 4 h, and 48 h at 25 °C, and a final spectrum was recorded after heating the sample at 60 °C for an additional 48 h. Aside from revealing the presence of multiple intermediates, this data

demonstrates that the tris(isocyanide) **Cr$_3$**(CN^{t}Bu)$_3$ is formed quantitatively, without signs of decomposition (Figure 5.9).

5.6.10.2 ^{1}H Reaction Monitoring: **Cr$_3$**(NTs)$_3$ + 3 equiv CN^{t}Bu

A 20 mL scintillation vial equipped with a magnetic stir bar was loaded with **Cr$_3$**(NTs)$_3$ (20 mg, 5.9 μmol, 1 equiv) and benzene-d_6 (0.6 mL). The mixture was stirred until homogeneous and then frozen within a −35 °C freezer. Upon thawing CN^{t}Bu (0.88 M in benzene-d_6; 20.1 μL, 17.7 μmol, 3 equiv) was added dropwise using a microsyringe. The sample was warmed to 25 °C with stirring, and then passed through a pipet filter into a J. Young NMR tube equipped with a mesitylene/benzene-d_6 (5% by volume) capillary. ^{1}H NMR spectra were collected after 30 min, 2 h, and 48 h at 25 °C. Ultimately, the reaction mixture converges toward a mixture of **Cr$_3$**(NTs)(CN^{t}Bu)$_2$ and an unidentified intermediate, likely the unidentified bis(imido) adduct **Cr$_3$**(NTs)$_2$(CN^{t}Bu) (Figure 5.11).

These results are plotted in comparison to the solution phase reactivity of **Cr$_3$**(NTs)$_3$(CN^{t}Bu)$_3$ observed upon dissolution of single crystals in toluene-d_8. In the absence of excess isocyanide, **Cr$_3$**(NTs)$_3$ and a mixture of **Cr$_3$**(NTs)$_3$(CN^{t}Bu)$_x$ (x = 1, 2, 3) forms immediately upon dissolution due to reversible coordination of isocyanide. After heating this sample at 60 °C for 24 h, the evolution of TsNCN^{t}Bu is observed, giving rise to a mixture of Cr(NTs)/Cr(CN^{t}Bu) nanoclusters nearly identical to that obtained independently upon treatment of **Cr$_3$**(NTs)$_3$ with 3 equivalents of isocyanide.

5.6.11 *X-ray Structure Determination*

Single crystals suitable for X-ray analysis were coated in deoxygenated paratone oil and mounted on a 20 μm CryoLoop™ (Hampton Research, 18 mm mount, 0.2 to 0.3 mm loop diameter). Data was collected either at –173 °C or –183 °C on a Bruker APEX II or Nonius Kappa CCD FR590 single crystal X-ray diffractometer, respectively, each equipped with a Mo source, as indicated for each sample. Unless indicated otherwise, all data was integrated and scaled using SAINT, SADABS within the APEX2 software package by Bruker.[59] Solution by direct methods (SHELXT[60] or SIR97[61,62]) produced a complete heavy atom phasing model consistent with the proposed structure. Structures were completed by difference Fourier synthesis with SHELXL.[63–65] Scattering factors are from Waasmair and Kirfel.[66] Hydrogen atoms were placed in

geometrically idealized positions and constrained to ride on their parent atoms with C–H distances in the range 0.95–1.00 Å. Isotropic thermal parameters U_{eq} were fixed such that they were $1.2U_{eq}$ of their parent atom U_{eq} for CHs and $1.5U_{eq}$ of their parent atom U_{eq} in case of methyl groups. All non-hydrogen atoms were refined anisotropically by full-matrix least-squares.

5.6.11.1 $\mathbf{Cr_3}(py)_3$

Large, dark red prismatic crystals of $\mathbf{Cr_3}(py)_3$ suitable for single crystal X-ray diffraction analysis were grown from a concentrated solution of the cluster in toluene layered with *n*-pentane (~1:5 ratio) at 25 °C over the course of 24 h. The compound crystallizes in the monoclinic space group C2/c, and the asymmetric unit features a singular cluster molecule with each edge Cr metal bound by an ancillary pyridine molecule. The contribution of toluene, *n*-pentane or diethyl ether solvent molecules to the diffraction pattern was removed using SQUEEZE (1911 eV in two voids). ISOR was applied for all carbon and nitrogen atoms to prevent non-positive definite displacement matrices. DELU was applied to all carbon, nitrogen and phosphorus atoms in order relate displacement parameters along bonds. 200 bad reflections were removed. A second, very faint Co_6Se_8 cluster, likely stemming from thermal disorder, was folded into the refined one, which is reflected in some notable rest electron density and a slightly elevated R1.

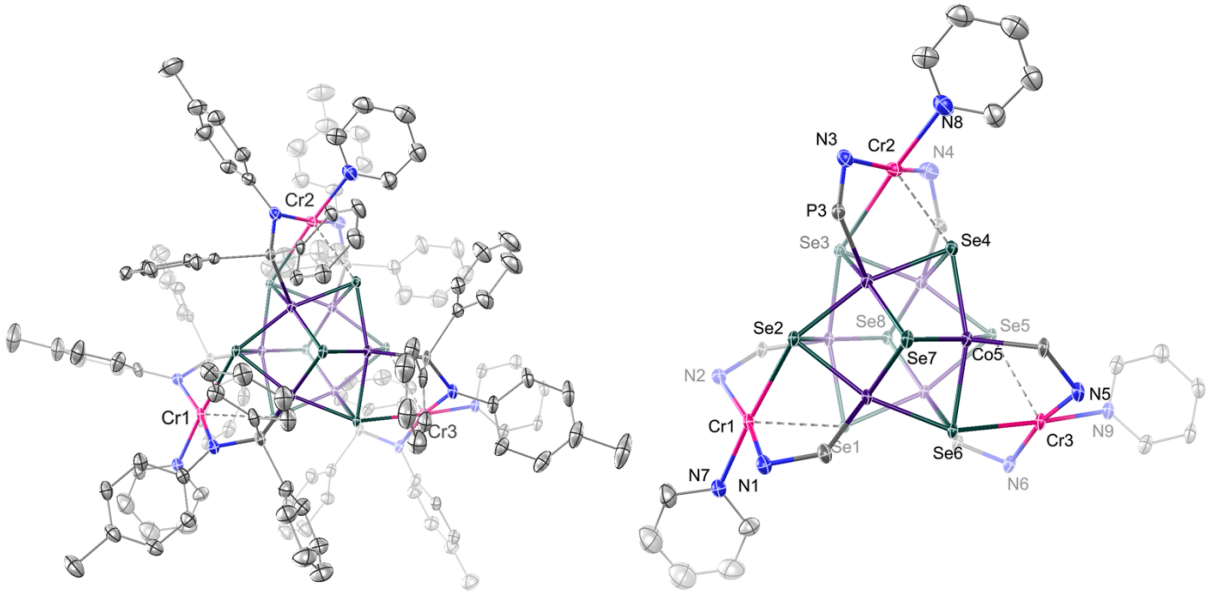


Figure 5.39. Solid-state structure of $\mathbf{Cr_3}(py)_3$ with thermal ellipsoids plotted at a 50% probability level. All hydrogen atoms are omitted for clarity. Selected interatomic distances (Å): Cr1-Se2 2.581(1), Cr1-Se1 2.726(1), Cr2-Se3 2.647(2), Cr2-Se4 2.703(2), Cr3-Se6 2.637(1), Cr3-Se5 2.719(2), Cr1-N7 2.102(7), Cr2-N8 2.150(8), Cr3-N9 2.116(7), Cr1-N1 2.022(7), Cr2-N3 2.059(8), Cr3-N6 2.047(7), Cr3…Co5 3.25(1).

5.6.11.2 $Cr_3(NTs)_3 \cdot 2\ CH_2Cl_2$

Dark red prismatic crystals of $Cr_3(NTs)_3$, suitable for single crystal X-ray analysis were grown by layering a concentrated solution of the cluster in DCM with *n*-pentane at 25 °C over the course of 48 h. The compound crystallizes in the mono space group $P2_1/n$, and the asymmetric unit contains a singular $Cr_3(NTs)_3$ cluster in addition to two DCM molecules. Some heavily disordered DCM molecules were also removed using SQUEEZE. Slight twinning required the application of a twin-law (ROTAX, applied with WinGX)[67], and ultimately afforded elevated R_1 and wR_2 values. Aromatic phenyl and tolyl rings were refined in an optimized geometry with AFIX 66 loops, and SAME commands were applied to geometrically similar moieties. 10 bad reflections were omitted from the refinement.

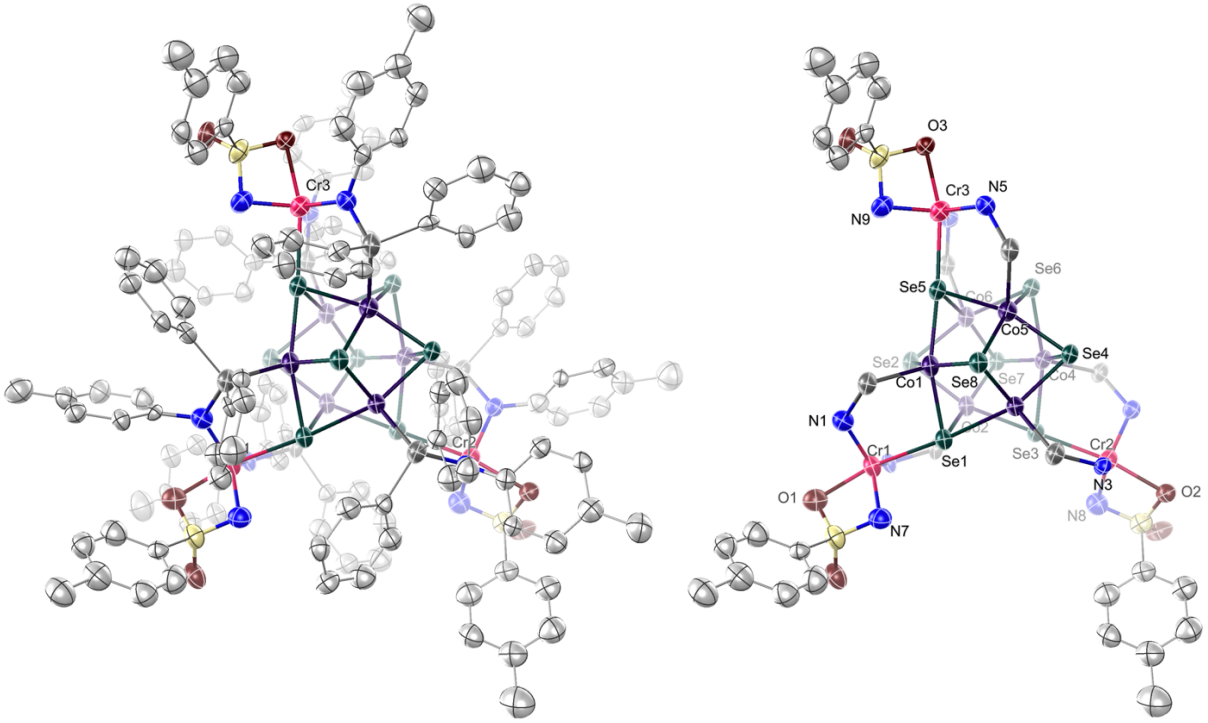


Figure 5.40. Solid-state structure of $Cr_3(NTs)_3 \cdot 2\ CH_2Cl_2$ with thermal ellipsoids plotted at a 50% probability level. All hydrogen atoms and co-crystallizing DCM molecules are omitted for clarity. Selected interatomic distances (Å) and angles (°): Cr1-Se1 2.513(5), Cr2-Se3 2.471(5), Cr3-Se6 2.463(5), Cr1-N7 1.81(2), Cr2-N8 1.82(2), Cr3-N9 1.84(2), Cr1-O1 2.12(2), Cr2-O2 2.10(2), Cr3-O3 2.05(2), Cr1-N1 1.88(2), Cr2-N3 1.91(2), Cr3-N5 1.87(2), Cr1…Co1 3.750(5), Cr1-N7-S1 95.2(1), Cr2-N8-S2 96.2(13), Cr3-N9-S3 95.8(13).

5.6.11.3 $\mathbf{Cr_3}(NTs)_3(CN^tBu)_3$

Dark red prismatic crystals of $\mathbf{Cr_3}(NTs)_3(CN^tBu)_3$ suitable for single crystal X-ray diffraction analysis were grown by layering a solution of $\mathbf{Cr_3}(NTs)_3$ and CN^tBu (10 equiv) with *n*-pentane at –35 °C over the course of 24 h. The crystals were transported to the diffractometer at –78 °C. Crystals that were transported at room temperature exhibited signs of decomposition, with X-ray analysis revealing the dissociation of CN^tBu at one edge site. The compound crystallizes in the triclinic space group $P\bar{1}$, and the asymmetric unit contains a singular $\mathbf{Cr_3}(NTs)_3(CN^tBu)_3$ cluster in addition to five toluene molecules, the contribution of which was removed with SQUEEZE. Three samples were measured – all of which exhibited significant positional disorder of the organic substituents. More specifically, three phosphinoamide ligands, two N-tosyl groups, and one CN^tBu ligand exhibit positional disorder and as a result they were modeled over two positions. Similar disorder is observed for Cr3. To handle the disorder, the displacement parameters of all carbon and nitrogen atoms as well as Cr2, Cr3, P1, and P6 were restrained using ISOR. Pairwise disordered atoms, whose displacement parameters were partially overlapping, also required DELU equivalents. 50 bad reflections were omitted (0.156%). Overall, the high degree of disorder affects all atoms, elongating their displacement parameters along one lattice direction.

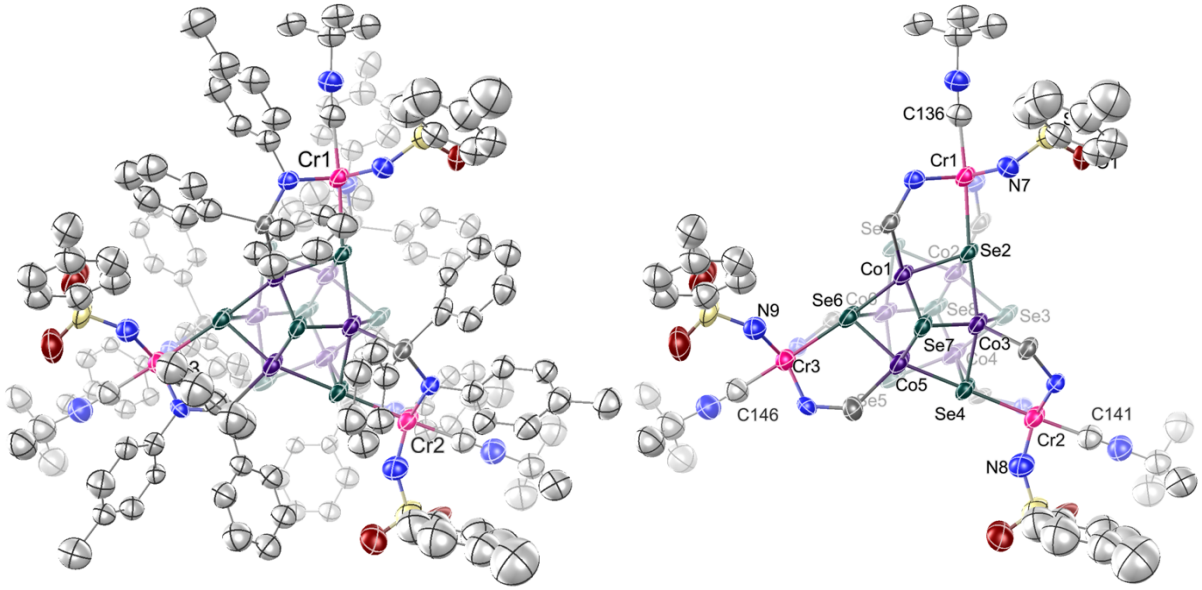


Figure 5.41. Solid-state structure of $\mathbf{Cr_3}(NTs)_3(CN^tBu)_3$ with thermal ellipsoids plotted at a 50% probability level. All hydrogen atoms and disorder are omitted for clarity. Selected interatomic distances (Å): Cr1-Se2 2.574(3), Cr2-Se4 2.605(3), Cr3-Se6 2.656(6), Cr1-N7 1.746(8), Cr2-N8 1.747(8), Cr3-N9 1.745(8), Cr1-C136 2.07(1), Cr2-C141 2.07(1), Cr3-C146 2.07(1), Cr1-N7-S1 143.7(6), Cr2-N8-S2 142.7(5), Cr3-N9-S3 144.5(6).

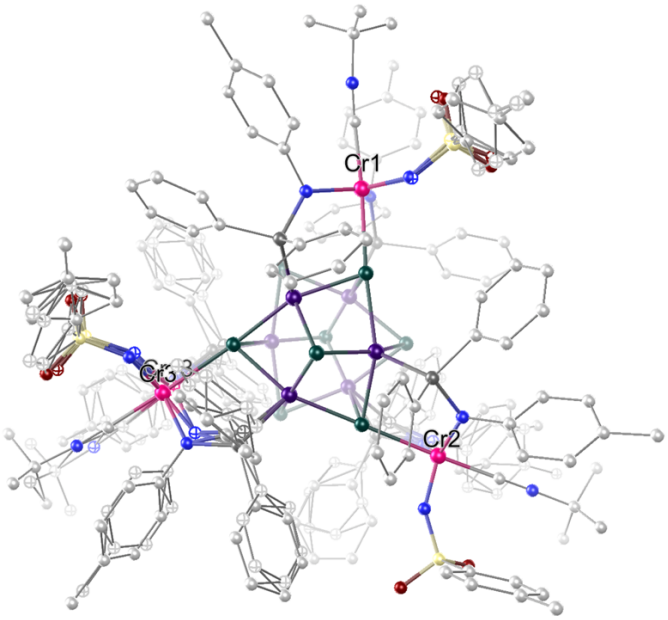


Figure 5.42. Solid-state structure of **Cr$_3$**(NTs)$_3$(CN^{t}Bu)$_3$ plotting both disordered components (each with ~50% abundance). The two components are compositionally identical but exhibit slight structural differences.

5.6.11.4 **Cr$_3$**(NTs)(CN^{t}Bu)$_2$

Dark red prismatic crystals of **Cr$_3$**(NTs)(CN^{t}Bu)$_2$ suitable for single crystal X-ray diffraction analysis were grown from a concentrated benzene solution layered with *n*-pentane at 25 °C over the course of 24 h. The compound crystallizes in the monoclinic space group P2$_1$/n, and the asymmetric unit contains a singular cluster molecule. The structure exhibits multiple instances of disorder, which required the phenyl groups to be optimized with AFIX 66 loops. In addition, ISOR was applied to the displacement parameters of all carbon and nitrogen atoms, and SAME restraints were required on symmetrically related phenyl and tolyl groups. The displacement parameters of related disordered atoms were linked with EADP cards, and for the N-tosyl group additional FLAT restraints were implemented on the 1:1 disordered tolyl moiety. The structure exhibits further chemical disorder with substoichiometric occupancy of the N-tosyl group at Cr1. Specifically, the refinement converged to a model with 90% occupancy of the N-tosyl ligand co-crystallized and 10% occupancy of **Cr$_3$**(CN^{t}Bu)$_2$Co$_6$Se$_8$L$_6$ exhibiting no surface ligands bound to Cr1, though presumably bound by a CN^{t}Bu ligand that is not detectable at this occupancy. The contribution of disordered solvent (benzene and *n*-pentane) to the diffraction pattern was removed using SQUEEZE.

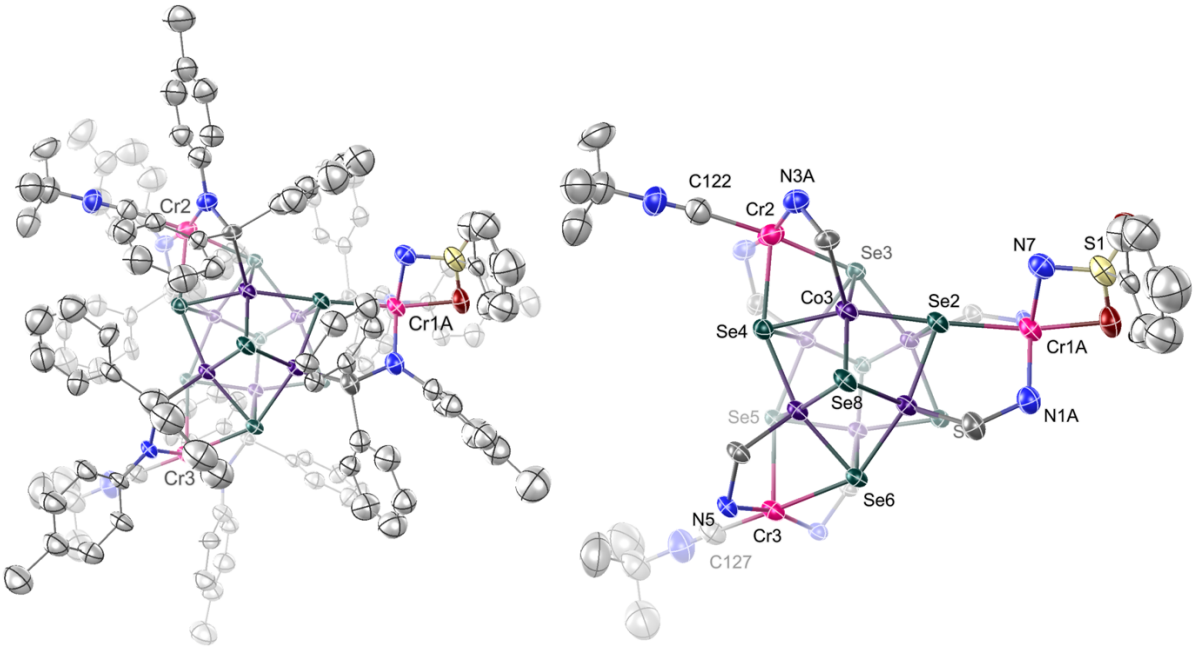


Figure 5.43. Solid-state structure of **Cr$_3$**(NTs)(CN^{t}Bu)$_2$ with thermal ellipsoids plotted at a 50% probability level. All hydrogen atoms and disorder are omitted for clarity. Selected interatomic distances (Å): Cr1A-Se2 2.444(2), Cr2-Se3 2.611(2), Cr2-Se4 2.663(2), Cr3-Se6 2.648(2), Cr3-Se5 2.655(2), Cr1A-N7 1.86(1), Cr1A-N1A 2.02(2), Cr3-N5 2.059(9), Cr2-C122 2.09(1), Cr3-C127 2.07(1).

5.6.11.5 X-ray Tables

Table 5.2. Crystallographic information for **Cr$_3$**(py)$_3$ and **Cr$_3$**(NTs)$_3$.

Compound	**Cr$_3$**(py)$_3$	**Cr$_3$**(NTs)$_3$ · 2 CH_2Cl_2
Empirical formula	$C_{129}H_{117}Co_6Cr_3N_9P_6Se_8$	$C_{137}H_{127}Co_6Cr_3N_9O_6P_6S_3Se_8Cl_4$
CCDC Number	2131447	2172819
Formula weight	3120.39	3560.53
Temperature (K)	90(2)	100(2)
Wavelength (Å)	0.71073	0.71073
Crystal system	Monoclinic	Monoclinic
Space group	C 2/c	$P2_1/n$
a (Å)	64.501(9)	14.1988(8)
b (Å)	15.308(2)	34.399(2)
c (Å)	33.309(4)	33(382(2)
α (°)	90	90
β (°)	116.246(6)	98.523(3)
γ (°)	90	90
Volume (Å^3)	29499(7)	16124.6(17)
Z	8	4
ρ^{calc} (g cm^{-1})	1.405	1.467
Absorption coefficient (mm^{-1})	2.953	2.815
F(000)	12400	7088
Crystal size (mm^3)	0.250 x 0.240 x 0.240	0.140 x 0.110 x 0.050
Theta range for data collection (°)	0.704 to 25.027	1.184 to 25.350
Index ranges	$-76\leq h\leq 68$, $-18\leq k\leq 18$, $0\leq l\leq 39$	$-17\leq h\leq 17$, $-41\leq k\leq 41$, $-40\leq l\leq 40$
Reflections collected	50456	57651
Independent reflections	23795 [R(int) = 0.0345]	57651 [R(int) = 0.1094]
Completeness to theta = 25.000°	98.9%	100%
Data / restraints / parameters	25795 / 1182 / 1456	57651 / 1605 / 1396
Goodness-of-fit on F^2	1.060	1.120
Final R indices [I>2sigma(I)]	R1 = 0.0790, wR2 = 0.1904	R1 = 0.1615, wR2 = 0.3687
R indices (all data)	R1 = 0.0943, wR2 = 0.1984	R1 = 0.2371, wR2 = 0.4055
Largest diff. peak and hole (e$^-$Å^{-3})	5.035 and –1.265	3.224 and –1.949

Table 5.3. Crystallographic information for **Cr$_3$**(NTs)$_3$(CN^{t}Bu)$_3$ and **Cr$_3$**(NTs)(CN^{t}Bu)$_2$.

Compound	**Cr$_3$**(NTs)$_3$(CN^{t}Bu)$_3$	**Cr$_3$**(NTs)(CN^{t}Bu)$_2$
Empirical formula	$C_{150}H_{150}Co_6Cr_3N_{12}O_6P_6S_3Se_8$	$C_{130.30}H_{126.30}Co_6Cr_3N_{8.90}O_{1.80}P_6S_{0.90}Se_8$
CCDC Number	2131448	2131446
Formula weight	3640.07	3201.63
Temperature (K)	100(2) K	100(2)
Wavelength (Å)	0.71073 Å	0.71073
Crystal system	Triclinic	Monoclinic
Space group	$P\bar{1}$	$P2_1/n$
a (Å)	18.5695(14)	17.8491(8)
b (Å)	24.0006(15)	46.0600(19)
c (Å)	24.270(3)	19.6997(8)
α (°)	112.899(5)	90
β (°)	103.803(5)	111.688(2)
γ (°)	106.371(4)	90
Volume (Å^3)	8786.6(13)	15049.2(11)
Z	2	4
ρ^{calc} (g cm^{-1})	1.376	1.413
Absorption coefficient (mm^{-1})	2.526	2.909
F(000)	3652	6381
Crystal size (mm^3)	0.300 x 0.150 x 0.130	0.160 x 0.130 x 0.100
Theta range for data collection (°)	1.232 to 25.350	1.305 to 25.350
Index ranges	$-22\leq h\leq 22$, $-28\leq k\leq 28$, $-29\leq l\leq 29$	$-21\leq h\leq 21$, $-55\leq k\leq 55$, $-23\leq l\leq 23$
Reflections collected	64080	54379
Independent reflections	32127 [R(int) = 0.0614]	27516 [R(int) = 0.1034]
Completeness to theta = 25.000°	99.8%	99.8%
Data / restraints / parameters	32127 / 3415 / 2073	27516 / 1819 / 1358
Goodness-of-fit on F^2	1.009	1.021
Final R indices [I>2sigma(I)]	R1 = 0.1140, wR2 = 0.2244	R1 = 0.0865, wR2 = 0.1754
R indices (all data)	R1 = 0.2287, wR2 = 0.3063	R1 = 0.1778, wR2 = 0.2125
Largest diff. peak and hole (e$^-$Å^{-3})	1.590 and –1.229	1.149 and –1.035

5.7 REFERENCES

(1) K. Nørskov, J.; Bligaard, T.; Hvolbæk, B.; Abild-Pedersen, F.; Chorkendorff, I.; H. Christensen, C. The Nature of the Active Site in Heterogeneous Metal Catalysis. *Chem. Soc. Rev.* **2008**, *37* (10), 2163–2171. https://doi.org/10.1039/B800260F.

(2) Tyo, E. C.; Vajda, S. Catalysis by Clusters with Precise Numbers of Atoms. *Nature Nanotechnology* **2015**, *10* (7), 577–588. https://doi.org/10.1038/nnano.2015.140.

(3) Du, X.; Jin, R. Atomically Precise Metal Nanoclusters for Catalysis. *ACS Nano* **2019**, *13* (7), 7383–7387. https://doi.org/10.1021/acsnano.9b04533.

(4) Taylor, H. S.; Armstrong, E. F. A Theory of the Catalytic Surface. *Proceedings of the Royal Society of London. Series A, Containing Papers of a Mathematical and Physical Character* **1925**, *108* (745), 105–111. https://doi.org/10.1098/rspa.1925.0061.

(5) Zambelli, T.; Wintterlin, J.; Trost, J.; Ertl, G. Identification of the "Active Sites" of a Surface-Catalyzed Reaction. *Science* **1996**, *273* (5282), 1688–1690. https://doi.org/10.1126/science.273.5282.1688.

(6) Tuxen, A.; Kibsgaard, J.; Gøbel, H.; Lægsgaard, E.; Topsøe, H.; Lauritsen, J. V.; Besenbacher, F. Size Threshold in the Dibenzothiophene Adsorption on MoS_2 Nanoclusters. *ACS Nano* **2010**, *4* (8), 4677–4682. https://doi.org/10.1021/nn1011013.

(7) Lauritsen, J.; Kibsgaard, J.; Olesen, G.; Moses, P.; Hinnemann, B.; Helveg, S.; Norskov, J.; Clausen, B.; Topsoe, H.; Lagsgaard, E.; Besenbacher, F. Location and Coordination of Promoter Atoms in Co- and Ni-Promoted MoS2-Based Hydrotreating Catalysts. *Journal of Catalysis* **2007**, *249* (2), 220–233. https://doi.org/10.1016/j.jcat.2007.04.013.

(8) Jaramillo, T. F.; Jorgensen, K. P.; Bonde, J.; Nielsen, J. H.; Horch, S.; Chorkendorff, I. Identification of Active Edge Sites for Electrochemical H_2 Evolution from MoS_2 Nanocatalysts. *Science* **2007**, *317* (5834), 100–102. https://doi.org/10.1126/science.1141483.

(9) Xu, Z.; Xiao, F.-S.; Purnell, S. K.; Alexeev, O.; Kawi, S.; Deutsch, S. E.; Gates, B. C. Size-Dependent Catalytic Activity of Supported Metal Clusters. *Nature* **1994**, *372* (6504), 346–348. https://doi.org/10.1038/372346a0.

(10) Zhao, S.; Austin, N.; Li, M.; Song, Y.; House, S. D.; Bernhard, S.; Yang, J. C.; Mpourmpakis, G.; Jin, R. Influence of Atomic-Level Morphology on Catalysis: The Case of Sphere and Rod-Like Gold Nanoclusters for CO_2 Electroreduction. *ACS Catal.* **2018**, *8* (6), 4996–5001. https://doi.org/10.1021/acscatal.8b00365.

(11) Kibsgaard, J.; Tuxen, A.; Knudsen, K. G.; Brorson, M.; Topsøe, H.; Lægsgaard, E.; Lauritsen, J. V.; Besenbacher, F. Comparative Atomic-Scale Analysis of Promotional Effects by Late 3d-Transition Metals in MoS_2 Hydrotreating Catalysts. *Journal of Catalysis* **2010**, *272* (2), 195–203. https://doi.org/10.1016/j.jcat.2010.03.018.

(12) Hong, X.; Chan, K.; Tsai, C.; Nørskov, J. K. How Doped MoS_2 Breaks Transition-Metal Scaling Relations for CO_2 Electrochemical Reduction. *ACS Catal.* **2016**, *6* (7), 4428–4437. https://doi.org/10.1021/acscatal.6b00619.

(13) Abbasi, P.; Asadi, M.; Liu, C.; Sharifi-Asl, S.; Sayahpour, B.; Behranginia, A.; Zapol, P.; Shahbazian-Yassar, R.; Curtiss, L. A.; Salehi-Khojin, A. Tailoring the Edge Structure of Molybdenum Disulfide toward Electrocatalytic Reduction of Carbon Dioxide. *ACS Nano* **2017**, *11* (1), 453–460. https://doi.org/10.1021/acsnano.6b06392.

(14) Degroot, M. W.; Corrigan, J. F. High Nuclearity Clusters: Metal–Chalcogenide Polynuclear Complexes. In *Comprehensive Coordination Chemistry II*; Elsevier, 2003; pp 57–123. https://doi.org/10.1016/B0-08-043748-6/06147-8.

(15) Anyushin, A. V.; Kondinski, A.; Parac-Vogt, T. N. Hybrid Polyoxometalates as Post-Functionalization Platforms: From Fundamentals to Emerging Applications. *Chem. Soc. Rev.* **2020**, *49* (2), 382–432. https://doi.org/10.1039/C8CS00854J.

(16) Jin, R.; Zeng, C.; Zhou, M.; Chen, Y. Atomically Precise Colloidal Metal Nanoclusters and Nanoparticles: Fundamentals and Opportunities. *Chem. Rev.* **2016**, *116* (18), 10346–10413. https://doi.org/10.1021/acs.chemrev.5b00703.

(17) Reed, C. J.; Agapie, T. A Terminal Fe^{III}–Oxo in a Tetranuclear Cluster: Effects of Distal Metal Centers on Structure and Reactivity. *J. Am. Chem. Soc.* **2019**, *141* (24), 9479–9484. https://doi.org/10.1021/jacs.9b03157.

(18) Amtawong, J.; Balcells, D.; Wilcoxen, J.; Handford, R. C.; Biggins, N.; Nguyen, A. I.; Britt, R. D.; Tilley, T. D. Isolation and Study of Ruthenium–Cobalt Oxo Cubanes Bearing a High-Valent, Terminal Ru^{V}–Oxo with Significant Oxyl Radical Character. *J. Am. Chem. Soc.* **2019**, *141* (50), 19859–19869. https://doi.org/10.1021/jacs.9b10320.

(19) Sridharan, A.; Brown, A. C.; Suess, D. L. M. A Terminal Imido Complex of an Iron–Sulfur Cluster. *Angew. Chem. Int. Ed.* **2021**, *60* (23), 12802–12806. https://doi.org/10.1002/anie.202102603.

(20) Bartholomew, A. K.; Juda, C. E.; Nessralla, J. N.; Lin, B.; Wang, S. G.; Chen, Y.; Betley, T. A. Ligand-Based Control of Single-Site vs. Multi-Site Reactivity by a Trichromium Cluster. *Angew. Chem. Int. Ed.* **2019**, *58* (17), 5687–5691. https://doi.org/10.1002/anie.201901599.

(21) Powers, T. M.; Betley, T. A. Testing the Polynuclear Hypothesis: Multielectron Reduction of Small Molecules by Triiron Reaction Sites. *J. Am. Chem. Soc.* **2013**, *135* (33), 12289–12296. https://doi.org/10.1021/ja405057n.

(22) Kibsgaard, J.; Jaramillo, T. F.; Besenbacher, F. Building an Appropriate Active-Site Motif into a Hydrogen-Evolution Catalyst with Thiomolybdate $[Mo_3S_{13}]^{2-}$ Clusters. *Nature Chem.* **2014**, *6* (3), 248–253. https://doi.org/10.1038/nchem.1853.

(23) Coucouvanis, D.; Mosier, P. E.; Demadis, K. D.; Patton, S.; Malinak, S. M.; Kim, C. G.; Tyson, M. A. The Catalytic Reduction of Hydrazine to Ammonia by the $MoFe_3S_4$ Cubanes and Implications Regarding the Function of Nitrogenase. Evidence for Direct Involvement of the Molybdenum Atom in Substrate Reduction. *J. Am. Chem. Soc.* **1993**, *115* (25), 12193–12194. https://doi.org/10.1021/ja00078a079.

(24) Luo, Z.; Castleman, A. W.; Khanna, S. N. Reactivity of Metal Clusters. *Chem. Rev.* **2016**, *116* (23), 14456–14492. https://doi.org/10.1021/acs.chemrev.6b00230.

(25) Carr, C. R.; Taheri, A.; Berben, L. A. Fast Proton Transfer and Hydrogen Evolution Reactivity Mediated by $[Co_{13}C_2(CO)_{24}]^{4-}$. *J. Am. Chem. Soc.* **2020**, *142* (28), 12299–12305. https://doi.org/10.1021/jacs.0c04034.

(26) Jin, R.; Li, G.; Sharma, S.; Li, Y.; Du, X. Toward Active-Site Tailoring in Heterogeneous Catalysis by Atomically Precise Metal Nanoclusters with Crystallographic Structures. *Chem. Rev.* **2021**, *121* (2), 567–648. https://doi.org/10.1021/acs.chemrev.0c00495.

(27) Chen, Y.; Wu, C.; Sung, P.; Chan, S. I.; Chen, P. P. Turnover of a Methane Oxidation Tricopper Cluster Catalyst: Implications for the Mechanism of the Particulate Methane Monooxygenase (PMMO). *ChemCatChem* **2020**, *12* (11), 3088–3096. https://doi.org/10.1002/cctc.202000322.

(28) Song, F.; Moré, R.; Schilling, M.; Smolentsev, G.; Azzaroli, N.; Fox, T.; Luber, S.; Patzke, G. R. $\{Co_4O_4\}$ and $\{Co_xNi_{4-x}O_4\}$ Cubane Water Oxidation Catalysts as Surface Cut-Outs of Cobalt Oxides. *J. Am. Chem. Soc.* **2017**, *139* (40), 14198–14208. https://doi.org/10.1021/jacs.7b07361.

(29) Luo, Z.; Khanna, S. N. Metal Cluster Catalysis. In *Metal Clusters and Their Reactivity*; Springer Singapore: Singapore, 2020; pp 215–239. https://doi.org/10.1007/978-981-15-9704-6_13.

(30) Ren, Y.; Yang, Y.; Zhao, Y.-X.; He, S.-G. Conversion of Methane with Oxygen to Produce Hydrogen Catalyzed by Triatomic Rh_3^- Cluster Anion. *JACS Au* **2022**, *2* (1), 197–203. https://doi.org/10.1021/jacsau.1c00469.

(31) Kephart, J. A.; Mitchell, B. S.; Chirila, A.; Anderton, K. J.; Rogers, D.; Kaminsky, W.; Velian, A. Atomically Defined Nano-Propeller $Fe_3Co_6Se_8(Ph_2PNTol)_6$: Functional Model for the Electronic Metal-Support Interaction Effect, and High Catalytic Activity for Carbodiimide Formation. *J. Am. Chem. Soc.* **2019**, *141* (50), 19605–19610. https://doi.org/10.1021/jacs.9b12473.

(32) Kephart, J. A.; Boggiano, A. C.; Kaminsky, W.; Velian, A. Inorganic Clusters as Metalloligands: Ligand Effects on the Synthesis and Properties of Ternary Nanopropeller Clusters. *Dalton Trans.* **2020**, *49* (45), 16464–16473. https://doi.org/10.1039/D0DT02416C.

(33) Kephart, J. A.; Romero, C. G.; Tseng, C.-C.; Anderton, K. J.; Yankowitz, M.; Kaminsky, W.; Velian, A. Hierarchical Nanosheets Built from Superatomic Clusters: Properties, Exfoliation and Single-Crystal-to-Single-Crystal Intercalation. *Chem. Sci.* **2020**, *11* (39), 10744–10751. https://doi.org/10.1039/D0SC03506H.

(34) Mitchell, B. S.; Kaminsky, W.; Velian, A. Tuning the Electronic Structure of Atomically Precise Sn/Co/Se Nanoclusters via Redox Matching of Tin(IV) Surface Sites. *Inorg. Chem.* **2021**, *60* (9), 6135–6139. https://doi.org/10.1021/acs.inorgchem.1c00313.

(35) Mitchell, B. S.; Krajewski, S. M.; Kephart, J. A.; Rogers, D.; Kaminsky, W.; Velian, A. Redox-Switchable Allosteric Effects in Molecular Clusters. *JACS Au* **2022**, *2* (1), 92–96. https://doi.org/10.1021/jacsau.1c00491.

(36) Campbell, C. T. Catalyst–Support Interactions: Electronic Perturbations. *Nat. Chem.* **2012**, *4* (8), 597–598. https://doi.org/10.1038/nchem.1412.

(37) Hili, R.; Yudin, A. K. Making Carbon-Nitrogen Bonds in Biological and Chemical Synthesis. *Nat. Chem. Biol.* **2006**, *2* (6), 284–287. https://doi.org/10.1038/nchembio0606-284.

(38) Kennemur, J. G.; Novak, B. M. Advances in Polycarbodiimide Chemistry. *Polymer* **2011**, *52* (8), 1693–1710. https://doi.org/10.1016/j.polymer.2011.02.040.

(39) Kephart, J.; Mitchell, B.; Kaminsky, W.; Velian, A. *Multi-Active Site Dynamics on a Molecular Cr/Co/Se Cluster Catalyst*; preprint; Chemistry, 2022. https://doi.org/10.26434/chemrxiv-2022-zkfsp.

(40) Yousif, M.; Tjapkes, D. J.; Lord, R. L.; Groysman, S. Catalytic Formation of Asymmetric Carbodiimides at Mononuclear Chromium(II/IV) Bis(Alkoxide) Complexes. *Organometallics* **2015**, *34* (20), 5119–5128. https://doi.org/10.1021/acs.organomet.5b00703.

(41) Dong, Y.; Clarke, R. M.; Zheng, S.-L.; Betley, T. A. Synthesis and Electronic Structure Studies of a Cr-Imido Redox Series. *Chem. Commun.* **2020**, *56* (21), 3163–3166. https://doi.org/10.1039/D0CC00108B.

(42) Laskowski, C. A.; Hillhouse, G. L. Group-Transfer Reactions of Ni(II)−Ni(II) Bridging Imido Complexes. Catalytic Formation of Carbodiimides and Isocyanates via Nitrene Transfer from Organoazides. *Organometallics* **2009**, *28* (20), 6114–6120. https://doi.org/10.1021/om900783u.

(43) A Search for All Cr...N Double Bond Lengths in the Cambridge Structural Database (Updated November 2020) Yielded 153 Hits between 1.55 and 1.874 Å (Mean 1.65(3) Å). A Similar Search for Cr...N Single Bond Lengths Yielded 3786 Hits between 1.763 and 2.443 Å (Mean 2.06(9) Å).

(44) Zdilla, M. J.; Abu-Omar, M. M. Mechanism of Catalytic Aziridination with Manganese Corrole: The Often Postulated High-Valent Mn(V) Imido Is Not the Group Transfer Reagent. *J. Am. Chem. Soc.* **2006**, *128* (51), 16971–16979. https://doi.org/10.1021/ja0665489.

(45) Zhou, W.; Patrick, B. O.; Smith, K. M. Influence of Redox Non-Innocent Phenylenediamido Ligands on Chromium Imido Hydrogen-Atom Abstraction Reactivity. *Chem. Commun.* **2014**, *50* (69), 9958–9960. https://doi.org/10.1039/C4CC04545A.

(46) Heins, S. P.; Morris, W. D.; Wolczanski, P. T.; Lobkovsky, E. B.; Cundari, T. R. Nitrene Insertion into C-C and C-H Bonds of Diamide Diimine Ligands Ligated to Chromium and Iron. *Angew. Chem. Int. Ed.* **2015**, *54* (48), 14407–14411. https://doi.org/10.1002/anie.201507463.

(47) Fan, X.; Wang, J.; Wu, K.; Zhang, L.; Zhang, J. Isomerism in Titanium-Oxo Clusters: Molecular Anatase Model with Atomic Structure and Improved Photocatalytic Activity. *Angew. Chem. Int. Ed.* **2019**, *58* (5), 1320–1323. https://doi.org/10.1002/anie.201809961.

(48) Zhang, Z.; Zandkarimi, B.; Alexandrova, A. N. Ensembles of Metastable States Govern Heterogeneous Catalysis on Dynamic Interfaces. *Acc. Chem. Res.* **2020**, *53* (2), 447–458. https://doi.org/10.1021/acs.accounts.9b00531.

(49) Somorjai, G. A.; Van Hove, M. A. Adsorbate-Induced Restructuring of Surfaces. *Progress in Surface Science* **1989**, *30* (3–4), 201–231. https://doi.org/10.1016/0079-6816(89)90009-9.

(50) Yan, B.; Krishnamurthy, D.; Hendon, C. H.; Deshpande, S.; Surendranath, Y.; Viswanathan, V. Surface Restructuring of Nickel Sulfide Generates Optimally Coordinated Active Sites for Oxygen Reduction Catalysis. *Joule* **2017**, *1* (3), 600–612. https://doi.org/10.1016/j.joule.2017.08.020.

(51) Zhang, Z.; Wei, Z.; Sautet, P.; Alexandrova, A. N. Hydrogen-Induced Restructuring of a Cu(100) Electrode in Electroreduction Conditions. *J. Am. Chem. Soc.* **2022**, *144* (42), 19284–19293. https://doi.org/10.1021/jacs.2c06188.

(52) Syres, K. L.; Thomas, A. G.; Flavell, W. R.; Spencer, B. F.; Bondino, F.; Malvestuto, M.; Preobrajenski, A.; Grätzel, M. Adsorbate-Induced Modification of Surface Electronic Structure: Pyrocatechol Adsorption on the Anatase TiO_2(101) and Rutile TiO_2(110) Surfaces. *J. Phys. Chem. C* **2012**, *116* (44), 23515–23525. https://doi.org/10.1021/jp308614k.

(53) *A Search for All Cr...C(CNtBu) Bond Lengths in the Cambridge Structural Database (Updated November 2020) Yielded 53 Hits between 1.87 and 2.068 Å (Mean 1.97(3) Å).*

(54) Hogarth, G.; Richards, I. Regioselective and Reversible Carbon–Nitrogen Bond Formation: Synthesis, Structure and Reactivity of Ureato-Bridged Complexes $[Mo_2(NAr)_2(\mu\text{-}X)\{\mu\text{-}ArNC(O)NAr\}(S_2CNR_2)_2]$ (Ar = Ph, p-Tol; X = S, NAr; R = Me, Et, Pr). *Dalton Trans.* **2005**, No. 4, 760–773. https://doi.org/10.1039/B417234P.

(55) Kim, J. Y.; Park, S. H.; Ryu, J.; Cho, S. H.; Kim, S. H.; Chang, S. Rhodium-Catalyzed Intermolecular Amidation of Arenes with Sulfonyl Azides via Chelation-Assisted C–H Bond Activation. *J. Am. Chem. Soc.* **2012**, *134* (22), 9110–9113. https://doi.org/10.1021/ja303527m.

(56) Passarelli, V.; Benetollo, F. Reactivity of Novel N,N'-Diphosphino-Silanediamine-Based Rhodium(I) Derivatives. *Inorg. Chem.* **2011**, *50*, 9958–9967. https://doi.org/10.1021/ic2004408.

(57) Evans, D. F. 400. The Determination of the Paramagnetic Susceptibility of Substances in Solution by Nuclear Magnetic Resonance. *J. Chem. Soc.* **1959**, 2003. https://doi.org/10.1039/jr9590002003.

(58) Weiss, S.; Aguila, M. J. B.; Kogut, E.; Warren, T. H. β-Diketiminato Nickel Imides in Catalytic Nitrene Transfer to Isocyanides. *Organometallics* **2013**, *32* (8), 2300–2308.

(59) Bruker APEX2 (Version 2.1-4), SAINT (Version 7.34A), SADABS (Version 2007/4), **2007** *BrukerAXS Inc,* Madison, Wisconsin, USA.

(60) Sheldrick, G.M. *Acta Cryst.* **2015**, *A71*, 3-8.

(61) Altomare, A.; Burla, C.; Camalli, M.; Cascarano, G. L.; Giacovazzo, C.; Guagliardi, A.; Moliterni, A.G.G.; Polidori, G.; Spagna, R. *J. Appl. Crystallogr.,* **1999**, *32*, 115-119.

(62) Altomare, A.; Cascarano, G. L.; Giacovazzo, C.; Guagliardi, A. *J. Appl. Crystallogr*., **1993**, *26*, 343-350.

(63) Sheldrick, G. M. *SHELXL-97, Program for the Refinement of Crystal Structures*, **1997**, University of Göttingen, Germany.

(64) Sheldrick, G. M. *Acta Cryst.* ***2015***, *C71*, 3–8.

(65) Mackay, S.; Edwards, C.; Henderson, A.; Gilmore, C.; Stewart, N.; Shankland, K.; Donald, A. *MaXus: A Computer Program for the Solution and Refinement of Crystal Structures from Diffraction Data*, **1997**, University of Glasgow, Scotland.

(66) Waasmaier, D.; Kirfel, A. *Acta Cryst.*, **1995**, *51*, 416-430.

(67) Cooper, R. I.; Gould, R. O.; Parsons, S.; Watkin, D. J. The Derivation of Non-Merohedral Twin Laws during Refinement by Analysis of Poorly Fitting Intensity Data and the Refinement of

Non-Merohedrally Twinned Crystal Structures in the Program *CRYSTALS*. *J Appl Crystallogr* **2002**, *35* (2), 168–174. https://doi.org/10.1107/S0021889802000249.

CHAPTER 6.

ALLOSTERIC ACTIVE SITE SPECIATION IN MOLECULAR CR/CO/SE CLUSTERS

6.1 ABSTRACT

At heterogeneous interfaces, surface active sites are differentiated based on their unique position on the supporting lattice. Here, we investigate the electronic origins of active site speciation within a Cr/Co/Se nanocluster, where the three edge metals are in formally equivalent chemical environments. Above, I demonstrated the capabilities of a new a molecular Cr/Co/Se nanocluster catalyst $Cr_3Co_6Se_8L^{Tol}_6$ (L^{Tol} = $Ph_2PN^{(-)}Tol$) and probed the mechanism by which the Cr edge metals facilitate azide activation and nitrene transfer by isolating of a series of catalytically competent Cr(imido) intermediates. Within this series of molecular Cr/Co/Se nanoclusters, comparative structural analysis reveals trends in how the three chemically equivalent Cr active sites are differentiated as they interact through a Co_6Se_8 support. Here, we utilize a combination of spectroscopic, electrochemical, and computational techniques to investigate the electronic

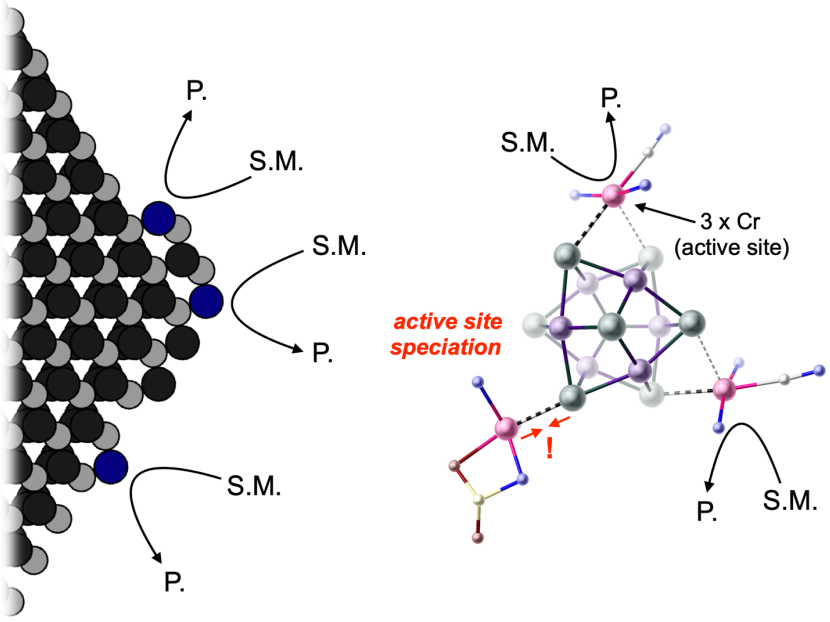


Figure 6.1. Cr/Co/Se nanoclusters enable a molecular investigation of the electronic forces that guide active site speciation.

structure of this system and pinpoint the mechanism by which our active sites are intertwined. Our computational analysis reveals how edge-support covalency draws lines of communication between neighboring active sites through the inorganic support. Owing to its allosteric character, edge-support binding is responsive to changes in oxidation state and supports a rich and well-behaved electrochemical profile. Drawing upon the chemical reversibility of edge-support binding, chemical redox transformations enable site-specific manipulation of Cr-Se bonding interactions and grant access to low-valent Cr(imido) edge sites with enhanced reactivity.

6.2 Introduction

The vast majority of industrial and pharmaceutical manufacturing processes rely on catalysis in some capacity,[1,2] and yet the absolute determination of catalytic active site identity remains one of the most challenging and elusive problems in all of surface science.[3–5] It is well-established that certain surface sites exhibit enhanced reactivity over their neighbors, which under the Taylor school of thought is understood to stem from their unique position on the supporting lattice.[6] Ultimately, this apparent irregularity along the surface landscape, wherein specific sites are imbued with enhanced reactivity, has led to the identification of "special sites" on catalytic surfaces.[7] For example, C–H activation of methane by Pt nanoparticles has been shown to correlate linearly with the number of Pt atoms along twin boundary sites,[8] and the activity of MoS_2 nanoflakes for electrocatalytic hydrogen evolution scales directly with the number of exposed edge sites.[9,10] At solid-state interfaces, the experimental identification of these sites is exceedingly challenging, typically requiring a well-defined model system, the access to which can present an obstacle of its own.[11] As one example, Au(111)-adsorbed MoS_2 nanoflakes have been imaged by scanning tunneling microscopy with atom-scale resolution to reveal both size-dependent and site-specific vacancy generation and substrate activation in hydrodesulfurization catalysis.[12] Moreover, heterogenous interfaces are often structurally dynamic, with active site correlation and surface restructuring effects giving rise to meta-stable surface phases during catalysis, complicating what was already a challenging problem.[13–17] Beyond a structural analysis, the electronic factors that lead to active site speciation and reactivity are complex and often poorly understood.[6,18,19]

Drawing upon Muetterties' cluster-surface analogy, molecular nanoclusters provide a well-defined environment to study metal-support interactions and active site identity and mechanism with atomic precision.[20] There are several reports of molecular metal oxide and sulfide clusters

that have been used to study the electronic properties and reactivity of heterogeneous catalysts for water oxidation and hydrogen evolution.[21–25] For example, Tilley and coworkers reported a cubane-type [$MnCo_3O_4$] cluster as a model for Mn-doped cobalt oxide, and demonstrated that the [Co_3O_4] core acts as a redox-reservoir to support ligand exchange chemistry at the exposed Mn site.[26] Further, Patzke reported a molecular [Co_4O_4] cubane cluster as a stable water oxidation catalyst, replicating the edge-site reactivity of heterogeneous water oxidation catalysts within atomically defined model system.[27] Although these systems successfully replicate catalytic behavior, some ambiguity often remains as to the true identity of the catalytically active species.[28–30] One powerful method to experimentally verify the identity of the catalytic active site is through the isolation and study reactive species formed upon substrate activation and transfer. To this end, there are a growing number of transition metal clusters that illustrate how the exposed polymetallic facets of a cluster core can engage in substrate activation.[31–33] Although these systems grant critical insights into the cooperative interaction of multiple metal centers during surface-based transformations, it can be argued that they do not capture the structural complexity of a surface-supported active site. The electronic interactions present within metal-support interfaces have been showcased in a several of molecular clusters wherein a substrate accessible surface metal is anchored directly to a polymetallic support.[22,34–37] However, within these systems the active site is often rigidly bound by the support, thereby inhibiting any coordinative dynamics between the surface metal and supporting lattice. Although these studies grant key insights regarding metal-support interactions, it is desirable to have a cluster platform in which multiple active sites are stabilized and differentiated on an inorganic support.

We have developed a well-defined nanocluster platform, $M_3Co_6Se_8L^{Tol}_6$ (M = Fe, Co, Cr, Zn; L^{Tol} = Ph_2PNTol, Ph = phenyl, Tol = 4-tolyl), in which three low-coordinate edge metals are dispersed on a Co_6Se_8 support.[38–42] Though a series of studies, we have explored the electronic and coordinative aspects of the metal-support interactions present within these clusters and demonstrated their utility as pre-templated building blocks for materials synthesis. We have demonstrated that this system is an excellent catalyst for the activation of tosyl azide (TsN_3) and subsequent transfer of this nitrene group to an isocyanide for carbodiimide synthesis.[38,41] We have also shown that the degree of electronic cooperativity between active site and support correlates directly with catalytic activity.[43] By equipping this cluster platform with Cr surface sites, we were able to localize redox chemistry to the edge metals, thereby taming the reactivity of key catalytic

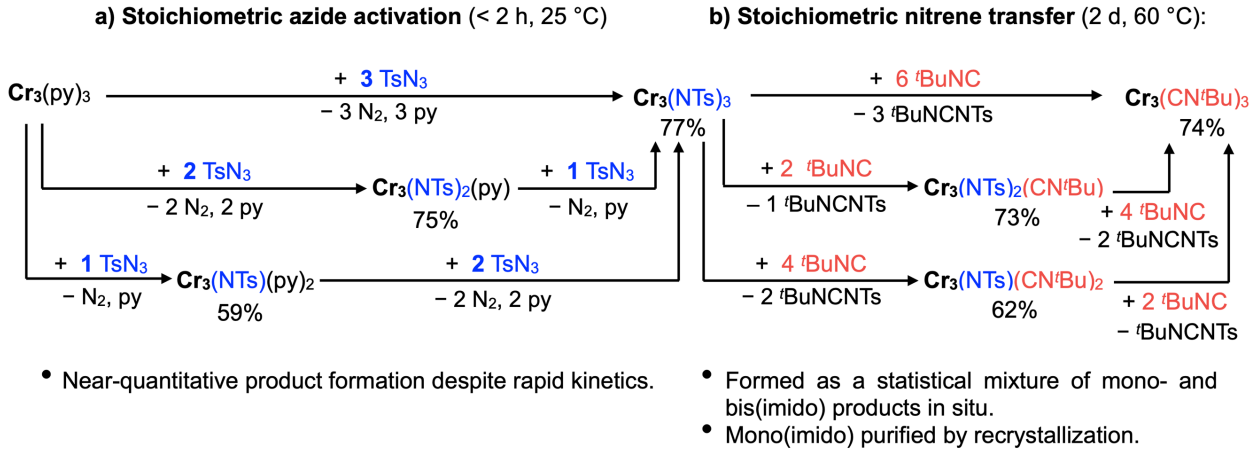
intermediates to grant their isolation. Ultimately, we found that through-cluster active site interactions regulated nitrene transfer kinetics between as the Cr edge sites become chemically differentiated on the cluster surface. Here, we explore the electronic origins of active site speciation within this Cr/Co/Se cluster in detail.

6.3 Site-differentiated Azide Activation and Nitrene Transfer

We previously demonstrated that all three of the Cr surface sites of **Cr$_3$**(py)$_3$ can be equipped with N-tosyl imido groups via treatment with tosyl azide, generating the isolable tris(imido) nanocluster **Cr$_3$**(NTs)$_3$. Through stoichiometric and catalytic nitrene transfer experiments, we showed that these Cr(NTs) edges readily react with two equivalents of *tert*-butyl isocyanide to afford the asymmetric carbodiimide, TsN=C=N^{t}Bu, in addition to an isocyanide-capped Cr(CN^{t}Bu) edge site. By manipulating the stoichiometry of CN^{t}Bu we were able to isolate the catalytically competent nitrene transfer intermediate **Cr$_3$**(NTs)(CN^{t}Bu)$_2$, which features a mixture of Cr(NTs) and Cr(CN^{t}Bu) edges.

Here, we explore how stoichiometric control over TsN$_3$ or CN^{t}Bu equivalency can grant access a complete family of nanoclusters bearing mixed Cr(py), Cr(NTs) and Cr(CN^{t}Bu) edge sites. To this end, treatment of **Cr$_3$**(py)$_3$ with one or two equivalents of TsN$_3$ yields the corresponding mono and bis(imido) nanoclusters, **Cr$_3$**(NTs)(py)$_2$ and **Cr$_3$**(NTs)$_2$(py), which are isolated in 59% and 75% yield, respectively (Scheme 6.1a). As we observed previously, ^{1}H NMR spectroscopy reveals that azide activation occurs rapidly, concluding within just 15 minutes of mixing the reagents at room temperature. Despite rapid azide activation kinetics, *in situ* reaction monitoring reveals the mono- and bis(imido) products are formed near-quantitatively (see Sections 5.6.10 and). Conversely, nitrene transfer proceeds more slowly and favors formation of product mixtures (Scheme 6.1b). For example, *in situ* ^{1}H NMR monitoring of the reaction of **Cr$_3$**(NTs)$_3$ with 4 equiv CN^{t}Bu reveals that after 48 h the major product **Cr$_3$**(NTs)(CN^{t}Bu)$_2$ is contaminated with both **Cr$_3$**(CN^{t}Bu)$_3$ and **Cr$_3$**(NTs)$_2$(CN^{t}Bu) (Figure 6.2). Similarly, treatment of **Cr$_3$**(NTs)$_3$ with 2 equiv CN^{t}Bu affords a new bis(imido) nanocluster, **Cr$_3$**(NTs)$_2$(CN^{t}Bu), that is contaminated with both **Cr$_3$**(NTs)$_3$ and **Cr$_3$**(NTs)(CN^{t}Bu)$_2$ (Figure 6.27). While the mono(imido) derivative, **Cr$_3$**(NTs)(CN^{t}Bu)$_2$, can be purified by bulk crystallization, which also enabled the determination of its single crystal X-ray structure (Figure 5.14), recrystallized samples of **Cr$_3$**(NTs)$_2$(CN^{t}Bu) remain contaminated with small amounts of these impurities.

Comparison of the ^{1}H NMR profiles of this nanocluster series reveals that the unique edge sites exhibit diagnostic paramagnetic ^{1}H resonances in distinct regions of the spectrum. This observation is perhaps unsurprising considering the electronic differences between reduced Cr(CN^{t}Bu)/Cr(py) and oxidized Cr(NTs) edge sites, which feature formal oxidation states of Cr(II) and Cr(IV), respectively. By mapping out the ^{1}H resonances associated with Cr(NTs), Cr(py) or Cr(CN^{t}Bu) edge sites we can draw key insights into the identity and symmetry of these products (Figure 6.3). Whereas **Cr$_3$**(py)$_3$ exhibits a single set of broad paramagnetic resonances due to rapid exchange of surface-bound pyridyl ligands, we showed that the Cr(NTs) edges of **Cr$_3$**(NTs)$_3$ are locked into a low-symmetry (α,α,β) conformation that persists even at elevated temperatures in solution. Notably, for each Cr(NTs) edge we observe a set of three N-tosyl-*H* resonances (Figure 6.4). By comparison, the mono(imido) cluster **Cr$_3$**(NTs)(py)$_2$ exhibits a complex ^{1}H NMR profile featuring a single set of Cr(NTs) resonances and desymmetrized Cr(py) resonances, suggesting after introduction of the imido group, the pyridyl ligands adopt a singular preferred conformation.



Scheme 6.1. Stoichiometric azide activation and nitrene transfer to yield a series of site-differentiated Cr(NTs)/Cr(py)/Cr(CN^{t}Bu) nanoclusters.

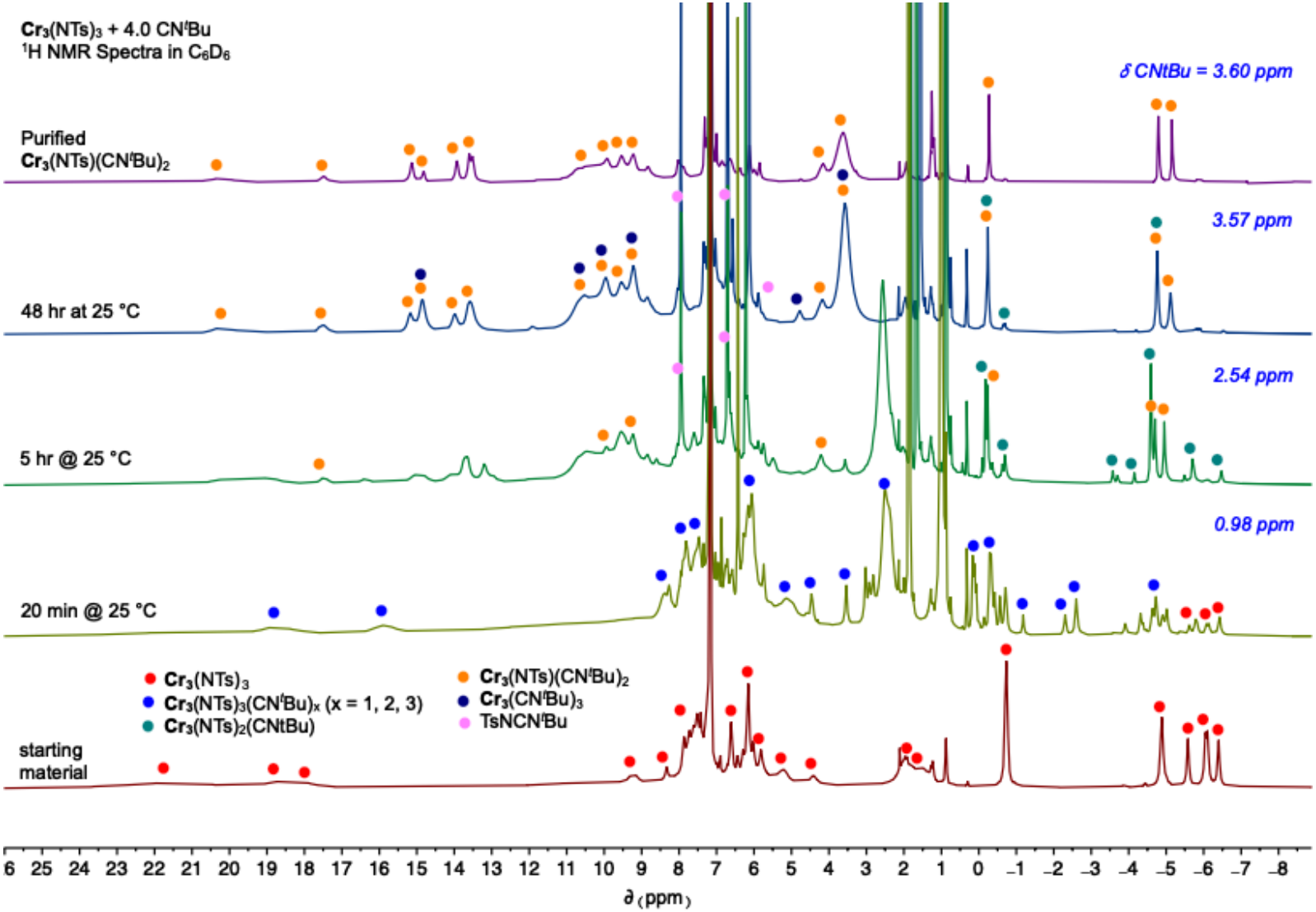


Figure 6.2. ^{1}H NMR (C_6D_6, 25 °C, 500 MHz) spectra tracking the reaction of **Cr$_3$**(NTs)$_3$ with CN^{t}Bu (4 equiv). Spectra recorded at different timepoints in the reaction were plotted in comparison to the starting material, **Cr$_3$**(NTs)$_3$, and the purified product, **Cr$_3$**(NTs)(CN^{t}Bu)$_2$.

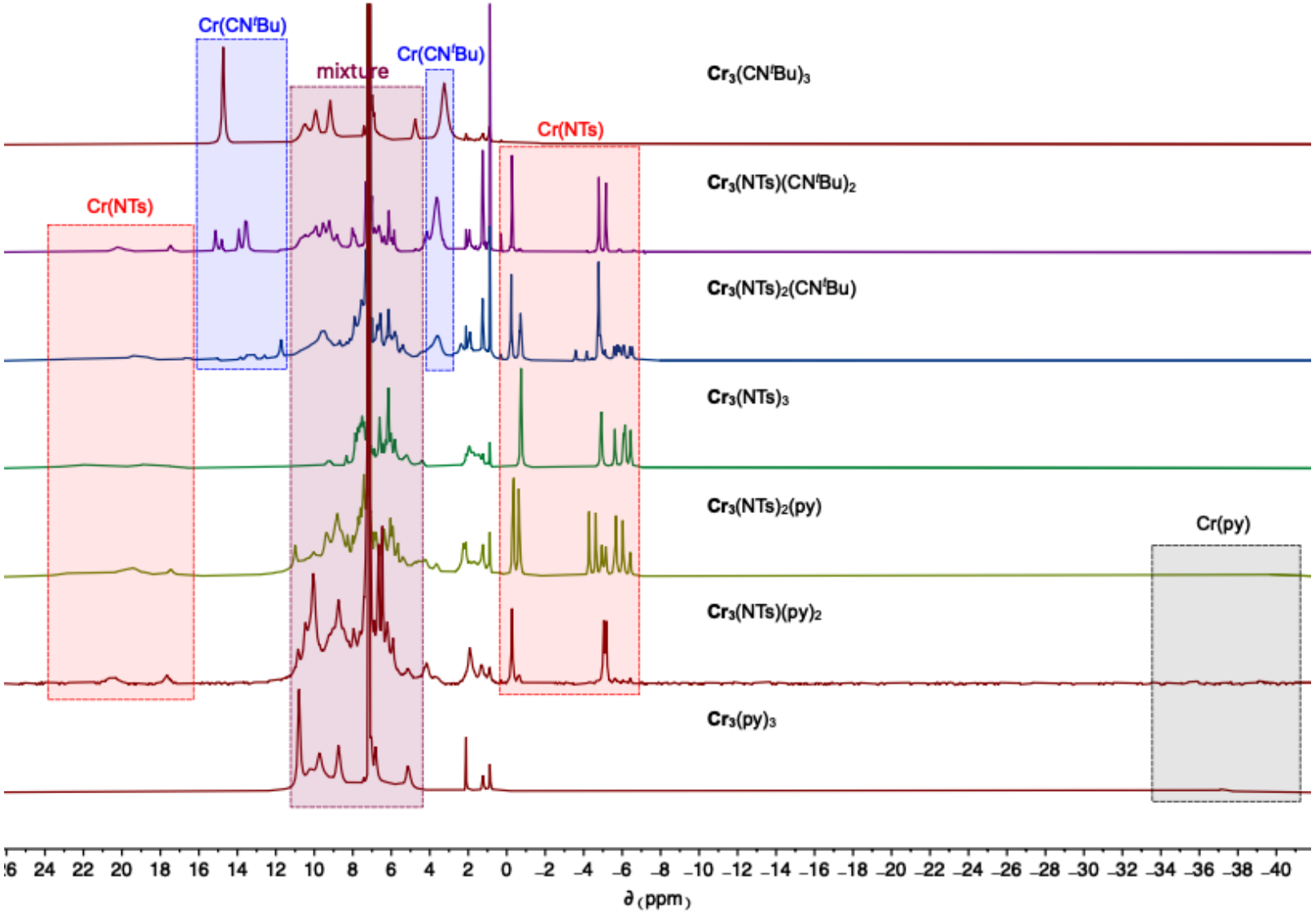


Figure 6.3. ^{1}H NMR (C_6D_6, 25 °C, 300 MHz) spectra of **Cr$_3$**(CN^{t}Bu)$_3$, **Cr$_3$**(NTs)(CN^{t}Bu)$_2$, **Cr$_3$**(NTs)$_2$(CN^{t}Bu), **Cr$_3$**(NTs)$_3$, **Cr$_3$**(NTs)$_2$(py), **Cr$_3$**(NTs)(py)$_2$, and **Cr$_3$**(py)$_3$ (listed from top to bottom), with boxes included to highlight diagnostic spectral features.

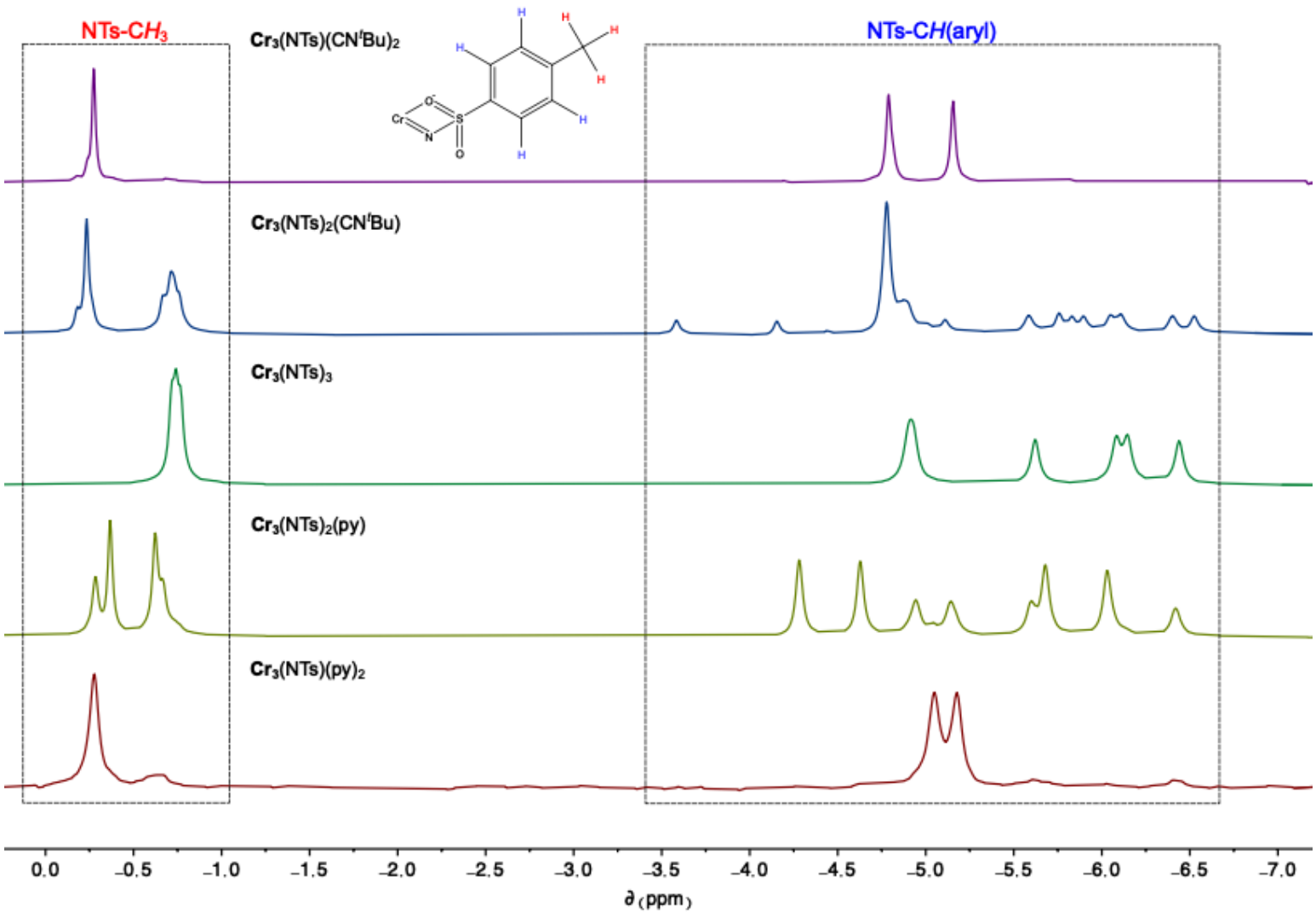


Figure 6.4. ^{1}H NMR (C_6D_6, 25 °C, 300 MHz) spectra of **Cr$_3$**(NTs)(CN^{t}Bu)$_2$, **Cr$_3$**(NTs)$_2$(CN^{t}Bu), **Cr$_3$**(NTs)$_3$, **Cr$_3$**(NTs)$_2$(py), and **Cr$_3$**(NTs)(py)$_2$, highlighting the N-tosyl ^{1}H region.

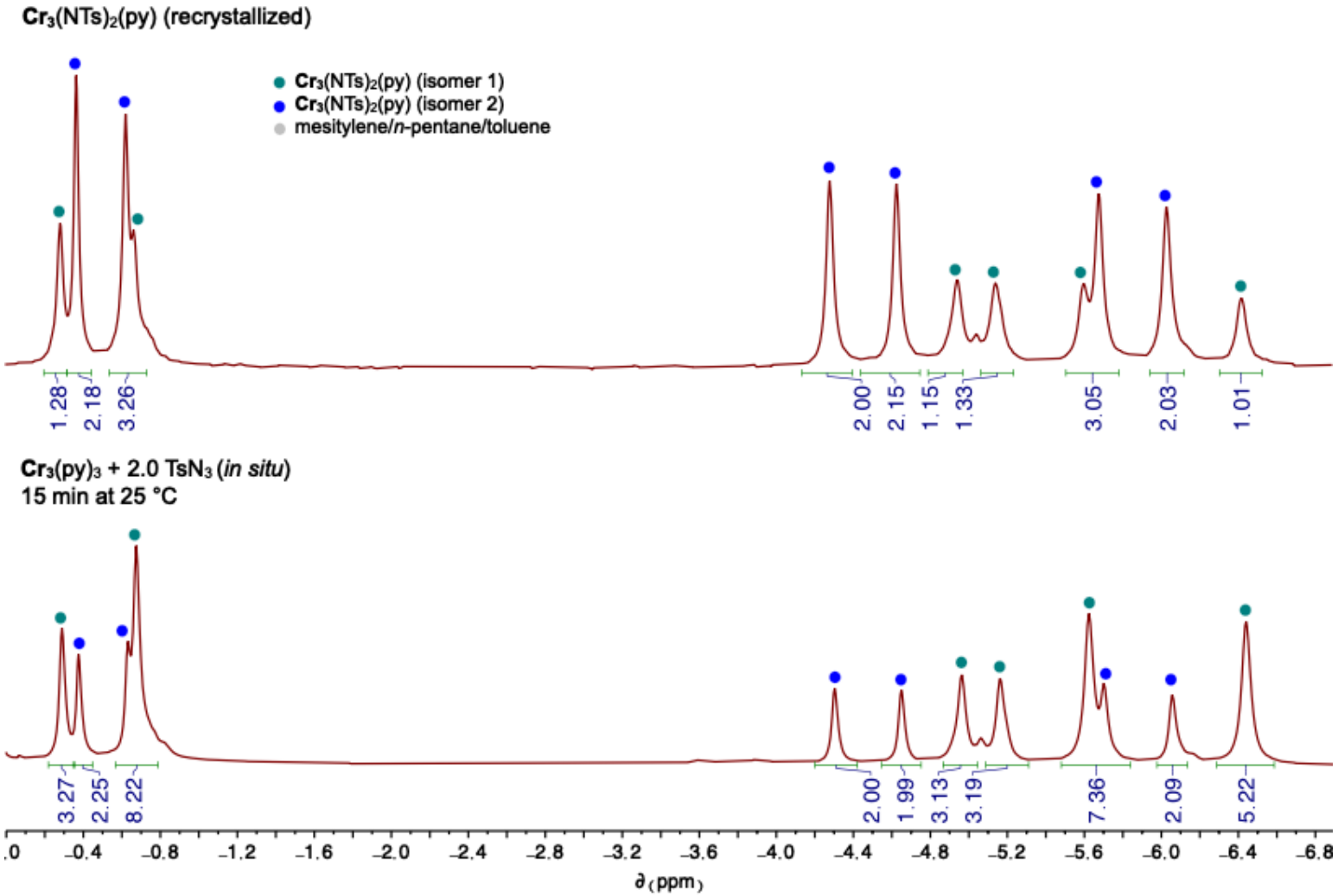


Figure 6.5. ^{1}H NMR (C_6D_6, 25 °C, 500 MHz) spectra tracking the reaction of **Cr$_3$**(py)$_3$ with TsN_3 (2 equiv). The *in situ* reaction mixture after 15 min is plotted in comparison to that of purified **Cr$_3$**(NTs)$_2$(py) in C_6D_6.

Due to the near-coincidence of its Cr(NTs) resonances with those observed for **Cr$_3$**(NTs)(CN^{t}Bu)$_2$, we predict that **Cr$_3$**(NTs)(py)$_2$ assumes the same conformation as the isocyanide-bound derivative, although it has proven difficult to grow high quality single crystals of this species. The selective formation a single mono(imido) product is intriguing in that it suggests either site-specific azide activation or, perhaps more plausibly, a rearrangement of the pyridyl ligands after imido formation.

This NMR analysis also reveals that in ensemble the differentiation of Cr-centers on the Co_6Se_8 surface can afford diastereomeric nanoclusters. This unique scenario is observed in the synthesis of the bis(imido) nanocluster, **Cr$_3$**(NTs)$_2$(py). Assuming a general preference for (α,α,β) isomerism, **Cr$_3$**(NTs)$_2$(py) could exist in three diastereomeric forms in which the Cr–Se bonds of the Cr(NTs) edges are oriented (α,α), *cis*-(α,β) or *trans*-(α,β), respectively. Here, α and β denote the top and bottom halves of the Co_6Se_8 support, respectively. Experimentally, **Cr$_3$**(py)$_3$ reacts with 2 equivalents of TsN_3 to form two bis(imido) products in a 3:2 ratio, best distinguished by the two complete sets of six NTs-*H* resonances (Figure 6.5). The purification of the products by recrystallization inverts this ratio to approximately 1:2 (75% combined isolated yield, see Section 6.12.7.1). The selective formation of two diastereomers in an unequal ratio may signify that azide activation proceeds at different rates at the two Cr(py) sites of the mono(imido) intermediate **Cr$_3$**(NTs)(py)$_2$. Notably, in contrast to the isocyanide and pyridyl derivatives of the mono(imido) **Cr$_3$**(NTs)(L)$_2$, the bis(imido) clusters **Cr$_3$**(NTs)$_2$(py) and **Cr$_3$**(NTs)$_2$(CN^{t}Bu) exhibit highly dissimilar Cr(NTs) ^{1}H resonances, indicating that the diastereomeric products formed upon imido-group installation may be distinct from those formed in nitrene transfer.

6.4 Crystallization of a Diastereomeric Bis(imido) Nanocluster

We were able to grow high-quality single crystals of one of these bis(imido) diastereomers and confirm its structure via X-ray diffraction analysis (Figure 6.6a). As anticipated from the NMR analysis, a defining structural feature is the orientation of the Cr(NTs)–Se bonds, which adopt a *trans*-(α,β) configuration where they are localized to Se atoms on opposite α/β-corners of the Co_6Se_8 support. This conformation may be favorable in that it maximizes the separation of contracted Cr(NTs)–Se bonds on the cluster support. As was observed for the tris(imido) **Cr$_3$**(NTs)$_3$, the two tosyl-imido groups coordinate the edge Cr via N/O-chelation to afford distorted

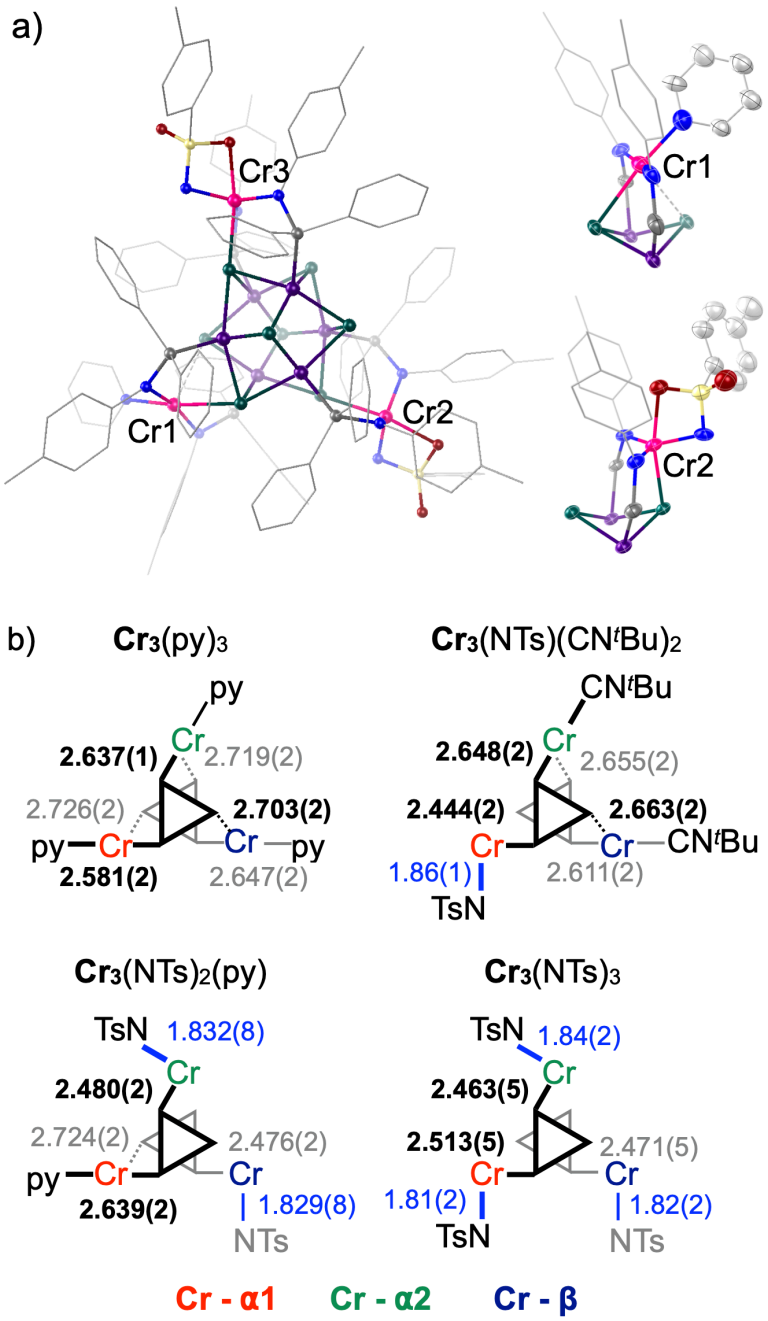


Figure 6.6. a) Single crystal X-ray structure of *trans*-(α,β,α)-**Cr$_3$**(NTs)$_2$(py) with insets highlighting Cr(py) and Cr(NTs) edge sites. b) Comparison of Cr···Se (α, black; β, gray) and Cr-NTs (blue) bond metrics across the crystallographically characterized Cr(NTs)/Cr(py)/Cr(CN^{t}Bu) series. Thermal ellipsoids plotted at 50% probability. Hydrogen atoms and co-crystallizing solvent omitted for clarity.

trigonal bipyramidal metal centers (τ_5 = 0.68, 0.71), while the third Cr remains capped by a pyridyl ligand in the pseudo-square pyramidal geometry observed for **Cr$_3$**(py)$_3$ (τ_5 = 0.10).

6.5 Structural Trends in Site-differentiated Cr/Co/Se Clusters

A comparative structural analysis of the Cr···Se and Cr–N_{Ts} bond lengths in **Cr$_3$**(py)$_3$, **Cr$_3$**(NTs)$_3$, **Cr$_3$**(NTs)$_2$(py), and **Cr$_3$**(NTs)(CN^{t}Bu)$_2$ enables us to parameterize the push-pull relationship between Cr(py)/Cr(NTs)/Cr(CN^{t}Bu) surface sites that differ in formal oxidation state, chemical environment, and α/β orientation on the Co_6Se_8 support (Figure 6.6b). Owing to their (α,α,β) configuration, the edge sites in these clusters can be categorized based on their unique position on the Co_6Se_8 support, denoted here as sites α1, α2, and β. Organization of this cluster series within the same α/β orientation exhumes several interesting conclusions, and ultimately points to the presence of a single Cr edge as a "special site" that favors either chemical or structural differentiation from its neighbors.

First, we note that the Cr···Se bond lengths at edge sites within the homoleptic clusters **Cr$_3$**(NTs)$_3$ and **Cr$_3$**(py)$_3$ vary widely despite exhibiting formally equivalent coordination environments. Further, in both **Cr$_3$**(NTs)$_3$ and **Cr$_3$**(py)$_3$ the *trans*-oriented α2 and β edges exhibit nearly identical edge-support bonding metrics, whereas that of the α1 oriented edge deviates significantly. In the case of **Cr$_3$**(py)$_3$, the α1 Cr···Se bond is at least 0.056 Å *shorter* than its neighbors. Interestingly, this trend is reversed in the case of **Cr$_3$**(NTs)$_3$, where the α1 Cr···Se bond is at least 0.042 Å *longer* than that of its neighbors. The bonding trends observed for **Cr$_3$**(NTs)$_3$ can be rationalized via an empirical analysis, in that Cr–Se bond length correlates directly with the number of non-bonding equatorial Se atoms that separate neighboring Cr–Se bonds. Along these lines of analysis the α1 edge is most "crowded" by its neighbors, and therefore has less electron density to draw from the Co_6Se_8 core in Cr–Se bonding. Conversely, the α2 edge has the greatest separation from its neighbors, and as a result exhibits the shortest Cr–Se bond length in **Cr$_3$**(NTs)$_3$. However, this empirical analysis breaks down when considering the trends observed for **Cr$_3$**(py)$_3$, where the α1 edge is still the most crowded by its neighbors, and yet it maintains a markedly shorter Cr–Se bond.

Expanding our analysis to include the heteroleptic clusters **Cr$_3$**(NTs)$_2$(py) and **Cr$_3$**(NTs)(CN^{t}Bu)$_2$, we parameterize the push-pull dynamic between edges of different chemical composition. Interestingly, within both of these site-differentiated clusters, it is the α1 "special site" that favors chemical differentiation from its neighbors. As observed in **Cr$_3$**(NTs)$_3$ and **Cr$_3$**(py)$_3$, *trans*-oriented α2 and β edges in **Cr$_3$**(NTs)$_2$(py) adopt nearly identical Cr–Se bonding

metrics, consistent with the trend observed in the homoleptic derivatives discussed above. Further, these Cr–Se bond are slightly longer than those observed at the α2 and β edge sites in **Cr$_3$**(NTs)$_3$, indicating that the α1 Cr(py) edge has an elongating effect on the neighboring Cr(NTs) edges. A more intriguing observation is made when comparing the Cr–Se bonds of the α1 Cr(py) edges in **Cr$_3$**(NTs)$_2$(py) and **Cr$_3$**(py)$_3$, where we observe an 0.058 Å elongation in the case of **Cr$_3$**(NTs)$_2$(py). Here, we find that the α2 and β Cr(NTs) edges have the same influence on the α1 edge that they did **Cr$_3$**(NTs)$_3$. Extraction of such trends is more challenging for **Cr$_3$**(NTs)(CN^{t}Bu)$_2$, as some variance is observed at the α2 and β Cr(CN^{t}Bu) edges where the shorter equatorial-oriented Cr–Se bonds of the Cr(CN^{t}Bu) edges differ by 0.037 Å. That said, by comparing the α1 Cr(NTs) edges of **Cr$_3$**(NTs)(CN^{t}Bu)$_2$ and **Cr$_3$**(NTs)$_3$, we find the α2 and β Cr(CN^{t}Bu) edges strengthen edge-support bonding at the α1 site by 0.069 Å. Notably, this is the same effect observed at the α1 Cr(py) edge of **Cr$_3$**(py)$_3$, where the α2 and β edges are also capped by L-type pyridyl ligands. As discussed above, this reinforcement in edge-support bonding at α1 site leads to decreased CN^{t}Bu binding affinity and nitrene transfer kinetics at Cr(NTs) edge in **Cr$_3$**(NTs)(CN^{t}Bu)$_2$, which highlights the paramount importance of the edge-support interaction strength within this system. In summary, the structural analysis presented in Figure 6.6 suggests that installation of Cr^{II}(L) (L = CN^{t}Bu or py) edges at positions α2 and β *reinforces* edge-support bonding at the α1 site, whereas installation N-tosyl imido groups at the α2 and β edges *weakens* Cr–Se bonding at the α1 site.

We previously rationalized the observed trends in M–Se as stemming from the inductive influence of the M edges on the Co$_6$Se$_8$ core. For example, the Cr^{II}(CN^{t}Bu) edges of **Cr$_3$**(NTs)(CN^{t}Bu)$_2$ may draw less electron density from the Co$_6$Se$_8$ core, and strength Cr–Se bonding at the remaining Cr^{IV}(NTs) edge relative to those in **Cr$_3$**(NTs)$_3$. While the edge sites likely do influence one another through inductive effects, this line of analysis cannot rationalize the inversion of bonding trends observed for **Cr$_3$**(py)$_3$ and **Cr$_3$**(NTs)$_3$. As a result, we turned to computational analysis to investigate the electronic origins of active site speciation within the Cr/Co/Se cluster series.

6.5.1 *Activation of Benzyl Azide Affords Benzaldimine-Bound Nanocluster*

Curious as to whether similar reactivity with a non-sulfonyl azide would yield a more linear nitrenoid group or alter the edge-support binding motif, we tested the reactivity of **Cr$_3$**(py)$_3$ with

both aromatic (ex. *p*-tolyl-N_3, *p*-MeO-phenyl-N_3) and aliphatic (benzyl-N_3) azides. While no reaction appears to transpire with the aromatic derivatives under either photolytic or thermal conditions, photolysis of **Cr$_3$**(py)$_3$ in the presence of benzyl azide (BnN_3, 3 equiv) promotes the evolution of nitrogen and the formation of new paramagnetic products. After prolonged irradiation (20 h), the major product lacks paramagnetic ^{1}H NMR resonances reminiscent of **Cr$_3$**(NTs)$_3$, and instead resembles the tris(pyridyl) starting material.

Single crystal X-ray characterization of this product reveals that after nitrogen extrusion each benzyl nitrenoid group has undergone an intramolecular 1,2-hydrogen atom shift to yield a benzaldimine ligand, NH=CH–Ph, at the edge sites (Figure 6.7).[44–50] There are several examples of this intramolecular transformation in the literature, although this is the first example reported at chromium. The tris(benzaldimine) cluster, **Cr$_3$**(NHCHPh)$_3$, exhibits a geometry highly similar to that observed for Cr$_3$(py)$_3$, with each Cr center bound κ^4 by the cluster-ligand and one benzaldimine ligand in square pyramidal geometry (τ_5 = 0.12). The Cr–N_{imine} distances range between 2.05(1) and 2.10(2) Å, comparable to the Cr–N_{py} distances observed in **Cr$_3$**(py)$_3$. This tris(benzaldimine) cluster **Cr$_3$**(NHCHPh)$_3$ exhibits the same (α,α,β) site differentiation that was observed for the pyridyl analogue, with the same trend in Cr···Se bond lengths. Additionally, the imino N–C bond lengths are highly contracted (avg. 1.26 Å) and N–C–C bond angles are observed

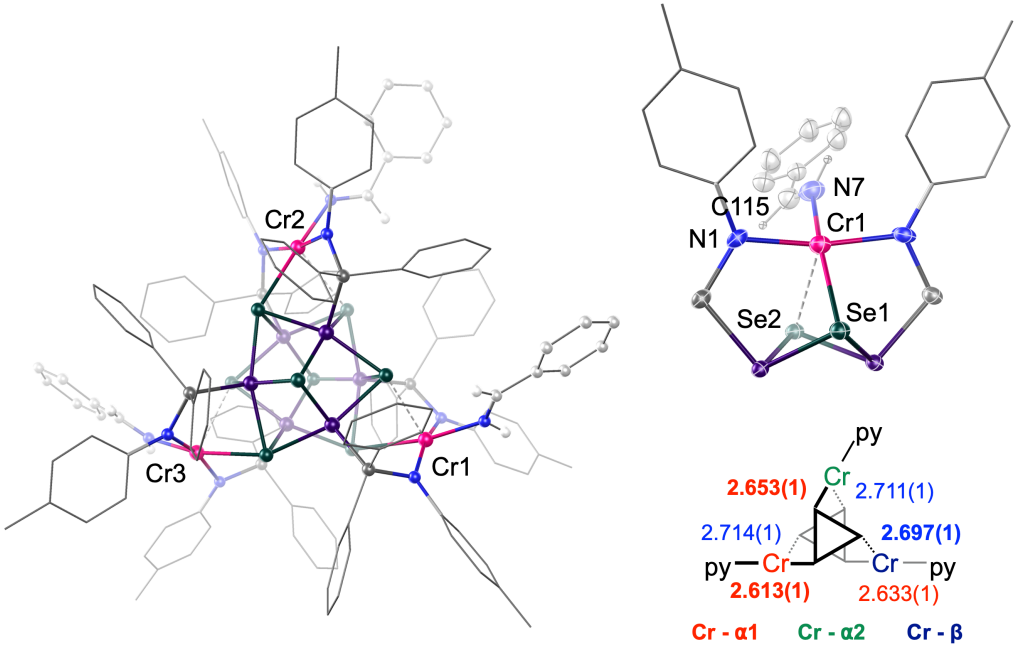


Figure 6.7. Single crystal X-ray structure of **Cr$_3$**(NHCHPh)$_3$ with an inset highlighting the Cr(NHCHPh) edge site. Select interatomic distances (Å): Cr1-N7 2.073(6), Cr1-Se1 2.633(1), Cr1-Se2 2.697(1), Cr1-N1 2.046(5), C115-N7 1.274(8).

between 123.7° and 127.7°, consistent with sp^2 hybridization at nitrogen and the presence of a N=C double bond. These data suggest that we form a nitrenoid intermediate with significant iminyl radical character favoring intramolecular H-atom abstraction.[51]

6.6 Computational Analysis Provides Molecular Orbital Basis for Active Site Differentiation

A computational analysis of the Cr(NTs)/Cr(py) cluster series, $\mathbf{Cr_3}(py)_3'$, $\mathbf{Cr_3}(NTs)(py)_2'$, $\mathbf{Cr_3}(NTs)_2(py)'$, and $\mathbf{Cr_3}(NTs)_3'$, reveals the electronic impact of imido group installation at the Cr surface sites and provides a molecular orbital basis for active site differentiation at the cluster surface. The $\mathbf{Cr_3}'$ clusters were optimized at the uBPV86/def2SVP level of theory, once again using a minimally adapted phosphinoamide ligand platform, $Ph_2PN^{(-)}Ph$, and sulfonyl imido group, $PhSO_2N^{2-}$. Analytical frequency calculations were performed to verify that optimization proceeds to a stable ground state geometry. Single-point electronics were then calculated at the uB3LYP+/cc-pVTZ level of theory. Spin-multiplicity assignments for these calculations were informed by solid-state magnetometry data collected for $\mathbf{Cr_3}(py)_3$ and $\mathbf{Cr_3}(NTs)_3$, which exhibits magnetic susceptibilities consistent with 3 x S = 2 Cr(II) or 3 x S = 1 Cr(IV) high spin electronic configurations, respectively (see Section 6.9). Further, as anticipated based on our magnetic analysis, Mulliken single-density analysis reveals that the majority of the unpaired spin localizes to the Cr edge sites, with minor contributions from the Co_6Se_8 core observed for $\mathbf{Co_3}(py)_3$ (Figure 6.8).

6.6.1 *Density of States Analysis*

As was the case in our computational analysis of $[\mathbf{Fe_3}]^+$, these systems are comprised of an exceedingly large number of electronic states, and so the overarching electronic structure of the Cr/Co/Se cluster core once again is most easily visualized via a density of states analysis. Partial density of states (*p*-DOS) plots were calculated for the Cr(NTs)/Cr(py) nanocluster series, $\mathbf{Cr_3}(py)_3'$, $\mathbf{Cr_3}(NTs)(py)_2'$, $\mathbf{Cr_3}(NTs)_2(py)'$, and $\mathbf{Cr_3}(NTs)_3'$, including contributions from Cr 3d, Se 4p, and Co 3d orbitals (Figure 6.9). At first glance, we recognize an appreciable amount of overlap between Cr 3d, Se 4p, and Co 3d orbitals, indicative of the covalency anticipated for a metal-selenide framework. Drawing back to our original hypothesis that metallation with Cr(II)

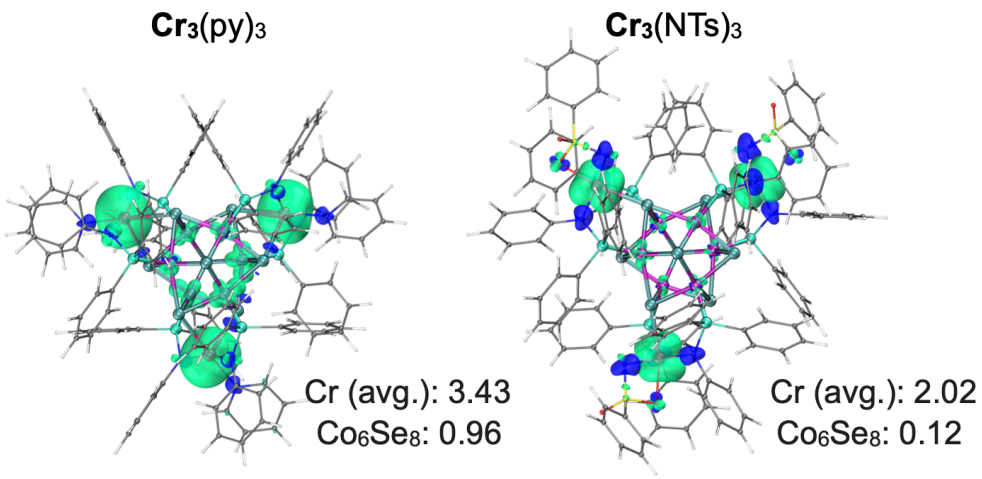


Figure 6.8. Mulliken spin density (*a*-*b*) isosurface plots (0.004 a.u.) of $\mathbf{Cr_3}(py)_3'$ and $\mathbf{Cr_3}(NTs)_3'$. Positive spin density values (green) are tabulated for the Cr edge metals and Co_6Se_8 core.

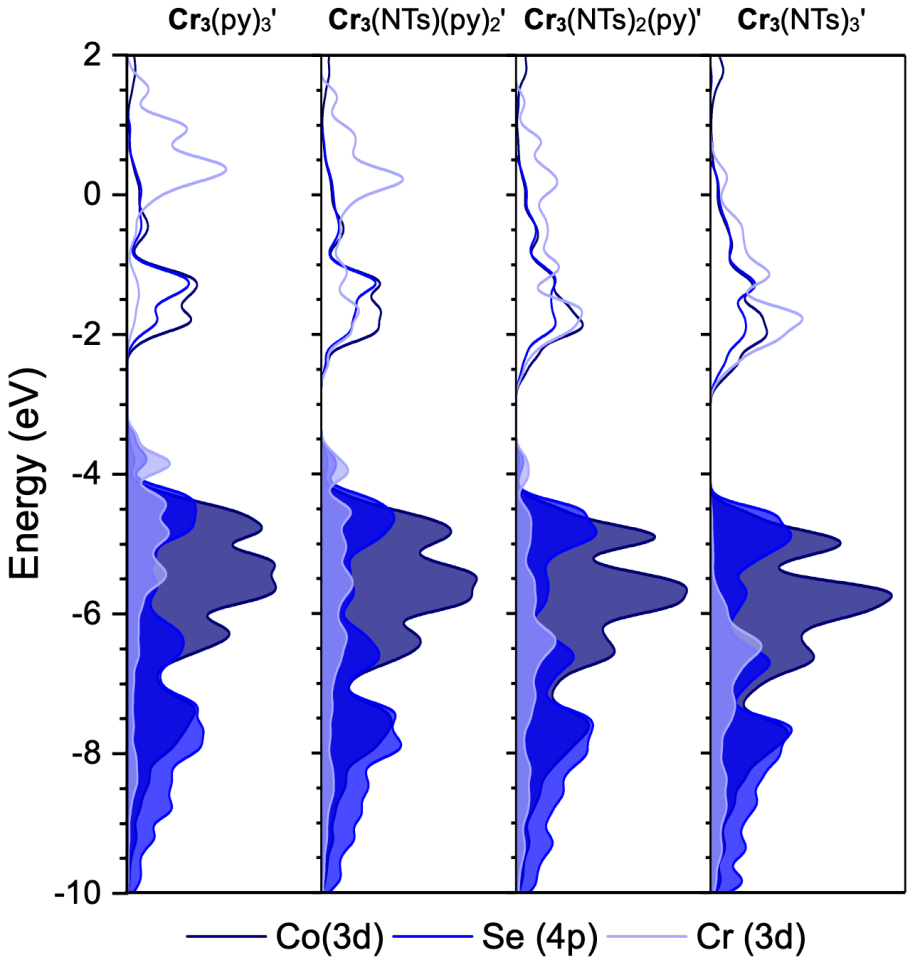


Figure 6.9. Partial density of states plots illustrating Co 3d , Se 4p and Cr 3d orbital contributions for $\mathbf{Cr_3}(py)_3'$, $\mathbf{Cr_3}(NTs)(py)_2'$, $\mathbf{Cr_3}(NTs)_2(py)'$, and $\mathbf{Cr_3}(NTs)_3'$. Calculations run at the uB3LYP+/cc-PVTZ level of theory.

would localize redox chemistry to the surface metals, *p*-DOS analysis of **Cr$_3$**(py)$_3$′ reveals that the HOMO is primarily localized to the Cr^{II}(py) edge sites, with minor contributions from the Co/Se core. However, as we traverse from **Cr$_3$**(py)$_3$′ to **Cr$_3$**(NTs)$_3$′ via installation of imido groups, these high-lying Cr(II) states are depleted until the highest filled states have little-to-no Cr 3d character. Ultimately, we note that as the Cr centers are oxidized, the remaining filled Cr 3d states are buried deep beneath the Fermi level, concentrating around –6.5 eV, which is a reflection not only of the depletion of Cr 3d states, but also the reinforced Cr–N^{Tol}, Cr–N^{Ts}, and Cr–Se bonding observed for Cr(NTs) edge sites in the solid state. Finally, with installation of the imido groups we observe an aggregation of Cr 3d contributions at unfilled states near the LUMO. This stands in contrast to **Cr$_3$**(py)$_3$′, wherein the LUMO primarily consists of Co 3d character.

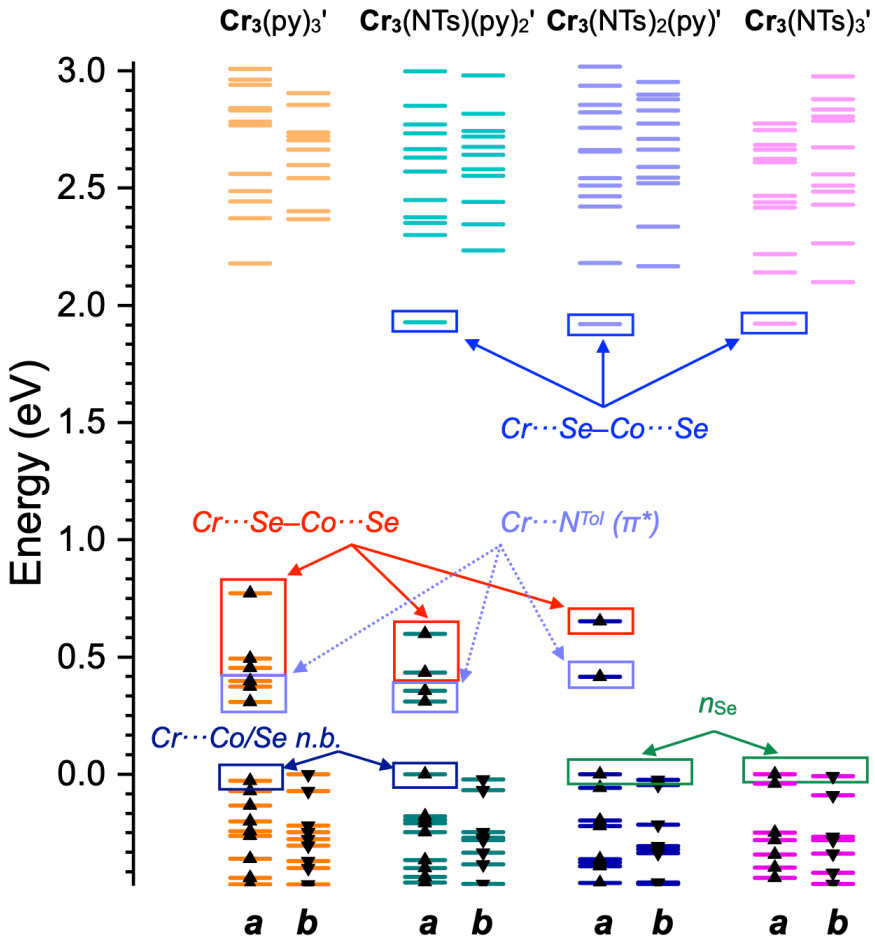


Figure 6.10. Frontier molecular orbital diagrams of **Cr$_3$**(py)$_3$′, **Cr$_3$**(NTs)(py)$_2$′, **Cr$_3$**(NTs)$_2$(py)′, and **Cr$_3$**(NTs)$_3$′, normalized to the highest-lying core-centered electronic states. Orbital topology is denoted in text that is color-coded to pair with representative molecular orbital plots provided below. Separate spin manifolds are denoted as *a* and *b*. All calculations run at the uB3LYP+/cc-PVTZ level of theory.

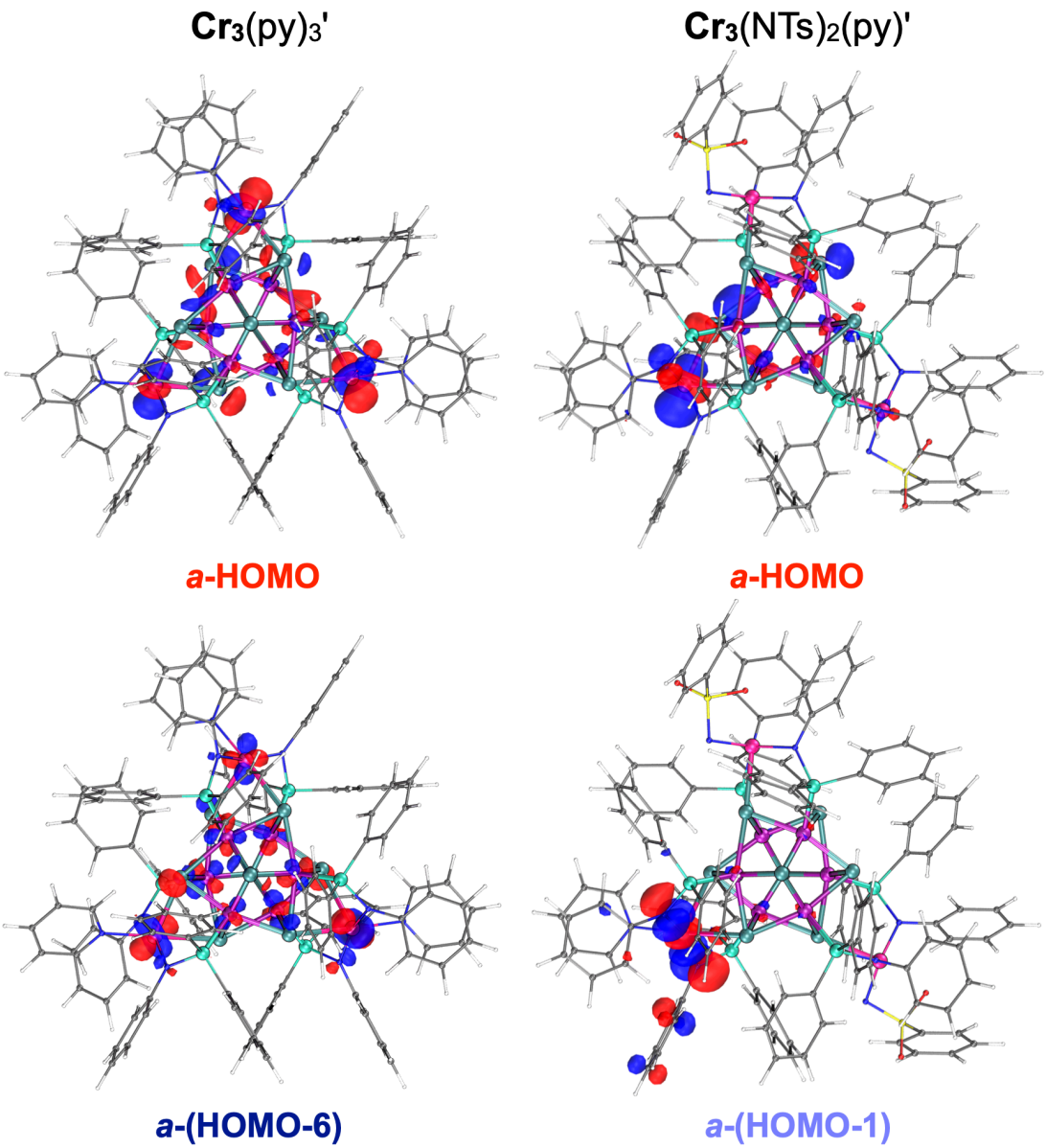


Figure 6.11. Isosurface plots (0.04 a.u.) for select frontier orbitals of **Cr**$_3$(py)$_3$′ and **Cr**$_3$(NTs)$_2$(py)′. All calculations run at the uB3LYP+/cc-PVTZ level of theory.

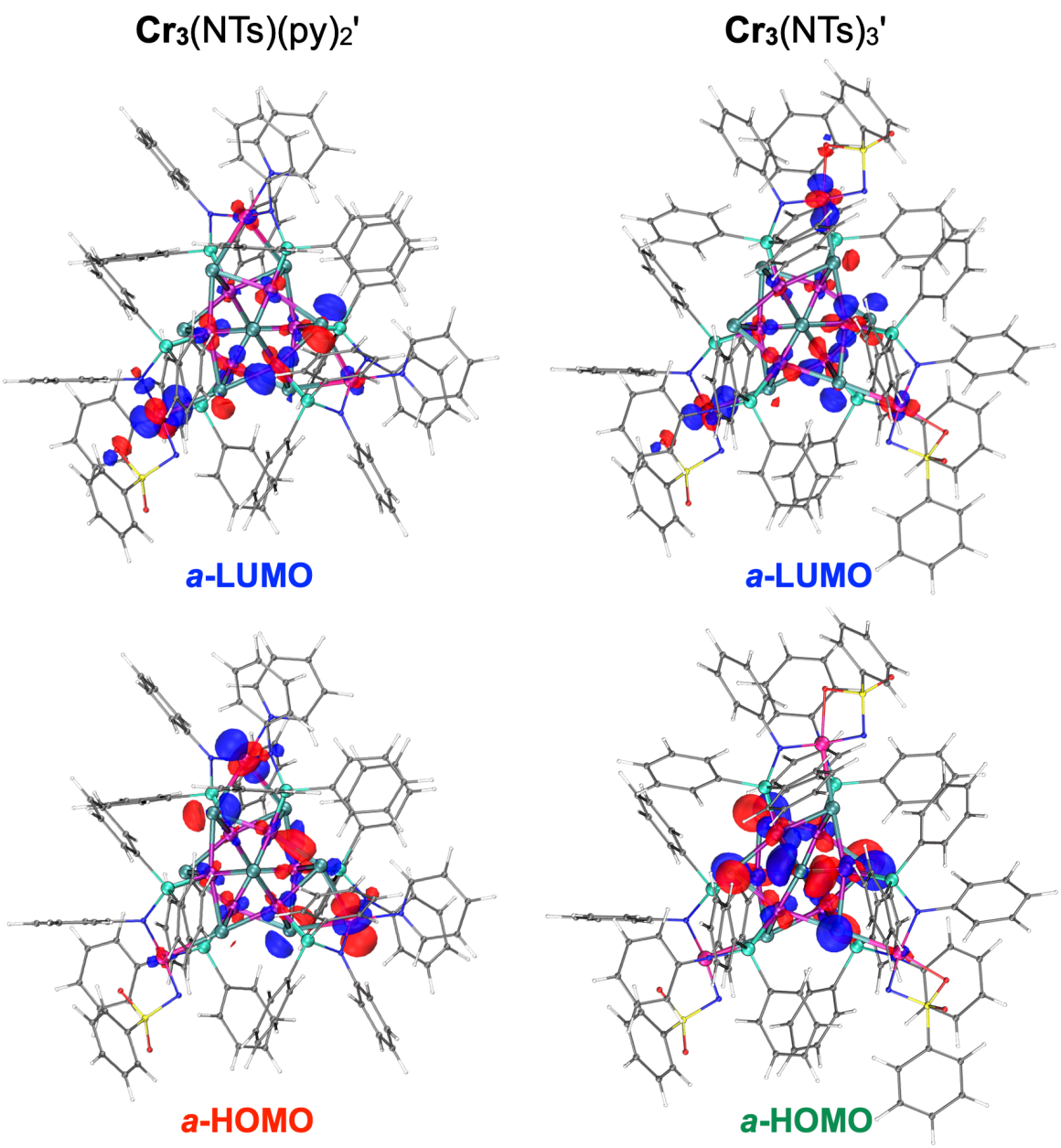


Figure 6.12. Isosurface plots (0.04 a.u.) for select frontier orbitals of **Cr$_3$**(NTs)(py)$_2$′ and **Cr$_3$**(NTs)$_3$′. All calculations run at the uB3LYP+/cc-PVTZ level of theory.

6.6.2 *Inspection of Frontier Molecular Orbitals*

A more detailed examination of the frontier molecular orbitals for this cluster series further clarifies the electronic signature of Cr(py) and Cr(NTs) edge sites and outlines the presence of multi-center Cr/Co/Se covalency in edge-support bonding. Molecular orbital diagrams for **Cr$_3$**(py)$_3$′, **Cr$_3$**(NTs)(py)$_2$′, **Cr$_3$**(NTs)$_2$(py)′, and **Cr$_3$**(NTs)$_3$′ are provided in Figure 6.10 and select orbital isosurface plots are provided in Figure 6.11 and Figure 6.12.

Several conclusions can be gleaned from a molecular orbital analysis of the Cr(py)/Cr(NTs) cluster series. As alluded to in the *p*-DOS analysis above, we find that each Cr(py) edge site introduces two Cr-centered states near the Fermi level. Although these orbitals are complex, especially when multiple Cr(py) edges are present as is the case for **Cr$_3$**(py)$_3$′, careful inspection of the corresponding isosurface plots grants key insights into their bonding character. The highest-lying of these Cr(II) orbitals adopt *Cr···Se–Co···Se* edge-support antibonding character as they project from each Cr(py) edge site into the Co_6Se_8 support. Notably, these singly-occupied *Cr···Se* antibonding orbitals are oriented along each axial Cr–Se bond, which are markedly weakened in the solid-state relative to their equatorial counterparts. The topology of this antibonding *Cr···Se–Co···Se* orbital can be most clearly viewed in the HOMO of **Cr$_3$**(NTs)$_2$(py)′, where there is a singular Cr(py) edge (Figure 6.11). By contrast, in the case of **Cr$_3$**(py)$_3$′, the three highest lying orbitals are composed of an admixture of *Cr···Se–Co···Se* orbitals stemming from the three Cr(py) edge sites. Immediately below these highest-filled orbitals, a second set of Cr-centered orbitals are observed, one for each pyridyl edge site, which can be more easily identified as a $Cr\cdots N^{Tol}$ π* interaction.

These high-lying Cr-centered orbitals are depleted as imido groups are installed at the edge sites. Formation of each Cr(NTs) edge is accounted for by a loss of two Cr-centered orbitals until these states are completed quenched in **Cr$_3$**(NTs)$_3$′, where the HOMO is centered on the Co_6Se_8 core. Once again, we observe excellent agreement here between experiment and theory. The depopulation of $Cr\cdots N^{Tol}$ π* orbitals is reflected in the solid-state where we note a 0.15 Å contraction in average Cr–N^{Tol} bond lengths between Cr(py) to Cr(NTs) edge sites, respectively (see Table 6.11). Similar trends cannot be drawn from the depopulation of the antibonding *Cr···Se–Co···Se* orbitals, as these axial Cr···Se interactions are completely absent in the κ^3-bound Cr(NTs) edge sites which bear a singular edge-support contact. Owing to the formal oxidation of Cr edge sites and elimination of these axial Cr···Se bonding interactions, we note that the highest lying

core-centered electronic states adopt increased Se 4p character. For example, orbital composition analysis of the **Cr$_3$**(py)$_3$′ *a*-HOMO-6, which is *Cr···Co/Se* non-bonding character, indicates Cr, Co and Se orbital contributions of 31.9%, 24.6%, and 30.5%, respectively. In contrast, the *a*-HOMO of **Cr$_3$**(NTs)$_3$′, predominantly of Se 4p lone pair character, exhibits Cr, Co and Se contributions of 1.5%, 26.7%, and 66.4%, respectively (see also Table 6.6). Finally, upon formation of Cr(NTs) edges, the LUMO adopts *Cr···Se–Co···Se* character. Each Cr(NTs) edge that is generated introduces one of these edge-support antibonding orbitals, which can once again be most clearly observed when there is a single Cr(NTs) edge present, as is the case for **Cr$_3$**(NTs)(py)$_2$ (Figure 6.12).

6.6.3 *Molecular Orbital Basis for Active Site Differentiation*

It is of particular importance that Cr···Se bonding interactions project from the Cr center into the Co_6Se_8 core, as this provides a molecular orbital basis for active site correlation. Here, it is essential to note that for each of these populated or unpopulated *Cr···Se–Co···Se* antibonding interactions, *Cr–Se···Co–Se* and *Cr–Se–Co–Se* bonding interactions can also be observed deeper down within the molecular orbital manifold (Figure 6.41). These various bonding/antibonding combinations are reminiscent to the orbital manifolds invoked in band-theory.[52] In an effort to break away from the sheer complexity of these molecular orbital plots, a qualitative model was put forth wherein edge-support bonding is treated within the confines of atomic orbitals that have appropriate spatial overlap. Along these lines of analysis, dative Cr–Se σ-bonding occurs via overlap of Cr $3d_{z2}$ or $3d_{x2-y2}$ orbitals with the Se $4p_z$ lone pair. However, this Se 4p orbital also has appropriate spatial overlap to interact with the in-line Co $3d_{x2-y2}$ orbital, which in turn overlaps with a distal Se $4p_z$. As implicated by our molecular orbital analysis, Cr···Se bonds *must* be treated as a symmetry adapted linear combination of Cr ($3d_{z2}$ or $3d_{x2-y2}$), Se_a $4p_z$, Co $3d_{x2-y2}$, and Se_b $4p_z$ orbitals (Figure 6.13). Accordingly, for the four orbitals involved in bonding, we may observe four unique orbital combinations, which range from all-bonding to all-antibonding in character. Drawing from our molecular orbital analysis above, we argue that these σ-bonding combinations account for the primary Cr–Se bonding interactions in **Cr$_3$**. Note that a similar treatment can be put forth in the case of the Fe···Se bonding interactions discussed in Chapter 3.

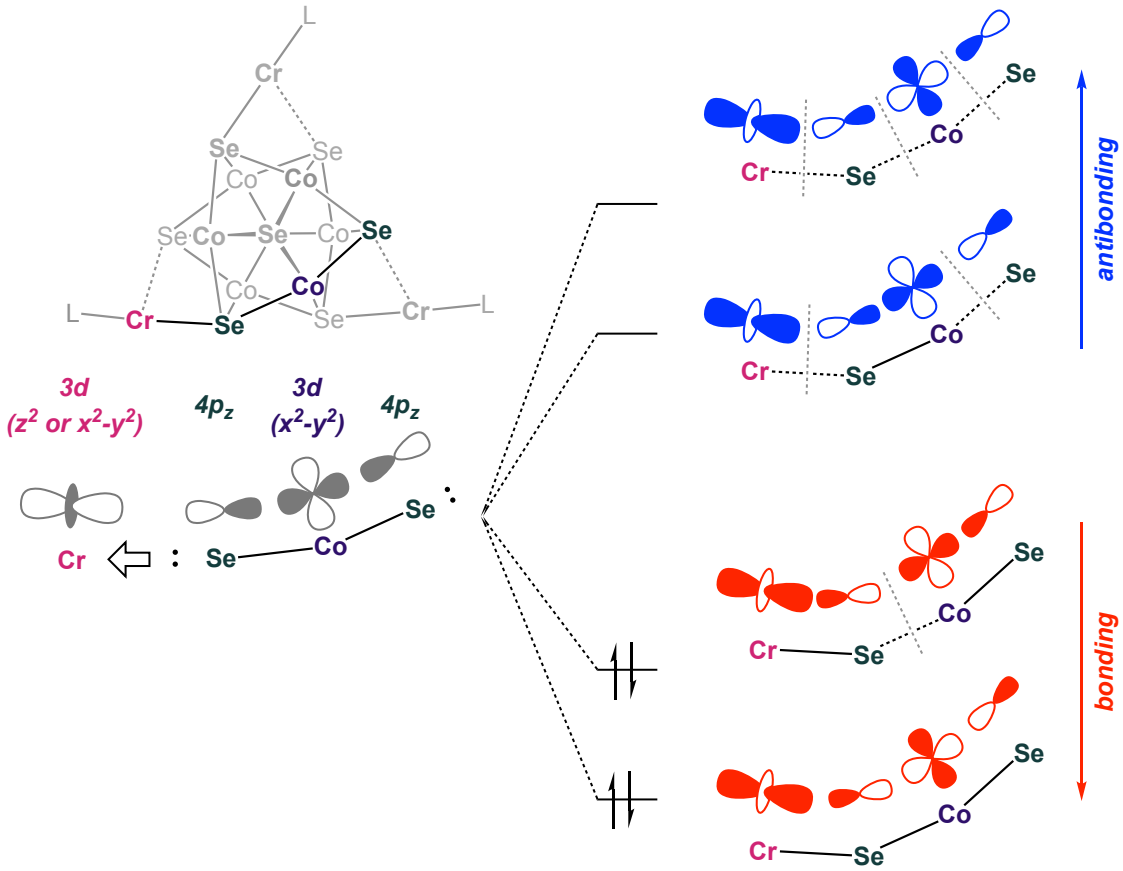


Figure 6.13. Dative Cr–Se σ-bonds form as a symmetry adapted linear combination of in-line Cr, Se, and Co atoms. Note that in the case of the weak axial Cr(py)–Se bond, the first antibonding state is singly occupied.

With a distilled model for edge-support bonding in hand, we set out to map the primary Cr···Se bonding interactions present within the **Cr$_3$** cluster series with the goal of rationalizing the observed trends in site-differentiation. In Figure 6.14, the highest populated Cr···Se bonding interactions are projected onto the solid-state structures of **Cr$_3$**(py)$_3$, **Cr$_3$**(NTs)(CN^{t}Bu)$_2$, **Cr$_3$**(NTs)$_2$(py), and **Cr$_3$**(NTs)$_3$, with bonding *Cr–Se···Co–Se* and antibonding *Cr···Se–Co···Se* interactions depicted in red and blue, respectively. It is important to note that Cr(py) and Cr(CN^{t}Bu) edges are treated equivalently, with one strong equatorial Cr–Se bond and one weakened Cr···Se axial bond in which the *Cr···Se–Co···Se* antibonding state is *singly-occupied*. Although the axial Cr···Se interactions are denoted as antibonding below, a net bonding interaction persists. The delocalized Cr/Co/Se bonds project from each Cr edge site to a distal Se atom. If this distal Se atom is engaged in bonding with a neighboring Cr edge, the two bonding interactions intersect at this atom as the bonding interactions begin to interfere with one another. Orbital interference is found to weaken the Cr–Se bond directly engaging with this Se atom. Ultimately,

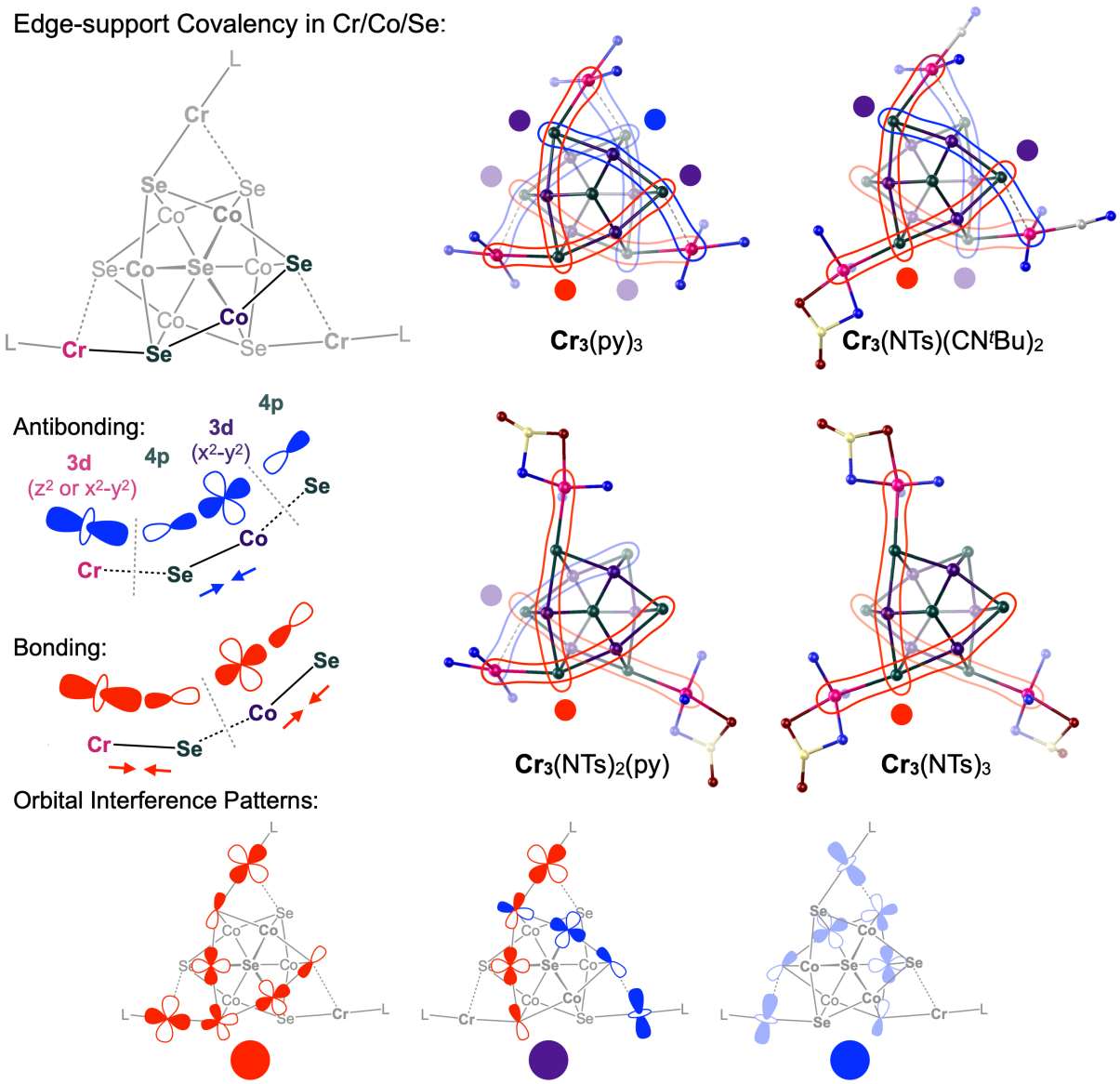


Figure 6.14. Qualitative depictions of the primary molecular orbitals responsible for Cr/Se/Co bonding. Red traces indicate topology of Cr–Se bonding interactions between Cr $3d_{z2}/3d_{x2-y2}$ and Se $4p_z$. Blue orbitals indicate topology of Cr–Se antibonding interactions between Cr $3d_{z2}/3d_{x2-y2}$ and Se $4p_z$, which are singly occupied along the weakened axial Cr–Se interactions present at Cr(py) edges. Red, purple, and blue dots denote Se atoms where these orbitals intersect via the provided interference patterns.

we find that these intersections only occur between Cr···Se interactions positioned on the same α or β cluster face. Further, owing to the C_1 symmetric (α,α,β) arrangement of the edge sites on the Co_6Se_8 support, the interference patterns impacting each Cr edge are distinct.

It is at these crossing points that the three edge sites engage in a game of intramolecular tug-of-war. Within the **Cr3** cluster series, there are three unique patterns in which these orbitals

intersect, denoted by the colored dots in Figure 6.14, that stem from the intersection of *Cr···Se–Co···Se* or *Cr–Se···Co–Se* orbitals with themselves (red and blue) or one-another (purple). In a comparison of the interactions present within **Cr$_3$** clusters, the simplest scenario is that of **Cr$_3$**(NTs)$_3$ where one must only account for the three Cr–Se bonds stemming from the Cr(NTs) edge sites. In this case, there is only one interference point present in the system, where the α-oriented *Cr–Se···Co–Se* bonds intersect at the Se directly bound to α1-Cr. Notably, it is this α1-Cr(NTs) edge that exhibits weakened bonding in solid-state. As the α2 *Cr–Se···Co–Se* bond projects onto this distal Se atom, it reinforces Co–Se bonding, and disrupts the α1 Cr–Se bond. This red crossing point is observed at the α1 site in all **Cr$_3$** clusters in this series and has a similar structural impact in the case of **Cr$_3$**(NTs)$_2$(py), where we observe weakened Cr–Se bonding at the α1 Cr(py) edge site relative to that in **Cr$_3$**(py)$_3$.

The opposite scenario is observed for **Cr$_3$**(py)$_3$ and **Cr$_3$**(NTs)(CN^{t}Bu)$_2$, wherein the α1 Cr edge exhibits strengthened Cr–Se bonding. Notably, in these clusters the α2 and β Cr^{II}(L) (L = py, CN^{t}Bu) edges also engage in weak axial *Cr···Se–Co···Se* bonds that project toward the Se atoms equatorially bound to the β and α2 edges, respectively (purple dots, Figure 6.14). We propose that the presence of these bonding interactions reinforces Cr–Se bonding at the α1 Cr edge by via a domino effect. Here, intersection at the Se atoms bound equatorially to the β and α2 edges weakens these equatorial Cr–Se bonds. The weakened Cr–Se bonding at the α2 edge diminishes its influence on the Se atom directly bound to the α1 edge. Owing to the decreased competition for this Se atom, the α1 Cr–Se bond is reinforced, and the bonding trends are inverted. Here, orbital interactions promote to differentiation of surface sites, whereas parallel examples in surface science typically evoke to inductive effects and strain fields.[53–55]

6.7 Edge-support Bonding Induces Ordered Structural Distortions within the Co/Se Support

The delocalized character of these *Cr–Se···Co–Se* bonds is also reflected in structural distortions observed within the Co$_6$Se$_8$ core. The Cr–Se bonds exercise a sort of *trans*-effect wherein the opposing Co–Se bonds are significantly elongated relative to those observed in Co$_6$Se$_8$L$^{Tol,H}_6$, which average 2.34 ± 0.01 Å (Figure 6.15). Conversely, the next in-line Co–Se bond is reinforced relative to those in Co$_6$Se$_8$L$^{Tol,H}_6$. These trends are perhaps most pronounced in the

case of **Cr$_3$**(NTs)$_3$, where no additional *Cr···Se–Co···Se* antibonding interactions are populated. Here, this structural distortion is most pronounced for in-line Cr, Se, Co, Se atoms along the α1 Cr edge, which exhibit Cr–Se, Se–Co, and Co–Se bond lengths of 2.513(5), 2.476(4) and 2.300(4) Å. Similar distortions propagate from Cr–Se bonds at all Cr(py), Cr(CN^{t}Bu), and Cr(NTs) edge sites. Finally, these distortions are either diminished or inverted along the weak axial Cr···Se bonds, ostensibly due to population of the antibonding *Cr···Se–Co···Se* interaction. Within this simplified

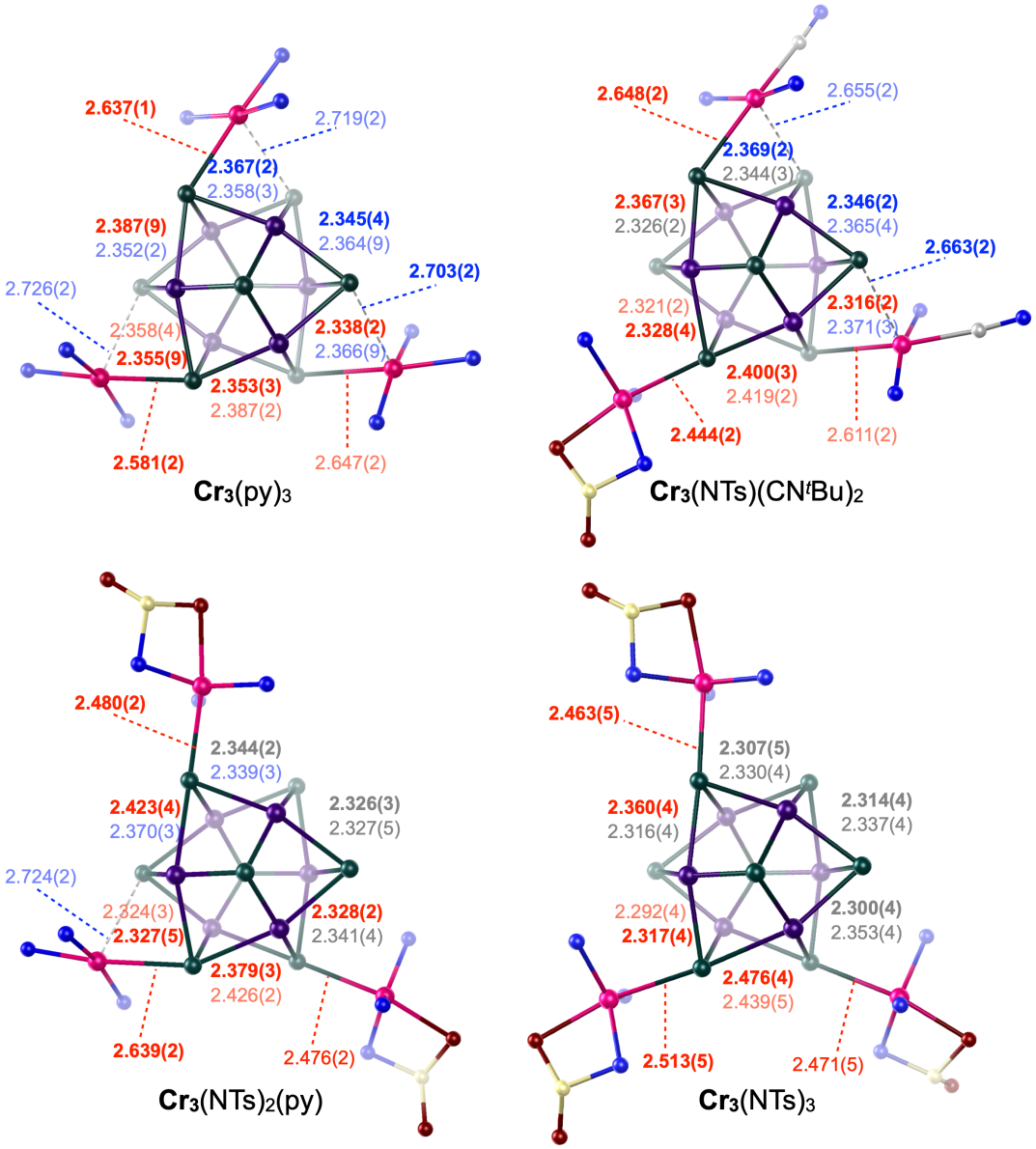


Figure 6.15. Single crystal X-ray comparison of **Cr$_3$**(py)$_3$, **Cr$_3$**(NTs)(py)$_2$, **Cr$_3$**(NTs)$_2$(py), and **Cr$_3$**(NTs)$_3$. Interatomic distances (Å), depicted in red or blue to pair with the orbital traces in Figure 6.14, are reflective of the presence of Cr–Se···Co–Se bonding interactions. All hydrogen atoms, chemical disorder, co-crystallizing solvents, and phosphinoamide carbon and phosphorous atoms are omitted to clarify the structure of the inorganic core.

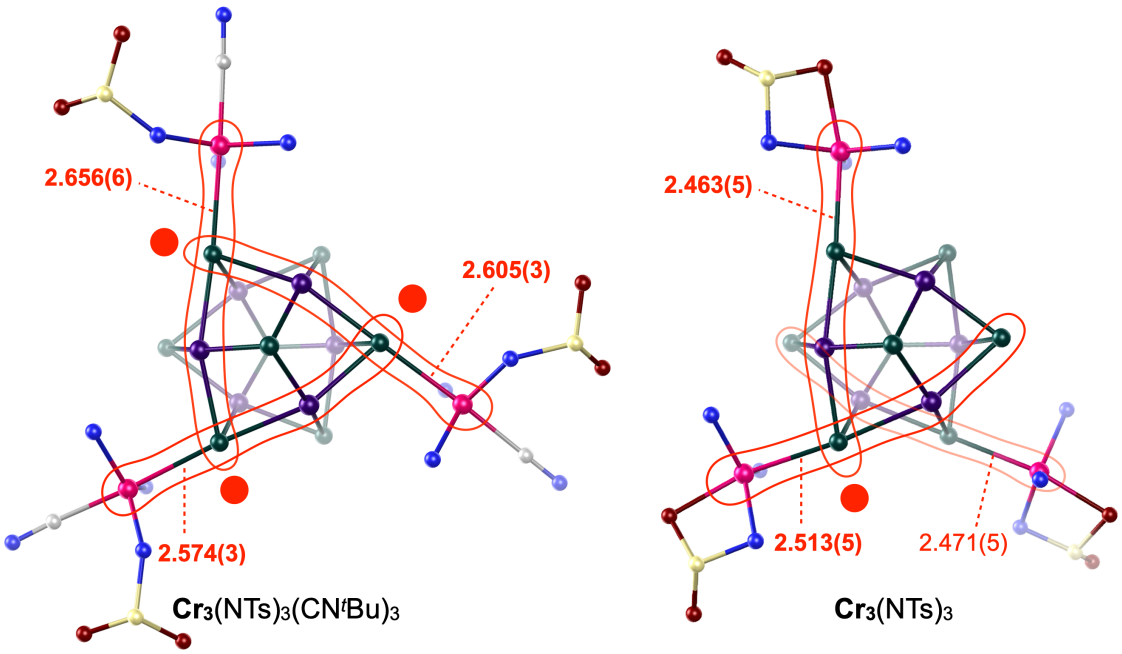


Figure 6.16. Comparison of the single crystal X-ray structures of **Cr$_3$**(NTs)$_3$(CN^{t}Bu)$_3$ and **Cr$_3$**(NTs)$_3$, with outlines to highlight the topology of *Cr–Se···Co–Se* bonding interactions. Orbital crossing points are denoted by red dots.

molecular framework, it becomes clear how interfacial metal-support bonding, which is ultimately responsive to substrate activation, promotes varying degrees of structural distortion and thereby polarization within a supporting lattice.

As a final note on the topological analysis of orbital interactions stemming from edge support bonding, these orbital crossing points can be used to rationalize the general (α,α,β) stereoselectivity. If these *Cr–Se···Co–Se* interactions are mapped onto the structures of (α,α,α)-**Cr$_3$**(NTs)$_3$(CN^{t}Bu)$_3$ and (α,α,β)-**Cr$_3$**(NTs)$_3$, which immediately recognize that the C_3 symmetric (α,α,α) maximizes the number of orbital crossing points (Figure 6.16). Under this symmetrical conformation, not only are Cr–Se bonds localized to the same α-Co_3Se_4 cluster half, but all of the edge sites compete for Se bonding with their neighbors. Along these lines of logic, it is unsurprising that we have only observed this conformation in the case of (α,α,α)-**Cr$_3$**(NTs)$_3$(CN^{t}Bu)$_3$ where Cr–Se bonds are markedly weakened.

6.8 Physicochemical Properties of Cr/Co/Se Nanoclusters

Having assessed the bonding interactions present within the **Cr$_3$** nanoclusters, we turned to further investigate their phyical properties. We first probed the physicochemical behavior of the site-

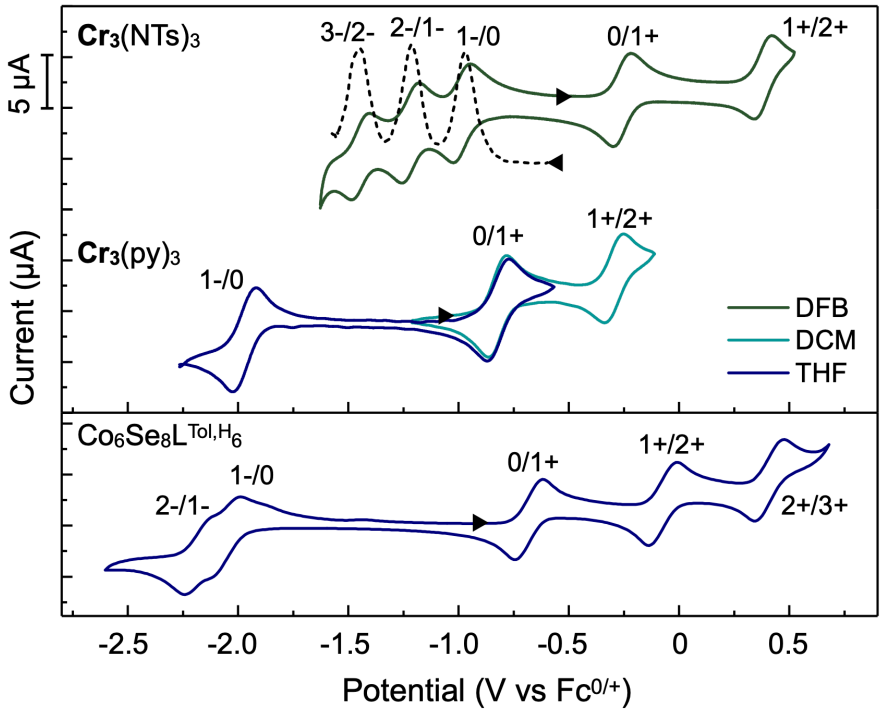


Figure 6.17. Cyclic voltammograms of $Co_6Se_8L^{Tol,H}_6$, $\mathbf{Cr_3}(py)_3$, and $\mathbf{Cr_3}(NTs)_3$ recorded at 50 mV/s with 0.1 M [^{n}Bu$_4$N][PF$_6$] as the supporting electrolyte. The dashed trace represents a differential pulse voltammogram collected in DFB. Open circuit potentials are denoted with black arrows.

differentiated Cr(NTs)/Cr(py) nanoclusters via electrochemical analysis. Cyclic voltammograms collected for $\mathbf{Cr_3}(NTs)_3$ in *o*-difluorobenzene (DFB) and $\mathbf{Cr_3}(py)_3$ in tetrahydrofuran (THF) and dichloromethane (DCM) reveal a surprisingly rich electrochemical behavior (Figure 6.17). Comparison of voltammograms collected for $\mathbf{Cr_3}(py)_3$ and $Co_6Se_8L^{Tol,H}_6$ confirmed that metallation with chromium makes oxidation more facile, as the (0/1+) redox couple shifts cathodically by 220 mV. Conversely, the first reductive couple is less impacted by chromium metallation, exhibiting a 120 mV anodic shift in the case of $\mathbf{Cr_3}(py)_3$. Analysis of $\mathbf{Cr_3}(py)_3$ by cyclic voltammetry in THF or DCM reveals the presence of only three redox couples, comprising two oxidations and one reduction. Notably, this is far fewer redox events than previously observed for either the unmetallated cluster-ligand, $Co_6Se_8L^{Tol,H}_6$, or its trimetallated derivatives, $\mathbf{Fe_3}$ and $\mathbf{Co_3}(py)_3$, suggesting that in the case of $\mathbf{Cr_3}(py)_3$, redox transitions are impeded due to involvement of the Cr(II) edge metals. Additionally, $\mathbf{Cr_3}(py)_3$ exhibits an electrochemical HOMO-LUMO separation of 1.16 eV, which is larger than that observed for $\mathbf{Fe_3}$ or $\mathbf{Co_3}(py)_3$ (0.79 and 1.01 eV, respectively), yet narrower than that of $Co_6Se_8L^{Tol,H}_6$ (1.44 eV).

As anticipated, installation of the tosyl imido groups has a pronounced effect on the electrochemical profile. Cyclic voltammograms collected for **Cr$_3$**(NTs)$_3$ reveal a set of three cascading one-electron reduction events narrowly separated at $E_{1/2}$ = –0.99, –1.22, and –1.44 V vs $Fc^{0/+}$. Notably, with the introduction of these redox couples, we observe a disappearance of the first reduction of **Cr$_3$**(py)$_3$. Supplementary differential pulse voltammetry analysis enables the clear resolution of three, remarkably well-behaved, one-electron reduction events. These redox couples are tentatively identified as isolated one-electron Cr(IV/III) reduction events occurring at each of the Cr(NTs) surface sites, suggesting that all three Cr(NTs) centers are redox-addressable. One might anticipate reduction of a reactive Cr(imido) center to be less well-behaved. However, drawing again from our computational analysis, the lowest unfilled molecular orbitals **Cr$_3$**(NTs)$_3$ exhibit predominantly *Cr···Se–Co···Se* antibonding character. Perhaps, population of these edge-support bonding states minimizes the effects of structural reorganization during redox manipulation. Further, the resolution of three distinct one-electron Cr(IV/III) reduction events likely stems from the structural inequivalence of the three Cr centers in their (α,α,β) arrangement on the inorganic support.

Further interpretation of this electrochemical data outlines deeper agreement between experiment and theory. The (0/1+) couple for **Cr$_3$**(NTs)$_3$ closely coincides with the (1+/2+) oxidation of **Cr$_3$**(py)$_3$ (–0.26 and –0.30 V vs $Fc^{0/+}$, respectively) whereas the first oxidation of **Cr$_3$**(py)$_3$ (–0.85 V vs $Fc^{0/+}$) appears to have disappeared completely in the tris(imido). The disappearance of the (0/+1) redox couple for **Cr$_3$**(py)$_3$ after oxidative group transfer at the Cr sites suggests this is a Cr(py)-centered redox couple, and that the second oxidation is the first Co_6Se_8-centered event. Once again, we note that this interpretation is in line with DFT analysis, as calculations indicated the HOMO of **Cr$_3$**(NTs)$_3$ is localized to the Co_6Se_8 core. This stands in contrast to the electrochemical behavior of **Fe$_3$**, where we observe predominantly core-localized redox chemistry. Electrochemical analysis of the site-differentiated clusters **Cr$_3$**(NTs)$_2$(py) and **Cr$_3$**(NTs)(py)$_2$ reveals a much more complex electrochemical behavior that is challenging to interpret (Figure 6.31). We simply note that these clusters appear to exhibit an admixture of redox events stemming from both Cr(py) and Cr(NTs) edge sites.

6.9 Magnetic Characterization

To probe their electronic properties further, **Cr$_3$**(py)$_3$ and **Cr$_3$**(NTs)$_3$ were characterized by variable temperature solid-state magnetometry between 2.5 and 300K (Figure 6.18). In the case of **Cr$_3$**(py)$_3$, its pseudo-square pyramidal geometry could give rise to diamagnetic d^4 Cr(II), but magnetic analysis reveals a magnetic susceptibility of 9.03 cm^3 mol^{-1} K at 298 K. This value is close to that expected for three S = 2 Cr(II) ions (9.0 cm^3 mol^{-1} K, g = 2.0).

Magnetic characterization of **Cr$_3$**(NTs)$_3$ supports the two-electron oxidation of all three edge sites upon azide activation, with a significant reduction in magnetic susceptibility as compared to **Cr$_3$**(py)$_3$. Below 50K, the tris(imido) nanocluster exhibits a magnetic susceptibility consistent with three S = 1 Cr(IV) centers (3.1 cm^3 mol^{-1} K vs 3.0 cm^3 mol^{-1} K, g = 2.0, respectively) although at temperatures above 50K, this value steadily increases to a maximum of 3.9 cm^3 mol^{-1} K at 300K. We attribute this steady increase to a slight contribution of temperature independent paramagnetism (2.8 x 10^{-3} cm^3 mol^{-1}).

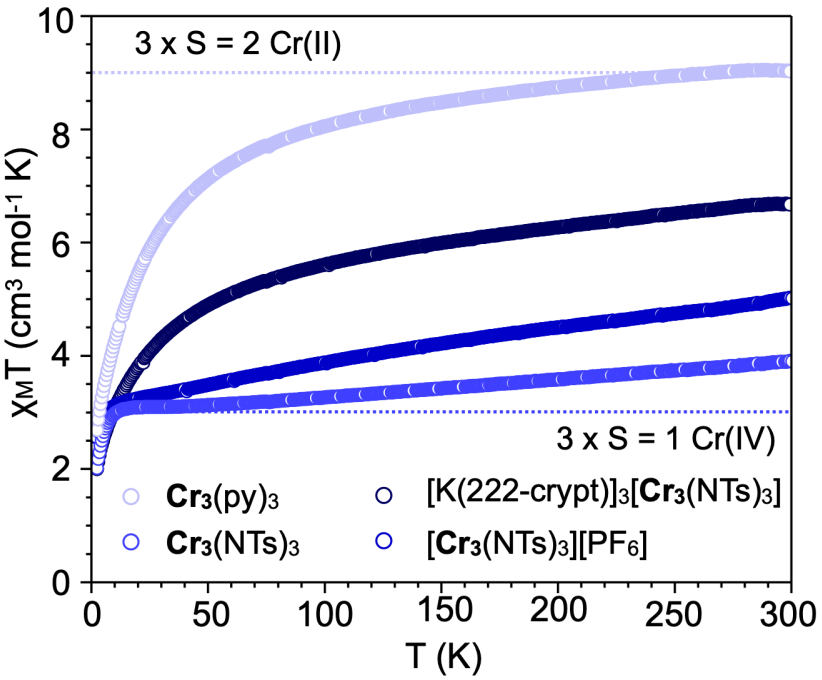


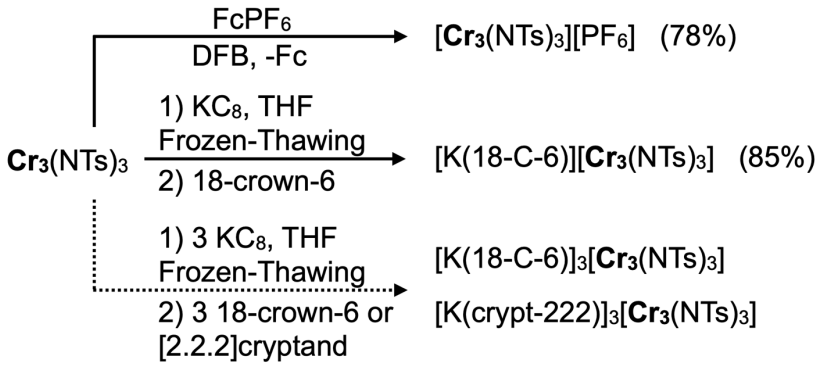
Figure 6.18. Variable-temperature dc magnetic susceptibility of **Cr$_3$**(py)$_3$ and **Cr$_3$**(NTs)$_3$, [**Cr$_3$**(NTs)$_3$][PF$_6$] and [K(2,2,2-crypt)]$_3$[**Cr$_3$**(NTs)$_3$] collected upon warming from 2.5 to 300 K with an applied field of 0.5 T.

6.10 CHEMICAL REDOX REACTIVITY OF $\mathbf{Cr_3}(NTs)_3$

Considering its well-behaved electrochemical behavior, we turned to investigate chemical redox manipulation of the tris(imido) nanocluster $\mathbf{Cr_3}(NTs)_3$ (Scheme 6.2). Chemical oxidation was easily achieved via treatment of $\mathbf{Cr_3}(NTs)_3$ with ferrocenium hexafluorophosphate ($FcPF_6$, 1 equiv) in DFB, affording the mono-oxidized product, $[\mathbf{Cr_3}(NTs)_3][PF_6]$, in good yields (78%). The mono-oxidized product appears to be indefinitely stable at room temperature and exhibits a beautiful ^{1}H NMR profile showcasing the site-differentiation of Cr(NTs) edges (Figure 6.19). The (α,α,β) C_1-symmetry of $[\mathbf{Cr_3}(NTs)_3][PF_6]$ is even more apparent that its neutral counterpart, as we observe the clear resolution and sharpening of innumerable peaks between 25 and –8 ppm. The presence of innumerable paramagnetic ^{1}H environments is apparent, but what is perhaps most striking is the isolation of all nine N-tosyl ^{1}H resonances between 0 and –8 ppm. Single crystals of $[\mathbf{Cr_3}(NTs)_3][PF_6]$, suitable for crystallographic analysis, were grown from a mixture of DFB and pentane. The solid-state structure of $[\mathbf{Cr_3}(NTs)_3][PF_6]$ reveals that the tris(imido) cluster is largely unperturbed by chemical oxidation (Figure 6.20a). We observe a slight elongation of Cr–Se bond lengths, which is consistent with oxidation primarily localizing to the Co_6Se_8. Solid-state magnetic analysis of $[\mathbf{Cr_3}(NTs)_3][PF_6]$ reveals a slight increase in magnetic susceptibility consistent with formation of an S = 1/2 Co_6Se_8 core.

Chemical reduction was investigated using potassium graphite (KC_8) in the presence of either 18-crown-6 (18-C-6) or [2.2.2]-cryptand (222-crypt) in THF or DFB (Scheme 6.2). Isolation of chemically reduced species has proven challenging, especially in the case of the trireduced derivatives, which exhibit extremely poor solubility even in polar aprotic solvents such as acetonitrile, THF or DFB. None the less, polycrystalline material, tentatively identified as the

Scheme 6.2. Chemical redox transformations of the tris(imido) nanocluster $\mathbf{Cr_3}(NTs)_3$.



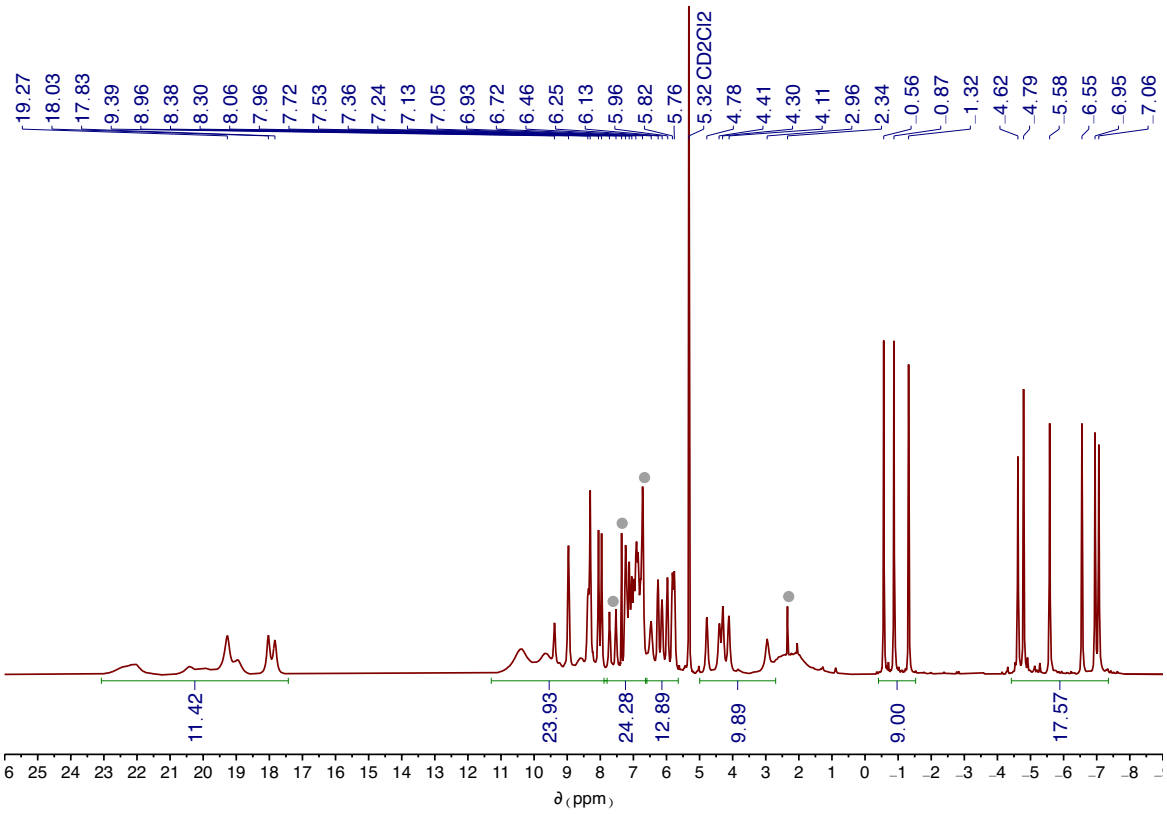


Figure 6.19. ^{1}H NMR (C_6D_6, 25 °C, 300 MHz) spectrum of [**Cr$_3$**(NTs)$_3$][PF_6]. Gray dot indicate solvent (toluene, *o*-DFB) resonances.

trireduced cluster [K(crypt-222)]$_3$[**Cr$_3$**(NTs)$_3$] is obtained upon treatment of **Cr$_3$**(NTs)$_3$ with three equivalents of KC_8 in the presence of 222-crypt in THF. This material was analyzed by solid-state magnetometry, which reveals a marked increase in magnetic susceptibility and a reasonable magnetic profile for three weakly interacting S = 3/2 Cr(III) ions (Figure 6.18). While this trireduced species appears to be challenging to synthetically manipulate, efforts are currently underway to confirm its identity crystallographically.

Encouraged by the observed magnetic response for [K(crypt-222)]$_3$[**Cr$_3$**(NTs)$_3$], we became interested in generating a mono-reduced derivative that might be more easily processed in lab. To this end, treatment of **Cr$_3$**(NTs)$_3$ with one equivalent of KC_8 in the presence of 18-C-6 in THF. Subsequent crystallization from a mixture of THF and *n*-pentane at –35 °C afforded the monoreduced product [K(18-C-6)][**Cr$_3$**(NTs)$_3$] as a crop of large blocky crystals suitable for single crystal X-ray analysis (85% isolated yield). Although this compound can be characterized in the solid-state (see below), upon dissolution this compound immediately undergoes disproportionation to afford a mixture of neutral **Cr$_3$**(NTs)$_3$ and other unidentified species tentatively identified as a

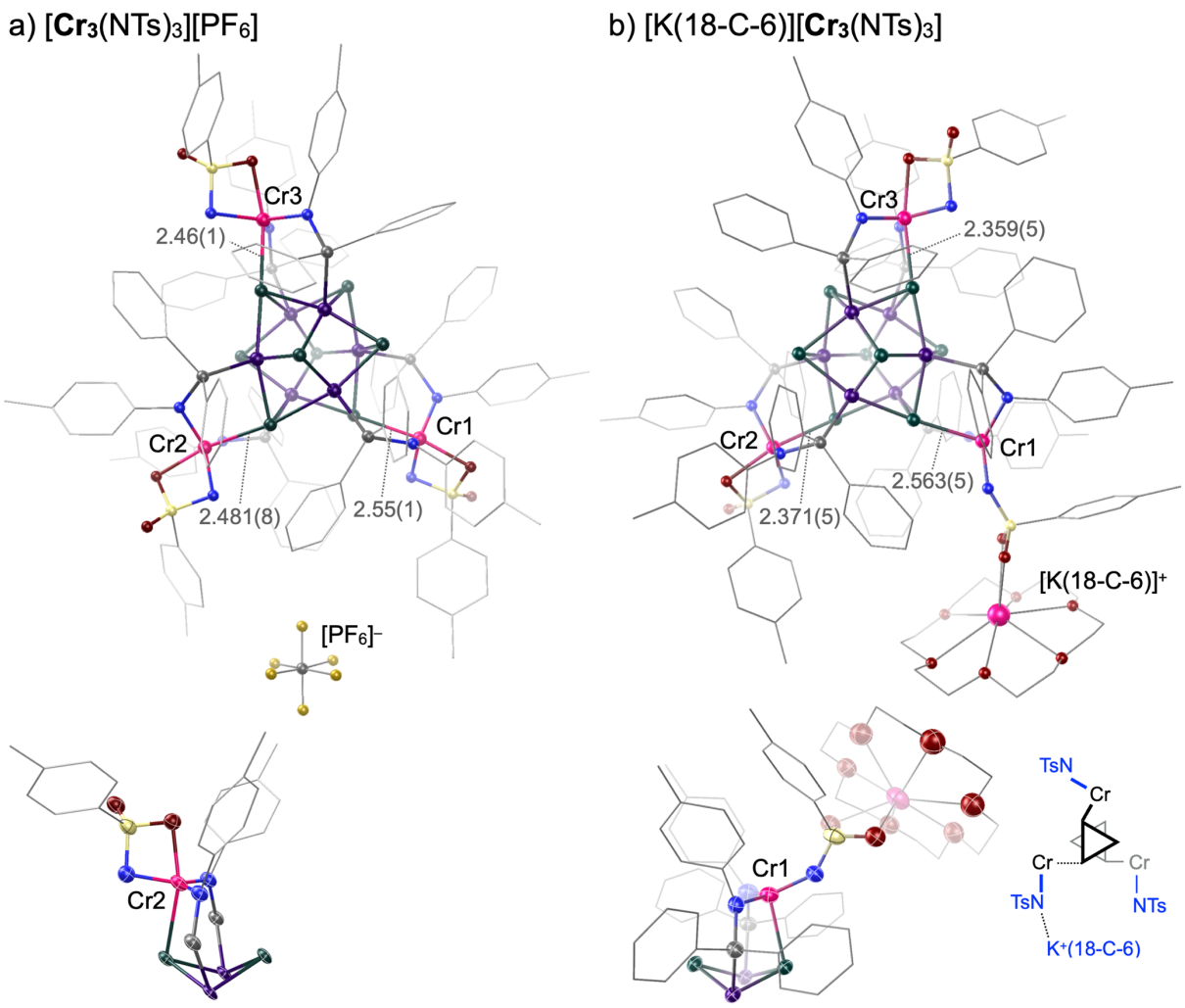


Figure 6.20. Single-crystal X-ray structures of a) [**Cr**$_3$(NTs)$_3$][PF$_6$] and b) [K(18-C-6)][**Cr**$_3$(NTs)$_3$]. Insets provided to highlight Cr(NTs) and [K(18-C-6)][Cr(NTs)] edge sites, with thermal ellipsoids plotted at 30% probability. All hydrogen atoms, positional disorder and solvent molecules omitted for clarity.

mixture of reduced [**Cr**$_3$(NTs)$_3$]$^{x-}$ (x = 1, 2, 3) clusters (Figure 6.24). This disproportionation is unsurprising considering the narrow separation (~200 mV) of the three reduction events observed electrochemically.

Single-crystal X-ray characterization of [K(18-C-6)][**Cr**$_3$(NTs)$_3$] enables us to draw several striking conclusions. In the solid-state, we find that the [K(18-C-6)]$^+$ counterion associates directly with the α1 Cr(NTs) edge site, as K$^+$ engages in chelation with the sulfonyl oxygen atoms (Figure 6.20b). This counterion association disrupts the N/O-chelation of the N-tosyl group at the Cr edge, affording a mono-coordinate N-tosyl imido analogous to those observed in **Cr**$_3$(NTs)$_3$(CN^{t}Bu)$_3$. This transformation affords a highly unusual trigonal pyramidal Cr(imido)

edge site featuring a completely open axial coordination site. The association of the $[K(18\text{-}C\text{-}6)]^+$ counterion at the α1 edge site is in agreement with our earlier bonding analysis that this edge is the most electron deficient. If treated as a reduced Cr(III)-imido complex, this compound would constitute the third example of this rare class of molecules.[56,57] However, turning again to our computational analysis, it is likely reduction is only partly localized to the Cr edge, with significant contribution from the Co_6Se_8 core. This observation is also reflected in the Cr–Se bonding parameters. At the reduced α1 Cr(NTs) edge, the Cr–Se bond is elongated by 0.05 Å relative to that of $\mathbf{Cr_3}(NTs)_3$, consistent with population of an antibonding *Cr···Se–Co···Se* interaction. Further, the Co_6Se_8 core appears to become much more electron rich as the α2 and β edges exhibit greatly shortened Cr–Se contacts. This is analogous to the enhanced edge support binding observed upon reduction of the Co_6Se_8 core in the case of $[\mathbf{Fe_3}]^-$. The $\mathbf{Cr_3}(NTs)_3$ cluster is unique in that it presents the opportunity for site-specific chemical redox transformations.

6.11 Conclusions

Drawing upon our initial investigation of the $\mathbf{Cr_3}$ nanocluster platform, we have thoroughly examined the effects of site-differentiation of the active sites on the surface of a Cr/Co/Se nanocluster. A comparative structural analysis revealed the presence of a Cr "special site" where edge-support bonding traits diverge from those of its neighbors. Detailed computational analysis reveals the electronic impact of imido group installation at the edge sites, and also provides a molecular orbital basis for the speciation of active sites on the cluster surface. Further, we demonstrate the evolution of delocalized edge-support bonding interactions that promote structural distortions within the Co_6Se_8 support. Analysis of the electrochemical response of $\mathbf{Cr_3}(py)_3$ reveals a markedly truncated redox profile relative to other $\mathbf{M_3}$ clusters, consistent with redox participation of the Cr(II) edge sites. Electrochemical analysis also indicates that reversible edge-support coordination at the edge sites minimizes structural reorganization upon chemical reduction, furnishing a rich redox profile in the case of $\mathbf{Cr_3}(NTs)_3$. Solid-state magnetic measurements confirm imido-group installation invokes a net two-electron oxidation at each of the edge sites, with a significant reduction in magnetic susceptibility. Finally, chemical redox transformations of $\mathbf{Cr_3}(NTs)_3$ confirm that this compound is chemically robust, withstanding both chemical oxidation and reduction.

6.12 Experimental Details

6.12.1 *General Information*

All syntheses were conducted under a dinitrogen atmosphere using a standard Schlenk line or an LC Technology Solutions glovebox equipped with a freezer set to −35 °C. All glassware was dried at 160 °C for a minimum of 12 h prior to use.

Solvents were purchased from Fischer Scientific and degassed, dried and purified using solvent purification columns housed in a stainless-steel cabinet and dispensed by a stainless-steel Schlenk line manufactured by JC Meyer Solvent Systems. Tetrahydrofuran (THF), diethyl ether (Et_2O), and methylene chloride (DCM) are passed through two packed columns of neutral alumina. *n*-Pentane, benzene, and toluene are passed through a column packed with alumina, and one containing Q5 reactant, a copper(II) oxide oxygen scavenger. All solvents were passed through an in-line, 2 μm filter, then stored over activated 3Å molecular sieves in the glovebox. 3Å molecular sieves were purchased from Sigma Aldrich and activated under vacuum at 300 °C for 48 h. Anhydrous pyridine (99.8%) was purchased from Sigma Aldrich and stored over activated 3Å molecular sieves for 72 h prior to use.

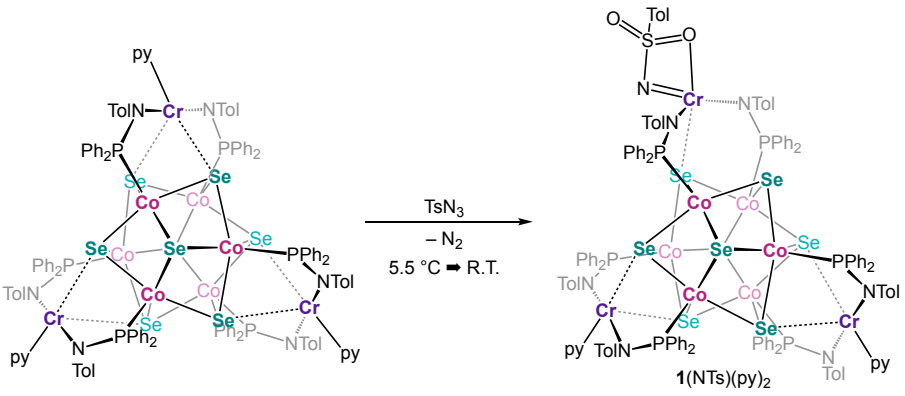
Deuterated solvents (benzene-d_6, toluene-d_8, DCM-d_2) were purchased from Sigma Aldrich, degassed and dried over activated 3Å molecular sieves in the glovebox for a minimum of 72 h. $CrCl_2$ (anhydrous, 99.9%-Cr, Strem Chemicals, Inc.) was dried under vacuum at 180 °C for 24 h prior to use. $Co_2(CO)_8$ (stabilized with 2-5% hexanes, Strem Chemicals, Inc.) was stored in the glovebox freezer, and used as received. Chlorodiphenylphosphine (97%, Alfa Aesar), selenium (99.5%, powder, 200 mesh, Sigma Aldrich), and *n*-butyl lithium (2.5 M in hexanes, Sigma Aldrich) were used as received. Tosyl azide was synthesized according to a literature procedure,[47] and it was dried over activated 3Å molecular sieves in diethyl ether prior to use and stored at –35 °C. *Tert*-butyl isocyanide (CN^tBu, 98%) was purchased from Sigma Aldrich, degassed, and stored over activated 3 Å molecular sieves in the glovebox for a minimum of 72 h prior to use. $Ph_2PN(H)Tol$ (Ph = phenyl, Tol = 4-tolyl; $L^{Tol,H}$), $Co_6Se_8L^{Tol,H}_6$, and $\mathbf{Li_6}(py)_6$ were prepared according to methods reported in the literature.[38,59]

UV-vis-*n*IR absorption spectra were acquired using a Varian Cary 5000 UV-Vis-*n*IR spectrophotometer, in *n*IR quartz cuvettes (Spectrocell Inc., 10 mm path length, 220–3500 nm spectral window). Attenuated total reflectance infrared (ATR-IR) spectra were recorded on a

Bruker Alpha IR instrument equipped with a Platinum ATR accessory housed within a nitrogen glovebox. NMR spectra were acquired at 25 °C unless indicated otherwise on Bruker 300, 500, or 700 MHz spectrometers. ^{1}H NMR spectra were referenced to residual deuterated solvent peaks. For variable-temperature NMR measurements, temperatures were calibrated using an 80% ethylene glycol/DMSO-d_6 external standard. Solution-phase magnetic susceptibilities were determined by the Evans method in benzene-d_6 using 5% (by volume) mesitylene in benzene-d_6 as an internal standard.[60]

Samples were prepared for elemental analysis by crushing single-crystalline material into a powder and then removing volatiles under reduced pressure for 12 h. Co, Se, P elemental analysis was conducted using a Perkin-Elmer Nexion 2000B inductively-coupled plasma mass spectrometer (ICP-MS). Prior to ICP-MS analysis, samples were digested in neat nitric acid (Fisher Scientific, ICP-MS grade) at 50 °C, and serial dilutions were performed with Milli-Q reference water.

6.12.2 *Synthesis and Isolation of $Cr_3(NTs)(py)_2Co_6Se_8L^{Tol}_6$, $\mathbf{Cr_3}(NTs)(py)_2$*



20 mL scintillation vial equipped with a magnetic stir bar was loaded with $\mathbf{Cr_3}(py)_3$ (0.200 g, 0.064 mmol, 1 equiv) and benzene (10 mL). The sample was stirred until homogeneous and then frozen within a –35 °C glovebox freezer. Upon thawing, a solution of TsN_3 in benzene (0.99 M, 0.065 mL, 0.064 mmol, 1 equiv) was added dropwise over the course of 1 minute to the cold, stirring solution, promoting the evolution of dinitrogen gas. The sample was slowly brought to 25 °C and stirred for a total of 2 hours. Over the course of this time, a fine black precipitate developed within the sample, which was collected on a fine porosity fritted glass funnel. The precipitate was washed

with benzene (3 x 3 mL) and *n*-pentane (3 x 3 mL), and volatiles were removed under reduced pressure to yield **Cr$_3$**(NTs)(py)$_2$ as a dark brown powder (0.121 g, 0.038 mmol, 59%).

^{1}H NMR (C_6D_6, 300 MHz) δ: 20.30 (s, $\nu_{1/2}$ = 237 Hz); 17.66 (s, $\nu_{1/2}$ = 114 Hz); 10.86 (s, $\nu_{1/2}$ = 80 Hz); 10.46 (s, $\nu_{1/2}$ = 82 Hz); 10.05 (s, $\nu_{1/2}$ = 120 Hz); 9.23 (bs); 9.03 (bs); 8.74 (s, $\nu_{1/2}$ = 116 Hz); 8.48 (bs); 7.96 (s, $\nu_{1/2}$ = 96 Hz); 6.66 (s, $\nu_{1/2}$ = 40 Hz); 6.47 (s, $\nu_{1/2}$ = 25 Hz); 6.21 (s, $\nu_{1/2}$ = 66 Hz); 5.91 (s, $\nu_{1/2}$ = 43 Hz); 5.14 (s, $\nu_{1/2}$ = 108 Hz); 4.18 (s, $\nu_{1/2}$ = 97 Hz); 1.93 (s, $\nu_{1/2}$ = 75 Hz); 1.31 (s, $\nu_{1/2}$ = 62 Hz); –0.28 (s, $\nu_{1/2}$ = 16 Hz); –5.05 (s, $\nu_{1/2}$ = 24 Hz); –5.18 (s, $\nu_{1/2}$ = 24 Hz); –35.75 (s, $\nu_{1/2}$ = 128 Hz); –39.07 (s, $\nu_{1/2}$ = 120 Hz) ppm. Elemental analysis found (calc.) for **Cr$_3$**(NTs)(py)$_2$ (Formula: $C_{131}H_{119}Co_6Cr_3N_9O_2P_6SSe_8$): Co 11.13 (11.01), Se 19.59 (19.67), P 5.76 (5.79).

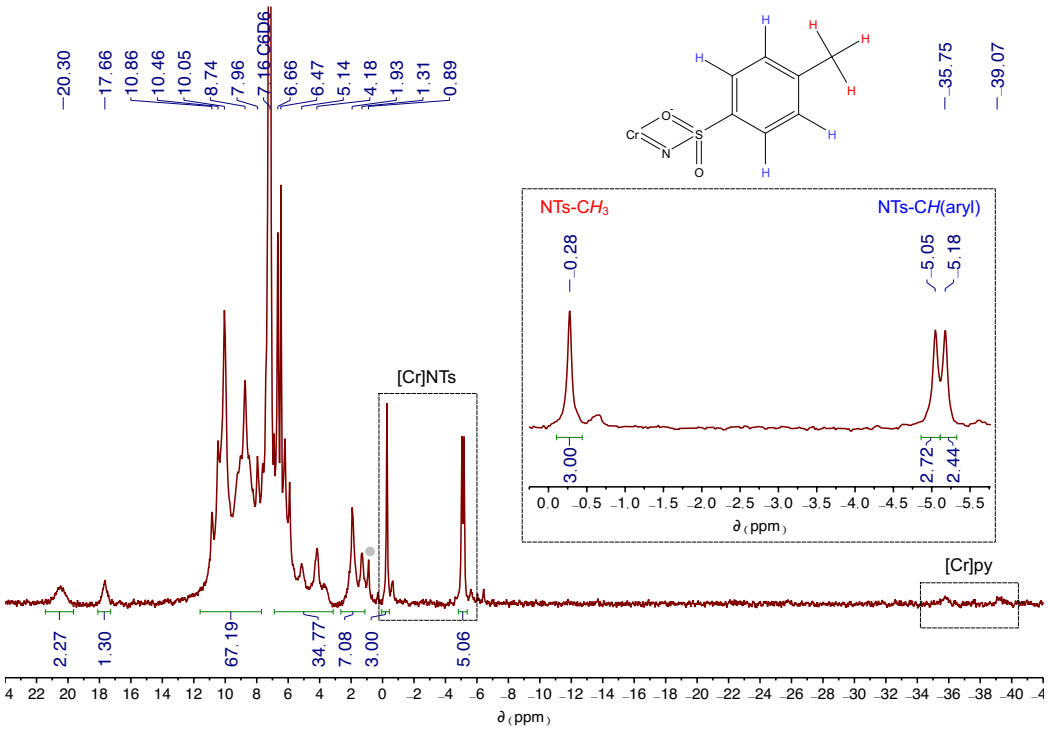
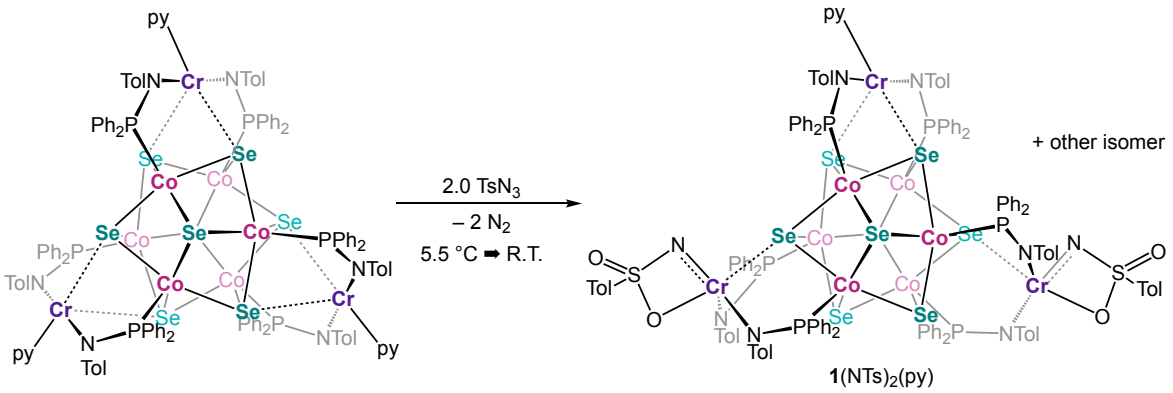


Figure 6.21. ^{1}H NMR (C_6D_6, 25 °C, 300 MHz) spectrum of **Cr$_3$**(NTs)(py)$_2$. Gray dot indicates *n*-pentane resonance.

6.12.3 *Synthesis and Isolation of $Cr_3(NTs)_2(py)Co_6Se_8L^{Tol}_6$,* ***$Cr_3(NTs)_2(py)$***



A 20 mL scintillation vial equipped with a magnetic stir bar was charged with $\mathbf{Cr_3}(py)_3$ (0.500 g, 0.16 mmol, 1 equiv) and benzene (16 mL). The sample was stirred until homogeneous and then frozen within a –35 °C freezer. Upon thawing, a solution of TsN_3 (0.97 M, 330 µL, 0.32 mmol, 2 equiv) was added dropwise to the cold, stirring solution. The sample was slowly warmed to room temperature, causing the effervescence of nitrogen gas. After 2 hours, the sample was cooled to room temperature, and passed through a plug of Celite. The filter cake was washed with a small amount of benzene (2 mL) and the filtrate was layered with *n*-pentane (30 mL) for crystallization. This sample was kept still at room temperature for 14 h to yield a crop of dark red-brown prismatic crystals, which were collected on a fritted glass funnel and washed with *n*-pentane (3 x 5 mL). Volatiles were removed under reduced pressure to yield $\mathbf{Cr_3}(NTs)_2(py)$ as a dark brown microcrystalline solid (365 mg, 0.12 mmol, 75%). The product is obtained in analytical purity, but as a mixture of two diastereomers. Crystals of the desired product suitable for single crystal X-ray analysis were grown via vapor diffusion of *n*-pentane into benzene concentrate at room temperature over the course of 24 h.

^{1}H NMR (C_6D_6, 300 MHz) δ: 22.22 (s, $\nu_{1/2}$ = 450 Hz); 19.35 (s, $\nu_{1/2}$ = 300 Hz); 17.46 (s, $\nu_{1/2}$ = 134 Hz); 10.99 (s, $\nu_{1/2}$ = 65 Hz); 10.03 (s, $\nu_{1/2}$ = 180 Hz); 9.37 (s, $\nu_{1/2}$ = 120 Hz); 8.80 (s, $\nu_{1/2}$ = 100 Hz); 8.57 (s, $\nu_{1/2}$ = 104 Hz); 8.27 (s, $\nu_{1/2}$ = 50 Hz); 8.01 (s, $\nu_{1/2}$ = 50 Hz); 7.71 (s, $\nu_{1/2}$ = 46 Hz); 7.60 (s, $\nu_{1/2}$ = 46 Hz); 7.43 (s, $\nu_{1/2}$ = 59 Hz); 6.90 (s, $\nu_{1/2}$ = 17 Hz); 6.79 (s, $\nu_{1/2}$ = 85 Hz); 6.49 (s, $\nu_{1/2}$ = 29 Hz); 6.37 (s, $\nu_{1/2}$ = 35 Hz); 6.04 (s, $\nu_{1/2}$ = 53 Hz); 5.93 (s, $\nu_{1/2}$ = 64 Hz); 5.67 (s, $\nu_{1/2}$ = 32 Hz); 5.42 (s, $\nu_{1/2}$ = 100 Hz); 4.78 (s, $\nu_{1/2}$ = 131 Hz); 4.58 (s, $\nu_{1/2}$ = 92 Hz); 4.24 (s, $\nu_{1/2}$ = 99 Hz); 3.65 (s, $\nu_{1/2}$ = 79 Hz); 2.25 (s, $\nu_{1/2}$ = 48 Hz); –0.28 (s, $\nu_{1/2}$ = 16 Hz); 10.99 (s, $\nu_{1/2}$ = 65 Hz); –0.37

(s, $\nu_{1/2}$ = 10 Hz);–0.62 (s, $\nu_{1/2}$ = 12 Hz); –0.66 (s, $\nu_{1/2}$ = 16 Hz); –4.28 (s, $\nu_{1/2}$ = 14 Hz); –4.63 (s, $\nu_{1/2}$ = 14 Hz); –4.94 (s, $\nu_{1/2}$ = 20 Hz); –5.14 (s, $\nu_{1/2}$ = 20 Hz); –5.59 (s, $\nu_{1/2}$ = 18 Hz); –5.68 (s, $\nu_{1/2}$ = 17 Hz); –6.03 (s, $\nu_{1/2}$ = 17 Hz); –6.41 (s, $\nu_{1/2}$ = 18 Hz); –39.52 (s, $\nu_{1/2}$ = 254 Hz) ppm. Elemental analysis found (calc.) for **Cr$_3$**(NTs)$_2$(py) (Formula: $C_{133}H_{121}Co_6Cr_3N_9O_4P_6S_2Se_8$): Co 10.85 (10.71), Se 19.02 (19.14), P 5.66 (5.63).

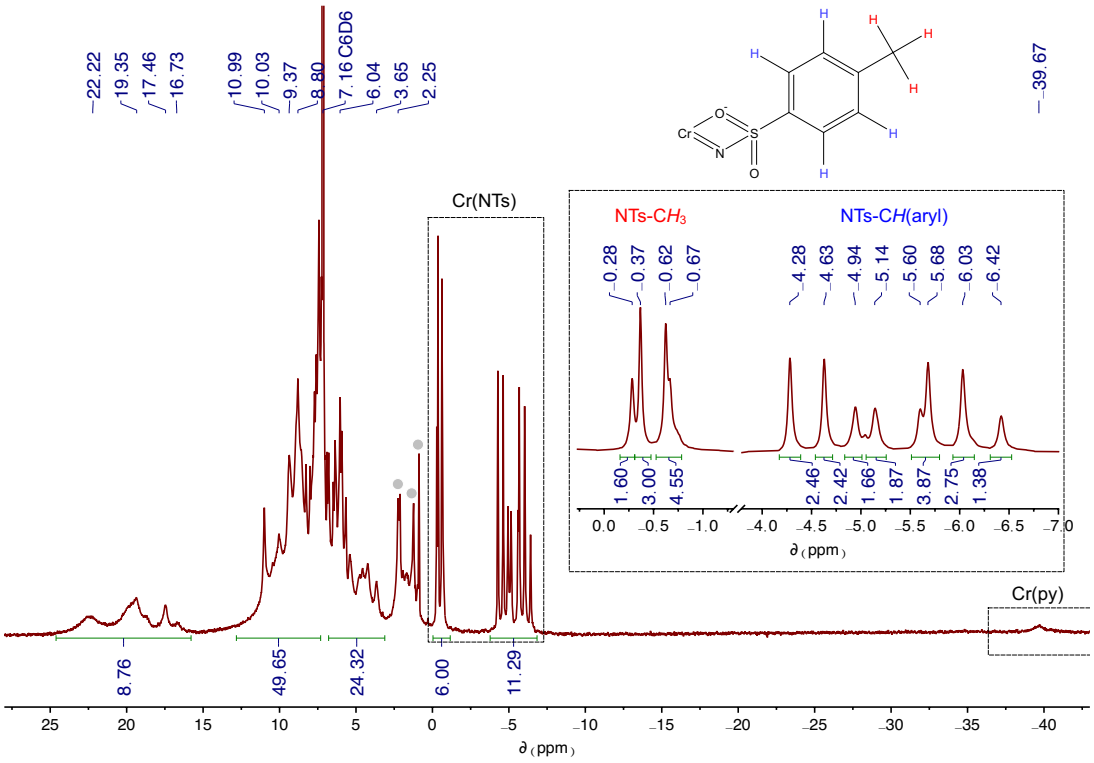


Figure 6.22. ^{1}H NMR (C_6D_6, 25 °C, 300 MHz) spectrum of **Cr$_3$**(NTs)$_2$(py). Gray dots indicate toluene/*n*-pentane resonances.

6.12.4 *Synthesis of Cr$_3$(NTs)$_2$(CN^{t}Bu)Co$_6$Se$_8$L$^{Tol}_6$, **Cr$_3$**(NTs)$_2$(CN^{t}Bu)*

A 20 mL scintillation vial equipped with a magnetic stir bar was charged with **Cr$_3$**(NTs)$_3$ (0.200 g, 0.059 mmol, 1 equiv) and benzene (10 mL). The sample was briefly stirred until homogeneous and then frozen within a –35 °C glovebox freezer. Upon thawing, CN^{t}Bu (13.3 µL, 0.118 mmol, 2 equiv) was added dropwise to the cold stirring solution using a microsyringe. The sample was slowly warmed to room temperature and then stirred for 48 h at 40 °C. The solution was then passed through a plug of Celite on a fritted glass funnel, and the filtrate was layered with *n*-pentane (50 mL) and kept still at 25 °C. After 24 h, a crop of dark red microcrystalline solids had developed

along the walls of the flask, which were collected on a fritted glass funnel and washed with *n*-pentane (3 x 4 mL) to yield **Cr$_3$**(NTs)$_2$(CN^{t}Bu) as a mixture of two isomers (0.142 g, 0.043 mmol, 73%). This product is contaminated with trace amounts of the mono- and tris(imido) clusters, **Cr$_3$**(NTs)(CN^{t}Bu)$_2$ and **Cr$_3$**(NTs)$_3$.

ATR-FTIR (crystals): ν_{CN} = 2196 cm^{-1}. ^{1}H NMR (C_6D_6, 300 MHz) δ: 22.43 (s, $\nu_{1/2}$ = 800 Hz); 19.38 (s, $\nu_{1/2}$ = 364 Hz); 18.85 (s, $\nu_{1/2}$ = 398 Hz); 16.58 (s, $\nu_{1/2}$ = 232 Hz); 13.84 (s, $\nu_{1/2}$ = 68 Hz); 13.51 (s, $\nu_{1/2}$ = 66 Hz); 13.42 (s, $\nu_{1/2}$ = 68 Hz); 13.26 (s, $\nu_{1/2}$ = 74 Hz); 13.10 (s, $\nu_{1/2}$ = 70 Hz); 12.58 (s, $\nu_{1/2}$ = 68 Hz); 11.78 (s, $\nu_{1/2}$ = 80 Hz); 9.63 (s, $\nu_{1/2}$ = 388 Hz); 9.48 (s, $\nu_{1/2}$ = 388 Hz); 7.92 (s, $\nu_{1/2}$ = 54 Hz); 7.54 (s, $\nu_{1/2}$ = 86 Hz); 6.72 (s, $\nu_{1/2}$ = 79 Hz); 6.56 (s, $\nu_{1/2}$ = Hz); 6.13 (s, $\nu_{1/2}$ = 57 Hz); 5.82 (s, $\nu_{1/2}$ = 60 Hz); 5.40 (s, $\nu_{1/2}$ = 110 Hz); 3.61 (s, $\nu_{1/2}$ = 250 Hz); 2.37 (s, $\nu_{1/2}$ = 103 Hz); 1.90 (s, $\nu_{1/2}$ = 59 Hz); –0.23 (s, $\nu_{1/2}$ = 15 Hz); –0.71 (s, $\nu_{1/2}$ = 29 Hz); –3.58 (s, $\nu_{1/2}$ = 23 Hz); –4.15 (s, $\nu_{1/2}$ = 22 Hz); –4.78 (s, $\nu_{1/2}$ = 29 Hz); –5.76 (s, $\nu_{1/2}$ = 25 Hz); –5.83 (s, $\nu_{1/2}$ = 25 Hz); –5.90 (s, $\nu_{1/2}$ = 25 Hz); –6.53 (s, $\nu_{1/2}$ = 29 Hz) ppm.

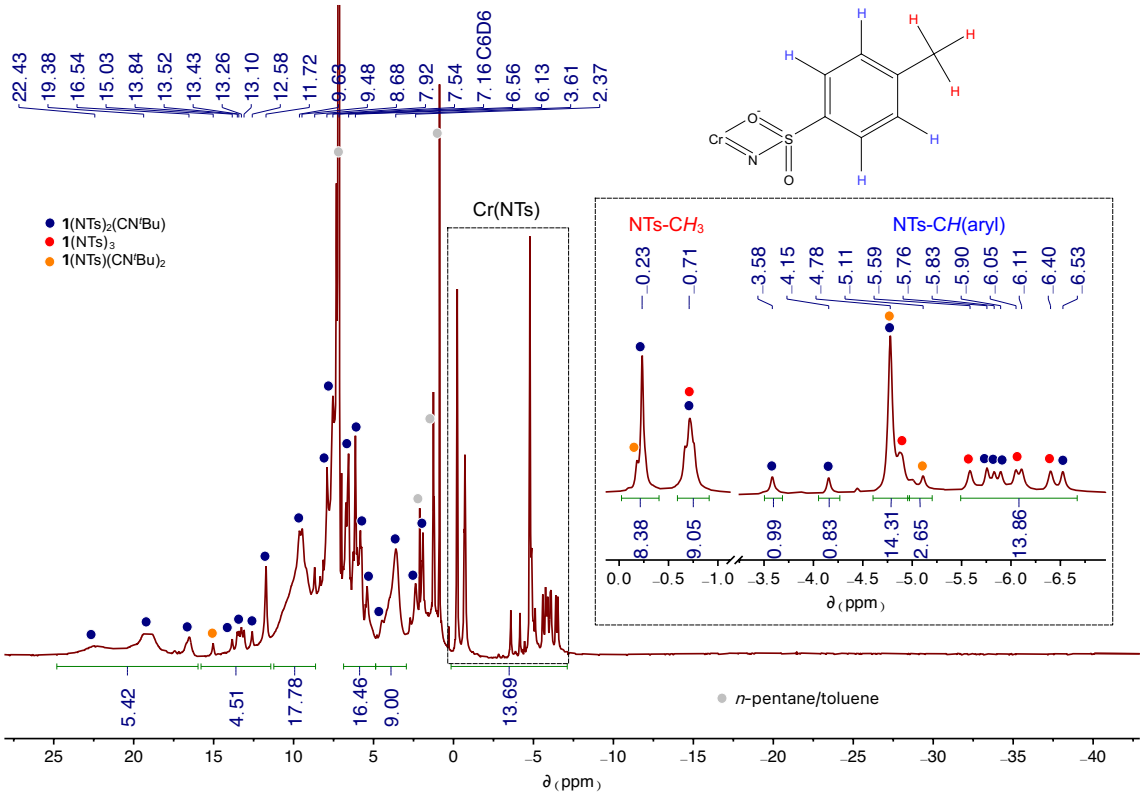
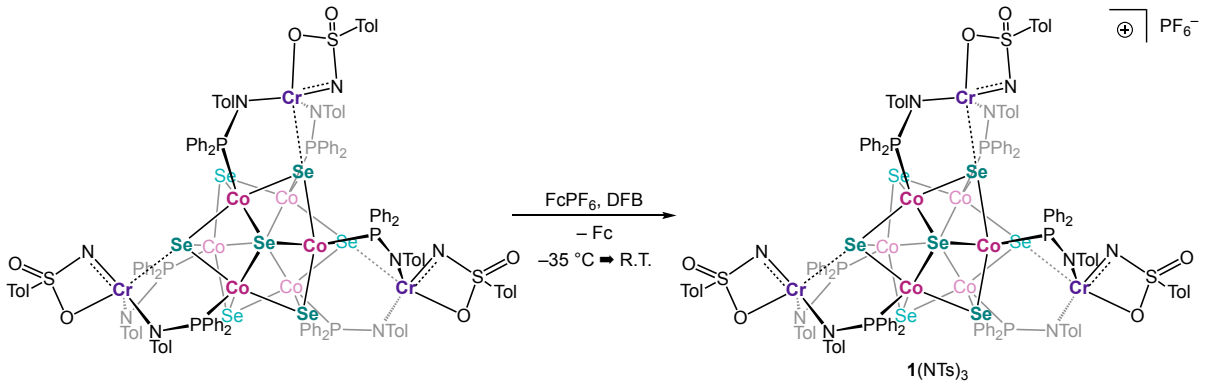


Figure 6.23. ^{1}H NMR (C_6D_6, 25 °C, 300 MHz) spectrum of **Cr$_3$**(NTs)$_2$(CN^{t}Bu). Gray dot indicates *n*-pentane or toluene resonances. Here, the trichromium cluster **Cr$_3$** is denoted as **1**.

6.12.5 *Synthesis and Isolation of [Cr$_3$(NTs)$_3$Co$_6$Se$_8$L$^{Tol}_6$][PF$_6$], [**Cr$_3$**(NTs)$_3$][PF$_6$]*



A 20 mL scintillation vial equipped with a magnetic stir bar was charged with **Cr$_3$**(NTs)$_3$ (0.200 g, 59 µmol, 1 equiv) and *o*-difluorobenzene (6 mL). The mixture was stirred until homogeneous and then cooled to –35 °C in a glovebox freezer. Solid ferrocenium hexafluorophosphate was added to the cold, stirring solution portion-wise, and the sample was stirred for 1 h at room temperature. The deep red-purple solution was then passed through a plug of Celite on a fritted glass funnel and the filtrate was layered with *n*-pentane and kept still at –35 °C for bulk crystallization. After 24 h, the mother liquor was decanted to yield a crop of dark red prismatic crystals, which were washed with *n*-pentane (3 x 5 mL) before volatiles were removed under reduced pressure to yield [**Cr$_3$**(NTs)$_3$][PF$_6$] as a dark red crystalline solid (0.163 g, 46 µmol, 78%).

^{1}H NMR (benzene-d_6, 300 MHz) δ: 22.36 (s, $\nu_{1/2}$ = 182 Hz); 22.06 (s, $\nu_{1/2}$ = 128 Hz); 20.39 (s, $\nu_{1/2}$ = 118 Hz); 19.92 (s, $\nu_{1/2}$ = 171 Hz); 19.27 (s, $\nu_{1/2}$ = 60 Hz); 18.96 (s, $\nu_{1/2}$ = 98 Hz); 18.03 (s, $\nu_{1/2}$ = 35 Hz); 17.83 (s, $\nu_{1/2}$ = 40 Hz); 10.41 (s, $\nu_{1/2}$ = 173 Hz); 9.67 (s, $\nu_{1/2}$ = 146 Hz); 9.67 (s, $\nu_{1/2}$ = 146 Hz); 9.39 (s, $\nu_{1/2}$ = 23 Hz); 8.96 (s, $\nu_{1/2}$ = 16 Hz); 8.61 (s, $\nu_{1/2}$ = 95 Hz); 8.38 (s, $\nu_{1/2}$ = 24 Hz); 8.30 (s, $\nu_{1/2}$ = 13 Hz); 8.06 (s, $\nu_{1/2}$ = 11 Hz); 7.24 (m); 7.13 (m); 7.05 (s, $\nu_{1/2}$ = 20 Hz); 6.99 (s, $\nu_{1/2}$ = 30 Hz); 6.93 (m); 6.72 (s, $\nu_{1/2}$ = 21 Hz); 6.46 (s, $\nu_{1/2}$ = 31 Hz); 6.25 (s, $\nu_{1/2}$ = 17 Hz); 6.13 (s, $\nu_{1/2}$ = 19 Hz); 5.96 (s, $\nu_{1/2}$ = 19 Hz); 5.82 (s, $\nu_{1/2}$ = 18 Hz); 5.76 (s, $\nu_{1/2}$ = 18 Hz); 4.78 (s, $\nu_{1/2}$ = 21 Hz); 4.41 (s, $\nu_{1/2}$ = 27 Hz); 4.30 (s, $\nu_{1/2}$ = 18 Hz); 4.11 (s, $\nu_{1/2}$ = 24 Hz); 2.96 (s, $\nu_{1/2}$ = 38 Hz); –0.56 (s, $\nu_{1/2}$ = 6 Hz); –0.87 (s, $\nu_{1/2}$ = 6 Hz); –1.32 (s, $\nu_{1/2}$ = 6 Hz); –4.62 (s, $\nu_{1/2}$ = 9 Hz); –4.79 (s, $\nu_{1/2}$ = 6 Hz); –5.58 (s, $\nu_{1/2}$ = 6 Hz); –6.55 (s, $\nu_{1/2}$ = 6 Hz); –6.95 (s, $\nu_{1/2}$ = 8 Hz); –7.06 (s, $\nu_{1/2}$ = 8 Hz) ppm. ^{31}P NMR (benzene-d_6, 121 MHz): no peaks observed between ±2000 ppm. Elemental analysis

found (calc.) for [**Cr$_3$**(NTs)$_3$][PF$_6$] (Formula: $C_{135}H_{123}Co_6Cr_3F_6N_9O_6P_7S_3Se_8$): Co 10.15 (10.00), Se 17.82 (17.87), P 6.29 (6.13).

6.12.6 *Synthesis of [K(18-crown-6)][Cr$_3$(NTs)$_3$Co$_6$Se$_8$L$^{Tol}_6$], [K(18-C-6][**Cr$_3$**(NTs)$_3$]*

A 10 mL round bottom flask equipped with a magnetic stir bar was loaded with **Cr$_3$**(NTs)$_3$ (0.100 g, 30 μmol, 1 equiv), 18-crown-6 (7.8 mg, 30 μmol, 1 equiv) and THF (6 mL). The dark brown slurry was stirred until mostly homogeneous, and then the solution was frozen within the glovebox coldwell. Upon thawing, freshly prepared potassium graphite (KC_8, 4 mg, 30 μmol, 1 equiv) was added as a solid to the cold, stirring mixture. The solution was stirred for 30 minutes and kept cold by periodically placing it within the glovebox coldwell. At this point, the cold solution was quickly passed through a plug of Celite on a fritted glass funnel, and the filtrate was layered with –35 °C *n*-pentane (15 mL). The layered sample was kept still at –35 °C for 48 hr to afford a crop of large blocky crystals, which were identified by single-crystal X-ray diffractometry as [K(18-C-6)][**Cr$_3$**(NTs)$_3$] (0.082 mg, 22 μmol, 74%). Note that in solution this compound undergoes disproportionation to afford a mixture with neutral **Cr$_3$**(NTs)$_3$ present as the major species in addition to several unidentified paramagnetic species, ostensibly a mixture of reduced [**Cr$_3$**(NTs)$_3$]^n (n = –1, –2, –3) clusters.

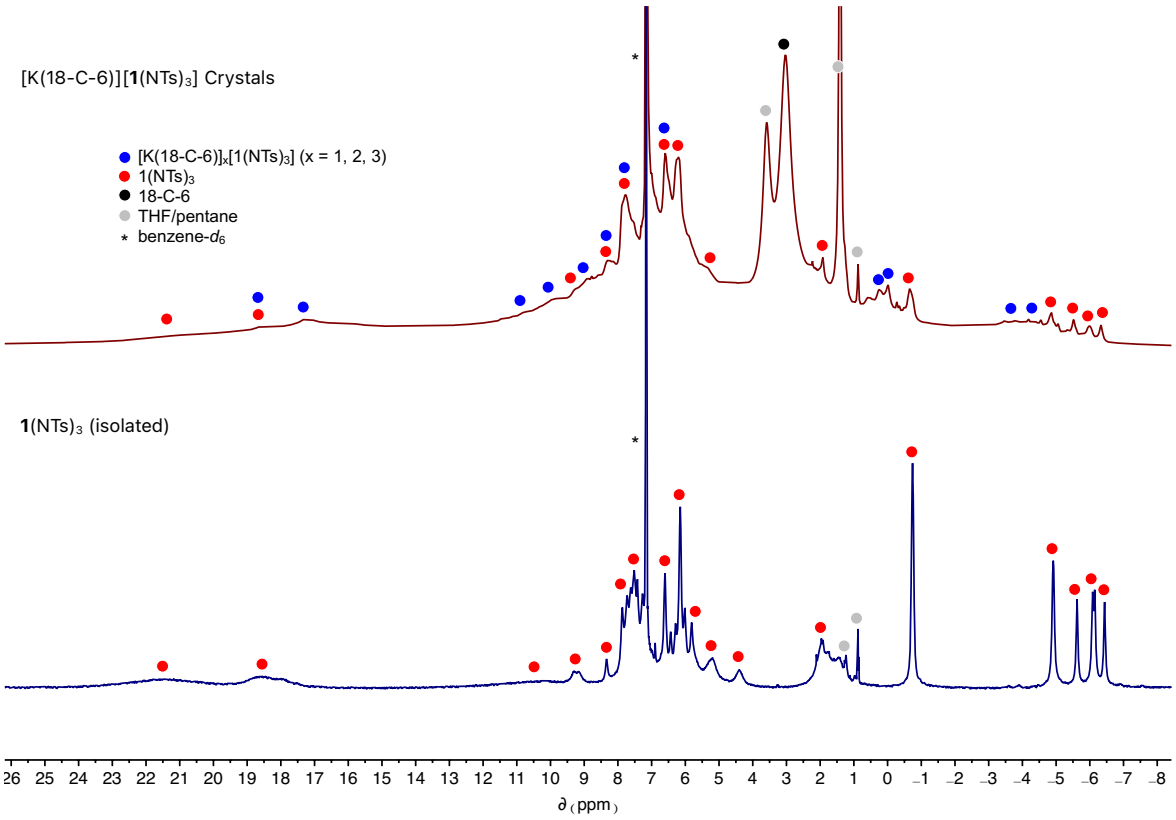


Figure 6.24. ^{1}H NMR (C_6D_6, 25 °C, 300 MHz) spectrum recorded for crystalline [K(18-C-6)][**Cr$_3$**(NTs)$_3$], revealing that the compound undergoes disproportionation in solution. Here, the trichromium cluster **Cr$_3$** is denoted as **1**.

6.12.7 *Stoichiometric Azide Activation and Nitrene Transfer Experiments*

6.12.7.1 ^{1}H Reaction Monitoring: **Cr$_3$**(py)$_3$ + 2 equiv TsN_3

A 20 mL scintillation vial equipped with a magnetic stir bar was charged with **Cr$_3$**(py)$_3$ (10 mg, 3.2 μmol, 1 equiv) and C_6D_6 (0.6 mL). The mixture was stirring until homogeneous and then frozen within a –35 °C glovebox freezer. Upon thawing, a solution of TsN_3 in C_6D_6 (1.0 M, 6.4 μL, 6.4 μmol, 2 equiv) was slowly added by microsyringe. The mixture was stirred and slowly brought to 25 °C before it was filtered through a pipet filter into a J. Young NMR tube equipped with a 5% mesitylene/C_6D_6 capillary. ^{1}H NMR analysis of this mixture reveals a ~2:1 mixture of the two isomers of **Cr$_3$**(NTs)$_2$(py), with little-to-no paramagnetic side products. Comparison of the ^{1}H NMR spectra collected after 15 min, 30 min, and 70 min reveals that the reaction was complete after just 15 min at 25 °C.

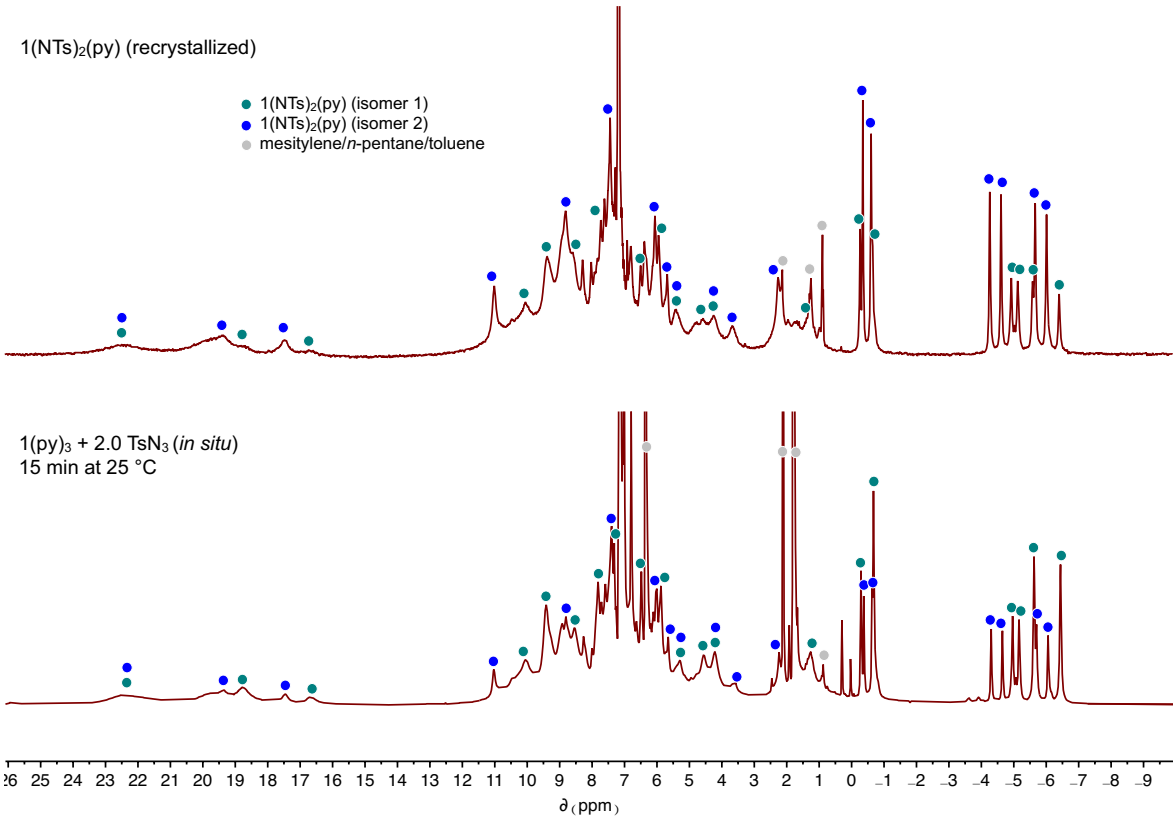


Figure 6.25. ^{1}H NMR (C_6D_6, 25 °C, 500 MHz) spectra tracking the reaction of **Cr$_3$**(py)$_3$ with TsN_3 (2 equiv). The *in situ* reaction mixture after 15 min is plotted in comparison to that of purified **Cr$_3$**(NTs)$_2$(py) in C_6D_6. Here, the trichromium cluster **Cr$_3$** is denoted as **1**.

6.12.7.2 ^{1}H Reaction Monitoring: **Cr$_3$**(py)$_3$ + 1 equiv TsN_3

A 20 mL scintillation vial equipped with a magnetic stir bar was loaded with **Cr$_3$**(py)$_3$ (10 mg, 3.2 μmol, 1 equiv) and THF-d_8. The solution was briefly stirred until homogeneous and cooled to –35 °C in the glovebox freezer. A solution of TsN_3 in C_6D_6 (0.994 M, 3.2 μL, 3.2 μmol, 1 equiv) was added to the cold, stirring solution using a microsyringe. The sample was slowly brought to 25 °C with stirring, and then passed through a pipet filter into a J. Young NMR tube equipped with a THF-d_8 capillary. Comparison of the ^{1}H NMR spectra collected after 30 min, 1 h, and 5 h indicates that the reaction was complete after just 30 minutes, and afforded **Cr$_3$**(NTs)(py)$_2$ as the major product. A similar result was observed when this reaction was run in C_6D_6, however, *in situ* monitoring was not feasible in that solvent as the mono-nitrenoid product has extremely poor solubility and crashes out as a dark brown solid.

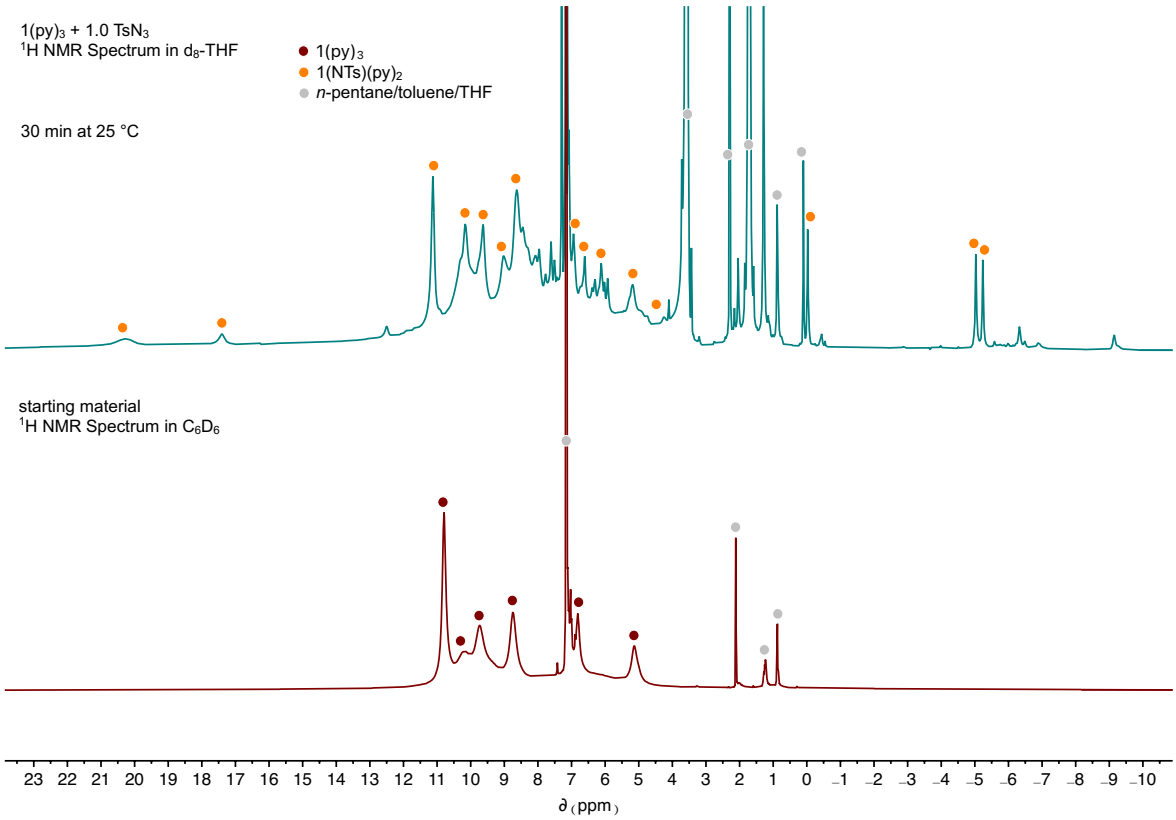


Figure 6.26. ^{1}H NMR (THF-d_8 {top}, benzene-d_6 {bottom}, 25 °C, 500 MHz) spectra tracking the reaction of **Cr$_3$**(py)$_3$ with TsN_3 (1 equiv). The *in situ* reaction mixture in THF-d_8 is plotted in comparison to that of the starting material in benzene-d_6. Here, the trichromium cluster **Cr$_3$** is denoted as **1**.

6.12.7.3 ^{1}H Reaction Monitoring: **Cr$_3$**(NTs)$_3$ + 4 equiv CN^{t}Bu

A 20 mL scintillation vial equipped with a magnetic stir bar was loaded with **Cr$_3$**(NTs)$_3$ (20 mg, 5.9 µmol, 1 equiv) and C_6D_6 (0.6 mL). The mixture was stirred until homogeneous and then frozen within a –35 °C freezer. Upon thawing CN^{t}Bu (26.6 µL, 23.6 µmol, 4 equiv) was added dropwise using a microsyringe. The sample was warmed to 25 °C with stirring, and then passed through a pipet filter into a J. Young NMR tube equipped with a 5% mesitylene/C_6D_6 capillary. ^{1}H NMR spectra were after 20 min, 5 h, and 48 h at 25 °C. This analysis confirmed that treatment with sub-stoichiometric amounts of isocyanide enables the isolation of the mono(imido)-bis(isocyanide) cluster, **Cr$_3$**(NTs)(CN^{t}Bu)$_2$, as the major product, however it appears to be contaminated with equal portions **Cr$_3$**(CN^{t}Bu)$_3$ and **Cr$_3$**(NTs)$_2$(CN^{t}Bu) in a statistical mixture of products.

6.12.7.4 ^{1}H Reaction Monitoring: **Cr$_3$**(NTs)$_3$ + 2 equiv CN^{t}Bu

A 20 mL scintillation vial equipped with a magnetic stir bar was loaded with **Cr$_3$**(NTs)$_3$ (20 mg, 5.9 µmol, 1 equiv) and C_6D_6 (0.6 mL). The mixture was stirred until homogeneous and then frozen within a –35 °C freezer. Upon thawing CN^{t}Bu (13.3 µL, 11.8 µmol, 2 equiv) was added dropwise using a microsyringe. The sample was warmed to 25 °C with stirring, and then passed through a pipet filter into a J. Young NMR tube equipped with a 5% mesitylene/C_6D_6 capillary. ^{1}H NMR spectra were after 20 min, 5 h, and 48 h at 25 °C. This analysis confirmed that treatment with sub-stoichiometric amounts of CN^{t}Bu enables the isolation of the bis(imido) **Cr$_3$**(NTs)$_2$(CN^{t}Bu) as a trapped intermediate, however it appears to be contaminated with small amounts of **Cr$_3$**(NTs)$_3$ and **Cr$_3$**(NTs)(CN^{t}Bu)$_2$.

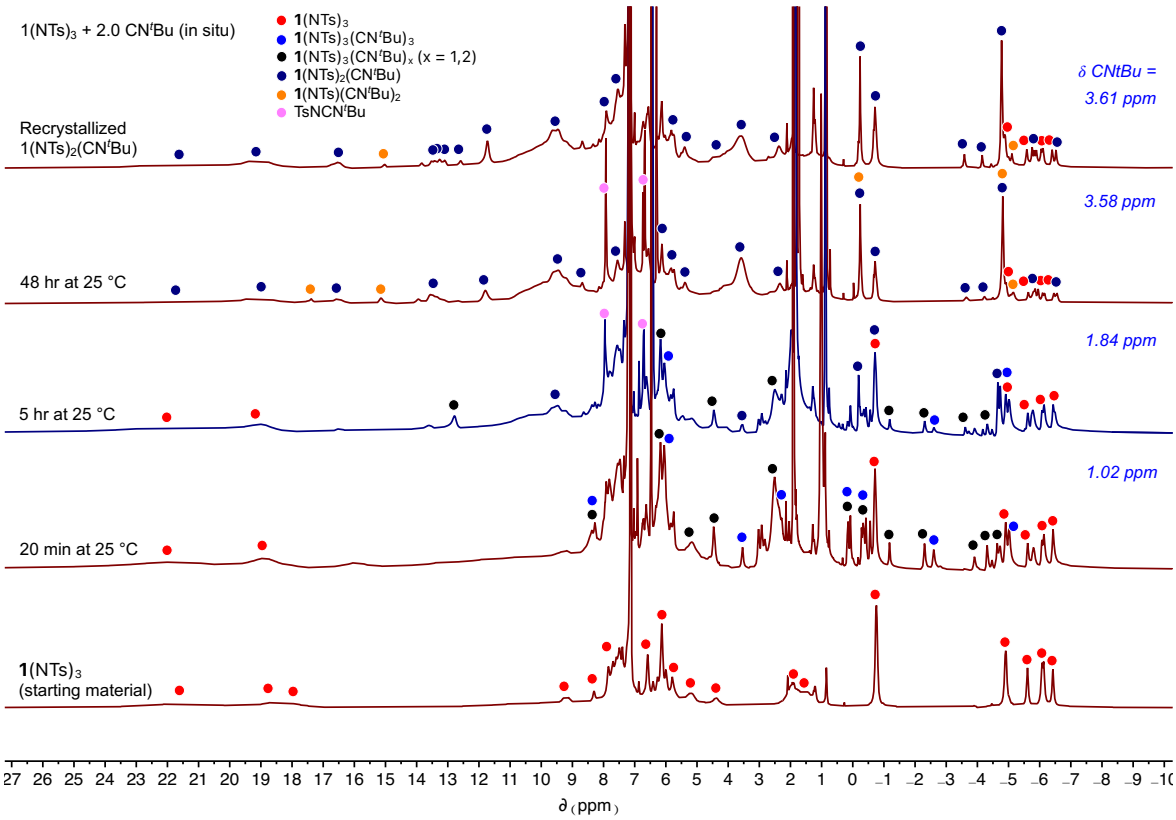


Figure 6.27. ^{1}H NMR (C_6D_6, 25 °C, 500 MHz) spectra tracking the reaction of **Cr$_3$**(NTs)$_3$ with CN^{t}Bu (2 equiv). Spectra recorded at different timepoints in the reaction were plotted in comparison to the starting material **Cr$_3$**(NTs)$_3$ and the purified product **Cr$_3$**(NTs)$_2$(CN^{t}Bu). Here, the trichromium cluster **Cr$_3$** is denoted as **1**.

6.12.8 *Electrochemical Analysis*

Table 6.1. Half-wave potentials ($E_{1/2}$) and open circuit potentials (OCP) of **Cr$_3$**(py)$_3$ and **Cr$_3$**(NTs)$_3$ recorded in 0.1 M [^{n}Bu$_4$N][PF$_6$] THF, DCM, or DFB solutions at 50 mV/s.

redox couple (n_{red}/n_{ox})	$E_{1/2}$ (V vs $Fc^{0/+}$)			
	$Co_6Se_8L^{Tol,H}{}_6$	**Cr$_3$**(py)$_3$		**Cr$_3$**(NTs)$_3$
	THF	THF	DCM	DFB
–3/–2	--	--	--	–1.44
–2/–1	--	--	--	–1.22
–1/0	–2.13	–2.01	--	–0.99
0/+1	–0.63	–0.85	–0.82	–0.26
+1/+2	–0.08	--	–0.30	0.38
+2/+3	0.41	--	--	--
OCP (V vs $Fc^{0/+}$)	–0.88	–1.15	–1.04	–0.46

Table 6.2. Diffusion coefficients (D_0) obtained by applying the Randles–Sevcik equation assuming n_e=1 for various oxidation states determined from cyclic voltammograms of **Cr$_3$**(py)$_3$ recorded in either THF or (DCM) and **Cr$_3$**(NTs)$_3$ recorded in DFB, with 0.1 M [^{n}Bu$_4$N][PF$_6$] supporting electrolyte.

oxidation state (n)	D_0 (10^{-6} cm^2/s)[a]	
	Cr$_3$(py)$_3$	**Cr$_3$**(NTs)$_3$
+2	(0.43)	0.16
+1	2.81 (2.82)	1.36
0	3.33 (2.65)	2.39
–1	1.23	4.94
–2	--	7.27
–3	--	0.03

[a] Diffusion coefficients calculated for each anodic and cathodic peak current density for scan rates ranging between 25 and 500 mV/s, then averaged for all scan rates to obtain the listed values.

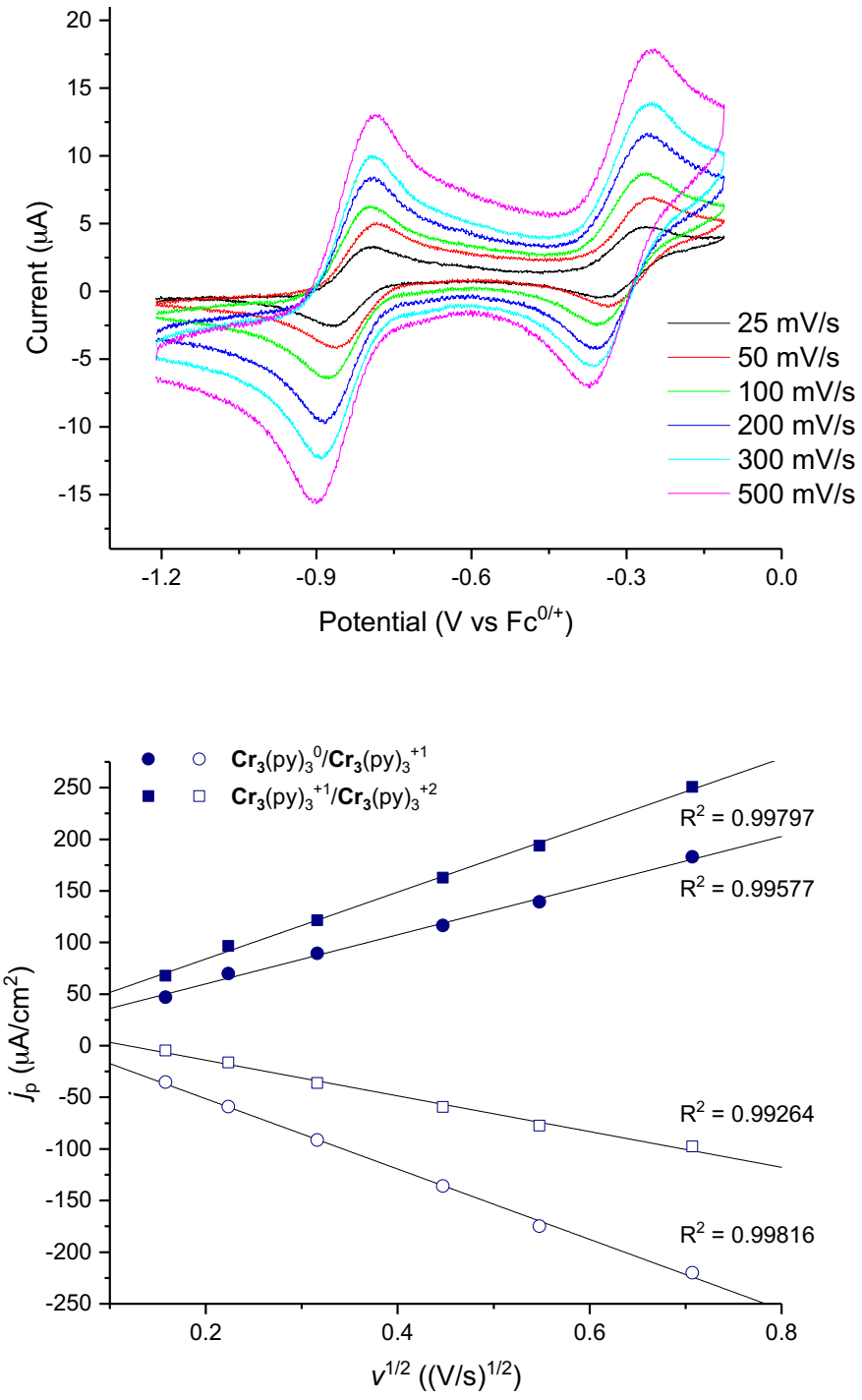


Figure 6.28. Cyclic voltammograms of **Cr$_3$**(py)$_3$ recorded between 25 and 500 mV s^{-1} in 0.1 M [^{n}Bu$_4$N][PF$_6$] DCM and referenced to ferrocene (top) and a plot of current density (j_p) versus the square root of scan rate ($v^{1/2}$) with linear fits used to model the data with the Randles–Sevcik equation (bottom).

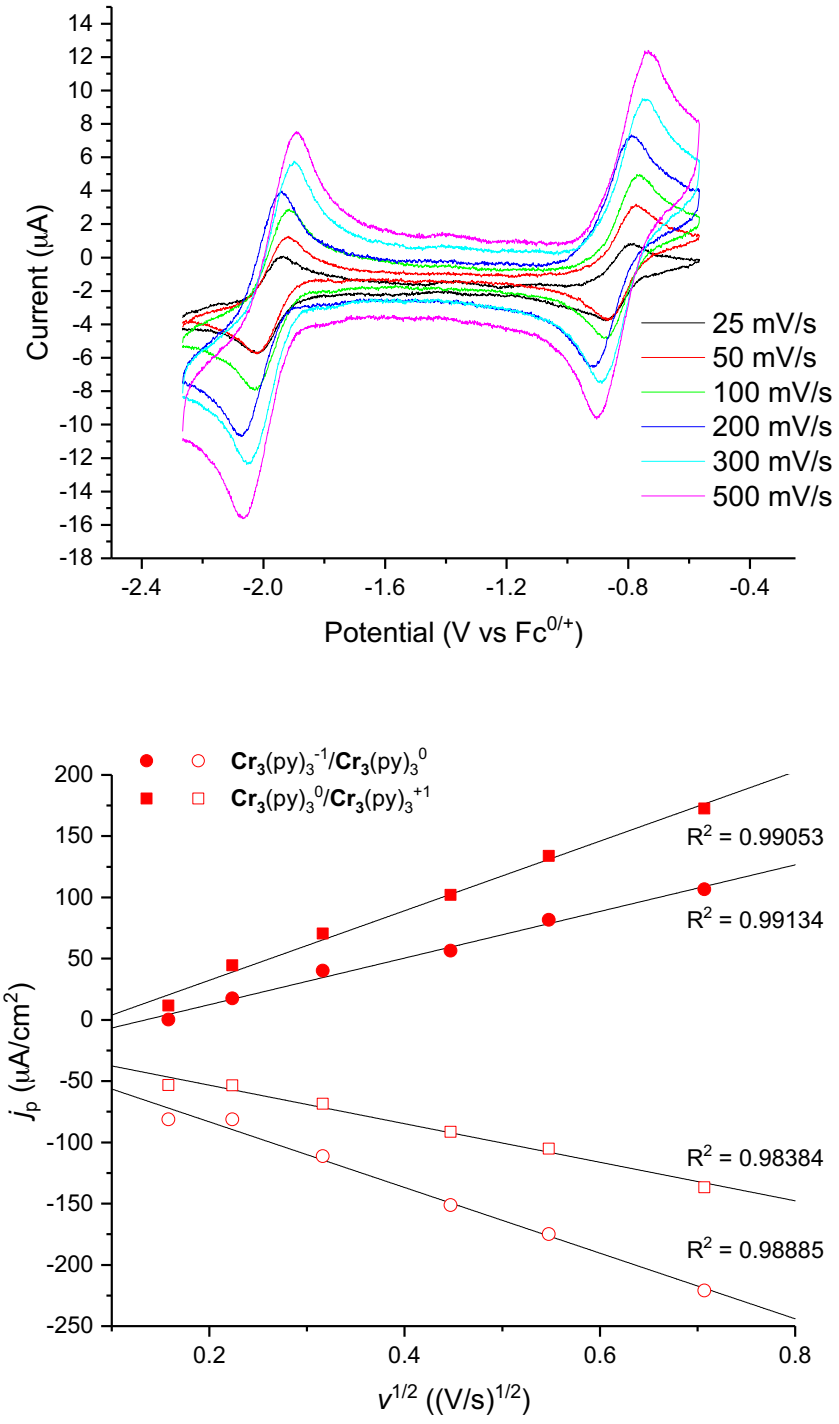


Figure 6.29. Cyclic voltammograms of $\mathbf{Cr_3}(py)_3$ recorded between 25 and 500 mV s^{-1} in 0.1 M [^{n}Bu$_4$N][PF$_6$] THF and referenced to ferrocene (top) and a plot of current density (j_p) versus the square root of scan rate ($v^{1/2}$) with linear fits used to model the data with the Randles–Sevcik equation (bottom).

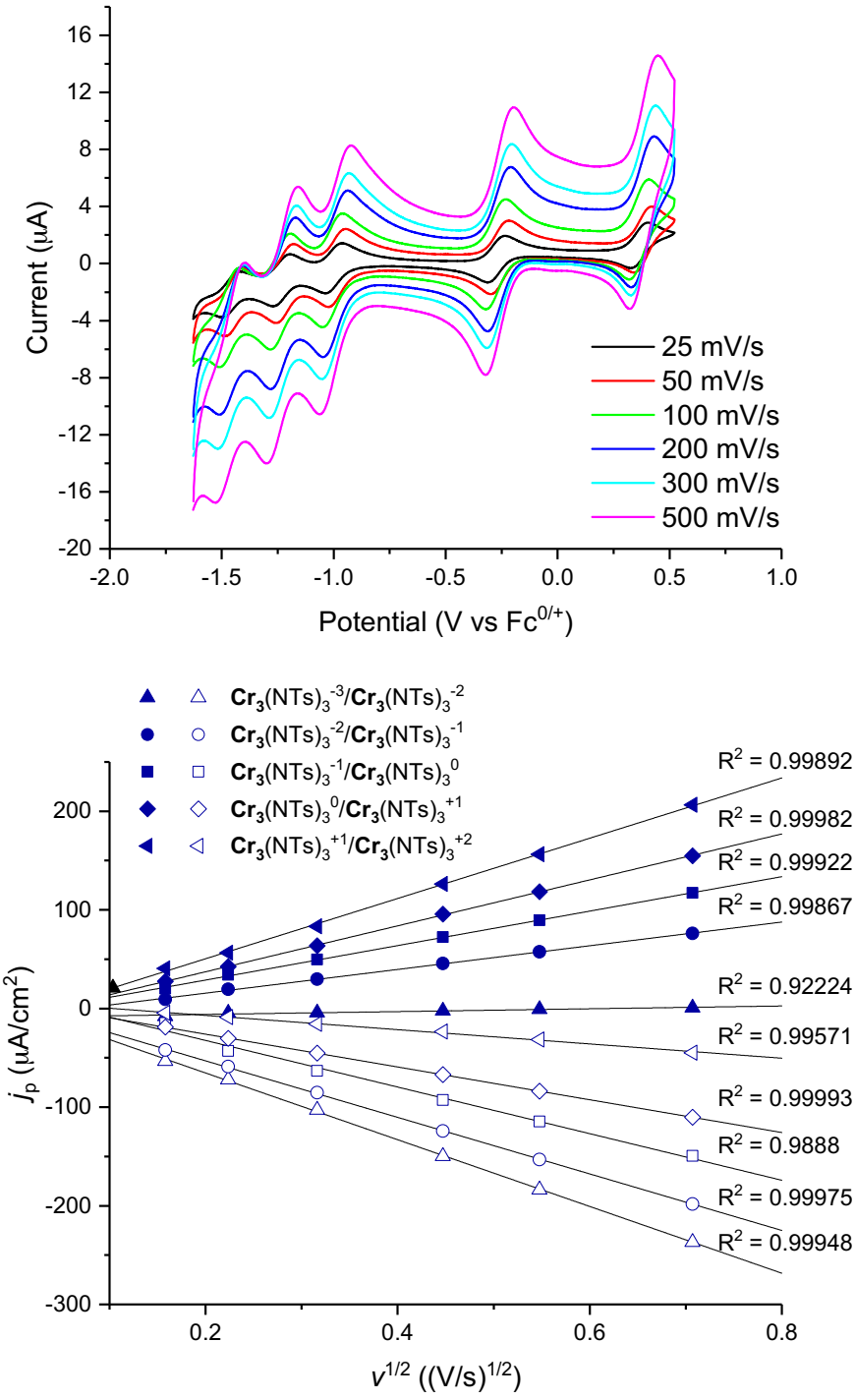


Figure 6.30. Cyclic voltammograms of **Cr$_3$**(NTs)$_3$ recorded between 25 and 500 mV s^{-1} in 0.1 M [^{n}Bu$_4$N][PF$_6$] DFB and referenced to ferrocene (top) and a plot of current density (j_p) versus the square root of scan rate ($v^{1/2}$) with linear fits used to model the data with the Randles–Sevcik equation (bottom).

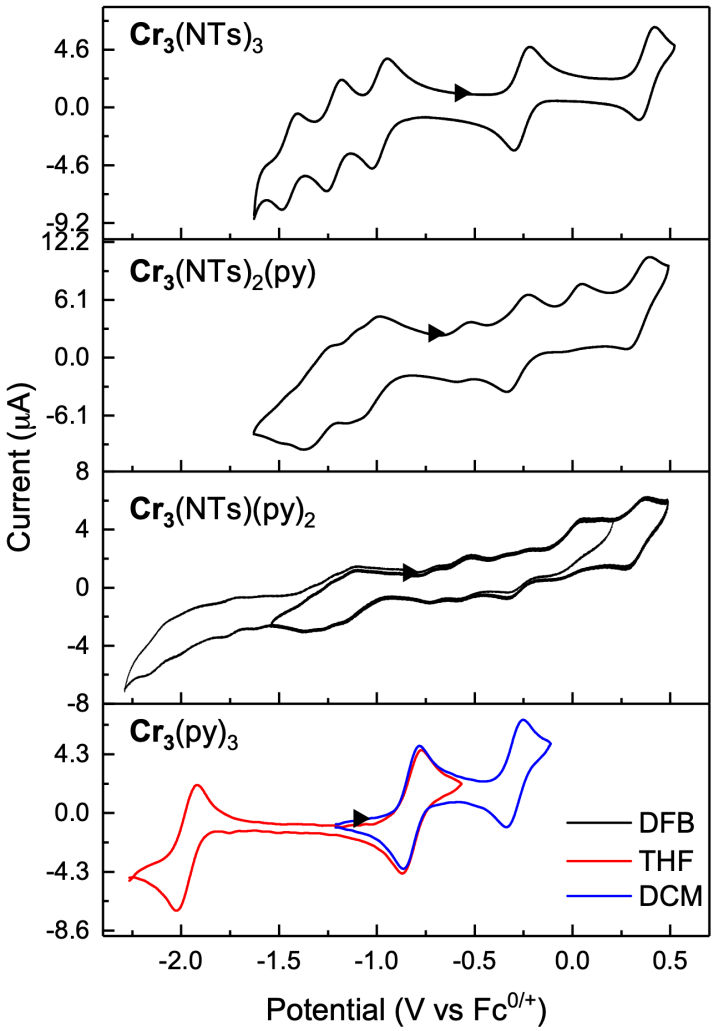


Figure 6.31. Cyclic voltammograms of **Cr$_3$**(py)$_3$, **Cr$_3$**(NTs)$_3$, **Cr$_3$**(NTs)$_2$(py) and **Cr$_3$**(NTs)(py)$_2$, recorded at 50 mV s^{-1} in 0.1 M [^{n}Bu$_4$N][PF$_6$] DFB, THF or DCM and referenced to ferrocene. Open circuit potentials denoted with black arrows. In the case of **Cr$_3$**(NTs)(py)$_2$, multiple potential windows were sample to verify the reversibility of the electrochemical events.

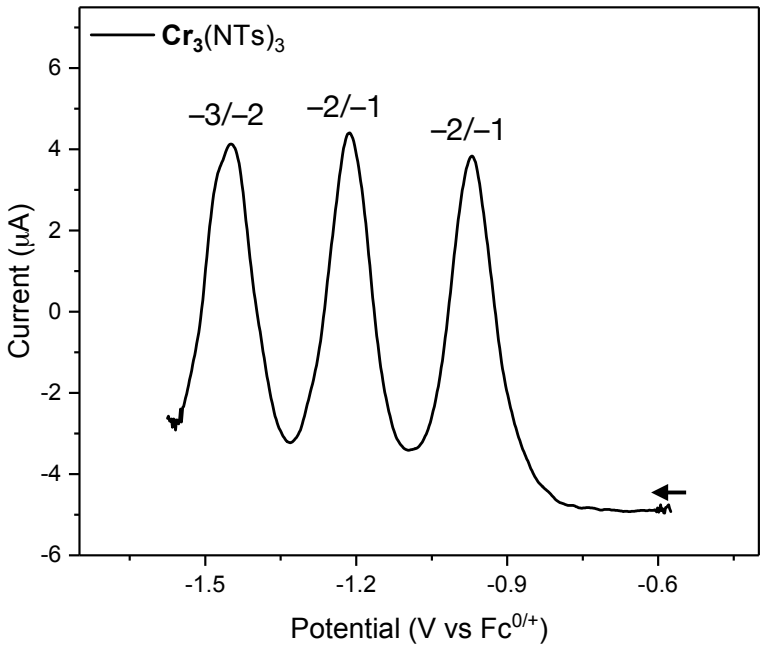


Figure 6.32. Differential pulse voltammogram of the three reduction processes of **Cr$_3$**(NTs)$_3$ in 0.1 M [^{n}Bu$_4$N][PF$_6$] in DFB solution. Step size = 2 mV, Pulse amplitude = 25 mV, Sample period = 2 s, Pulse time = 0.5 s.

6.12.9 *Magnetic Measurements*

Direct Current (*dc*) Magnetic susceptibility data for **Cr$_3$**(py)$_3$, **Cr$_3$**(NTs)$_3$, [**Cr$_3$**(NTs)$_3$][PF$_6$], and [K(222-crypt)]$_3$[**Cr$_3$**(NTs)$_3$] were collected on warming from 5 to 300 K under applied fields of 0.1, 0.5, and 1 T using a Quantum Design Inc. PPMS DynaCool equipped with a 14 T magnet. To prepare these samples, crystalline material was loaded within a VSM powder sample holder (P125E, Quantum Design Inc.) that was carefully sealed with a thin loop of epoxy. Crushed crystalline solids were placed under vacuum at 60 °C for 2 hours prior to analysis. All magnetic susceptibility data was corrected for diamagnetic contributions from the analyte calculated using Pascal's constants,[61] as well as for the susceptibility of the capsule and sample holder. Magnetization data was recorded at 50 K between –14 and 14 T to confirm the absence of any ferromagnetic impurities. Further, variable-temperature *dc* magnetic susceptibility does not decrease with increasing field strength, providing further support that these samples are free of ferromagnetic impurities. Susceptibility data (0.5 T applied field) for **Cr$_3$**(py)$_3$ provides a reasonable value for three weakly interacting Cr(II) (S = 2) ions, with $S_{Tot} = 6$ at 298 K. In contrast,

the observed room temperature magnetic susceptibility of **Cr$_3$**(NTs)$_3$ is greater than that expected for three S = 1 Cr(IV) ions. However, at below 50 K we find that the magnetic susceptibility converges toward a reasonable value for three S = 1 Cr(IV) ions. This data was modeled using PHI in order to extract the g-value and also to approximate the contributions of temperature independent paramagnetism in the case of **Cr$_3$**(NTs)$_3$, but a quantitative model was not developed due to the complexity of the system.[62] Variable-temperature variable-field reduced magnetization data supports the presence of a high-spin ground state, but magnetic saturation is not reached under applied fields of up to 7 T and temperatures down to 2.5 K. Accordingly, the selected spin multiplicity for DFT analysis was assigned based on the observed magnetic susceptibility at 298 K.

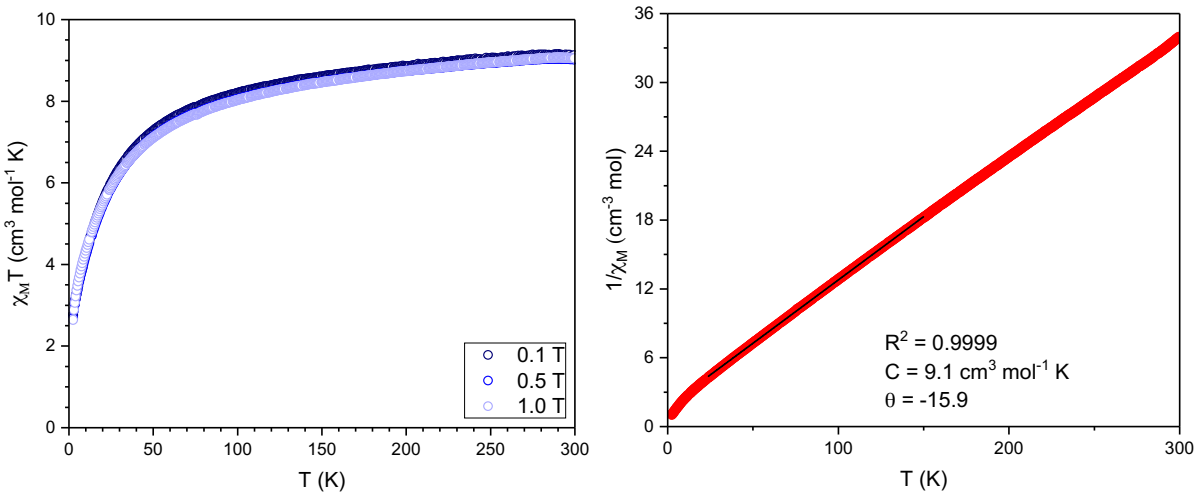


Figure 6.33. (left) Variable-temperature *dc* magnetic susceptibility (χ_MT, filled circles) data recorded for **Cr$_3$**(py)$_3$ upon warming from 5 to 300K under applied fields of 0.1, 0.5, and 1.0 T. (right) Reciprocal molar susceptibility ($1/\chi_M$) data recorded for **Cr$_3$**(py)$_3$ upon warming from 5 to 300K with an applied field of 0.5 T. A linear fit to the data between 25 and 150 K was used to calculate Curie (C) and Weiss (θ) constants.

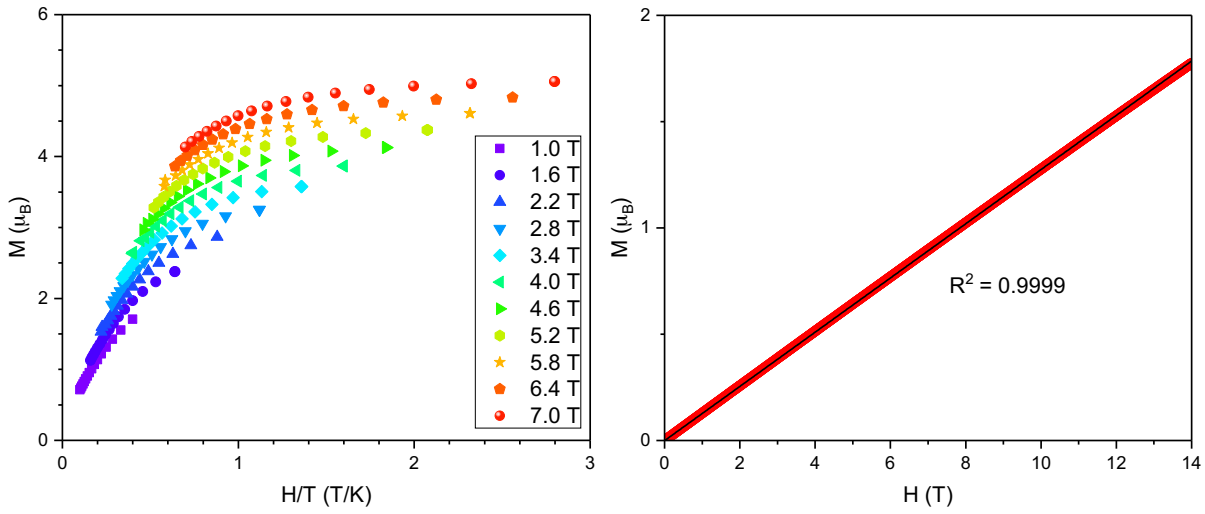


Figure 6.34. (left) Variable-temperature, variable-field reduced magnetization data for **Cr$_3$**(py)$_3$, collected upon warming from 2.5 to 10 K at each applied field. This plot confirms the presence of a high-spin ground state, but the sample resists magnetic saturation under applied magnetic fields up to 7.0 T. (right) Magnetization of **Cr$_3$**(py)$_3$ recorded on sweeping the applied field from 0 and 14 T at 50 K.

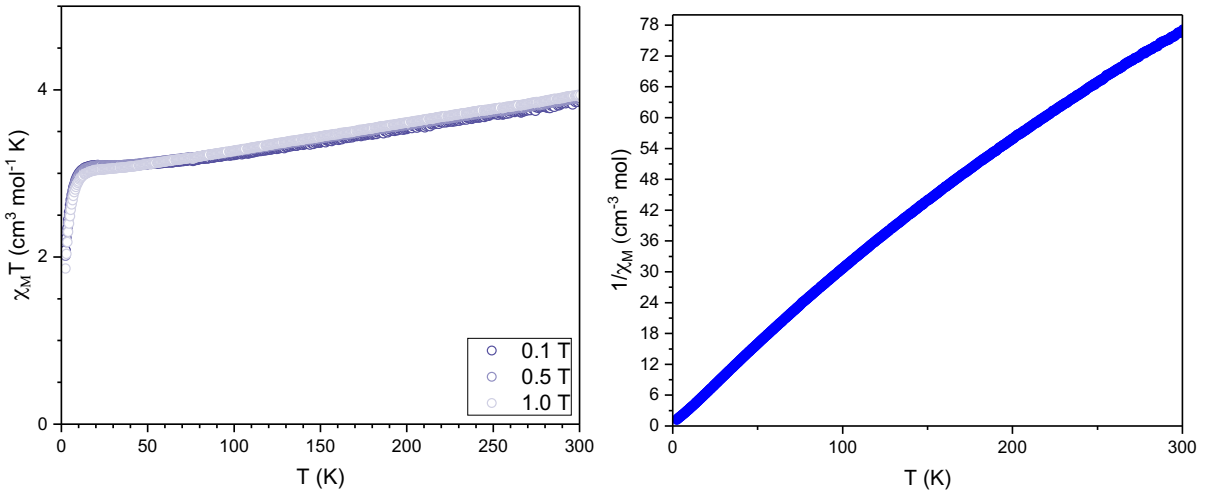


Figure 6.35. (left) Variable-temperature *dc* magnetic susceptibility (χ_MT, filled circles) data recorded for **Cr$_3$**(NTs)$_3$ upon warming from 5 to 300K under applied fields of 0.1, 0.5, and 1.0 T. (right) Reciprocal molar susceptibility ($1/\chi_M$) data recorded for **Cr$_3$**(NTs)$_3$ upon warming from 5 to 300K with an applied field of 0.5 T.

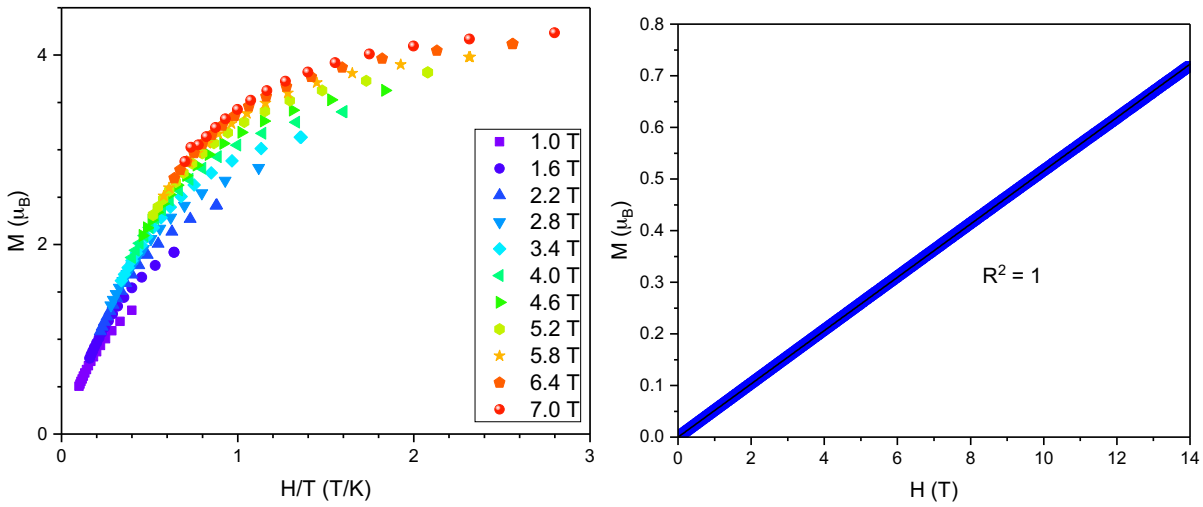


Figure 6.36. (left) Variable-temperature, variable-field reduced magnetization data for **Cr$_3$**(NTs)$_3$, collected upon warming from 2.5 to 10 K at each applied field. This plot confirms the presence of a high-spin ground state, but the sample resists magnetic saturation under applied magnetic fields up to 7.0 T. (right) Magnetization of **Cr$_3$**(NTs)$_3$ recorded on sweeping the applied field from 0 and 14 T at 50 K.

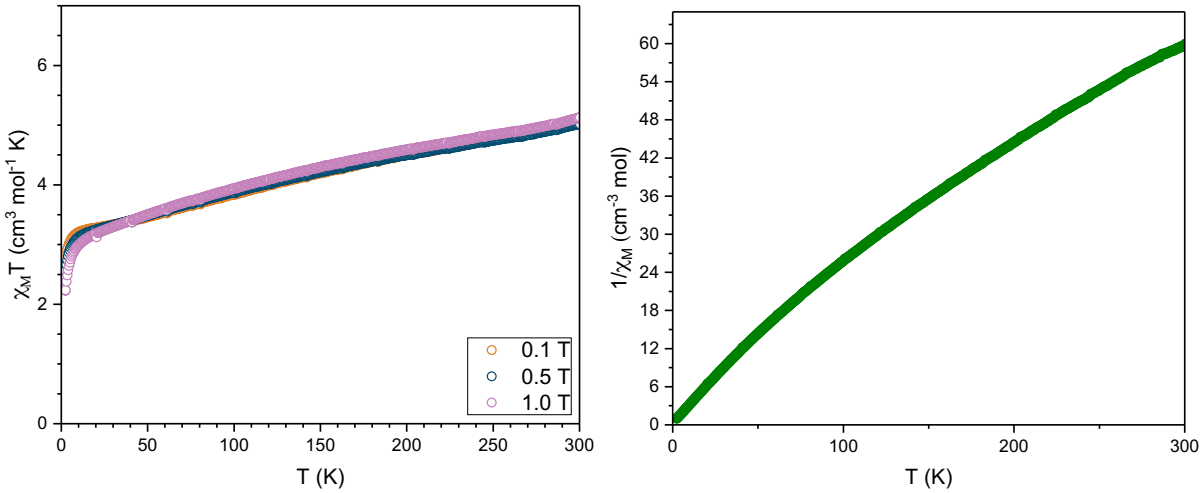


Figure 6.37. (left) Variable-temperature *dc* magnetic susceptibility (χ_MT, filled circles) data recorded for [**Cr$_3$**(NTs)$_3$][PF$_6$] upon warming from 5 to 300K under applied fields of 0.1, 0.5, and 1.0 T. (right) Reciprocal molar susceptibility ($1/\chi_M$) data recorded for [**Cr$_3$**(NTs)$_3$][PF$_6$] upon warming from 5 to 300K with an applied field of 0.5 T.

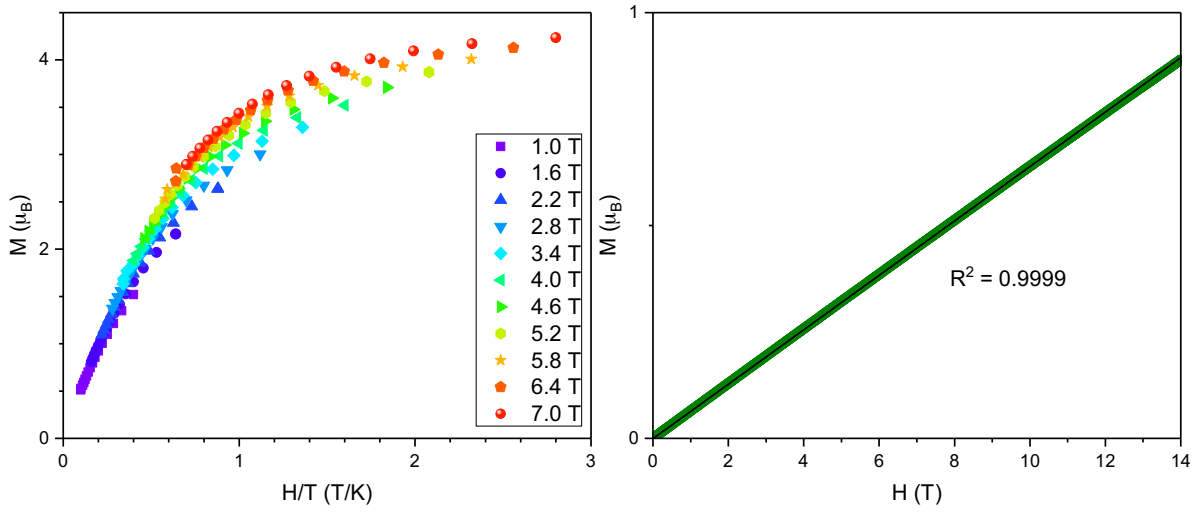


Figure 6.38. (left) Variable-temperature, variable-field reduced magnetization data for [**Cr$_3$**(NTs)$_3$][PF$_6$], collected upon warming from 2.5 to 10 K at each applied field. This plot confirms the presence of a high-spin ground state, but the sample resists magnetic saturation under applied magnetic fields up to 7.0 T. Magnetization of [**Cr$_3$**(NTs)$_3$][PF$_6$] recorded on sweeping the applied field from 0 and 14 T at 50 K.

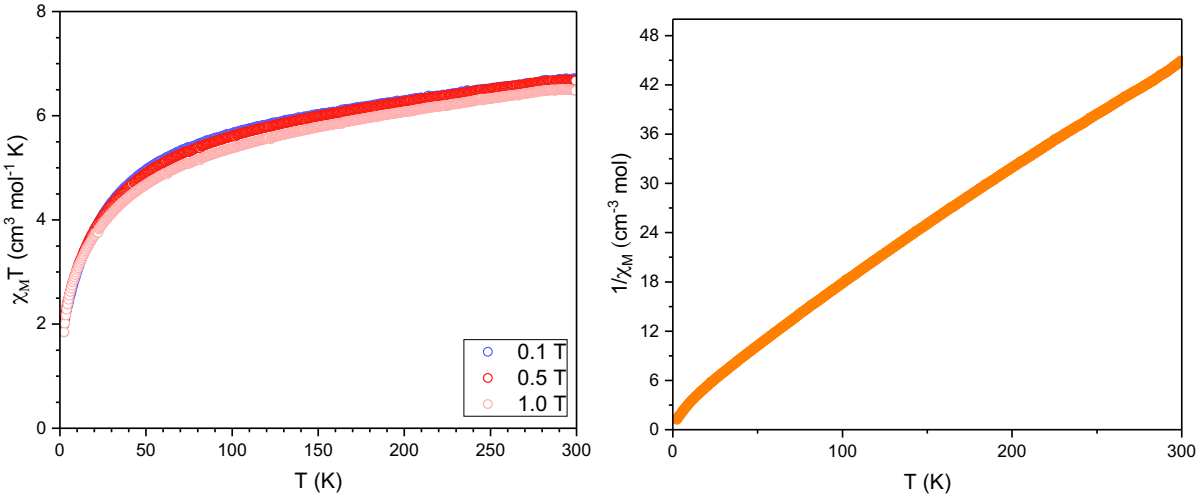


Figure 6.39. (left) Variable-temperature *dc* magnetic susceptibility (χ_MT, filled circles) data recorded for [K(222-crypt)]$_3$[**Cr$_3$**(NTs)$_3$] upon warming from 5 to 300K under applied fields of 0.1, 0.5, and 1.0 T. (right) Reciprocal molar susceptibility ($1/\chi_M$) data recorded for [K(222-crypt)]$_3$[**Cr$_3$**(NTs)$_3$] upon warming from 5 to 300K with an applied field of 0.5 T.

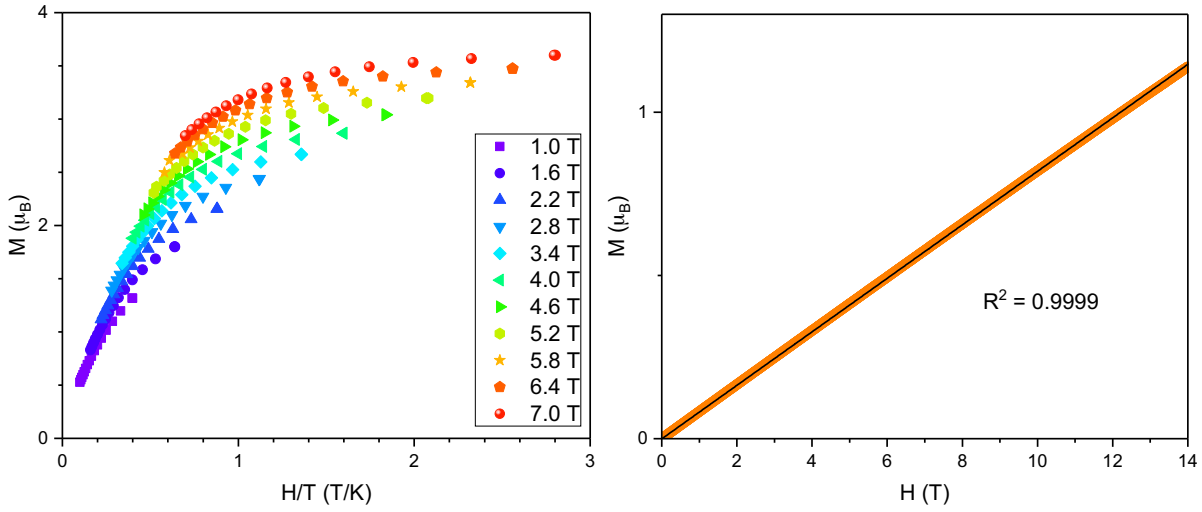


Figure 6.40. (left) Variable-temperature, variable-field reduced magnetization data for [K(222-crypt)]$_3$[**Cr$_3$**(NTs)$_3$], collected upon warming from 2.5 to 10 K at each applied field. This plot confirms the presence of a high-spin ground state, but the sample resists magnetic saturation under applied magnetic fields up to 7.0 T. (right) Magnetization of [K(222-crypt)]$_3$[**Cr$_3$**(NTs)$_3$] recorded on sweeping the applied field from 0 and 14 T at 50 K.

6.12.10 *DFT Calculations*

All calculations were performed using Gaussian 16, Revision B.01 quantum chemistry program package for the Linux operating system.[63] The initial starting point geometries were adapted from the corresponding crystallographically obtained structures and optimized to a stationary point, followed by analytical frequency calculations (Hessian) to confirm that no imaginary frequencies were present. The geometry optimizations were performed using DFT calculations at a pure GGA functional level using Becke's 1988 gradient-corrected exchange functional[64] and Perdew's 1986 electron correlation functional[65] (BPV86) and def2SVP[66,67] as a basis set. Using the optimized geometries, single point calculations were conducted using B3LYP+[68–71] as a functional and the correlation consistent basis set, cc-pVTZ.[72–76] These single point calculations were used to generate density of states plots, orbital energy diagrams, and spin density calculations. Multiwfn was used to generate partial density of states plots.[77]

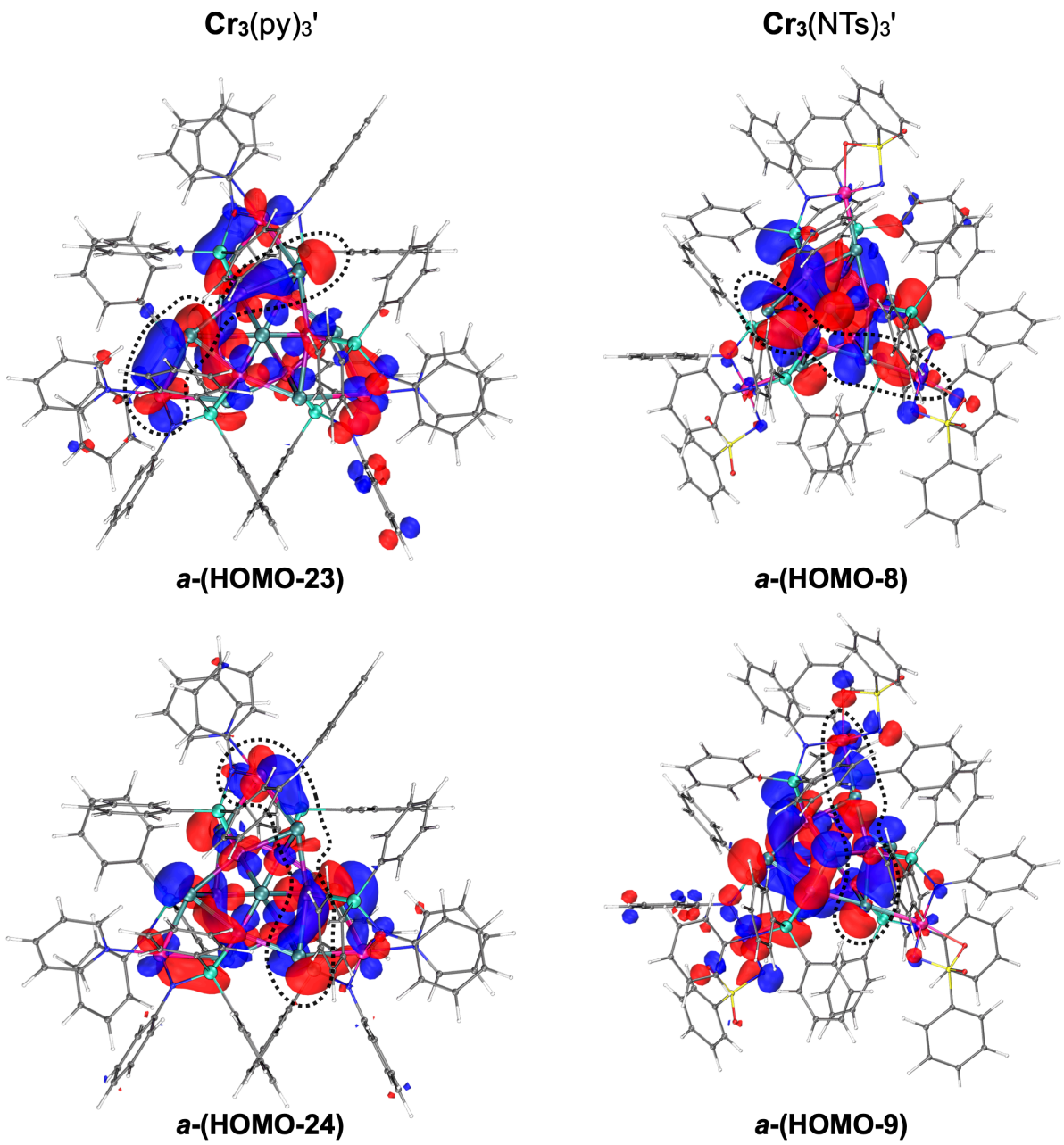


Figure 6.41. Isosurface plots (0.04 a.u.) for select molecular orbitals of **Cr$_3$**(py)$_3$′ and **Cr$_3$**(NTs)$_3$′. The orbitals are illustrative of the following interactions: 1) **Cr$_3$**(py)$_3$′ *a*-(HOMO-23) depicts the *Cr–Se···Co–Se* bonding orbital that projects along the axial Cr–Se bond, and represents a bonding counterpart to the HOMO; 2) **Cr$_3$**(py)$_3$′ *a*-(HOMO-24) depicts an analogous equatorial *Cr–Se···Co–Se* bonding orbital; 3) **Cr$_3$**(NTs)$_3$′ *a*-(HOMO-8) exhibits *Cr–Se···Co–Se* character, confirming presence of the same bonding motif at Cr(NTs) edge sites; 4) **Cr$_3$**(NTs)$_3$′ *a*-(HOMO-9) exhibits *Cr–Se–Co–Se* all-bonding character. Outlines included to aid inspection, which is admittedly very challenging, even for the author. All calculations run at the B3LYP+/cc-PVTZ level of theory.

Table 6.3. Comparison of bond metrics of the DFT optimized structures of **Cr$_3$**(py)$_3$′ and **Cr$_3$**(NTs)$_3$′ to those extracted from the single-crystal X-ray diffraction structures of **Cr$_3$**(py)$_3$ and **Cr$_3$**(NTs)$_3$. Parameters listed from top to bottom correspond to α1, α2, and β edge sites, respectively.

Compound	Interatomic Distance (Å)				
	Cr…Se	Cr–N^{L} (L = ^{a}py, ^{b}NTs)	Cr–N^{Tol}	Co–P (avg.)	Co–Se (avg.)
Cr$_3$(py)$_3$	2.581(2) 2.726(2) 2.637(1) 2.719(2) 2.647(2) 2.703(2)	2.102(7)^{a} 2.150(8)^{a} 2.116(7)^{a}	2.022(7) 2.058(7) 2.059(8) 2.039(8) 2.048(7) 2.047(7)	2.16	2.35
Cr$_3$(py)$_3$′ (calc.)	2.6223 2.6838 2.6194 2.6435 2.6182 2.6860	2.1076^{a} 2.1191^{a} 2.1166^{a}	2.0400 2.0466 2.0546 2.0598 2.0465 2.0716	2.17	2.37
Cr$_3$(NTs)$_3$	2.513(5) 2.463(5) 2.471(5)	1.81(2)^{b} 1.84(2)^{b} 1.82(2)^{b}	1.88(2) 1.89(2) 1.87(2) 1.88(2) 1.91(2) 1.93(2)	2.13	2.35
Cr$_3$(NTs)$_3$′ (calc.)	2.5406 2.5191 2.5473	1.8330^{b} 1.8334^{b} 1.8208^{b}	1.9035 1.9046 1.9018 1.9072 1.9107 1.9336	2.15	2.35

Table 6.4. Comparison of bond metrics of the DFT optimized structures of **Cr$_3$**(NTs)(py)$_2$′ and **Cr$_3$**(NTs)$_2$(py)′ to those extracted from the single-crystal X-ray diffraction structures of **Cr$_3$**(NTs)(CN^{t}Bu)$_2$ and **Cr$_3$**(NTs)$_2$(py). Parameters listed from top to bottom correspond to α1, α2, and β edge sites, respectively.

Compound	Interatomic Distance (Å)				
	Cr…Se	Cr–N^L (L = ^{a}py, ^{b}NTs)	Cr–N^{Tol}	Co–P (avg.)	Co–Se (avg.)
Cr$_3$(NTs)(CN^{t}Bu)$_2$	2.444(3) 2.648(2) 2.655(3) 2.611(3) 2.663(4)	2.02(2)^b -- --	1.86(1) 1.939(9) 2.05(1) 2.059(9) 1.84(3) 2.04(1)	2.15	2.35
Cr$_3$(NTs)(py)$_2$′ (calc.)	2.5410 2.6133 2.6547 2.5970 2.6667	1.8228^b 2.1126^a 2.1174^a	1.9111 1.9314 2.0576 2.0621 2.0478 2.0624	2.16	2.37
Cr$_3$(NTs)$_2$(py)	2.639(3) 2.724(5) 2.480(5) 2.476(2)	2.07(1)^a 1.832(9)^b 1.829(8)^b	2.042(8) 2.054(8) 1.914(8) 1.926(8) 1.905(7) 1.905(8)	2.15	2.34
Cr$_3$(NTs)$_2$(py)′ (calc.)	2.6263 2.6421 2.5051 2.5279	2.1095^a 1.8349^b 1.8298^b	2.0372 2.0425 1.9013 1.9069 1.9066 1.9078	2.16	2.36

Table 6.5. Total energies calculated for **Cr$_3$**(py)$_3$′, **Cr$_3$**(NTs)(py)$_2$′, *trans*-(α,β,α)-**Cr$_3$**(NTs)$_2$(py)′, *cis*-(α,β,α)-**Cr$_3$**(NTs)$_2$(py)′, *trans*-(α,α,β)-**Cr$_3$**(NTs)$_2$(py)′, **Cr$_3$**(NTs)$_3$′, and **Cr$_3$**(NTs)$_3$(CN′Bu)$_3$′ calculated at the B3LYP+/cc-pVTZ level of theory.

Compound	**Total Energy (eV)**
Cr$_3$(py)$_3$′	-1029565.8427643
Cr$_3$(NTs)(py)$_2$′	-1045469.9542480
trans-(α,β,α)-**Cr$_3$**(NTs)$_2$(py)′	-1061374.0254424
cis-(α,β,α)-**Cr$_3$**(NTs)$_2$(py)′	-1061373.9959997
(α,α,β)-**Cr$_3$**(NTs)$_2$(py)′	-1061373.8304346
Cr$_3$(NTs)$_3$′	-1077277.9960690
Cr$_3$(NTs)$_3$(CNMe)$_3$′	-1088043.8896469

Table 6.6. Composition analysis for the highest lying core-centered orbitals of **Cr$_3$**(py)$_3$′, **Cr$_3$**(NTs)(py)$_2$′, **Cr$_3$**(NTs)$_2$(py)′, and **Cr$_3$**(NTs)$_3$′ at the B3LYP+/cc-pVTZ level of theory. Orbital composition analysis conducted using Multiwfn (see Ref. 62)

Compound	**Orbital**	**%Cr**	**%Co**	**%Se**
Cr$_3$(py)$_3$′	*a*-HOMO–6	31.9	24.6	30.5
Cr$_3$(NTs)(py)$_2$′	*a*-HOMO–4	14.4	25.6	45.1
Cr$_3$(NTs)$_2$(py)′	*a*-HOMO–2	2.4	38.1	55.5
Cr$_3$(NTs)$_3$′	*a*-HOMO	1.5	26.7	66.4

Table 6.7. Hirshfeld spin-density (α−β) values calculated for **Cr$_3$**(py)$_3$′, **Cr$_3$**(NTs)(py)$_2$′, *trans*-(α,α,β)-**Cr$_3$**(NTs)$_2$(py)′, and **Cr$_3$**(NTs)$_3$′ at the B3LYP+/cc-pVTZ level of theory.

Compound	Hirshfeld Spin-density								
	Cr1	Cr2	Cr3	Co_6Se_8 core	N^{Tol} (avg.)	N^{Ts} (avg.)	Total Spin	% on Cr edges	% on Co_6Se_8
Cr$_3$(py)$_3$′	3.45[b]	3.40[b]	3.43[b]	0.96	0.04	--	12	85.7	8.0
Cr$_3$(NTs)(py)$_2$′	3.41[b]	3.41[b]	2.06[a]	0.72	0.02	–0.06	10	88.7	7.2
trans-(α,α,β)-**Cr$_3$**(NTs)$_2$(py)′	3.39[a]	2.01[a]	2.04[a]	0.49	0.00	–0.05	8	93.0	6.1
Cr$_3$(NTs)$_3$′	2.04[a]	2.02[a]	2.02[a]	0.12	–0.02	–0.05	6	101.1	1.9

[a]Cr(NTs) edge site; [b]Cr(py) edge site.

Table 6.8. Hirshfeld charges calculated for **Cr$_3$**(py)$_3$′, **Cr$_3$**(NTs)(py)$_2$′, *trans*-(α,α,β)-**Cr$_3$**(NTs)$_2$(py)′, and **Cr$_3$**(NTs)$_3$′ at the B3LYP+/cc-pVTZ level of theory.

Compound	Hirshfeld Charge (a.u.)		
	Cr1	Cr2	Cr3
Cr$_3$(py)$_3$′	0.43[b]	0.43[b]	0.43[b]
Cr$_3$(NTs)(py)$_2$′	0.43[b]	0.43[b]	0.56[a]
trans-(α,α,β)-**Cr$_3$**(NTs)$_2$(py)′	0.43[b]	0.56[a]	0.56[a]
Cr$_3$(NTs)$_3$′	0.56[a]	0.56[a]	0.56[a]

[a]Cr(NTs) edge site; [b]Cr(py) edge site.

6.12.11 *X-ray Structure Determination*

Single crystals suitable for X-ray analysis were coated in deoxygenated paratone oil and mounted on a 20 µm CryoLoop™ (Hampton Research, 18 mm mount, 0.2 to 0.3 mm loop diameter). Data was collected either at –173 °C or –183 °C on a Bruker APEX II or Nonius Kappa CCD FR590 single crystal X-ray diffractometer, respectively, each equipped with a Mo source, as indicated for each sample. Unless indicated otherwise, all data was integrated and scaled using SAINT, SADABS within the APEX2 software package by Bruker.[78] Solution by direct methods (SHELXT[79] or SIR97[80,81]) produced a complete heavy atom phasing model consistent with the proposed structure. Structures were completed by difference Fourier synthesis with SHELXL.[82–84] Scattering factors are from Waasmair and Kirfel.[85] Hydrogen atoms were placed in geometrically idealized positions and constrained to ride on their parent atoms with C–H distances in the range 0.95–1.00 Å. Isotropic thermal parameters U_{eq} were fixed such that they were $1.2U_{eq}$ of their parent atom U_{eq} for CHs and $1.5U_{eq}$ of their parent atom U_{eq} in case of methyl groups. All non-hydrogen atoms were refined anisotropically by full-matrix least-squares.

6.12.11.1 *trans*-(α,β,α)-$\mathbf{Cr_3}(NTs)_2(py)$

Dark red prismatic crystals of *trans*-(α,β,α)-$\mathbf{Cr_3}(NTs)_2(py)$ suitable for single crystal X-ray diffraction analysis were grown from a concentrated solution of the cluster in benzene layered by *n*-pentane at 25 °C over the course of 14 h. The compound crystallizes in the triclinic space group $P\bar{1}$, and the asymmetric unit contains a singular cluster molecule and six benzene solvent molecules. The solid-state structure reveals that two Cr edge metals are bound by a tosyl nitrenoid group, while the third Cr center is bound by a pyridyl ligand. The structure exhibits multiple instances of chemical disorder including the tolyl groups of both tosyl imido substituents, one tolyl amido substituent, and two benzene solvent molecules. The disordered tolyl substituents were structurally related via SAME and the benzene molecules were idealized with AFIX 66 .. AFIX 0 loops. The overall displacement parameters of all carbon atoms were restrained with ISOR and linked along interatomic bonds using DELU. Seven bad reflections were removed.

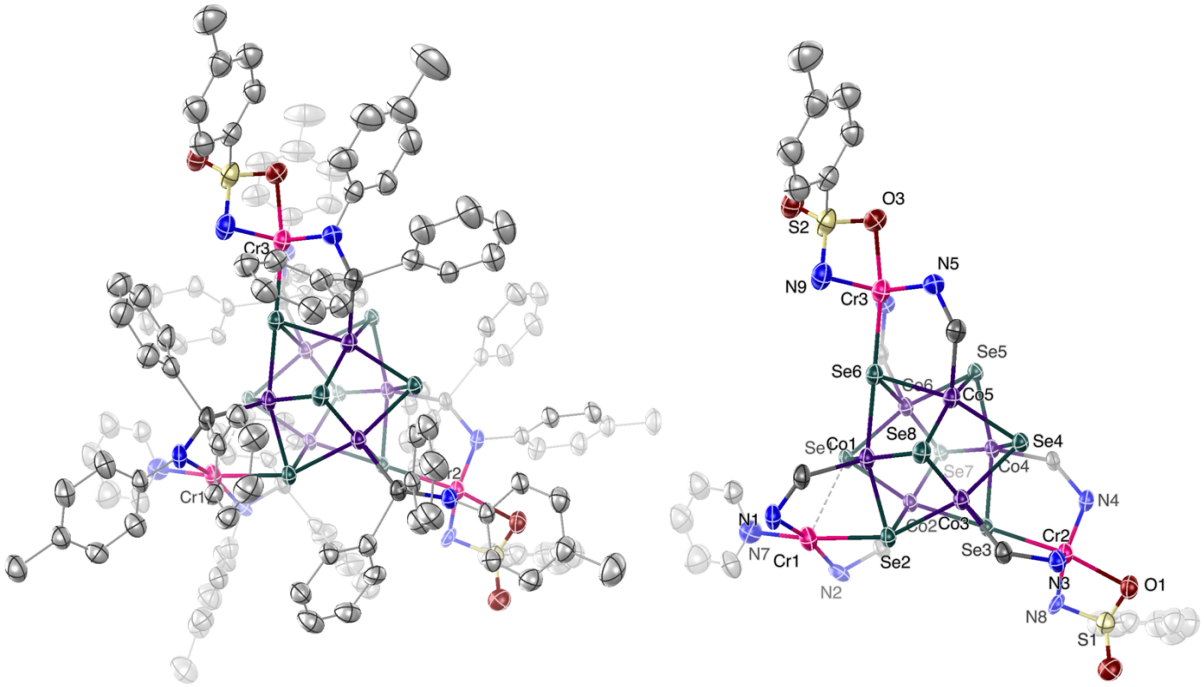


Figure 6.42. Solid-state structure of *trans*-(α,β,α)-**Cr$_3$**(NTs)$_2$(py) with thermal ellipsoids plotted at 50% probability. All hydrogen atoms, co-crystallizing solvent molecules and instances of chemical disorder are omitted for clarity. Selected interatomic distances (Å) and angles (°): Cr1-N7 2.073(8), Cr2-N8 1.829(8), Cr3-N9 1.832(8), Cr2-O1 2.097(6), Cr3-O3 2.062(6), Cr1-Se2 2.6392(16), Cr1-Se1 2.7243(17), Cr2-Se3 2.4755(15), Cr3-Se6 2.4801(17), Cr1-N1 2.053(7), Cr2-N3 1.904(7), Cr3-N5 1.926(7), Cr2-N8-S1 95.5(4), Cr3-N9-S2 94.5(4).

6.12.11.2 **Cr$_3$**(NHCHPh)$_3$

Dark red prismatic crystals of **Cr$_3$**(NHCNPh)$_3$ suitable for single crystal X-ray analysis were grown from a concentrated benzene solution layered with *n*-pentane at 25 °C over the course of 24 h. The compound crystallizes in the monoclinic space group C2/c, and the asymmetric unit contains a singular cluster molecule. The contribution of ca. five benzene solvent molecules per cluster to the diffraction pattern was removed using SQUEEZE. Several of the organic substituents on the cluster exhibit disorder and were therefore modeled over two positions, and these disordered groups were further stabilized with some ISOR and SAME restraints. The displacement parameters of the disordered atoms were linked using EADP. Additionally, some phenyl groups were optimized with AFIX 66 loops. A total of 30 bad reflections were removed.

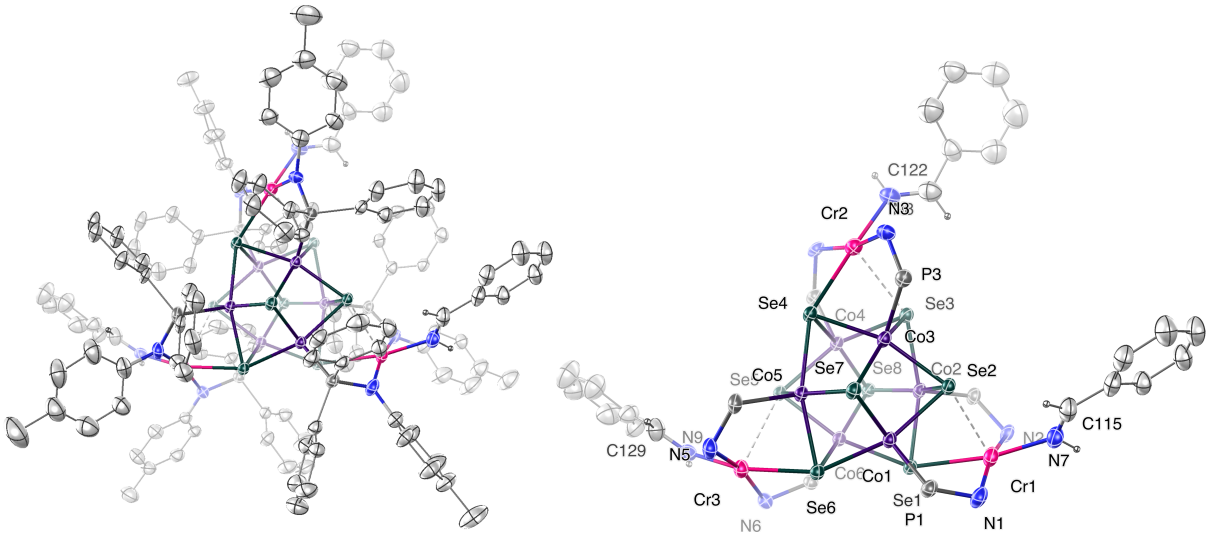


Figure 6.43. Solid-state structure of $\mathbf{Cr_3}(NHCHPh)_3$ with thermal ellipsoids plotted at 50% probability. All hydrogen atoms, co-crystallizing solvent molecules and instances of chemical disorder are omitted for clarity. Selected interatomic distances (Å) and angles (°): Cr1-N7 2.073(6), Cr2-N8 2.095(17), Cr3-N9 2.053(6); Cr1-Se1 2.633(1), Cr1-Se2 2.697(1), Cr2-Se4 2.653(1), Cr2-Se3 2.711(1), Cr3-Se6 2.613(1), Cr3-Se5 2.714(1), Cr1-N1 2.046(5), Cr1-N2 2.053(6), Cr2-N3 2.051(5), Cr2-N4 2.062(5), C122-N8 1.252(17), C115-N7 1.274(8), C129-N9 1.237(13).

6.12.11.3 $[\mathbf{Cr_3}(NTs)_3][PF_6]$

Dark red prismatic crystals of $[\mathbf{Cr_3}(NTs)_3][PF_6]$, suitable for single crystal X-ray diffraction analysis, were grown by layering a concentrated *o*-difluorobenzene solution of the oxidized cluster layered *n*-pentane at –35 °C over the course of 48 h. The compound crystallizes in the triclinic space group $P\bar{1}$, and the asymmetric unit contains two $[\mathbf{Cr_3}(NTs)_3]^+$ clusters, two $[PF_6]^-$ anions, four explicitly refined *o*-difluorobenzene molecules. Residual electron density indicates the presence of additional disordered solvent molecules, the contribution of which to the diffraction pattern was removed with SQUEEZE. All phenyl groups were optimized with AFIX 66 loops. In addition, SAME restraints were required between locally equivalent moieties as well as global ISOR and DELU and a few EADP stabilizations for displacement parameters. A total of 50 bad peaks were excluded from the refinement. In addition, the full scattering range was limited to a resolution of 0.86 Å since there was no good data beyond a resolution of 1Å. The structure is of sufficient quality to be included in a publication for demonstrating connectivity and interatomic distances between heavy atoms (Co, Se, Cr).

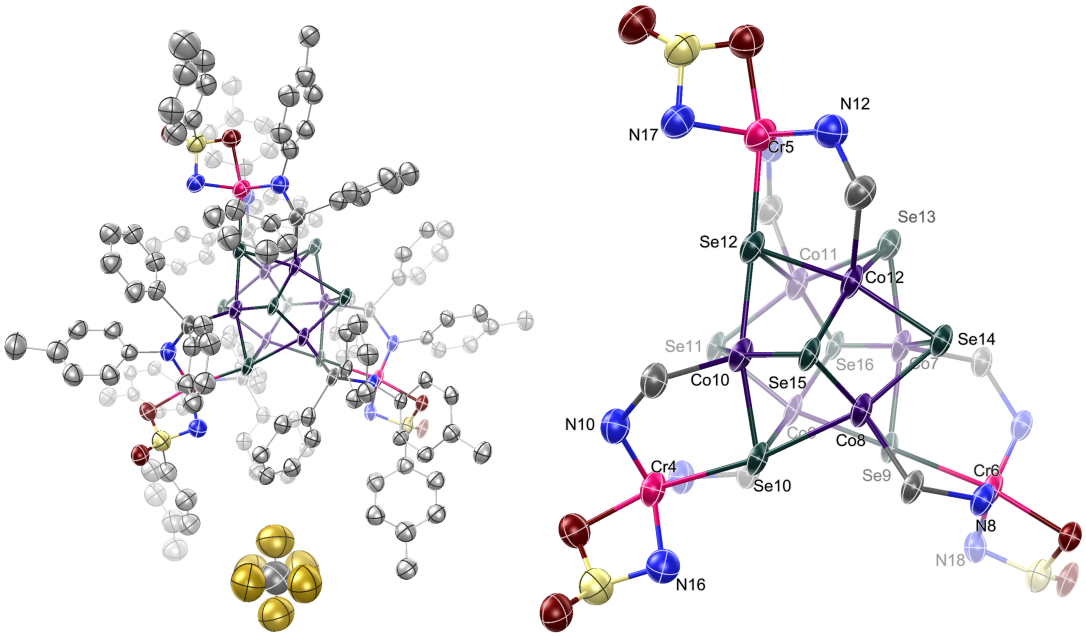


Figure 6.44. Solid-state structure of [**Cr$_3$**(NTs)$_3$][PF$_6$] with thermal ellipsoids plotted at 50% probability. All hydrogen atoms, co-crystallizing solvent molecules and instances of chemical disorder are omitted for clarity. Selected interatomic distances (Å) and angles (°): Cr4-N16 1.81(3), Cr5-N17 1.92(3), Cr6-N18 1.80(2), Cr5-O9 2.04(2), Cr4-Se10 2.547(6), Cr5-Se12 2.469(7), Cr6-Se9 2.499(6), Se10-Co8 2.546(5), Co8-Se14 2.280(6), Cr4-N10 1.91(3), Cr5-N12 1.98(3), Cr6-N8 1.88(3).

6.12.11.4 [K(18-C-6)][**Cr$_3$**(NTs)$_3$]

Large, blocky crystals of [K(18-C-6)][**Cr$_3$**(NTs)$_3$], suitable for single-crystal X-ray analysis, were grown over the course of 48 h by layering a concentrated solution of the reduced cluster in THF with *n*-pentane at –35 °C. The compound crystallizes in the triclinic space group P$\bar{1}$, and the asymmetric unit contains of a singular [**Cr$_3$**(NTs)$_3$]$^-$ molecule where one Cr(NTs) edge is bound to a [K(18-crown-6)]$^+$ counterion. The contribution of disordered mostly THF solvent to the diffraction pattern was removed with SQUEEZE. Since the data was weak, a few restraints were needed, including DELU for P, C, N, O, ISOR for C, N, O, FLAT for two toluene molecules, DFIX for two too close C in the crown, and two hydrogen atoms, as well as an EADP for atoms C1, C101 of a disordered phenyl group. Another toluene in the vicinity of the crown is disordered as well.

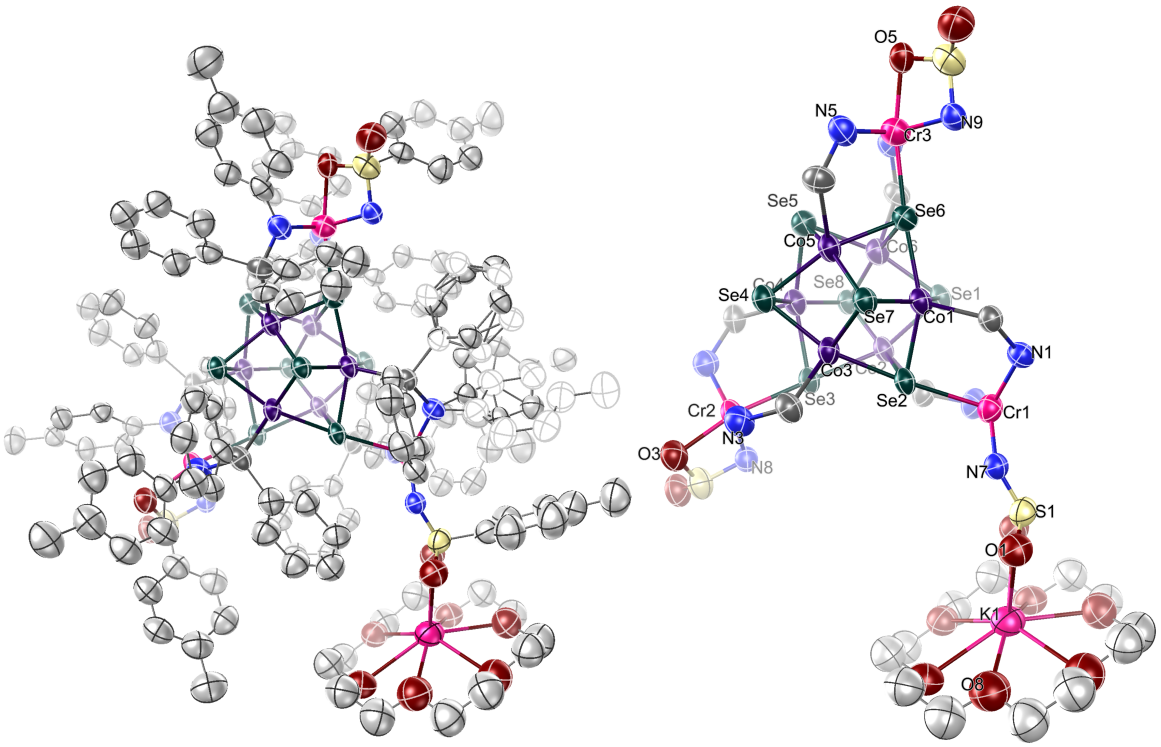


Figure 6.45. Solid-state structure of [K(18-C-6)][**Cr**$_3$(NTs)$_3$] with thermal ellipsoids plotted at 50% probability. All hydrogen atoms, co-crystallizing solvent molecules and instances of chemical disorder are omitted for clarity. Selected interatomic distances (Å) and angles (°): Cr1-Se2 2.563(5), Cr2-Se3 2.371(5), Cr3-Se6 2.359(5), Cr1-N7 1.732(19), Cr2-N8 1.78(2), Cr3-N9 1.75(2), Cr1-N1 1.873(17), Cr1-N2 1.797(16), Cr2-N3 1.821(16), Cr3-N5 1.786(17), Cr2-O3 1.977(18), Cr3-O5 1.988(17), Co3-Se2 2.263(4), Co3-Se4 2.230(4), Co1-Se6 2.299(4), Co1-Se2 2.221(4).

6.12.11.5 X-ray Tables

Table 6.9. Crystallographic information for **Cr$_3$**(NTs)(CN^{t}Bu)$_2$, **Cr$_3$**(NHCHPh)$_3$, and **Cr$_3$**(NTs)$_2$(py).

Compound	**Cr$_3$**(NHCHPh)$_3$	**Cr$_3$**(NTs)$_2$(py)
Empirical formula	$C_{135}H_{123}Co_6Cr_3N_9P_6Se_8$	$C_{169}H_{157}Co_6Cr_3N_9O_4P_6S_2Se_8$
Formula weight	3198.50	3769.23
Temperature (K)	100(2)	100(2)
Wavelength (Å)	0.71073	0.71073
Crystal system	Monoclinic	Triclinic
Space group	C 2/c	$P\bar{1}$
a (Å)	37.789(3)	16.9339(11)
b (Å)	16.071(1)	19.4579(13)
c (Å)	50.347(4)	24.7724(16)
α (°)	90	85.522(3)
β (°)	104.506(4)	84.182(3)
γ (°)	90	72.832(3)
Volume (Å^3)	29600(4)	7748.6(9)
Z	8	2
ρ^{calc} (g cm^{-1})	1.435	1.615
Absorption coefficient (mm^{-1})	2.944	2.853
F(000)	12736	3788
Crystal size (mm^3)	0.300 x 0.150 x 0.120	0.310 x 0.090 x 0.070
Theta range for data collection (°)	1.485 to 28.421	1.407 to 28.509
Index ranges	$-50\leq h\leq 50$, $-21\leq k\leq 21$, $-65\leq l\leq 66$	$-22\leq h\leq 22$, $-25\leq k\leq 25$, $-32\leq l\leq 32$
Reflections collected	65744	77084
Independent reflections	35076 [R(int) = 0.0527]	38857 [R(int) = 0.1036]
Completeness to theta = 25.000°	98.8	99.9%
Data / restraints / parameters	35076 / 717 / 1542	38857 / 1939 / 1758
Goodness-of-fit on F^2	1.044	1.023
Final R indices [I>2sigma(I)]	R1 = 0.0677, wR2 = 0.1441	R1 = 0.0769, wR2 = 0.1682
R indices (all data)	R1 = 0.1137, wR2 = 0.1605	R1 = 0.1933, wR2 = 0.2190
Largest diff. peak and hole (e$^-$Å^{-3})	1.572 and –1.042	1.802 and –1.003

Table 6.10. Crystallographic information for [**Cr$_3$**(NTs)$_3$][PF$_6$] and [K(18-C-6)][**Cr$_3$**(NTs)$_3$].

Compound	[**Cr$_3$**(NTs)$_3$][PF$_6$]	[K(18-C-6)][**Cr$_3$**(NTs)$_3$]
Empirical formula	$C_{147}H_{131}Co_6Cr_3F_{10}N_9O_6P_7S_3Se_8$	$C_{147}H_{147}Co_6Cr_3KN_9O_{12}P_6S_3Se_8$
Formula weight	3763.83	3694.09
Temperature (K)	100(2)	100(2)
Wavelength (Å)	0.71073	0.71073
Crystal system	Triclinic	Triclinic
Space group	$P\bar{1}$	$P\bar{1}$
a (Å)	21.709(3)	13.5208(13)
b (Å)	24.113(3)	21.561(2)
c (Å)	33.995(5)	28.037(3)
α (°)	93.730(9)	92.559(7)
β (°)	106.949(9)	98.400(7)
γ (°)	95.659(9)	101.903(6)
Volume (Å^3)	16857(4)	7888.0(14)
Z	4	2
ρ^{calc} (g cm^{-1})	1.483	1.555
Absorption coefficient (mm^{-1})	2.653	2.843
F(000)	7492	3702
Crystal size (mm^3)	0.170 x 0.080 x 0.050	0.22 x 0.100 x 0.070
Theta range for data collection (°)	1.000 to 24.407	1.170 to 25.027
Index ranges	$-20\leq h\leq 20$, $-23\leq k\leq 23$, $-32\leq l\leq 32$	$-16\leq h\leq 16$, $-25\leq k\leq 25$, $-33\leq l\leq 33$
Reflections collected	55417	55679
Independent reflections	55417 [R(int) = 0.2452]	27844 [R(int) = 0.2112]
Completeness to theta = 25.000°	99.9%	100.0
Data / restraints / parameters	55417 / 4314 / 3019	27844 / 2658 / 1599
Goodness-of-fit on F^2	1.030	0.941
Final R indices [I>2sigma(I)]	R1 = 0.1725, wR2 = 0.3207	R1 = 0.1243, wR2 0.2849
R indices (all data)	R1 = 0.4758, wR2 = 0.4142	R1 = 0.3593, wR2 0.4034
Largest diff. peak and hole (e$^-$Å^{-3})	2.533 and –2.016	1.357 and –1.155

Table 6.11. Select interatomic distances for **Cr$_3$**(py)$_3$, **Cr$_3$**(NTs)$_2$(py), **Cr$_3$**(NTs)$_3$ · 2 CH_2Cl_2, **Cr$_3$**(NTs)$_3$(CN^{t}Bu)$_3$, and **Cr$_3$**(NTs)(CN^{t}Bu)$_2$.

Compound	Interatomic Distance (Å)								
	Cr–N_{NTs}	Cr–N_{Tol}	Cr–Se (κ^3)	Cr–Se (κ^4)	Cr–O_{NTs}	Cr–C_{CNtBu}	Cr–N_{py}	Co–Se	τ_5
Cr$_3$(py)$_3$	--	2.022(7) 2.058(7) 2.059(8) 2.039(8) 2.048(7) 2.047(7)	--	2.581(1) 2.726(1) 2.647(2) 2.703(2) 2.637(1) 2.719(2)	--	--	2.102(7) 2.150(8) 2.116(7)	2.296(3) - 2.469(3) Avg. 2.35 ∑ 56.34	0.08 0.15 0.17
Cr$_3$(NTs)$_2$(py)	-- 1.832(8) 1.829(8)	2.053(7) 2.042(8) 1.904(7) 1.905(7) 1.926(7) 1.915(7)	-- 2.476(2) 2.480(2)	2.639(2) 2.724(2) -- --	-- 2.097(6) 2.062(6)	--	2.073(8) -- --	2.305(1) - 2.426(1) Avg. 2.34 ∑ 56.27	0.10 0.68 0.71
Cr$_3$(NTs)$_3$ · 2 CH_2Cl_2	1.81(2) 1.82(2) 1.84(2)	1.88(2) 1.90(2) 1.91(2) 1.93(2) 1.87(2) 1.88(2)	2.513(5) 2.471(5) 2.463(5)	--	2.12(2) 2.10(2) 2.05(2)	--	--	2.292(4) - 2.476(4) Avg. 2.34 ∑ 56.15	0.70 0.73 0.64
Cr$_3$(NTs)$_3$(CN^{t}Bu)$_3$	1.746(8) 1.747(8) 1.745(8)	1.931(6) 1.915(8) 1.931(7) 1.83(1) 1.95(1) 1.93(1)	2.574(3) 2.605(3) 2.656(6)	--	--	2.07(1) 2.07(1) 2.07(1)	--	2.313(3) - 2.414(2) Avg. 2.34 ∑ 56.21	0.81 0.79 0.84
Cr$_3$(NTs)(CN^{t}Bu)$_2$	1.862(9)	2.02(2) 1.939(9) 1.84(2) 2.04(1) 2.059(9) 2.050(9)	2.444(2)	2.611(2) 2.663(2) 2.646(2) 2.655(2)	2.082(9)	2.07(1) 2.09(1)	--	2.309(2) - 2.419(2) Avg. 2.35 ∑ 56.34	0.61 0.18 0.17

6.13 REFERENCES

(1) *Synthesis of Solid Catalysts*, 1st ed.; De Jong, K. P., Ed.; Wiley, 2009. https://doi.org/10.1002/9783527626854.

(2) Kaiser, S. K.; Chen, Z.; Faust Akl, D.; Mitchell, S.; Pérez-Ramírez, J. Single-Atom Catalysts across the Periodic Table. *Chem. Rev.* **2020**, *120* (21), 11703–11809. https://doi.org/10.1021/acs.chemrev.0c00576.

(3) Nørskov, J. K.; Studt, F.; Abild-Pedersen, F.; Bligaard, T. *Fundamental Concepts in Heterogeneous Catalysis*; Wiley: Hoboken, New Jersey, 2015.

(4) Nørskov, J. K.; Bligaard, T.; Hvolbæk, B.; Abild-Pedersen, F.; Chorkendorff, I.; Christensen, C. H. The Nature of the Active Site in Heterogeneous Metal Catalysis. *Chem. Soc. Rev.* **2008**, *37* (10), 2163. https://doi.org/10.1039/b800260f.

(5) Meirer, F.; Weckhuysen, B. M. Spatial and Temporal Exploration of Heterogeneous Catalysts with Synchrotron Radiation. *Nat Rev Mater* **2018**, *3* (9), 324–340. https://doi.org/10.1038/s41578-018-0044-5.

(6) Vogt, C.; Weckhuysen, B. M. The Concept of Active Site in Heterogeneous Catalysis. *Nat Rev Chem* **2022**, *6* (2), 89–111. https://doi.org/10.1038/s41570-021-00340-y.

(7) Hammer, B. Special Sites at Noble and Late Transition Metal Catalysts. *Top Catal* **2006**, *37* (1), 3–16. https://doi.org/10.1007/s11244-006-0004-y.

(8) Huang, W.; Johnston-Peck, A. C.; Wolter, T.; Yang, W.-C. D.; Xu, L.; Oh, J.; Reeves, B. A.; Zhou, C.; Holtz, M. E.; Herzing, A. A.; Lindenberg, A. M.; Mavrikakis, M.; Cargnello, M. Steam-Created Grain Boundaries for Methane C–H Activation in Palladium Catalysts. *Science* **2021**, *373* (6562), 1518–1523. https://doi.org/10.1126/science.abj5291.

(9) Jaramillo, T. F.; Jorgensen, K. P.; Bonde, J.; Nielsen, J. H.; Horch, S.; Chorkendorff, I. Identification of Active Edge Sites for Electrochemical H_2 Evolution from MoS_2 Nanocatalysts. *Science* **2007**, *317* (5834), 100–102. https://doi.org/10.1126/science.1141483.

(10) Gordon, C. P.; Engler, H.; Tragl, A. S.; Plodinec, M.; Lunkenbein, T.; Berkessel, A.; Teles, J. H.; Parvulescu, A.-N.; Copéret, C. Efficient Epoxidation over Dinuclear Sites in Titanium Silicalite-1. *Nature* **2020**, *586* (7831), 708–713. https://doi.org/10.1038/s41586-020-2826-3.

(11) Somorjai, G. A.; Contreras, A. M.; Montano, M.; Rioux, R. M. Clusters, Surfaces, and Catalysis. *Proc. Natl. Acad. Sci. U.S.A.* **2006**, *103* (28), 10577–10583. https://doi.org/10.1073/pnas.0507691103.

(12) Tuxen, A.; Kibsgaard, J.; Gøbel, H.; Lægsgaard, E.; Topsøe, H.; Lauritsen, J. V.; Besenbacher, F. Size Threshold in the Dibenzothiophene Adsorption on MoS_2 Nanoclusters. *ACS Nano* **2010**, *4* (8), 4677–4682. https://doi.org/10.1021/nn1011013.

(13) Xu, L.; Papanikolaou, K. G.; Lechner, B. A. J.; Je, L.; Somorjai, G. A.; Salmeron, M.; Mavrikakis, M. Formation of Active Sites on Transition Metals through Reaction-Driven Migration of Surface Atoms. *Science* **2023**, *380* (6640), 70–76. https://doi.org/10.1126/science.add0089.

(14) Ertl, G. Oscillatory Kinetics and Spatio-Temporal Self-Organization in Reactions at Solid Surfaces. *Science* **1991**, *254* (5039), 1750–1755. https://doi.org/10.1126/science.254.5039.1750.

(15) Yan, B.; Krishnamurthy, D.; Hendon, C. H.; Deshpande, S.; Surendranath, Y.; Viswanathan, V. Surface Restructuring of Nickel Sulfide Generates Optimally Coordinated Active Sites for Oxygen Reduction Catalysis. *Joule* **2017**, *1* (3), 600–612. https://doi.org/10.1016/j.joule.2017.08.020.

(16) Zou, N.; Zhou, X.; Chen, G.; Andoy, N. M.; Jung, W.; Liu, G.; Chen, P. Cooperative Communication within and between Single Nanocatalysts. *Nature Chem* **2018**, *10* (6), 607–614. https://doi.org/10.1038/s41557-018-0022-y.

(17) Zhang, Z.; Zandkarimi, B.; Alexandrova, A. N. Ensembles of Metastable States Govern Heterogeneous Catalysis on Dynamic Interfaces. *Acc. Chem. Res.* **2020**, *53* (2), 447–458. https://doi.org/10.1021/acs.accounts.9b00531.

(18) Fields, M.; Tsai, C.; Chen, L. D.; Abild-Pedersen, F.; Nørskov, J. K.; Chan, K. Scaling Relations for Adsorption Energies on Doped Molybdenum Phosphide Surfaces. *ACS Catal.* **2017**, *7* (4), 2528–2534. https://doi.org/10.1021/acscatal.6b03403.

(19) Nørskov, J. K.; Bligaard, T.; Rossmeisl, J.; Christensen, C. H. Towards the Computational Design of Solid Catalysts. *Nature Chem* **2009**, *1* (1), 37–46. https://doi.org/10.1038/nchem.121.

(20) Muetterties, E. L.; Rhodin, T. N.; Band, Elliot.; Brucker, C. F.; Pretzer, W. R. Clusters and Surfaces. *Chem. Rev.* **1979**, *79* (2), 91–137. https://doi.org/10.1021/cr60318a001.

(21) Petel, B. E.; Brennessel, W. W.; Matson, E. M. Oxygen-Atom Vacancy Formation at Polyoxovanadate Clusters: Homogeneous Models for Reducible Metal Oxides. *J. Am. Chem. Soc.* **2018**, *140* (27), 8424–8428. https://doi.org/10.1021/jacs.8b05298.

(22) Arnett, C. H.; Chalkley, M. J.; Agapie, T. A Thermodynamic Model for Redox-Dependent Binding of Carbon Monoxide at Site-Differentiated, High Spin Iron Clusters. *Journal of the American Chemical Society* **2018**, *140* (16), 5569–5578. https://doi.org/10.1021/jacs.8b01825.

(23) Dornsiepen, E.; Pieck, F.; Tonner, R.; Dehnen, S. [{$PhSn)_3SnS_6$}{$(MCp)_3S_4$}] (M = W, Mo): Minimal Molecular Models of the Covalent Attachment of Metal Chalcogenide Clusters on Doped Transition Metal Dichalcogenide Layers. *J. Am. Chem. Soc.* **2019**, *141* (41), 16494–16500. https://doi.org/10.1021/jacs.9b09209.

(24) Kibsgaard, J.; Jaramillo, T. F.; Besenbacher, F. Building an Appropriate Active-Site Motif into a Hydrogen-Evolution Catalyst with Thiomolybdate [Mo3S13]2− Clusters. *Nature Chem* **2014**, *6* (3), 248–253. https://doi.org/10.1038/nchem.1853.

(25) Ullman, A. M.; Nocera, D. G. Mechanism of Cobalt Self-Exchange Electron Transfer. https://doi.org/10.1021/ja404469y.

(26) Nguyen, A. I.; Suess, D. L. M.; Darago, L. E.; Oyala, P. H.; Levine, D. S.; Ziegler, M. S.; Britt, R. D.; Tilley, T. D. Manganese–Cobalt Oxido Cubanes Relevant to Manganese-Doped Water Oxidation Catalysts. *J. Am. Chem. Soc.* **2017**, *139* (15), 5579–5587. https://doi.org/10.1021/jacs.7b01792.

(27) Song, F.; Moré, R.; Schilling, M.; Smolentsev, G.; Azzaroli, N.; Fox, T.; Luber, S.; Patzke, G. R. {Co_4O_4} and {$Co_xNi_{4-x}O_4$} Cubane Water Oxidation Catalysts as Surface Cut-Outs of Cobalt Oxides. *J. Am. Chem. Soc.* **2017**, *139* (40), 14198–14208. https://doi.org/10.1021/jacs.7b07361.

(28) Stracke, J. J.; Finke, R. G. Electrocatalytic Water Oxidation Beginning with the Cobalt Polyoxometalate $[Co_4(H_2O)_2(PW_9O_{34})_2]^{10-}$: Identification of Heterogeneous CoO_x as the Dominant Catalyst. *J. Am. Chem. Soc.* **2011**, *133* (38), 14872–14875. https://doi.org/10.1021/ja205569j.

(29) Surendranath, Y.; Lutterman, D. A.; Liu, Y.; Nocera, D. G. Nucleation, Growth, and Repair of a Cobalt-Based Oxygen Evolving Catalyst. *J. Am. Chem. Soc.* **2012**, *134* (14), 6326–6336. https://doi.org/10.1021/ja3000084.

(30) Ullman, A. M.; Liu, Y.; Huynh, M.; Bediako, D. K.; Wang, H.; Anderson, B. L.; Powers, D. C.; Breen, J. J.; Abruña, H. D.; Nocera, D. G. Water Oxidation Catalysis by Co(II) Impurities in $Co(III)_4O_4$ Cubanes. *J. Am. Chem. Soc.* **2014**, *136* (50), 17681–17688. https://doi.org/10.1021/ja5110393.

(31) Powers, T. M.; Betley, T. A. Testing the Polynuclear Hypothesis: Multielectron Reduction of Small Molecules by Triiron Reaction Sites. *J. Am. Chem. Soc.* **2013**, *135* (33), 12289–12296. https://doi.org/10.1021/ja405057n.

(32) Lee, Y.; Anderton, K. J.; Sloane, F. T.; Ermert, D. M.; Abboud, K. A.; García-Serres, R.; Murray, L. J. Reactivity of Hydride Bridges in High-Spin $[3M^{-3}(\mu\text{-H})]$ Clusters ($M = Fe^{II}$, Co^{II}). *J. Am. Chem. Soc.* **2015**, *137* (33), 10610–10617. https://doi.org/10.1021/jacs.5b05204.

(33) Osei, M. K.; Mirzaei, S.; Bogetti, X.; Castro, E.; Rahman, M. A.; Saxena, S.; Hernández Sánchez, R. Synthesis of Square Planar Cu_4 Clusters. *Angew. Chem. Int. Ed.* **2022**, *61* (41). https://doi.org/10.1002/anie.202209529.

(34) de Ruiter, G.; Thompson, N. B.; Lionetti, D.; Agapie, T. Nitric Oxide Activation by Distal Redox Modulation in Tetranuclear Iron Nitrosyl Complexes. *J. Am. Chem. Soc.* **2015**, *137* (44), 14094–14106. https://doi.org/10.1021/jacs.5b07397.

(35) McSkimming, A.; Suess, D. L. M. Dinitrogen Binding and Activation at a Molybdenum–Iron–Sulfur Cluster. *Nat. Chem.* **2021**, *13* (7), 666–670. https://doi.org/10.1038/s41557-021-00701-6.

(36) Ye, M.; Thompson, N. B.; Brown, A. C.; Suess, D. L. M. A Synthetic Model of Enzymatic $[Fe_4S_4]$–Alkyl Intermediates. *J. Am. Chem. Soc.* **2019**, *141* (34), 13330–13335. https://doi.org/10.1021/jacs.9b06975.

(37) Li, F.; Meyer, R. L.; Carpenter, S. H.; VanGelder, L. E.; Nichols, A. W.; Machan, C. W.; Neidig, M. L.; Matson, E. M. Nitric Oxide Activation Facilitated by Cooperative Multimetallic Electron Transfer within an Iron-Functionalized Polyoxovanadate–Alkoxide Cluster. *Chemical Science* **2018**, *9* (30), 6379–6389. https://doi.org/10.1039/C8SC00987B.

(38) Kephart, J. A.; Mitchell, B. S.; Chirila, A.; Anderton, K. J.; Rogers, D.; Kaminsky, W.; Velian, A. Atomically Defined Nano-Propeller $Fe_3Co_6Se_8(Ph_2PNTol)_6$: Functional Model for the Electronic Metal-Support Interaction Effect, and High Catalytic Activity for Carbodiimide Formation. *Journal of the American Chemical Society* **2019**, *141* (50), 19605–19610. https://doi.org/10.1021/jacs.9b12473.

(39) Kephart, J. A.; Romero, C. G.; Tseng, C.-C.; Anderton, K. J.; Yankowitz, M.; Kaminsky, W.; Velian, A. Hierarchical Nanosheets Built from Superatomic Clusters: Properties, Exfoliation and Single-Crystal-to-Single-Crystal Intercalation. *Chem. Sci.* **2020**, *11* (39), 10744–10751. https://doi.org/10.1039/D0SC03506H.

(40) Kephart, J. A.; Boggiano, A. C.; Kaminsky, W.; Velian, A. Inorganic Clusters as Metalloligands: Ligand Effects on the Synthesis and Properties of Ternary Nanopropeller Clusters. *Dalton Trans.* **2020**, *49* (45), 16464–16473. https://doi.org/10.1039/D0DT02416C.

(41) Kephart, J.; Mitchell, B.; Kaminsky, W.; Velian, A. *Multi-Active Site Dynamics on a Molecular Cr/Co/Se Cluster Catalyst*; preprint; Chemistry, 2022. https://doi.org/10.26434/chemrxiv-2022-zkfsp.

(42) Mitchell, B. S.; Krajewski, S. M.; Kephart, J. A.; Rogers, D.; Kaminsky, W.; Velian, A. Redox-Switchable Allosteric Effects in Molecular Clusters. *JACS Au* **2022**, *2* (1), 92–96. https://doi.org/10.1021/jacsau.1c00491.

(43) Mitchell, B. S.; Chirila, A.; Kephart, J. A.; Boggiano, A. C.; Krajewski, S. M.; Rogers, D.; Kaminsky, W.; Velian, A. Metal–Support Interactions in Molecular Single-Site Cluster Catalysts. *J. Am. Chem. Soc.* **2022**, *144* (40), 18459–18469. https://doi.org/10.1021/jacs.2c07033.

(44) Zars, E.; Gravogl, L.; Gau, M.; Carroll, P. J.; Meyer, K.; Mindiola, D. J. Iron(II) Mediated Deazotation of Benzyl Azide: Trapping and Subsequent Transformations of the Benzaldimine Fragment. *Inorg. Chem.* **2022**, *61* (2), 1079–1090. https://doi.org/10.1021/acs.inorgchem.1c03243.

(45) Risse, J.; Scopelliti, R.; Severin, K. Beyond Click-Chemistry: Transformation of Azides with Cyclopentadienyl Ruthenium Complexes. *Organometallics* **2011**, *30* (12), 3412–3418. https://doi.org/10.1021/om200295c.

(46) Russell, S. K.; Lobkovsky, E.; Chirik, P. J. N−N Bond Cleavage in Diazoalkanes by a Bis(Imino)Pyridine Iron Complex. *J. Am. Chem. Soc.* **2009**, *131* (1), 36–37. https://doi.org/10.1021/ja8075132.

(47) Albertin, G.; Antoniutti, S.; Castro, J. Preparation of Imine Complexes of Ruthenium and Osmium Stabilised by [MCl(η_6-p-Cymene)(PR_3)]+ Fragments. *Journal of Organometallic Chemistry* **2010**, *695* (4), 574–579. https://doi.org/10.1016/j.jorganchem.2009.11.008.

(48) Albertin, G.; Antoniutti, S.; Baldan, D.; Castro, J.; García-Fontán, S. Preparation of Benzyl Azide Complexes of Iridium(III). *Inorg. Chem.* **2008**, *47* (2), 742–748. https://doi.org/10.1021/ic701907y.

(49) Albertin, G.; Antoniutti, S.; Bonaldo, L.; Botter, A.; Castro, J. Azo Complexes of Osmium(II): Preparation and Reactivity of Organic Azide and Hydrazine Derivatives. *Inorg. Chem.* **2013**, *52* (6), 2870–2879. https://doi.org/10.1021/ic302483e.

(50) Albertin, G.; Antoniutti, S.; Bacchi, A.; Celebrin, A.; Pelizzi, G.; Zanardo, G. Reactions of Manganese and Rhenium Complexes with Organic Azides: Preparation of Tetraazabutadiene Derivatives. *Dalton Trans.* **2007**, No. 6, 661. https://doi.org/10.1039/b613964g.

(51) Hakey, B. M.; Darmon, J. M.; Akhmedov, N. G.; Petersen, J. L.; Milsmann, C. Reactivity of Pyridine Dipyrrolide Iron(II) Complexes with Organic Azides: C–H Amination and Iron Tetrazene Formation. *Inorg. Chem.* **2019**, *58* (16), 11028–11042. https://doi.org/10.1021/acs.inorgchem.9b01560.

(52) Hoffmann, R. How Chemistry and Physics Meet in the Solid State. *Angew. Chem. Int. Ed. Engl.* **1987**, *26* (9), 846–878. https://doi.org/10.1002/anie.198708461.

(53) Stepanyuk, V. S.; Negulyaev, N. N.; Niebergall, L.; Longo, R. C.; Bruno, P. Adatom Self-Organization Induced by Quantum Confinement of Surface Electrons. *Phys. Rev. Lett.* **2006**, *97* (18), 186403. https://doi.org/10.1103/PhysRevLett.97.186403.

(54) Nilius, N.; Rienks, E. D. L.; Rust, H.-P.; Freund, H.-J. Self-Organization of Gold Atoms on a Polar FeO(111) Surface. *Phys. Rev. Lett.* **2005**, *95* (6), 066101–066101. https://doi.org/10.1103/PhysRevLett.95.066101.

(55) Li, S.; Duan, S.; Zha, Z.; Pan, J.; Sun, L.; Liu, M.; Deng, K.; Xu, X.; Qiu, X. Structural Phase Transitions of Molecular Self-Assembly Driven by Nonbonded Metal Adatoms. *ACS Nano* **2020**, *14* (5), 6331–6338. https://doi.org/10.1021/acsnano.0c02995.

(56) Dong, Y.; Clarke, R. M.; Zheng, S.-L.; Betley, T. A. Synthesis and Electronic Structure Studies of a Cr-Imido Redox Series. *Chem. Commun.* **2020**, *56* (21), 3163–3166. https://doi.org/10.1039/D0CC00108B.

(57) Monillas, W. H.; Yap, G. P. A.; MacAdams, L. A.; Theopold, K. H. Binding and Activation of Small Molecules by Three-Coordinate Cr(I). *J. Am. Chem. Soc.* **2007**, *129* (26), 8090–8091. https://doi.org/10.1021/ja0725549.

(58) Kim, J. Y.; Park, S. H.; Ryu, J.; Cho, S. H.; Kim, S. H.; Chang, S. Rhodium-Catalyzed Intermolecular Amidation of Arenes with Sulfonyl Azides via Chelation-Assisted C–H Bond Activation. *J. Am. Chem. Soc.* **2012**, *134* (22), 9110–9113. https://doi.org/10.1021/ja303527m.

(59) Passarelli, V.; Benetollo, F. Reactivity of Novel N,N'-Diphosphino-Silanediamine-Based Rhodium(I) Derivatives. *Inorg. Chem.* **2011**, *50*, 9958–9967. https://doi.org/10.1021/ic2004408.

(60) Evans, D. F. 400. The Determination of the Paramagnetic Susceptibility of Substances in Solution by Nuclear Magnetic Resonance. *J. Chem. Soc.* **1959**, 2003. https://doi.org/10.1039/jr9590002003.

(61) Bain, G. A.; Berry, J. F. Diamagnetic Corrections and Pascal's Constants. *Journal of Chemical Education* **2008**, *85* (4), 532. https://doi.org/10.1021/ed085p532.

(62) Chilton, N. F.; Anderson, R. P.; Turner, L. D.; Soncini, A.; Murray, K. S. PHI: A Powerful New Program for the Analysis of Anisotropic Monomeric and Exchange-Coupled Polynuclear *d*- and *f*-Block Complexes. *J. Comput. Chem.* **2013**, *34* (13), 1164–1175. https://doi.org/10.1002/jcc.23234.

(63) Frisch, M. J.; Trucks, G. W.; Schlegel, H. B.; Scuseria, G. E.; Robb, M. A.; Cheeseman, J. R.; Scalmani, G.; Barone, V.; Petersson, G. A.; Nakatsuji, H.; Li, X.; Caricato, M.; Marenich, A. V.; Bloino, J.; Janesko, B. G.; Gomperts, R.; Mennucci, B.; Hratchian, H. P.; Ortiz, J. V.; Izmaylov, A. F.; Sonnenberg, J. L.; Williams; Ding, F.; Lipparini, F.; Egidi, F.; Goings, J.; Peng, B.; Petrone, A.; Henderson, T.; Ranasinghe, D.; Zakrzewski, V. G.; Gao, J.; Rega, N.; Zheng, G.; Liang, W.; Hada, M.; Ehara, M.; Toyota, K.; Fukuda, R.; Hasegawa, J.; Ishida, M.; Nakajima, T.; Honda, Y.; Kitao, O.; Nakai, H.; Vreven, T.; Throssell, K.; Montgomery Jr., J. A.; Peralta, J. E.; Ogliaro, F.; Bearpark, M. J.; Heyd, J. J.; Brothers, E. N.; Kudin, K. N.; Staroverov, V. N.; Keith, T. A.; Kobayashi, R.; Normand, J.; Raghavachari, K.; Rendell, A. P.; Burant, J. C.; Iyengar, S. S.; Tomasi, J.; Cossi, M.; Millam, J. M.; Klene, M.; Adamo, C.; Cammi, R.; Ochterski, J. W.; Martin, R. L.; Morokuma, K.; Farkas, O.; Foresman, J. B.; Fox, D. J. *Gaussian 16 Rev. A.03*; Wallingford, CT, 2016.

(64) Becke, A. D. Density-Functional Exchange-Energy Approximation with Correct Asymptotic Behavior. *Phys. Rev. A* **1988**, *38* (6), 3098–3100. https://doi.org/10.1103/PhysRevA.38.3098.

(65) Perdew, J. P. Density-Functional Approximation for the Correlation Energy of the Inhomogeneous Electron Gas. *Phys. Rev. B* **1986**, *33* (12), 8822–8824. https://doi.org/10.1103/PhysRevB.33.8822.

(66) Weigend, F.; Ahlrichs, R. Balanced Basis Sets of Split Valence, Triple Zeta Valence and Quadruple Zeta Valence Quality for H to Rn: Design and Assessment of Accuracy. *Phys. Chem. Chem. Phys.* **2005**, *7* (18), 3297. https://doi.org/10.1039/b508541a.

(67) Weigend, F. Accurate Coulomb-Fitting Basis Sets for H to Rn. *Phys. Chem. Chem. Phys.* **2006**, *8* (9), 1057. https://doi.org/10.1039/b515623h.

(68) Becke, A. D. Density-functional Thermochemistry. III. The Role of Exact Exchange. *The Journal of Chemical Physics* **1993**, *98* (7), 5648–5652. https://doi.org/10.1063/1.464913.

(69) Miehlich, B.; Savin, A.; Stoll, H.; Preuss, H. Results Obtained with the Correlation Energy Density Functionals of Becke and Lee, Yang and Parr. *Chemical Physics Letters* **1989**, *157* (3), 200–206. https://doi.org/10.1016/0009-2614(89)87234-3.

(70) Lee, C.; Yang, W.; Parr, R. G. Development of the Colle-Salvetti Correlation-Energy Formula into a Functional of the Electron Density. *Phys. Rev. B* **1988**, *37* (2), 785–789. https://doi.org/10.1103/PhysRevB.37.785.

(71) Yanai, T.; Tew, D. P.; Handy, N. C. A New Hybrid Exchange–Correlation Functional Using the Coulomb-Attenuating Method (CAM-B3LYP). *Chemical Physics Letters* **2004**, *393* (1–3), 51–57. https://doi.org/10.1016/j.cplett.2004.06.011.

(72) Dunning, T. H. Gaussian Basis Sets for Use in Correlated Molecular Calculations. I. The Atoms Boron through Neon and Hydrogen. *The Journal of Chemical Physics* **1989**, *90* (2), 1007–1023. https://doi.org/10.1063/1.456153.

(73) Woon, D. E.; Dunning, T. H. Gaussian Basis Sets for Use in Correlated Molecular Calculations. III. The Atoms Aluminum through Argon. *The Journal of Chemical Physics* **1993**, *98* (2), 1358–1371. https://doi.org/10.1063/1.464303.

(74) Wilson, A. K.; van Mourik, T.; Dunning, T. H. Gaussian Basis Sets for Use in Correlated Molecular Calculations. VI. Sextuple Zeta Correlation Consistent Basis Sets for Boron through Neon. *Journal of Molecular Structure: THEOCHEM* **1996**, *388*, 339–349. https://doi.org/10.1016/S0166-1280(96)80048-0.

(75) Peterson, K. A.; Woon, D. E.; Dunning, T. H. Benchmark Calculations with Correlated Molecular Wave Functions. IV. The Classical Barrier Height of the $H+H_2 \rightarrow H_2+H$ Reaction. *The Journal of Chemical Physics* **1994**, *100* (10), 7410–7415. https://doi.org/10.1063/1.466884.

(76) Kendall, R. A.; Dunning, T. H.; Harrison, R. J. Electron Affinities of the First-row Atoms Revisited. Systematic Basis Sets and Wave Functions. *The Journal of Chemical Physics* **1992**, *96* (9), 6796–6806. https://doi.org/10.1063/1.462569.

(77) Lu, T.; Chen, F. Multiwfn: A Multifunctional Wavefunction Analyzer. *Journal of Computational Chemistry* **2012**, *33* (5), 580–592. https://doi.org/10.1002/jcc.22885.

(78) Bruker APEX2 (Version 2.1-4), SAINT (Version 7.34A), SADABS (Version 2007/4), **2007** *BrukerAXS Inc,* Madison, Wisconsin, USA.

(79) Sheldrick, G.M. *Acta Cryst.* **2015** *A71,* 3-8.

(80) Altomare, A.; Burla, C.; Camalli, M.; Cascarano, G. L.; Giacovazzo, C.; Guagliardi, A.; Moliterni, A.G.G.; Polidori, G.; Spagna, R. *J. Appl. Crystallogr.,* **1999***, 32,* 115-119.

(81) Altomare, A.; Cascarano, G. L.; Giacovazzo, C.; Guagliardi, A. *J. Appl. Crystallogr.,* **1993***, 26*, 343-350.

(82) Sheldrick, G. M. *SHELXL-97, Program for the Refinement of Crystal Structures,* **1997***,* University of Göttingen, Germany.

(83) Sheldrick, G. M. *Acta Cryst.* **2015**, *C71*, 3–8.

(84) Mackay, S.; Edwards, C.; Henderson, A.; Gilmore, C.; Stewart, N.; Shankland, K.; Donald, A. *MaXus: A Computer Program for the Solution and Refinement of Crystal Structures from Diffraction Data,* **1997**, University of Glasgow, Scotland.

(85) Waasmaier, D.; Kirfel, A. *Acta Cryst.,* **1995**, *51*, 416-430.

APPENDIX A

Table A.1. Optimized atomic coordinates of **Fe₃′**.

Atom	x	y	z	Atom	x	y	z
C	-3.4925223	0.8119278	-6.4134661	C	-2.3729613	-7.7533713	-3.0229268
C	-4.4164202	1.0490936	-5.3825577	C	-1.9064953	-6.4339697	-2.9197383
C	-5.5605811	5.9097834	-3.0094315	C	-4.0636642	-3.5147676	-1.7613719
C	-2.146563	1.1794203	-6.2389998	C	-0.4332202	6.5263735	-2.0277836
C	-6.26015	6.368943	-1.8810111	C	-0.9801854	5.2594166	-1.7780732
C	-4.0018302	1.6645305	-4.189505	C	3.1048683	1.2822454	-4.0140201
C	-4.6519551	4.8450476	-2.9106586	C	-2.3929414	-8.6019977	-1.9036079
C	0.0449589	-2.437107	-6.2409915	C	-8.0994364	1.9699131	0.6494141
C	-1.7244084	1.7812964	-5.0419249	C	-8.7466555	1.8103631	1.8883608
C	-5.033806	-3.5693574	-4.3937514	C	-1.4501383	-5.9207246	-1.6766428
C	1.0152097	-3.4375177	-6.4269907	C	-6.7187836	1.767888	0.5373115
C	2.4652968	2.6384228	-6.4104794	C	-7.9840807	1.4499292	3.0117572
C	-6.0313136	5.7482243	-0.6394137	C	-5.9319149	1.4140406	1.6664773
C	-2.6561541	2.0482651	-4.0130539	C	4.8098034	-1.4181658	-4.1744896
C	-0.6706541	6.1638878	-4.4158045	C	-6.597769	1.2573532	2.9109835
C	-1.2256626	4.8963798	-4.1693627	C	-5.7238436	-3.1830455	2.0328922
C	2.0886389	1.295058	-6.2360392	C	5.6220604	-2.5384348	-4.4205123
C	-3.6557404	-3.4272901	-4.1568637	C	-1.9426107	-8.1066531	-0.6662247
C	-5.928527	-3.6856413	-3.3191125	C	-4.9600275	-2.03409	1.7815575
C	-0.6808586	-2.3661742	-5.0402796	C	-1.4870032	-6.7879817	-0.5515431
C	-4.4106054	4.2101812	-1.663559	C	6.5267027	1.5791079	-2.9149005
C	1.2577316	-4.3682618	-5.4035668	C	4.5162331	-1.0242795	-2.8523452
C	-5.1173123	4.6935594	-0.5295285	C	7.9024167	1.8360241	-3.0169844
C	3.1480931	3.3073522	-5.3814837	C	-6.0003618	-3.5769519	3.3535067
C	-0.2707061	6.9813547	-3.3477216	C	-4.4665098	-1.2540712	2.8514133
C	-1.3807262	4.4278911	-2.8479425	C	5.8546893	1.7080789	-1.6704882
C	-0.4612808	-3.3185733	-4.0189902	C	6.1565799	-3.2736777	-3.3515457
C	2.3924615	0.6219256	-5.0410274	C	0.0969497	6.5400452	2.0362472
C	0.5237739	-4.3105882	-4.2069414	C	-5.5175793	-2.8052195	4.4213822
C	-3.1566926	-3.3927596	-2.8380856	C	0.7093111	5.3039528	1.7836268
C	-5.4370093	-3.664118	-2.0024361	C	-4.7586123	-1.6485676	4.1738371
C	3.4673291	2.6338587	-4.1905104	C	5.0627607	-1.7666811	-1.7814825

Table A.1. Optimized atomic coordinates of **Fe₃′** (continued).

Atom	x	y	z	Atom	x	y	z
C	8.6478372	2.2348861	-1.8950242	C	0.8055493	-2.3577468	5.039037
C	5.8788514	-2.8794185	-2.0312541	C	-1.0624676	-4.4294764	5.3832934
C	6.6247029	2.1011903	-0.5427277	C	3.804706	-3.3462376	4.1651785
C	-0.0804086	6.9872117	3.356949	C	6.0963869	-3.4334872	3.3439846
C	-3.1701079	1.1159624	4.0155682	C	0.0801168	-2.4625836	6.2374367
C	7.9943736	2.3673521	-0.6562115	C	-0.8548207	-3.4979118	6.4137484
C	-3.5907059	2.4505859	4.1920962	C	2.0958501	1.2864831	6.238117
C	1.848359	-6.6897845	0.5064307	C	5.1858066	-3.4298384	4.4116739
C	1.161687	4.4966716	2.8512409	C	4.370234	1.2828906	5.3832373
C	4.880015	4.9397589	0.5186961	C	3.4598663	0.9929158	6.4126924
C	2.3732378	-7.9837552	0.6069995	H	-3.8192835	0.3377128	-7.3518318
C	4.1972863	4.4286376	1.6553047	H	-5.4703377	0.7561135	-5.5051076
C	1.7413728	-5.8477556	1.6459869	H	-5.7258667	6.3828667	-3.9903649
C	5.7412125	6.0385078	0.6227552	H	-1.414441	0.9959217	-7.0406812
C	0.3710223	6.1940108	4.4228434	H	-5.4059222	-3.5969387	-5.4296347
C	-2.4313692	0.4862364	5.0431194	H	-0.1505636	-1.7010191	-7.0361478
C	0.9917895	4.9579924	4.1734452	H	2.2225802	3.1639598	-7.3469979
C	-3.3022057	3.1365257	5.3838165	H	-4.1297491	4.4953326	-3.8114109
C	4.2414024	-3.2662157	1.7744764	H	1.5842636	-3.4882226	-7.3681491
C	4.4067851	5.0814947	2.8989315	H	-0.558758	6.5142991	-5.4535834
C	3.3182706	-3.2574022	2.8441024	H	-4.725064	1.8511065	-3.3820229
C	5.938682	6.6767113	1.8608614	H	-1.5510396	4.2792261	-5.0186321
C	2.8255688	-8.4771278	1.8443282	H	1.5510922	0.7626435	-7.0360021
C	2.5587251	2.1863458	4.0144917	H	-2.9690715	-3.3597231	-5.0122186
C	0.6207837	-3.3096589	4.0106423	H	-7.0077279	-3.7980324	-3.5047824
C	-0.3286829	-4.3373357	4.1886808	H	-0.6615718	2.0387185	-4.9153884
C	5.6182949	-3.3576387	2.0243685	H	-6.5654393	6.0934624	0.2595308
C	2.2001003	-6.3591124	2.8889525	H	-1.4169241	-1.5588066	-4.9051932
C	-2.1577752	1.171288	6.2386568	H	3.4383727	4.3620644	-5.5037976
C	-2.5920022	2.4971831	6.4131376	H	2.0224083	-5.1490899	-5.5347567
C	5.2619359	6.1901499	2.9917162	H	0.1635462	7.9742782	-3.5409048
C	1.6422516	1.8670639	5.0420823	H	-2.7218381	-8.1223104	-4.0004325
C	3.9233208	1.8768435	4.1909366	H	-1.8886658	-5.796606	-3.8140873
C	2.7368508	-7.6524891	2.9782273	H	-4.9293409	4.2227629	0.4486691

Table A.1. Optimized atomic coordinates of **Fe₃′** (continued).

Atom	x	y	z	Atom	x	y	z
H	2.0655467	-0.4216111	-4.9147347	H	6.2582457	6.4044463	-0.2779976
H	-6.1332533	-3.7623268	-1.1558093	H	8.5586641	2.675033	0.237937
H	0.7136745	-5.0395769	-3.4055757	H	-2.0605672	-0.5425732	4.9167175
H	4.0027021	3.1572772	-3.3847968	H	-3.6379437	4.1776289	5.5063225
H	4.4178257	-0.8428781	-5.0249504	H	-0.490339	-5.0664708	3.3810612
H	-0.1259913	7.1651294	-1.1858486	H	0.2481688	6.5393998	5.4610666
H	-1.1065308	4.9100796	-0.7412902	H	6.3276295	-3.3650785	1.1829278
H	-8.6770594	2.2483943	-0.2457955	H	1.3569791	4.3605052	5.0206009
H	-3.6852035	-3.5019321	-0.7270579	H	0.5671987	2.0667884	4.9146656
H	-6.2201433	1.8776116	-0.4389382	H	3.9022784	4.7116472	3.8017666
H	-8.4724109	1.3199747	3.9905321	H	4.6355651	2.1043844	3.3841994
H	5.9651103	1.2823984	-3.8110002	H	2.1274628	-5.7409343	3.7939917
H	-6.1056056	-3.7807419	1.1913164	H	1.5148041	-1.5254651	4.9107803
H	5.84277	-2.8306545	-5.4588592	H	-1.7994468	-5.237604	5.5074505
H	-4.7494351	-1.7300868	0.7441301	H	-1.598267	0.6621753	7.0387376
H	-6.0231886	0.9898906	3.8080436	H	-2.3729471	3.0323285	7.3500521
H	8.3958084	1.7261383	-3.9956753	H	5.4033338	6.676329	3.9699771
H	-0.2504635	7.1600865	1.195971	H	3.1061015	-3.3651482	5.01352
H	-6.5957308	-4.4823302	3.5474538	H	3.0857951	-8.0206898	3.9559792
H	-1.9522713	-8.7522012	0.2258232	H	7.178084	-3.4995498	3.5373145
H	0.8476659	4.9606952	0.7463685	H	1.3742485	1.0609209	7.0385964
H	-1.1514287	-6.4005507	0.4236894	H	0.24795	-1.7260687	7.0385204
H	6.7932409	-4.1507494	-3.5444199	H	-1.4237033	-3.5754045	7.3531962
H	1.5123055	-6.3022481	-0.4686489	H	5.4385453	1.0479348	5.5062349
H	-4.1469799	2.9512064	3.3860191	H	5.5483461	-3.5003855	5.4489263
H	-5.7378209	-3.0973358	5.4598672	H	3.8115096	0.534723	7.350024
H	4.7153672	4.4548203	-0.4568594	N	-3.5296443	3.1279447	-1.4933247
H	-0.5665205	7.9553443	3.5524133	N	-0.9551472	-4.6169797	-1.5004421
H	-4.4078423	-1.0456231	5.0231164	N	-4.5463318	1.253804	1.4924515
H	4.8520812	-1.4603475	-0.7446717	N	4.478081	1.484418	-1.4958711
H	2.436523	-8.6107507	-0.2960301	N	3.3705381	3.3037626	1.4900544
H	6.1221248	2.1903541	0.4335666	N	1.1770976	-4.5701935	1.4849192
H	6.3008187	-3.4484142	-1.1889876	P	-2.1250945	2.7878326	-2.3986012
H	3.8723951	-3.2084422	0.7384161	P	-1.3605499	-3.2266976	-2.4006456

Table A.1. Optimized atomic coordinates of **Fe$_3$′** (continued).

Atom	x	y	z	Atom	x	y	z
P	3.4753834	0.4452607	-2.4024549	Se	-2.7391701	-0.2574413	-1.0365056
P	-3.4979215	0.2645648	2.4024312	Se	1.1465597	2.5024087	-1.0376339
P	1.9879834	2.8967837	2.4009162	Se	-1.2748758	2.432909	1.0563173
P	1.5196165	-3.1701175	2.3962418	Se	1.5939163	-2.2447743	-1.0410546
Fe	-3.4175838	1.8605856	0.0028306	Se	-1.4657166	-2.3222556	1.0549073
Fe	0.0955325	-3.890832	-0.0088965	Se	2.7466632	-0.1116629	1.0518881
Fe	3.3218529	2.0292275	-0.0050806	Se	0.0040669	-0.0021796	2.6862989
Co	-1.0153419	1.4064518	-1.1278239	H	6.6103494	7.5446418	1.9416583
Co	-0.7093921	-1.5802595	-1.1284968	H	9.7258248	2.4377272	-1.9831172
Co	1.7231406	0.1766123	-1.1307769	H	-9.833005	1.9627748	1.9754388
Co	-1.7318871	0.0831405	1.137124	H	-6.9735984	7.2024234	-1.9663335
Co	0.9428563	1.460399	1.1383107	H	-2.7574204	-9.6365001	-1.9926112
Co	0.7972101	-1.5458275	1.1353472	H	3.2446471	-9.491664	1.9221936
Se	-0.0015322	0.001059	-2.6771252	--	--	--	--

Table A.2. Optimized atomic coordinates of *cis*-(α,β)-[**Fe$_3$**(CNMe)$_2$]$^+$.

Atom	x	y	z	Atom	x	y	z
C	-4.2074612	0.9189296	-6.0677915	C	-0.948595	6.6342383	-2.4260974
C	-0.9840239	-3.6426949	-6.7391777	C	-1.3167166	4.228779	-2.6580059
C	-3.0257619	1.6670252	-6.1843831	C	0.1528484	-8.1605125	-2.2863639
C	-2.3172487	-3.6104027	-6.3024219	C	-3.6805237	-3.5129929	-1.9265348
C	2.0376408	2.2429313	-6.7522033	C	-1.671537	5.4749061	-2.099481
C	-4.7854329	0.732737	-4.8005702	C	-5.8735956	4.1394888	-1.0160958
C	1.559236	0.9592667	-6.4344316	C	7.7371233	1.2052721	-3.2958771
C	0.0577733	-3.5755689	-5.7970664	C	-1.0583393	-6.0325076	-2.0846846
C	2.8482708	2.9285269	-5.8326101	C	6.3379053	1.2798098	-3.2345435
C	-2.4212537	2.2248728	-5.0450025	C	0.0422308	-6.8692442	-1.7577829
C	-2.613654	-3.5121755	-4.9318767	C	5.7860296	-3.4510681	-3.8124533
C	-5.7848967	5.3903481	-3.5104978	C	-5.5967423	-4.7143604	-1.0072447
C	-4.1819163	1.2838851	-3.6598919	C	4.1824709	-1.212619	-3.1682209
C	-6.9305772	5.5370529	-2.7120617	C	-4.2080081	-4.591787	-1.1871689
C	1.8919218	0.3643548	-5.2067145	C	8.5005646	1.0651923	-2.1235628
C	-2.9924017	2.0379854	-3.7692905	C	5.663262	1.2116606	-1.9881135
C	-0.2340328	-3.465279	-4.4298253	C	5.4798081	-3.163518	-2.471344
C	-4.6874095	4.6340139	-3.0715945	C	4.6796835	-2.0575482	-2.1502032
C	-1.5741265	-3.4338635	-3.9817241	C	7.8449734	0.9871456	-0.883241
C	-5.944934	-2.6645329	-2.2667232	C	-7.8191978	1.160902	0.8824032
C	3.1836249	2.3347307	-4.6023756	C	6.4451229	1.049788	-0.8158255
C	-1.90779	-7.8313841	-3.5179143	C	-6.4182957	1.1933581	0.8157123
C	-0.8216937	-8.6528395	-3.1732282	C	-8.4735472	1.2511845	2.1225579
C	-4.5588394	-2.5370039	-2.4500183	C	-5.633676	1.3364523	1.9886017
C	0.5214025	5.3200533	-3.8431734	C	-0.2034124	-6.8675053	1.7513113
C	2.7177791	1.0435143	-4.2824718	C	-0.3441476	-8.1565406	2.2781891
C	0.1393471	6.5633148	-3.3108654	C	-4.7229176	-1.9538177	2.1505543
C	-0.1892193	4.1567915	-3.5071604	C	-7.7078171	1.3729373	3.2954342
C	-6.9631437	4.9009873	-1.4585516	C	-5.5465233	-3.0424045	2.4717231
C	-6.4680297	-3.7556002	-1.5501801	C	-6.3072852	1.4172578	3.2348323
C	5.297385	-2.6173252	-4.8303167	C	5.9671905	4.0044265	1.0191766
C	-2.0330191	-6.5404329	-2.9829184	C	0.9175096	-6.0579782	2.0775493
C	4.5052217	-1.5011377	-4.5121988	C	4.1002942	-4.6878302	1.1815886
C	-4.699053	3.9887349	-1.8042475	C	5.4859779	-4.8423988	1.0027899

Table A.2. Optimized atomic coordinates of *cis*-(α,β)-[**Fe**$_3$(CNMe)$_2$]$^+$ (continued).

Atom	x	y	z	Atom	x	y	z
C	7.0736044	4.740761	1.4623465	C	-1.9860529	2.2861282	6.7536707
C	1.7977813	5.4321879	2.1038155	C	-1.5354423	0.9926542	6.4350888
C	1.1011582	6.6075374	2.4303721	C	3.0688268	1.5929911	6.1859747
C	-4.2069052	-1.1203354	3.1686749	C	2.2291006	-3.6813443	6.2984561
C	4.7902779	3.8778031	1.8080374	C	0.895383	-3.675445	6.7348503
C	0.6197417	-8.6734581	3.162696	C	4.2312366	0.8155516	6.0674354
C	3.5974381	-3.5997482	1.9244897	H	-4.6832666	0.4902959	-6.9628704
C	1.4149934	4.1943809	2.6624347	H	-0.7553516	-3.7289626	-7.8124875
C	0.0119534	6.5612798	3.3152139	H	-3.1398555	-3.6729558	-7.0311928
C	6.3789316	-3.9064937	1.5503732	H	1.780603	2.7061951	-7.7170965
C	-5.8579711	-3.3239743	3.8129024	H	-2.5689371	1.8284187	-7.1727635
C	0.2864297	4.1480192	3.512006	H	0.9218973	0.4132521	-7.1463858
C	-0.3977989	5.3270462	3.8479	H	-5.7241763	0.1663912	-4.7009434
C	1.8811422	-6.5904842	2.9734521	H	-5.736186	5.8737709	-4.4987518
C	4.4978422	-2.6467007	2.4527152	H	1.1072583	-3.6151283	-6.1267192
C	5.8807678	-2.8061471	2.2704944	H	3.2341623	3.9302878	-6.0781882
C	7.0560938	5.3746328	2.7172689	H	-3.6642556	-3.5120845	-4.6086777
C	-2.6928043	1.1026818	4.2836174	H	-1.5086429	2.8227798	-5.1683806
C	-3.1307953	2.4034225	4.6044132	H	-6.6232717	-1.9054879	-2.6854174
C	1.7258208	-7.8788453	3.5067903	H	-3.8104948	4.5516356	-3.7257432
C	4.7938921	4.5204226	3.0767734	H	-2.6781035	-8.1998075	-4.2130743
C	-4.5349931	-1.4024532	4.5127141	H	-4.161635	-1.673059	-3.0053284
C	-5.3508031	-2.501473	4.8308514	H	1.5068334	-0.6401909	-4.9744332
C	5.9081168	5.2514507	3.5163687	H	-4.6486535	1.1473784	-2.673271
C	1.492215	-3.4746095	3.9782295	H	1.3837861	5.2444611	-4.5220878
C	3.0403418	1.9640437	3.7708274	H	5.5397263	-2.8283202	-5.8832572
C	0.1516919	-3.4674861	4.4260257	H	4.1480618	-0.8486617	-5.3212144
C	4.2104009	1.1802952	3.659426	H	0.6909432	7.4764582	-3.5837007
C	-2.7822525	2.989318	5.834762	H	0.1568878	3.189601	-3.9019207
C	-1.8813368	0.4055709	5.2072533	H	0.5901351	-3.4149994	-3.7005423
C	2.4763772	2.1654767	5.0475076	H	3.8160614	2.8716811	-3.8799103
C	2.5286806	-3.5872731	4.9282987	H	-7.555527	-3.854662	-1.412444
C	-0.1436953	-3.5739153	5.7928043	H	-7.8549665	4.9829736	-0.8174913
C	4.802078	0.6146925	4.7992205	H	8.2377723	1.2620192	-4.2750194

Table A.2. Optimized atomic coordinates of *cis*-(α,β)-[**Fe$_3$**(CNMe)$_2$]$^+$ (continued).

Atom	x	y	z	Atom	x	y	z
H	-2.898823	-5.9244717	-3.2598819	H	4.67141	1.0313079	2.6718618
H	1.0156597	-8.7852555	-2.0087596	H	-1.2616117	5.2709768	4.5269013
H	-1.24712	7.6012423	-1.9927784	H	4.1204845	-1.7760111	3.011359
H	5.7560488	1.3987955	-4.1594611	H	6.5763043	-2.0649569	2.6929588
H	-2.5274383	5.5356362	-1.4129227	H	2.7620484	-5.9959774	3.2496474
H	6.4086241	-4.3235065	-4.0632192	H	3.9159743	4.4558446	3.7315483
H	-5.9362947	3.6261264	-0.044601	H	-4.1632754	-0.7582078	5.3217624
H	0.8208125	-6.4820376	-1.0802633	H	2.488208	-8.2667352	4.200098
H	-5.9977596	-5.57176	-0.445067	H	-3.1465042	3.9990009	6.0809407
H	-8.4031967	1.0528765	-0.0446843	H	-1.5178961	-0.6068891	4.9745235
H	-3.5264441	-5.3413213	-0.7593713	H	-5.5969385	-2.707726	5.8838516
H	-5.9005924	1.088518	-0.1496571	H	5.8708392	5.7337021	4.5056914
H	8.4268956	0.8650742	0.0434061	H	1.5793309	2.7862157	5.172376
H	5.8603843	-3.8041645	-1.662398	H	3.5789199	-3.6171632	4.6052603
H	4.4474053	-1.8473644	-1.0947094	H	-1.1939903	-3.5831941	6.1221173
H	5.9257825	0.9549737	0.1496996	H	5.7262072	0.0250546	4.6981028
H	-0.9736391	-6.460558	1.0758178	H	-1.7186934	2.7433439	7.7186435
H	-1.2221853	-8.7599631	2.0011655	H	-0.9096671	0.4327388	7.1465052
H	-4.4868342	-1.7483242	1.0949728	H	2.618021	1.7660258	7.1751507
H	6.0176751	3.4921933	0.0463775	H	3.0492828	-3.7708655	7.0271495
H	-5.9413351	-3.6743256	1.6627311	H	0.6639457	-3.7585762	7.8078152
H	3.4018744	-5.4196588	0.7503044	H	4.6978123	0.3753513	6.9617584
H	7.9664552	4.8045633	0.8206531	N	-3.6256751	3.2350899	-1.2759787
H	5.8673894	-5.7069297	0.4378976	N	-1.127668	-4.7573688	-1.4893572
H	2.6548424	5.473679	1.4172428	N	4.2537365	1.3292325	-1.866094
H	1.4212928	7.5675105	1.9968436	N	-4.2218943	1.4234057	1.8674425
H	-8.2075943	1.4390074	4.2744365	N	1.0167098	-4.7840684	1.4837821
H	-5.723393	1.5222753	4.1601617	N	3.7000703	3.1492262	1.2789824
H	-3.7519667	2.9542431	3.8826175	P	-2.2782752	2.7107109	-2.1869735
H	-0.5190667	7.4866169	3.587771	P	-1.853996	-3.35198	-2.149507
H	7.4639693	-4.0306596	1.4135904	P	3.1698672	0.2541062	-2.6608824
H	-6.4990188	-4.182948	4.0636548	P	-3.1622821	0.3239604	2.6617681
H	-0.6703574	-3.3896818	3.6967496	P	1.7749628	-3.3967111	2.1462601
H	-0.081304	3.1890523	3.9072863	P	2.3411434	2.6548476	2.1896961

Table A.2. Optimized atomic coordinates of *cis*-(α,β)-[**Fe$_3$**(CNMe)$_2$]$^+$ (continued).

Atom	x	y	z	Atom	x	y	z
Fe	-3.4640757	2.7957209	0.6715745	H	0.5064654	-9.6839487	3.5826467
Fe	3.5279721	2.7178534	-0.6692382	H	9.5981952	1.0102894	-2.1780495
Fe	-0.0474132	-4.0938079	-0.002372	H	7.9268172	5.9472295	3.0699176
Co	-1.0447222	1.3062315	-1.065053	H	-9.5721336	1.2199248	2.1764704
Co	-0.9430319	-1.7095447	-1.0471834	H	-7.7881871	6.1294179	-3.0641913
Co	1.4656748	-0.1253472	-1.3517074	C	3.8095819	4.5411415	-1.4374416
Co	-1.4673866	-0.0929826	1.3518436	C	-3.7067084	4.6240202	1.441744
Co	1.0749327	1.2801298	1.0671141	C	4.4956645	6.9842752	-1.9811259
Co	0.9032935	-1.7322024	1.0451446	H	3.612057	7.653762	-1.9874401
Se	-0.3984382	-0.1833017	-2.7567218	H	5.2080437	7.330285	-1.2047395
Se	-2.7185425	-0.2230191	-0.6142122	H	4.9915394	7.0404298	-2.9710046
Se	1.1895242	2.1865984	-1.1252307	C	-4.3441052	7.0801543	1.9860016
Se	1.3329663	-2.5029166	-1.2054639	H	-3.4481232	7.7330062	1.987853
Se	-1.1382874	2.2123241	1.1286634	H	-5.0530255	7.4385132	1.2120465
Se	-1.3906921	-2.4726171	1.2020453	H	-4.8347265	7.1467665	2.977845
Se	2.7128555	-0.2870569	0.6141764	N	-3.9728542	5.7426212	1.7196221
Se	0.3947617	-0.1960492	2.7568445	N	4.0983901	5.6542544	-1.7147333
H	-0.7320107	-9.6651401	-3.5945168	--	--	--	--

Table A.3. Optimized atomic coordinates of *trans*-(α,β)-[**Fe$_3$**(CNMe)$_2$]$^+$.

Atom	x	y	z	Atom	x	y	z
C	0.5557183	4.15265	-6.6344403	C	5.0436092	4.9944401	-0.6870979
C	-3.0452168	-2.3613067	-6.8191109	C	3.2425559	3.8214007	-1.8439127
C	1.8357342	4.4490967	-6.141141	C	-5.7392573	-4.5485159	-3.5867006
C	-4.1711346	-1.6054847	-6.45272	C	-4.3362379	1.0528336	-2.8640115
C	3.5396177	-0.3693868	-6.4612847	C	3.6720002	4.7777888	-0.9014482
C	-0.4271356	3.652703	-5.7628292	C	-0.9661329	6.624556	-1.7165181
C	2.3493592	-1.1027414	-6.3120235	C	6.8656606	-4.7316011	-2.3374777
C	-1.9928502	-2.5276738	-5.9041124	C	-5.3140099	-2.4410045	-2.406919
C	4.4292681	-0.2626109	-5.3802711	C	5.9928706	-3.6321505	-2.3466773
C	2.1365567	4.2461098	-4.7837071	C	-4.8503444	-3.6614642	-2.9635025
C	-4.2442189	-1.0187394	-5.1797315	C	1.6282833	-6.859709	-3.4432832
C	1.0037581	8.0946858	-3.0576318	C	-6.1897377	2.5508448	-2.3388896
C	-0.1284666	3.4400556	-4.4093726	C	2.1195393	-4.1443004	-2.8296906
C	-0.2773134	8.6463295	-2.8869044	C	-5.475799	1.3631435	-2.0979165
C	2.0525652	-1.7246718	-5.0898406	C	6.6091355	-5.8358327	-1.5069257
C	1.1582112	3.7327105	-3.905301	C	4.8432664	-3.6130181	-1.5173101
C	-2.0616814	-1.9369062	-4.631586	C	1.0416516	-6.2752139	-2.3087313
C	1.3095314	6.8209854	-2.5553967	C	1.2863001	-4.9272235	-2.0029965
C	-3.186877	-1.1755863	-4.2532634	C	5.4713532	-5.8293873	-0.6804136
C	-4.6101068	3.1523945	-4.0841237	C	-3.0721794	7.4264217	3.3091907
C	4.1341395	-0.8880069	-4.1555459	C	4.5989951	-4.7315473	-0.6809344
C	-7.5853656	-3.0441724	-3.1110212	C	-2.8462637	6.0892737	2.9491051
C	-7.1109131	-4.245925	-3.663796	C	-2.2164481	8.4499824	2.8692565
C	-3.9019064	1.9632529	-3.8529582	C	-1.7397482	5.7386914	2.1321563
C	5.5723699	3.2855983	-2.3340601	C	-5.3844068	-4.7038572	0.6213564
C	2.9478097	-1.6315196	-4.0021012	C	-6.3946402	-5.6319804	0.9112775
C	5.995594	4.2570718	-1.4095282	C	-4.4917898	3.000052	1.4449618
C	4.2033257	3.0572547	-2.5437865	C	-1.1145786	8.115773	2.0616714
C	-1.2599034	7.9019261	-2.2102615	C	-5.8901521	3.079596	1.5176562
C	-5.7597126	3.4481076	-3.3298866	C	-0.8753474	6.7834545	1.7051029
C	2.4691358	-6.0921414	-4.2661506	C	6.5273545	-2.5428012	1.7649168
C	-6.6991141	-2.1488852	-2.4917064	C	-4.4131208	-4.3333223	1.5953311
C	2.7166062	-4.7438998	-3.9625599	C	-1.6355047	-5.7958801	1.096095
C	0.3275998	6.0614739	-1.8689043	C	-0.971724	-7.0323271	1.0165311

Table A.3. Optimized atomic coordinates of *trans*-(α,β)-[**Fe$_3$**(CNMe)$_2$]$^+$ (continued).

Atom	x	y	z	Atom	x	y	z
C	5.0436092	4.9944401	-0.6870979	C	-0.2086927	3.0012623	6.8115259
C	3.2425559	3.8214007	-1.8439127	C	-0.9718217	1.910605	6.3596365
C	-5.7392573	-4.5485159	-3.5867006	C	2.5876228	-1.4579507	6.4313047
C	-4.3362379	1.0528336	-2.8640115	C	-1.9889484	-3.1180179	6.1456784
C	3.6720002	4.7777888	-0.9014482	C	-2.9302661	-2.1154462	6.4247947
C	-0.9661329	6.624556	-1.7165181	C	2.6413683	-2.8540355	6.2985416
C	6.8656606	-4.7316011	-2.3374777	H	0.3215148	4.3139501	-7.6977862
C	-5.3140099	-2.4410045	-2.406919	H	-2.9894554	-2.8226183	-7.8170766
C	5.9928706	-3.6321505	-2.3466773	H	-5.0040508	-1.4739531	-7.1601775
C	-4.8503444	-3.6614642	-2.9635025	H	3.7713139	0.1187835	-7.4201172
C	1.6282833	-6.859709	-3.4432832	H	2.6090808	4.8499823	-6.814137
C	-6.1897377	2.5508448	-2.3388896	H	1.6434909	-1.1876976	-7.1522271
C	2.1195393	-4.1443004	-2.8296906	H	-1.4338471	3.4216833	-6.1431472
C	-5.475799	1.3631435	-2.0979165	H	1.7833714	8.665846	-3.58526
C	6.6091355	-5.8358327	-1.5069257	H	-1.1106343	-3.1252444	-6.1808866
C	4.8432664	-3.6130181	-1.5173101	H	5.3648491	0.3075368	-5.4908447
C	1.0416516	-6.2752139	-2.3087313	H	-5.136634	-0.4375349	-4.9057986
C	1.2863001	-4.9272235	-2.0029965	H	3.1400668	4.497479	-4.4121582
C	5.4713532	-5.8293873	-0.6804136	H	-4.2666377	3.8521063	-4.861389
C	-3.0721794	7.4264217	3.3091907	H	2.3228628	6.4155492	-2.6805821
C	4.5989951	-4.7315473	-0.6809344	H	-8.6571598	-2.7975207	-3.1665709
C	-2.8462637	6.0892737	2.9491051	H	-3.0122626	1.7296783	-4.4589965
C	-2.2164481	8.4499824	2.8692565	H	1.1173006	-2.2952759	-4.9858489
C	-1.7397482	5.7386914	2.1321563	H	-0.9028083	3.0476986	-3.7320869
C	-5.3844068	-4.7038572	0.6213564	H	6.3129659	2.6985248	-2.898311
C	-6.3946402	-5.6319804	0.9112775	H	2.9404505	-6.5447662	-5.1520363
C	-4.4917898	3.000052	1.4449618	H	3.3817779	-4.1570858	-4.6122876
C	-1.1145786	8.115773	2.0616714	H	7.0697442	4.4397942	-1.251627
C	-5.8901521	3.079596	1.5176562	H	3.8844206	2.2864366	-3.2627779
C	-0.8753474	6.7834545	1.7051029	H	-1.2320122	-2.0768167	-3.9225885
C	6.5273545	-2.5428012	1.7649168	H	4.8273122	-0.8024782	-3.3051065
C	-4.4131208	-4.3333223	1.5953311	H	-2.2710932	8.3149033	-2.0732082
C	-1.6355047	-5.7958801	1.096095	H	7.7521486	-4.727756	-2.9908858
C	-0.971724	-7.0323271	1.0165311	H	-7.0684082	-1.2039808	-2.0678318

Table A.3. Optimized atomic coordinates of *trans*-(α,β)-[**Fe$_3$**(CNMe)$_2$]$^+$ (continued).

Atom	x	y	z	Atom	x	y	z
H	-5.3575721	-5.4887595	-4.0137715	H	2.9812506	4.2333432	4.8605562
H	5.3669132	5.7496526	0.0451361	H	0.6035819	-4.1285344	3.0992205
H	6.1865055	-2.7724971	-3.0045807	H	1.7489961	-6.3285961	2.9781487
H	2.9239724	5.3580482	-0.340939	H	-3.7455697	-4.7335849	3.6397215
H	1.4326205	-7.9156426	-3.6855264	H	5.6910157	-0.3024844	4.2268614
H	-1.7449515	6.0332499	-1.2085175	H	-3.7968781	2.8151313	4.8042595
H	-3.7788319	-3.8988223	-2.8907676	H	-5.5000522	-6.4040759	4.1222793
H	-7.0981482	2.7715441	-1.7565886	H	0.6472958	4.9328027	6.2891384
H	-3.9388605	7.6688038	3.9437744	H	-2.0568886	1.0246112	4.7108955
H	-5.8019168	0.6612064	-1.3156493	H	-6.2771186	2.9140504	4.9221778
H	-3.5381396	5.3134729	3.29829	H	7.7024164	-1.2874468	5.2605348
H	5.2625999	-6.6885837	-0.024423	H	2.7794042	0.4606539	5.4539704
H	0.3869755	-6.8660845	-1.6510217	H	-0.9433149	-4.2475614	4.6271469
H	0.8242116	-4.483174	-1.1089929	H	-4.2958158	-0.6516427	5.5642806
H	3.7133678	-4.7173366	-0.0288127	H	2.9833021	-4.5121295	4.9304556
H	-5.3097266	-4.2842905	-0.3957745	H	0.1824234	3.0146942	7.8403975
H	-7.1265509	-5.8901087	0.1304791	H	-1.1734707	1.0583084	7.0259799
H	-3.9960219	3.0283166	0.4617269	H	2.3880389	-1.0029225	7.4135608
H	6.174453	-2.9388993	0.7994749	H	-1.5067928	-3.6683327	6.9680782
H	-6.4725001	3.1774681	0.5897184	H	-3.1931646	-1.8752168	7.4664176
H	-2.5764117	-5.6493982	0.5492384	H	2.4855051	-3.5011548	7.1752188
H	8.2200649	-3.8882329	1.8238977	N	0.5821462	4.7875497	-1.3161363
H	-1.4126463	-7.8448731	0.4186161	N	-4.4230291	-1.5658197	-1.7227639
H	5.8672433	1.2675842	2.0422761	N	3.9878888	-2.4746748	-1.4811145
H	6.7043927	3.5175933	2.7433084	N	-1.4374358	4.4270333	1.7131692
H	-0.4264183	8.8993802	1.7094186	N	-3.4919889	-3.3228321	1.2305437
H	0.0029317	6.5283685	1.0903924	N	4.6666631	-0.9744951	1.7284139
H	-0.2316137	4.9060317	3.9585804	P	1.437213	3.5144999	-2.0892769
H	5.2759291	5.0019348	4.1791144	P	-3.3610726	-0.4958876	-2.5340287
H	0.7512518	-8.207052	1.644167	P	2.5149594	-2.3967644	-2.3627008
H	-7.636955	3.1286959	2.8194411	P	-1.8678595	2.9367885	2.4391215
H	-3.7111722	-1.2085062	3.2096999	P	-1.9464875	-3.0992371	1.9319393
H	2.126908	2.0284026	4.1243659	P	3.3597435	-0.1921627	2.5033708
H	3.3517273	-3.0446089	2.9479376	Fe	-0.3569868	3.9363778	0.163997

Table A.3. Optimized atomic coordinates of *trans*-(α,β)-[**Fe$_3$**(CNMe)$_2$]$^+$ (continued).

Atom	x	y	z	Atom	x	y	z
Fe	4.5679387	-1.0597404	-0.2660153	H	-7.8067554	-4.9447808	-4.1521389
Fe	-4.4452294	-1.9112481	0.2062592	H	-6.3203519	4.3763353	-3.5180849
Co	0.7159011	1.7176797	-1.0920577	H	-2.4024478	9.4957651	3.1555812
Co	-1.5871123	-0.0998341	-1.3521481	H	-0.5095969	9.6469507	-3.2810453
Co	1.037523	-1.2285292	-1.2695606	H	-7.2333211	-6.9900607	2.3982149
Co	-0.98438	1.4315423	1.1366466	C	-6.0972775	-1.3370146	1.1030138
Co	1.6386589	0.0120296	1.180838	C	-8.3029546	-0.8186148	2.3695875
Co	-0.819518	-1.5250589	0.942749	H	-8.4821734	-1.6085889	3.1267364
Se	0.150019	0.252711	-2.8697505	H	-8.235878	0.1633003	2.8806381
Se	-1.617228	2.2751858	-1.0602584	H	-9.161441	-0.8027684	1.667926
Se	2.6955122	0.3876902	-0.890198	N	-7.1069723	-1.0899557	1.6686885
Se	-1.0260683	-2.3408315	-1.2371509	C	6.3500349	-0.3353414	-0.7485742
Se	1.207693	2.383682	1.1741433	C	8.8791288	0.2414448	-0.807262
Se	-2.7174052	-0.1753043	0.7053606	H	9.0563635	1.3202186	-0.6233107
Se	1.3973597	-2.2541001	0.7923343	H	9.3739925	-0.346811	-0.0075822
Se	-0.1321529	-0.1362001	2.6905103	H	9.3289099	-0.0294411	-1.7836658
H	9.0148279	-3.0777033	4.0767615	N	7.4920556	-0.031035	-0.820207
H	7.2925506	-6.6983993	-1.5037023	--	--	--	--

Table A.4. Optimized atomic coordinates of (α,α)-[**Fe$_3$**(CNMe)$_2$]$^+$.

Atom	x	y	z	Atom	x	y	z
C	3.1716016	-2.222958	6.3922213	C	5.8963598	3.5125549	2.3742564
C	-2.9160911	-1.9351338	6.7871009	C	4.1789269	1.8052921	2.7079187
C	3.0763453	-0.8228567	6.4031095	C	-6.7847821	-3.1102941	2.7911269
C	-2.2023217	-3.1122427	6.5156081	C	-0.7999122	-4.5350997	2.4697869
C	0.4728994	3.8941256	6.4707347	C	5.40435	2.2171166	2.1429893
C	3.3816304	-2.8915585	5.1742222	C	6.6913463	-2.2247398	1.4602268
C	-0.261256	2.7078603	6.2945211	C	-3.6232206	7.4038831	2.7986587
C	-3.2604761	-1.0735982	5.7307089	C	-4.4268581	-3.6184262	2.3315633
C	0.5335708	4.8362272	5.4302915	C	-2.8645443	6.2240991	2.786613
C	3.187879	-0.0932206	5.2072585	C	-5.5774998	-2.8098225	2.1422827
C	-1.8333078	-3.430757	5.197234	C	-6.337221	2.9192764	3.4022777
C	7.7221879	-1.1594479	3.8286021	C	-0.5870173	-6.9173394	1.9678966
C	3.484196	-2.1676128	3.976486	C	-3.5610582	3.0110998	2.8869285
C	8.4380221	-2.1663146	3.1602797	C	-1.3096498	-5.71296	1.8881626
C	-0.9364943	2.4667083	5.0870407	C	-3.9088582	8.0889494	1.6056026
C	3.3893036	-0.7577368	3.9797485	C	-2.3738563	5.6925943	1.5653235
C	-2.8805908	-1.3810157	4.4159444	C	-5.8588418	2.7955165	2.0863493
C	6.508041	-0.6746343	3.3189048	C	-4.4810392	2.8338895	1.8293071
C	-2.1620549	-2.5648987	4.1323351	C	-3.4314171	7.5713427	0.3882144
C	1.1701085	-5.7806568	3.2010382	C	5.4627828	-5.7204459	-0.5256785
C	-0.1406124	4.599296	4.2196664	C	-2.6848039	6.3870328	0.3665509
C	-5.7306629	-5.0079831	3.8729448	C	4.5746754	-4.6361898	-0.5664472
C	-6.8696982	-4.2116423	3.6594595	C	6.5389007	-5.7949359	-1.4279338
C	0.4550097	-4.5755239	3.1183464	C	4.739355	-3.5997353	-1.5202348
C	3.936206	4.0211406	3.7126186	C	-6.3337441	-3.4130003	-1.3138634
C	-0.893137	3.4192532	4.0434582	C	-7.5214131	-4.0024335	-1.7676802
C	5.1704225	4.4144462	3.1683146	C	1.2010121	-4.989692	-1.5252156
C	3.433633	2.7325559	3.4721081	C	6.7178663	-4.7716505	-2.3741937
C	7.9083547	-2.6960901	1.9704038	C	0.9710482	-6.3681176	-1.6597265
C	0.6525529	-6.9553609	2.6263981	C	5.8282903	-3.6866833	-2.4236663
C	-5.4295965	3.0938743	4.4588801	C	0.4771479	7.0911683	-0.7918228
C	-4.5237277	-4.7214827	3.218373	C	-5.6001882	-2.4929231	-2.1163493
C	-4.0480858	3.1458889	4.2047346	C	-5.9809796	0.6637611	-1.6133871
C	5.9638909	-1.1903091	2.1112616	C	-6.8844916	1.740012	-1.6109131

Table A.4. Optimized atomic coordinates of (α,α)-[$\mathbf{Fe_3}(CNMe)_2]^+$ (continued).

Atom	x	y	z	Atom	x	y	z
C	0.5783872	8.4643454	-1.0436632	C	2.9097265	-0.9285408	-6.640846
C	3.617392	4.6821475	-2.1569666	C	1.71508	-1.5718413	-6.2701876
C	4.9964027	4.8103122	-2.3937373	C	0.1579699	3.2920782	-6.4774435
C	1.9144881	-4.2816895	-2.5152982	C	-3.1378568	-0.7324663	-6.4358202
C	0.6878931	6.1361785	-1.8230181	C	-2.5808263	-2.0045315	-6.6391377
C	-8.0389752	-3.6802682	-3.0337791	C	-1.1626829	3.7668584	-6.4880775
C	-4.7568134	0.7592998	-2.3098919	H	3.093707	-2.7917713	7.3312546
C	2.8977735	3.6030974	-2.7129772	H	-3.2109461	-1.6918862	7.8194352
C	5.672093	3.862661	-3.1787592	H	-1.9348974	-3.7985853	7.3336739
C	-6.5739998	2.9304676	-2.2884386	H	0.9967906	4.083998	7.4200263
C	1.4486251	-7.0572335	-2.787326	H	2.9237495	-0.2863245	7.3520803
C	3.5935839	2.6231919	-3.4581803	H	-0.310402	1.9613565	7.1017254
C	4.9689657	2.7633315	-3.7008293	H	3.4839832	-3.9875564	5.1583126
C	-6.1474082	-2.1692023	-3.3878009	H	8.1130134	-0.7357486	4.7669453
C	-4.4368422	1.9733957	-2.9613454	H	-3.8343792	-0.1551907	5.9276464
C	-5.3438302	3.0455221	-2.9573726	H	1.1004737	5.7707081	5.5629767
C	0.9068169	8.9310145	-2.3293977	H	-1.2906335	-4.366731	5.0043683
C	2.5766981	-1.8978082	-4.008101	H	3.1347013	1.0026898	5.2479848
C	3.7640609	-1.2382827	-4.3794507	H	2.1406293	-5.8036602	3.7197634
C	-7.3434928	-2.7544259	-3.8293751	H	5.9825086	0.1184377	3.8659578
C	1.0260342	6.619826	-3.1148638	H	-5.782307	-5.8696805	4.5566488
C	2.3972118	-4.9837695	-3.6431668	H	0.8755535	-3.6640586	3.571352
C	2.1623867	-6.3617098	-3.7774044	H	-1.4991398	1.5288496	4.9636473
C	1.133126	7.9980271	-3.355038	H	3.6625237	-2.6988434	3.02999
C	-3.1857141	-1.1074691	-4.0191731	H	3.3469089	4.7240052	4.3200071
C	0.2525191	3.5376775	-4.0481717	H	-5.7960888	3.2027001	5.4912274
C	-2.6239598	-2.3863017	-4.2339225	H	-3.3524794	3.3073739	5.0406724
C	-1.0781393	4.0136195	-4.0665258	H	5.5595826	5.427083	3.3545537
C	3.9309644	-0.7594738	-5.6918649	H	2.442519	2.4654777	3.869724
C	1.5456465	-2.0482529	-4.961573	H	-3.159182	-0.6970274	3.598901
C	0.8637441	3.1783292	-5.267471	H	-0.0911082	5.336771	3.4050881
C	-3.4403684	-0.286181	-5.1376161	H	8.436662	-3.5017515	1.4373135
C	-2.3269849	-2.8315297	-5.5307564	H	-3.9913398	7.794939	3.7598436
C	-1.7770107	4.1309831	-5.2773216	H	-3.6436579	-5.3579584	3.3881158

Table A.4. Optimized atomic coordinates of (α,α)-[**Fe$_3$**(CNMe)$_2$]$^+$ (continued).

Atom	x	y	z	Atom	x	y	z
H	-7.6631577	-2.4672481	2.6260842	H	5.4926048	2.0014349	-4.2979099
H	6.8578605	3.8162397	1.932465	H	-3.4656287	2.0975585	-3.4634298
H	-2.6414995	5.7152856	3.7340504	H	-5.0832707	3.9816478	-3.4744787
H	5.976605	1.5129173	1.5226529	H	-5.6338522	-1.4579001	-4.0450445
H	-7.4188433	2.8839619	3.6033938	H	1.2055116	5.914678	-3.9371125
H	6.2749938	-2.6852354	0.5501044	H	2.9657079	-4.4540692	-4.4211695
H	-5.4943761	-1.9255639	1.4918822	H	-7.7353655	-2.4774122	-4.8205949
H	-1.0034152	-7.8344258	1.5225463	H	4.8698168	-0.2591597	-5.9766192
H	5.3164213	-6.5140002	0.2233298	H	0.6002116	-2.5399698	-4.6841822
H	-2.2832254	-5.6804478	1.3773751	H	2.5477583	-6.8949809	-4.6599805
H	3.7404684	-4.5671748	0.146936	H	1.3969445	8.3446619	-4.3663082
H	-3.6505891	8.089273	-0.5581211	H	1.9026768	2.8236668	-5.2901301
H	-6.5592588	2.6642641	1.2482469	H	-3.902563	0.7018804	-5.0117532
H	-4.1189543	2.7314946	0.7944226	H	-1.9026601	-3.8371099	-5.6766055
H	-2.3333324	5.9723254	-0.5917925	H	-2.8050654	4.5247428	-5.2769799
H	-5.9788705	-3.6416927	-0.2954306	H	3.0430086	-0.5594411	-7.6693281
H	-8.0567094	-4.7050699	-1.1100762	H	0.9034497	-1.6987907	-7.0025189
H	0.8269899	-4.4633214	-0.6344155	H	0.6528834	3.0125458	-7.4199973
H	0.2398249	6.7338603	0.2230975	H	-3.3509568	-0.0781424	-7.2949737
H	0.421519	-6.900581	-0.8687873	H	-2.3561957	-2.3557974	-7.6579426
H	-6.2344905	-0.2600582	-1.0761492	H	-1.7095077	3.863983	-7.4383225
H	0.4053968	9.1766628	-0.2224215	N	4.7710369	-0.7318277	1.5068314
H	-7.8442702	1.6394506	-1.080993	N	-3.245138	-3.3124139	1.6072903
H	3.1016141	5.4306921	-1.5409057	N	-1.5838355	4.527535	1.4845912
H	5.541055	5.6649137	-1.9643076	N	3.8728562	-2.4685366	-1.5264981
H	7.5566781	-4.8196556	-3.086109	N	-4.3850048	-1.9879791	-1.5930049
H	5.963703	-2.8911766	-3.1705617	N	0.5588279	4.772437	-1.4928555
H	4.5571967	-1.1025988	-3.6289201	P	3.5314819	0.104365	2.3360597
H	6.7485723	3.9780051	-3.3794492	P	-1.7510102	-2.9430152	2.3616224
H	-7.2847667	3.7707808	-2.2887044	P	-1.767637	3.1126074	2.4412596
H	1.272931	-8.1392534	-2.891898	P	2.322881	-2.4903335	-2.2646657
H	-2.429591	-3.0470916	-3.37507	P	-3.5431949	-0.639657	-2.2425242
H	3.0715614	1.732487	-3.8405536	P	1.0874803	3.4147518	-2.3895011
H	-1.5603236	4.3143592	-3.1245193	Fe	4.5065631	-0.9601132	-0.4585375

Table A.4. Optimized atomic coordinates of (α,α)-[**Fe$_3$**(CNMe)$_2$]$^+$ (continued).

Atom	x	y	z	Atom	x	y	z
Fe	-0.4035469	3.9950937	0.0225778	H	-7.8144821	-4.4440363	4.1734059
Fe	-3.4372631	-3.232358	-0.3539595	H	1.2156418	-7.8986447	2.6947503
Co	1.6872174	0.183832	1.1689988	H	7.2355966	-6.6460577	-1.392294
Co	-0.7267905	-1.3989092	1.2294549	H	9.3888056	-2.5418907	3.5671147
Co	-0.9070129	1.5387296	1.207131	H	-8.977174	-4.1320494	-3.3887421
Co	0.9252228	-1.2461601	-1.1576485	C	6.1689451	-0.1310658	-1.1589069
Co	0.556392	1.7037734	-1.1605076	C	-3.4370254	-5.0495905	-1.1468427
Co	-1.7405268	-0.145359	-1.1198842	C	8.5875571	0.7289256	-1.5427438
Se	0.0520613	0.1039482	2.8206604	H	8.6170038	1.8370927	-1.5579882
Se	1.4865892	-2.1111099	0.9467409	H	9.2266017	0.3608737	-0.7143811
Se	1.2617596	2.5535483	1.0019197	H	8.9933176	0.3498329	-2.5022678
Se	-2.6355004	-0.0679116	1.0434882	C	-3.6690698	-7.3392081	-2.347575
Se	2.5593401	0.4099297	-1.0107665	H	-4.468826	-7.262169	-3.111645
Se	-1.1566155	-2.3805106	-0.8719119	H	-2.7195645	-7.6225434	-2.8454104
Se	-1.7590962	2.2217933	-0.943274	H	-3.947582	-8.1317326	-1.6239589
Se	-0.1142729	0.1070938	-2.7834701	N	-3.5260501	-6.1013957	-1.6807987
H	0.9914834	10.0098806	-2.5271116	N	7.2595902	0.2781335	-1.3674624
H	-4.5019301	9.0154218	1.6231723	--	--	--	--

Table A.5. Optimized atomic coordinates of (α,α,β)-[$\mathbf{Fe_3}(CNMe)_2(THF)]^+$.

Atom	x	y	z	Atom	x	y	z
C	-0.9831732	4.1194787	6.1762262	C	-6.785242	1.3339779	2.3005091
C	3.3325511	0.6801527	6.9008985	C	-4.3685812	1.5394966	2.6044369
C	-1.8481376	3.0165168	6.2455914	C	7.2564531	-1.1702327	3.5745256
C	3.6077878	1.9801065	6.4504395	C	3.4980858	3.3767161	2.1017132
C	-2.7223594	-2.0117704	6.6566897	C	-5.5736017	1.9892617	2.0247997
C	-0.6825077	4.6844332	4.925156	C	-3.9083229	6.1261926	1.0845434
C	-1.4129744	-1.578268	6.3830762	C	-1.8254772	-7.7137054	3.1345011
C	3.0014897	-0.3218103	5.971554	C	5.7261575	0.4671058	2.5660256
C	-3.4081168	-2.7875891	5.7077059	C	-1.8350191	-6.3115624	3.1010977
C	-2.4087326	2.4772036	5.0751572	C	6.1213848	-0.8748886	2.804597
C	3.5508848	2.283376	5.0788171	C	2.8863757	-5.9823802	3.8386773
C	-5.2364322	6.0712681	3.5400033	C	4.7543264	5.2140376	1.0994971
C	-1.2348137	4.1446549	3.7536884	C	0.7474595	-4.2661002	3.1488277
C	-5.2719708	7.2443676	2.7690609	C	4.543529	3.8350931	1.2751215
C	-0.7935249	-1.921092	5.1703321	C	-1.6921915	-8.4589025	1.949721
C	-2.1060211	3.0343573	3.8155694	C	-1.7066674	-5.615535	1.8712274
C	2.9292943	-0.0187969	4.604152	C	2.6553746	-5.6456701	2.493789
C	-4.5527815	4.9303508	3.0927398	C	1.5996353	-4.789195	2.1501381
C	3.199114	1.2894592	4.1416512	C	-1.5541998	-7.7824662	0.7258715
C	2.8442474	5.690928	2.5243966	C	-0.7808343	7.8890277	-0.7737112
C	-2.7893398	-3.1324704	4.4925967	C	-1.5517271	-6.3801251	0.686583
C	7.6180714	1.1981609	3.9451778	C	-0.9096366	6.4928526	-0.7267295
C	8.0163187	-0.1350381	4.1458043	C	-0.8260982	8.5658877	-2.0042736
C	2.6310366	4.3151491	2.705529	C	-1.1063283	5.7363998	-1.9105283
C	-5.6074609	-0.2544866	3.7097201	C	6.8223564	-2.0042417	-0.5744676
C	-1.472863	-2.7111833	4.2159421	C	8.1500175	-2.388441	-0.8034928
C	-6.8083535	0.2201737	3.1550698	C	2.1030638	4.6207306	-2.0914901
C	-4.3924694	0.3885905	3.4245737	C	-1.0000717	7.827012	-3.1877191
C	-4.5981609	7.2593202	1.5349542	C	3.2359528	5.3861468	-2.4046752
C	3.9117235	6.1450274	1.7294221	C	-1.1404219	6.4320324	-3.1469636
C	2.0457962	-5.4669427	4.8374879	C	-4.4688189	-5.7102406	-1.1899802
C	6.4893239	1.5003543	3.1686182	C	5.877027	-1.9295819	-1.6328385
C	0.9781281	-4.6191986	4.4962509	C	4.0365342	-4.5642259	-1.2255403
C	-3.870475	4.9244246	1.844862	C	3.9836497	-5.9670382	-1.143198

Table A.5. Optimized atomic coordinates of (α,α,β)-[$\mathbf{Fe_3}$(CNMe)$_2$(THF)]$^+$ (continued).

Atom	x	y	z	Atom	x	y	z
C	-5.263188	-6.7635454	-1.6615931	C	-2.3236441	2.2309896	-6.7139446
C	-5.6919879	-1.4117566	-2.1124247	C	-1.0659941	1.6817452	-6.4072583
C	-6.8277514	-0.639483	-2.4076013	C	-1.9997878	-2.7898628	-6.2805576
C	1.2429512	4.1624752	-3.1149805	C	3.5169595	-2.3629266	-6.2566643
C	-4.3066932	-4.5073743	-1.9319699	C	3.4745434	-1.023445	-6.6745191
C	8.5827716	-2.7263778	-2.0985255	C	-1.2897779	-3.9982161	-6.2085724
C	3.086193	-3.8615251	-1.9948302	H	-0.5517165	4.5448364	7.0950305
C	-4.4396497	-1.0885641	-2.6760173	H	3.3859234	0.4436284	7.9746724
C	-6.7271832	0.4664651	-3.2667233	H	3.8817257	2.7681393	7.168575
C	2.9743593	-6.679921	-1.8096553	H	-3.2057021	-1.7465943	7.6094768
C	3.5373743	5.6930229	-3.7429759	H	-2.1002656	2.5722065	7.2206607
C	-4.3365599	0.0558918	-3.4989972	H	-0.8660623	-0.9674464	7.1172506
C	-5.4767719	0.8158581	-3.8046559	H	-0.0231601	5.5637853	4.8622669
C	6.3303255	-2.271365	-2.9351703	H	-5.7516944	6.03512	4.5126242
C	2.0597602	-4.5828038	-2.6473243	H	2.8032474	-1.3496863	6.3120336
C	2.0092341	-5.982431	-2.5572019	H	-4.430787	-3.1380998	5.9175765
C	-5.9213914	-6.6653726	-2.9002346	H	3.7934818	3.3017029	4.7441502
C	-1.0804121	2.8171651	-4.2408968	H	-3.1007225	1.6287216	5.1601511
C	-2.3462948	3.3543682	-4.550441	H	2.1729042	6.4162719	3.0091928
C	7.6594394	-2.6661832	-3.1554849	H	-4.5567621	4.0331185	3.7240672
C	-4.9744673	-4.4294718	-3.1852855	H	8.1968781	2.0187217	4.3972497
C	1.5468395	4.4839099	-4.4558377	H	1.7876917	3.971974	3.3250533
C	2.6909831	5.2385881	-4.7664367	H	0.2300952	-1.5694838	4.9731343
C	-5.7631191	-5.4913025	-3.6541067	H	-1.0037254	4.599309	2.7788522
C	3.2214009	-1.672895	-3.9265595	H	-5.6058377	-1.1380025	4.3653683
C	-2.3265989	-2.8078603	-3.8584632	H	2.2123447	-5.7321817	5.8929079
C	3.167188	-0.3293317	-4.3603065	H	0.3173696	-4.2418467	5.2893514
C	-1.6100961	-4.0235087	-3.7939369	H	-7.7616884	-0.2801035	3.3860097
C	-2.9619517	3.0653404	-5.7816039	H	-3.4607302	-0.0279127	3.8363956
C	-0.4502047	1.9677511	-5.1779995	H	2.6767584	-0.8130181	3.8835529
C	-2.5171392	-2.198137	-5.1157102	H	-3.3272316	-3.7370579	3.7474895
C	3.3969475	-2.687153	-4.8941524	H	-4.5931816	8.1705879	0.9163338
C	3.3034739	-0.0063528	-5.7193085	H	-1.9283289	-8.2308917	4.1012531
C	-1.1006553	-4.6146803	-4.9601829	H	6.195818	2.548308	3.0136544

Table A.5. Optimized atomic coordinates of (α,α,β)-[**Fe$_3$**(CNMe)$_2$(THF)]$^+$ (continued).

Atom	x	y	z	Atom	x	y	z
H	7.5374696	-2.2212248	3.7450683	H	-5.3773789	1.6911325	-4.4638697
H	-7.7188961	1.7049312	1.8503192	H	1.294848	-4.0503153	-3.2338358
H	-1.949559	-5.7432686	4.0349967	H	1.2093941	-6.5343593	-3.0742885
H	-5.5602383	2.8652367	1.3612407	H	5.6391366	-2.2224616	-3.78468
H	3.7193897	-6.6501349	4.1069272	H	-4.8844255	-3.5279978	-3.8041218
H	-3.3627375	6.172673	0.1298501	H	0.882587	4.1571986	-5.2682582
H	5.4934778	-1.6851299	2.4026872	H	7.9754994	-2.9267028	-4.1778213
H	5.5891496	5.5620898	0.4714284	H	-3.9435969	3.5052945	-6.0172744
H	-0.6326711	8.4508022	0.1615717	H	0.5312041	1.524088	-4.9524875
H	5.1827059	3.1002663	0.7638784	H	2.9118646	5.4822964	-5.8171047
H	-0.8406876	5.9556234	0.2311883	H	-6.2632203	-5.3914893	-4.6301984
H	-1.435304	-8.3505503	-0.2097545	H	-3.087485	-1.2642933	-5.2046019
H	3.3006957	-6.0486298	1.6994412	H	3.4603262	-3.740702	-4.5875681
H	1.4347571	-4.5323711	1.0923041	H	3.2722665	1.0486501	-6.032659
H	-1.4077542	-5.8462687	-0.2648382	H	-0.5639348	-5.573655	-4.8959289
H	6.4928423	-1.7629701	0.4467613	H	-2.8038941	2.009687	-7.6794066
H	8.8498746	-2.43547	0.0454642	H	-0.5578755	1.0235133	-7.1282318
H	1.8822129	4.3873561	-1.0383283	H	-2.1640488	-2.3021397	-7.2536494
H	-3.937736	-5.8240712	-0.2326909	H	3.6523571	-3.1686275	-6.9945395
H	3.8836452	5.743849	-1.5909131	H	3.5760538	-0.7719351	-7.7413603
H	4.8285518	-4.017616	-0.6964912	H	-0.893305	-4.4645457	-7.123278
H	-5.3530655	-7.6792884	-1.0562431	N	-3.1858146	3.8105677	1.3094742
H	4.7473702	-6.5047755	-0.5603777	N	4.5980753	0.7213514	1.7523736
H	-5.7763451	-2.2818216	-1.4464323	N	-1.7584758	-4.2004313	1.7770677
H	-7.8000501	-0.9131363	-1.9697562	N	-1.2899795	4.3329559	-1.8089273
H	-1.0321095	8.3440392	-4.1595006	N	4.5654407	-1.5048487	-1.3300226
H	-1.285259	5.8700844	-4.0804917	N	-3.5205012	-3.4736978	-1.373808
H	-2.8465585	4.0044747	-3.8174896	P	-2.7784148	2.4082545	2.1962259
H	-7.6225243	1.0575651	-3.5147392	P	3.2145356	1.5607051	2.3077353
H	2.9363515	-7.7779824	-1.745165	P	-0.6542492	-3.1785879	2.6114322
H	4.4279394	6.2924752	-3.9868903	P	-0.2662016	3.2076184	-2.6140147
H	3.0192151	0.4761639	-3.6240962	P	3.1195058	-2.014736	-2.0912331
H	-3.3620323	0.3758696	-3.8973711	P	-2.9530458	-2.1182023	-2.2459636
H	-1.4695698	-4.5198114	-2.8223076	Fe	-2.7130471	3.6428053	-0.6288165

Table A.5. Optimized atomic coordinates of (α,α,β)-[**Fe$_3$**(CNMe)$_2$(THF)]$^+$ (continued).

Atom	x	y	z	Atom	x	y	z
Fe	-3.0957322	-3.3798834	0.582608	H	-7.6325637	4.0480444	-1.9605992
Fe	4.1142629	-0.1092357	0.0165307	H	-7.2073958	5.5983997	-1.1360468
Co	-1.4354772	1.1191554	1.067289	H	-6.9341103	5.4117673	-2.9085767
Co	1.5788473	0.8181941	1.0970992	C	-7.4017851	-4.2494523	1.8040519
Co	-0.1475956	-1.4902624	1.3320482	H	-8.0535559	-3.3526005	1.8114012
Co	0.0396248	1.4769207	-1.3213315	H	-7.7444185	-4.9402768	1.0067895
Co	-1.4995832	-0.9738521	-1.0949555	H	-7.4919797	-4.7615163	2.7831723
Co	1.525899	-0.9852481	-1.0387498	N	-6.0579776	-3.8757828	1.5761491
Se	-0.0145557	0.3487162	2.7602626	C	-4.9319211	-3.6148692	1.3217833
Se	0.2138084	2.6985293	0.6675419	C	-4.5127752	4.0368383	-1.409308
Se	-2.4414287	-1.0686774	1.0795969	N	-5.6058706	4.3991355	-1.680308
Se	2.2379389	-1.4558326	1.1842036	O	5.8455803	1.1622593	-0.9465983
Se	-2.2856342	1.2960716	-1.1371502	C	7.1798214	1.3824172	-0.4075985
Se	2.4139203	1.2397416	-1.1182081	C	5.8263016	1.4801822	-2.3668116
Se	-0.0365653	-2.7060771	-0.6497381	C	8.095217	1.4592702	-1.627643
Se	0.0375183	-0.3634974	-2.7599041	H	7.182343	2.332633	0.1729908
H	-6.5392549	-7.4946506	-3.2757535	H	7.418547	0.5542462	0.2847613
H	-1.6885844	-9.5588059	1.9820051	C	7.1798799	2.1310817	-2.6641929
H	8.9040663	-0.3653531	4.7536565	H	5.6879635	0.5344565	-2.932804
H	4.0808848	7.2244623	1.5966608	H	4.9591636	2.1433841	-2.5615758
H	-0.7198981	9.660468	-2.0425047	H	8.3755922	0.4374194	-1.9571904
H	-5.8078333	8.135823	3.1276952	H	9.02535	2.0255865	-1.4248218
H	9.6221378	-3.0385946	-2.2789123	H	7.5029467	1.9659947	-3.7105201
C	-6.9082779	4.8868865	-1.9324883	H	7.1344451	3.2269772	-2.4920503

Table A.6. Optimized atomic coordinates of *trans*-(α,β)-[**Fe$_3$**(CNMe)(THF)]$^+$.

Atom	x	y	z	Atom	x	y	z
C	0.0748849	3.9447774	6.7869242	C	-4.5636425	5.3571574	1.0331195
C	2.7486654	-2.8705635	6.6982601	C	-2.8227919	4.0297914	2.1153355
C	-1.1590417	4.4435713	6.3422168	C	5.2843131	-5.1647846	3.4119173
C	3.9385643	-2.1910201	6.389797	C	4.4388387	0.5611878	2.8931691
C	-3.9525104	-0.0290849	6.1933409	C	-3.2120521	4.9980122	1.166566
C	0.9398736	3.3180927	5.8735549	C	1.5636869	6.4979927	1.9948922
C	-2.6865873	-0.6399826	6.1826141	C	-6.2326718	-5.1767195	2.7567232
C	1.7114924	-2.9191814	5.7522663	C	5.0680835	-2.9841124	2.3116469
C	-4.7791258	-0.1242504	5.0616313	C	-5.3634896	-4.0769161	2.7017805
C	-1.5315826	4.3141758	4.9935003	C	4.4882056	-4.1783808	2.8128582
C	4.0905011	-1.5609689	5.1443969	C	-1.2831886	-6.6745427	3.6324952
C	-0.3104704	8.0817001	3.3428633	C	6.4224667	1.8964924	2.4047634
C	0.5678866	3.1804276	4.5283169	C	-2.0031125	-4.0271926	2.9495067
C	1.011755	8.5372652	3.206422	C	5.5970488	0.7923621	2.1267312
C	-2.2538297	-1.3500435	5.0513521	C	-6.5017346	-5.9382677	1.6059973
C	-0.6755143	3.6714366	4.0727182	C	-4.7334965	-3.710656	1.4834874
C	1.8590657	-2.283604	4.5085743	C	-1.0828509	-6.2036496	2.3233683
C	-0.7041199	6.8478704	2.8033274	C	-1.4367132	-4.8899157	1.9840075
C	3.0483519	-1.5955254	4.1889101	C	-5.8733115	-5.5960412	0.3959831
C	4.9226288	2.5741946	4.1918563	C	3.6105048	7.334796	-3.1478782
C	-4.3509514	-0.8381128	3.9286438	C	-4.9929702	-4.505416	0.3365772
C	7.2644274	-3.8143558	3.021017	C	3.2951387	6.0065405	-2.8231919
C	6.6758824	-4.9892282	3.5191395	C	2.8692241	8.4050845	-2.6206355
C	4.1022067	1.4681102	3.9223304	C	2.212288	5.712738	-1.9541787
C	-5.157478	3.7723692	2.7783184	C	4.9619534	-5.0760232	-0.8098385
C	-3.0921164	-1.4730508	3.9206808	C	5.8961484	-6.0734057	-1.1244791
C	-5.5372836	4.7560596	1.8479067	C	4.76623	2.7299166	-1.3737506
C	-3.8107828	3.3938396	2.9006048	C	1.7913685	8.127424	-1.7607693
C	1.9459462	7.7365945	2.5256707	C	6.1664666	2.7050648	-1.4529383
C	6.0883098	2.7900066	3.4354166	C	1.4635705	6.8052759	-1.4383847
C	-1.8546787	-5.8283904	4.5957886	C	-6.4333122	-2.1873169	-1.9838336
C	6.4717966	-2.8202541	2.4259157	C	4.0500576	-4.5773534	-1.7841739
C	-2.219931	-4.5139096	4.2570049	C	1.1270605	-5.7896287	-1.3787401
C	0.2284242	6.0318125	2.1131119	C	0.3435449	-6.9563415	-1.3567826

Table A.6. Optimized atomic coordinates of *trans*-(α,β)-[**Fe$_3$**(CNMe)(THF)]$^+$ (continued).

Atom	x	y	z	Atom	x	y	z
C	-7.5903471	-2.6861884	-2.5947953	C	0.4137367	3.2477307	-6.6801812
C	-5.2027778	2.3209458	-2.6925932	C	1.1395468	2.1079641	-6.292582
C	-5.6595497	3.6168581	-2.9861698	C	-2.4160878	-0.5798466	-6.6310164
C	3.9837538	2.7571489	-2.549578	C	1.859194	-2.9999111	-6.310408
C	-5.6733192	-1.1404023	-2.5706407	C	2.8608938	-2.0434413	-6.5357306
C	5.9301207	-6.6336666	-2.412093	C	-2.4887611	-1.9809954	-6.6643218
C	0.7159338	-4.6683941	-2.131	H	0.3657329	4.0480343	7.8434906
C	-3.8897803	1.9305172	-3.0297638	H	2.6317918	-3.3660592	7.6743116
C	-4.810368	4.5401703	-3.616912	H	4.7607415	-2.154109	7.1207028
C	-0.8644498	-7.0155012	-2.0704832	H	-4.2903184	0.5256706	7.0819488
C	6.8072856	2.6877743	-2.7045373	H	-1.8392628	4.9464489	7.0465408
C	-3.0309739	2.8757075	-3.6378436	H	-2.025727	-0.5584934	7.0588564
C	-3.4946922	4.1660669	-3.9389535	H	1.911493	2.9291014	6.2146462
C	4.089865	-5.163867	-3.0779497	H	-1.0534049	8.698631	3.8719245
C	-0.5179246	-4.72365	-2.8199272	H	0.7799836	-3.4605265	5.977925
C	-1.2960284	-5.8922399	-2.7964699	H	-5.7695365	0.356949	5.0605499
C	-8.0332339	-2.1632	-3.8230926	H	5.032873	-1.042744	4.9153333
C	1.4879164	3.0697593	-4.0715029	H	-2.4969523	4.7224113	4.6635898
C	0.7391077	4.2011326	-4.4593363	H	4.6533917	3.2716764	4.9997309
C	5.0127597	-6.1769715	-3.3753929	H	-1.7481099	6.520167	2.8986422
C	-6.1267157	-0.633301	-3.8195283	H	8.3527981	-3.6668594	3.1004665
C	4.6329553	2.7320752	-3.8036451	H	3.1996172	1.2959221	4.5294423
C	6.0362025	2.6936241	-3.8784076	H	-1.2524572	-1.8054709	5.0554516
C	-7.2864676	-1.1386822	-4.4270298	H	1.2536239	2.692819	3.8184809
C	2.0908241	-2.7162095	-3.89149	H	-5.9152397	3.29877	3.4214504
C	-2.9432621	-0.5839381	-4.2446151	H	-2.030931	-6.1940313	5.6191029
C	3.0971052	-1.7522202	-4.1287482	H	-2.6888195	-3.8730961	5.0170792
C	-3.0148841	-1.9945265	-4.2864207	H	-6.5933178	5.0536843	1.7583572
C	0.2108701	4.2887559	-5.7594306	H	-3.530821	2.6113853	3.6230435
C	1.6676399	2.0146956	-4.9952448	H	1.0412414	-2.3362804	3.7745508
C	-2.6432728	0.1161782	-5.4315801	H	-4.9832981	-0.8956691	3.0306453
C	1.4777477	-3.3377335	-4.9997967	H	2.9878342	8.0741116	2.4143002
C	3.4818462	-1.4228717	-5.4369139	H	-6.71148	-5.4380677	3.713345
C	-2.7923371	-2.6857779	-5.487157	H	6.9309745	-1.8968073	2.0449035

Table A.6. Optimized atomic coordinates of *trans*-(α,β)-[**Fe$_3$**(CNMe)(THF)]$^+$ (continued).

Atom	x	y	z	Atom	x	y	z
H	4.8134892	-6.0827662	3.7962955	H	-2.8155926	4.8852882	-4.4210636
H	-4.8536331	6.1201425	0.2949748	H	-0.8858289	-3.8441064	-3.3692778
H	-5.1783602	-3.4798241	3.6060317	H	-2.2504123	-5.9231035	-3.3442444
H	-2.4454865	5.4802133	0.5414905	H	3.4014548	-4.8201142	-3.8591317
H	-1.0007257	-7.7044508	3.8993398	H	-5.5681412	0.1626955	-4.3285876
H	2.3034315	5.8618262	1.4827109	H	4.0467556	2.7760785	-4.7325122
H	3.4010719	-4.3159192	2.7175479	H	5.0162608	-6.613569	-4.3865174
H	7.3419564	2.0535543	1.8193064	H	-0.3545949	5.185719	-6.0554947
H	4.4565869	7.5320806	-3.824538	H	2.215396	1.1050178	-4.7057658
H	5.8495027	0.095021	1.3138961	H	6.5265176	2.6899269	-4.8642814
H	3.8993889	5.1926854	-3.2418415	H	-7.606088	-0.720602	-5.3942668
H	-6.0555049	-6.1949516	-0.5099286	H	-2.6019941	1.2135281	-5.4390909
H	-0.6473031	-6.8600094	1.5553843	H	0.7149121	-4.1138687	-4.8524425
H	-1.278216	-4.5359694	0.9536864	H	4.2792457	-0.6809398	-5.5979818
H	-4.4662444	-4.2639605	-0.5990714	H	-2.8747836	-3.7833942	-5.5073639
H	4.8970834	-4.7015668	0.2254899	H	0.004131	3.3230855	-7.6991575
H	6.5842699	-6.4302351	-0.3427957	H	1.2912895	1.2780827	-6.9991682
H	4.2778898	2.7447077	-0.3864823	H	-2.1901922	-0.0154727	-7.548592
H	-6.0886166	-2.626616	-1.0367792	H	1.3720771	-3.5012389	-7.1607221
H	6.7581464	2.709533	-0.5255384	H	3.1655893	-1.7899812	-7.5626916
H	2.0657385	-5.7547949	-0.8098408	H	-2.3221323	-2.5228426	-7.6077611
H	-8.1443098	-3.5039571	-2.1076293	N	-0.1121964	4.7955448	1.5205949
H	0.6895288	-7.8293208	-0.7820445	N	4.2678176	-2.006318	1.6537017
H	-5.8771259	1.6000382	-2.2104932	N	-3.8760589	-2.5939209	1.3683347
H	-6.6902239	3.9014345	-2.7248401	N	1.8250857	4.4130941	-1.5689087
H	1.1919096	8.9486418	-1.3388592	N	3.2150156	-3.5056817	-1.3882466
H	0.6051327	6.597485	-0.7796178	N	-4.5263574	-0.6781853	-1.8927527
H	0.5733434	5.021157	-3.7474228	P	-1.0429494	3.5524622	2.2597584
H	-5.1707725	5.5530651	-3.8529769	P	3.3145795	-0.8672496	2.502036
H	-1.4736541	-7.9320028	-2.0551588	P	-2.525961	-2.3439014	2.3843035
H	7.9069786	2.6882198	-2.7645009	P	2.1410575	2.9259015	-2.346534
H	3.5975839	-1.2648691	-3.277164	P	1.7121144	-3.1075754	-2.1009197
H	-1.9864634	2.617587	-3.8703785	P	-3.2705823	0.2366893	-2.6040637
H	-3.2727016	-2.5529446	-3.3743693	Fe	0.7621264	3.9509003	0.0058873

Table A.6. Optimized atomic coordinates of *trans*-(α,β)-[**Fe$_3$**(CNMe)(THF)]$^+$ (continued).

Atom	x	y	z	Atom	x	y	z
Fe	-3.880808	-1.2368686	-0.0828031	H	1.3129223	9.5071924	3.6296221
Fe	4.2889051	-2.2481223	-0.2904872	H	6.6508367	-7.4274601	-2.6589292
Co	-0.502721	1.7464184	1.1465263	C	5.9878438	-1.7435015	-1.139705
Co	1.6019817	-0.2407146	1.3254142	C	8.2373028	-1.284633	-2.351275
Co	-1.1535549	-1.138647	1.2061854	H	8.3688826	-2.0217567	-3.169046
Co	1.16	1.4412328	-1.0923684	H	8.2408604	-0.2626806	-2.7819977
Co	-1.6440257	0.2505401	-1.1655021	H	9.0886378	-1.3841225	-1.6477925
Co	0.717293	-1.4865768	-1.0441594	N	7.0190229	-1.5284859	-1.6790417
Se	-0.1060358	0.178929	2.8498909	O	-5.9794535	-0.4790969	0.7766383
Se	1.875647	2.1296053	1.1183659	C	-7.1333718	-1.1994201	1.2692049
Se	-2.6738046	0.6775755	0.9510982	C	-6.3932745	0.8958664	0.6634109
Se	0.8250942	-2.4037618	1.0966393	C	-8.3667795	-0.5079663	0.6427831
Se	-0.9516033	2.5448292	-1.0550375	H	-7.0129152	-2.2630312	0.9954178
Se	2.7248555	-0.3397417	-0.7417612	H	-7.1532971	-1.1323327	2.3812781
Se	-1.5780781	-2.0839078	-0.9246828	C	-7.8083219	0.8267514	0.0776331
Se	0.137653	0.0443883	-2.6956005	H	-6.3899166	1.3640316	1.6748733
H	-8.9401096	-2.5558751	-4.3062942	H	-5.6481181	1.4218872	0.0388153
H	-7.1875334	-6.7972709	1.6545824	H	-9.1536184	-0.3433694	1.4049813
H	7.2986585	-5.7657185	3.9884693	H	-8.8061165	-1.1242247	-0.1641324
H	6.735884	3.6530302	3.6525143	H	-8.4194214	1.706473	0.3593416
H	3.1247455	9.4433748	-2.879266	H	-7.7636975	0.7851063	-1.0288143

Table A.7. Optimized atomic coordinates of (α,α,β)-[**Fe$_3$**(CNMe)(THF)$_2$]$^+$.

Atom	x	y	z	Atom	x	y	z
C	0.8924304	3.7969134	6.8087988	C	-4.3913664	4.8800156	1.4275254
C	2.3590974	-3.5429258	6.6417263	C	-2.4487336	3.8581541	2.5055298
C	-0.100973	4.6612789	6.3208273	C	4.8370891	-5.9180308	3.3401533
C	3.6147081	-2.9819194	6.3561147	C	4.4015382	-0.1780886	2.9182836
C	-4.0079197	-0.1031657	6.2225705	C	-3.0336271	4.5247061	1.407889
C	1.3942745	2.7798384	5.9804938	C	1.7719002	6.1649154	2.6802576
C	-2.8251225	-0.861462	6.1737762	C	-6.8709967	-4.7162578	2.519076
C	1.326163	-3.4527678	5.6939734	C	4.7253404	-3.7144137	2.2696
C	-4.8278559	-0.0220087	5.0851093	C	-5.8750812	-3.7283355	2.5151705
C	-0.6003141	4.5015115	5.0183169	C	4.0887479	-4.8845577	2.7584896
C	3.836634	-2.3314649	5.1317629	C	-2.1283697	-6.8470982	3.2910063
C	-0.2366464	8.1078477	2.8627065	C	6.4295659	1.0494264	2.332149
C	0.900681	2.6213936	4.6753895	C	-2.5236292	-4.0997747	2.7531964
C	1.0601189	8.4070795	3.3152221	C	5.5117956	0.0169506	2.0728282
C	-2.472573	-1.5459587	4.999859	C	-7.2206741	-5.3890741	1.3351592
C	-0.1131932	3.4685403	4.1824809	C	-5.195914	-3.3878377	1.3160598
C	1.543727	-2.7951093	4.4722603	C	-1.8500882	-6.3300831	2.0140012
C	-0.5292004	6.8497644	2.311698	C	-2.0427122	-4.9671092	1.7464929
C	2.7993735	-2.2242053	4.1763131	C	-6.5449679	-5.0737399	0.1434974
C	5.1304199	1.7222497	4.2715671	C	5.3488506	6.1911888	-2.4624857
C	-4.47964	-0.7087192	3.9090153	C	-5.5390863	-4.0959333	0.1348871
C	6.8798484	-4.6605847	2.9616005	C	4.3075626	5.2506202	-2.4759105
C	6.2358488	-5.8126555	3.444413	C	5.8582529	6.6852516	-1.2491337
C	4.213789	0.6907371	4.0149985	C	3.7449965	4.7740223	-1.2620306
C	-4.6231064	3.8549614	3.6186663	C	4.2457995	-5.8011761	-0.8752664
C	-3.3107315	-1.4952597	3.8632453	C	5.0515718	-6.9050941	-1.1888409
C	-5.1870272	4.5599284	2.5418176	C	5.0979076	1.6060783	-1.5414805
C	-3.2651558	3.4943713	3.5984438	C	5.3195552	6.2111297	-0.0395894
C	2.0618882	7.4255739	3.2229856	C	6.4492423	1.3084745	-1.7701847
C	6.2425814	1.9039633	3.4312341	C	4.2881002	5.2632812	-0.0452124
C	-2.6163567	-5.9953926	4.2943848	C	-6.6553921	-1.5218254	-2.066811
C	6.1357451	-3.6208635	2.3821566	C	3.4601712	-5.1485828	-1.8682683
C	-2.82059	-4.6305798	4.027397	C	0.4021908	-6.0049918	-1.5740628
C	0.4755557	5.8555416	2.2000815	C	-0.5148679	-7.0692901	-1.6206744

Table A.7. Optimized atomic coordinates of (α,α,β)-[**Fe$_3$**(CNMe)(THF)$_2$]$^+$ (continued).

Atom	x	y	z	Atom	x	y	z
C	-7.8645166	-1.8497639	-2.6917232	C	0.5759836	3.8412671	-6.2131083
C	-4.9252662	2.8075455	-2.6205342	C	1.054767	2.5256593	-6.082632
C	-5.2506406	4.1470736	-2.8936174	C	-2.4575401	-0.2225512	-6.6547205
C	4.25399	1.9670904	-2.6156164	C	1.6073903	-3.2441181	-6.3882971
C	-5.7671607	-0.5596399	-2.6175128	C	2.6193458	-2.290246	-6.5748901
C	5.0765509	-7.417173	-2.4968062	C	-2.6819091	-1.6052405	-6.740099
C	0.154743	-4.818867	-2.2973832	H	1.2774541	3.9180613	7.8329686
C	-3.6566013	2.2929914	-2.9616593	H	2.1874719	-4.0552027	7.6009009
C	-4.3139126	4.9898526	-3.5135096	H	4.4336502	-3.0557569	7.087886
C	-1.6957804	-6.9581814	-2.3723993	H	-4.2849028	0.4287044	7.1456863
C	6.9754178	1.3548368	-3.0735111	H	-0.4926259	5.4702501	6.9562272
C	-2.7046197	3.1587655	-3.5479909	H	-2.1676368	-0.9182526	7.0546185
C	-3.0403688	4.4912826	-3.8373935	H	2.1730777	2.0984442	6.3561925
C	3.4911491	-5.6838403	-3.1839441	H	-1.0340491	8.8638286	2.9379365
C	-1.0511837	-4.7019925	-3.0269648	H	0.3429304	-3.90201	5.9018057
C	-1.9643852	-5.767573	-3.0693443	H	-5.750014	0.5788019	5.1113487
C	-8.2338283	-1.2348232	-3.9016424	H	4.8296183	-1.9097539	4.9188192
C	1.7673371	2.9999279	-3.7938115	H	-1.3740371	5.1915924	4.653432
C	1.2636321	4.3123113	-3.9197778	H	4.9754578	2.388163	5.1342556
C	4.2832494	-6.8021169	-3.4820722	H	-1.547416	6.6273881	1.9635988
C	-6.1479964	0.0393944	-3.849966	H	7.9743462	-4.5676432	3.0401141
C	4.7886958	2.0138778	-3.920434	H	3.3506645	0.5494203	4.6834922
C	6.1408522	1.7026387	-4.1475485	H	-1.5348571	-2.1207148	4.9761028
C	-7.3604781	-0.2951831	-4.4726825	H	1.3085719	1.8293379	4.0306016
C	1.7649118	-2.9796328	-3.9605018	H	-5.2418435	3.5871641	4.4888471
C	-2.9852481	-0.2576727	-4.2683121	H	-2.8529165	-6.3944703	5.2927471
C	2.7829745	-2.0195645	-4.1596975	H	-3.2261473	-3.9830104	4.8174874
C	-3.2107968	-1.6493414	-4.3630257	H	-6.2473588	4.8549196	2.5680512
C	0.6764616	4.7284672	-5.12814	H	-2.8407144	2.935309	4.4454752
C	1.6409296	2.1026148	-4.8783189	H	0.7292923	-2.7366256	3.7347826
C	-2.6093971	0.4488515	-5.429569	H	-5.104504	-0.627393	3.0076552
C	1.1847435	-3.5907411	-5.0924998	H	3.0784068	7.6386867	3.5884165
C	3.210012	-1.6822421	-5.4527021	H	-7.3853173	-4.9594281	3.4619949
C	-3.0629603	-2.315499	-5.5892037	H	6.6382681	-2.7156583	2.0121843

Table A.7. Optimized atomic coordinates of (α,α,β)-[**Fe$_3$**(CNMe)(THF)$_2$]$^+$ (continued).

Atom	x	y	z	Atom	x	y	z
H	4.3225097	-6.8162248	3.7152004	H	-2.2945993	5.1406993	-4.3200692
H	-4.8274619	5.4120341	0.5682904	H	-1.2872558	-3.7686228	-3.5603355
H	-5.6250644	-3.1991944	3.4457296	H	-2.8956967	-5.6654099	-3.6473839
H	-2.414612	4.7649362	0.5301384	H	2.9012982	-5.2151448	-3.9805761
H	-1.971827	-7.9162257	3.5012734	H	-5.4913784	0.7730131	-4.3345846
H	2.5458081	5.3845517	2.6381049	H	4.157612	2.3186151	-4.767381
H	2.9950966	-4.9641882	2.67133	H	4.2833301	-7.1956395	-4.5108014
H	7.3024457	1.1860797	1.6750219	H	0.3041886	5.7604135	-5.224493
H	5.7626918	6.5481075	-3.418616	H	1.9956409	1.064469	-4.7893853
H	5.6499213	-0.6510921	1.2087669	H	6.5462631	1.7557852	-5.1697641
H	3.9109836	4.8944935	-3.4365774	H	-7.6205284	0.1904858	-5.4261336
H	-6.789687	-5.6070399	-0.7883311	H	-2.4483653	1.5346187	-5.3964959
H	-1.4788188	-6.9884413	1.2147803	H	0.412794	-4.363431	-4.9737632
H	-1.8243034	-4.576443	0.7404961	H	4.0138813	-0.9408693	-5.5807938
H	-4.978346	-3.8812638	-0.7874235	H	-3.263412	-3.3962647	-5.649686
H	4.1835978	-5.4531682	0.1694563	H	0.1228806	4.1732384	-7.1598909
H	5.645194	-7.3800693	-0.3925745	H	0.9709828	1.8191122	-6.9222846
H	4.7000635	1.577782	-0.5148657	H	-2.170703	0.3475276	-7.5516729
H	-6.3710992	-2.0331632	-1.1361007	H	1.143096	-3.7351317	-7.2573346
H	7.0989025	1.0503105	-0.9203235	H	2.9531157	-2.0267107	-7.5902251
H	1.3173719	-6.1018367	-0.9748404	H	-2.572208	-2.126858	-7.7030305
H	-8.518697	-2.6063868	-2.2307812	N	0.2234547	4.5862548	1.6158416
H	-0.2953473	-7.9970899	-1.0700804	N	3.9692923	-2.689314	1.6310402
H	-5.6716263	2.1485748	-2.156628	N	-4.208795	-2.3797279	1.2530575
H	-6.250189	4.5273109	-2.632485	N	2.6787056	3.857773	-1.2049077
H	5.716228	6.5745605	0.9212134	N	2.7578806	-3.9876665	-1.4675397
H	3.8870652	4.867856	0.8997954	N	-4.5768388	-0.2659352	-1.9205474
H	1.3279037	5.0006944	-3.061425	P	-0.6660032	3.3534767	2.4158316
H	-4.5749002	6.0343687	-3.7428666	P	3.137045	-1.4793963	2.5105818
H	-2.4102432	-7.7945373	-2.4099675	P	-2.8432056	-2.3388787	2.2798006
H	8.041342	1.1408384	-3.2495479	P	2.5216284	2.4746699	-2.1843491
H	3.2587661	-1.5370876	-3.2911639	P	1.3257213	-3.3894146	-2.1873538
H	-1.6884925	2.8027426	-3.7768019	P	-3.2177117	0.5290879	-2.5935206
H	-3.527743	-2.2100136	-3.4712204	Fe	-4.0196219	-0.9723052	-0.1343236

Table A.7. Optimized atomic coordinates of (α,α,β)-[**Fe$_3$**(CNMe)(THF)$_2$]$^+$ (continued).

Atom	x	y	z	Atom	x	y	z
Fe	3.9520442	-2.9017988	-0.314763	O	-6.0335149	-0.0035853	0.7887177
Co	-0.3556929	1.5600243	1.2260229	C	-7.2609541	-0.6296126	1.2464672
Co	1.4966361	-0.6448889	1.3646283	C	-6.2778981	1.4136956	0.6871882
Co	-1.3435949	-1.2389844	1.1617224	C	-8.40996	0.3519534	0.9057961
Co	1.2869423	1.1279799	-1.0202536	H	-7.3459718	-1.609392	0.7414097
Co	-1.6030852	0.2978102	-1.1594433	H	-7.1907499	-0.820101	2.3398865
Co	0.5124431	-1.7067889	-1.0756585	C	-7.707764	1.5075399	0.157931
Se	-0.1881555	-0.110133	2.8709713	H	-6.17403	1.8875197	1.6909679
Se	2.0031593	1.7010819	1.2014126	H	-5.5012011	1.8390915	0.025227
Se	-2.6257731	0.7636582	0.9573732	H	-8.8951146	0.7175443	1.8330638
Se	0.4897024	-2.7053003	1.036229	H	-9.1940637	-0.1267252	0.2885727
Se	-0.6449229	2.5063122	-0.9475701	H	-8.1746127	2.4937578	0.349351
Se	2.625433	-0.812193	-0.690496	H	-7.7181282	1.3254255	-0.9360557
Se	-1.8388191	-2.0440072	-1.0051301	Fe	1.1899685	3.8115682	0.1016367
Se	0.1462229	-0.071947	-2.6917719	O	0.7204487	6.1841709	-1.0213646
H	-9.1817796	-1.4930104	-4.3964912	C	1.515314	7.3934062	-0.9197324
H	-8.0053944	-6.1602763	1.3439047	C	-0.6572977	6.5358191	-1.2861479
H	6.821128	-6.6254002	3.900498	C	0.7486077	8.4312488	-1.7376894
H	6.9636349	2.7103219	3.6341249	H	1.5983922	7.6977106	0.1480891
H	6.6713854	7.4264236	-1.2460872	H	2.527471	7.1661879	-1.3028999
H	1.2859019	9.3949418	3.7442163	C	-0.708184	8.0693931	-1.4016887
H	5.695122	-8.2929042	-2.7438535	H	-0.9691276	6.0239333	-2.2227297
C	5.703804	-2.6520064	-1.1768948	H	-1.2949234	6.1518563	-0.4633953
C	7.9575053	-2.6484527	-2.4638011	H	0.9520434	8.2977425	-2.8212829
H	8.0570156	-1.7257399	-3.0708328	H	1.0153884	9.4717462	-1.4671087
H	8.8125199	-2.7120685	-1.7607779	H	-1.4374134	8.4151384	-2.1605573
H	7.9876205	-3.5292315	-3.136698	H	-0.9936475	8.5186692	-0.4285093
N	6.7401598	-2.6346516	-1.7475273	--	--	--	--

Table A.8. Optimized atomic coordinates of *cis*-(α,β)-[**Fe$_3$**(THF)$_2$]$^+$.

Atom	x	y	z	Atom	x	y	z
C	-3.7806606	0.7224966	-6.3694333	C	-0.6385351	6.4654575	-2.7296903
C	-0.1998869	-3.6872429	-6.7912336	C	-1.0445467	4.057173	-2.8788701
C	-2.5695793	1.4295777	-6.4229949	C	0.5002733	-8.247369	-2.2600921
C	-1.5689504	-3.5553707	-6.5124006	C	-3.4216194	-3.6668212	-2.3072234
C	2.6032036	1.8419361	-6.6290404	C	-1.4085302	5.335614	-2.4073025
C	-4.4512087	0.592935	-5.1414132	C	-5.7460748	4.0070423	-1.565178
C	2.1629808	0.5486559	-6.2946031	C	7.9715168	1.1442858	-2.7673784
C	0.7225972	-3.7435443	-5.7311749	C	-0.7478386	-6.131534	-2.1990784
C	3.2768698	2.6148177	-5.6692037	C	6.5689133	1.1601349	-2.775307
C	-2.0287588	2.0035624	-5.2599148	C	0.3049409	-6.9647296	-1.7347613
C	-2.0196208	-3.4801893	-5.1829688	C	6.1672275	-3.6178745	-3.0593622
C	-5.439032	5.2687879	-4.0343674	C	-5.3969644	-4.9521081	-1.667735
C	-3.9110491	1.1600055	-3.9769318	C	4.4837243	-1.3742182	-2.6895904
C	-6.6595207	5.3921028	-3.3513999	C	-4.0006795	-4.7906369	-1.6816878
C	2.4039538	0.0284922	-5.0131354	C	8.6840113	1.1172083	-1.5553247
C	-2.6930487	1.8746153	-4.0225613	C	5.8354439	1.1459956	-1.5596069
C	0.2777766	-3.6578043	-4.403931	C	5.7201729	-3.273985	-1.7722648
C	-4.3756562	4.5303571	-3.4926687	C	4.8811219	-2.1654078	-1.5880675
C	-1.0995654	-3.5258116	-4.1152147	C	7.9724047	1.0871485	-0.3439772
C	-5.6558342	-2.8531821	-2.8655383	C	-7.9694137	1.108495	0.3450041
C	3.5172556	2.0958728	-4.3840033	C	6.5691783	1.0881642	-0.3458195
C	-1.3723146	-7.9163143	-3.760607	C	-6.5661883	1.105787	0.3466204
C	-0.3372835	-8.7349496	-3.2795434	C	-8.6807382	1.14042	1.5564685
C	-4.2617721	-2.6865562	-2.8828559	C	-5.8321255	1.1616489	1.5602956
C	0.8972344	5.0575836	-3.975819	C	-0.3245535	-6.9641893	1.7342995
C	3.099992	0.7930376	-4.049037	C	-0.5235092	-8.246258	2.2596688
C	0.5080171	6.3323594	-3.5294682	C	-4.8870772	-2.1518477	1.5877616
C	0.1400666	3.9243015	-3.638526	C	-7.9679874	1.1655692	2.7684148
C	-6.8029945	4.7480205	-2.1100535	C	-5.7291684	-3.258166	1.7716519
C	-6.227088	-3.9885612	-2.2640946	C	-6.5653477	1.1776892	2.7761195
C	5.7800465	-2.8374877	-4.1597578	C	5.7569119	3.9914091	1.5661328
C	-1.5828535	-6.6339829	-3.2311206	C	0.7306957	-6.1340502	2.1984755
C	4.9486725	-1.7193688	-3.9774188	C	3.9873566	-4.8018409	1.6810662
C	-4.4969916	3.8823544	-2.2324931	C	5.3832069	-4.9670415	1.6671757

Table A.8. Optimized atomic coordinates of *cis*-(α,β)-[**Fe$_3$**(THF)$_2$]$^+$ (continued).

Atom	x	y	z	Atom	x	y	z
C	6.8156848	4.7295484	2.1112655	C	-2.5974131	1.8476715	6.6295229
C	1.4230778	5.3308242	2.4079526	C	-2.1609324	0.553212	6.2947462
C	0.6562084	6.4627562	2.730448	C	2.5732992	1.4201797	6.4229969
C	-4.4871275	-1.3623247	2.6895506	C	1.558492	-3.5606665	6.5117814
C	4.5075147	3.869631	2.2333974	C	0.1890337	-3.6887571	6.7904372
C	0.3127902	-8.7362552	3.2789933	C	3.7826847	0.7102124	6.3693181
C	3.4112695	-3.6765927	2.306758	H	-4.2070451	0.282185	-7.2835786
C	1.0556995	4.0533699	2.8795624	H	0.1485061	-3.7578119	-7.8330838
C	-0.4905942	6.3327691	3.5303787	H	-2.3002181	-3.5219572	-7.3344738
C	6.2158582	-4.0058142	2.263753	H	2.4206538	2.2457628	-7.6366117
C	-6.1767819	-3.6014408	3.0587197	H	-2.0388022	1.5455922	-7.3802567
C	-0.1291724	3.9237154	3.6393669	H	1.6266002	-0.0636665	-7.0352117
C	-0.8832101	5.059051	3.9767653	H	-5.4129734	0.0596053	-5.0919292
C	1.5644203	-6.6389036	3.2303851	H	-5.3040406	5.7548572	-5.0131633
C	4.2539911	-2.6986812	2.8826455	H	1.7971668	-3.8649639	-5.9367436
C	5.6476019	-2.8690249	2.8653769	H	3.628662	3.6264457	-5.9257527
C	6.6738194	5.3735784	3.3528238	H	-3.0981141	-3.4031704	-4.9863115
C	-3.0972603	0.8008846	4.0492431	H	-1.0901653	2.568058	-5.3360831
C	-3.5106963	2.1048604	4.3845245	H	-6.3024668	-2.0896018	-3.3243083
C	1.3502606	-7.9206204	3.7599028	H	-3.4410988	4.4591316	-4.0629337
C	4.3877925	4.5175379	3.4937785	H	-2.0349074	-8.2796981	-4.5614692
C	-4.9526625	-1.7067838	3.9773485	H	-3.8298909	-1.7864918	-3.3472386
C	-5.787102	-2.8226686	4.1593791	H	2.0487279	-0.984463	-4.7694118
C	5.4530141	5.2531124	4.0357327	H	-4.4508105	1.0663543	-3.0233743
C	1.0894638	-3.5293173	4.1145537	H	1.8022255	4.9344088	-4.5888483
C	2.69823	1.8659921	4.0227835	H	6.1331511	-3.0918992	-5.1709652
C	-0.2882785	-3.6574967	4.4030888	H	4.6727312	-1.1097525	-4.8491599
C	3.9145068	1.1484539	3.977031	H	1.0983672	7.2204067	-3.8032078
C	-3.2688028	2.622756	5.6698691	H	0.4931194	2.9334592	-3.9624689
C	-2.4034162	0.0340925	5.0131415	H	1.008485	-3.7086941	-3.5813916
C	2.0340524	1.995984	5.2600865	H	4.0305381	2.7019906	-3.6239661
C	2.0095233	-3.4864863	5.182416	H	-7.3200777	-4.1183298	-2.2570042
C	-0.7334881	-3.742261	5.7302652	H	-7.7562921	4.8072	-1.5615967
C	4.453119	0.5795818	5.1413487	H	8.5156997	1.15767	-3.7246362

Table A.8. Optimized atomic coordinates of *cis*-(α,β)-[**Fe$_3$**(THF)$_2$]$^+$ (continued).

Atom	x	y	z	Atom	x	y	z
H	-2.4052592	-6.0196637	-3.621388	H	4.4541792	1.0539414	3.023513
H	1.3223536	-8.8691177	-1.8733917	H	-1.788454	4.9383378	4.5899073
H	-0.9470564	7.4569198	-2.3640407	H	3.8244712	-1.7975691	3.3471926
H	6.0297584	1.1951682	-3.7323949	H	6.2962467	-2.107261	3.3243252
H	-2.3113637	5.4438374	-1.7920084	H	2.3886531	-6.0269481	3.6205173
H	6.8201439	-4.4922906	-3.2034163	H	3.4530421	4.4484998	4.0639962
H	-5.8917784	3.4835751	-0.6091424	H	-4.6747953	-1.0983442	4.8493005
H	0.978707	-6.5817148	-0.9508044	H	2.0119235	-8.2859247	4.56066
H	-5.835391	-5.8430575	-1.1923923	H	-3.6176258	3.6353483	5.9266681
H	-8.5097413	1.067731	-0.6134572	H	-2.0511049	-0.9798137	4.7691449
H	-3.3528874	-5.5448817	-1.212087	H	-6.1406314	-3.0765829	5.1705635
H	-6.008989	1.0322198	-0.59996	H	5.319228	5.7392078	5.0146811
H	8.5124579	1.0449364	0.614576	H	1.0967998	2.5626858	5.3363638
H	6.0184919	-3.8724634	-0.8991068	H	3.0882504	-3.4124498	4.9858967
H	4.5393019	-1.9113228	-0.5726658	H	-1.808416	-3.8607197	5.9356871
H	6.0116578	1.0160753	0.6006832	H	5.4136067	0.0439637	5.091784
H	-0.9973042	-6.5792153	0.9504364	H	-2.4137116	2.2507063	7.6372017
H	-1.3474423	-8.8656318	1.8730996	H	-1.626324	-0.0608584	7.0351885
H	-4.5448857	-1.8981426	0.5723927	H	2.0426421	1.537043	7.3802213
H	5.9013209	3.4679016	0.6099199	H	2.2897585	-3.5294712	7.3339431
H	-6.0294363	-3.8553541	0.8982799	H	-0.1596694	-3.7585675	7.8322348
H	3.3375662	-5.5542599	1.2112938	H	4.2078597	0.2684696	7.2833365
H	7.7691348	4.7865104	1.5628394	N	-3.4673211	3.1419686	-1.6062024
H	5.8192872	-5.8590796	1.1917166	N	-0.9076661	-4.864558	-1.6025704
H	2.3261204	5.4365713	1.7925402	N	4.4206834	1.2195203	-1.5049014
H	0.967375	7.4533787	2.3647634	N	-4.4171932	1.2313758	1.5053952
H	-8.5119873	1.180368	3.7257553	N	0.8941003	-4.8675244	1.6020014
H	-6.0259152	1.2112689	3.7331049	N	3.4759912	3.1320355	1.6068561
H	-4.0220966	2.712791	3.6246621	P	-2.0668641	2.5767788	-2.4151524
H	-1.0784988	7.2224096	3.804207	P	-1.5839602	-3.4681974	-2.3237238
H	7.3084984	-4.1384928	2.2566972	P	3.4142851	0.1035103	-2.3530327
H	-6.8320919	-4.474101	3.2025516	P	-3.4136738	0.1125185	2.353168
H	-1.0190369	-3.7062112	3.5804584	P	1.5741638	-3.4729978	2.3231048
H	-0.4849008	2.9338401	3.9633397	P	2.074	2.5702865	2.415563

Table A.8. Optimized atomic coordinates of *cis*-(α,β)-[**Fe$_3$**(THF)$_2$]$^+$ (continued).

Atom	x	y	z	Atom	x	y	z
Fe	-3.5466272	2.5060873	0.2796205	C	-3.5241107	5.6270291	0.869059
Fe	3.5538428	2.4968752	-0.2792457	C	-5.6596622	6.117696	1.7969562
Fe	-0.0055399	-4.1972428	-0.0003348	H	-6.1913393	3.9695062	1.5546639
Co	-0.9548757	1.1983202	-1.151737	H	-5.2436512	4.3443949	3.0330989
Co	-0.8281129	-1.8086087	-1.1298848	C	-4.2345793	6.688436	1.7064902
Co	1.5924344	-0.1931284	-1.193077	H	-2.4383466	5.5363066	1.0700195
Co	-1.5928702	-0.1888388	1.1927576	H	-3.6901636	5.7864814	-0.2180765
Co	0.9583527	1.1952191	1.1516704	H	-6.2529	6.5380816	2.6321466
Co	0.8230182	-1.811485	1.1290085	H	-6.2108612	6.3064218	0.8530223
Se	-0.1226448	-0.2767272	-2.7713164	H	-3.7745913	6.7619446	2.7138947
Se	-2.6608473	-0.3404855	-0.8766002	H	-4.1926933	7.6908545	1.2378181
Se	1.2759463	2.133238	-1.0189626	O	4.167072	4.3558345	-1.2425695
Se	1.4513728	-2.5781756	-1.0670561	C	5.4104856	4.6079879	-1.9668454
Se	-1.2697086	2.1366764	1.0192312	C	3.5394085	5.6177638	-0.8680281
Se	-1.4588402	-2.5743878	1.0657737	C	5.6761475	6.1032625	-1.7958822
Se	2.659828	-0.3484262	0.8762966	H	6.2025527	3.9537493	-1.5536616
Se	0.1218833	-0.2779822	2.7708484	H	5.2558711	4.3310362	-3.032148
H	-0.1807618	-9.7405231	-3.6973927	C	4.2524524	6.6774651	-1.7054119
H	0.1534245	-9.7413723	3.6968664	H	2.4534137	5.5297002	-1.0689213
H	9.7842264	1.1079995	-1.5563108	H	3.7059348	5.7767035	0.2191145
H	7.5049377	5.9501398	3.7850776	H	6.2704235	6.5222588	-2.6310321
H	-9.7809738	1.1341366	1.5576275	H	6.2277885	6.290587	-0.8519268
H	-7.4891913	5.9708926	-3.7834571	H	3.7926564	6.7520803	-2.7128229
O	-4.1549205	4.366614	1.2434152	H	4.2129854	7.6799791	-1.2367363
C	-5.3976296	4.6217712	1.9678067	--	--	--	--

Table A.9. Optimized atomic coordinates of (α,α,β)-**Cr**$_3$(py)$_3$′.

Atom	x	y	z	Atom	x	y	z
C	2.2614292	1.8836515	-6.9541461	C	5.6871637	2.8705964	-3.6912703
C	3.1952657	0.8670976	-6.70364	C	6.9252466	-1.1497221	-2.084578
C	1.3469999	-3.4252472	-6.4461895	C	4.6251552	3.2093792	-2.8083437
C	0.3866038	-2.418072	-6.2487882	C	-5.5831679	-3.9478795	-3.4345127
C	-2.697737	0.7977175	-6.1333205	C	-2.8371996	-3.5014384	-2.905595
C	-4.0732142	0.5301917	-6.2480819	C	5.9009067	-0.1875969	-2.0295238
C	1.6477343	2.5421196	-5.8730451	C	-0.8081748	6.3381185	-2.2550757
C	1.5671658	-4.3794199	-5.4394545	C	-4.899504	4.7293577	-2.7343541
C	3.5171437	0.5075245	-5.3819941	C	-2.6358709	-8.4327934	-1.7273019
C	-0.3482481	-2.362168	-5.0530057	C	4.4861219	-6.1049037	-1.2453212
C	-1.0303054	5.8002937	-4.6119963	C	-5.6991255	5.8815834	-2.7582
C	-2.1854617	1.3953681	-4.9694618	C	-1.3377121	5.0836176	-1.9203502
C	-4.9347997	0.8701582	-5.1930681	C	4.1621186	-7.3038202	-1.8978069
C	1.9567239	2.1747877	-4.5554808	C	-1.3368755	-5.8844036	-1.6466987
C	2.8960681	1.150815	-4.2930641	C	3.4543024	-5.2961752	-0.7541044
C	0.8271062	-4.3297264	-4.2453899	C	-5.1143368	-3.9186045	-2.1082861
C	5.4209036	-2.6839714	-3.2196781	C	-3.7553874	-3.6903092	-1.8487753
C	-1.5674369	4.5440189	-4.2768962	C	2.8070339	-7.6429995	-2.0330791
C	5.9454105	5.2023711	-4.3799961	C	-4.5271166	4.1215267	-1.5029873
C	-0.1419705	-3.3262893	-4.0402676	C	-8.5548133	0.3785596	-1.5990606
C	4.8782618	5.5540264	-3.5346268	C	1.8330983	-6.7785734	-1.517854
C	4.3943188	-1.7272447	-3.1593704	C	-2.319334	-7.8329273	-0.4953917
C	-0.6457069	6.6984501	-3.6043868	C	-7.4909356	-0.5356879	-1.6532516
C	-4.6803612	-3.7551688	-4.4915573	C	-6.1652512	6.4667215	-1.5675283
C	-3.3151689	-3.5400801	-4.2307516	C	-1.6967732	-6.5767172	-0.4552092
C	6.6908221	-2.3974047	-2.6869787	C	-8.3079325	1.6585244	-1.082301
C	-3.0488399	1.7552238	-3.9095632	C	-6.2305727	-0.1434394	-1.1882025
C	-4.4264217	1.4814707	-4.0340099	C	-7.0177116	1.9773171	-0.6391753
C	6.329866	3.8522992	-4.460552	C	-4.9845433	4.7463588	-0.3066499
C	4.221031	4.5737523	-2.7763461	C	-5.7985439	5.887519	-0.3391739
C	-2.3200982	-7.7494283	-2.9154256	C	3.7588696	5.910381	0.8188544
C	4.6323386	-0.4588846	-2.5819181	C	4.3248707	7.1737242	1.0354123
C	-1.6793659	-6.5018302	-2.883157	C	5.8479599	1.9950015	1.4536999
C	-1.7184867	4.1682971	-2.9263769	C	6.2365926	3.8189867	0.0625461

Table A.9. Optimized atomic coordinates of (α,α,β)-**Cr**$_3$(py)$_3$′ (continued).

Atom	x	y	z	Atom	x	y	z
C	4.6705385	-2.3027228	1.4440597	C	1.4390273	-2.9529359	4.1397917
C	6.0668447	-2.1677532	1.5072675	C	3.4908766	2.501052	4.3400743
C	7.1719344	2.0057248	1.9090344	C	0.0339463	4.9732457	4.1920767
C	3.2754047	5.1070414	1.889706	C	0.550492	-3.9893976	4.4958986
C	-0.2424063	5.2292128	1.7945355	C	-0.8281881	6.0641921	4.403127
C	7.5750888	3.8966803	0.4706579	C	-3.0433343	0.3993786	4.2374494
C	4.4112977	7.7037567	2.3345841	C	-4.8578832	-2.1656926	4.2016011
C	8.0561936	2.9774128	1.4139926	C	-3.2918085	1.7606987	4.5032121
C	-1.0996259	6.3187936	2.0049614	C	-5.5380704	-3.3749715	4.4258906
C	2.1566043	-5.6130867	2.2583715	C	1.7491479	-1.9621798	5.0989026
C	3.3012463	-5.8338527	3.0719298	C	1.2229642	2.1012348	5.1190137
C	-4.2884888	-2.9097747	1.9627092	C	3.9958856	2.0483186	5.5709628
C	3.9130005	-2.5813925	2.6037028	C	-2.4179834	-0.3873759	5.2311462
C	-4.9690473	-4.11702	2.184451	C	0.0208322	-4.0618121	5.7955028
C	6.7338102	-2.2859614	2.7390462	C	-2.9611294	2.3187448	5.750238
C	1.3462634	-6.7510908	1.9789044	C	1.7288721	1.672018	6.3569523
C	3.6086481	-7.1106143	3.5671902	C	1.2320073	-2.0469614	6.4013158
C	0.33098	4.5379661	2.8846203	C	3.1155803	1.6427665	6.5877296
C	3.361713	5.6687686	3.1953558	C	0.3715126	-3.1002443	6.7567965
C	-5.910235	0.9043561	2.3664935	C	-2.0980809	0.1680251	6.479937
C	1.6656939	-8.0256538	2.4639114	C	-2.3743311	1.5213787	6.7465435
C	3.9153595	6.9404603	3.4052237	H	2.0189465	2.171818	-7.9889644
C	2.8020008	-8.220979	3.2688018	H	3.692123	0.3529843	-7.5412863
C	-6.3333847	2.2129072	2.7238546	H	1.9252466	-3.4622652	-7.3824345
C	-6.8758034	-0.1343792	2.4475174	H	0.2151478	-1.6594641	-7.0276198
C	-4.2168503	-1.9211542	2.9665281	H	-2.0133299	0.5396551	-6.9564748
C	-1.4006258	6.7374681	3.3131533	H	-4.4710619	0.0571714	-7.1593184
C	-7.6450495	2.4705716	3.1512387	H	2.3176962	-5.1725923	-5.5825335
C	5.9913117	-2.5439568	3.9030138	H	0.9261922	3.3538813	-6.0524366
C	4.5954548	-2.6957592	3.8358067	H	-0.9220927	6.0793285	-5.6718261
C	-8.1836854	0.1250538	2.8853367	H	4.2688608	-0.2753672	-5.2083105
C	-5.5940965	-4.3550458	3.4213732	H	5.2244081	-3.6609643	-3.6876036
C	-8.5798087	1.4257023	3.242977	H	-1.8857834	3.8640724	-5.0798826
C	2.10126	2.5443232	4.1044543	H	-1.0810984	-1.5539293	-4.91004

Table A.9. Optimized atomic coordinates of (α,α,β)-**Cr**$_3$(py)$_3$′ (continued).

Atom	x	y	z	Atom	x	y	z
H	-1.1029113	1.5756543	-4.8917902	H	3.6522334	5.5291809	-0.2085592
H	-5.0348358	-3.7840924	-5.5336262	H	-6.7891012	2.9748595	-0.236481
H	-2.620592	-3.4179301	-5.0737408	H	4.6841024	7.7582382	0.1732145
H	-6.0132344	0.6622413	-5.2699594	H	-2.5792253	-8.3375439	0.4487981
H	4.5336033	6.5991038	-3.4833301	H	-1.5057484	-6.0816745	0.5109612
H	3.4022779	-1.9718042	-3.5692294	H	4.1586892	-2.1785737	0.4757674
H	-0.2254624	7.6811237	-3.8684749	H	6.6273738	-1.9597692	0.5833972
H	-2.5689417	-8.1990296	-3.8900445	H	5.1272849	1.2417264	1.8095885
H	7.4964638	-3.146196	-2.7415914	H	-0.0021028	4.905696	0.7695501
H	-1.4243125	-5.996245	-3.8253676	H	5.8345363	4.5172801	-0.6848663
H	0.99559	-5.0739701	-3.454059	H	-4.6563754	4.3230315	0.6575563
H	1.4718531	2.6995113	-3.7162409	H	-1.5420933	6.8415874	1.1429932
H	7.151859	3.5548031	-5.1312333	H	-6.1315162	6.3417773	0.6077562
H	3.3388603	4.8388818	-2.1714303	H	-3.7945752	-2.721807	0.9983958
H	-4.5643825	4.2824952	-3.6806436	H	7.4922631	1.2521353	2.6425694
H	-5.0993836	1.7568062	-3.2091991	H	-4.9981627	-4.8818432	1.3926473
H	-5.9696755	6.3248875	-3.7298912	H	3.9686753	-4.9975541	3.3077356
H	-6.6486874	-4.1327374	-3.6429049	H	8.2220383	4.6768836	0.0450781
H	5.5290243	-5.7887972	-1.1026139	H	9.1017642	3.0155683	1.755974
H	6.0143233	1.8242178	-3.7647048	H	0.4350011	-6.6161761	1.3748909
H	7.9162421	-0.9158678	-1.6644368	H	7.828854	-2.1800188	2.7908632
H	4.9507582	-7.9655337	-2.2874314	H	4.5060494	-7.2351624	4.1944312
H	6.0801238	0.7934581	-1.5641829	H	-5.6049288	3.0358304	2.6579814
H	-0.5156495	7.0383191	-1.4574918	H	-6.594637	-1.1504826	2.141309
H	3.6655843	-4.360948	-0.2179418	H	1.0063585	-8.8737362	2.2194422
H	-9.5585281	0.0975948	-1.9528976	H	4.1759262	2.8439106	3.5507191
H	2.492902	-8.5732724	-2.5276811	H	-2.0760274	7.5908272	3.4800829
H	-1.4725438	4.8063429	-0.8640982	H	-7.9351385	3.4981582	3.4223771
H	-7.6207611	-1.5511548	-2.0533879	H	2.9991433	5.0977754	4.0597076
H	-5.8093396	-4.0809736	-1.2696777	H	0.2734028	-4.7479275	3.7517008
H	-9.1017662	2.4156625	-1.0147386	H	3.9633168	7.3375553	4.4318799
H	-3.3870449	-3.6775415	-0.8117761	H	-6.1225931	-5.3041044	3.6016299
H	0.7630486	-7.0175415	-1.6038192	H	-8.9078344	-0.7037063	2.9361105
H	-5.370879	-0.8310147	-1.222616	H	-3.7415163	2.3849402	3.7194251

Table A.9. Optimized atomic coordinates of (α,α,β)-**Cr$_3$**(py)$_3$′ (continued).

Atom	x	y	z	Atom	x	y	z
1	H	6.4999201	-2.6390784	P	-1.0546457	-3.2643955	-2.4187405
2	H	4.0385327	-2.9246661	P	-2.4212327	2.5453188	-2.3435909
3	H	2.3949313	-1.1111808	P	2.0646193	-2.8391706	2.3942743
4	H	0.4843412	4.4714652	P	1.4685606	3.1243176	2.4544714
5	H	0.1352472	2.0892277	P	-3.4157736	-0.2888002	2.5493822
6	H	-2.1749571	-1.4427124	Cr	3.3602766	2.7796384	-0.080033
7	H	-1.0447708	6.3923958	Cr	0.7199369	-4.2923473	-0.0520857
8	H	-4.8393392	-1.4034732	Cr	-4.0880705	1.5728922	0.0830071
9	H	5.0838865	2.0250172	Co	1.6541569	0.3534876	-1.1608229
10	H	-6.031197	-3.5481623	Co	-0.5726505	-1.5754965	-1.1532671
11	H	-0.6643857	-4.8830151	Co	-1.1439564	1.2935975	-1.1080534
12	H	-3.1666533	3.3832072	Co	1.0683382	-1.3592742	1.1664471
13	H	1.0265463	1.3534652	Co	0.6170654	1.5523832	1.230778
14	H	1.4997909	-1.2750714	Co	-1.6790819	-0.2902364	1.2446173
15	H	3.5090859	1.3029944	Se	-0.0313829	0.0509438	-2.7246634
16	H	-1.6220172	-0.4640128	Se	1.7490031	-2.0506422	-1.0025937
17	H	-0.0301427	-3.1669082	Se	0.8747798	2.6149407	-0.8849286
18	H	-2.1266342	1.9545401	Se	-2.6736854	-0.4889991	-0.8934207
19	N	3.9800088	2.2852491	Se	2.6581559	0.4125449	0.9780237
20	N	-0.6485969	-4.6658814	Se	-0.9659783	-2.5851541	0.9987603
21	N	-3.7691383	2.9487757	Se	-1.7164808	2.0706949	1.0841314
22	N	2.1449294	-5.6195949	Se	0.0348914	-0.0641785	2.8037836
23	N	-5.9904599	1.0943682	H	-3.1322073	-9.4143933	-1.7612111
24	N	5.3791449	2.8873336	H	3.050172	-9.2193455	3.6596026
25	N	2.7622885	3.8302806	H	6.4580296	5.9672894	-4.982798
26	N	1.786926	-4.3724718	H	4.8465018	8.6995356	2.508134
27	N	-4.6025434	0.7100592	H	-6.7955843	7.3683447	-1.5959284
28	P	3.2932513	0.8294118	H	-9.607256	1.6230558	3.5852098

Table A.10. Optimized atomic coordinates of **Cr$_3$**(NTs)(py)$_2$′.

Atom	x	y	z	Atom	x	y	z
C	6.0479149	-4.7458597	-5.2625868	C	-1.9468022	-4.8540642	-1.249853
C	5.9687357	-3.3648491	-5.5093957	C	-2.491798	-4.0147655	-2.2459201
C	5.3799926	-5.2663282	-4.1406844	C	-0.7512319	2.6705598	-4.756784
C	5.2590743	-2.5131792	-4.6498373	C	-3.2980886	-1.4357687	-3.4027837
C	1.1753499	-2.1108795	-7.1376524	C	7.3816073	1.811311	1.4407459
C	4.6579464	-4.4216993	-3.2872446	C	-4.8211913	0.0264218	-4.6328524
C	1.9820566	-0.9638865	-7.0859539	C	6.7541713	2.9462777	0.9012358
C	0.9236759	-2.8322591	-5.9567658	C	0.6690438	4.4879276	-3.9868563
C	4.5893721	-3.0161074	-3.4987538	C	0.1518256	-5.233136	2.1915508
C	2.535277	-0.5375398	-5.8652162	C	-0.3377611	3.5376505	-3.7200861
C	3.3786454	-7.5893797	-0.2844429	C	6.6316171	0.9011805	2.2076932
C	1.4659637	-2.4016036	-4.7370836	C	-4.4580579	-0.6348915	-3.4460766
C	2.2789777	-1.2469469	-4.6744574	C	-6.5952257	-4.7872797	-2.1855107
C	3.8767178	-8.257524	0.8483926	C	4.7057437	-2.9495592	3.2474569
C	3.0625501	-6.2238938	-0.2222923	C	-0.668903	-6.2221382	2.752293
C	5.5528264	0.4267263	-3.0418319	C	-5.7040708	-3.7039225	-2.1239894
C	6.4498166	1.4827119	-3.2767302	C	1.0812663	-4.5288546	2.9892813
C	4.1868144	0.5580691	-3.3654785	C	5.3902869	3.1815698	1.1462594
C	5.9926825	2.6831276	-3.8451164	C	5.6490707	-2.5397966	4.2058529
C	4.0447882	-7.5347868	2.0432568	C	-6.9248383	-5.507557	-1.0253592
C	3.7267284	1.7834033	-3.9003098	C	3.32916	-2.7126051	3.4446162
C	-2.0041345	-6.7531508	-2.7714512	C	5.2641931	1.1245569	2.4362247
C	4.6283803	2.8301456	-4.1535515	C	-0.5792782	-6.5206663	4.1234849
C	-2.5504103	-5.9284621	-3.7673332	C	-5.1043538	-3.3296495	-0.8952985
C	0.8175803	3.7264102	-6.2963641	C	-9.121698	-1.3163532	-2.9991637
C	-2.8673582	-0.8896463	-5.7477077	C	4.6347785	2.2831593	1.926256
C	-0.1799137	2.7700584	-6.03607	C	-9.9527627	-0.2320726	-3.3301179
C	3.2637212	-5.4658225	0.9668848	C	-6.3435757	-5.1371143	0.199686
C	-2.4912206	-1.5360271	-4.5598877	C	1.1758959	-4.845536	4.3601881
C	-1.7109334	-6.2125103	-1.507811	C	-3.418309	4.1321037	-3.492679
C	-2.8002159	-4.5703745	-3.506059	C	-5.4369288	-4.0708478	0.2630769
C	3.7499034	-6.1648939	2.107019	C	0.346083	-5.8322163	4.9231635
C	-4.0355437	-0.1073449	-5.788543	C	5.2297625	-1.8829343	5.3746823
C	1.2416797	4.5839515	-5.2676326	C	-8.2358461	-1.2257777	-1.9128842

Table A.10. Optimized atomic coordinates of **Cr$_3$**(NTs)(py)$_2$′ (continued).

Atom	x	y	z	Atom	x	y	z
C	-4.7894957	4.4230549	-3.5901762	C	1.1683177	2.9351319	5.9697301
C	-2.8571185	3.7500056	-2.255455	C	2.2506151	2.8006223	6.8571156
C	2.9178251	-2.0431904	4.6194364	C	-2.709084	2.726468	4.0657167
C	-9.9106371	0.9490466	-2.5672685	C	-6.2214083	-0.910501	3.6457684
C	-1.4052693	6.758062	-2.1945971	C	-2.306254	-1.6183906	7.173085
C	3.8610031	-1.6354047	5.5775804	C	-3.3917494	-0.0485493	5.6600688
C	-1.0660056	5.9921437	-1.0456126	C	-5.1249134	3.6478024	2.9797117
C	-8.2031316	-0.0381102	-1.1661489	C	-6.5967861	-2.9267604	4.966532
C	-9.0373072	1.0516906	-1.4737433	C	-3.2416423	-0.5957372	6.9441819
C	-1.9523141	8.0439129	-2.0694362	C	-3.1542592	4.0256888	4.3498424
C	-5.6126472	4.3368034	-2.4561413	C	-7.0019942	-1.647617	4.5490886
C	-3.6916568	3.6734129	-1.1192601	C	-4.3666744	4.490172	3.8073761
C	3.9586266	5.4963674	3.182532	H	6.472538	-2.9337495	-6.3893017
C	2.752774	5.3181214	2.4479593	H	5.4024348	-6.3483514	-3.9344063
C	-1.3375449	6.5702994	0.2264351	H	0.7534841	-2.4504856	-8.0964349
C	2.6663306	2.6127362	4.0611461	H	2.1983515	-0.397551	-8.0053321
C	-2.1751559	8.6147559	-0.8036843	H	0.3051893	-3.742752	-5.9839742
C	3.7472061	2.4922456	4.9581066	H	3.2095657	-8.1412693	-1.2227719
C	-5.0597758	3.9618253	-1.2201636	H	5.2284374	-1.4391344	-4.8737556
C	4.2224587	6.6918091	3.8674586	H	4.1002782	-4.8557209	-2.4422476
C	-1.8674514	7.8639436	0.3449357	H	3.1840186	0.3494739	-5.854611
C	1.8288346	6.4001144	2.4655462	H	1.2628514	-2.9749445	-3.8183548
C	-1.6681298	-1.5437024	4.8248044	H	2.6091214	-5.7184176	-1.0903623
C	1.3741941	2.840085	4.5860133	H	5.9128218	-0.5221472	-2.617754
C	-4.6198571	-2.741284	3.5580151	H	1.2627056	3.8023726	-7.3006102
C	3.3071783	7.7580248	3.8473198	H	7.5147435	1.3598155	-3.0255844
C	-1.5236511	-2.0939597	6.1084654	H	-2.232193	-0.9916603	-6.6411758
C	2.1036683	7.597956	3.1389224	H	-1.8087897	-7.816796	-2.9777527
C	3.5387864	2.581349	6.3463088	H	-2.7942384	-6.3437155	-4.7575668
C	-5.018367	-1.4501096	3.1386384	H	-0.5154961	2.0896039	-6.8333561
C	-2.6020423	-0.5142171	4.5845447	H	6.6995801	3.502531	-4.0502905
C	-3.4763599	1.8706452	3.2432337	H	-1.5563391	-2.1156692	-4.5401119
C	-5.4012641	-3.47062	4.4667298	H	2.6589638	1.9290594	-4.1260932
C	-4.682794	2.3433228	2.6915385	H	4.2540681	3.7671332	-4.5937563

Table A.10. Optimized atomic coordinates of **Cr$_3$**(NTs)(py)$_2$′ (continued).

Atom	x	y	z	Atom	x	y	z
H	4.4217959	-8.044376	2.9443746	H	1.8537985	-1.8231663	4.7894851
H	-4.3260853	0.4053673	-6.7187784	H	4.7036217	4.6906956	3.2096125
H	-1.2833263	-6.8513596	-0.7199221	H	-2.2014457	8.6125769	-2.979582
H	-3.2447584	-3.9449374	-4.2927036	H	4.7674641	2.336813	4.5798785
H	2.0172354	5.3413278	-5.4628528	H	-1.0540072	-1.9315143	3.9987746
H	8.4556008	1.6383256	1.2677618	H	3.5207989	-1.1120039	6.4839686
H	-1.709145	-4.4328568	-0.2612481	H	-9.0070919	1.954237	-0.8469264
H	3.907229	-5.6184888	3.047559	H	-1.161077	5.9556608	1.1237479
H	-1.5263275	1.911647	-4.5712388	H	-6.6882157	4.5585098	-2.5358536
H	7.3313336	3.6625327	0.2961451	H	-3.2707441	3.3798596	-0.1453722
H	5.0298911	-3.4612742	2.3299905	H	5.1680895	6.7897346	4.4243709
H	0.0841928	-5.0052158	1.1167359	H	-3.6761602	-3.1540493	3.1706408
H	-7.0397282	-5.0664816	-3.1538981	H	0.8596186	6.2714087	1.9577723
H	-1.3871778	-6.7618465	2.1160975	H	-0.7951641	-2.9031205	6.2698457
H	7.1092625	0.0052604	2.6333782	H	-2.0663406	8.2780247	1.3461561
H	-5.470254	-3.1349683	-3.0344811	H	0.5225714	2.9492679	3.895467
H	-5.725184	0.6535749	-4.6433892	H	-5.6964498	3.8721029	-0.328562
H	6.7185686	-2.741661	4.0374568	H	4.3969941	2.4881672	7.0301619
H	0.9945816	5.1568199	-3.1766227	H	-5.2803111	1.7030028	2.0288695
H	-9.1639122	-2.2465161	-3.5861094	H	1.3566673	8.4076705	3.1248306
H	-2.7849312	4.2129417	-4.3874817	H	-5.0701321	-4.4706551	4.7873721
H	4.901596	4.0818363	0.7450104	H	-1.7634511	2.3650675	4.4985358
H	-5.07204	-0.5057764	-2.5424322	H	-6.5584846	0.0772637	3.30364
H	-1.2271548	-7.2933099	4.5653734	H	-2.1904128	-2.0468658	8.1808568
H	4.6893384	0.3906489	3.0220039	H	0.1543834	3.1127026	6.3602631
H	-5.2133347	4.7223058	-4.5616146	H	-6.07811	3.996472	2.5536292
H	-7.588844	-2.0706114	-1.6356219	H	2.088688	2.8729792	7.9437726
H	-6.5927687	-5.6873799	1.120092	H	-4.1354147	0.7438091	5.4947514
H	1.9109191	-4.3325872	4.9969782	H	-2.5507237	4.6801034	4.9978202
H	-1.2222466	6.3387739	-3.1939359	H	-7.9427223	-1.2161017	4.9250199
H	5.9675525	-1.5614569	6.1260941	H	-4.7172414	5.5096515	4.0310317
H	-4.9798001	-3.7874275	1.2208499	H	-3.8665147	-0.221062	7.7695662
H	0.4339706	-6.0686378	5.9951454	N	3.8863737	-2.220964	-2.5745628
H	-10.570168	1.7937471	-2.8189919	N	3.0029462	-4.0879856	0.944775

Table A.10. Optimized atomic coordinates of **Cr$_3$**(NTs)(py)$_2$′ (continued).

Atom	x	y	z	Atom	x	y	z
N	-4.1854956	-2.2419817	-0.7915979	H	-7.2127041	-3.4997078	5.6768166
N	-0.4549462	4.7283146	-1.1029026	H	-2.6001169	9.6259605	-0.7136374
N	2.4351481	4.1643744	1.7090986	H	-7.629015	-6.3520482	-1.075706
N	-5.6041668	0.6498293	-0.2711716	H	3.5224442	8.6935066	4.385459
N	-4.1928175	-0.7185662	2.2201751	C	6.1305991	-4.3707583	-0.312987
O	-6.6925583	-1.3112706	0.6899695	C	6.2921329	-2.0503409	-0.2317223
O	-7.7609368	1.0047621	1.2068964	C	7.5156549	-4.5140227	-0.1567385
P	3.0045614	-0.8292449	-3.0031577	H	5.4782648	-5.2516244	-0.4013993
P	-2.7588827	-2.2268049	-1.8091422	C	7.6821653	-2.1111597	-0.0742618
P	2.1218613	-3.2493276	2.1283143	H	5.7601113	-1.0866848	-0.2461495
P	-1.0500214	3.4197156	-2.0038902	C	8.3118105	-3.3652464	-0.0399405
P	2.8204979	2.5834461	2.2009861	H	7.952628	-5.522375	-0.1336281
P	-2.8249651	0.1738907	2.8692157	H	8.2519016	-1.1759996	0.020809
Cr	3.4512974	-2.9081285	-0.6801343	H	9.4033774	-3.4454248	0.0765839
Cr	1.0842083	4.2279952	0.1523028	C	2.0721744	6.9856516	-0.7723368
Cr	-4.6502336	-0.7666404	0.3650407	C	3.478094	5.2339237	-1.3796904
Co	1.626123	-0.3735099	-1.3997885	C	2.9394647	7.9313332	-1.3365695
Co	-1.07143	-1.2543977	-0.8906478	H	1.1301422	7.2963256	-0.2989118
Co	1.0828596	-1.6525858	1.099901	C	4.3946689	6.1160055	-1.9645307
Co	-0.4772074	1.623264	-0.9309998	H	3.6464835	4.1459209	-1.3933858
Co	1.5430502	1.2206621	1.0967295	C	4.1266474	7.4940131	-1.9406232
Co	-1.1288162	0.1689362	1.5495945	H	2.6748335	8.9972012	-1.291361
Se	0.8866074	-2.6301371	-1.1015192	H	5.3046267	5.7121858	-2.4305203
Se	-0.2766493	0.062276	-2.6544365	H	4.8304251	8.2132806	-2.3865991
Se	3.0751523	-0.5458936	0.4723582	N	2.3343092	5.6562469	-0.7869257
Se	1.8279367	1.9930304	-1.0977681	N	5.5228657	-3.1599964	-0.3539123
Se	-1.1869211	-2.1362709	1.2794134	S	-7.0616234	0.1358454	0.2230034
Se	-2.5262132	0.4586412	-0.2998186	H	-10.644397	-0.3099177	-4.1830998
Se	0.7901596	-0.1112944	2.8393929	H	6.6084684	-5.4071528	-5.9404167
Se	-0.4857756	2.5052158	1.2965343	H	4.1161657	-9.3307648	0.8052865

Table A.11. Optimized atomic coordinates of *trans*-(α,β)-**Cr$_3$**(NTs)$_2$(py)′.

Atom	x	y	z	Atom	x	y	z
C	-1.7777871	-2.1932992	7.2113113	C	2.2396044	-4.614103	1.9585062
C	-2.8404705	-1.2822019	7.0961566	C	-3.6517642	1.2650041	3.533345
C	1.2401786	2.7310595	6.6974713	C	9.8889183	-3.1649018	1.5173036
C	-1.0243145	-2.5274578	6.0745018	C	8.5264614	-0.6978115	1.6059423
C	3.4077718	-2.0708423	5.5720301	C	2.581447	8.4590992	2.7503468
C	2.1932227	1.8769515	6.1152391	C	-4.8081518	3.7261304	4.2883999
C	4.5912426	-1.3117562	5.5461891	C	6.5732206	-5.6307647	1.2956735
C	-3.148413	-0.708631	5.8525637	C	0.7617335	-6.5317848	1.6069171
C	0.5769213	3.676284	5.8989221	C	3.248198	6.2690285	1.8923672
C	-5.9863148	-4.0273344	5.2403823	C	5.8544201	-4.4258167	1.318295
C	-1.3266342	-1.9507211	4.8306333	C	6.8172944	3.3957713	1.7770045
C	2.8487258	-2.5449763	4.3755382	C	1.1224241	-5.2024421	1.3339681
C	-4.8100245	-4.401544	4.5692372	C	4.0153937	3.0957285	2.0351456
C	5.2034897	-1.0233878	4.3154367	C	-4.9651637	1.5825209	3.1349045
C	-6.5555965	-2.7670798	4.9888948	C	-5.5391778	2.8090636	3.5172899
C	2.485945	1.9706958	4.7461657	C	6.2451339	-6.6379865	0.3720192
C	-2.3926167	-1.0363174	4.7043711	C	1.2547306	8.0044995	2.8368455
C	2.6403951	-6.7203369	3.1345222	C	8.9471409	-2.8593722	0.5209398
C	0.8686243	3.7732883	4.5267929	C	1.9176763	5.7830269	1.9951212
C	2.9982384	-5.3901671	2.8645139	C	8.2795336	-1.6251082	0.5789522
C	10.1506611	-2.2491131	2.5514515	C	0.9312558	6.6897472	2.470333
C	-4.2081018	-3.5224025	3.6567004	C	4.7866316	-4.2119662	0.4167306
C	9.4685326	-1.0200229	2.5962685	C	6.0498007	2.9603232	0.6832261
C	-5.9547329	-1.8820578	4.0818194	C	4.6599383	2.8143082	0.8122225
C	3.4757496	-2.2836776	3.1370871	C	5.1903864	-6.4293582	-0.5330053
C	1.836432	2.9337514	3.9407418	C	4.4662174	-5.2289003	-0.5106179
C	4.6512637	-1.5046186	3.1147988	C	-4.8245411	-4.9938494	0.1976455
C	1.5207819	-7.2946453	2.5089459	C	-5.6230805	-6.1439587	0.1246508
C	-2.9105295	2.1979169	4.2943223	C	-5.0528791	-3.9031009	-0.6709864
C	-3.4907042	3.4173258	4.6739014	C	-6.6607235	-6.2276862	-0.8197015
C	6.1863205	3.6793618	3.0006336	C	-1.4766012	-5.0418769	-1.6171745
C	4.7958371	3.5306783	3.1312595	C	-2.5538832	6.3433873	0.4501418
C	-4.7702102	-2.2503022	3.4055804	C	-1.1982791	-6.3693356	-1.9803868
C	3.5700712	7.5810988	2.2736246	C	-3.2516741	7.546854	0.6277551

Table A.11. Optimized atomic coordinates of *trans*-(α,β)-**Cr$_3$**(NTs)$_2$(py)′ (continued).

Atom	x	y	z	Atom	x	y	z
C	-9.1517499	-2.4106768	-0.5980898	C	-4.6446562	3.5117195	-3.0902931
C	-8.3854755	-1.2339544	-0.6316951	C	4.5125681	-4.3971616	-4.7731014
C	-4.6032045	3.0770588	-0.6977618	C	-6.0456274	3.6125485	-3.0440441
C	-6.1039574	-3.9907596	-1.6119747	C	2.9705972	2.2461874	-4.1794298
C	-6.8969444	-5.1462048	-1.6855197	C	-1.532643	3.4725836	-3.6123161
C	-6.0010386	3.1766869	-0.6539978	C	6.3685775	-2.8657584	-5.0954789
C	-2.5269287	-4.330234	-2.2295797	C	-2.9862969	-2.0357983	-4.4842123
C	-1.9734829	-7.0065425	-2.9627094	C	2.2864323	-0.9298279	-4.7170935
C	-2.400557	5.7566919	-0.8378922	C	1.1703585	-1.7756058	-4.8832037
C	2.2598067	5.661173	-1.5283145	C	3.6211963	3.433722	-4.5465119
C	0.600099	7.1746973	-0.9164015	C	5.7166233	-4.068324	-5.4182831
C	-3.848618	8.1922124	-0.4701312	C	-0.7089815	4.5704835	-3.9340549
C	-10.096243	-2.6305001	-1.6137826	C	-5.2002698	-0.3249469	-4.3001817
C	5.0062187	1.4667356	-3.0891194	C	-1.8956166	2.5663136	-4.6347137
C	-8.5368526	-0.2815217	-1.6534983	C	3.0610799	-0.5958163	-5.8510184
C	-3.3038266	-4.9810275	-3.2151173	C	-3.479197	-1.4010025	-5.634517
C	-3.909473	3.2428506	-1.9159548	C	0.8374022	-2.2785796	-6.1512722
C	-3.0274005	-6.3090263	-3.5767076	C	-4.5899047	-0.5428866	-5.5460544
C	-6.7265886	3.4477903	-1.8265978	C	-0.2641828	4.7686432	-5.2530519
C	3.0040694	6.6664241	-2.1558953	C	-1.4545276	2.7698418	-5.9524656
C	4.610339	-2.3145755	-3.4931459	C	-0.6364924	3.8696665	-6.2660709
C	5.652133	2.6623403	-3.4554899	C	2.7223916	-1.0942853	-7.1186716
C	1.2876584	8.235032	-1.5211243	C	1.6096205	-1.9373377	-7.2732472
C	3.9654133	-3.5303327	-3.8155812	H	-1.5382029	-2.6437575	8.1871231
C	-3.0226373	6.416353	-1.9330971	H	-3.4411865	-1.0166122	7.9796534
C	3.666937	1.2443236	-3.4650736	H	1.0114658	2.6547211	7.77174
C	-3.6097153	-1.8381715	-3.2318971	H	2.9128308	-2.293304	6.529929
C	-3.7361225	7.6093818	-1.7449762	H	5.0334372	-0.9435276	6.4850206
C	2.5131367	7.9812698	-2.153967	H	2.709296	1.1218029	6.7274363
C	-4.7164395	-0.9682189	-3.1469636	H	-0.1930066	-3.2448034	6.1538581
C	5.8225933	-1.9922751	-4.1435049	H	-0.1706876	4.3500284	6.3459042
C	-10.263878	-1.6874495	-2.643327	H	-3.9882573	-0.0036322	5.7765942
C	-9.4836271	-0.5178852	-2.6637842	H	-4.3548571	-5.3865487	4.7569932
C	4.9670778	3.6428936	-4.1907153	H	3.24361	-7.3114576	3.8407225

Table A.11. Optimized atomic coordinates of *trans*-(α,β)-**Cr$_3$**(NTs)$_2$(py)′ (continued).

Atom	x	y	z	Atom	x	y	z
H	-7.4847927	-2.4688145	5.498935	H	6.5314211	2.7062953	-0.2718692
H	1.9196587	-3.1342179	4.4072728	H	4.073182	2.4610639	-0.0487383
H	6.1243743	-0.4217991	4.2816567	H	-2.1345058	5.8078943	1.3176729
H	9.671022	-0.3052425	3.4086323	H	3.6377303	-5.0581587	-1.2119623
H	3.8756795	-4.9557969	3.3631326	H	-0.8644399	-4.534792	-0.8592257
H	3.226397	1.2846476	4.3062717	H	-0.3629312	-6.9015652	-1.5001555
H	-0.7306156	-2.2198387	3.9462168	H	-3.3506512	7.9716461	1.639282
H	6.7784023	4.0245821	3.8627777	H	-8.997369	-3.1449243	0.2056304
H	-1.8773087	1.9691522	4.6003128	H	-4.0492231	2.8665732	0.2294955
H	4.3149498	3.7725658	4.0897241	H	-6.5229745	3.0265816	0.3016698
H	-2.9081035	4.1313217	5.2763528	H	2.6124564	4.6188412	-1.5113408
H	1.2381795	-8.3360081	2.7282496	H	-1.7548836	-8.046003	-3.2527772
H	4.6128318	7.9247873	2.1825218	H	-0.3625866	7.3393024	-0.4105801
H	-3.2818126	-3.8004857	3.1317787	H	5.5500498	0.7129164	-2.5032951
H	0.3443909	4.5076792	3.9014079	H	-6.2954663	-3.1409516	-2.2823203
H	-6.4204664	-0.9107138	3.8667873	H	-7.7121611	-5.1971281	-2.4240202
H	7.4019668	-5.7801426	2.0053065	H	-10.703296	-3.5487583	-1.6015395
H	6.1173982	-3.6355533	2.0354171	H	6.7052599	2.8120823	-3.1717114
H	5.1393725	-1.2673432	2.1566546	H	-5.201343	-0.7821933	-2.1759041
H	10.4199201	-4.1286947	1.485482	H	-7.9123639	0.6249078	-1.6554614
H	4.0309342	5.6137989	1.4898999	H	3.018662	-3.7731465	-3.3103246
H	7.9783749	0.2563446	1.6284001	H	-7.8237704	3.5357064	-1.7892691
H	-5.2621746	4.6832302	4.5886529	H	3.9587915	6.4052389	-2.6335684
H	7.9079746	3.511124	1.6763261	H	6.3521969	-1.0683436	-3.874507
H	-0.1245577	-6.9666584	1.1200121	H	-4.1317166	-4.4498768	-3.7047615
H	0.4616648	8.6758922	3.2024739	H	-3.6434171	-6.8012595	-4.3450047
H	-5.5419835	0.8824874	2.514919	H	0.8569331	9.2455381	-1.4835854
H	0.5266155	-4.5965566	0.6379678	H	0.5603823	-2.0514641	-4.0104777
H	-6.5716373	3.0374587	3.211126	H	3.078694	8.7947853	-2.6333908
H	-4.0097919	-4.9188241	0.9313374	H	-2.926899	5.9921266	-2.9422773
H	-5.4329376	-6.9823053	0.8125773	H	-0.4221113	5.2717744	-3.1370295
H	8.7191049	-3.5694122	-0.2869319	H	5.4823854	4.568285	-4.4933712
H	-0.1095239	6.3376297	2.5475907	H	-4.204676	8.0970379	-2.6146473
H	4.9280115	-7.2087263	-1.2650466	H	-2.1094764	-2.6962229	-4.5636792

Table A.11. Optimized atomic coordinates of *trans*-(α,β)-**Cr$_3$**(NTs)$_2$(py)′ (continued).

Atom	x	y	z	Atom	x	y	z
H	3.9926561	-5.3369342	-5.016203	P	2.6836339	-2.8537884	1.5523758
H	1.9175752	2.0938781	-4.4642672	P	2.1550082	3.0205762	2.1129806
H	-9.6120518	0.2175866	-3.4727287	P	-2.8735473	-2.5831425	-1.6937307
H	7.3197375	-2.6043543	-5.5848519	P	-2.0541262	3.2158757	-1.8453606
H	-4.1252166	3.6607633	-4.0475021	P	2.7678892	-0.3209205	-3.0243491
H	-6.0619633	0.3539598	-4.2155975	S	-7.2567796	-0.8773159	0.7328141
H	-2.5281608	1.694477	-4.4090964	S	7.1571451	-1.1602327	-0.7575938
H	-6.6044652	3.8341661	-3.9669197	Cr	-4.7471407	-1.4013601	0.670485
H	3.0709371	4.1965386	-5.1184825	Cr	4.6334626	-1.6028191	-0.7243751
H	3.9409769	0.0543076	-5.7454705	Cr	0.0951748	4.3410226	0.1054574
H	-0.0318858	-2.9451905	-6.2608976	Co	-1.2798691	-0.075154	1.584053
H	0.3721095	5.6360837	-5.4885873	Co	1.11884	-1.5519964	0.8525567
H	-2.988378	-1.5742311	-6.6047363	Co	1.1857274	1.4291043	0.9997868
H	-4.9760584	-0.0429929	-6.4479712	Co	-1.246182	-1.4194311	-0.9023471
H	-1.7488498	2.0572438	-6.738094	Co	-1.0638655	1.5399414	-0.8710685
H	3.3388088	-0.8246117	-7.9900502	Co	1.2276043	-0.0798673	-1.5424522
H	-0.2901292	4.0239681	-7.2997877	Se	0.7650211	-0.1285751	2.706241
H	1.3465198	-2.3302478	-8.2676989	Se	-1.0426564	-2.3668278	1.231714
N	-4.1312888	-1.3652234	2.4741244	Se	-0.9511218	2.3072021	1.3950616
N	4.0287069	-2.9970275	0.4276377	Se	2.8253838	-0.1190667	0.1727216
N	1.513439	4.4949511	1.5676959	Se	-2.866076	0.0874369	-0.1261664
N	5.8784022	-0.3758138	-0.166877	Se	0.8538121	-2.3856103	-1.3267878
N	-5.9475189	-0.1082838	0.1847303	Se	1.1316854	2.297553	-1.2098697
N	-4.221531	-2.7405605	-0.5826559	Se	-0.7980483	0.0711214	-2.6698516
N	1.0727201	5.904374	-0.920536	H	-11.005683	-1.8665931	-3.4366844
N	-1.6207217	4.5968608	-0.9625442	H	6.1489892	-4.7500648	-6.1668758
N	4.025148	-1.4389253	-2.5184992	H	10.8893868	-2.4955957	3.3294285
O	-6.6275227	-2.2490764	1.1559528	H	-6.461481	-4.7181614	5.9538895
O	-8.0696204	-0.1922257	1.7690792	H	-7.2859387	-7.132007	-0.8778407
O	6.4797675	-2.4881792	-1.246758	H	2.841271	9.4868697	3.0463641
O	7.9893736	-0.4505042	-1.7625195	H	-4.4062086	9.1308213	-0.3317528
P	-2.8377317	-0.3278961	3.0428424	H	6.8120274	-7.5815782	0.3550829

Table A.12. Optimized atomic coordinates of *cis*-(α,β)-**Cr$_3$**(NTs)$_2$(py)′.

Atom	x	y	z	Atom	x	y	z
C	-2.9327246	-0.6880519	-7.0736136	C	-3.4249912	-6.4798389	-2.5096264
C	-2.8844009	0.7092089	-6.9532075	C	4.8955377	-6.5956546	-2.1461389
C	2.38835	-3.0966391	-5.9580947	C	-6.8824161	-0.6910751	-2.7951265
C	1.0206948	-2.7977117	-5.8307912	C	3.34663	6.3455605	-3.6384857
C	2.3018643	2.8151934	-6.664429	C	5.5661616	5.4863841	-3.159988
C	3.570463	2.7120453	-6.0691669	C	-3.5880116	3.0484199	-3.0760875
C	-3.1091798	-1.4765939	-5.9223804	C	5.7275921	-5.6845904	-1.4773156
C	1.1518237	2.6015782	-5.8881612	C	-5.9956376	0.3765303	-3.1111272
C	6.7293951	-7.0707364	-3.6812452	C	-1.1880408	-4.781534	-2.1590053
C	3.1039804	-3.5568081	-4.8412964	C	1.3287453	-6.7270998	-2.119199
C	-3.0127514	1.318378	-5.6917756	C	1.2469859	-8.1288587	-2.1297069
C	0.3728806	-2.9647244	-4.596818	C	-4.9668424	5.0639286	-2.9140615
C	7.5513951	-6.1582634	-2.9952176	C	6.6148044	-0.6671739	-1.8066935
C	3.6896271	2.3994873	-4.7062084	C	2.7852897	5.3436433	-2.8342851
C	-8.3340624	-0.1688894	-4.6815751	C	5.0083954	4.4838223	-2.3521353
C	5.4087611	-7.2915549	-3.2532268	C	4.2679878	0.8787134	-2.0131184
C	-3.2226826	-0.8715246	-4.6622759	C	-4.7970944	3.6817183	-2.7199341
C	1.2707289	2.2913349	-4.5235226	C	-3.1407043	-5.936584	-1.2447956
C	-3.177751	0.5349373	-4.5317109	C	3.6080649	4.3986276	-2.1818137
C	-2.5855209	-6.1832197	-3.5944082	C	-2.0360901	-5.0898999	-1.0730664
C	-2.7128458	5.2163984	-3.8038693	C	1.2637359	-6.0071499	-0.8996031
C	2.4570653	-3.7336696	-3.6052254	C	1.1206001	-8.8462063	-0.9286855
C	-7.4571175	0.8719095	-5.0310513	C	6.3737004	0.3734306	-0.8966277
C	-8.0312301	-0.9512868	-3.5536963	C	5.2015948	1.1422287	-0.9912422
C	-1.4697801	-5.3461628	-3.4207807	C	-7.8020751	-3.6719718	0.4960771
C	1.0806754	-3.4562249	-3.4752203	C	1.1247223	-6.7424225	0.3014326
C	-2.5413951	3.8363387	-3.6066073	C	1.0662509	-8.1420633	0.2867138
C	2.5374513	2.1894814	-3.9139817	C	9.0239752	4.8971543	0.2140738
C	7.056219	-5.461965	-1.8819916	C	8.2570045	6.0586836	0.0079079
C	-3.9276833	5.8348438	-3.4609942	C	-6.6575628	-2.8649063	0.4109959
C	4.7397385	6.4206043	-3.8074177	C	8.4452418	3.7665535	0.8153253
C	5.6726335	-0.9483027	-2.8105151	C	6.9113018	6.0976883	0.4037519
C	4.5010426	-0.1853635	-2.9125342	C	-8.527463	-3.7532692	1.6981412
C	-6.3134565	1.1459658	-4.2663652	C	0.384052	6.644032	-0.1778795

Table A.12. Optimized atomic coordinates of *cis*-(α,β)-**Cr$_3$**(NTs)$_2$(py)′ (continued).

Atom	x	y	z	Atom	x	y	z
C	7.0976352	3.7887643	1.2145959	C	0.1746115	3.7285957	3.6284295
C	-6.2138417	-2.0842973	1.5156796	C	-3.9485239	-4.3491671	5.1509319
C	6.3486354	4.9567768	1.0015942	C	1.7101023	-2.0647857	4.4505587
C	0.2665744	8.0361811	-0.3032084	C	5.1157242	0.9314029	3.8535837
C	-2.5265363	4.9778574	0.6645577	C	0.3507501	-2.2438509	4.7829276
C	-3.5667056	5.9176202	0.5811769	C	1.489691	3.9385673	4.089238
C	-8.0814219	-3.0199144	2.8120628	C	-3.3451874	0.1430442	4.9112447
C	-3.5435338	-3.9657843	2.4043661	C	-0.8443332	3.4225947	4.5592677
C	0.9921012	6.0730815	0.9623498	C	2.6786311	-2.1607428	5.4746147
C	-6.9486047	-2.1964516	2.7279533	C	-5.6590767	1.7191516	4.6932485
C	5.0432793	-1.4781484	2.4002805	C	-0.0330376	-2.5134547	6.1060483
C	-3.5362511	-5.2619198	2.9396985	C	1.7744493	3.8717846	5.4654526
C	6.2700846	-0.835359	2.644479	C	-3.6852639	1.042943	5.9349551
C	-1.6409734	4.9816634	1.7624853	C	-4.841669	1.835386	5.8292029
C	-3.7410953	6.8708032	1.5979927	C	-0.5549493	3.3687819	5.9308611
C	2.7394489	-4.4399891	3.003143	C	2.2919115	-2.4222736	6.7988386
C	0.758277	8.8808204	0.706132	C	0.9359699	-2.5983038	7.1192318
C	4.0179626	-4.8433867	3.4483271	C	0.7552828	3.5947041	6.3893967
C	-3.746773	-2.8415468	3.2356662	H	-2.8441	-1.1626193	-8.0631532
C	3.8510607	-0.9305225	2.9118006	H	2.8963498	-2.9605961	-6.9254228
C	1.6002024	-5.1097822	3.5081694	H	-2.7605728	1.3374422	-7.8491664
C	1.4864497	6.9283956	1.9721253	H	2.2110072	3.0552552	-7.7352787
C	4.1478708	-5.8890786	4.3746369	H	0.451548	-2.4179926	-6.6929542
C	-3.731544	-5.4577303	4.3183433	H	4.4789348	2.8758519	-6.6690005
C	6.3110891	0.360971	3.3782161	H	-3.1648463	-2.5730856	-6.0052131
C	1.370313	8.3198339	1.8401389	H	0.1525858	2.6603723	-6.3458756
C	-1.8174087	5.9515463	2.7747092	H	4.1775944	-3.7851107	-4.924428
C	-2.8624471	6.8856002	2.6935051	H	8.5897076	-5.9949942	-3.3224739
C	1.7359719	-6.1506599	4.4391679	H	-3.0042843	2.4158141	-5.6234991
C	3.0114591	-6.5454227	4.8769013	H	-2.7916427	-6.6124547	-4.587222
C	-4.1767029	0.0008036	3.7777235	H	-0.6920321	-2.7027899	-4.512391
C	-3.9618219	-3.0489924	4.6139198	H	4.7693458	-8.0165589	-3.7794569
C	3.890629	0.2911794	3.6209331	H	-1.888678	5.8116909	-4.2260906
C	-5.331096	0.8047241	3.6777339	H	-0.8119037	-5.1441099	-4.2775013

Table A.12. Optimized atomic coordinates of *cis*-(α,β)-**Cr$_3$**(NTs)$_2$(py)′ (continued).

Atom	x	y	z	Atom	x	y	z
H	-7.6652483	1.49172	-5.9178069	H	-2.4013308	4.2391078	-0.140586
H	-8.6861902	-1.7900703	-3.2685962	H	-4.2349513	5.9013925	-0.2929661
H	-1.5778154	3.3740177	-3.8652464	H	1.0765572	-6.1972289	1.2537692
H	4.6889717	2.3205112	-4.2563487	H	0.9709947	-8.6863158	1.238947
H	5.8436489	-1.7775329	-3.5129775	H	-0.2136664	8.4637824	-1.1971528
H	-3.35859	-1.4967539	-3.7650707	H	-3.4024209	-3.8155219	1.3230088
H	3.7628999	-0.4241861	-3.6936495	H	5.0231392	-2.3992675	1.8034174
H	0.366813	2.1055321	-3.9259981	H	6.6218236	2.9140414	1.6838511
H	-4.0613754	6.9163378	-3.6171488	H	-3.3735945	-6.1264773	2.2778257
H	3.0328964	-4.0707822	-2.7310985	H	7.1954049	-1.2873661	2.2558065
H	1.4466013	-6.1811131	-3.0652034	H	4.9130471	-4.354695	3.0412659
H	1.2871345	-8.6641369	-3.0915085	H	-8.6300187	-3.0821233	3.7654421
H	2.6897005	7.074949	-4.1372309	H	-4.5569987	7.6077552	1.5335876
H	-4.298192	-7.1360064	-2.6470358	H	-6.6293458	-1.6183312	3.6065394
H	7.6887103	-4.765645	-1.3130555	H	0.6044549	-4.7872476	3.1690677
H	6.65952	5.5394977	-3.2786477	H	-5.9749904	0.7010308	2.7923393
H	-5.6586951	1.9726945	-4.57018	H	5.1532347	-6.1969575	4.701564
H	-6.6334545	-1.3460378	-1.9450332	H	-3.7215331	-6.4745956	4.7400488
H	3.8682304	-6.7688219	-1.7938809	H	7.2747441	0.8553402	3.5790281
H	7.5303549	-1.272425	-1.7240708	H	1.9953462	6.4976458	2.8448867
H	-5.9240964	5.5374833	-2.6450301	H	-0.4184713	-2.1844697	3.9988257
H	1.6969594	5.2730559	-2.6989434	H	0.8360234	-6.6532935	4.8263155
H	5.6562033	3.7578682	-1.8414779	H	2.302953	4.1404171	3.3779241
H	-5.6150826	3.0761475	-2.3032007	H	-1.1299117	5.9849011	3.6313532
H	-3.7917243	-6.1657147	-0.3872671	H	-2.9827902	7.6349736	3.4910557
H	-8.1147302	-4.2623476	-0.3798773	H	1.7729443	8.9721479	2.6306026
H	-1.8196731	-4.6635596	-0.081814	H	-4.1569623	-2.1951599	5.2782437
H	-6.0514628	-2.8535558	-0.5092225	H	2.9618028	0.7446802	4.0006685
H	7.0969716	0.5872648	-0.0959088	H	-1.8730563	3.2328611	4.2150473
H	5.0059679	1.9454206	-0.2643413	H	-2.4211609	-0.4466618	5.0018286
H	8.710247	6.9426828	-0.4664144	H	5.133352	1.8845994	4.4019467
H	-0.0060714	5.9729774	-0.9571031	H	3.7445522	-2.0340956	5.2385188
H	9.0460457	2.8582634	0.9757597	H	-4.1194861	-4.4926763	6.2292659
H	6.2989045	6.9967899	0.2429507	H	-6.5632499	2.3399036	4.5963509

Table A.12. Optimized atomic coordinates of *cis*-(α,β)-**Cr$_3$**(NTs)$_2$(py)′ (continued).

Atom	x	y	z	Atom	x	y	z
H	-1.0982561	-2.6623461	6.340312	Se	-2.9021143	1.50888	0.614337
H	2.8055273	4.0474356	5.8086618	Se	-0.6452671	-2.4496846	1.2947212
H	-3.0364702	1.1247401	6.8205582	Se	1.8015549	1.5213103	0.9669271
H	-1.361383	3.1461922	6.6460796	Se	-0.6896912	0.4038854	2.7898015
H	3.0605725	-2.4925216	7.5838389	S	5.105081	-4.7408138	-0.0681429
H	-5.1026026	2.5440416	6.6304167	S	4.6475725	5.0420909	1.6055624
H	0.6350593	-2.8047196	8.1581639	O	3.8802099	-5.5330109	0.5021152
H	0.9796367	3.5501632	7.4664705	O	6.2696074	-4.5607194	0.8379056
Co	-1.8708815	0.6635448	-1.370111	O	3.7885469	5.6218064	0.4246164
Co	-0.3203837	-1.7612553	-0.9086706	O	4.6927744	5.8791429	2.8291879
Co	1.0713093	0.7747428	-1.1332516	Cr	2.7393279	-3.7639823	0.1987178
Co	-2.0622287	-0.6249395	1.1878958	Cr	-4.8328707	-0.1135807	-0.3427024
Co	-0.5352879	1.8257574	0.9374665	Cr	2.704344	3.8276612	0.4628885
Co	0.8478991	-0.6919105	1.426171	H	1.063563	-9.9453564	-0.9397736
N	-4.8888402	0.6060851	-2.2755256	H	3.1197124	-7.3640234	5.6050772
N	1.33085	-4.5819926	-0.8446254	H	-9.4202102	-4.39267	1.7707566
N	3.0124771	3.3802584	-1.3675918	H	-9.2305147	-0.3755	-5.2853479
N	4.3525494	-3.3875086	-0.5553579	H	5.1802369	7.2075167	-4.4389217
N	-5.1055812	-1.2374158	1.3486882	H	10.0795904	4.8740159	-0.0971977
N	1.0941391	4.6454561	1.0684499	H	0.6703193	9.9737622	0.6066453
N	2.5702617	-3.3690588	2.0611013	H	7.1246961	-7.6195988	-4.5498223
N	4.0186401	3.5596498	1.7143871	C	-7.7934324	0.5143001	0.1768423
P	-3.3937825	1.2145631	-2.8075652	C	-6.395757	2.3679437	0.3422144
P	0.2362882	-3.6319838	-1.8281825	C	-8.9245078	1.291311	0.4619145
P	2.6784931	1.8210714	-2.096359	H	-7.8822722	-0.5674185	0.0035378
P	-3.7742496	-1.1802666	2.3954864	C	-7.4752688	3.2091148	0.6370866
P	-0.2310395	3.7682161	1.8170397	H	-5.3653219	2.7543461	0.3006924
P	2.215027	-1.7655263	2.6844637	C	-8.768408	2.6651648	0.694942
Se	-0.2267447	-0.3092551	-2.7422111	H	-9.9119886	0.8098279	0.4975233
Se	-2.7215816	-1.5308987	-0.9671604	H	-7.2899388	4.277105	0.8205111
Se	-0.4557075	2.502663	-1.2710348	H	-9.6380596	3.3011232	0.9202055
Se	1.9574835	-1.4455127	-0.5002794	N	-6.5454474	1.0390775	0.1136858

Table A.13. Optimized atomic coordinates of (α,α,β)-**Cr**$_3$(NTs)$_2$(py)′.

Atom	x	y	z	Atom	x	y	z
C	-3.6509118	0.3842614	7.0057946	C	-2.7963556	-3.2117457	3.1063132
C	-3.9903662	-0.9510726	6.7330005	C	-5.6297288	-0.8879831	2.7562378
C	2.5848945	3.475337	6.2326819	C	-1.4872605	4.760123	2.8880869
C	1.2578615	3.0127412	6.1888672	C	2.5045963	6.8610553	1.5473802
C	3.137348	-2.2369232	6.7659287	C	2.8088505	8.2159225	1.7466607
C	4.3586741	-1.8507261	6.1893109	C	-3.5565003	-5.5199463	2.8999827
C	-3.0856635	1.1769184	5.9935267	C	6.8198331	1.9793275	1.86431
C	1.9758888	-2.2645994	5.9774378	C	4.0370698	-4.5871195	2.8860018
C	3.1459311	4.0761103	5.0946509	C	6.0605184	-3.3065617	2.4566114
C	-3.764627	-1.4923622	5.45734	C	4.7483098	0.0781007	2.1223993
C	0.4981969	3.158882	5.0180495	C	-3.6903452	-4.1582146	2.5702911
C	4.4195205	-1.4924197	4.8334911	C	-3.7734786	5.4750569	2.3770915
C	-7.8450353	-0.2002449	4.3806271	C	4.6707802	-3.4842886	2.271128
C	-2.8515745	0.6350852	4.719482	C	-2.600108	4.7934399	2.0197633
C	2.0352189	-1.9043788	4.6215406	C	1.1661414	6.3819441	1.584665
C	-3.1884742	-0.7048896	4.435165	C	1.7841089	9.1433976	1.999132
C	-2.7516339	6.1216536	4.482297	C	6.7000124	0.9338009	0.9346334
C	-1.6225124	-5.0073631	4.2779714	C	5.668955	-0.0134654	1.0584806
C	2.386394	4.2187033	3.9197929	C	-8.2028935	1.7782107	-0.4040548
C	-7.6357936	-1.5339868	3.9908975	C	0.1434474	7.3396348	1.8186612
C	-6.9473543	0.7930973	3.9538379	C	0.4531613	8.6921753	2.0298687
C	-1.5753983	5.4406059	4.122924	C	10.0624959	-3.1722356	-0.2087819
C	1.0497564	3.7771811	3.8726762	C	9.4451163	-4.402592	0.0810032
C	-1.7536535	-3.6492046	3.9542645	C	-6.9234053	1.2350319	-0.2282783
C	3.2549878	-1.5131462	4.0324457	C	9.3447195	-2.1603021	-0.8694602
C	-2.527642	-5.948136	3.7527845	C	8.1107302	-4.630224	-0.290165
C	6.1529066	-5.2986533	3.8582786	C	-8.7780587	1.8492108	-1.6847055
C	5.8898979	2.0859003	2.9134398	C	1.582122	-6.067218	0.4359788
C	4.8518651	1.1497592	3.037118	C	8.0078793	-2.3724104	-1.2472121
C	-6.5378788	-1.8801337	3.1888246	C	-6.1921055	0.7256544	-1.3273268
C	-3.8550568	6.139019	3.6140945	C	7.4099204	-3.6081264	-0.9524228
C	-5.8518902	0.4543263	3.1453965	C	1.6130294	-7.4479452	0.6825219
C	4.7728381	-5.4865199	3.6703127	C	-1.5116873	-4.9167709	-0.7660992
C	6.7918435	-4.2064361	3.2470068	C	-2.4383611	-5.9710301	-0.7894719

Table A.13. Optimized atomic coordinates of (α,α,β)-**Cr**$_3$(NTs)$_2$(py)′ (continued).

Atom	x	y	z	Atom	x	y	z
C	-8.0588309	1.3570294	-2.7865186	C	1.6277429	2.5454111	-4.3863342
C	-4.0806932	3.5024257	-1.4614664	C	5.0508677	-0.5271783	-4.2706363
C	2.223846	-5.5255831	-0.7010537	C	-8.3228493	-5.2549474	-3.25999
C	-6.7851029	0.7919186	-2.6131486	C	0.3096325	3.0481271	-4.4531739
C	5.2187594	1.8316442	-2.7539638	C	2.4738329	-3.5458226	-3.9878806
C	-4.4759401	4.8205373	-1.7362507	C	-2.7623777	0.3292168	-4.7117525
C	-7.4323828	-3.6081419	-1.7284624	C	-8.8679519	-4.2187807	-4.0400269
C	6.3895745	1.1605845	-3.149027	C	0.1313665	-3.0461304	-4.4347448
C	-0.4895175	-4.8413335	-1.7322491	C	2.3446728	2.388225	-5.5942319
C	-2.3428844	-6.9718046	-1.7685234	C	-4.1618338	-2.094553	-4.9207748
C	3.7537607	4.6574795	-2.47499	C	-0.271339	3.3942894	-5.683435
C	2.2919174	-8.308452	-0.1963697	C	2.7415719	-3.489126	-5.3685258
C	3.8567238	5.1039543	-3.8192744	C	-2.7345124	-0.3974143	-5.9124771
C	-4.0714332	2.5232726	-2.4789988	C	-3.4378907	-1.6102338	-6.0221481
C	-7.9719466	-2.5618649	-2.4922148	C	0.4056409	-2.9877989	-5.8088069
C	3.9561805	1.3487398	-3.1532044	C	1.7588824	2.7233583	-6.8274511
C	4.6409659	5.2381002	-1.5224317	C	0.4502931	3.2294371	-6.8785646
C	2.906947	-6.3966047	-1.579113	C	1.7116756	-3.2131111	-6.281104
C	-7.6050402	-4.9559966	-2.0921688	H	-3.8305297	0.8078827	8.0061802
C	4.7960064	6.0818762	-4.1824972	H	3.1800176	3.3627204	7.1520855
C	-4.8552165	5.18786	-3.0393447	H	-4.4408752	-1.5795241	7.5166925
C	6.3099252	-0.0098892	-3.9194672	H	3.0911354	-2.5148869	7.8304014
C	2.9403909	-7.7752379	-1.323632	H	0.8110272	2.5271829	7.0699675
C	-0.3985625	-5.8540276	-2.7153886	H	5.276382	-1.8300039	6.7970609
C	-1.3169505	-6.9141902	-2.7273032	H	-2.827351	2.2284606	6.19262
C	5.5661632	6.2259722	-1.8904249	H	1.0123636	-2.5596356	6.4207935
C	5.6527703	6.656474	-3.2270322	H	4.1832571	4.4449074	5.1190269
C	-3.5250029	-0.1305164	-3.6131719	H	-4.0459536	-2.5358678	5.2568676
C	-4.4690489	2.8980648	-3.78031	H	-2.8004688	6.6470278	5.4488817
C	3.8813465	0.1452245	-3.8909024	H	-0.5363714	2.785781	5.0006462
C	-8.6968016	-2.8784193	-3.6531629	H	-0.809594	-5.3328844	4.9453389
C	-4.2091982	-1.3590136	-3.7231758	H	-0.7148572	5.4557647	4.80662
C	1.1639918	-3.3382833	-3.5147492	H	-8.3388911	-2.3192745	4.3093691
C	-4.8495221	4.222344	-4.0585246	H	-7.0977938	1.8421412	4.2529599

Table A.13. Optimized atomic coordinates of (α,α,β)-$\mathbf{Cr_3}(NTs)_2(py)'$ (continued).

Atom	x	y	z	Atom	x	y	z
H	-1.0481825	-2.9173796	4.3772241	H	1.100035	-7.8528364	1.5686687
H	5.384108	-1.1986135	4.3971168	H	-3.7827972	3.2167767	-0.4408019
H	5.9677808	2.9079642	3.641448	H	5.2936606	2.7426788	-2.1471785
H	-2.4125714	1.2654751	3.9320809	H	7.4236366	-1.5938035	-1.7609593
H	4.1188977	1.2581477	3.8512859	H	-4.4852919	5.5667146	-0.9267072
H	1.1219606	-1.9257638	4.0097113	H	7.3703264	1.5673737	-2.8563287
H	-2.4275021	-7.0141151	4.0095137	H	-7.8369033	-1.5187661	-2.1718202
H	2.830547	4.6805066	3.0288522	H	3.1803025	4.6879134	-4.5772794
H	3.3134232	6.1381782	1.354479	H	-8.4942307	1.4067539	-3.797106
H	3.8591802	8.5463847	1.7127242	H	-3.0713741	-7.7974279	-1.788366
H	4.2625942	-6.3428164	4.137771	H	-6.2423923	0.3906476	-3.4800745
H	-4.7774345	6.6682957	3.8992316	H	4.597409	4.8676151	-0.4852076
H	7.8742776	-4.0539675	3.3795105	H	-7.1928602	-5.7514311	-1.4550822
H	-6.3973347	-2.9210314	2.8681497	H	-4.769074	-1.7549984	-2.8630357
H	-5.1396224	1.2245554	2.8130262	H	4.8496579	6.4084053	-5.2334235
H	7.6331147	2.7154792	1.7687984	H	-5.1648575	6.221956	-3.2569004
H	-4.2752092	-6.243616	2.4857496	H	7.2264839	-0.5301654	-4.2382444
H	2.9577568	-4.7257591	2.7327743	H	3.4378932	-5.9823969	-2.44691
H	6.5639367	-2.4591564	1.9708461	H	-0.273091	3.1739256	-3.5270429
H	-4.4888932	-3.8431689	1.8859453	H	6.238564	6.6507735	-1.1281037
H	-4.6356002	5.4777622	1.6919884	H	3.2938886	-3.7393112	-3.2839102
H	-8.752952	2.1545435	0.4722284	H	0.3937783	-5.8160991	-3.4762218
H	-2.5375659	4.2730914	1.0528375	H	-1.2312242	-7.6971827	-3.4965782
H	-6.4753351	1.1851679	0.7734075	H	3.4851259	-8.4388264	-2.013175
H	7.4135796	0.848379	0.1013611	H	-9.1342565	-2.0675057	-4.2552387
H	5.5770649	-0.8247994	0.3195659	H	-4.4943527	2.152226	-4.5868787
H	10.0061139	-5.1923708	0.6038208	H	2.902548	-0.2741523	-4.1730107
H	1.0461019	-5.3864275	1.1142083	H	-0.8970381	-2.8742616	-4.0802764
H	9.8282451	-1.1969917	-1.0932417	H	-2.1783769	1.2583692	-4.6351214
H	7.6112887	-5.5823331	-0.0596357	H	4.9755634	-1.4662742	-4.8370075
H	-1.5994903	-4.1419113	0.0082194	H	3.3760329	2.0085347	-5.5781519
H	-3.2440732	-5.9907275	-0.0421906	H	-5.157614	4.4943471	-5.0800771
H	-0.90571	7.0184602	1.8127934	H	-8.4654574	-6.3050476	-3.5577247
H	-0.3652924	9.4075496	2.2091659	H	-4.6988387	-3.0530051	-4.9852191

Table A.13. Optimized atomic coordinates of (α,α,β)-**Cr$_3$**(NTs)$_2$(py)′ (continued).

Atom	x	y	z	Atom	x	y	z
H	-1.2978227	3.7924259	-5.7050783	Se	-2.2660512	-1.5059041	-0.4002553
H	3.7672078	-3.6747258	-5.7234184	Se	-0.5528481	2.7664734	-0.9888546
H	-2.1463047	-0.0161887	-6.761223	Se	2.3293815	-0.9110591	-0.8259226
H	-0.4100529	-2.7647119	-6.5131684	Se	-0.214711	-0.0839475	-2.5971604
H	2.3367866	2.5883779	-7.7551644	S	-6.4702595	-3.2522424	-0.2433976
H	-3.4133612	-2.1814627	-6.9633072	S	5.7294554	-3.9334882	-1.5300043
H	-0.0054319	3.4956516	-7.8449607	O	-6.8101029	-4.3300193	0.7231707
H	1.9237383	-3.1723185	-7.360918	O	-6.8216891	-1.7841404	0.1835822
Co	-1.313025	-0.6058036	1.555779	O	4.9952663	-4.6647876	-0.3517365
Co	-0.1251575	2.0516244	1.2175726	O	5.8703862	-4.7239357	-2.7789299
Co	1.5523891	-0.3103876	1.279019	Cr	1.5674284	4.2396587	-0.4752963
Co	-1.6719581	0.6847092	-0.9208402	Cr	-4.751966	-1.3650118	0.0573361
Co	0.1210146	-1.5893808	-0.8166012	Cr	3.6372247	-3.0544636	-0.3472312
Co	1.1829208	1.2010595	-1.2270963	H	2.0189866	10.2057526	2.1654587
N	-4.4926857	-1.2103837	1.9417232	H	6.384127	7.4244014	-3.5212175
N	0.9194912	5.017753	1.301139	H	-9.7793765	2.284877	-1.8230522
N	3.8964439	-2.5763596	1.4764914	H	-8.7070063	0.0648024	5.0121392
N	-4.8972703	-3.06627	-0.5891087	H	6.7296827	-6.0044382	4.4757949
N	-4.8952119	0.1694336	-1.1082344	H	11.1095256	-3.0008868	0.0847083
N	2.1667347	-4.1122466	-0.9424682	H	2.3190701	-9.3917195	-0.0015761
N	2.810377	3.724985	-2.0111158	H	-9.4361867	-4.4595023	-4.9516605
N	4.8823884	-2.5615693	-1.5944073	C	1.742842	7.0484449	-1.6972057
P	-2.9273857	-1.3987237	2.7260651	C	-0.3957595	6.1488311	-1.8087938
P	0.0757329	3.9276014	2.2926282	C	1.3152589	8.2443034	-2.2894581
P	3.3179146	-1.0996134	2.2209433	H	2.7928877	6.9142339	-1.4031293
P	-3.5266958	0.8048736	-2.0053925	C	-0.8996119	7.3084885	-2.4080498
P	0.7371165	-3.4479793	-1.7111472	H	-1.050911	5.2891196	-1.5994426
P	2.3957619	2.2356446	-2.7000925	C	-0.0302358	8.3819233	-2.6558688
Se	0.1817799	0.5265	2.968205	H	2.0432755	9.0510396	-2.4533748
Se	-2.3922954	1.4323117	1.2049926	H	-1.9656989	7.3549792	-2.6719673
Se	0.3102378	-2.2841418	1.4131648	H	-0.3962436	9.3087804	-3.1233354
Se	2.2133451	1.993095	0.7777183	N	0.9071329	6.0080637	-1.4613748

Table A.14. Optimized atomic coordinates of (α,α,α)-**Cr**$_3$(NTs)$_2$(py)′.

Atom	x	y	z	Atom	x	y	z
C	3.5459249	-0.7694508	6.9983748	C	2.855454	3.0031738	3.2403142
C	3.9431528	0.5602891	6.7809525	C	5.6392804	0.6501134	2.8284234
C	-3.2588171	-4.1263381	5.5802578	C	1.4621781	-4.7008	2.8733158
C	-2.0929207	-3.3571509	5.7397271	C	-0.3413697	-7.3197668	2.1111953
C	-3.1246308	2.1170248	6.787869	C	-0.0248345	-8.6846845	2.0400084
C	-4.356006	1.8043318	6.1879914	C	3.6558917	5.303879	3.1166999
C	2.9650987	-1.5005842	5.9493814	C	-6.8759777	-1.8982964	1.8139747
C	-1.9540384	2.1102124	6.0126761	C	-3.9812943	4.5599178	2.972678
C	-3.4564269	-4.8453738	4.3899836	C	-6.026828	3.3506387	2.4502545
C	3.7574215	1.1578745	5.5242067	C	-4.7580227	-0.0522037	2.095211
C	-1.1309798	-3.3084031	4.7170482	C	3.7632843	3.9533185	2.7352443
C	-4.4171613	1.4842021	4.8227943	C	3.7509067	-5.4677731	2.4702336
C	7.8201966	-0.1197043	4.4621737	C	-4.6288113	3.4972157	2.3039707
C	2.7732722	-0.902827	4.6934403	C	2.5535095	-4.9093656	2.0007313
C	-2.0141448	1.7889691	4.6467588	C	-0.2261534	-6.4808444	0.9684177
C	3.1655046	0.4327908	4.4653467	C	0.4081196	-9.2654235	0.8346099
C	2.7997642	-5.6295385	4.6980144	C	-6.7148858	-0.8603182	0.8810354
C	1.7202565	4.7740855	4.4854951	C	-5.6614054	0.0600241	1.0186355
C	-2.4922672	-4.8006832	3.3682479	C	8.1895483	-1.9695244	-0.3689188
C	7.6402606	1.2272089	4.1045902	C	0.2502021	-7.0790116	-0.2325564
C	6.9103748	-1.0851065	3.9984986	C	0.5463922	-8.44869	-0.3018146
C	1.5951191	-5.0770824	4.2258761	C	-9.983543	3.4162503	-0.1844739
C	-1.3154176	-4.0390282	3.52109	C	-9.3924484	4.6857116	-0.0451498
C	1.8250259	3.427213	4.1098418	C	6.9181943	-1.4059087	-0.1982399
C	-3.2435525	1.4706606	4.0344238	C	-9.2358731	2.3422639	-0.6958493
C	2.6395202	5.7178518	3.9910341	C	-8.0554399	4.8885102	-0.4185321
C	-6.1012821	5.2949143	3.9181013	C	8.7917098	-1.9994174	-1.6386194
C	-5.9589134	-2.0319622	2.8719141	C	-1.4756494	6.0868469	0.5849959
C	-4.8984151	-1.1228177	3.0062313	C	-7.8933404	2.5287211	-1.0691379
C	6.5593848	1.6141039	3.2978788	C	6.2236326	-0.8350929	-1.2905793
C	3.8808044	-5.8234535	3.8244211	C	-7.3207162	3.8014919	-0.9236083
C	5.8319231	-0.7056873	3.1854195	C	-1.4857433	7.4625966	0.8594807
C	-4.7123787	5.4509499	3.7708403	C	1.6420264	4.8950367	-0.6074262
C	-6.7537856	4.2426206	3.253357	C	2.5919081	5.9285364	-0.5866251

Table A.14. Optimized atomic coordinates of (α,α,α)-**Cr**$_3$(NTs)$_2$(py)′ (continued).

Atom	x	y	z	Atom	x	y	z
C	8.1082881	-1.4462151	-2.7343093	C	-1.552609	-2.0739814	-4.5648102
C	3.9920517	-3.5812222	-1.5692103	C	-5.6107485	0.2464752	-3.6303016
C	-2.1036321	5.5821418	-0.5762479	C	8.4422345	5.1749895	-3.0338286
C	6.8432298	-0.8610107	-2.5650892	C	-0.3781137	-2.8289816	-4.7838068
C	-5.1222911	-2.4203047	-2.8976509	C	-2.3505964	3.6275837	-3.9022161
C	4.3435116	-4.9001913	-1.8925697	C	2.844318	-0.2625904	-4.7071049
C	7.5260763	3.4968776	-1.5524153	C	8.9947227	4.1548766	-3.8297782
C	-6.4399868	-1.9745046	-3.0936013	C	0.008076	3.2042249	-4.3430349
C	0.6197554	4.8832739	-1.5764069	C	-2.0858984	-1.3230591	-5.6315832
C	2.5200268	6.9702871	-1.524125	C	4.2947699	2.1380354	-4.8277741
C	-2.5980287	-4.8297465	-3.4021143	C	0.2426681	-2.8364578	-6.0415041
C	-2.1288663	8.3538912	-0.0156698	C	-2.6115127	3.5752476	-5.2841423
C	-3.3805005	-4.6736661	-4.5818621	C	2.839788	0.5034229	-5.883039
C	4.0711123	-2.5557054	-2.5366542	C	3.5689715	1.7041966	-5.9488397
C	8.0726824	2.4662939	-2.3323008	C	-0.2579537	3.1580752	-5.7190636
C	-4.0343408	-1.5404078	-3.0853609	C	-1.4565094	-1.3239977	-6.8886605
C	-2.0482884	-6.1227094	-3.173537	C	-0.293522	-2.0809659	-7.0998144
C	-2.7504202	6.4835	-1.451056	C	-1.5686561	3.3455247	-6.1946008
C	7.707822	4.8521161	-1.8828855	H	3.6931531	-1.2366145	7.9846155
C	-3.6131546	-5.7509006	-5.4494802	H	-4.0111207	-4.1632509	6.3834553
C	4.7689676	-5.2192375	-3.1934827	H	4.4071755	1.1401162	7.5937146
C	-6.6866763	-0.6439676	-3.473591	H	-3.0781515	2.3653642	7.8596422
C	-2.7626248	7.8569887	-1.1677445	H	-1.9299866	-2.7843726	6.6656676
C	0.5534581	5.9358434	-2.5187357	H	-5.2809806	1.8120189	6.7849475
C	1.4953623	6.9745792	-2.4863405	H	2.6612411	-2.5476543	6.1006566
C	-2.2946425	-7.1985862	-4.0363995	H	-0.9830999	2.3484235	6.4737511
C	-3.0853307	-7.0260497	-5.1855048	H	-4.3657337	-5.4511362	4.2531062
C	3.6074852	0.1469524	-3.5895279	H	4.0823402	2.1961269	5.3671149
C	4.5161404	-2.8820457	-3.8356715	H	2.8855726	-5.9197378	5.7568463
C	-4.2932939	-0.1954624	-3.4279611	H	-0.2343393	-2.686959	4.8559856
C	8.8142067	2.8067012	-3.4758997	H	0.9165066	5.088717	5.1690121
C	4.3169824	1.3641641	-3.6538082	H	0.7506615	-4.9566463	4.9193318
C	-1.0372297	3.4527994	-3.4245313	H	8.3531295	1.9910097	4.4522521
C	4.8553573	-4.2063289	-4.1614194	H	7.0376064	-2.1440953	4.2719633

Table A.14. Optimized atomic coordinates of (α,α,α)-**Cr$_3$**(NTs)$_2$(py)′ (continued).

Atom	x	y	z	Atom	x	y	z
H	1.1081803	2.6928334	4.5084868	H	-0.9843535	7.8394641	1.7644289
H	-5.3895217	1.2478411	4.3690802	H	3.6526172	-3.3355686	-0.5512829
H	-6.0641467	-2.8512911	3.5993738	H	-4.9293571	-3.4645774	-2.6127032
H	2.3242639	-1.4885475	3.8779862	H	-7.2877182	1.7025617	-1.4711945
H	-4.1778644	-1.2494519	3.8286411	H	4.2738405	-5.6869446	-1.1257447
H	-1.0944542	1.7848535	4.0444707	H	-7.2774666	-2.6769509	-2.9586244
H	2.5600074	6.7749596	4.2884732	H	7.9298609	1.4167329	-2.0372709
H	-2.6439502	-5.3615988	2.4349849	H	-3.8138607	-3.6956127	-4.8267571
H	-0.6960957	-6.8923875	3.0596142	H	8.5650663	-1.4643704	-3.736444
H	-0.1273695	-9.3069343	2.9433486	H	3.2665233	7.7797835	-1.509506
H	-4.1914647	6.2759876	4.2807753	H	6.3280346	-0.4128896	-3.4258073
H	4.8222483	-6.2574041	4.1950347	H	-1.3864167	-6.2693699	-2.3053669
H	-7.8429895	4.116281	3.3534315	H	7.2896677	5.6345888	-1.2337432
H	6.4416732	2.6654272	3.0031806	H	4.8767288	1.7210414	-2.7767471
H	5.110413	-1.4543891	2.8253358	H	-4.2240789	-5.5841422	-6.3509642
H	-7.7170564	-2.6032374	1.7184147	H	5.0343676	-6.2562017	-3.4509661
H	4.3857025	6.0294545	2.72593	H	-7.7187873	-0.2982567	-3.6416914
H	-2.8951065	4.6741795	2.8508947	H	-3.2695533	6.0966301	-2.3385902
H	-6.5401099	2.5345034	1.9230488	H	0.0477091	-3.4259886	-3.9624848
H	4.5527273	3.6507463	2.0350529	H	-1.8456788	-8.1797372	-3.8137065
H	4.590584	-5.6235702	1.7755775	H	-3.1793499	3.7928368	-3.2011773
H	8.7113761	-2.3949344	0.5021241	H	-0.237861	5.9449847	-3.2816116
H	2.4527353	-4.6373088	0.9393257	H	1.429384	7.7898837	-3.2233034
H	6.4476943	-1.3890782	0.7941253	H	-3.278885	8.5453839	-1.8548674
H	-7.414106	-0.7603004	0.0371438	H	9.2572198	2.0081934	-4.0903505
H	-5.53767	0.8710184	0.2841202	H	4.6045271	-2.1005707	-4.6030794
H	-9.9779914	5.5262621	0.3577762	H	-3.4693364	0.5273753	-3.5257008
H	-0.9658111	5.3817174	1.2586393	H	1.038878	3.0545726	-3.9857149
H	-9.6994678	1.3499745	-0.8061133	H	2.2418607	-1.1824872	-4.6656417
H	-7.58215	5.8754567	-0.3126209	H	-5.7859714	1.3010463	-3.8863052
H	1.708667	4.0867851	0.1342519	H	-3.0068251	-0.7390692	-5.4949632
H	3.3969131	5.8996053	0.1612007	H	5.1967523	-4.4429903	-5.1811137
H	0.4191533	-6.4289476	-1.1059431	H	8.5921424	6.2310666	-3.305692
H	0.9117473	-8.8758345	-1.2492174	H	4.85248	3.0863261	-4.8580592

Table A.14. Optimized atomic coordinates of (α,α,α)-**Cr$_3$**(NTs)$_2$(py)′ (continued).

Atom	x	y	z	Atom	x	y	z
H	1.1473019	-3.4446226	-6.1963242	Se	2.3180296	1.4185763	-0.3475148
H	-3.6423679	3.7243571	-5.6405201	Se	0.4709171	-2.7449167	-1.1689933
H	2.2476342	0.1617775	-6.7456952	Se	-2.2764633	1.0007892	-0.8260811
H	0.567481	2.9700023	-6.4222075	Se	0.2729796	0.1799549	-2.6014934
H	-1.8890308	-0.7322231	-7.7101642	S	6.5455107	3.1105432	-0.0875054
H	3.5632153	2.3056924	-6.8712948	S	-5.6255667	4.0921554	-1.4808961
H	0.1897316	-2.0912512	-8.0892503	O	6.8909525	4.1537744	0.9142291
H	-1.7743347	3.3108317	-7.2758883	O	6.8732508	1.6252765	0.2975805
Co	1.3293323	0.5008844	1.5653035	O	-4.8759635	4.7603799	-0.2722365
Co	0.0631428	-2.0816981	1.0995804	O	-5.7419425	4.9364892	-2.6965056
Co	-1.5480913	0.3097245	1.2608295	Cr	-1.5955138	-4.2448691	-0.5882992
Co	1.7011474	-0.7274425	-0.9600002	Cr	4.8016224	1.2365702	0.136097
Co	-0.0526592	1.6228265	-0.7653505	Cr	-3.564296	3.1305468	-0.3069364
Co	-1.2007737	-1.1051458	-1.3117306	H	0.6487356	-10.338138	0.7853961
N	4.5174489	1.0134085	2.009791	H	-3.2748235	-7.8664705	-5.870065
N	-0.5769051	-5.1209257	0.9583916	H	9.7861736	-2.4515006	-1.7735708
N	-3.8614423	2.5968564	1.493952	H	8.6689841	-0.4166876	5.0973232
N	4.9731622	2.9565744	-0.451574	H	-6.6745676	5.9951111	4.5451228
N	4.9342473	-0.2588832	-1.0767348	H	-11.03406	3.2649263	0.1075036
N	-2.066281	4.173686	-0.8475099	H	-2.1394646	9.4332576	0.2011013
N	-2.3419595	-3.8091911	-2.4679375	H	9.5760507	4.4142827	-4.7279196
N	-4.8125133	2.7050935	-1.5882024	C	-4.5023935	-4.7004787	-0.0368356
P	2.9481188	1.2048786	2.7844707	C	-3.352858	-6.7226749	-0.1492192
P	-0.0847203	-3.9890685	2.1210384	C	-5.7197854	-5.3580496	0.1771123
P	-3.3022456	1.0953131	2.2133201	H	-4.4453584	-3.6016675	-0.0677711
P	3.5715596	-0.8415366	-2.0164782	C	-4.5307519	-7.4514992	0.0604657
P	-0.6282936	3.5117623	-1.6147218	H	-2.3872795	-7.2338006	-0.2741605
P	-2.2963774	-2.1529574	-2.8552544	C	-5.7406205	-6.7606891	0.2236128
Se	-0.2122264	-0.6316824	2.9152252	H	-6.6335278	-4.761386	0.3062282
Se	2.3489391	-1.5603306	1.1433453	H	-4.4859353	-8.5494175	0.0891743
Se	-0.2409651	2.2541056	1.4820082	H	-6.6832691	-7.3056959	0.3845673
Se	-2.260616	-1.9356806	0.6453707	N	-3.3332776	-5.368174	-0.200341

Table A.15. Optimized atomic coordinates of **Cr$_3$**(NTs)$_3$′.

Atom	x	y	z	Atom	x	y	z
C	2.7928866	-2.3937651	6.9948396	C	0.9297168	-7.3461663	2.5625244
C	3.6325055	-1.2704348	6.9176075	C	-6.9920882	-5.1718873	1.3353323
C	-4.0391849	-2.6231369	5.5832156	C	5.2459602	-2.884361	3.2596497
C	-2.6360447	-2.7087295	5.6000755	C	-2.1629609	6.8181911	3.8148486
C	-2.2339247	3.0080553	6.7200813	C	-4.4873371	6.5244549	3.1772225
C	-3.4513234	3.2205004	6.0518526	C	3.7039135	1.6477914	3.56065
C	2.0690162	-2.7981168	5.8612787	C	-7.4632343	-4.0239001	0.6802354
C	-1.1115891	2.5749946	5.9962839	C	5.5260416	-1.5110242	3.0762409
C	-9.0218112	-5.1760994	2.6863408	C	-0.6875459	-5.078575	2.0510976
C	-4.730087	-2.8180871	4.3768608	C	-3.6265833	-6.2493071	1.5902506
C	3.7471074	-0.553762	5.7157939	C	-3.9147431	-7.6207143	1.5017904
C	-1.9324158	-2.9935637	4.4195255	C	5.2378157	3.5429978	3.6288301
C	-9.4814268	-4.0285552	2.0146269	C	-6.9222698	0.9440259	1.3810146
C	-3.5475996	3.0005853	4.6691268	C	-1.8015636	5.7370797	2.9985711
C	7.1915994	-3.1175766	4.703538	C	-4.1299485	5.4444882	2.355727
C	-7.7845155	-5.7475904	2.342411	C	-4.2852917	1.8206162	1.8479959
C	2.1761886	-2.0779587	4.660658	C	4.9050221	2.2605175	3.1542491
C	-1.2067798	2.3539061	4.6127007	C	1.0333301	-6.6648265	1.3378907
C	3.0162424	-0.9484051	4.5724959	C	-2.7806198	5.035611	2.260591
C	0.0116263	-6.9007746	3.5260381	C	0.2355029	-5.5388227	1.0876881
C	3.1668982	3.6230867	4.8967112	C	-3.2047161	-5.5235247	0.448184
C	-4.0284655	-3.1090403	3.1930392	C	-3.8101146	-8.2945701	0.2736878
C	7.4813725	-1.7548539	4.5179782	C	-6.3397519	1.9047271	0.5405304
C	6.0702788	-3.6791301	4.0699246	C	-5.0234643	2.3407116	0.7660167
C	-0.7968623	-5.7798135	3.2711446	C	6.9628666	-4.9056997	-0.4419178
C	-2.6228091	-3.2158372	3.2053534	C	-3.0936678	-6.2173826	-0.779637
C	2.8322084	2.3445966	4.4275728	C	-3.4033659	-7.5810048	-0.8669631
C	-2.4229984	2.5637125	3.9318432	C	-7.6677782	7.0092335	-0.4712465
C	-8.7059775	-3.4473501	0.9998098	C	-6.6473239	7.9215244	-0.1454323
C	4.3746912	4.2259178	4.4994501	C	5.9523126	-3.9506693	-0.261248
C	-3.5076497	7.215107	3.9109235	C	-7.3524416	5.7901123	-1.0949064
C	-6.179519	0.4064789	2.4456904	C	-5.3091074	7.6226934	-0.4435583
C	-4.8644791	0.8334902	2.6759872	C	7.9340835	-4.7296301	-1.4424224
C	6.6569915	-0.9538331	3.7140997	C	1.1769651	6.2909003	0.7507671

Table A.15. Optimized atomic coordinates of **Cr$_3$**(NTs)$_3$′ (continued).

Atom	x	y	z	Atom	x	y	z
C	-6.0165537	5.4742254	-1.3972476	C	4.2539323	-4.0761859	-3.6338528
C	5.8980693	-2.7972637	-1.0757186	C	-3.6171964	1.4576485	-3.7865315
C	-5.0125993	6.3975457	-1.0654991	C	10.3784739	-0.3135599	-2.2722327
C	1.6706719	7.5656242	1.0659171	C	4.8602368	0.1000587	-3.3417911
C	3.6516147	4.0049005	-0.3224813	C	0.7964298	3.7633364	-3.3322501
C	4.9157418	4.6037371	-0.2006927	C	4.233789	-5.4080125	-4.0772905
C	7.888805	-3.5846559	-2.2561285	C	-2.1050239	-1.3616419	-4.6392518
C	2.6174531	-4.6256289	-1.9251563	C	-4.6000919	2.4149452	-4.0742007
C	0.4689778	6.0726464	-0.4526151	C	9.4796065	1.8666724	-2.8895598
C	6.8833024	-2.6226862	-2.0744517	C	-0.8127853	-1.8601464	-4.9040249
C	-5.3147332	0.003498	-2.8092947	C	-0.3400643	4.4115533	-3.8534077
C	2.5951329	-5.9567503	-2.3714613	C	3.2820378	-1.1942421	-4.6658697
C	8.5632693	0.656886	-1.0066084	C	10.3897329	0.816413	-3.1079835
C	-6.2971254	0.9642247	-3.1087508	C	1.7281304	3.1755887	-4.2182278
C	2.7684667	4.398179	-1.3465595	C	-2.9961501	-1.1700523	-5.7190146
C	5.3040826	5.6155723	-1.0926614	C	5.1702525	0.869883	-4.4773445
C	-3.8110704	-3.454864	-3.4287232	C	-0.4204165	-2.1641715	-6.2172382
C	1.4577586	8.6428445	0.1894284	C	-0.5310712	4.4884684	-5.2454146
C	-5.1023364	-3.5015251	-3.999426	C	3.6010093	-0.4305755	-5.7988551
C	3.4392344	-3.6683816	-2.5531384	C	4.5511544	0.6020917	-5.7091507
C	9.4601328	-0.4034979	-1.212583	C	1.5330773	3.2590053	-5.604361
C	-3.9739753	0.236388	-3.171971	C	-2.5989829	-1.4688613	-7.0317246
C	-2.8330771	-4.3714095	-3.8811232	C	-1.3104319	-1.9667257	-7.285251
C	0.2560518	7.1605251	-1.3284444	C	0.4031119	3.9171515	-6.1228853
C	8.559425	1.7952254	-1.8319018	H	2.706099	-2.9560527	7.937574
C	-5.4021551	-4.4421899	-4.9962018	H	-4.5905503	-2.3976331	6.5091439
C	3.4020104	-6.3511811	-3.4510345	H	4.2105093	-0.949099	7.7977315
C	-5.9459536	2.1633941	-3.7495844	H	-2.1614437	3.1774394	7.8056736
C	0.7459111	8.4341568	-1.0044916	H	-2.0810029	-2.544073	6.5362623
C	3.1670773	5.4170345	-2.2430566	H	-4.3369403	3.5625256	6.6091373
C	4.4249256	6.0236882	-2.1109463	H	1.4170302	-3.6840539	5.9068603
C	-3.1364992	-5.3052426	-4.8832925	H	-0.1554851	2.3969393	6.5123237
C	-4.4236427	-5.3450563	-5.4455317	H	-5.8282748	-2.7484788	4.348056
C	3.9233071	-0.9503621	-3.4311778	H	-10.456592	-3.5889965	2.2747347

Table A.15. Optimized atomic coordinates of **Cr$_3$**(NTs)$_3$′ (continued).

Atom	x	y	z	Atom	x	y	z
H	4.416897	0.3164938	5.6684822	H	-6.9067859	2.3153263	-0.3078189
H	-0.085671	-7.4322846	4.4854174	H	-4.5648637	3.0824347	0.0941061
H	-0.8343826	-3.0438645	4.4500095	H	-6.8949392	8.8746978	0.3463847
H	-7.4311277	-6.6546929	2.8559608	H	1.3461564	5.4389731	1.4261686
H	2.4809447	4.1514511	5.5767369	H	-8.1514956	5.0769543	-1.3489331
H	-1.5216077	-5.4579534	4.0318034	H	-4.5016098	8.3243593	-0.1889421
H	8.3649719	-1.307398	4.9990985	H	3.3627418	3.2143099	0.3834858
H	5.8329982	-4.7456795	4.2066521	H	5.5974803	4.2577125	0.5891775
H	1.8911263	1.8734985	4.7511591	H	-2.7721203	-5.6640596	-1.6722919
H	-4.5066237	3.1726349	4.1614171	H	-3.3196415	-8.0909592	-1.8390474
H	-6.621734	-0.3630434	3.0956509	H	2.22717	7.7161713	2.0039801
H	1.609273	-2.4051308	3.7764056	H	1.9869662	-4.3127102	-1.0813622
H	-4.2859478	0.3909516	3.5013278	H	-5.5998176	-0.9190487	-2.2872188
H	-0.3255837	2.010084	4.0526351	H	-5.7460658	4.5238685	-1.8823522
H	4.6399157	5.2281798	4.8700216	H	1.933353	-6.6868157	-1.8806122
H	-4.5796086	-3.2363399	2.2500516	H	-7.3442781	0.7580135	-2.8390523
H	-3.7313264	-5.7298939	2.5527432	H	9.4258077	-1.2851268	-0.5568235
H	-4.2290017	-8.1658479	2.4058273	H	-5.8806064	-2.8176698	-3.6354273
H	-1.3859168	7.3559767	4.3796976	H	8.6474754	-3.4333948	-3.0399098
H	1.5635128	-8.2235585	2.7636247	H	6.2947447	6.0870663	-0.9967132
H	-9.0586935	-2.5684869	0.4414016	H	6.8547437	-1.7228716	-2.7047804
H	-5.5428734	6.8318092	3.2379428	H	-1.8252726	-4.3260931	-3.4415113
H	6.9048887	0.1036242	3.550342	H	7.8385445	2.6062002	-1.6494843
H	4.3601678	-3.3114587	2.765861	H	5.3493927	0.3257475	-2.3815919
H	-6.0278925	-5.6152134	1.0470595	H	-6.417387	-4.4711471	-5.4214725
H	-7.9512485	0.5998247	1.1969407	H	3.3816789	-7.3932638	-3.8058593
H	6.1884082	4.0004586	3.3144506	H	-6.7199718	2.9073662	-3.9960501
H	-0.7529414	5.4186786	2.9175521	H	-0.3231775	7.0081898	-2.2494626
H	-4.8952608	4.9105912	1.7754679	H	-0.1077209	-2.017953	-4.0746482
H	5.581558	1.7477597	2.4574575	H	-2.3589969	-6.0048612	-5.2276896
H	1.7517705	-7.0044599	0.5765363	H	-1.090849	4.845833	-3.1800938
H	6.991054	-5.795981	0.2051297	H	2.4911032	5.7402563	-3.047284
H	0.3266122	-5.0016305	0.1320148	H	4.7192426	6.8196817	-2.8123431
H	5.1859474	-4.0818731	0.5151865	H	0.5628859	9.2739497	-1.6927596

Table A.15. Optimized atomic coordinates of **Cr$_3$**(NTs)$_3$′ (continued).

Atom	x	y	z	Atom	x	y	z
H	11.0890783	-1.1361939	-2.4457516	P	-1.6849349	-3.5619955	1.6350692
H	4.9100213	-3.3510261	-4.1346173	P	-2.5200163	2.3126855	2.0929997
H	-2.5681686	1.662576	-4.0514178	P	3.4360318	-1.9199403	-1.9190283
H	2.6161127	2.6544006	-3.8275709	P	1.0926762	3.6158257	-1.5067164
H	2.5326419	-1.9960197	-4.7462753	P	-2.648296	-1.0243559	-2.8919646
H	-4.3091175	3.3637221	-4.5481517	Se	-0.4034494	-0.5510677	2.8082779
H	-4.0103275	-0.7883185	-5.5353597	Se	1.7568178	-2.3147836	1.0893802
H	4.8750439	-5.7087613	-4.9201065	Se	0.7456671	2.1621445	1.5439466
H	9.4869042	2.7498758	-3.5465709	Se	-2.6187593	-0.9216333	0.3100927
H	5.9083373	1.6818089	-4.3921982	Se	2.944628	0.5581162	-0.1895125
H	0.5892238	-2.5602559	-6.4062569	Se	-0.2182443	-2.5412586	-1.3481758
H	-1.4200591	5.007077	-5.6359062	Se	-1.4398082	1.915168	-0.9227699
H	3.0991569	-0.6403281	-6.7559214	Se	0.7568769	0.250512	-2.6368895
H	2.2691004	2.7997488	-6.281576	S	-6.4692917	-3.2295972	-0.6015248
H	-3.3062437	-1.3135191	-7.8608879	S	7.4571045	0.6255515	0.4192425
H	4.8060236	1.1986131	-6.5989232	S	-3.3037439	6.0574539	-1.540986
H	-1.0005992	-2.201557	-8.3154348	O	-5.4434845	-4.2998168	-1.1095533
H	0.2516001	3.9802032	-7.2117199	O	-7.4443171	-2.7085295	-1.5953387
Co	1.5397711	-0.0367118	1.5984726	O	8.1364109	1.4068788	1.4834799
Co	-0.5490532	-1.891316	0.8793172	O	7.1929689	-0.8887596	0.7420111
Co	-1.1712883	0.9160411	1.1700607	O	-2.4244709	6.3546078	-0.2712428
Co	1.6395885	-1.1942831	-0.9808214	O	-3.0253431	6.9193417	-2.7161191
Co	0.8488259	1.6215939	-0.723376	Cr	-3.9159549	-2.9157631	-0.6004435
Co	-1.1565429	-0.4311239	-1.4675803	Cr	5.1516731	-0.4870648	0.4297722
N	4.6603626	-0.7160298	2.2528517	Cr	-1.825717	4.3561178	-0.3338182
N	-2.8898186	-4.131539	0.4980706	H	-4.0430956	-9.3681904	0.2062442
N	-2.3879962	3.9313306	1.433941	H	-4.6642015	-6.0794997	-6.229572
N	-5.440216	-2.1487669	0.035528	H	8.7254228	-5.481431	-1.585724
N	5.9726943	1.0934745	-0.0074539	H	7.8415028	-3.7415193	5.3362888
N	4.8507318	-1.8405084	-0.8791537	H	-3.7907528	8.0637012	4.5526363
N	-0.0129857	4.7568702	-0.7618383	H	-8.7156214	7.2510182	-0.2361833
N	-3.4704457	-2.5007486	-2.4108513	H	1.8419235	9.6441739	0.4380736
N	-3.0624547	4.4679447	-1.6826083	H	11.1114047	0.8794714	-3.9367665
P	3.2037851	-0.0372149	2.9600206	H	-9.6374334	-5.6325225	3.4766462

Table A.16. Optimized atomic coordinates of **Cr$_3$**(NTs)(CNMe)$_2$′.

Atom	x	y	z	Atom	x	y	z
C	6.3079095	-4.6861533	-5.2637988	C	-2.0234628	-4.7720206	-1.2361469
C	6.0928842	-3.3262369	-5.5428943	C	-2.5557255	-3.9134354	-2.2226509
C	5.6925074	-5.2418406	-4.1279581	C	-0.8058975	2.6480479	-4.7689267
C	5.297774	-2.5296912	-4.7052612	C	-3.2880617	-1.3067096	-3.3651277
C	1.1905063	-2.0222998	-7.1991277	C	7.5313766	1.6852738	1.1226731
C	4.8847441	-4.4556675	-3.2958377	C	-4.7774393	0.2078913	-4.5729103
C	2.0455089	-0.911653	-7.1324634	C	6.8863828	2.8207464	0.6051982
C	0.9076574	-2.7482062	-6.0280802	C	0.8718432	4.2813808	-4.1125285
C	4.6718535	-3.0700443	-3.5460306	C	0.1843079	-5.227959	2.0923052
C	2.61668	-0.5259908	-5.906549	C	-0.2353303	3.4762076	-3.7759309
C	3.7990736	-7.5418718	-0.2292089	C	6.8181897	0.7964393	1.9455363
C	1.4675456	-2.3577721	-4.8028426	C	-4.4202297	-0.4660983	-3.3914828
C	2.3304526	-1.2408443	-4.7259928	C	-6.684471	-4.5435921	-2.1025347
C	4.2727585	-8.1580392	0.9427909	C	4.71989	-2.8826646	3.2514771
C	3.376785	-6.2055339	-0.2075159	C	-0.6438215	-6.2301589	2.6177746
C	5.6467828	0.2598989	-2.8866171	C	-5.7569069	-3.4906427	-2.0526663
C	6.6047618	1.2749703	-3.0418075	C	1.105591	-4.5470842	2.9191134
C	4.3240859	0.4481542	-3.3383735	C	5.5438549	3.0795187	0.9273574
C	6.2532327	2.4919504	-3.6490519	C	5.6344511	-2.4621061	4.2326884
C	4.3077266	-7.4123583	2.1341137	C	-7.0168125	-5.2581017	-0.9395441
C	3.9654273	1.6909951	-3.9086714	C	3.3322617	-2.7168957	3.4435435
C	-2.1651546	-6.6647002	-2.760588	C	5.4716797	1.0439946	2.2573954
C	4.9302537	2.6976718	-4.0764032	C	-0.5691572	-6.5664738	3.98104
C	-2.7002369	-5.82072	-3.7462537	C	-5.1230612	-3.1425007	-0.8335951
C	0.803554	3.4654827	-6.407467	C	-9.1237625	-1.0132106	-2.8536969
C	-2.8733015	-0.7758294	-5.7163027	C	4.8290256	2.2057679	1.7721139
C	-0.2929654	2.6504152	-6.0761249	C	-9.8989279	0.1084321	-3.1953461
C	3.4385816	-5.423492	0.979387	C	-6.4017773	-4.91287	0.2763455
C	-2.5020391	-1.4344662	-4.5336592	C	1.1860701	-4.9022272	4.281546
C	-1.8354209	-6.1366222	-1.5007295	C	-3.2460843	4.3389947	-3.381602
C	-2.9018161	-4.4559152	-3.4787321	C	-5.4592626	-3.8774729	0.3276786
C	3.9028933	-6.0691499	2.1584881	C	0.3494396	-5.9026697	4.8086647
C	-4.0141486	0.046584	-5.7402027	C	5.175509	-1.8655983	5.4188583
C	1.3866537	4.2781188	-5.4210669	C	-8.2206277	-0.9510887	-1.7796031

Table A.16. Optimized atomic coordinates of **Cr$_3$**(NTs)(CNMe)$_2$′ (continued).

Atom	x	y	z	Atom	x	y	z
C	-4.5968879	4.7247657	-3.4051397	C	1.4684335	3.0039947	5.9101096
C	-2.6502415	3.9014576	-2.1791648	C	2.530787	2.7243243	6.7876793
C	2.8808404	-2.1031414	4.6339743	C	-2.4592743	2.8467994	4.0697408
C	-9.7831584	1.2994446	-2.4556509	C	-6.0839674	-0.7139402	3.7274989
C	-0.8992164	6.7714727	-2.4022074	C	-2.1250399	-1.5112568	7.1854046
C	3.7955319	-1.6862047	5.6152658	C	-3.1905555	0.0911775	5.6923382
C	-0.5748768	6.071356	-1.2084951	C	-4.8922462	3.8188933	3.0689266
C	-8.1147003	0.2464055	-1.0558639	C	-6.4830672	-2.7265686	5.0468133
C	-8.8922208	1.3743837	-1.3742611	C	-3.0318891	-0.4597054	6.9739484
C	-1.2911357	8.1183537	-2.3645992	C	-2.8655874	4.1560389	4.3657025
C	-5.3652527	4.6792959	-2.2310552	C	-6.8657616	-1.4366881	4.6413135
C	-3.4293489	3.8666393	-1.0023074	C	-4.0863493	4.6460496	3.8662236
C	4.3470641	5.3305174	3.1002617	H	6.5568233	-2.8660994	-6.430014
C	3.1710007	5.2903042	2.298677	H	5.8248713	-6.3099521	-3.8921307
C	-0.692364	6.782886	0.0168801	H	0.754458	-2.3302901	-8.1622171
C	2.9128651	2.5556197	3.986295	H	2.2854691	-0.342501	-8.0441224
C	-1.3679041	8.8149365	-1.1458942	H	0.2507673	-3.6309748	-6.0677517
C	3.9750458	2.2875589	4.8730498	H	3.7338875	-8.1141993	-1.1682463
C	-4.777443	4.2499505	-1.0294046	H	5.1706729	-1.4681983	-4.9512228
C	4.7887611	6.5263682	3.6861588	H	4.3867632	-4.9198047	-2.4317255
C	-1.0682568	8.1331138	0.0468395	H	3.3040316	0.3312163	-5.8845864
C	2.4685013	6.51823	2.1358519	H	1.2410523	-2.9342314	-3.8914649
C	-1.5316722	-1.457472	4.8247795	H	2.942898	-5.7462719	-1.1103069
C	1.6569772	2.9182105	4.5233451	H	5.9194328	-0.6960248	-2.4156481
C	-4.526746	-2.5806691	3.6052152	H	1.2034225	3.4650913	-7.4333084
C	4.0911667	7.7307479	3.4954458	H	7.6345669	1.1105329	-2.6893072
C	-1.3793884	-2.0118361	6.1057417	H	-2.2556593	-0.8999019	-6.6191814
C	2.9238795	7.7116336	2.7112388	H	-2.0065654	-7.7334377	-2.9718478
C	3.7828435	2.368538	6.2639839	H	-2.9725437	-6.2256408	-4.7333256
C	-4.9022854	-1.2787144	3.197968	H	-0.7513388	2.0026176	-6.8386011
C	-2.4377953	-0.3995786	4.6017036	H	7.0085469	3.2821164	-3.7830448
C	-3.2740491	2.0068203	3.2767955	H	-1.5878516	-2.0465069	-4.526473
C	-5.3092295	-3.2957534	4.524308	H	2.9279682	1.8856933	-4.2209712
C	-4.4888421	2.5047942	2.7675137	H	4.6382698	3.6523977	-4.5406902

Table A.16. Optimized atomic coordinates of **Cr$_3$**(NTs)(CNMe)$_2$′ (continued).

Atom	x	y	z	Atom	x	y	z
H	4.6625937	-7.8815625	3.0657141	H	1.8068095	-1.9351447	4.7999081
H	-4.3011388	0.5682555	-6.6665586	H	4.9322274	4.4165466	3.2598536
H	-1.4162615	-6.7911745	-0.7212907	H	-1.5362616	8.6325168	-3.307769
H	-3.3381593	-3.8147601	-4.2572424	H	4.969992	2.0266203	4.4857994
H	2.2443246	4.9216926	-5.6732936	H	-0.9473976	-1.8647818	3.9864533
H	8.5879822	1.4905343	0.8806992	H	3.4239844	-1.2077334	6.5339725
H	-1.7570438	-4.3611593	-0.2505047	H	-8.8049878	2.2858602	-0.7659604
H	3.954339	-5.506685	3.1009168	H	-0.5244779	6.2313964	0.955632
H	-1.6585731	1.9952341	-4.5273141	H	-6.4252682	4.9763671	-2.2524981
H	7.4331142	3.5159528	-0.0503569	H	-2.9801661	3.5322179	-0.0544827
H	5.0766972	-3.3498554	2.322363	H	5.7033978	6.5110686	4.3003123
H	0.1294262	-4.9707465	1.02312	H	-3.60028	-3.0139884	3.1989729
H	-7.1554216	-4.8032794	-3.0638219	H	1.535615	6.5207229	1.5527232
H	-1.3569006	-6.7510181	1.9603902	H	-0.6747891	-2.8444444	6.2539268
H	7.3075752	-0.1043883	2.3471849	H	-1.1518567	8.6501428	1.0159443
H	-5.5214223	-2.9248666	-2.9646875	H	0.8217497	3.14313	3.8407399
H	-5.6594207	0.8657911	-4.570596	H	-5.3716083	4.1946421	-0.1061678
H	6.7141684	-2.6084135	4.0712035	H	4.6268689	2.1607684	6.9401774
H	1.324082	4.9156571	-3.3359852	H	-5.1231977	1.8777815	2.1269593
H	-9.2234642	-1.9501497	-3.422646	H	2.3440973	8.6357487	2.5568097
H	-2.6554127	4.3885488	-4.3074006	H	-4.9961096	-4.3047261	4.8349126
H	5.0381991	3.9716477	0.5294044	H	-1.5060817	2.4663275	4.4686047
H	-5.0168918	-0.317264	-2.4792145	H	-6.4042009	0.2825382	3.394679
H	-1.2229881	-7.349652	4.3946764	H	-2.002894	-1.942948	8.1910387
H	4.9226293	0.320211	2.8788074	H	0.4838859	3.2911188	6.3104829
H	-5.0475528	5.0667021	-4.3500176	H	-5.8530632	4.1867537	2.6773465
H	-7.6152074	-1.8234264	-1.4939495	H	2.3824487	2.790914	7.8766088
H	-6.6525336	-5.4589697	1.1987966	H	-3.9117453	0.9068544	5.5414302
H	1.9160353	-4.4097165	4.939872	H	-2.2250383	4.7991543	4.9889545
H	-0.8316414	6.2529996	-3.3686196	H	-7.7897589	-0.9852941	5.0349634
H	5.8914793	-1.5374638	6.1881953	H	-4.4056269	5.6736662	4.099192
H	-4.9760757	-3.6136849	1.2782692	H	-3.6278022	-0.0648483	7.8112432
H	0.426631	-6.1692037	5.8743591	N	3.8855183	-2.3265106	-2.6481891
H	-10.398661	2.1741722	-2.7161446	N	3.056316	-4.0737121	0.9158592

Table A.16. Optimized atomic coordinates of **Cr$_3$**(NTs)(CNMe)$_2$′ (continued).

Atom	x	y	z	Atom	x	y	z
N	-4.1662562	-2.0866143	-0.7422263	Se	1.9869268	1.9555409	-1.1810431
N	-0.1314444	4.7367119	-1.1763176	Se	-1.1298524	-2.0660034	1.2877775
N	2.6835609	4.1375573	1.6595465	Se	-2.4198029	0.560468	-0.2929569
N	-5.4842385	0.8504531	-0.1989395	Se	0.9291428	-0.075177	2.7922755
N	-4.0765357	-0.5629855	2.2673181	Se	-0.3186655	2.5516887	1.2772631
O	-6.6208859	-1.0766502	0.7776668	S	-6.9496829	0.3820506	0.3173585
O	-7.6066079	1.2709238	1.3125012	H	-10.604428	0.0528522	-4.0386595
P	3.0692991	-0.8868916	-3.0474764	H	6.9330901	-5.3047604	-5.9253195
P	-2.7551591	-2.118624	-1.7795649	H	4.5952804	-9.2102113	0.9314108
P	2.1587008	-3.2513041	2.0974748	H	-7.0998111	-3.2882022	5.765366
P	-0.8569804	3.4565634	-2.0223695	H	-1.6737932	9.8719842	-1.1244134
P	3.0375845	2.5410459	2.1236475	H	-7.7493423	-6.0786413	-0.9806189
P	-2.6754413	0.2937202	2.889882	H	4.4439259	8.6649753	3.9579909
Cr	3.4329764	-2.9103249	-0.7310121	C	2.5776775	5.4444399	-0.8387374
Cr	1.3550232	4.1369877	0.0929106	C	5.4047817	-3.2189096	-0.4530475
Cr	-4.5666699	-0.5965224	0.4203104	C	4.1424109	7.2157461	-1.9009346
Co	1.7130219	-0.423082	-1.429457	H	4.5464787	7.8425418	-1.0800361
Co	-1.0238158	-1.1999988	-0.8882317	H	4.9880531	6.7522348	-2.4480679
Co	1.1528676	-1.6402238	1.0628138	H	3.5732406	7.8615617	-2.5995454
Co	-0.3241944	1.6553989	-0.9425588	C	7.9502538	-3.6630586	-0.2602631
Co	1.688632	1.2397512	1.031104	H	8.294473	-4.0571028	-1.2382136
Co	-1.0037125	0.239905	1.5410127	H	8.515834	-2.7384129	-0.026821
Se	0.8719847	-2.6446526	-1.123716	H	8.1573766	-4.418236	0.524548
Se	-0.1954048	0.0784027	-2.6598373	N	3.2986603	6.2179631	-1.3659872
Se	3.1780988	-0.5918448	0.427572	N	6.5663784	-3.3892818	-0.3189562

Table A.17. Optimized atomic coordinates of **Cr$_3$**(NTs)$_3$(CNMe)$_3$′.

Atom	x	y	z	Atom	x	y	z
C	3.8307526	-3.0095098	-2.5496696	H	6.2944131	-1.2461071	-4.1787439
C	4.4396258	-2.0486796	-3.3888255	H	7.7409441	-2.8520252	-2.8952707
C	5.8359388	-1.9927271	-3.5118543	H	3.5191217	-4.2548623	-4.7756469
C	6.6453009	-2.8907918	-2.791869	H	2.9126415	-4.732597	-7.1375771
C	1.5544253	-3.4695076	-4.2406261	H	0.5984701	-4.2314025	-7.9778441
C	2.5029508	-4.027724	-5.126876	H	-1.1055799	-3.2568665	-6.4107775
C	2.1594427	-4.2993949	-6.4612769	H	-0.4959831	-2.7776994	-4.0390859
C	0.8645343	-4.0232593	-6.9298119	H	3.5713136	-6.3334623	-2.4776012
C	-0.0885613	-3.4797246	-6.0530811	H	3.2027839	-8.382633	-3.8590234
C	0.2543233	-3.2047105	-4.7199887	H	-1.0657578	-7.5838801	-3.8994148
C	1.4685113	-5.7812251	-2.4267173	H	-0.6777287	-5.510732	-2.5344489
C	2.5586553	-6.596847	-2.8119732	H	-2.9552406	-2.601694	-4.3423722
C	2.3429518	-7.7563009	-3.5729584	H	-3.8349303	-4.925545	-4.5099586
C	1.0436337	-8.1190583	-3.9696235	H	-5.6738538	-5.694111	-2.9765568
C	-0.0434092	-7.310585	-3.5949291	H	-3.8316459	1.4804326	-8.0764954
C	0.1650605	-6.1520281	-2.8321493	H	-2.1144765	2.4280096	-6.5087045
C	-4.2793431	-2.0329755	-2.703547	H	-2.0096039	1.6428497	-4.1420003
C	-3.7512146	-2.9325004	-3.6576413	H	-0.6481274	3.6227663	-4.6154788
C	-4.2494845	-4.2400416	-3.7544693	H	-2.2410518	5.5144947	-4.9152452
C	-5.2764467	-4.670479	-2.8938812	H	-2.0853736	7.5426292	-3.4372556
C	-3.6526307	0.2358347	-4.3503502	H	1.907806	4.8744777	-5.1128554
C	-3.7847508	1.1351433	-7.0319129	H	2.7135928	4.4524988	-7.4239764
C	-2.826389	1.6666919	-6.1541576	H	3.4018809	2.1389248	-8.1240108
C	-2.7613108	1.2203633	-4.824102	H	3.271087	0.2524182	-6.4682497
C	-0.5807638	4.5006693	-3.9549202	H	2.4651326	0.6800492	-4.1468125
C	-1.474805	5.5677633	-4.1261723	P	1.973127	-3.0981544	-2.4611918
C	-1.3895211	6.7008721	-3.2963245	P	-3.5697104	-0.3205936	-2.5715768
C	2.125356	2.8018128	-4.4632505	Se	-0.0227874	-0.1257769	-3.2447821
C	2.2018578	3.8560108	-5.4025897	C	-5.7893875	-3.7882003	-1.9306956
C	2.6596994	3.6179319	-6.7079046	C	-4.6185184	-0.288225	-5.2400232
C	3.0486342	2.325178	-7.0977758	C	-4.6821582	0.1581622	-6.5692869
C	2.9794645	1.2717984	-6.1720246	C	-5.8679782	1.1300709	-2.6196785
C	2.5214999	1.5098643	-4.8657533	C	-7.0646243	0.4012075	-2.8122925
H	3.8164171	-1.3493299	-3.9663218	C	-8.0831098	0.9139912	-3.6316915

Table A.17. Optimized atomic coordinates of **Cr$_3$**(NTs)$_3$(CNMe)$_3$′ (continued).

Atom	x	y	z	Atom	x	y	z
C	-7.9253204	2.153423	-4.2759681	C	1.0678102	-3.918758	4.0550762
C	-6.7399694	2.886754	-4.0838963	C	-2.5596325	-3.9325224	2.4081778
C	-5.7209706	2.3818194	-3.2637991	C	-0.7191107	-6.046026	1.5390047
H	-5.3328244	-1.0477067	-4.8928307	C	-0.3238045	-6.8761499	2.6142252
H	-5.4421895	-0.2614932	-7.2463436	C	-1.4717402	4.9922397	1.2493533
H	-7.2045022	-0.553685	-2.2882945	C	0.4164823	4.5537403	-2.9547296
H	-9.0107257	0.3355323	-3.7647483	C	-0.4133615	6.7507377	-2.2892756
H	-6.6054845	3.860177	-4.5810897	C	0.479381	5.6783326	-2.1102141
H	-4.7911542	2.9471293	-3.1047449	C	3.9327638	4.4126326	-2.7572239
C	-2.8070533	-4.703358	3.5678435	C	3.8774669	5.8047585	-3.001922
C	-1.7491998	-6.4928975	0.6779979	C	4.8356832	6.4190849	-3.8241805
C	-2.369752	-7.7322595	0.8896571	C	5.8585296	5.659936	-4.4190856
C	-1.9717539	-8.5519569	1.9607572	C	5.9243126	4.2761017	-4.1739489
C	-0.9434587	-8.119408	2.8162709	C	4.9721764	3.6576442	-3.3513334
H	-1.9909838	-4.9197266	4.2712888	C	4.8098589	-0.1284279	2.0682714
H	-3.1733341	-8.059443	0.2117451	C	5.6775873	0.0432488	3.1716027
H	-0.6169411	-8.7551267	3.6543247	C	6.839375	-0.7338396	3.2873514
C	-4.0903425	-5.2092579	3.8221888	C	7.147425	-1.6940402	2.3090505
C	-5.1437425	-4.940579	2.9312644	C	6.2796617	-1.8849024	1.2229478
C	-4.9104935	-4.1619016	1.7853518	C	5.1165902	-1.1081598	1.102577
C	-7.2652769	-1.7497376	5.1553852	C	2.9542573	1.571036	3.500819
C	-8.1571826	-0.8225227	5.7254235	C	2.752539	0.6032613	4.5104157
H	-4.2649824	-5.8182854	4.7228061	C	2.375752	0.9962268	5.8032394
H	-6.1533763	-5.3310761	3.1339338	C	2.1756898	2.3568568	6.098433
H	-5.7384207	-3.9006296	1.111146	C	2.3428245	3.3197339	5.0897716
H	-6.7624821	-2.4958587	5.7899369	C	2.727403	2.9309837	3.7936004
H	-9.5105347	0.8421202	5.3545857	C	5.5545679	2.5897787	1.3067414
C	6.0468815	-3.8330206	-1.9409032	C	5.9998212	3.353063	2.4115535
C	4.6463171	-3.8892695	-1.811119	C	7.3724037	3.5387176	2.6426264
C	-0.1031987	-3.2202547	3.7007968	C	8.3237988	2.9594163	1.7849689
C	-0.7256079	-2.3830812	4.6538715	C	7.8891098	2.1937867	0.6875442
C	-0.2016147	-2.2758116	5.9506978	C	6.5202489	2.0102449	0.4494691
C	0.954595	-2.992405	6.3089968	C	1.5351073	-6.7881976	0.1295923
C	1.5892604	-3.8074331	5.3578953	C	2.0711373	-9.2928059	0.3121752

Table A.17. Optimized atomic coordinates of **Cr$_3$**(NTs)$_3$(CNMe)$_3$′ (continued).

Atom	x	y	z	Atom	x	y	z
C	5.0462009	4.7369205	-0.2764992	H	1.2216894	5.7356085	-1.3015785
C	7.0595657	6.3230051	-0.5047914	H	3.0985337	6.4064678	-2.5148229
C	5.3480556	-5.4506926	2.5983678	H	4.780078	7.505067	-3.9984715
C	5.0312077	-4.5473117	3.6256629	H	6.7227204	3.6711478	-4.6315577
C	6.0336225	-4.163904	4.5297545	H	5.0145009	2.5769913	-3.1523104
C	7.3361338	-4.6802925	4.4061923	H	5.4555282	0.8024815	3.9345002
C	7.6445557	-5.5677379	3.3609385	H	7.5109698	-0.5815	4.1464259
C	6.6496377	-5.9573106	2.44855	H	8.057773	-2.3052622	2.4005827
C	2.9388236	7.1237671	2.7338583	H	6.4984026	-2.6438532	0.4587141
C	1.7802525	6.9286314	3.5048274	H	4.4469845	-1.2591522	0.2431317
C	1.8272708	7.1958172	4.88248	H	2.8903408	-0.4659612	4.2873059
C	4.1332607	7.5797362	3.3138946	H	2.2303557	0.2304138	6.5803855
Co	0.9782315	-1.424912	-1.5613212	H	1.8856598	2.665438	7.1151401
Co	-0.6397167	-1.5912399	0.7960252	H	2.1809534	4.3870846	5.3037897
Co	-1.6751469	-0.2270195	-1.5880326	H	2.8457895	3.6908531	3.0052944
Co	-1.072327	1.3575662	0.6950357	H	5.2561934	3.8116447	3.0781188
Co	0.6702552	1.4595303	-1.6640202	H	7.700268	4.139086	3.5060611
Co	1.7059078	0.2593371	0.6963461	H	8.6248364	1.7313719	0.0111377
Cr	1.5593336	-4.7776452	0.2961783	H	6.1713556	1.4159988	-0.4072614
Cr	3.2876326	3.8035727	-0.0088891	H	4.0139684	-4.1387984	3.7015478
H	6.6601901	-4.5470951	-1.3700982	H	5.7960899	-3.4508047	5.333576
H	4.2002091	-4.6239712	-1.1259272	H	8.6659529	-5.9658267	3.2563934
H	-1.632203	-1.816832	4.3892671	H	6.8593479	-6.6568496	1.6261933
H	-0.7038113	-1.6254599	6.682976	H	0.8518504	6.5823453	3.0289306
H	1.3589742	-2.9164534	7.3305981	H	5.0117756	7.7347992	2.671764
H	2.4923992	-4.3752077	5.6304088	N	1.6517449	-4.6060874	-1.6227971
H	1.5743269	-4.5485796	3.307806	N	-0.0883631	-4.7796244	1.2952775
H	-3.4457411	-3.066823	0.618361	N	2.9735061	3.7598203	-1.9118877
H	-2.0542818	-5.8459757	-0.1568755	N	4.1573833	2.4161845	1.0306703
H	0.4985309	-6.5559709	3.2678652	N	1.6695068	-7.9548553	0.1180389
H	-0.6603505	6.9402544	0.7503775	N	3.0650751	-4.905079	1.191405
H	-1.0226503	4.5057841	0.3710554	N	6.03327	5.363237	-0.3931474
H	-0.9330212	2.6687437	4.3023991	N	2.6724628	5.202936	0.831036
H	-0.3213967	7.6285616	-1.6323191	O	4.7307292	-6.7278731	0.3444353

Table A.17. Optimized atomic coordinates of **Cr$_3$**(NTs)$_3$(CNMe)$_3$′ (continued).

Atom	x	y	z	Atom	x	y	z
O	3.3701	-7.1716264	2.4558866	C	-6.6125905	2.0684022	-0.1617396
O	1.6441337	7.4911107	0.4316992	C	-8.9597963	3.0970965	-0.3952021
O	4.179609	7.3641275	0.4015915	C	-7.6728513	-0.7879742	2.9721836
P	-0.8436142	-3.3555322	2.0008655	C	-7.0167555	-1.7377005	3.7733472
P	1.5505981	3.1014863	-2.713395	C	-8.8064306	0.1211413	4.9110165
P	3.384549	1.0205465	1.7811262	C	-8.5678338	0.1412301	3.5264997
S	4.0499235	-6.1770281	1.5613772	C	3.0183781	7.6507883	5.4783579
S	2.8874075	6.8361124	0.9408327	C	4.1687462	7.8417106	4.6940479
Se	1.6074082	-2.1468302	0.5712806	Cr	-4.9535295	0.9735889	0.1184665
Se	-1.0991744	-2.4975304	-1.317211	H	-6.5958193	-4.0989534	-1.2497401
Se	-2.6687665	-0.3181384	0.5187458	H	-5.6928428	-1.8131355	-1.0521287
Se	-1.5904533	2.1163386	-1.4627855	H	-3.3601736	4.2907523	4.0290909
Se	1.0486577	2.4640951	0.4058465	H	-3.0586581	6.7353088	4.3683236
Se	2.6575047	0.224985	-1.4445307	H	-1.722279	8.0833476	2.717035
Se	0.0187732	0.0652908	2.3346606	H	-4.5975765	0.6611768	3.0861182
C	-3.6221617	-3.6676843	1.5223382	H	-4.8421213	-0.2703192	5.3827943
C	-5.287052	-2.4780122	-1.827475	H	-3.1486725	0.2753134	7.1614192
C	-2.2169561	4.2288193	2.1694939	H	-1.182277	1.7414666	6.5937401
C	-2.7772007	4.869441	3.2991984	H	-5.8875752	2.7276165	3.156439
C	-2.6067336	6.2487006	3.4899358	H	-7.3364423	4.7227026	3.5939182
C	-1.8654287	7.0023028	2.563668	H	-5.6634118	6.6900994	0.1014484
C	-1.2909501	6.3711765	1.4476558	H	-4.22214	4.6814176	-0.3270891
C	-2.7719132	1.7600802	3.5475901	H	-6.3280829	-2.4628519	3.3170728
C	-3.8545512	0.9132969	3.8587321	H	-9.0758114	0.8545839	2.8622937
C	-3.9848319	0.3806573	5.1545709	H	0.921802	7.0546207	5.4926793
C	-3.0366847	0.6841104	6.144865	H	5.0994907	8.2040144	5.1575276
C	-1.9413905	1.509244	5.831195	N	-4.8152826	0.6368059	-1.7769985
C	-1.8025428	2.0359393	4.5384756	N	-4.1404343	2.4323816	1.1084721
C	-4.9587329	3.5769401	1.3860884	N	-7.6305109	2.6415742	-0.2852079
C	-5.8398057	3.6023046	2.4926546	N	-5.8670198	-0.2041633	1.0214157
C	-6.654566	4.7213409	2.7287602	O	-7.3928497	-2.2167855	0.7402284
C	-6.5978597	5.8363807	1.8743082	O	-8.486049	0.0726187	0.59871
C	-5.7200646	5.820747	0.774956	P	-2.534452	2.432373	1.8314208
C	-4.9090932	4.7036914	0.5312847	S	-7.4057151	-0.7870756	1.1752738

Table A.17. Optimized atomic coordinates of **Cr$_3$**(NTs)$_3$(CNMe)$_3$′ (continued).

Atom	x	y	z	Atom	x	y	z
H	-2.4613271	-9.5240011	2.1274081	H	2.8067193	-9.2964066	1.1435312
H	-8.3505989	-0.8396401	6.8090912	H	-9.6310162	2.2253342	-0.2538236
H	6.6030689	6.1444727	-5.0697272	H	-9.1632246	3.860038	0.3820916
H	9.3996066	3.1001711	1.9724877	H	-9.1266435	3.5420396	-1.3956901
H	-7.2315106	6.7161446	2.0661457	H	-8.7231753	2.5478322	-4.9243066
H	3.0476429	7.8620077	6.5584691	H	8.1161902	-4.3825583	5.1238795
H	0.8791473	-9.0276978	-4.5692078	H	7.5474888	6.2428959	-1.4959188
H	2.5414856	-9.6809843	-0.6127833	H	7.8162196	6.1617781	0.2883242
H	1.1964563	-9.9200706	0.5723713	H	6.5998175	7.3259994	-0.3901518

VITA

Jon Kephart was born in 1993 in Brookings, SD to Kevin and Lucy Kephart, and has three sisters Josephine, Natalie, and Abigail. His interest in chemistry was first piqued by an excellent high-school instructor, Chad Caldwell. Beyond the classroom, Jon exercised his scientific interests though his summer job at McCrory Gardens where he mowed lawns, trimmed trees, and designed flower-beds. At McCrory, Jon conducted many of his first experiments, which ranged from attempts at different styles of plant propagation to tabulating the spontaneous "close-packing" of plastic pots suspended in water. It was at this stage in his life that Jon became interested in pursuing a career in science.

After high school, Jon headed west to Laramie, WY, where he attended the University of Wyoming from 2012-2016. At Wyoming, he enjoyed studying the many different facets of the central science. Beyond the typical undergraduate curriculum, Jon undertook graduate level courses on several topics, his favorites including physical inorganic chemistry, advanced organic synthesis, and photochemistry. He also pursued undergraduate research in several different labs. As an NSF-REU student at the University of Utah, Jon spent a summer investigating the kinetics of [2+2+2] cycloaddition catalysis in the lab of Prof. Janis Louie. Janis encouraged Jon to continue on in the field of inorganic chemistry, so upon returning to Wyoming, he began working with Prof. Elliott Hulley. In the Hulley lab, Jon investigated the synthesis of iron organometallics equipped with bifunctional ligand platforms with the goal of developing an olefin metathesis catalyst. Through a serendipitous discovery, Jon found that aerobic oxidation of the bis(neopentyl) complex (tmeda)Fe($CH_2{}^tBu$)$_2$ induced the self-assembly of a magic-sized iron-oxo cluster, $Fe_9O_6(CH_2{}^tBu)_6(tmeda)_3$. This result led to one of Jon's first publications, and, most importantly, left him determined to study nanocluster chemistry further in graduate school. After graduating in December 2016 with a Bachelor of Science degree in Chemistry (*magna cum laude*), Jon conducted post-baccalaureate research under the joint supervision of Profs. John Hoberg and Bruce Parkinson. Here, he spent six months investigating the self-assembly and characterization of covalent organic frameworks. It was late in his time at the University of Wyoming that Jon had the great fortune of meeting his future wife, Sally, who was also pursuing her undergraduate degree in chemistry at Wyoming.

In July 2017, Jon continued his westward journey to Seattle, WA, where he pursued graduate studies in inorganic chemistry at the University of Washington. At UW, Jon joined the lab of Prof. Alexandra Velian as her first student, which granted him the experience of setting up an inorganic synthesis laboratory space. Staying true to his goal of investigating cluster chemistry, Jon's graduate research entailed a deep-dive into nanocluster synthesis and characterization as he developed a new class of M/Co/Se "nanopropeller" clusters. As a graduate student, Jon enjoyed many opportunities to present his work, most notably attending two ACS National Meetings, two Gordon Research Conferences, and three ORCAS conferences. In recognition of his research accomplishments, Jon has received several accolades including the 2023 ACS Division of

Inorganic Chemistry Young Investigator Award and the 2022 UW Inorganic Division Research Trailblazer Award. Outside of lab, Jon has enjoyed hiking in the Cascade Range, where he and Sally summitted Mt. Stuart and Mt. Cashmere; exploring the Olympic Peninsula; climbing at Seattle Bouldering Project; attending concerts at The Neptune; and drinking barrel-aged stouts at Holy Mountain Brewing. After over five years of tinkering with clusters in lab, Jon completed his Ph.D. in April 2023. Following graduation, Jon and Sally will move to Cambridge, MA, where he will pursue postdoctoral research at the Massachusetts Institute of Technology in the lab of Prof. Yogesh Surendranath.